Crystal Engineering Study of Porphyrins, DPMs, BODIPYs, and Cubanes

Submitted by

Keith J. Flanagan

B. A. (mod.) Medicinal Chemistry

Trinity College Dublin, the University of Dublin

A thesis submitted to Trinity College Dublin, the University of Dublin, for the degree of

Doctor of Philosophy

May 2019

Under the supervision of Prof. Dr. Mathias O. Senge

Declaration.

I declare that this thesis has not been submitted as an exercise for a degree at this or any other university and it is entirely my own work. I agree to deposit this thesis in the University's open access institutional repository or allow the Library to do so on my behalf, subject to Irish Copyright Legislation and Trinity College Library conditions of use and acknowledgement.

Signed:_____

April 2019 Trinity College Dublin

Summary of Work.

This thesis consists of three topics, each covering an aspect of crystal engineering: for porphyrins (Chapter 1), BODIPYs and tris(dipyrrinato)metal(III) complexes (Chapter 2), and cubanes (Chapter 3). Each chapter contains its own introduction, results, discussion, and experimental section. There is also a general introduction which briefly describes crystal engineering.

Chapter 1.1 covers the synthesis and subsequent X-ray crystallographic investigation on the efficacy of highly substituted [5,10,15,20-tetraaryl-(X)-2,3,7,8,12,13,17,18-octaethylporphyrin (OETArXP)] as a potential scaffold for molecular cages. A library of porphyrins with a variety of functional groups, such as halogens, alkyl and nitrogenous groups was established through a modified Lindsey porphyrin condensation reaction, followed by a metal insertion, using Cu(II), Pd(II), and Ni(II). Coupled with this, is a detailed discussion on the crystal structures of OETArXP and their metal complexes, conducted to assess if these compounds can be used for molecular cages. Depending on the substitution type employed, the structures of these compounds revealed a plethora of intermolecular and intramolecular interactions. The metal(II) centres were found to not affect the overall crystal structure of the porphyrin to any significant degree. The inclusion of solvent showed a large impact on the crystal packing of these compounds, by creating layers of solvent between sheets of porphyrin. However, these compounds were found unsuitable as a scaffold for a molecular cage due to their tight crystal packing. Moving forward, this section outlines current on-going efforts in this project which involve the synthesis of large porphyrin scaffolds through a copper-catalysed azide-alkyne cycloaddition in order to increase the size of the porphyrin moiety and the type of functional groups available.

Chapter 1.2 gives a detailed discussion on the structure of all core *N*-methyl-substituted porphyrins that have been synthesised in our lab, and that currently exist in the literature. This chapter focuses mainly on the effects that occur when a methyl group is inserted into the core of a porphyrin in both planar and nonplanar porphyrins. This chapter also contains a short comparison with regards to specific topics such as the effects of core-substitution in planar porphyrins *vs* nonplanar porphyrin, electron withdrawing groups *vs.* electron donating groups, and low-substitution *vs.* high substitution.

Chapter 2.1 discusses our recently published results on a family of functionalised BODIPY compounds bearing either an anthracene, pyrene, or perylene on the *meso*-position and a variety of alkyl core substituents (methyl or ethyl). A structural relationship was established between the alkyl-substitution pattern and their effects the dihedral angle between the BODIPY, and the *meso*-substituent in the structure. This will be combined with an investigation into how the hydrogen-fluorine interactions behave in the crystal packing to determine their potential as directive contacts in the crystal structure. Also, this chapter covers the X-ray crystallographic results of three compounds that were achieved by to the sensitisation of oxygen and subsequent [4+2] cycloaddition to the anthracene moiety of BODIPY-anthracene-dyad (BAD) systems the through the photoactivated oxidative addition of singlet oxygen. In this section, a brief description is given on the reaction mechanism and how the structure of the BAD systems can influence product formation.

Chapter 2.2 discusses five new structures of tris(dipyrrinato)metal(III) complexes with either an iron(III), gallium(III), or indium(III) centres. In this chapter, the structural difference between the metal(III) complexes of the *meso*-pentafluorophenyl structures and their *para*-substituted derivatives was established. There were clear changes observed in the crystal packing and the hydrogen-fluorine interactions, as a result of increased symmetry in the *para*-substituted derivatives forming an attractive kaleidoscope-like pattern.

Chapter 3 contains a detailed structural analysis of all currently available (published and current results from our group) 1,4-disubstituted cubane structures with an emphasis on examining how the cubane scaffold interacts in its solid-state environment. In this regard, the interactions between the cubane hydrogen atoms and acids, ester, halogens, ethynyl, nitrogenous groups and other cubane scaffolds were catalogued. This established several new cubane interaction profiles such as; the catemer formation seen in ester, the preferences of halogen-hydrogen interactions over direct halogen-bonding and the stabilising effects caused by the cubane hydrogens interacting with ethynyl groups.

Publications.

1. "Not Your Usual Bioisostere: Solid State Study of 3D Interactions in Cubanes" Keith J. Flanagan, Stefan S. R. Bernhard, Shane Plunkett, and Mathias O. Senge, *Chem. Eur. J*., **2019**, Accepted Manuscript, DOI:org/10.1002/chem.201806432.

2. "The role of π–π stacking and hydrogen-bonding inter-actions in the assembly of a series of isostructural group IIB coordination compounds" Taraneh Hajiashrafi, Roghayeh Zekriazadeh, Keith J. Flanagan, Farnoush Kia, Antonio Bauzá, Antonio Frontera, and Mathias O. Senge, *Acta Cryst*.*Sect. C* **2019**, *75*, 178–188.

3. "Fluorescent imidazole-based chemosensors for the reversible detection of cyanide and mercury ions" Ganapathi Emandi, Keith J. Flanagan, and Mathias O. Senge, *Photochem. Photobiol. Sci.* **2018**, 17, 1450–1461.

4. "*N*-Substitution: The Neglected Path to Nonplanar Porphyrins" Marie Roucan, Keith Flanagan, John O'Brien, and Mathias O. Senge, *Eur. J. Org. Chem.* **2018**, *46*, 6432–6446.

5. "Pre-/Post-functionalization in Dipyrrin Metal Complexes – Antitumor and Antibacterial Activity of Glycosylated Gallium Complexes" Claudia S. Gutsche, Susanna Gräfe, Burkhard Gitter, Keith J. Flanagan, Mathias O. Senge, Nora Kulak and Arno Wiehe, *Dalton Trans*. **2018**, *47*, 12373–12384.

6. "Sterically induced distortions of nickel(II) porphyrins – Comprehensive investigation by DFT calculations and resonance Raman spectroscopy" Julian Schindler, Stephan Kupfer, Aoife A. Ryan, Keith J. Flanagan, Mathias O. Senge, and Benjamin Dietzek, *Coord. Chem. Rev*., **2018**, *360*, 1–16.

7. "BODIPY-pyrene and perylene dyads as heavy atom-free singlet oxygen sensitizers" Mikhail A. Filatov, Safakath Karuthedath, Pavel M. Polestshuk, Susan Callaghan, Keith J. Flanagan, Thomas Wiesner, Frédéric Laquai, and Mathias O. Senge, *ChemPhotoChem.*, **2018**, *2*, 606–615.

8. "Control of triplet state generation in heavy atom-free BODIPY-anthracene dyads by media polarity and structural factors" Mikhail A. Filatov, Safakath Karuthedath, Pavel M. Polestshuk, Susan Callaghan, Keith J. Flanagan, Maxime Telitchko, Thomas Wiesner, Frédéric Laquai, and Mathias O. Senge, *Phys. Chem. Chem. Phys.*, **2018**, *20*, 8016–8031.

9. "Cubane cross-coupling and cubane-porphyrin arrays" Stefan S. R. Bernhard, Gemma M. Locke, Shane Plunkett, Alina Meindl, Keith J. Flanagan, and Mathias O. Senge, *Chem. Eur. J*., **2018**, *24*,1026–1030.

10. "Lactones and flavonoids isolated from the leaves of globimetula braunii" Muhammad Kamal Ja'afar, Shajarahtunnur Jamil, Norazah Basar, Mohd

Bakri Bakar, Satyajit D. Sarker, Keith J. Flanagan, and Mathias O. Senge, *Nat. Prod. Commun*., **2017**, *12*,1455–1458.

11. "Merging triptycene, BODIPY and porphyrin chemistry: Synthesis and properties of mono- and trisubstituted triptycene-dye arrays" Ganapathi Emandi, Yasser M. Shaker, Keith J. Flanagan, Jessica M. O'Brien, and Mathias O. Senge, *Eur. J. Org. Chem*., **2017**, *45*, 6680–6692

12. "Delayed release singlet oxygen sensitizers based on pyridone-appended porphyrins" Susan Callaghan, Mikhail A. Filatov, Elisabeth Sitte, Huguette Savoie, Ross W. Boyle, Keith J. Flanagan, and Mathias O. Senge, *Photochem. Photobiol. Sci.*, **2017**, *16*, 1371–1374.

13. "Synthesis of long-wavelength absorbing porphyrin m-benzoic acids as molecular tectons for surface studies" Alina Meindl, Aoife A. Ryan, Keith J. Flanagan, and Mathias O. Senge, *Heterocycles*, **2017**, *94,*1518–1541.

14. "Generation of triplet excited states via photoinduced electron transfer in *meso*-anthra-BODIPY: fluorogenic response towards singlet oxygen in solution and in vitro" Mikhail A. Filatov, Safakath Karuthedath, Pavel M. Polestshuk, Huguette Savoie, Keith J. Flanagan, Cindy Sy, Elisabeth Sitte, Maxime Telitchko, Frédéric Laquai, Ross W. Boyle and Mathias O. Senge, *J. Am. Chem. Soc*., **2017**, *139*, 6282–6285.

15. "Synthesis of a family of highly substituted porphyrin thioethers via nitro displacement in 2,3,7,8,12,13,17,18-octaethyl-5,10,15,20-tetranitroporphyrin" Marc Kielmann, Keith J. Flanagan, Karolis Norvaiša, Daniela Intrieri and Mathias O. Senge, *J. Org. Chem*., **2017**, *82*, 5122–5134.

16. "Sequential nucleophilic substitution of the α-pyrrole- and p-aryl-position of *meso*-pentafluorophenyl-substituted BODIPYs" Claudia S. Gutsche, Benjamin F. Hohlfeld, Keith J. Flanagan, Mathias O. Senge, Nora Kulak and Arno Wiehe, *Eur. J. Org. Chem*., **2017**, 3187–3196.

17. "Comparative synthetic strategies for the generation of 5,10- and 5,15-substituted push-pull porphyrins" Alina Meindl, Shane Plunkett, Aoife A. Ryan, Keith J. Flanagan, Susan Callaghan and Mathias O. Senge, *Eur. J. Org. Chem.*, **2017**, 3565–3583.

18. "Nucleophilic aromatic substitution on pentafluorophenyl–substituted dipyrranes and tetrapyrroles as a route to multifunctionalized chromophores for potential application in photodynamic therapy" Claudia S. Gutsche, Marlene Ortwerth, Susanna Gräfe, Keith J. Flanagan, Mathias O. Senge, Hans-Ulrich Reissig, Nora Kulak and Arno Wiehe, *Chem. Eur. J.*, **2016**, *22*, 13953–13964.

19. “Crystal structure of 5-tert-butyl-10,15,20-triphenylporphyrin” Keith J. Flanagan, Ebrahim Mohamed Mothi, Lisa Kötznera and Mathias O. Senge, *Acta Cryst*., **2016**, *E72*, 128–132.

20. “Conformational and structural studies of *meso* monosubstituted metalloporphyrins – Edge-on molecular interactions of porphyrins in crystals” Mathias O. Senge, Keith J. Flanagan, Aoife A. Ryan, Claudia Ryppa, Mandy Donath and Brendan Twamley, *Tetrahedron*, **2016**, *72*, 105–115.

21. “Crystal structure of [5-n-butyl-10-(2,5-dimethoxyphenyl)-2,3,7,8,13,12,17,18-octaethylporphyrinato]nickel(II)” Keith J. Flanagan, Ebrahim M. Mothi, Lisa Kötznera and Mathias O. Senge, *Acta Cryst*., **2015**, *E71*, 1397–1400.

22. “Crystal structure of 4-(methoxycarbonyl)phenylboronic acid” Keith J. Flanagan and Mathias O. Senge, *Acta Cryst*., **2015**, *E71*, 1151–1154.

23. “Crystal structures of 2-furylbenzimidazoles with antiangiogenic inhibition of VEGF in cell line MCF-7” Keith J. Flanagan, Yasser M. Shaker, Ahmed Temirak, Hoda I. El Diwani and Mathias O. Senge, Heterocycles, **2015**, *91*, 1603–1613.

24. “Highly strained tertiary sp^3 scaffolds: synthesis of functionalized cubanes and exploration of their reactivity under Pd(II) catalysis” Shane Plunkett, Keith J. Flanagan, Brendan Twamley and Mathias O. Senge, *Organometallics*, **2015**, *34*, 1408–1414.

Notes on Publications:

This thesis contains details that have been previously published in the above peer reviewed papers. Below is a list, by chapter, of the papers that have been used in the writing of this thesis.

Chapter 1 contains details from papers 4 and 6.

Chapter 2 contains details from papers 5, 7, 8, and 14.

Chapter 3 contains details from papers 1, 9 and 24.

Conference Abstracts.

K. Flanagan and M. O. Senge, “Preparation of non-covalent organic frameworks using dodecasubstituted porphyrins” in 31st European Crystallographic Meeting, (22.08.18 – 27.08.18), Oviedo, Spain, Abstract MS21-P02.

K. J. Flanagan and M. O. Senge, “Synthesis and Structural Chemistry of Dodecasubstituted Porphyrins” in Tetrapyrrole Discussion Group Meeting (11.09.17–13.03.17), The University of Sheffield, Sheffield, UK, Abstract 32.

M. Kielmann, K. J. Flanagan, K. Norvaiša, D. Intrieri, and M. O. Senge, “Recent Discoveries in the Aromatic Nucleophilic Substitution (SNAr) Chemistry of Highly Substituted Porphyrins” in Tetrapyrrole Discussion Group Meeting, (11.09.17–13.03.16), The University of Sheffield, Sheffield, UK, Abstract 33.

K. J. Flanagan and M. O. Senge, “Preparation of non-covalent organic frameworks using dodecasubstituted porphyrins, in 24th Congress and General Assembly of the International Union of Crystallography (IUCr 2017), (21.08.17–28.09.16) Hyderabad International Convention Centre, Hyderabad, India, Abstract 1094.

K. J. Flanagan and M. O. Senge, “A conformational study of porphyrins with ‘few’ substituents” in TetraPyrrole Discussion Group Meeting, (21.03.2016–22.03.2016), Liverpool, England, Abstract 16.

K. J. Flanagan and M. O. Senge, “Structural chemistry of dodecasubstituted porphyrins” in ORCHEM 2016 (05.09.2016–07.09.2016), Weimar, Germany, Abstract T126.

K. J. Flanagan and M. O. Senge, “A conformational study of porphyrins with ‘few’ substituents” in ORCHEM 2016, (05.09.2016–07.09.2016), Weimar, Germany, Abstract T127.

K. J. Flanagan and M. O. Senge, “Structural chemistry of dodecasubstituted porphyrins” in Centre for Synthesis and Chemical Biology (CSCB) "Recent Advances in Synthesis and Chemical Biology XV, (09.12.2016), Dublin, Ireland, Abstract P37.

J. M. O’Brien, K. J. Flanagan, C. Moylan and M. O. Senge. “Recent advancements towards the functionalization of triptycene scaffolds”, Centre for Synthesis and Chemical Biology (CSCB) "Recent Advances in Synthesis and Chemical Biology XIV", (11.12.15) Royal College of Surgeons in Ireland, Dublin, Ireland.

L. Rodgers, C. Moylan, K. J. Flanagan, and M. O. Senge. “Hexasubstituted triptycene scaffold as molecular building blocks” GDCH Wissenschaftsforum, (30.08.15–02.09.15), Dresden, Germany, Abstract ORG 076.

L. Rodgers, C. Moylan, K. J. Flanagan, R. Eckert and M. O. Senge. “Hexasubstituted triptycene synthons as molecular scaffold building blocks”, Centre

for Synthesis and Chemical Biology (CSCB) "Recent Advances in Synthesis and Chemical Biology XIII", (12.12.14) University College Dublin, Ireland.

Acknowledgements.

First and foremost, I would like to thank Prof. Dr. Mathias O. Senge for giving me the opportunity to work within his research groups and for the support, guidance and encouragement he has continually provided in all my ventures. Without his help, I would not have had a chance to explore my interest and learn new topic I had never considered before. I would also like to thank Science Foundation Ireland for providing financial support for this research.

Special thanks are due to Dr. Brendan Twamley for the introduction to and continued support in X-ray crystallography throughout my studies. Brendan has always had the answer to my long lists of questions and was always generous with giving me his time. I would like to thank all the members of the Senge group past and present. In particular, I would like to thank Alina Meindl, Marc Kielmann, Marie Roucan, Gemma Locke, Elisabeth Sitte, Jessica O'Brien, Susan Callaghan, Karolis Norvaiša, Bhavya Khurana, Dáire Gibbons, Zoi Melissari, Piotr Gierlich, and Harry Sample for their help, advice, proof reading my thesis, friendship, and making the lab a welcoming and enjoyable place to work. I would like to thank our two postdocs, Dr. Nitika Grover and Dr. Ganapathi Emandi, who have endured my enquiries throughout my studies and provided so much guidance. A special thanks to our previous postdocs, Dr. Mikhail Filatov, who provided compounds, support, and understanding while working on the BODIPY chapter of this thesis, and Dr. Stefan Bernhard, whose work with cubane synthesis allowed me to compile chapter three of this thesis and whose continued support and friendship has been invaluable.

A special thanks is due to all my collaborators who provided the necessary compounds for my publications, especially Dr. Arno Wiehe who has given me many opportunities to expand my scope of studies in a variety of areas for many years.

Many thanks are due to all the technical and administrative staff in the chemistry department, particularly to Dr. John O'Brien and Dr. Manuel Reuther for NMR analysis, to Dr. Martin Feeney and Dr. Gary Hessman for HRMS measurements.

I would like to thank Dermot Gillen, who has been a friend and a source of excellent company for many years. Our friendship may have starting by studying for exams in a library, but it has blossomed into one I will treasure for all my days. To Aaron Keogh for being a great friend every day of our studies and always up for a pint in

the gingerman. To Hannah Dalton, for being X-ray buddies over the years and always starting my days with welcoming conversation. To all the other 7th floor chemist who made the days fly by with great conversation and many great nights out.

Finally, I would like to thank my family for always being there with support and encouragement throughout my studies. Without my family this journey would not have been possible. Much of my success is due to always knowing that they will help me stand back up when I stumble.

Abbreviation.

A	acceptor
Ar	aryl
Ax	axial
BODIPY	(4,4-difluoro-4-bora-3a,4a-diaza-s-indacenes)
BAD	BODIPY-anthracene-dyad
BPyrD	BODIPY-pyrene-dyad
BPerD	BODPIY-perylene-dyad
Br	bromine
BXD	BODPIY-X-dyad
calcd.	calculated
bs	broad singlet
D	donor
d	doublet
dd	doublet of doublets
DDQ	2,3-dichloro-5,6-dicyanobenzoquinone
DPM	dipyrromethene
DBU	1,8-diazabicyclo [5.4.0]undec-7-ene
eq.	equivalents
Eq	equatorial
ESI	electrospray ionization
Et	ethyl
EDG	electron donating group
EWG	election withdrawing group
HRMS	high resolution mass spectrometry
LRMS	low resolution mass spectrometry
m	multiplet
M.p.	melting point
MALDI	matrix-assisted laser desorption ionization
MeOH	methanol
NMR	nuclear magnetic resonance
NSD	Normal-coordinate structural decomposition
OAc	acetate
OEP	2,3,7,8,12,13,17,18-octaethylporphyrin
OETArXP	5,10,15,20-tetraaryl-(X)-substituted-2,3,7,8,12,13,17,18-octaethylporphyrins
Ph	phenyl
ppm	parts per million
Rf	retention factor
r.t.	room temperature
s	singlet
t	triplet
TEA	triethylamine
TFA	trifluoroacetic acid
THF	tetrahydrofuran
TLC	thin layer chromatography
TPP	5,10,15,20-tetraphenylporphyrin
TBAF	tetra-*n*-butylammonium fluoride
UV	ultraviolet
vis	visible
v/v	volume to volume
XRD	X-ray diffraction

X-ray Commands Used.

DFIX: The distance between the first and second named atom, the third and fourth, fifth and sixth etc. (if present) is restrained to a target distance with an estimated standard deviation.

ISOR: The named atoms are restrained with effective standard deviation s so that their Uij components approximate to isotropic behaviour; however, the corresponding isotropic U is free to vary.

EADP: The same isotropic or anisotropic displacement parameters are used for all the named atoms. The displacement parameters (and possibly free variable references) are taken from the named atom which precedes the others in the atom list, and the actual values, free variable references etc. given for the Uij of the other atoms are ignored. The atoms involved must either be all isotropic or all anisotropic. An atom should not appear in more than one EADP instruction.

SIMU: Atoms closer than dmax are restrained with effective standard deviation to have the same Uij components.

SADI: The distances between the first and second named atoms, the third and fourth, fifth and sixth etc. (if present) are restrained to be equal with an effective standard deviation.

Contents

General Introduction.

Crystal Engineering.

The field of crystal engineering has advanced rapidly since its inception[1] due to the optimisation of X-ray crystallographic procedures, the relatively low-cost of powerful computers, developments in crystal structure visualisation, databases, and improvements in reflection analysis and processing. In short, the whole process to obtain a crystal structure of even large molecules is now less time consuming and relatively inexpensive.[2] This has left the field of crystal engineering with the tools to advance at a rapid pace with the backing of large databases to bolster any growth in a positive direction. Crystal engineering is the designed growth of functional molecular crystals that has progressed from analysis of crystal structures in terms of intermolecular interactions, to the construction of crystals with pre-desired topologies, to property optimisation and design.[2] Crystal engineering has grown and developed over the past 50 years as a natural outcome of the interplay between crystallography and chemistry.[3] The key principle of crystal engineering is the understanding of how a molecule or ion can be controlled by treating them as molecular building blocks that engage in self-assembly.[4]

Chemistry has to do with molecules while crystallography has to do with crystals, which are extended, ordered assemblies of molecules. The interplay between chemistry and crystallography is, therefore, the interplay between the structure and properties of molecules on one hand and those of extended assemblies of molecules on the other.[5] Crystal engineering relies on the use of non-covalent bonding to achieve the organisation of the molecules or ions in the solid state.

There are two main strategies were traditionally used in crystal engineering, hydrogen-bonding and coordination of molecules and/or ions.[6] In purely organic systems a large focus is put on the use of hydrogen-bonds to form such self-assembly molecules.[6] Whereas, the use of coordination to metals has featured heavily in inorganic systems.[6] This has also developed into the field of supramolecular chemistry.[7] However, over the past two decades, the use of halogen-bonds has proven an effective method for providing additional control in crystal design through the attractive interaction between an electrophilic region on a halogen atom and a nucleophilic region of a molecule or molecular fragment.[8] Other intermolecular forces, such as π···π and ionic interactions can also be employed as a synthetic handle for designed systems.[6]

History of Crystal Engineering.

The first example of X-ray diffraction was demonstrated by Bragg in 1921. He determined that the structural unit of benzene shows little to no changes in structural size from one crystal to another.[9] Additionally, Bragg showed that there was also an interplay between the unit cell parameters of naphthalene and anthracene. Two of the axial lengths were almost identical while the third was 8.66 Å in naphthalene and 11.66 Å in anthracene. With no further information, Bragg was able to conclude that the long direction of the molecules coincided with this third non-equal axis. With this information, it could be concluded that the width of a benzene ring was approximately 2.5 Å. This appears to be the first published example of the correlation between the properties of crystals and molecular structures. Building on this, Bernal, who was a student of Bragg, was able to accurately calculate and correct formulas for steroids and bile acids, that had been proposed previously by Wieland, Windaus, and Ruzicka, through the use of the unit cell parameters of a number of aromatic hydrocarbons related to phenanthrene.[10] As impressive as these examples are, the true question of crystal engineering is usually the reverse. If given a molecule, what is its crystal structure? The above two examples focus on primary crystal structure determination and subsequent molecular determination. Crystal engineering focuses on what can be determined by crystal synthesis and trying to design a crystal structure by using molecular building blocks.

The first attempt to answer such a question was demonstrated by Robertson, also a previous student of Bragg, using a selection of polynuclear aromatic hydrocarbons.[11] Robertson classified these compounds into two groups. The first group consisted of molecules that could be characterised by a smaller molecular area in comparison to the molecular thickness. This group consisted of hydrogen-rich molecules like naphthalene or anthracene and are characterised in the crystal structure by a short monoclinic axis of around 5.4−8.0 Å. The second group consisted of molecules that could be characterised by a large molecular area in comparison to the molecular thickness. This group consisted of carbon-rich molecules like coronene and ovalene that yield graphitic crystal structures and are characterised in the crystal structure by a short monoclinic axis of around 4.6−5.4 Å. With this, Robertson was able to derive a crystal property from a molecular property, thus being the first time, someone approached the topic of crystal

engineering. A question which appears to have sprung from the seed planted by Bragg and passed to his successors.

While its inception can be traced back to Bragg and his students, the actual conception and terming of this field of study fell to Pepinsky, who introduced the term into the literature in a meeting abstract of the American Physical Society in 1955.[1a] The term is, however, generally associated with Schmidt, who was a student of Dorothy Crowfoot Hodgkin, and who correlated the solid-state reactivity of a large number of photodimerisable compounds to their crystal structures on the basis of topochemical principles.[1b, 1c] This principle postulates the minimum molecular movement in solid-state reactions. This was essentially a recount of Bragg's work extracting molecular property from crystal property. He realised that any real progress could not be made until such a time that a full predictive protocol could be obtained for a crystal structure of a molecular solid from the structure of a molecule itself. He termed this futuristic project '*the phase of crystal engineering*'.[1c] Following this, a number of developments were made over the years which focused on solid-state investigations, and over the course of these studies, the outcomes of these reactions were correlated on a basis of topochemical principles during the 70's and 80's.[12] In tandem to these developments, which are strictly chemical in nature, Kitaigorodskii stated that the packing of a molecular solid was determined by the consideration of the size and shape.[13]

Following this and throughout the 80's and 90's, there were several attempts to appreciate the role of intermolecular interactions in crystal engineering. In 1986 Desiraju and Sarma attempted to rationalise Schmidt's observations on the unit cell parameters of chloroaromatic compounds based on the short halogen-bond distance between chlorine moieties.[14] In 1989, Desiraju wrote a book which attempted to correlate the chemical point of view of interactions with Kitaigorodskii's physical point of view based on the close-packing.[5a] It described organic crystal structures as being predominantly governed by Kitaigorodskii's close-packing principles. This is invoked by a geometrical argument, which states that minor deviations to the close-packing, is dependent on chemical factors that lead to the formation of the crystal structure, and as such can be engineered. In short, interactions which are directional can function as a handle to drive crystal design. These discoveries coincided well with the Etter and Steiner identification of

hydrogen-bonding as a directional force that is both strong and important in the determination of a crystal structure in 1990.[15]

While the first detailed descriptions of molecular crystals were centred around pure organic compounds such as hydroquinone by Powell[16] in 1948 and adamantane-1,3,5,7-tetracarboxylic acid by Ermer in 1989,[17] it has become more commonly associated with polymers and metal-organic frameworks.[18] Such metal-organic coordination compounds have been described as early as the 1990's by Robson.[19] Both pure organic and metal-organic compounds fall into the definition of crystal engineering. In both cases, the understanding of crystal structure is undertaken through the intermolecular interactions and attempts to define a reliable design strategy using these interactions and use such knowledge to direct the design of a crystal towards a property that is desired.[5a] The field of crystal engineering is an evolving subject covering many fields such as polymorphs,[20] pseudo polymorphs,[21] co-crystals,[22] coordination polymers,[23] metal-organic frameworks,[23] hydrogen-bonding,[24] and halogen-bonding.[8c]

What is Crystal Engineering?

The question we are asking, when trying to synthesise a crystal structure of a molecule is "how do the molecules recognise each other from the earliest stages of nucleation towards a final crystal structure?" The core problem in crystal engineering is that crystal structures cannot easily be predicted from the molecular structure. Therefore, information can be postulated by functional groups. But the complete behaviour of such compounds is little understood. The behaviour of a functional group during crystallisation is inherently dependent on the nature and positioning of all other functional groups in the molecule. For example, the crystal structure of 3-iodonitrobenzene need not be closely related to that of either iodobenzene or nitrobenzene to exhibit similar properties of both.[25] Additionally, it need not even be related closely to that of 4-iodonitrobenzene, which implies that the molecular structure is independent of the crystal structure in this case and the crystal structure is only an emergent property.[6, 26] A further complication outlined by Desiraju and co-workers, is that of the hydrocarbon portion of the molecule which can also interact as an effective functional group by competing readily with classical hydrogen-bonding, thus further complicating the predictability of such compounds.[27]

Another question to be addressed is that of building the crystal. In an ideal world, individual molecules would aggregate, nucleate and then crystallise. This sequential process is not always followed in such a clear order.[28] For example, a mid-size cluster of crystals may re-dissolve due to not being able to grow further and thus follow an alternate path of nucleation, i.e. use an alternate crystal packing pattern. The classical example of this is acetic acid. In this structure it is postulated that up to 90% of the liquid is made up of a dimer, however, the only known experimental crystal structures show that an infinite catemer is formed.[29] The rationalisation of such an observation is that the dimer is formed very easily but is unable to grow further because very weak methyl··· methyl interactions are the main cohesive interactions in the further assembly of dimers. The catemer is preferred because its formation provides a pathway for crystal growth quite readily in at least one dimension. Currently, it is not understood how the molecular crystals are built, if the events are sequential with small clusters stacking to in an orderly increase of size or if the whole event is much more irregular. The answer to such a question lies outside the current abilities of X-ray crystallography and will probably first come from alternate spectroscopy fields or molecular modelling.[30] If a sequential crystal is regular, this leads to a favourable situation for the crystal engineers. In these cases, the structure of the final crystals can be related more accurately to the structure of smaller and smaller modules, until in the end, even a basic recognition unit such as the carboxylic acid dimer or a phenol···phenol catemer is a good enough approximation to parts of the final structure.[6] Such structural modularity is desirable, but it is a casualty when the crystallisation events are irregular. Both these difficulties together constitute a formidable challenge in the prediction or anticipation of crystal structures from molecular structures. With this complication currently in mind, it is time for the crystal engineer to think on a larger and simpler scale. This is done through the use of supramolecular tecton.[31] Supramolecular synthons are structural units within molecules which can be formed and/or assembled by known or conceivable synthon operations involving intermolecular interactions (Figure GI1).

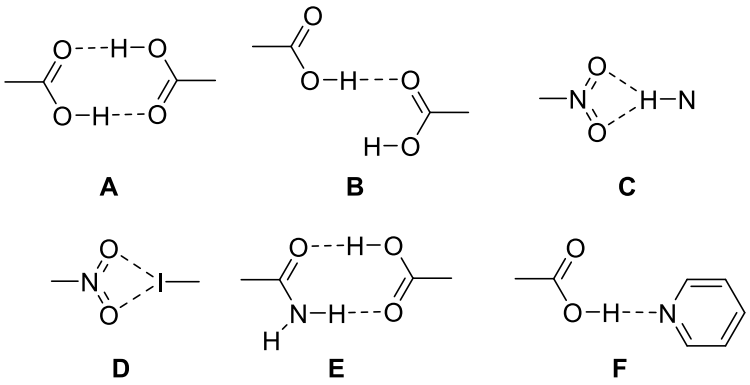

Figure GI1: Selection of supramolecular synthons.[6] Dimer (**A**) and catemer (**B**) implicated in the crystal packing in acids. The nitro···amino (**C**) and nitro···iodo (**D**) synthons show the similarity between hydrogen-bonding and halogen-bonding. Amide···acid (**E**) and acid···pyridine (**F**) heterosynthons are of relevance in the formation of pharmaceutical co-crystals.

Synthons are simply any unit that conveys the essential features of a crystal structure and are a reasonable approximation to the whole crystal. The closer the structure of a small synthon is to the actual crystal, the more useful it is to the entire structure. Small clusters are good templates for larger clusters so that the final crystal can be analysed easily as a collection of robust synthons that were formed from the earlier stages of molecular association.[32] The crystal growth in such instances can be viewed as a sequence of kinetically controlled events with robust synthons forming strong and directional interactions. Building from this the new synthons are formed from slightly weaker and less directional interactions. Following this principle, building up a crystal can be rationalised as a series of logical steps with chemical backing. The use of synthons is a practical concept that is aimed at the design of molecular crystal structures; however, the whole process is essentially a game of probability.[33] The more times a specific synthon is seen in the literature, this increases the probability of predicting the structure of new molecules that contain this specific synthon. Unfortunately, these occurrences are by no means universal.[6] Flaws in the building process lead to a lack of easily observable correspondences between molecular and crystal structures increasing the difficulties in crystal engineering.

In a general sense, molecular and crystal structures are not related in easily perceived ways. Competition between synthons becomes a complication,[34] sometimes even with just a small increase in molecular functionality, leading to polymorphism, however, this leaves us with two topics that are considered the most

important in crystal engineering: (i) intermolecular interactions, (ii) supramolecular interactions.

Intermolecular Interactions.

A synthon is the product of recognition events between molecules in a crystal structure. But to organise which synthon might or might not form, there is a need to understand which the properties of intermolecular interactions are the primary reasons for resulting synthon. To say a synthon is a set of specific interactions between two molecules is an oversimplification of this process.[6] A more accurate view of this is to imagine a synthon as a function of three-body interactions which is limited to the *n*-body interaction. Simply put interactions which merge into a general body of close-packing.[6, 35] Ideally, the issues to be considered are highly directional and atom-specific interactions that are kinetically favoured. Close-packing, on the other hand, is generally considered to be thermodynamically favoured.[36] This results in two cases of crystal engineering, the chemical recognition, and the geometrical recognition. The chemical recognition is a product of interactions based on atom pairing, whereas the geometrical is a product of close-packing. This can result in a case where both processes are observed, leading to polymorphism of crystals structures. All interactions, chemical or geometrical, arise from electrostatics, the above statement raises questions as to whether the chemical and geometrical models are related to one another and if the basis for the chemical model arises from the geometrical model?

An example of this was purposed by Desiraju and Boese using the crystal structure of fluorobenzene in terms of a specific C−H···F−C hydrogen-bond.[37] This crystal packing is seen to adopt an uncommon tetragonal space group ($P4_12_12$) and is isomorphous to benzonitrile, pyridine hydrofluoride, and pyridine-*N*-oxide. They suggested the simple argument that considering the three later structures are all equivalent to fluorobenzene, with regards to their interaction profiles and recognised hydrogen-bond donors. Therefore, the C−H···F−C interactions in fluorobenzene can be considered to be hydrogen-bonding partner. This would be the chemical element of crystal engineering. However, the different space group adopted by fluorobenzene suggests that there is also a geometrical element because of close-packing. Therefore, both processes are important in the crystal packing and thus, should be a consideration for crystal engineering.

It can be considered that while nearly all structures are close-packed, there are some deviations to this feature. These deviations from close-packing owe to chemical factors and in turn lead to the formation of crystal structures that can be engineered in a systematic manner. Directionality, as it exists in organic crystals, is the handle that permits crystal design, and pattern recognition is one of the first steps in the crystal engineering strategy.[6] There are currently two major processes to achieve directionality in a predictable chemical manner: Either through hydrogen-bonding or halogen-bonding. All other interaction types can be considered to be an artefact of close-packing in a crystal structure. Hydrogen-bonding, as of the official definition, is classified as being directional and influences crystal packing modes in chemically understandable ways.[24] Simply put they are an attractive interaction between a hydrogen atom from a molecule or a molecular fragment, D−H···A in which D is more electronegative than H, and an atom or a group of atoms in the same or different molecule where there is evidence of bond formation.[24, 38]

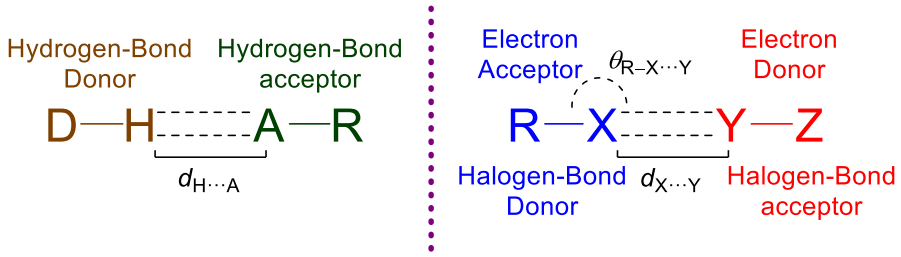

Figure GI2: Representation of hydrogen-bonding (left) and halogen-bonding (right).

Halogen-bonds are the second method to achieve chemical directionality in a crystal structure. The current IUPAC recommendations state that "*a halogen-bond R−X···Y−Z occurs when there is evidence of a net attractive interaction between an electrophilic region on a halogen atom X belonging to a molecule or a molecular fragment R−X (where R can be another atom, including X, or a group of atoms) and a nucleophilic region of a molecule, or molecular fragment, −Z*".[38] In this definition, halogen atoms behave electrophilic in contacts. As such this suggests that halogen-bonds and hydrogen-bonds can have similar effects on crystal packing.[6] This can be clearly seen when taking the examples of 4-dichlorobenzene, γ-hydroquinone, and 1,4-diethynylbenzene (Figure GI3).[39] The significance of the halogen-bond in crystal engineering is that its strength is an intermediate between the strong (O−H···O) and weak (C−H···O) hydrogen-bonds.

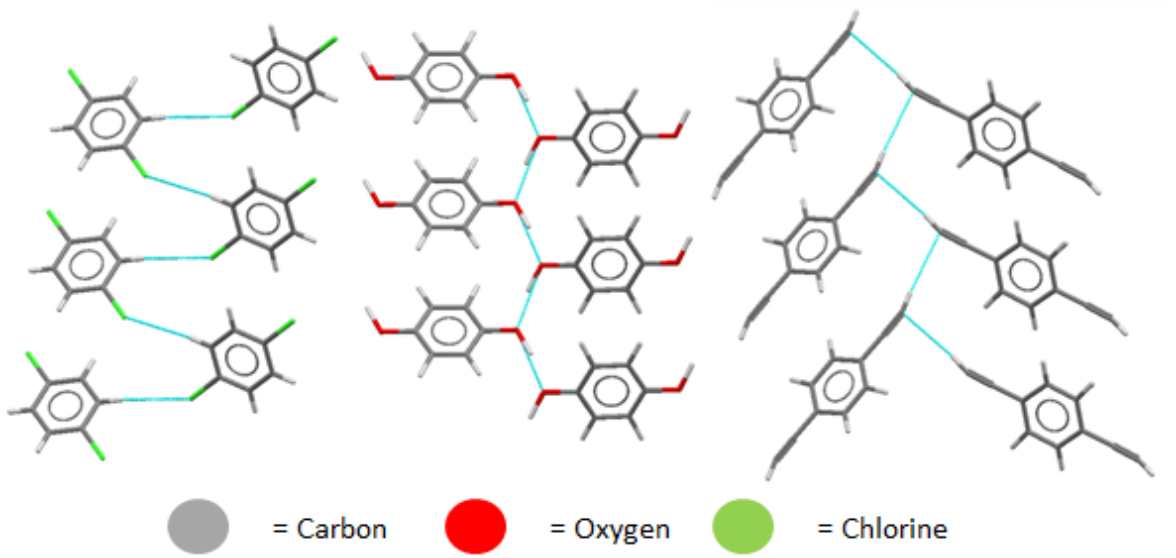

Figure GI3: The equivalent crystal structures of 1,4-dichlorobenzene, γ-hydroquinone, and 1,4-diethynylbenzene. Note, that the respective halogen-bond, hydrogen-bond, and C−H···π interaction in these three structures are chemically and crystallographic equivalent.[39]

Supramolecular Interactions.

It is generally accepted that in the first step of crystallisation, the most directional interactions tend to be formed first. This is due to the process being a kinetic phenomenon.[6] This initial contact is believed to be stable through several stages of crystallisation, leading to the idea of a supramolecular synthon. If these interactions are stabilising, then a retrosynthetic approach to their formation is possible, which is the general idea of crystal engineering.[3b, 40] Synthons can be directed by either specific anisotropic interactions, such as carboxylic acid and carboxamide dimers, or shape filling, such as tetraphenyls and hexaphenyls.[41] Such connections are often considered node connections and can be disassembled in a retrosynthetic manner. This retrosynthetic step is implemented in the design of crystal structures of MOFs and coordination polymers because the linker interactions are very strong.[42] The one caveat to this process is that small clusters may not be the best model for a larger array. Therefore, this process works better when small clusters are a good approximation of the larger array. The ideal synthon is one which is present throughout the crystal structure, irrespective of other functional groups being present in these molecules. For example, if the functionalities M^1 and M^2 are present, then the synthon $M^1\cdots M^2$ (S^1) is robust if it appears in all molecules (Figure GI4). The mere presence of M^1 and M^2 ensures the appearance of S^1. As such, the architecture through which information content

passes from molecular structure to crystal structure is a means of simplifying a crystal structure without losing too much information. The complete crystal structure is an energy and structural space of great complexity and a 'good' synthon helps one to traverse this landscape with maximum efficiency. This comes into place when considering adding more functional groups such as M^1, M^2, M^3, and M^4. This results in a larger potential of synthons $M^1\cdots M^2$ (S^1), $M^1\cdots M^3$ (S^2), $M^1\cdots M^4$ (S^3), etc., all of which would also be chemically possible to achieve. However, a good synthon results in S^1 consistently without interference from the other possible synthons. This is the key element in the use of the synthon theory to design increasingly complex structures.[43] When the interactions are weak, the synthons are not so robust and fidelity of crystal structures within the same (molecular) family is poor. When the hydrogen-bonding is strong and predictable, considerable control is possible in the design strategy.

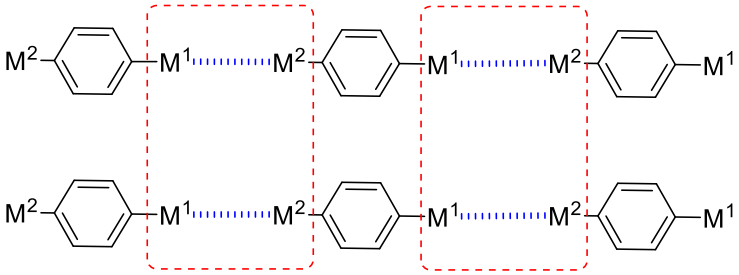

Figure GI4: Representation of a synthon (S^1) in a co-crystal structure. Repeating unit highlighted with red dashed box.

The final field which will be covered here is the study of co-crystals or multicomponent molecular crystals. This field has boomed over the past number of years with a large number of contributions.[44] This topic, on first glance, may appear backward for a few reasons, none more so that crystallisation has been a technique for purification for millennia. However, the benefits of such complexes are undeniable, and the improbability only lasts until someone succeeds. The formation of such co-crystallisation complexes is driven by enthalpy and characterised by distinctive intermolecular interactions (D···A) that are more favourable than interactions of the types (D···D and A···A) between individual components.[6] Co-crystals have been known to chemists ever since Wöhler crystallised quinhydrone from 1,4-benzoquinone and hydroquinone in 1844.[45] The main benefits of co-crystals is the practical implications in the pharmaceutical industry that was put forward by Zaworotko and Almarsson in 2004.[46] It was suggested that active

pharmaceutical ingredient (API), a drug molecule, may be induced to form a pharmaceutical co-crystal by suitable complexation with another molecule known as a co-former, which is selected on the basis of complementarity of molecular recognition sites with the API.[47] This complex between API and co-former forms a synthon called a hetero-synthon, because the two components that constitute this synthon arise from different molecules. The pharmaceutical co-crystal is designed to optimise a property of interest. If the API is too soluble or insoluble, combining it with a co-former to form a co-crystal can be used to improve its solubility. Other properties that have been optimised by co-crystal formation include increasing shelf life,[48] stability to moisture loss,[49] hardness and brittleness,[50] and bioavailability.[51] As a result, co-crystal screening has become a very important part of drug development in recent years.[52]

The synthon approach is based on chemistry rather than on geometry or topology, it is more than just a way of describing crystals. Synthons are not a static motif. The prevalence of the supramolecular synthon is not confined to crystals but also to the solution from which the crystal is obtained. For these reasons, it is likely that the supramolecular synthon will continue to be used in operational crystal engineering for some time to come.

Final Remarks.

In essence, crystal engineering is the logical process to design functional crystal structures. This process relies heavily on the identification and implementation of specific synthons in useful ways. Both intermolecular interactions and supramolecular features are of key importance to designing useful structures for applications, such as co-crystal of APIs as mentioned above. Crystal engineering is an ever-improving field and has benefited from the use of modern technology and the discovery of new interaction profiles. In this thesis, the basic principles of crystal engineering will be applied to porphyrins, dipyrromethanes, and cubanes, in an effort to learn their secrets and add to this ever-growing field.

Strength and Determinants of Intermolecular and Intramolecular Interactions.

During the following chapters there is one question which is repeatedly of concern. How can one determine the importance of the interaction? Unlike in a covalent bond there is no specific determinant (angle, length, or strength) which quantifies a bond,

but rather a range of determinants based of the atoms involved and a potential for significance, which will be the focus of this section. In each of the chapters included in this thesis all intermolecular or intramolecular interactions will be quantified based on the following topics and the techniques used to determine their importance, as bonds, will be discussed.

A final comment is warranted on what this thesis considers to be a relevant interaction or an interaction that forms as a result of crystal packing. For this, two terms will be used. Either an interaction is described as a bond and is directive (it is of length less than the sum of the van der Waals radii of the atoms involved and of suitable angle) to fall into this category, or an interaction is a short contact (it is a result of close packing forms due to crystallisation processes rather) and does not direct the packing structure in any manner. The first case is of significant importance as it describes an interaction that is considered strong, whereas the second case describes an interaction potential and is not actual bond.

Hydrogen Bonding.

As stated before, hydrogen-bonding as of the official definition is classified as being directional and influences crystal packing modes in chemically understandable ways.[24] This however is rather vague and an intentionally open description of a hydrogen bond. This is done due to the simple fact that new forms of hydrogen bonds can be discovered, and strength and determinants of a hydrogen bond are subject to interpretation. In this section, I will discuss the classical limits to a hydrogen bond and how the compounds in this thesis are determined to be relevant hydrogen bonds or short contacts.

There are two criteria to evaluate the presence and the strength of a hydrogen bond. The first is to look at the distance between the H (hydrogen) and the A (acceptor) atom, which should be shorter than the sum of their van der Waals radii. The larger this distance is the weaker the bond is. The second method is to evaluate the angle formed by the D–H···A, the closer this angle is to 180°, the stronger the hydrogen bond is. For weak hydrogen interactions, the relative bond strength is usually less than 50 kJ/mol with most less than 30 kJ/mol. For strong hydrogen bonds the relative bond strength is greater than 50 kJ/mol with some being greater than 100 kJ/mol.[53] The strength is also affected by the electronegativity of the acceptor. Greater

electronegativity of the hydrogen bond acceptor will lead to an increase in hydrogen bond strength. One of the final aspects which affects hydrogen bonding is the amount of contacts that are present between molecules. With two or more hydrogen bonds between molecules then the strength of the bonds increases in accordance with the sum of interactions compared to a single bond.[54]

Non-classical hydrogen bonding follows a similar classification as above in hydrogen bonding but generally are considered weak hydrogen bonds. A typical example of a non-classical hydrogen bond is that of C–H···O interactions, such as those reported by Johnston and Cheong.[55]

However, while these are tidy determinants to observe if hydrogen bonding is occurring or not, they fall short in many cases and should be taken as a rule of thumb. As pointed out by Desiraju in his 2011 publication "a bond by any other name" there are significant discrepancies in using the above description.[24] The determination of true bonding, or close contact, is subject to experience. Not every interaction which falls under these rules is a hydrogen bond and not every interaction which falls outside these rules is not a hydrogen bond.

Halogen Bonding.

Halogen bonding occurs when there is evidence of a net attractive interaction between an electrophilic region on a halogen atom and the nucleophilic region of a molecule where the second atom is; F, Cl, Br, I, halide, etc. or N, O, S, Se, etc. Generally, halogen bonds are considered weaker than hydrogen bonds and range from 5–180 kJ/mol.[56] The determinants for such a bond follow similar lines to hydrogen bonding. The stronger the bond, the shorter the sum of the van der Waals radii between the two interacting atoms. For interactions which involve halides or non-halogen atoms, usually the closer the angle is to 180°, the stronger the interaction is. However, with halogen-halogen interactions there are two halogen bond types observed (type I and type II). In type I halogen bonding, the interactions between atoms are symmetrical with $\theta_1=\theta_2$ as seen in Figure GI5A. In type II halogen bonding the interactions are bent were where θ_1 ~180° and θ_2 ~90° (Figure GI5B). Type I interactions are geometry-based contacts that arise from close-packing and are not true halogen bonds according to the IUPAC definition. Type II interactions arise from the pairing between the electrophilic area on one halogen

atom and the nucleophilic area on the other halogen. These are considered true halogen bonds. Halogen bonding are seen mainly in iodine and bromine, however sometimes can include chlorine. They are typically substituted in molecular environments that are electron-withdrawing. The three pairs of unshared electrons on the halogen atom, form a belt of negative electrostatic potential around its central region, leaving a positive "σ-hole" on the outermost portion of its surface, centred around the R–X axis.[57] This σ-hole can interact favourably with negative sites on another molecules, giving rise to halogen bonding.

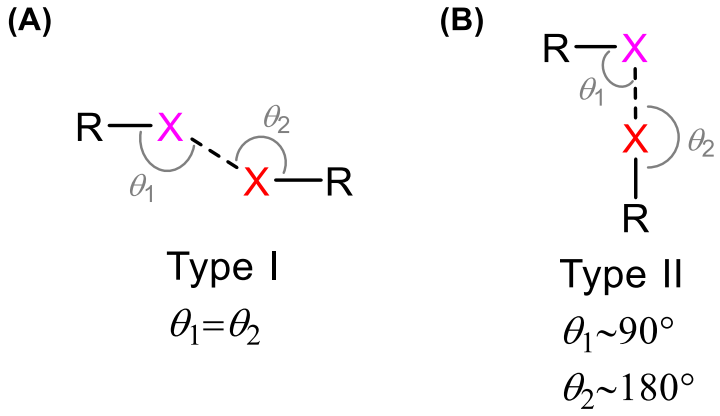

Figure GI5: Structural scheme for type I (A) and type II (B) halogen···halogen short contacts. (X = halogen atom, and R = C, N, O, halogen atom, etc.).

π-Interactions.

π-Interactions are a type of non-covalent interaction that involves an electron rich π-system that can interact with another π-system (π-stacking), a cation, or an anion.[58] Other types included the C–H···π interactions.[58] π-π interactions are not due to an attractive electronic interaction between the two π-systems but occur when the attractive interactions between π-electrons and the σ-framework outweigh unfavourable contributions such as π-electron repulsion.[58] For π-stacking three motifs are seen, sandwich, t-shaped, and parallel displaced (Figure GI6). In highly aromatic systems these type of interactions are quite prolific. The relative strength of these interactions are difficult to calculate, however, Hunter and Sanders described the attractive interaction between a porphyrin-porphyrin π-system at the optimum geometry calculated as being less than 1 kJ/mol, however their experimental estimate was 48 kJ/mol.[58]

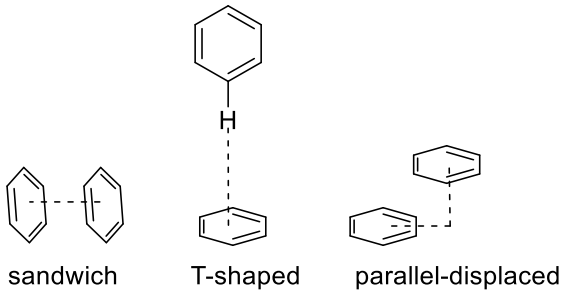

Figure GI6: π-Stacking motifs seen in aromatic systems.

Cation π-interactions are where an adjacent cation is seen to interact with the face of an electron rich π-system (Figure GI7A).[59] They are considered to be similar in strength to hydrogen bonds or salt bridges with studies on Li^+ interacting with a benzene molecule, at 158 kJ/mol.[60] By substituting the aromatic ring, the strength of the interaction can be increased with electron donating groups or decrease with electron withdrawing groups. Conversely, anion π-interactions occur between a highly electron deficient π-system and an anion (Figure GI7B).[61]

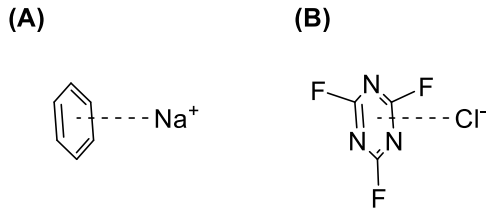

Figure GI7: Representation of cation π-interactions (A) and anion π-interactions (B).

In alkyne and alkene compounds, the presence of weak nonclassical hydrogen bonding interactions are evident between hydrogen atoms and the π-system. In these systems the hydrogen atoms are seen to be directionally important and usually point towards the centroid of the C=C or C≡C bonds. Although mostly linear there are two common motifs seen in hydrocarbon molecules are either along a perpendicular direction (Figure GI8A) or a herringbone arrangement (Figure GI8B).[62] For C–H interaction involving aromatic systems an interaction profile similar to T-shaped aromatic compounds is also possible (Figure GI8C).[63] The distance of such bonds is similar to hydrogen bonds – usually below the sum of the van der Waals radii – with angles close to 180° or 90°. The strength of such interactions is less than traditional hydrogen bonds and more similar to the strength of π-stacked systems. However, as has been shown, the strength of these interactions can be increased by substituting with electron donating groups and lowered by using electron withdrawing groups.[63]

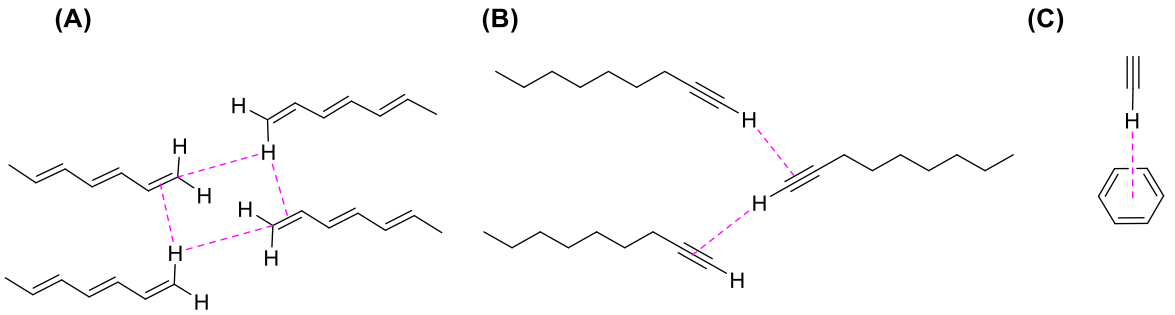

Figure GI8: Representation of C–H···π interactions along a perpendicular direction (A), herringbone (B), and linear carbons with aromatic ring (C).

Metallophilic Interactions.

Metallophilic interactions are non-covalent interactions between heavy metal atoms, gold···gold interactions.[64] For these to occur, the interaction bond distance should be less than the van der Waals radii between the two interacting atoms. Metallophilic interactions can either be intermolecular or intramolecular with the former being prominent in forming supramolecular assemblies,[65] subject to the element of choice and oxidation sate of the metal atoms involved. This type of interaction is enhanced by relativistic effects with the major contribution to this being the electron correlation of the closed-shell components.[65] While a significant interaction, their strength is similar to that of hydrogen bonding (29–46 kJ/mol), however, they can easily be broken by solvation of complexes.[66] The most notable application of metallophilic interactions is the polymerization of metal atoms which can be manipulated to form nucleated clusters such as gold nanoparticles.[67]

Analysis of Interactions.

Throughout this thesis, non-covalent interactions between molecules will be a major focus, however, without extensive computational calculation, determining their strength or significance is non-trivial. For this, we have used several characteristic techniques to determine their significance. For chapter 1, we have used a program named crystalexplorer to visualize specific interactions (O···H, Cl···H, F···H, etc.), where they are located in the molecular structure, and what percentage of the short contacts are associated with the specific interactions. This is done through using Hirschfeld surface analysis and generating fingerprint plots (Figure GI9). Through this method the X-ray crystallographic data can be uploaded, and generate surfaces based on *ab initio* quantum mechanical property densities. By using this generated surface, the internal distance *di* (distance from the atom position to the Hirshfeld

surface) and external distance *de* (distance from the Hirschfeld surface to an atom from the adjacent molecule) can be mapped to reveal detailed information about the intermolecular interaction for the individual molecule (*di vs. de*). These interactions can be separated and mapped using fingerprint plots to give visual information on the interactions and their significance. For example, Figure GI9 shows a simple interpretation of this process for the currently unpublished data of (4-(tert-butyl)benzyl)(2-(phenylsulfonyl)ethyl)sulfane which was determined by myself and the original compound was provided by Marie Roucan from the Senge group.

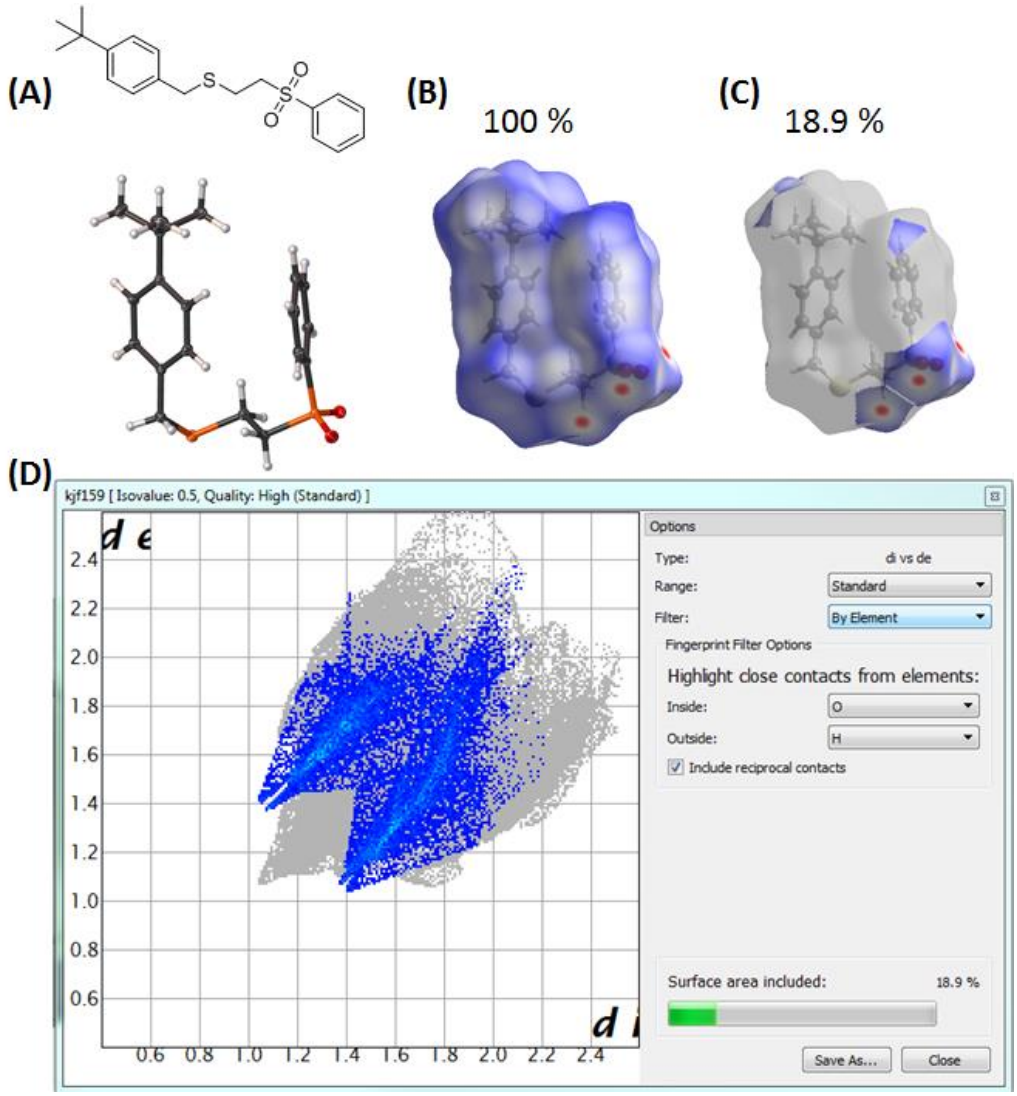

Figure GI9: Example of Hirschfeld surface analysis and fingerprint plots using (4-(tert-butyl)benzyl)(2-(phenylsulfonyl)ethyl)sulfane. (A) Molecular structure and crystal structure of (4-(tert-butyl)benzyl)(2-(phenylsulfonyl)ethyl)sulfane, (B) Hirschfeld surface of showing all (100%) interactions calculated, (C) Hirschfeld surface of showing all O···H (18.9% of total surface) interactions calculated, (D) output window from crystal explorer showing the fingerprint plot showing all O···H (blue dots (greyed out zone and blue dots combined represent all interactions)) mapped as a function of *de* vs *di*.

From this example, (Figure GI9A) shows the molecular and crystal structure (4-(tert-butyl)benzyl)(2-(phenylsulfonyl)ethyl)sulfane, (Figure GI9B) shows the Hirschfeld surface of all interactions (100% coverage), (Figure GI9C) shows the Hirschfeld surface indicating only the interactions we are interesting in seeing (18.9%). In this case, we are focusing on the O···H interactions. It can be clearly seen which oxygen atoms and which hydrogen atoms are important in these interactions. Figure GI9D shows the fingerprint plot output window from crystalexplorer. From this we can isolate the interactions we are interested in seeing and how much these interactions contribute to all the calculated interactions. In Figure GI9C we see that the most prominent O···H interactions are actually on the CH_2 group close to the SO_2 moiety and make up 18.9% of all the interaction seen in this structure. Moving to the OLEX2 output, it can be clearly seen that this interaction is between O1···H13C at a distance of 2.523(5) Å and a C–H···O angle of 137.9(8)° (Figure GI10). In Figure GI9C it is also seen that this interaction is highlighted in red compared to the rest of the surface which is blue. The colour code goes from blue to white, to red, demonstrating increasing significance in that order.

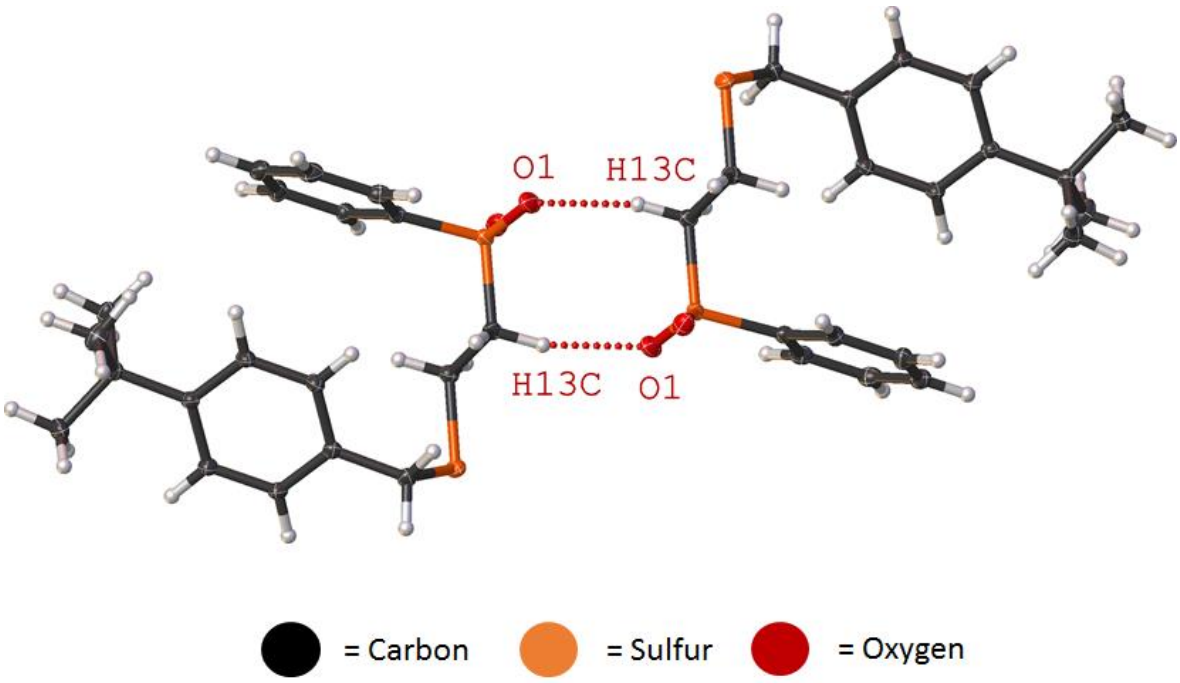

Figure GI10: Expanded view of 4-(tert-butyl)benzyl)(2-(phenylsulfonyl)ethyl)sulfane in the crystal structure showing the interaction between O1···H13C (2.523(5) Å, C–H···O angle of 137.9(8)°).

For chapter two, the determination is much simpler as we are looking at one specific interaction group, H···F interactions. For this chapter the bond length and angles

are listed in each relevant image. In the text contacts are listed as bonds (significant) or close contact (as a result of close packing and thus less significant). In this chapter's conclusion I will also outline my opinion of the importance of these interactions, but a discussion on strength is subjective to current hydrogen bonding theory.

Chapter three is the most complicated chapter to determine the strength of interactions. This is due to the fact that in this chapter we are outlining a new concept of C–H···A (where A is an acceptor) interaction type which are considered weak to begin with. However, these interactions provide an important discussion on how the implications of shape determine crystal packing and subsequently, the interactions of molecules overall for processes like protein interactions for drug related compounds. Therefore, I have listed these interactions in a table below each image in which the interactions are discussed and in the main text and conclusions for each interaction profile, their importance is discussed in terms of close packing or true bonds.

Chapter 1:
Crystal Engineering of Porphyrins.

Nomenclature of Porphyrins.

The term tetrapyrrole is often used to describe porphyrins as a class of molecules consistent of pyrrole rings linked together by methene bridges in a macrocyclic pattern.[68] The porphyrin skeleton contains twenty carbon atoms of the macrocyclic ring and four internal nitrogen atoms (Figure 1:1). Carbon atoms are classified as C_a (α) for the eight pyrrole carbons connected to core nitrogen atoms, C_b (β) for the eight peripheral pyrrole carbons or C_m (*meso*) for the four carbons in the methene bridges. The porphyrin macrocycle contains 22 π-electrons, 18 of which take part in the aromatic system. The other four π-electrons possess more double bond character. The porphyrin macrocycle retains a high degree of flexibility, which when included with the internalised nitrogen atoms and the adjustable core size allows for the insertion of a large variety of metals, forming metalloporphyrins.

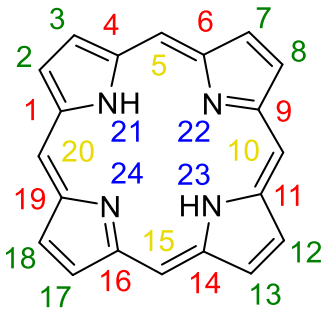

1, 4, 6, 9, 11, 14, 16, 19 = α carbons = C_a
2, 3, 7, 8, 12, 13, 17, 18 = β carbons = C_b
5, 10, 15, 20 = *meso* carbons = C_m
21, 22, 23, 24 = core nitrogen atoms

Figure 1:1: IUPAC nomenclature of porphyrins.

Porphyrins are scaffold systems that can be functionalised at a plethora of locations around the periphery, sixteen in total (C_a, C_b, and C_m), as well as by metal coordination. The structural chemistry of porphyrin metal complexes is one of the largest explored areas of coordination chemistry. There are many reviews available on metal coordination,[69] aspects of macrocycle modification,[70] supramolecular chemistry[71] and nonplanar systems.[72] Due to their impressive optical and photophysical properties,[73] chemical stability,[74] conformational flexibility[72a, 75] and biological relevance;[76] porphyrins have long been studied as molecular scaffolds. Applications for the tetrapyrrole macrocycle have been found in areas as diverse as optics,[77] light harvesting,[78] surface chemistry[79] and cancer therapy.[80] Continuous research into the properties of porphyrinoid systems means they are among the most studied classes of organic compounds. The search for further applications for this robust scaffold, however, requires equally focused research into

their synthetic availability. As such, the development of novel synthetic avenues to substituted porphyrin scaffolds remains an ongoing challenge.

Nonplanar Porphyrins.

The role of porphyrins in nature is a well-established research topic. To date, more than 150 different natural tetrapyrroles with functions ranging from oxygen transport, electron transport and transfer, and photosynthesis have been identified.[81] This has led to many industrial applications in processes such as modelling electron transfer, optics, supramolecular chemistry, and solar cells.[82] One of the most notable of these practical uses is photodynamic therapy (PDT), which has been used as a cancer treatment[83] and as a treatment for cataracts.[84] However, as with many biological molecules, porphyrin-related compounds have also played the villain in human history, namely in genetic disorders such as porphyria, caused by mutations in one or more of the genes associated with heme synthesis, resulting in the formation of the toxic uroporphyrin I and other such compounds.[85] Biological studies have established that by conformational control of the porphyrin macrocycle nature regulates biological reactions facilitated by porphyrin-dependent molecules.[72b] The realisation that porphyrins exhibit a considerable degree of conformational flexibility and that physicochemical properties are associated with different macrocycle conformations has resulted in a major boost to the field of porphyrin chemistry, allowing the development of conformationally designed systems.[86] In 2000, Senge wrote extensively on the synthesis and properties of highly substituted porphyrins in the Porphyrin Handbook.[87]

Usually, a large degree of substitution results in a higher degree of nonplanarity. Figure 1:2A shows the structure of 2,3,7,8,12,13,17,18-octaethylporphyrin[88] which is almost completely planar in comparison to the nonplanar 2,3,7,8,12,13,17,18-octaethyl-5,10,15,20-tetraphenylporphyrin[89] (Figure 1:2B), in which the macrocyclic ring is completely distorted. Thus, the latter is due to the effect of the higher degree of substitution as well as the effects of the substituent's electronic and steric effects.

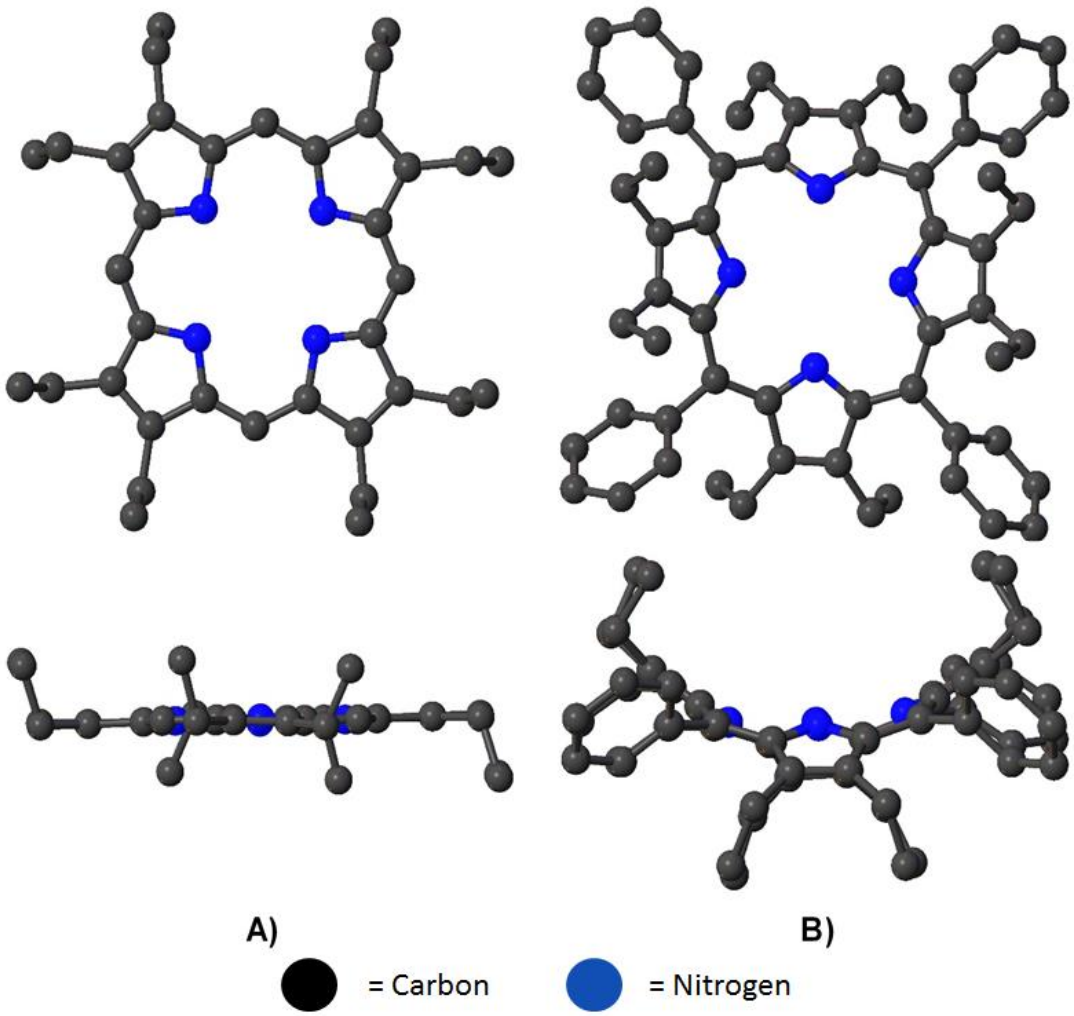

Figure 1:2: X-ray structure of the planar 2,3,7,8,12,13,17,18-octaethylporphyrin[88] (A) and nonplanar 2,3,7,8,12,13,17,18-octaethyl-5,10,15,20-tetraphenylporphyrin[89] (B) showing the difference higher substitution pattern has on the distortion of the macrocycle. Structures are drawn isotropically with hydrogen atoms omitted.

Nonplanar porphyrins, reported by Senge *et al.*, with an increased number of *meso* substituents, demonstrated bathochromic shifts (red shift) of the absorption bands compared to their planar counterparts, which is an indication of increased distortion of the macrocyclic ring.[86c] Nonplanar porphyrins have significantly lower fluorescence quantum yields, larger Stokes shifts and shorter lifetimes of the lowest excited state than their planar counterparts.[90] This has resulted in an increased focus on the synthesis and structural elucidation of numerous highly substituted porphyrins for biomimetic studies.[72]

Nonplanar porphyrins typically display much greater solubility in polar solvents compared to their more planar counterparts.[81] This can be rationalised due to reduced π-stacking. They form more complex molecular structures such as cages

or channels, allowing easier access for solvent molecules.[91] This results in increased solubility and contributes to altered photophysical properties.

Planar porphyrins, when subjected to alterations that distort the macrocyclic ring typically display an increase in basicity.[92] The NH hydrogens rarely take part in any interaction, except in organolithium, *N*-methylation reactions, or deprotonation.[93] However, it should be noted that pre-deformed structures such as highly substituted porphyrins show an increase in reactivity in such reactions owing to the accessibility of the NH hydrogens. The porphyrin macrocycles can be protonated forming the corresponding dication more easily by weak acids, such as acetic acid, than planar porphyrins.[92a, 94]

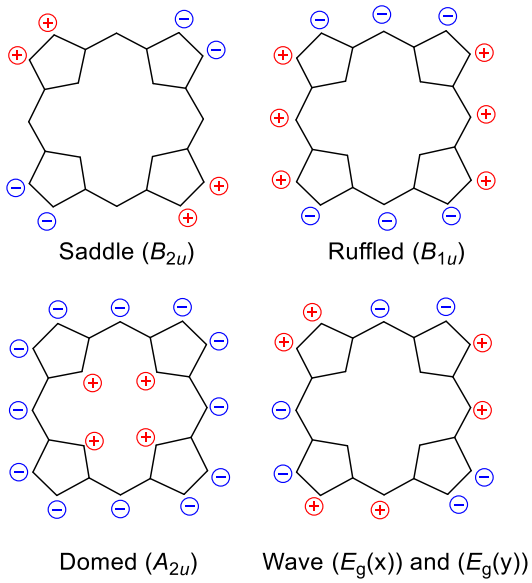

Figure 1:3: Representation of four main distortion modes observed in porphyrins. Only the most significant displacements are shown. (+) indicates displacements above the plane and (-) indicates displacements below the plane.

In order to compare planar and nonplanar porphyrins a system of classification is necessary. For this purpose, the four main distortion modes, ruffled (B_{1u}), saddled (B_{2u}), domed (A_{2u}) and wave (E_g(x)) and (E_g(y)), as described by Scheidt and Lee, are used to classify the distortion of porphyrins from the 24-atom least-squares plane (Figure 1:3).[95] Typically, highly substituted nonplanar porphyrins exhibit either a ruffled, saddle, domed distortion mode. Ruffled distortions are usually associated with metalloporphyrins with small metal ions such as Ni(II), where the nitrogen-metal bonds are shortened and can result in ring distortions.[95-96] Saddle porphyrins are usually more prevalent in dodecasubstituted porphyrin structures as these structures frequently involve steric crowding that is reduced *via* saddling of

the macrocyclic ring.[86c, 95] The domed distortion mode is usually found in five-coordinated porphyrin complexes where the axial ligand causes the out-of-plane displacement of the central metal or in metalloporphyrin which incorporates large metal ions like Ti(III).[97]

How to Make a Nonplanar Porphyrin.

Before beginning any project, it is important to consider what is the best method to achieve the desired target. In this case, we are hoping to make a nonplanar porphyrin. Senge has summarised this topic in his ChemComm article and as a chapter in the Porphyrin Handbook, listing out all possible way to make a nonplanar porphyrin.[72a, 87] These were 1) introduction of sterically demanding groups, 2) metalation, 3) axial ligands, 4) degrees of reduction, 5) alteration of the conjugated system, 6) *N*-substitution, 7) cation radical formation, 8) "strapping" of the macrocycle *via* covalent linkage, 9) heteroatom substitution (Figure 1:4).

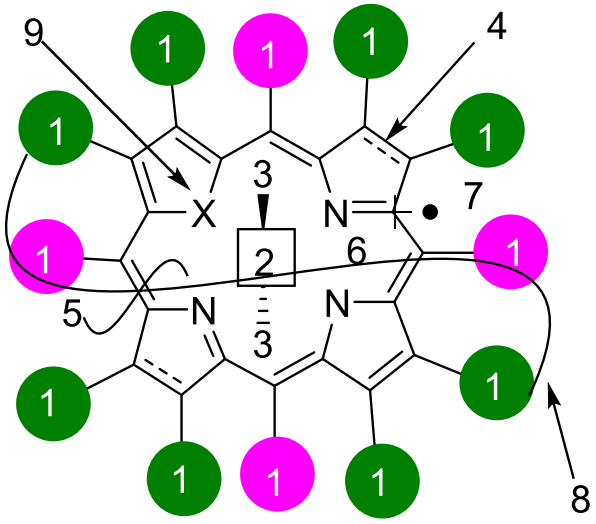

Figure 1:4: Representation of the possible chemical modification used to make the macrocycle nonplanar. Variations can be achieved by several different methods (1–9).

The introduction of sterically demanding groups is a simple process that involves selecting an appropriate aldehyde (conventionally something bulky) and pyrrole (with functionalised *β*-carbons) and subsequently reacting them together using standard porphyrin condensation reaction. *Peri*-interactions usually cause the macrocycle to adopt a conformation in which less strain is applied resulting in a nonplanar porphyrin (Figure 1:2B). Metalation is also a simple procedure to achieve

nonplanarity. The core of the porphyrin system will readily accept most metal ions either directly into the core or as a sit-atop complex and as stated above different metals will deform the porphyrin macrocycle, such as Ni(II) causing ruffling and Ti(III) causing doming (Figure 1:5A).[95-96, 98] A similar effect is seen with axial ligands in porphyrin complexes where the ligand will affect displacement of ions in the metal complex and induce alternate distortions from the parent metal complex (Figure 1:5B).[99]

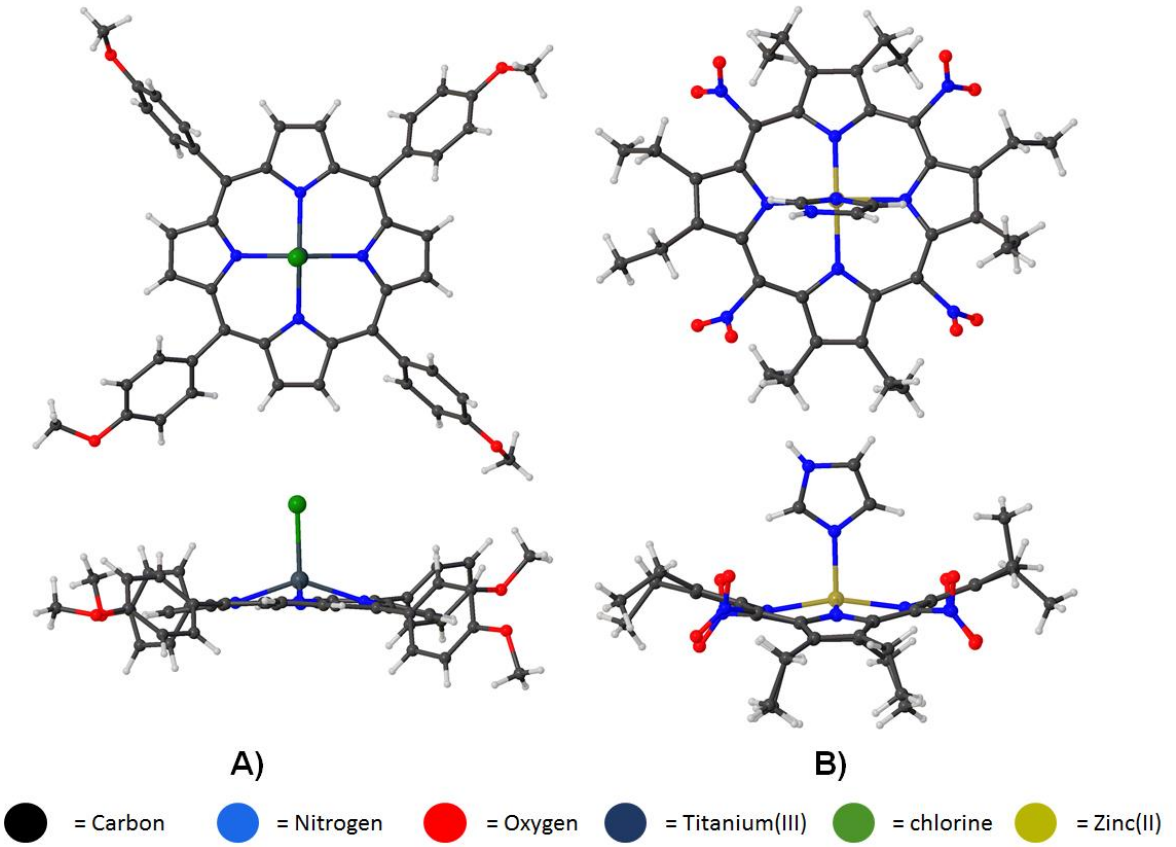

Figure 1:5: Distortion induced by metal (A) and axial ligand (B) in porphyrins.[99b, 100]

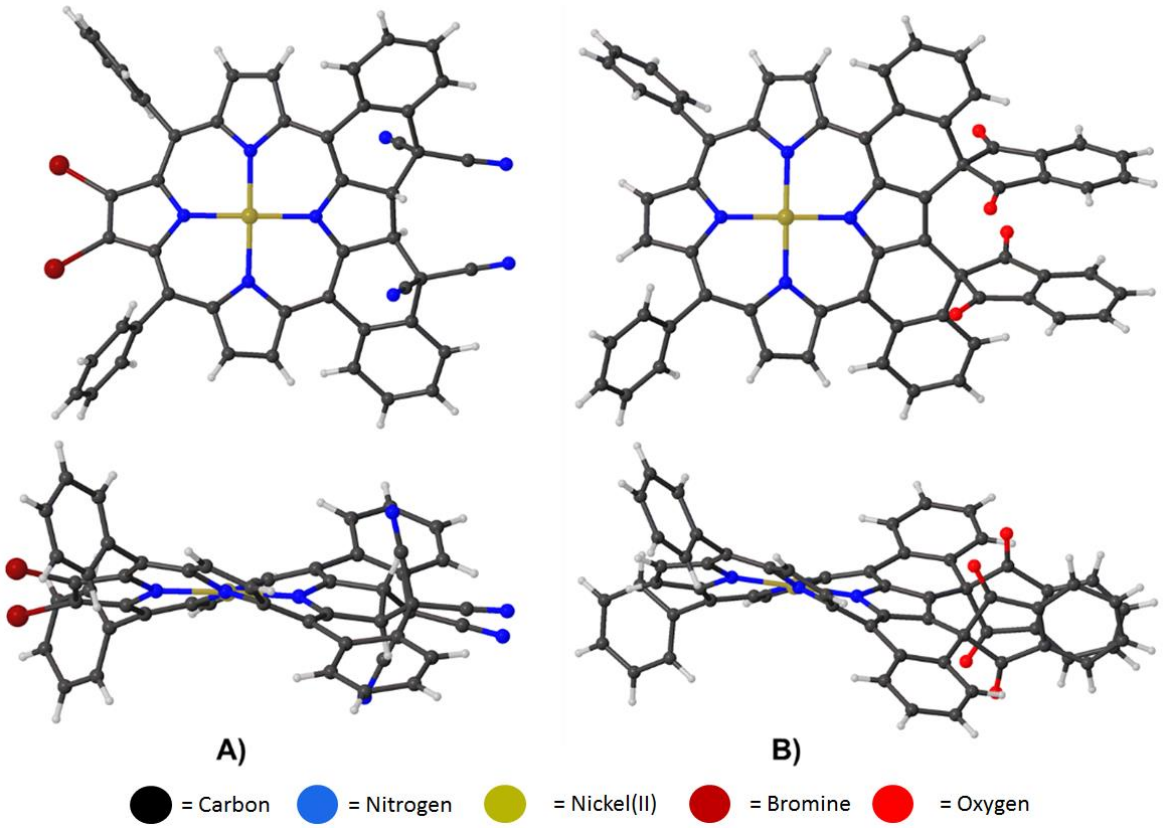

Figure 1:6: Structure reported by Chaudhri *et al.* showing fused chlorin (A) and fused porphyrin (B) systems showing their effects on nonplanarity.[101]

Reducing the porphyrin systems or altering the conjugation of the macrocycle is commonly employed as a method of achieving nonplanarity.[102] Typically, both of these methods focus on the modification of a pyrrole unit by either fusing a moiety to the *β*-positions or by reducing the pyrrole unit. This causes the porphyrin to adopt a more nonplanar conformation to accommodate the strain incorporated by this method (Figure 1:6).[101]

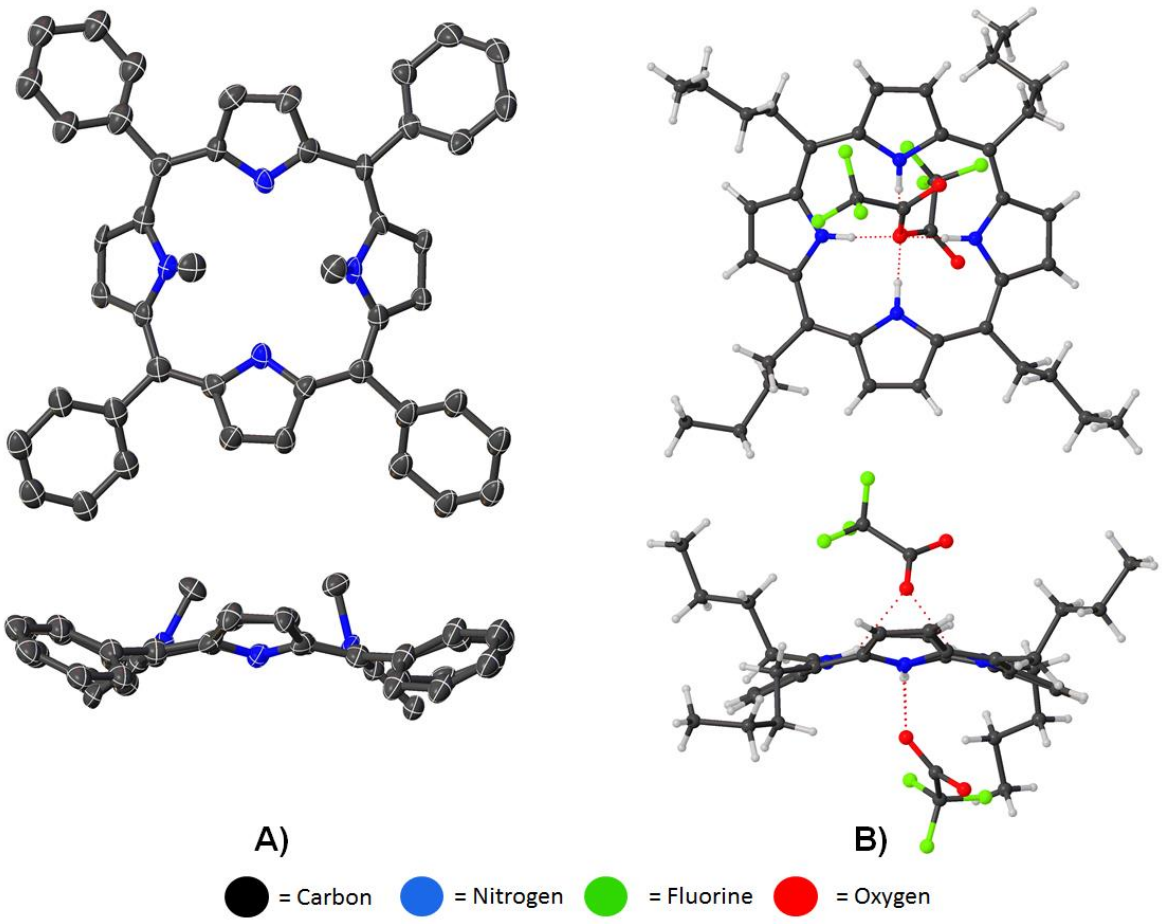

Figure 1:7: *N*-substituted porphyrin (A) (hydrogen atoms omitted) and dication porphyrins (B) showing their effects on nonplanarity.[93, 103]

N-substituted porphyrins result from direct alkylation of free base porphyrins with a methyl unit inserted into the core of the macrocycle. This was achieved by Jackson and co-workers using reagents such as methyl iodide or methyl trifluoromethanesulfonate.[104] This method allows for the rapid preparation of nonplanar, core distorted porphyrins due to the increase in bulk in the porphyrin core (Figure 1:7A).[93, 105] Porphyrin cations are an effective method towards the nonplanarity of porphyrins. Every free base porphyrin has the potential to become a dication when subjected to an acidic environment. This causes the core of the porphyrin to accept two protons. The inclusion of an additional two hydrogen atoms into the porphyrin core causes an up-and-down displacement of the N–H units causing the macrocycle to become more distorted and thus, leading to nonplanarity (Figure 1:7B).[103]

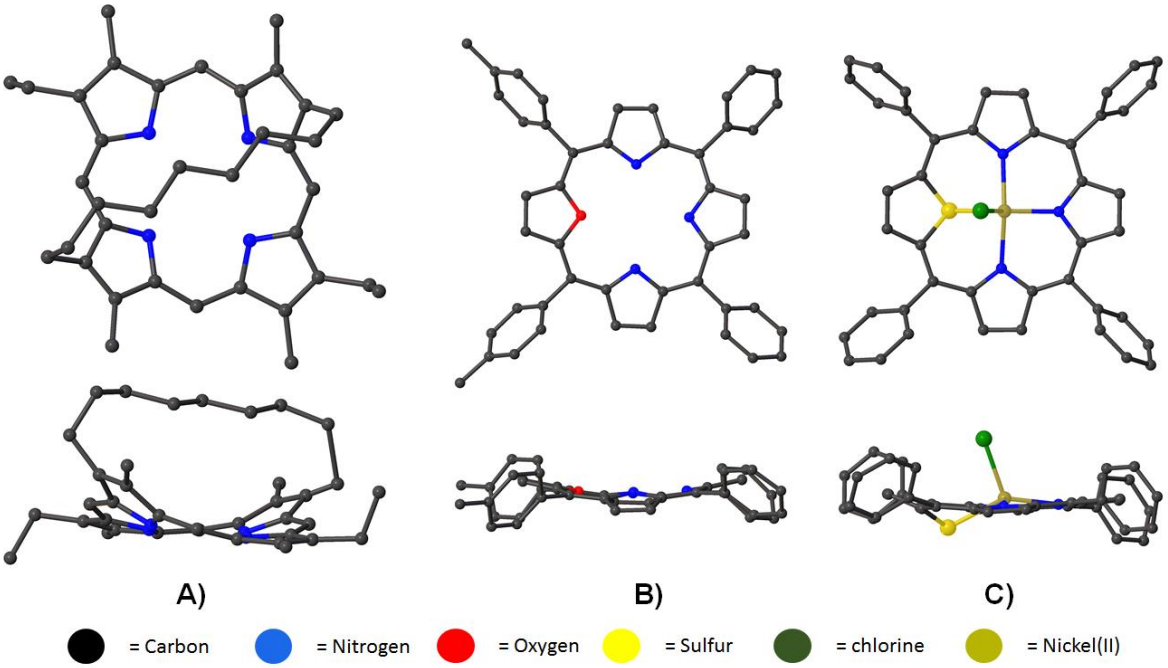

Figure 1:8: Strapped porphyrins (A) and heteroatom porphyrins (B and C) showing their effects on nonplanarity. Hydrogen atoms have been omitted.[106]

The strapping of a porphyrin macrocycle is another method to achieve nonplanarity. This method is similar to that of highly substituted porphyrins, where the covalently bound strap between *meso-meso* or *β-β* can overload the periphery with substituents. The main difference between these two methods is that the length of the strap can be used to control the degree of nonplanarity. The shorter the strap the more nonplanar the porphyrin.[106a] Finally, heteroatom substituted porphyrins have several interesting properties one of which is due to the electron-withdrawing effect of the heteroatom, these porphyrinoids can stabilise unusual oxidative states of the central metal ion. The distortion of these molecules is a result of large heteroatoms shrinking the core of the macrocycle and distorting the ring.[106b, 106c, 107]

Porphyrins in Crystal Engineering.

The use of nonplanar porphyrins as potential non-covalent organic frameworks has been a hitherto ignored area for framework chemistry. The concept of crystal engineering of porphyrins has been around for over three decades with Byrn *et al*. purposed the idea that the highly ordered 'porous' structure of porphyrin clathrates can be used as some form of 'porphyrin sponge'.[108] In this regard, a tetraphenylporphyrin host was reported to trap a variety of guests within its crystal using strictly hydrogen-bonding and Van der Waals forces. Since then, crystal

engineering of porphyrins has focused on the use of planar porphyrins with a variety of non-covalent interactions such as hydrogen-bonds, metal coordination and halogen-bonding interactions.[108-109] Goldberg and co-workers have published several articles on the use of 5,10,15,20-tetraarylporphyrins bearing either a carboxylic acid, pyridine or amine functionality forming non-covalent systems through hydrogen-bonds and metal coordination.[109a-d, 109f, 109h, 109j-m] These complexes have been reported to be of use in a range of areas in material sciences, such as molecular sieves, due to the formation of a three-dimensional lattice in which more than 50% of the crystal volume consisted of open straight channels.[109d, 109f]

Titi *et al.* reported on the self-assembly of tetraarylporphyrins through halogen-bonding.[109g] In this, the authors discussed the use of a 5,10,15-tris(4-iodophenyl)-20-(pyridin-4-yl)porphyrin forming a chiral architecture through C-I···N and C-I···π interactions. Additionally, they reported the six-coordinate tin complex of this compound which featured the pyridine ligand of the tin metal centre interacting with the 4-iodophenyl groups of the neighbouring molecules, forming a three-dimensional complex. Similar works have been reported by Patra *et al*. who utilised the coordination of tin to carboxylic acids to form a supramolecular organised network by exploiting cooperative hydrogen-bonding with axial bound ligands.[110]

Other areas such as the use of etioporphyrin as a chiral separator for fullerene molecules have been documented but investigations into the effect of distortion on the formation of such interactions and frameworks have been lacking.[111] The field of fullerene chemistry, namely C_{60}, $C_{60}O$, C_{70} and C_{80} fullerenes, has seen many contributions to crystal engineering with the co-crystallisation of fullerenes and 2,3,7,8,12,13,17,18-octaethylporphyrin containing various metal centres (Ni(II), Zn(II), Ag(II), Pd(II) and Fe(III)).[112] However, these systems are predominantly planar. Ghiassi *et al*. recently published an article featuring the crystal engineering of etioporphyrin-1 for the use of the chiral separation of fullerene molecules and compared this to planar Ni(II)OEP.[111] In this, they showed that the use of etioporphyrin has a much higher capacity to separate the individual fullerene units due to the host-guest complex formed during co-crystallisation.

However, with all the advances made in the crystal engineering of planar porphyrins, investigation of their nonplanar counterparts has been practically unexplored with

regards to non-covalent interactions and their applications in the synthesis of molecular cages. The main benefit of this is that with higher degrees of distortion, the *meso*-substituted groups themselves are forced further from the plane of the porphyrin ring. This allows for the potential of interactions to take place between co-facial molecules as seen in fullerene chemistry rather than the inline molecules. This application has been touched on by people such as Gilday *et al*. in which the planar 5,10,15,20-tetrakis(3-(azidomethyl)phenyl)porphyrin was 'strapped' with tetra(prop-2-yn-1-yl) benzene-1,2,4,5-tetracarboxylate through a copper(I)-catalysed azide-alkyne cycloaddition.[113] The authors carried out successful anion binding studies which showed a 1:1 receptor to anion-binding stoichiometry and a clearly visible colour change depending on the anion.

The structural properties of porphyrins have attracted significant interest since they were first described, there has been a significant number of structures of nonplanar porphyrins published over the years.[86a, 86c, 94a, 96a, 96d, 99b, 105, 114] In terms of crystal engineering, the emphasis to date has mainly focused on planar porphyrin species, such as the studies done by Goldberg and co-workers.[108-111]. With this in mind, a larger series of highly substituted free base and metalloporphyrins with an aim to investigate their structural properties in the solid state was envisioned.

Nonplanar Porphyrin Cages

Nonplanar porphyrin has many interesting potentials as molecular cages which has yet to be realised. However, there are two main reason why one would embark on such an investigation. The first reason is a simple comparison between planar and nonplanar porphyrin. In nonplanar porphyrins the inherent distortion is an attractive building block for creating a structure with a large cavity size. As seen in Figure 1:2, the distorted macrocycle forms a domed shaped cavity. The combination of two such units through appropriate peripheral connective group would result in the formation of a complete cage.

The second reason is the increased potential nonplanar porphyrins have in small molecule activation compared to their planar counter-parts. Due to the distortion of the macrocycle both the imine and the amine groups are now expressed outside the porphyrin plane allowing for them to interact with their environment more easily. This has the added benefit of making the nonplanar porphyrin more basic and easier to

be protonated. For a practical benefit this nonplanarity has potential in a variety of areas such as sensing and binding of small molecules as illustrated in a review by Kielmann and Senge[115] or as an organocatalyst as demonstrated by Roucan *et al*..[116] Both of these functions would be a desirable property to have in a non-covalent organic framework which is why nonplanar porphyrins were chosen as the model for our design.

Objectives.

In Chapter 1.1, highly substituted porphyrins will be the central target molecule. The objective of this chapter is to investigate if molecular cages may be designed from 5,10,15,20-tetraaryl-(X)-substituted-2,3,7,8,12,13,17,18-octaethylporphyrins (OETArXPs). To accomplish this, an investigation into the structural properties of OETArXP derivatives using X-ray diffraction (XRD) techniques was suggested as the most appropriate course of action. With this in mind, the first objective is to synthesise a library of OETArXP compounds which present a variety of functional groups on the *meso*-phenyl substituent. A series of halogen (fluorine to iodine), nitrogenous (azido, cyano), alkyl (TMS-acetylene, butyl) and chained (benzyloxy) porphyrins have been chosen as the initial target molecules. Following this, selection of tetravalent metal complexes [Cu(II), Ni(II) and Pd(II)] of these porphyrins will also be synthesised to allow for an investigation of the effects of metal complexes on the structural properties of these porphyrins. The final step to this chapter will focus how the inclusion of solvents can effect the crystal packing. This will allow for the investigation of solvent effects within this series of porphyrins. All pyrroles, porphyrins and their metal counterparts, aldehydes **1:25** and **1:27**, azides, and triazole porphyrins included in this chapter were synthesized by me during the course of this study.

In chapter 1.2, *N*-methyl-substituted porphyrins will be central to this discussion. The objective of this chapter will be to conduct a systematic structural discussion on the effects of *N*-methyl-substitution of porphyrins using XRD for samples published by our group and literary samples. The first topic to examine is how both planar and nonplanar porphyrins are affected by an increase in *N*-methyl-substitution. Accompanying this will be an investigation into the differences in distortion between electron withdrawing or donating groups. This will be one of the first structural discussion on all *N*-methyl-substituted porphyrins published to date.

Chapter 1.1 Investigation of OETArXPs for the Use as Molecular Cages.

For this project, several groups of porphyrins were chosen to highlight different aspects of possible interactions, Figure 1:9. A series of compounds **1:1–1:6** bearing a halogen in either the *ortho*- or *para*-position of the *meso*-aryl residue were prepared to examine the effects of halogen functionalisation on the interaction profile of OETArXP. A pair of alkyl porphyrin, 4-butlyphenyl-OETArXP (**1:7**) and 4-((trimethylsilyl)ethynyl)phenyl-OETArXP (**1:8**) were synthesised to investigate hydrophobic effects and compound **1:18** could be used as a synthetic handle for synthesising larger porphyrin arrays. Following this two benzyloxy chained porphyrins, 4-benzyloxyphenyl-OETArXP (**1:9**), and 3,4-dibenzyloxyphenyl-OETArXP (**1:10**), where chosen as they are bulky groups and can be used to investigate steric effects. Two nitrogenous porphyrins, 4-cyanophenyl-OETArXP (**1:11**) and 4-azidophenyl-OETArXP (**1:12**), were also synthesised as part of this series. Cyanophenyl groups due to their electron rich nature and 2-D connections, provide an interesting tecton for the synthesis of a non-covalent network.[109m] Such moieties have been used as a weak hydrogen-bond acceptor in supramolecular arrays and as suitable halogen-bond acceptors. Goldberg and co-workers have utilised this specific moiety link porphyrin systems through non-covalent interactions.[109m] 4-azidophenyl-OETArXP was chosen for its potential for further modification either through click reactions or reduction to the amine functionality.[113]

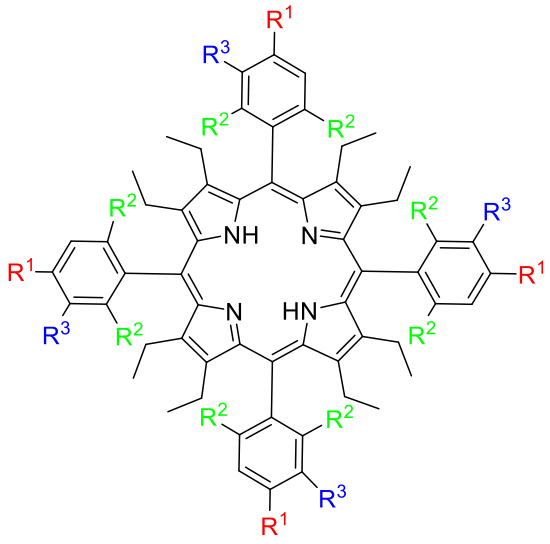

1:1-1:12

1:1 = R^1 = F; R^2 = H; R^3 = H (30 %)
1:2 = R^1 = Cl; R^2 = H; R^3 = H (28 %)
1:3 = R^1 = Br; R^2 = H; R^3 = H (33 %)
1:4 = R^1 = I; R^2 = H; R^3 = H (14 %)
1:5 = R^1 = H; R^2 = F; R^3 = H (20 %)
1:6 = R^1 = H; R^2 = Cl; R^3 = H (17 %)
1:7 = R^1 = Butyl; R^2 = H; R^3 = H (11 %)
1:8 = R^1 = TMS acetylene; R^2 = H; R^3 = H (52 %)
1:9 = R^1 = benzyloxy; R^2 = H; R^3 = H (37 %)
1:10 = R^1 = benzyloxy; R^2 = H; R^3 = benzyloxy (28 %)
1:11 = R^1 = CN; R^2 = H; R^3 = H (29 %)
1:12 = R^1 = N_3; R^2 = H; R^3 = H (21 %)

Figure 1:9: Free base porphyrins synthesised in this section.

Pyrrole Synthesis.

The preparation of 3,4-diethylpyrrole (**1:22**) began with the synthesis of 4-acetoxy-3-nitrohexane (**1:16**) and ethyl isocyanoacetate (**1:20**) according to previously reported methods (Schemes 1:1-1:2).[117] With the starting materials to hand, a condensation reaction between compounds **1:16** and **1:20** was performed to afford 3,4-diethylpyrrole-2-carboxylate (**1:21**). Two methods established in the literature were attempted for this condensation as outlined in Scheme 1:3.[118],[119] Both pathways afforded the desired product in high yields. Method 1 utilised 1,8-diazabicyclo[5.4.0]undec-7-ene (DBU) to achieve the product on a four-hour timescale, while Method 2 used potassium carbonate over 3 days. Even though Method 1 is less time consuming, Method 2 was chosen as it allowed for large-scale (>60 g) synthesis of the desired compound using comparatively cheap reagents and resulted in a much higher yield.

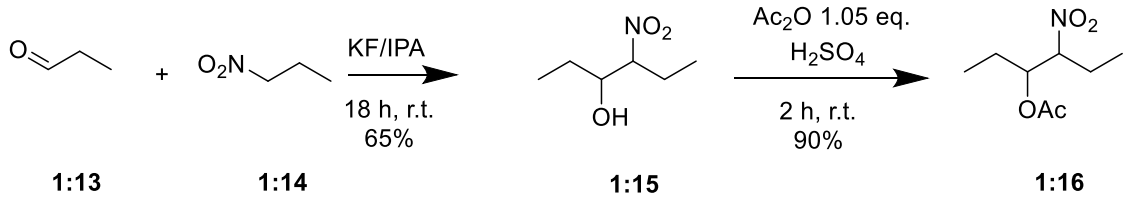

Scheme 1:1: Synthesis of 4-acetoxy-3-nitrohexane (**1:16**).

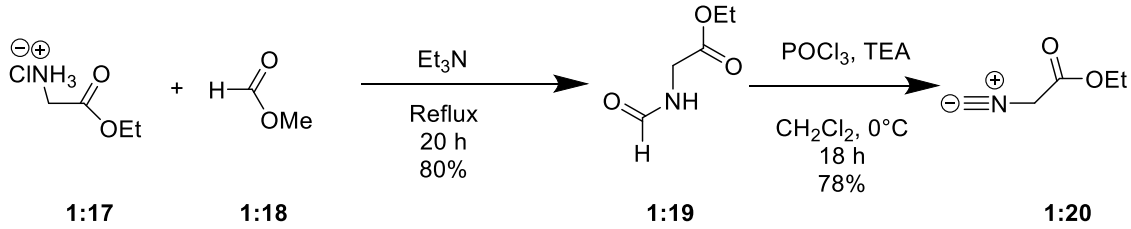

Scheme 1:2: Synthesis of ethyl isocyanoacetate (**1:20**).

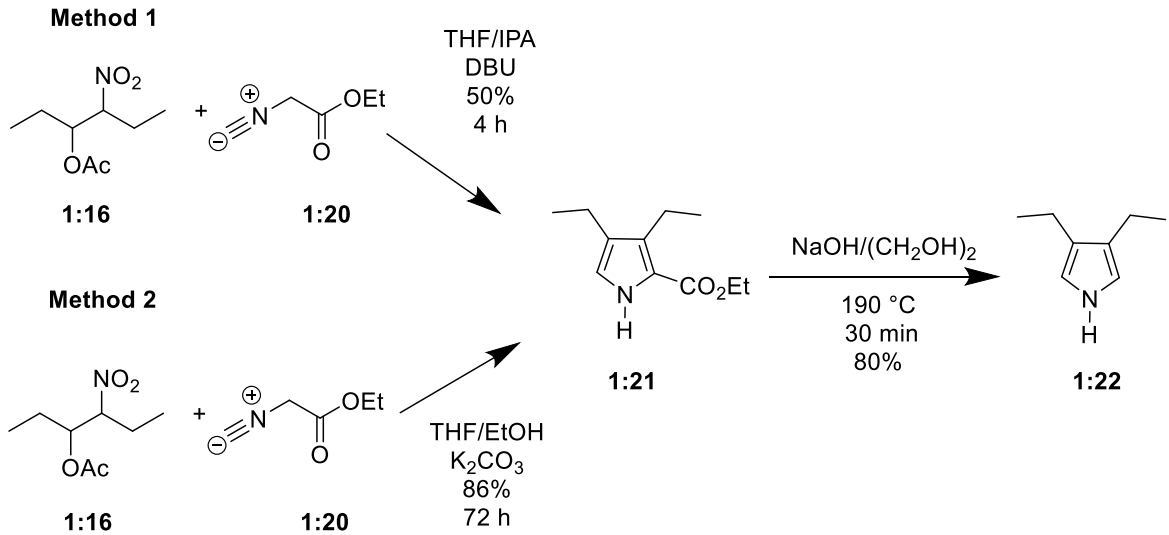

Scheme 3: Synthesis of 3,4-diethylpyrrole (**1:22**).

Aldehyde Synthesis.

The synthesis of the 4-((trimethylsilyl)ethynyl)benzaldehyde for compound **1:8** was achieved by using a Sonogashira cross-coupling between 4-iodobenzaldehyde and TMS-acetylene using a similar procedure as reported by Sasaki *et al*. (Scheme 1:4).[120] The 4-azidobenzaldehyde for compound **1:12** was achieved employing a procedure reported by Grimes *et al*. (Scheme 1:5).[121]

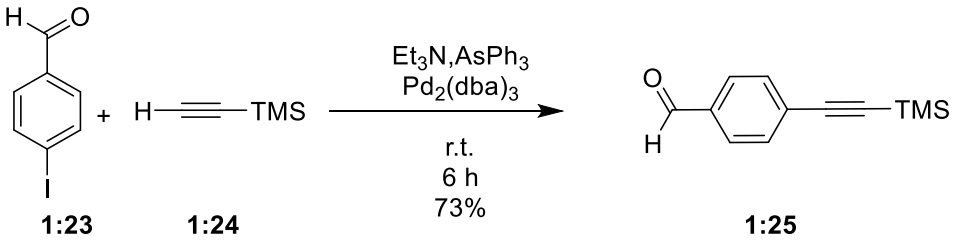

Scheme 1:4: Synthesis of 4-((trimethylsilyl)ethynyl)benzaldehyde (**1:25**).

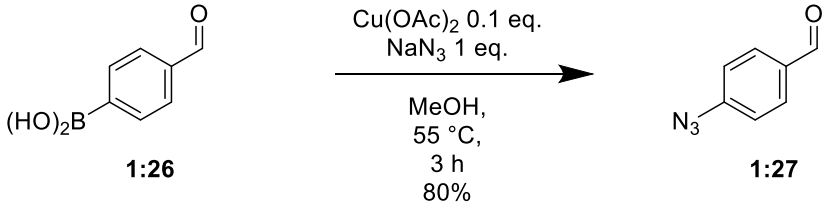

Scheme 1:5: Synthesis of 4-azidobenzaldehyde (**1:27**).

Synthesis of Free Base OETArXP.

The synthesis of free base 5,10,15,20-tetraaryl-(X)-substituted-2,3,7,8,12,13,17,18-octaethylporphyrins (OETArXP) (**1:1–1:12**) was achieved following a modified condensation method related to the Lindsey condensation for 5,10,15,20-tetraarylsubstituted porphyrins (Scheme 1:6).[122] The synthesis of compound **1:3** and **1:6** were previously reported by Schindler *et al.* and Hoshino *et al*., respectively.[123] The synthesis of such porphyrin systems was relatively straightforward. Initially, the porphyrinogen was formed and subsequently oxidised by DDQ. Following this, the free base porphyrin was concentrated and then filtered through a plug of silica gel using EtOAc as an eluent. This was then purified by column chromatography on silica gel using EtOAc:*n*-hexane (1:1, v/v) solution as an eluent. Each compound was then set-up for crystallisation by dissolving in a minimum of CH_2Cl_2 and layering with MeOH. A shiny green flaky solid was obtained. On further examination, thin layer chromatography (TLC) analysis showed two green spots with very similar R_f values present in every reaction sample, which could be the result of atropisomerism (see NMR section). Additional purification was

carried out as needed, e.g., use of multiple crystallisations or column chromatography on aluminium oxide, depending on the compound properties.

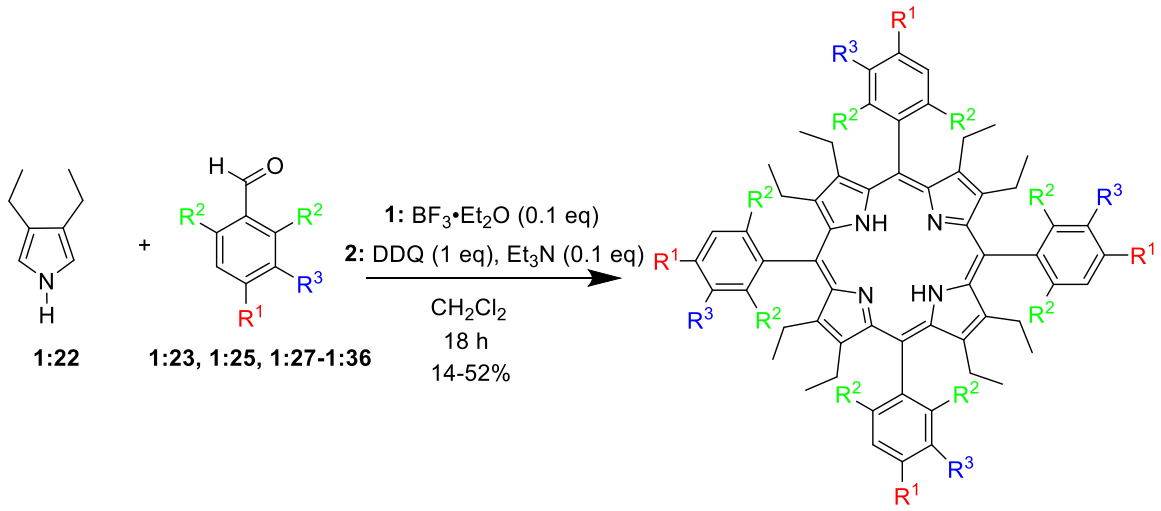

1:28 = R^1 = F; R^2 = H; R^3 = H
1:29 = R^1 = Cl; R^2 = H; R^3 = H
1:30 = R^1 = Br; R^2 = H; R^3 = H
1:23 = R^1 = I; R^2 = H; R^3 = H
1:31 = R^1 = H; R^2 = F; R^3 = H
1:32 = R^1 = H; R^2 = Cl; R^3 = H
1:33 = R^1 = Butyl; R^2 = H; R^3 = H
1:25 = R^1 = TMS acetylene; R^2 = H; R^3 = H
1:34 = R^1 = benzyloxy; R^2 = H; R^3 = H
1:35 = R^1 = benzyloxy; R^2 = H; R^3 = benzyloxy
1:36 = R^1 = CN; R^2 = H; R^3 = H
1:27 = R^1 = N_3; R^2 = H; R^3 = H

1:1 = R^1 = F; R^2 = H; R^3 = H (30%)
1:2 = R^1 = Cl; R^2 = H; R^3 = H (28%)
1:3 = R^1 = Br; R^2 = H; R^3 = H (33%)
1:4 = R^1 = I; R^2 = H; R^3 = H (14%)
1:5 = R^1 = H; R^2 = F; R^3 = H (20%)
1:6 = R^1 = H; R^2 = Cl; R^3 = H (17%)
1:7 = R^1 = Butyl; R^2 = H; R^3 = H (11%)
1:8 = R^1 = TMS acetylene; R^2 = H; R^3 = H (52%)
1:9 = R^1 = benzyloxy; R^2 = H; R^3 = H (37%)
1:10 = R^1 = benzyloxy; R^2 = H; R^3 = benzyloxy (28%)
1:11 = R^1 = CN; R^2 = H; R^3 = H (29%)
1:12 = R^1 = N_3; R^2 = H; R^3 = H (21%)

Scheme 1:6: Synthesis of free base OETArXPs.

The ^{1}H NMR spectra of the free base compounds are remarkably similar. Particularly, the CH_2 protons of the ethyl groups show splitting into two groups of signals, characteristic of the OETArXPs. Figure 1:10 shows the ^{1}H NMR spectrum of 5,10,15,20-tetrakis(2,6-dichlorophenyl)-2,3,7,8,12,13,17,18-octaethylporphyrin (**1:6**). Signals (a) are representing the CH_2 protons of the OETArXP and exhibit splitting due to atropisomers present in the structure of the compound at lower temperatures. This explanation was confirmed by carrying out ^{1}H NMR experiments at different temperatures for compound **1:1** (Figure 1:11). At 25°C two distinct broad signals are present one at 1.89 ppm and one overlapping with the DMSO-d_6 peak at 2.50 ppm (this was confirmed in the 2D NMR). At 30-40°C the signals are hard to distinguish before they begin to coalesce at 50°C (2.25 ppm) with complete overlap of both signals and a sharper signal seen in the final two traces (75°C and 90°C).

When the temperature is increased, the molecule gains a degree of flexibility which removes the distinction of spin state for each molecule and resulting in the formation of one single peak at 2.25 ppm at temperatures of >40 °C. It should also be noted that the temperature of coalescence is located between 30–40 °C. This result is in line with previous studies conducted by Medforth *et al*. on 2,3,5,7,8,12,13,15,17,18-decaalkylporphyrins in which *cis* and *trans* conformations contributed to the splitting of signals at low temperatures.[124] signals (b) is characteristic of the CH_3 group of the ethyl group and integrates for 24 protons. Both signals (a) and (b) are characteristics of the OETArXP and feature in all ^{1}H NMR spectra of the compounds listed. The signal (e) at -1.28 ppm is characteristic of all free base porphyrins. This peak denotes the internal nitrogen protons and they typically feature in the negative region of the spectra due to the anisotropic effect of the macrocyclic ring. Initially, it was observed in this series of OETArXPs, this characteristic signal was absent. Due to the nonplanarity of the ring, the NH hydrogens can interact with their environment more readily, which allows the interactions of protons with the lone pair of the nitrogen atoms with acidic solvents. However, the addition of a small amount of deuterated pyridine resulted in the appearance of the NH protons in the spectra as seen in Figure 1:10. The aromatic region of the ^{1}H NMR contains the distinct structural information for each compound. Signals (c) and (d) show the substitution pattern of 2,6-dichlorophenyl in Figure 1:10.

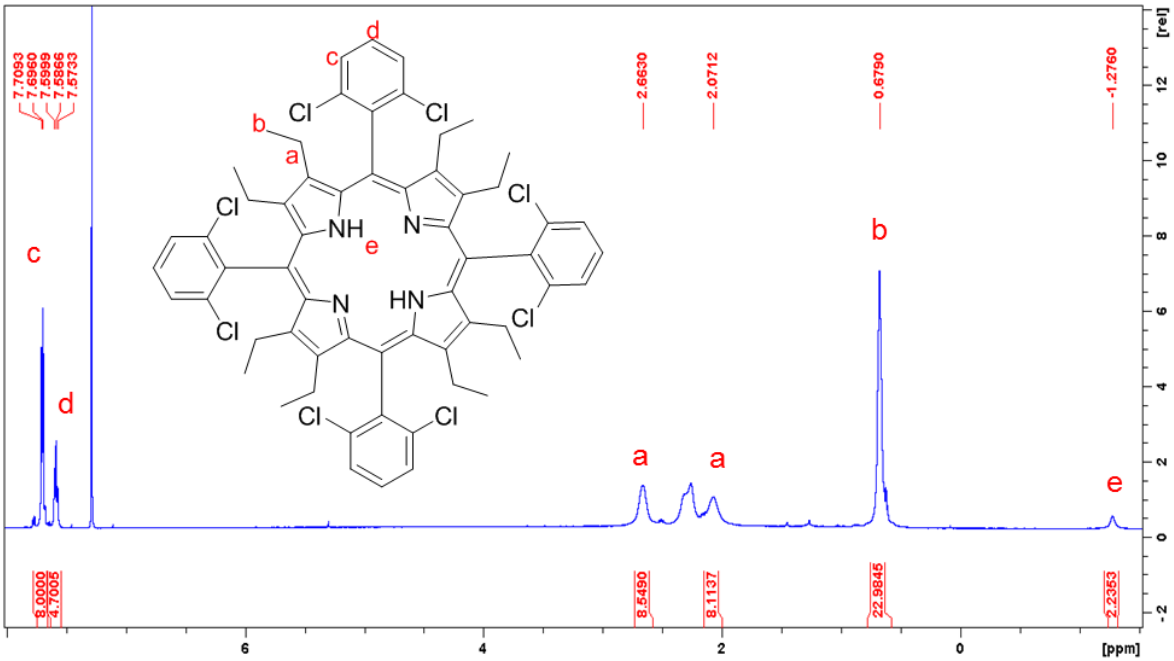

Figure 1:10: ^{1}H NMR spectrum of 5,10,15,20-tetrakis(2,6-dichlorophenyl)-2,3,7,8,12,13,17,18-octaethylporphyrin **1:6** in DMSO-d_6 (r.t.).

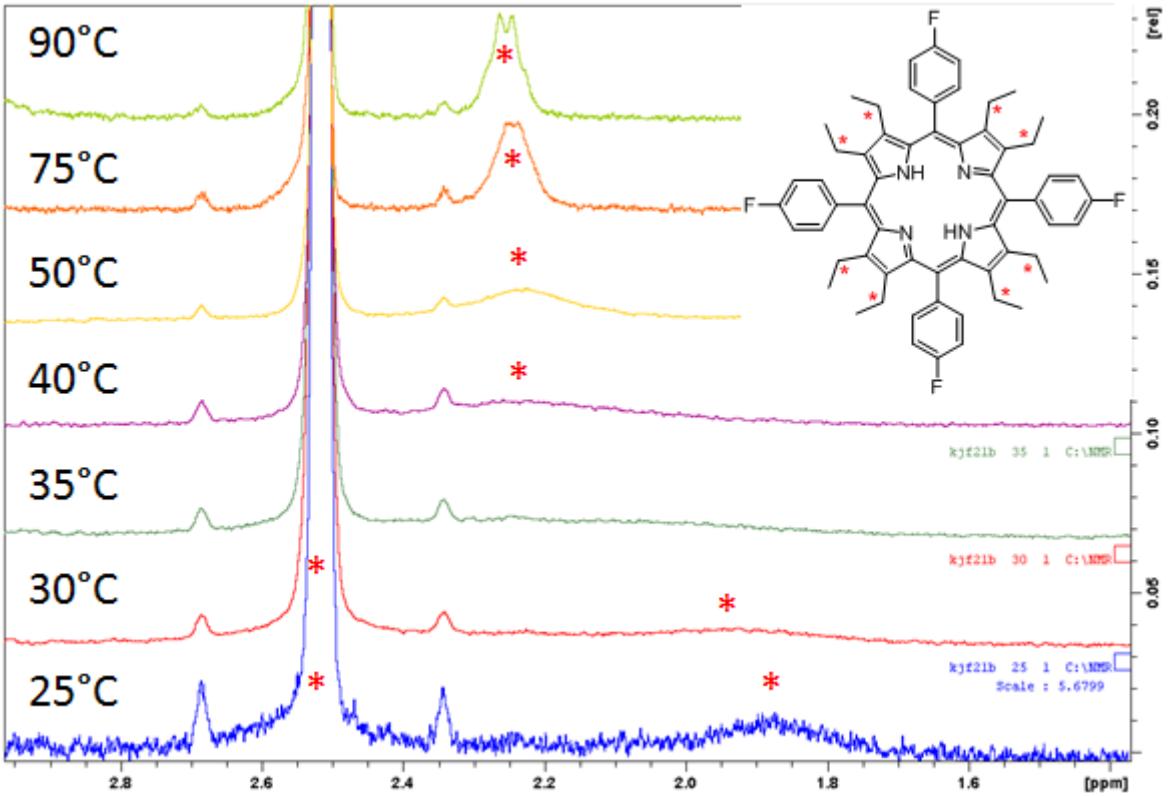

Figure 1:11: Variable temperature ^{1}H NMR spectroscopic study of 2,3,7,8,12,13,17,18-octaethyl-5,10,15,20-tetrakis(4-fluorophenyl)-porphyrin **1:1** in DMSO-d_6. In ascending order, the temperature at which each experiment was carried out is indicated on the right-hand side of the figure (25°C, 30°C, 35°C, 40°C, 50°C, 75°C, and 90°C). The CH_2 protons being examined in this experiment are indicated in the chemdraw and in each trace by a red '*'. At 25°C two distinct peaks are present one at 1.89 ppm and one overlapping with the DMSO signal at 2.50 ppm (this was confirmed in the 2D NMR). At 30-40°C the signals are hard to distinguish before they begin to coalesce at 50°C (2.25 ppm) with complete overlap of both signals and a sharper signal seen in the final two traces (75°C and 90°C).

Metal Insertion into OETArXP.

When choosing which metals to insert into the free base porphyrins there was one concern which had to be addressed. We did not want the metal to be the driving force for interactions either through an axial ligand as seen in the works of Golberg and co-workers or by metallophilic interactions.[109g] This was due to our initial design plan, which was to create an over cage structure. Either of the above mentioned would occupy the void we hoped to create and make this project futile. For this reason I focused on using metal which would be tetra-coordinating such as nickel(II), copper(II), and palladium(II).

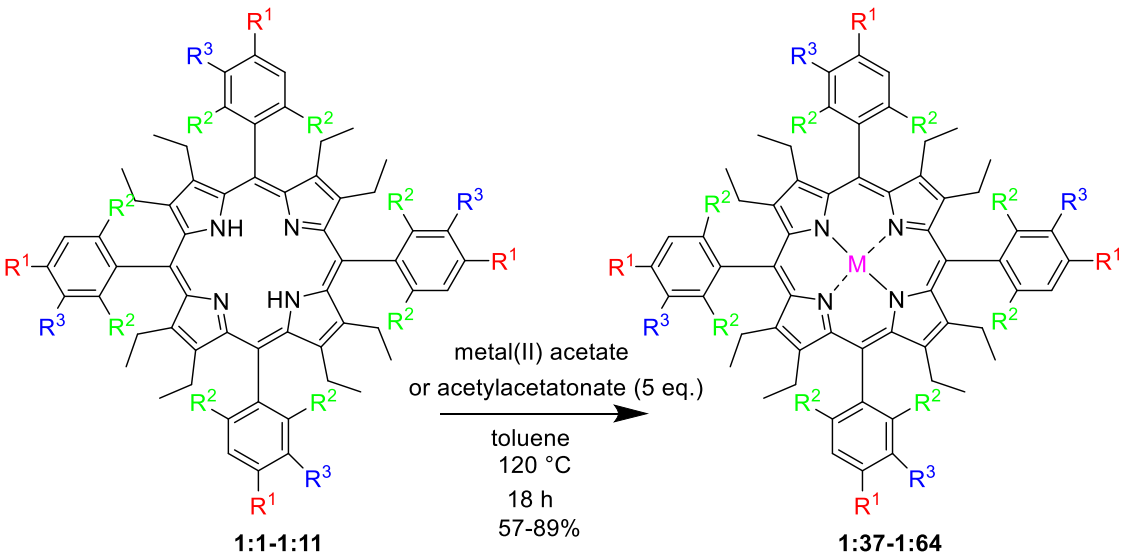

1:37 = R^1 = F; R^2 = H; R^3 = H; M = Ni(II) (72%)
1:38 = R^1 = F; R^2 = H; R^3 = H; M = Pd(II) (85%)
1:39 = R^1 = F; R^2 = H; R^3 = H; M = Cu(II) (89%)
1:40 = R^1 = Cl; R^2 = H; R^3 = H; M = Ni(II) (82%)
1:41 = R^1 = Cl; R^2 = H; R^3 = H; M = Pd(II) (63%)
1:42 = R^1 = Cl; R^2 = H; R^3 = H; M = Cu(II) (78%)
1:43 = R^1 = Br; R^2 = H; R^3 = H; M = Ni(II) (77%)
1:44 = R^1 = Br; R^2 = H; R^3 = H; M = Pd(II) (62%)
1:45 = R^1 = Br; R^2 = H; R^3 = H; M = Cu(II) (88%)
1:46 = R^1 = I; R^2 = H; R^3 = H; M = Ni(II) (85%)
1:47 = R^1 = I; R^2 = H; R^3 = H; M = Pd(II) (57%)
1:48 = R^1 = I; R^2 = H; R^3 = H; M = Cu(II) (85%)
1:49 = R^1 = H; R^2 = F; R^3 = H; M = Ni(II) (74%)
1:50 = R^1 = H; R^2 = F; R^3 = H; M = Cu(II) (80%)
1:51 = R^1 = H; R^2 = Cl; R^3 = H; M = Ni(II) (80%)
1:52 = R^1 = H; R^2 = Cl; R^3 = H; M = Pd(II) (63%)
1:53 = R^1 = H; R^2 = Cl; R^3 = H; M = Cu(II) (86%)
1:54 = R^1 = CN; R^2 = H; R^3 = H; M = Ni(II) (81%)
1:55 = R^1 = CN; R^2 = H; R^3 = H; M = Pd(II) (86%)
1:56 = R^1 = CN; R^2 = H; R^3 = H; M = Cu(II) (79%)
1:57 = R^1 = butyl; R^2 = H; R^3 = H; M = Ni(II) (81%)
1:58 = R^1 = TMS; R^2 = H; R^3 = H; M = Ni(II) (78%)
1:59 = R^1 = benzyloxy; R^2 = H; R^3 = H; M = Ni(II) (75%)
1:60 = R^1 = benzyloxy; R^2 = H; R^3 = H; M = Pd(II) (75%)
1:61 = R^1 = benzyloxy; R^2 = H; R^3 = H; M = Cu(II) (85%)
1:62 = R^1 = benzyloxy; R^2 = H; R^3 = R^1; M = Ni(II) (83%)
1:63 = R^1 = benzyloxy; R^2 = H; R^3 = R^1; M = Pd(II) (67%)
1:64 = R^1 = benzyloxy; R^2 = H; R^3 = R^1; M = Cu(II) (81%)

Scheme 1:7: Synthesis of metal(II) porphyrin compounds.

The synthesis of the metallated derivatives of OETArXP was achieved by the addition of nickel(II) acetylacetonate to a solution of **1:1** in toluene and heating to 120 °C for 18 h. It was found by TLC analysis that complete conversion did not occur. However, on the addition of a further 2.5 eq. of nickel(II) acetylacetonate, the starting material was consumed. The purification of the compound involved passing the crude material through a plug of silica gel using CH_2Cl_2 as an eluent. The compounds were subsequently crystallised from CH_2Cl_2 and MeOH. The solution was then decanted, and the resulting crystals were dried under high vacuum and collected to afford compound **1:37**. This procedure was repeated using the appropriate metal(II) acetate or metal(II) acetylacetonate to yield compounds **1:38–1:64** (Scheme 1:7). The synthesis of compound **1:43** was previously reported by Schindler *et al*.[123a]

X-ray Crystallographic Studies of Nonplanar Porphyrins.

General Remarks.

Crystal packing studies of highly substituted nonplanar porphyrins is a well-established field.[72a, 86a, 86c, 94a, 96a, 96d, 99b, 105, 114, 125] However, detailed studies in the crystal engineering of nonplanar porphyrins have not been conducted to date. An investigation into the intermolecular and crystal packing effects of both halogenated and non-halogenated substituted derivatives was undertaken on the synthesised OETArXP (**1:1–1:12**) and the metalloporphyrin derivatives (**1:37–1:64**). Single crystals of compounds **1:1–1:12** proved difficult to obtain with only the free base derivative **1:6A** (where A denotes the $CDCl_3$ solvated versions) of reasonable quality. However, the metalloporphyrin derivatives (**1:37–1:64**) provided 13 samples of sufficient quality for X-ray diffraction, **1:37**, **1:38**, **1:40**, **1:43B**, **1:45**, **1:49**, **1:51A**, **1:52**, **1:53**, **1:53A**, and **1:54** (where 'A' denotes the $CDCl_3$ solvated versions and 'B' denotes the CH_2Cl_2 solvate version). All structures included in this section were collected as part of this thesis by myself.

As stated previously in the discussion of the ^{1}H NMR spectra of compound **1:6**, the CH_2 protons of the ethyl groups can be seen as a split signal. In comparison to the solid state, in the crystal structure, the two distinct orientations of the ethyl groups can be seen. The first example is where the ethyl groups at C2, C3, C12 and C13 are pointing above the plane and the ethyl groups at C7, C8 C17 and C18 are pointing below the plane as seen in compounds **1:54**. The second most common orientation is where the ethyl groups at C2, C7, C12 and C17 are pointing above the plane and C3, C8, C13 and C18 are pointing below the plane as seen in compound **1:37**. This is not a strict rule, as other conformations are possible as can be seen in compound **1:40**. This is in-line with much earlier observations varied out by Gentemann *et al.*[126] In this study the authors calculated the activation barrier for highly substituted porphyrins through the use of variable temperature NMR experiment. As a result, it is not evident at any stage in the crystal structure that all ethyl groups point in the same direction, which results in the signals splitting into two signals in the ^{1}H NMR spectra. The X-ray structures provide a graphical representation of this interaction. It can be seen from the crystal structures (Figure 1:12) that the porphyrin rings are severely distorted. The tilt angles of the pyrrole rings are larger compared to planar porphyrins as shown previously in Figure 1:2.

This is a result of the higher degree of distortion in the 24-atom macrocyclic ring. The phenyl groups exhibit a similar tilt angle from the 24-atom least-squares plane of 38–59˚ with the largest deviation associated with compound **1:52** (47.1–59.0°). The average N–metal bonds are comparable with other nonplanar porphyrins found in the literature for both Cu(II) and Ni(II) complexes, Table 1:1.[86a, 86b]

The conformational analysis of porphyrins requires the determination of specific geometrical parameters complemented by a visual description. The simplest depiction of this is the displacement of atoms from the 24-atom least-squares plane as a skeletal deviation plot (Figure 1:15). It should be noted that atoms, which deviate the most from the 24-atom least-squares plane, are the *β*-carbons (Figure 1:15). The *β*-carbons are featured in an alternating pattern above and below the 24-atom macrocycle least-squares plane and the nitrogen atoms are all close to the mean plane. As previously stated this results in a saddle type porphyrin structure.

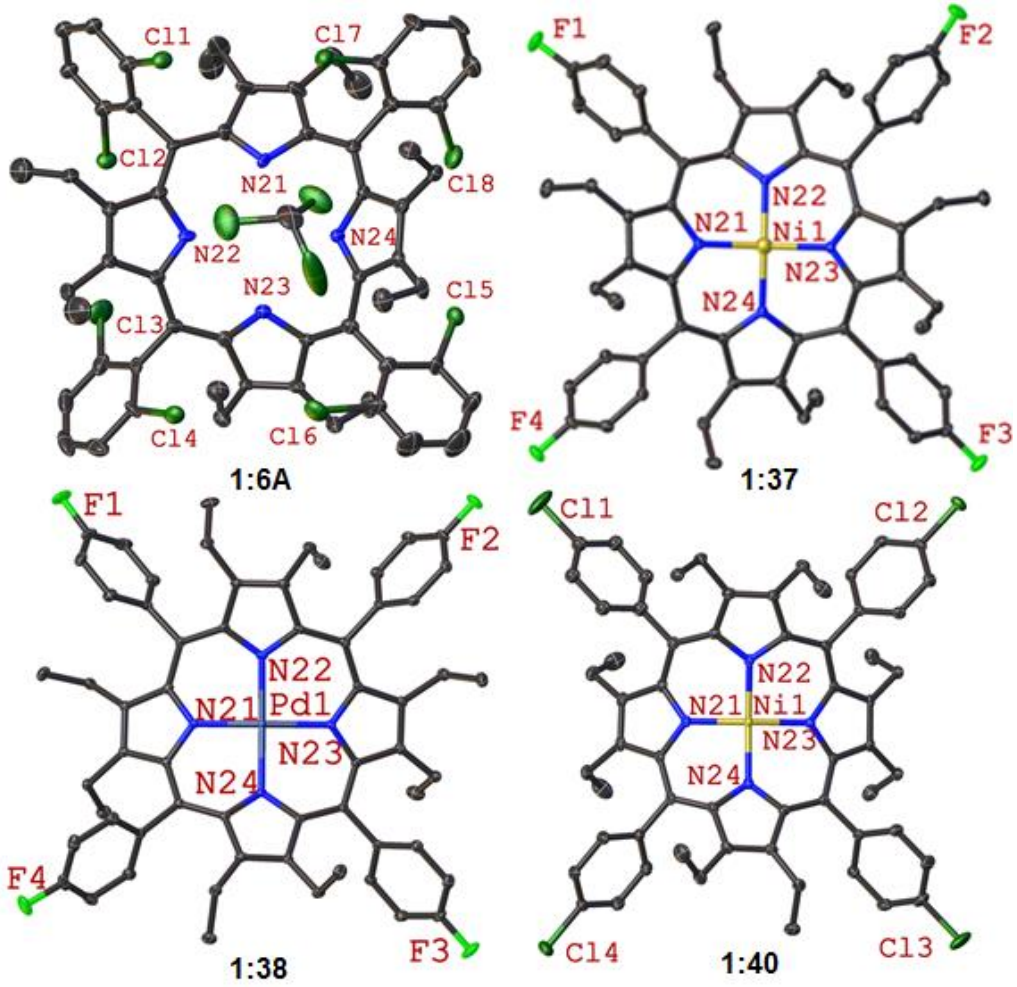

Figure 1:12: Molecular structure of OETArXPs (thermal displacement given as 50% probability). Hydrogen atoms, deuterium atoms and minor disordered moieties have been omitted for clarity.

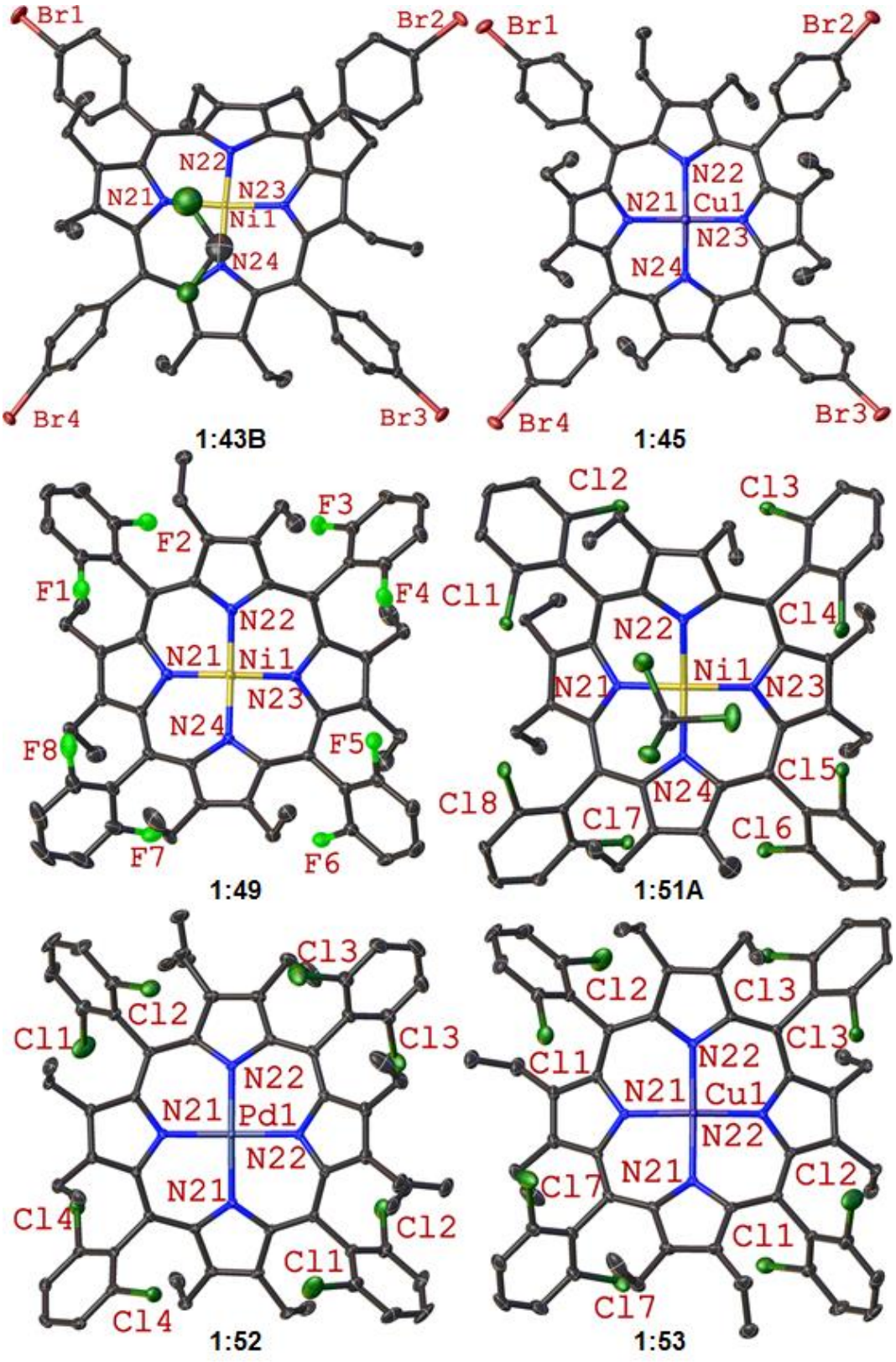

Figure 1:12 (continued): Molecular structure of OETArXPs (thermal displacement given as 50% probability). Hydrogen atoms and minor disordered moieties have been omitted for clarity.

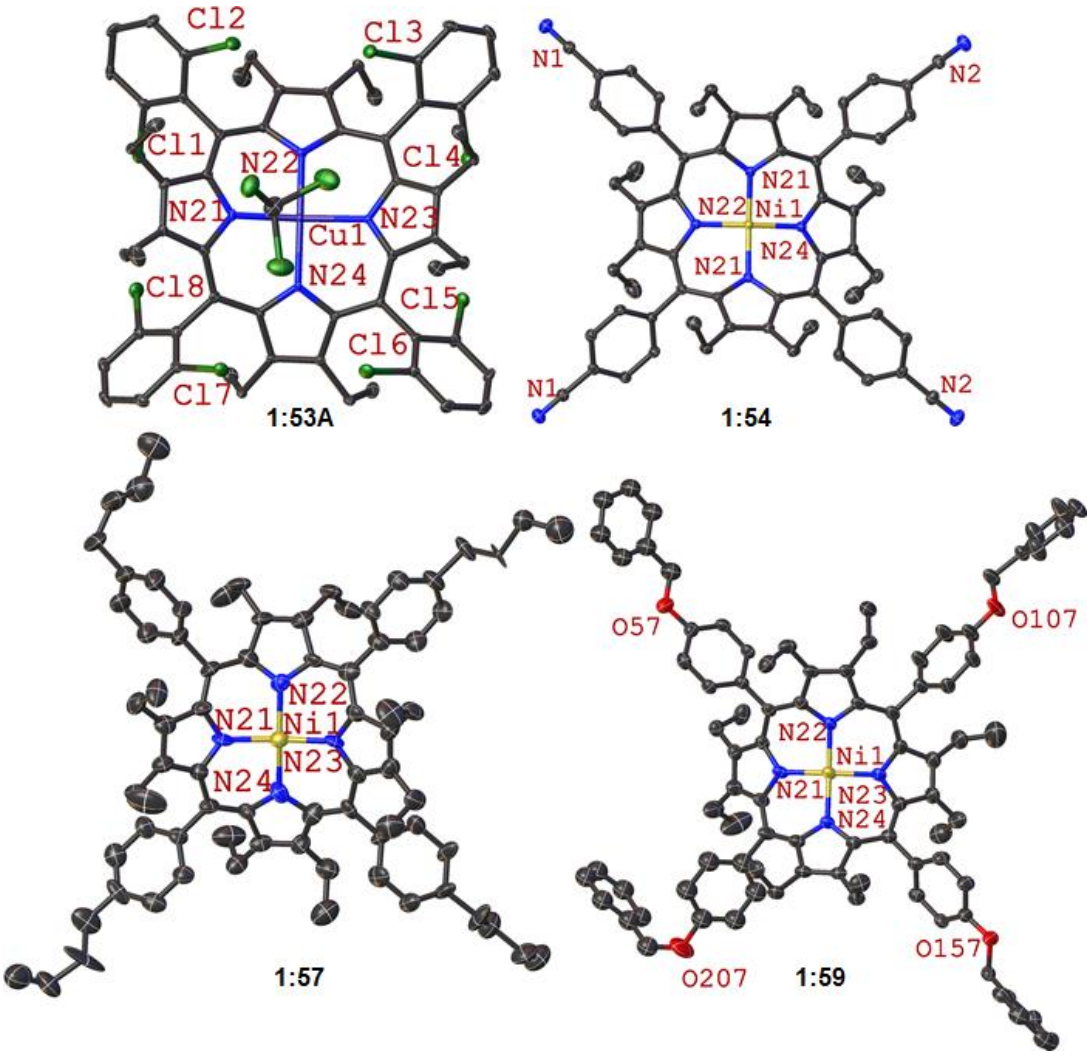

Figure 1:12 (continued): Molecular structure of OETArXPs (thermal displacement given as 50% probability). Hydrogen atoms, deuterium atoms and minor disordered moieties have been omitted for clarity.

Due to the bulky aryl groups present, steric crowding favours this conformation. This saddle type distortion is also evident in the molecular structures shown in Figure 1:12. In comparison to previous studies conducted within the group on unsymmetrical decasubstituted OEP structures, the porphyrin structure presented here show similar overall out-of-plane contributions for saddle distorted porphyrins, with regards to the 24-atom least-squares plane, Figure 1:16.[86c] There are two other features of these compounds that are general to all of these structures. These are the effects that metals and solvents have on the crystal packing within this series. While the structures will be discussed in individual detail it feels prudent to highlight these effects to avoid needless repetition. Changing the metal(II) centre has only marginal effects on the structure of the porphyrin rings. N–metal bond lengths are increased depending on the size of the metal, however, this has little to

no effect on the other structural parameters highlighted in Table 1:1. This is seen clearly in the crystal packing of the structures of **1:37** and **1:38** (Figure 1:13). Both compounds are structurally similar with no solvent molecules presented. The only difference between the structures is the metal(II) centre [Ni(II) (**1:37**) and Pd(II) (**1:38**)] and as such, both compounds result in identical packing patterns.

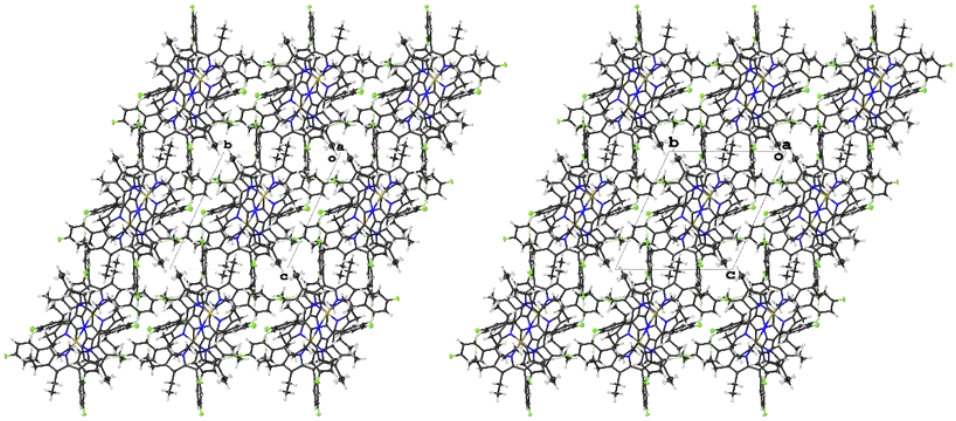

Figure 1:13: Crystal packing image (looking down the *a*-axis) of compounds **1:37** (left) and **1:38** (right) showing the similarities between the crystal packing of two alternate metal complexes of OETArXP structures. Thermal displacement is given at 50% probability.

Solvent inclusion has much more of an effect on the porphyrin structures. This is clearly seen in the structure of **1:53** and **1:53A** in which the inclusion of solvent results in a small decrease in the N–Metal bond lengths. The phenyl ring tilt angles show a ~7° decrease and pyrrole tilt angles show a ~18° decrease as a result of including the solvent. However, the most obvious difference is seen in the crystal packing of **1:53** and **1:53A**, in which the packing pattern alters significantly from the tightly stacked structure of **1:53** to the much looser patter on **1:53A** in which the porphyrin layers are separated by a solvent channel (Figure 1:14).

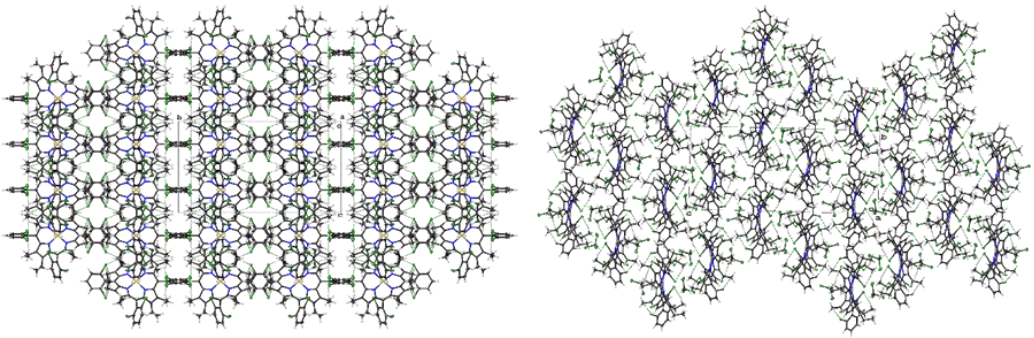

Figure 1:14: Crystal packing image (looking down the *a*-axis) of compounds **1:53** (left) and **1:53A** (right) showing the differences caused by the inclusion of solvent to OETArXP structures. Thermal displacement is given at 50% probability.

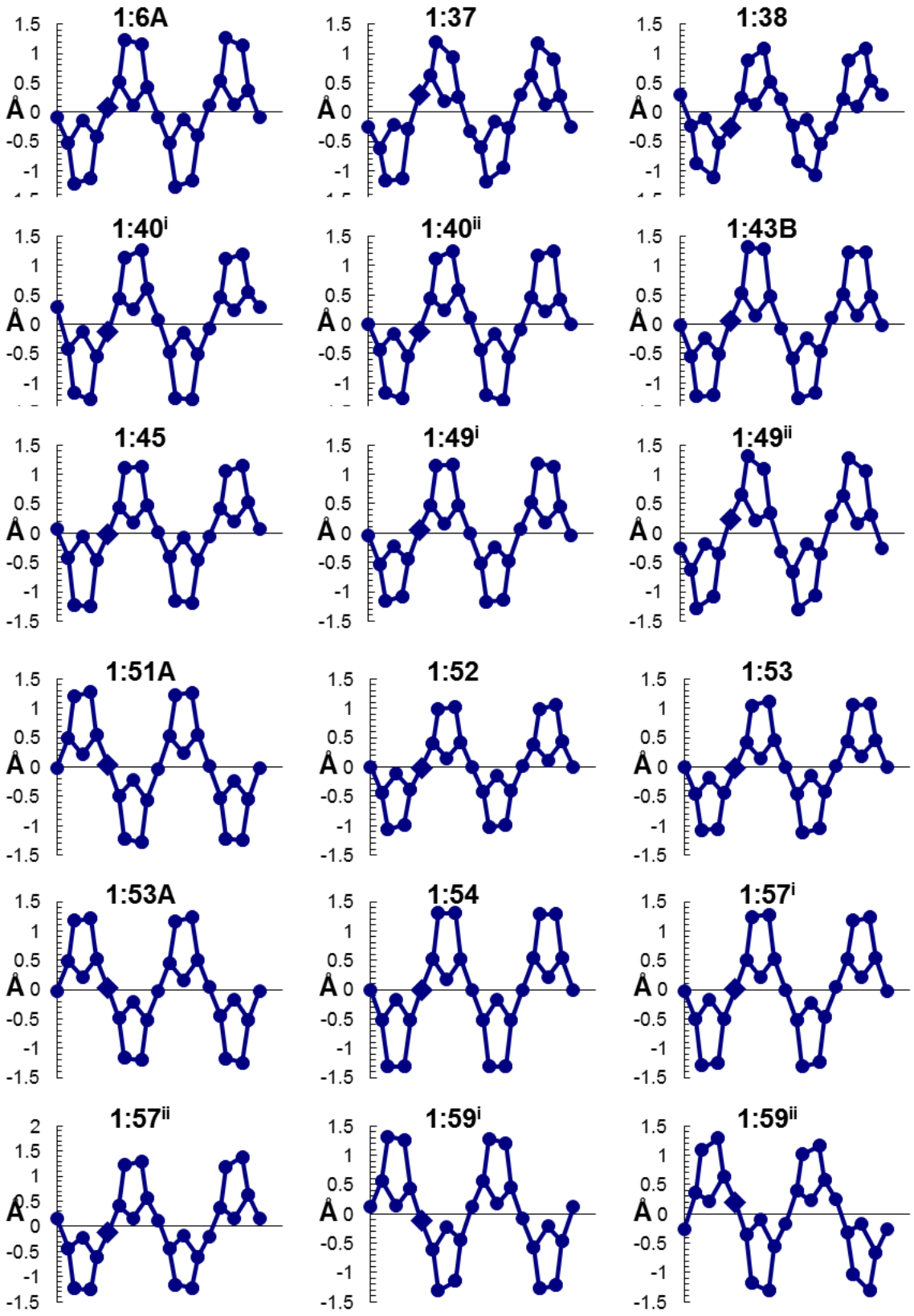

Figure 1:15: View of skeletal deviations plot (C20 to C20) from the crystal structure of all determined compounds. The structures that have more than one molecule are indicated by (i) for the first macrocycle ring and (ii) for the second macrocycle ring. Atoms deviations are calculated using the 24-atom least-squares plane.

Table 1:1: Selected geometrical parameters of OETArXP crystal structures.

Compound	1:6A	1:37	1:38	1:40[i]	1:40[ii]	1:43B
Pyrrole tilt angle (°)						
N21	21.8(3)	25.2(4)	25.9(7)	30.5(7)	29.7(7)	27.3(7)
N22	30.5(3)	26.4(4)	24.6(7)	26.7(6)	26.6(6)	32.3(8)
N23	31.2(3)	26.5(4)	23.9(6)	31.5(6)	30.5(6)	27.4(8)
N24	30.8(3)	25.2(4)	26.0(6)	25.5(7)	28.1(7)	30.1(8)
Phenyl ring tilt angle (°)						
C5	52.3(3)	54.6(4)	56.0(6)	45.6(11)	45.0(7)	38.5(8)
C10	43.5(3)	53.7(4)	52.7(7)	40.1(6)	42.0(6)	38.7(8)
C15	42.0(3)	49.7(4)	50.2(7)	42.7(6)	40.4(6)	56.8(6)
C20	47.7(3)	51.6(4)	53.4(6)	46.4(6)	46.9(6)	48.7(8)
N-Metal bond length (Å)						
N21	n/a	1.913 (1)	2.008(2)	1.923(2)	1.917(2)	1.896(2)
N22	n/a	1.917 (1)	2.007(2)	1.903(2)	1.904(2)	1.914(3)
N23	n/a	1.927 (1)	2.013(2)	1.914(2)	1.912(2)	1.892(2)
N24	n/a	1.923 (1)	2.020(2)	1.903(2)	1.905(2)	1.917(2)

[a] bond length or angle generated and calculated over symmetry.

Table 1:1 (continued): Selected geometrical parameters of OETArXP crystal structures.

Compound	1:45	1:49[i]	1:49[ii]	1:51A	1:52	1:53
Pyrrole tilt angle (°)						
N21	32.8(11)	24.7(6)	28.6(6)	28.6(5)	25.1(7)	46.6(12)
N22	26.1(11)	27.0(6)	28.8(6)	28.8(10)	23.5(8)	47.9(12)
N23	30.1(11)	25.5(6)	29.3(6)	28.1(10)	23.5(8)[a]	44.6(12)
N24	24.9(11)	27.6(6)	29.4(6)	27.6(10)	25.1(7)[a]	45.0(13)
Phenyl ring tilt angle (°)						
C5	40.8(11)	53.7(6)	47.2(6)	44.2(10)	59.0(8)	58.2(6)
C10	46.6(10)	45.9(6)	53.0(6)	44.3(10)	51.0(10)	46.9(8)
C15	46.5(10)	47.3(6)	48.0(7)	46.0(10)	59.0(8)[a]	58.2(6)[a]
C20	41.6(10)	47.2(7)	49.9(7)	47.4(10)	47.1(10)	49.7(9)
N-Metal bond length (Å)						
N21	1.975(4)	1.908(2)	1.902(2)	1.905(3)	2.010(2)	1.977(17)
N22	1.970(4)	1.923(2)	1.886(2)	1.904(3)	2.014(2)	1.973(17)
N23	1.982(4)	1.912(2)	1.902(2)	1.902(3)	2.010(2)	1.973(17)
N24	1.961(3)	1.923(2)	1.903(2)	1.896(3)	2.014(2)	1.977(17)

[a] bond length or angle generated and calculated over symmetry.

Table 1:1 (continued): Selected geometrical parameters of OETArXP crystal structures.

Compound	1:53A	1:54	1:57[i]	1:57[ii]	1:59[i]	1:59[ii]
Pyrrole tilt angle (°)						
N21	27.4(13)	31.9(4)	30.8(4)	28.0(5)	37.7(13)	28.2(12)
N22	26.9(13)	31.8(6)	28.9(4)	31.2(4)	28.4(12)	32.3(12)
N23	29.0(12)	31.9(4)	29.7(4)	28.0(5)	29.8(13)	24.2(16)
N24	29.1(12)	30.1(6)	27.2(4)	31.8(4)	29.1(12)	29.5(12)
Phenyl ring tilt angle (°)						
C5	46.6(12)	38.2(4)	42.8(5)	41.6(6)	36.7(11)	42.7(2)
C10	47.9(12)	38.2(4)[a]	34.8(4)	39.5(4)	46.5(16)	50.1(12)
C15	44.6(12)	40.0(4)[a]	37.2(5)	37.5(5)	42.9(12)	53.8(13)
C20	45.0(13)	40.0(4)	37.0(4)	30.1(5)	34.7(2)	42.9(11)
N-Metal bond length (Å)						
N21	1.967(4)	1.907(13)	1.918(12)	1.887(13)	1.911(4)	1.908(3)
N22	1.964(4)	1.903(18)	1.919(12)	1.900(14)	1.898(4)	1.919(3)
N23	1.963(4)	1.907(13)	1.884(12)	1.892(13)	1.902(4)	1.907(4)
N24	1.960(4)	1.902(18)	1.898(12)	1.895(12)	1.901(4)	1.903(3)

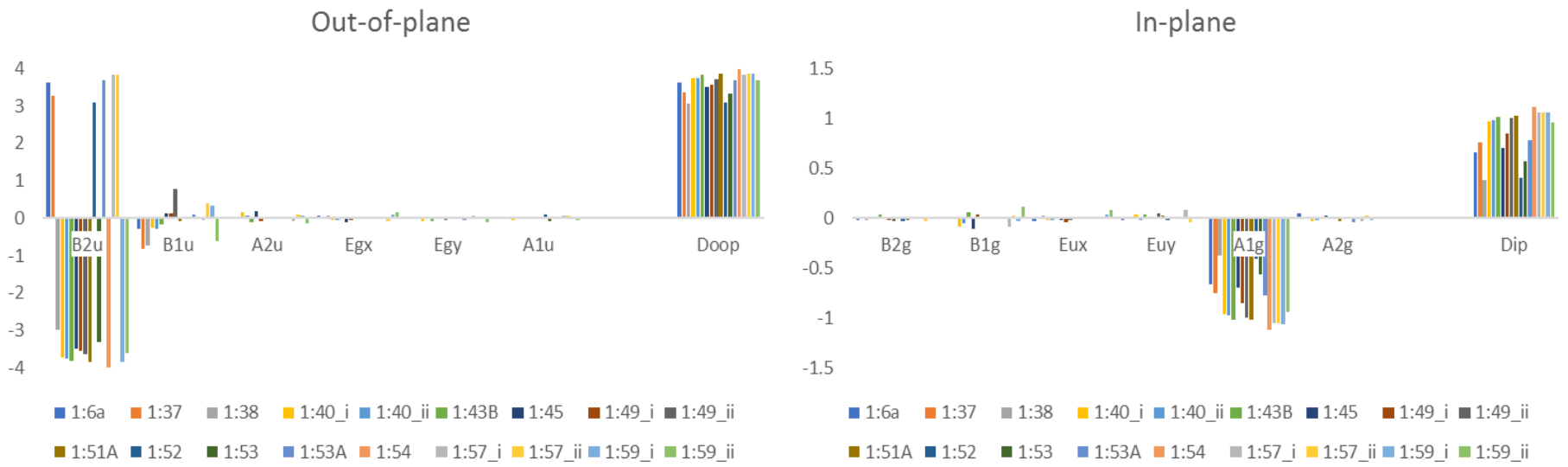

Figure 1:16: Out-of-plane (left) and in-plane (right) distortion modes of the OETArXP crystal structures.

Increasing the Size of the Halogen.

As outlined previously the main objective of this project was the crystal engineering of highly substituted porphyrin species for the investigation the influence of substituent type and pattern on crystal packing. With this in mind, the increase in halogen size is of particular interest, as larger halogens opening up the possibility towards a more dynamic crystal packing, with the size of the atom influencing the packing pattern achieved. Five crystals structures (**1:37**, **1:38**, **1:40**, **1:43B**, and **1:45**) have been determined in this series with fluorine being the smallest and bromine being the largest halogen atoms included.

The structure of **1:37** shows several interactions between the hydrogen and fluorine atoms (Figure 1:17). The first of these is the reciprocated C–F···H contact between the F1···H17E (2.447(1) Å, 102.7(1)°) (Figure 1:17a). This tethers the *para*-fluoro atom to the ethyl group of the porphyrin ring. The second contact F2···H202 (2.447(1) Å, 102.7(1)°) binds the *para*-fluoro atom to the aromatic hydrogens on the opposite side of the porphyrin ring (Figure 1:17b). This has the effect of forming a cupping type pattern between overlapping porphyrin molecules involving three macrocycle rings. In addition, there is a type of edge-on interaction of porphyrin rings, facilitated by a C–F···H contact (2.442(1) Å, 120.4(1)°) between the F3···H106, forming a tight network between the macrocycle planes.

These interactions can also be highlighted using fingerprint plots and Hirshfeld surfaces (Figure 1:18), in which the H···F contacts are indicated by the coloured spots and can be seen to be centred aryl substitutions. These contacts combined, result in a tight packing pattern with the overlapped cupping and the edge-on interactions contributing towards the presence of a little space between the porphyrin layers as seen in Figure 1:19.

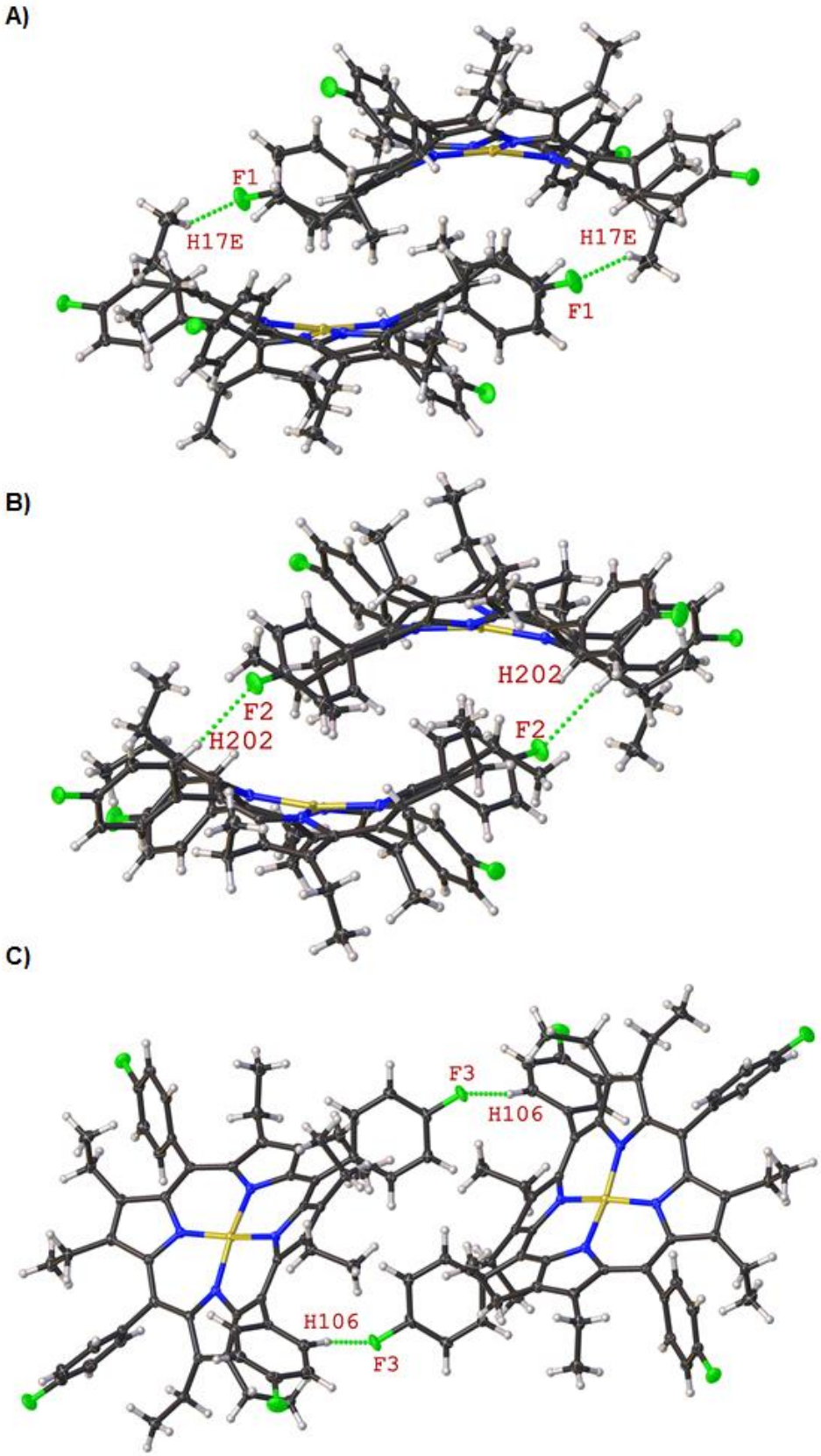

Figure 1:17: Expanded view of compound **1:37** showing the H···F contacts involved in the face-to-face (A and B, C–F1···H17E (2.447(1) Å, 102.7(1)°) and C–F2···H202 (2.447(1) Å, 102.7(1)°)) and edge-on interactions (C, C–F3···H106 (2.442(1) Å, 120.4(1)°)). Thermal displacement is given at 50% probability. Interactions are indicated by green dashed lines.

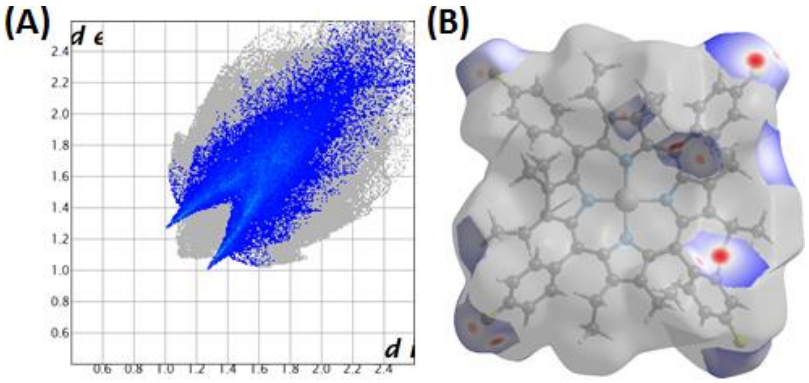

Figure 1:18: Fingerprint plots (A) and Hirshfeld surfaces (B) of compound **1:37** showing the H···F interactions which occupy 19.5% of total surface contacts. H···F interactions represented in the Hirschfeld surface (B) are coloured blue and red. The grey areas highlight all other contacts which are not the focus of this discussion.

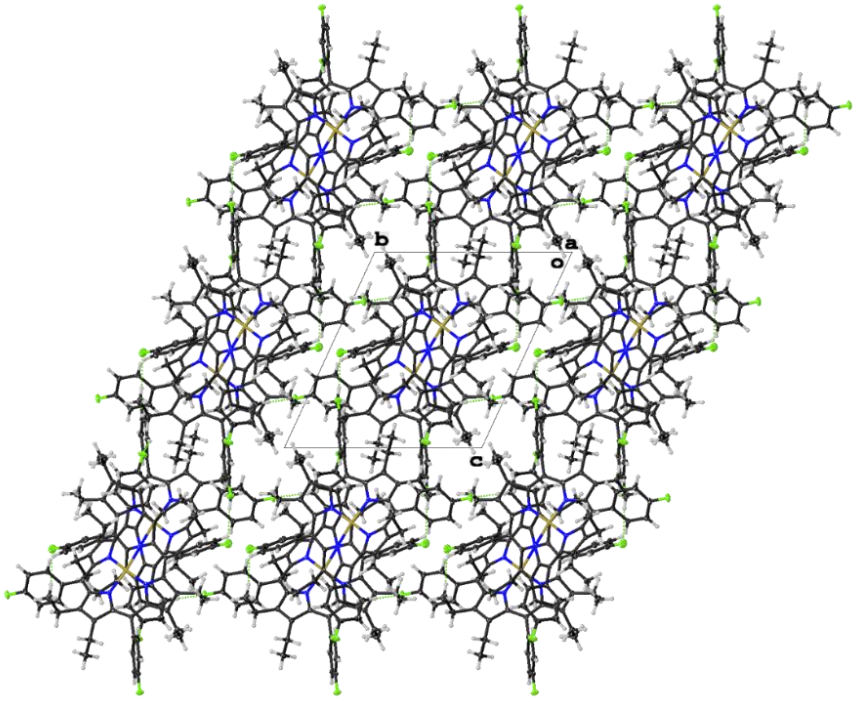

Figure 1:19: Crystal packing of compound **1:37** looking down the *a*-axis. Thermal displacement is given at 50% probability.

The structure of **1:38** shows similar types of interactions as seen in compound **1:37**, in which the C–H···F interaction of the cupping moiety is between F1···H13C (2.502(2) Å, 107.5(1)°) and F4···H160 (2.507(2) Å, 136.1(1)°) this, as before, binds three of the macrocycles in the aforementioned cupping pattern (Figure 1:20). The edge-on interaction is seen between F3···H206 (2.435(2) Å, 118.6(1)°) and results in a similar tight network between the macrocycle planes as with compound **1:37** (Figure 1:20). This is validated by comparing the fingerprint plots and Hirshfeld surfaces (Figure 1:21) which are identical to that of compound **1:37** with most of the H···F interactions centred on the aryl substitutes. While looking down the *a*-axis of

the crystal packing (Figure 1:22) the offset overlapped pattern caused by the cupping interaction between the porphyrin is quite evident and the edge-on interactions hold the porphyrin macrocycle in almost rhombic shape.

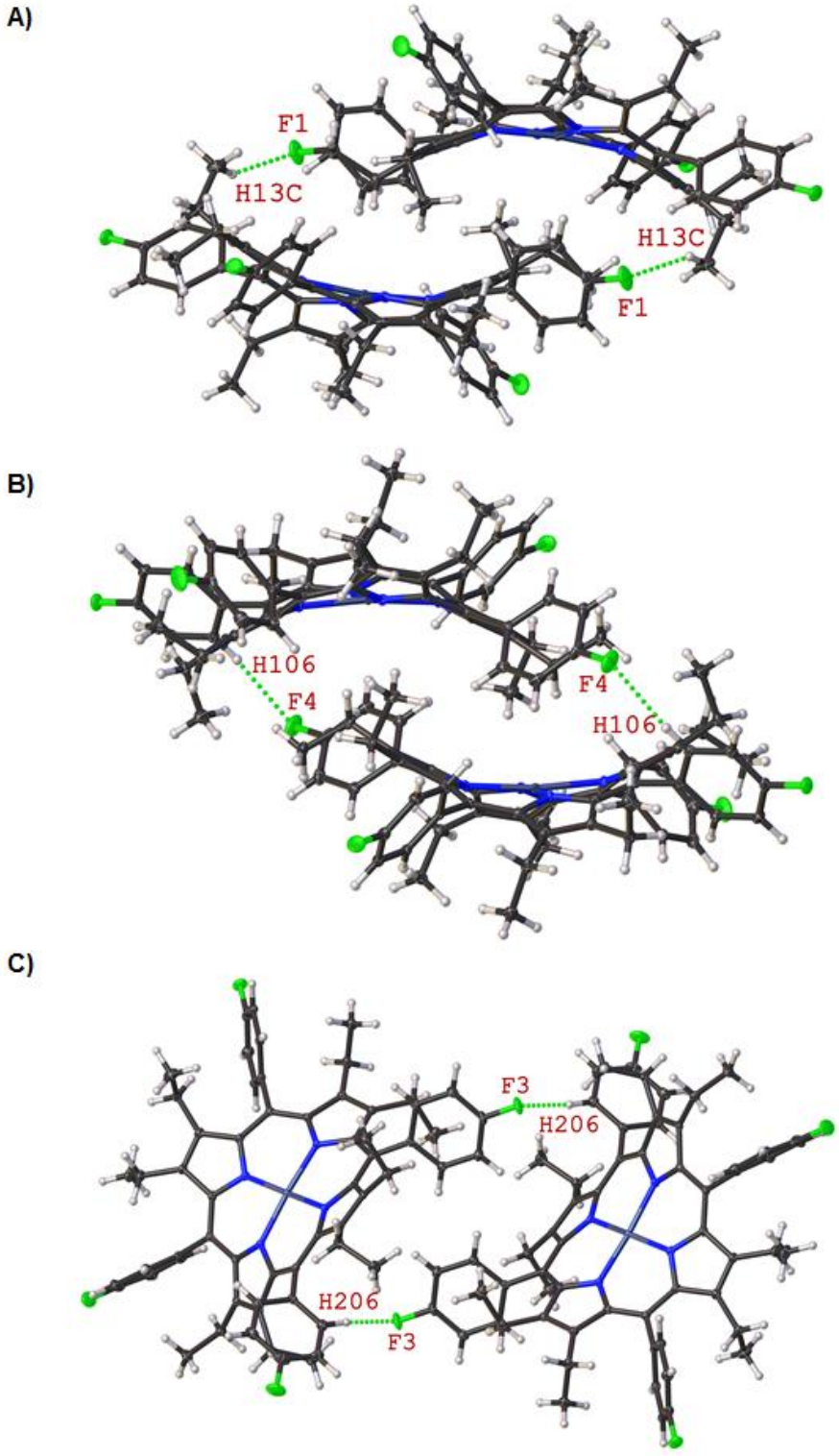

Figure 1:20: Expanded view of compound **1:38** showing the H···F contacts involved in the face-to-face (A and B, C–F1···H13C (2.502(2) Å, 107.5(1)°) and C–F4···H160 (2.507(2) Å, 136.1(1)°)) and edge-on interactions (C, C–F3···H206 (2.435(2) Å, 118.6(1)°)). Thermal displacement is given at 50% probability. Interactions are indicated by green dashed lines.

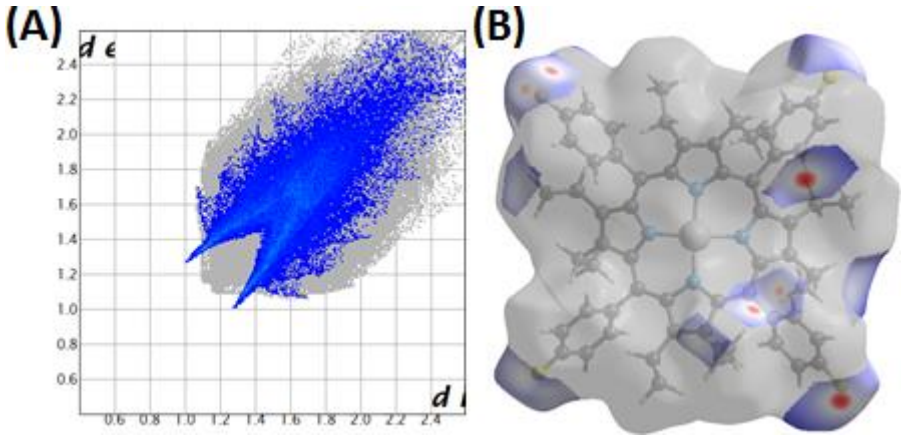

Figure 1:21: Fingerprint plots (A) and Hirshfeld surfaces (B) of compound **1:38** showing the H···F interactions which occupy 19.5% of total surface contacts. H···F interactions represented in the Hirschfeld surface (B) are coloured blue and red. The grey areas highlight all other contacts which are not the focus of this discussion.

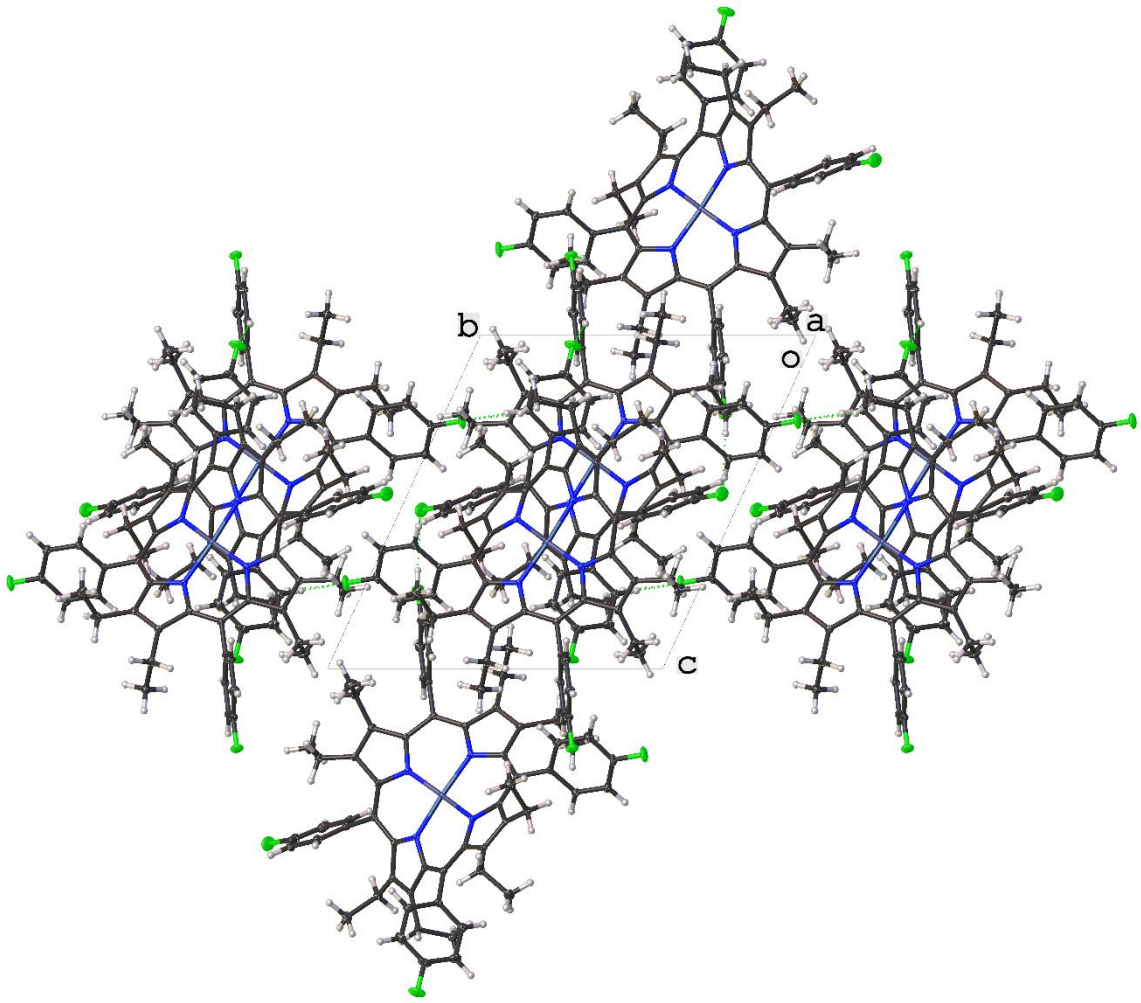

Figure 1:22: Crystal packing of compound **1:38** looking down the *a*-axis. Thermal displacement is given at 50% probability.

The structure of **1:40** marks the first increase in the size of the halogen. This results in quite a dramatic change in the nature of halogen–hydrogen interactions. There

are no interactions involved in the overlapped cupping pattern seen in the fluorine counterparts and the reciprocal nature of the interactions has now been eliminated. This is seen through the two Cl···H interactions between the Cl2_2···H17E_1 (2.864(7) Å, 97.9(8)°) and Cl2_1···H17D_2 ((2.854(7) Å, 133.3(8)°). This forms a linear network of Cl···H contacts between the two independent molecules which are repeated throughout the structure (Figure 1:23). The Hirshfeld surface analysis and the fingerprint plots (Figure 1:24) show that most of the Cl···H interactions between the porphyrin macrocycles are directed towards the ethyl groups and the edge of the porphyrin. This is different from the fluorine derivatives above where the F···H interactions favoured the aryl moiety. This minor change appears to have a profound change in the crystal packing of compound **1:40**. As seen in Figure 1:25, the cupping pattern observed previously in the fluorine series is now combined with face-to-face layered type pattern. The first two rows of porphyrins form a channel with the next layer partaking in cupping pattern (Figure 1:25). This pattern is repeated through the crystal packing in a 2×2 network looking down the *b*-axis.

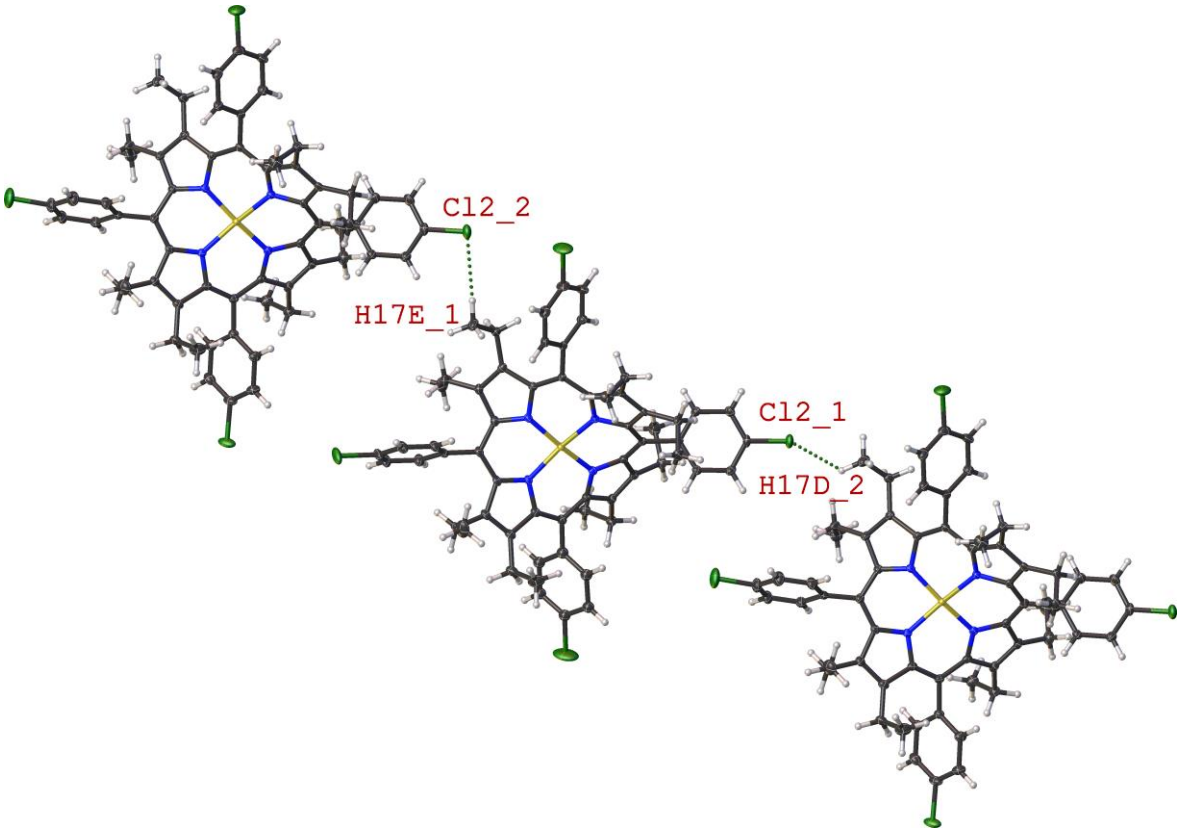

Figure 1:23: Expanded view of compound **1:40** showing the H···Cl contacts involved in the edge-on interactions C–Cl2_2···H17E_1 (2.864(7) Å, 97.9(8)°) and C–Cl2_1···H17D_2 ((2.854(7) Å, 133.3(8)°). Thermal displacement is given at 50% probability. Interactions indicated by green dashed lines.

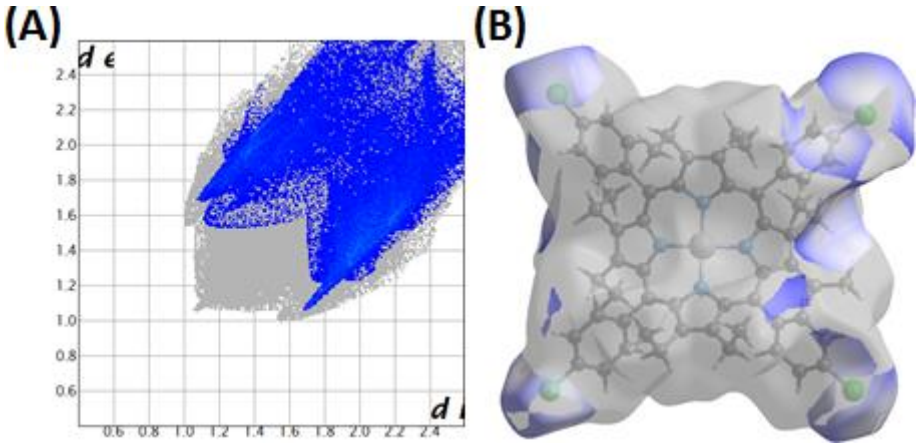

Figure 1:24: Fingerprint plots (A) and Hirshfeld surfaces (B) of compound **1:40** showing the H···Cl interactions which occupy 23.3% of total surface contacts. H···Cl interactions represented in the Hirschfeld surface (B) are coloured blue. The grey areas highlight all other contacts which are not the focus of this discussion.

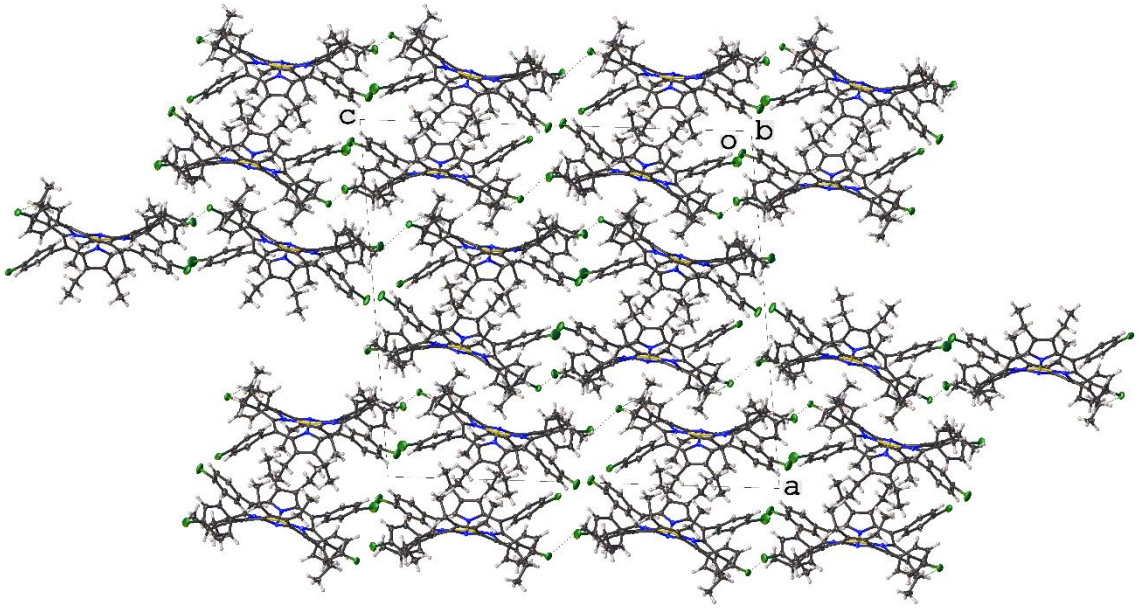

Figure 1:25: Crystal packing of compound **1:40** looking down the *b*-axis. Thermal displacement is given at 50% probability.

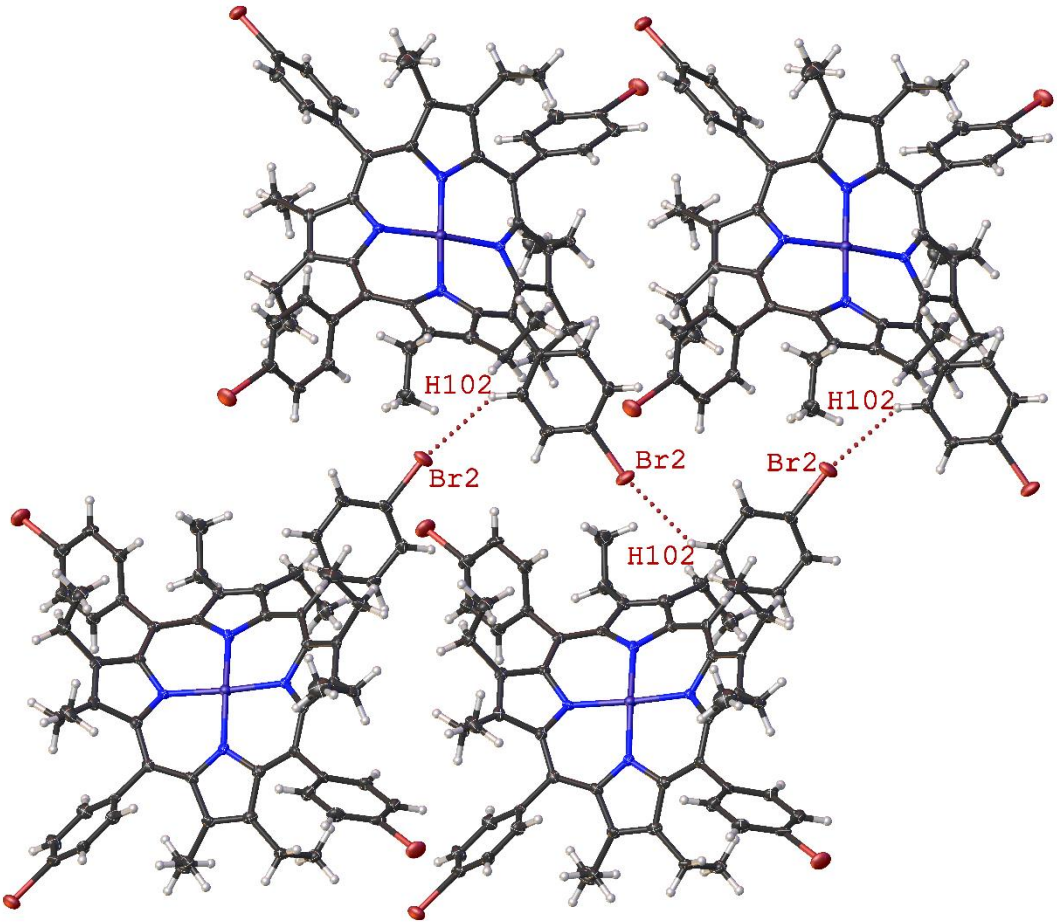

Figure 1:26: Expanded view of compound **1:45** showing H···Br intermolecular contacts (C–Br2···H102 (3.026(5) Å, 159.9(1)°)) involved in the edge-on interactions. Thermal displacement is given at 50% probability. Interactions are indicated by red dashed lines.

The inclusion of a bromine atom marks the final increase in halogen size. There are two structures involved in this section, compound **1:45** and **1:43B**. For the Cu(II) derivative, compound **1:45**, the first interaction is between C–Br2···H102 (3.026(5) Å, 159.9(1)°) (Figure 1:26) and results in a Br···H network between the *para*-bromine of one porphyrin macrocycle and the *ortho*-hydrogen of the next porphyrin ring in a head-to-head pattern. This is coupled with a second Br···H contact between C–Br2···H155 (3.051(6) Å, 98.2(1)°) which forms an orthogonal orientation between the porphyrin macrocycles, partnered with a face-to-face interaction between the two hydrogen contributing porphyrin rings (Figure 1:27). The final short contact of note is that between C–Br2···Br3 (3.867(8) Å, 106.4(1)°) which is reciprocated between porphyrin rings and aids in forming linear sheets of repeating porphyrin head-to-head dimers (Figure 1:27). Looking at the Hirshfeld surfaces and fingerprint plots (Figure 1:28) it can be seen that most of the Br···H interactions are centred on the aryl groups with little indication of any ethyl group contribution to such

interactions. The Br···H interactions resemble the fluorine series in character more than that of the chlorine series above but indicate a strong preference for the aromatic portion of the porphyrin macrocycle rather than the alkyl. The crystal packing of compound **1:45** resembles that of compound **1:40**, where the face-to-face channels of porphyrins coupled with the next layer forming the cupping pattern, appears to be inherent for this class of compound, Figure 1:29. What is of high interest is the arrangement of the Br···H and Br···Br interactions as they are placed throughout the crystal system as a whole. From Figure 1:29, it is clear that Br···Br interactions are strictly between the channel section of the packing arrangement. Also, the Br···H interactions are the driving force behind that of the cupping pattern is seen in this series forming quite an elaborate mesh-like network throughout the crystal packing.

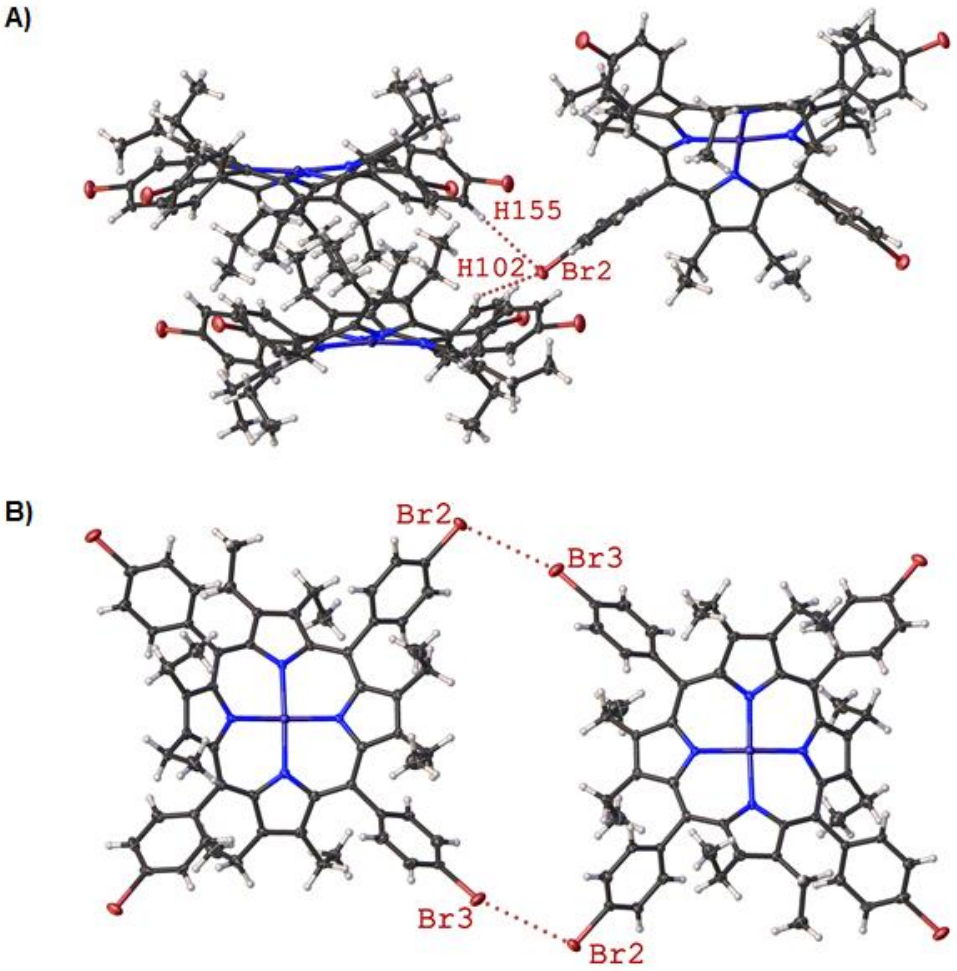

Figure 1:27: Expanded view of compound **1:45** showing H···Br (A, C–Br2···H102 (3.026(5) Å, 159.9(1)°) and C–Br2···H155 (3.051(6) Å, 98.2(1)°)) and Br···Br (B, C–Br2···Br3 (3.867(8) Å, 106.4(1)°)) intermolecular contacts involved in the edge-on interactions. Thermal displacement is given at 50% probability. Interactions indicated by red dashed lines.

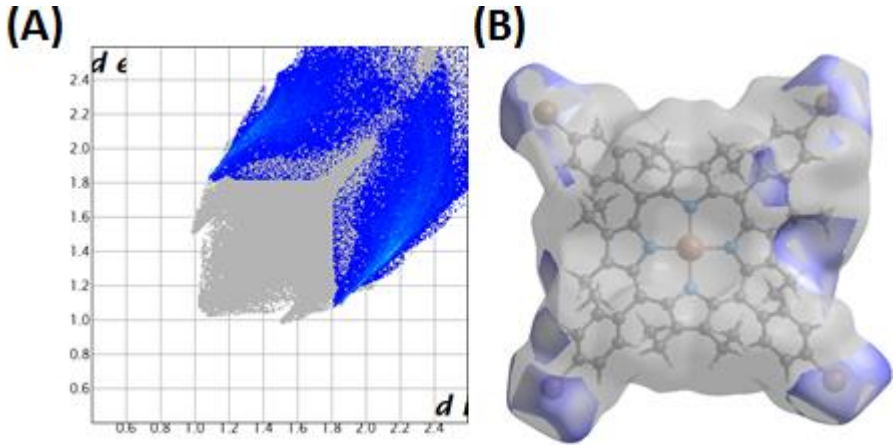

Figure 1:28: Fingerprint plots (A) and Hirshfeld surfaces (B) of compound **1:45** showing the H···Br interactions which occupy 22.8% of total surface contacts. H···Br interactions represented in the Hirschfeld surface (B) are coloured blue. The grey areas highlight all other contacts which are not the focus of this discussion.

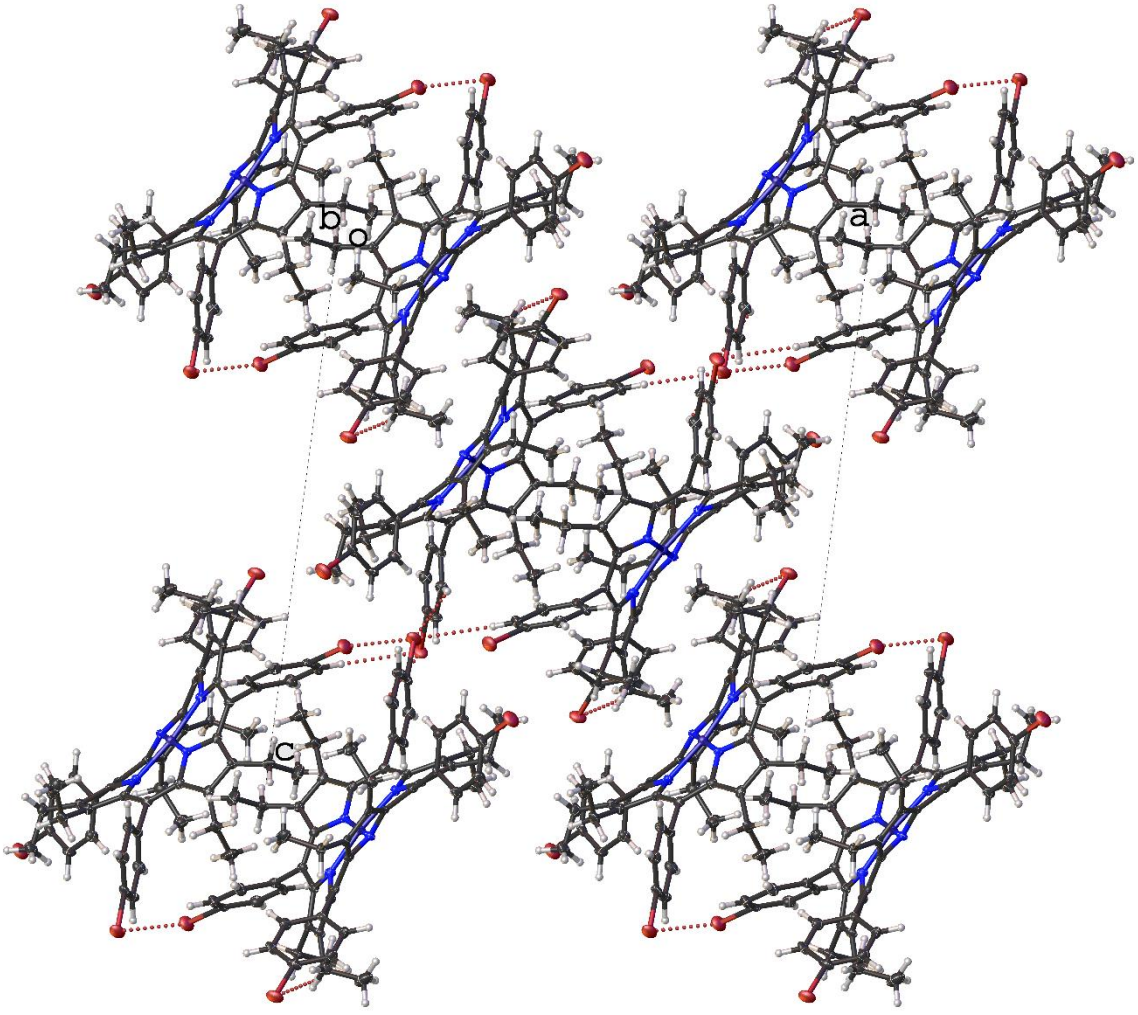

Figure 1:29: Crystal packing of compound **1:45** looking down the *b*-axis. Thermal displacement is given at 50% probability.

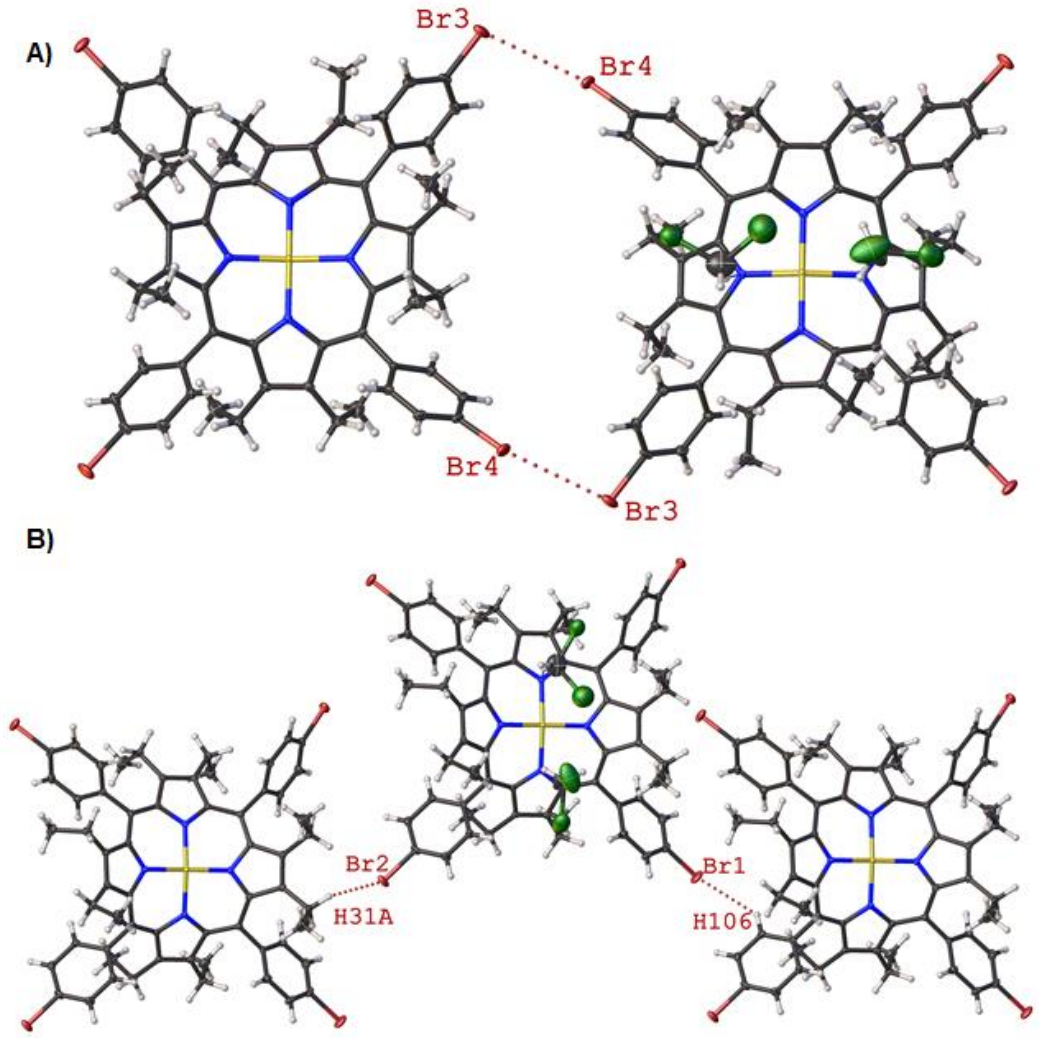

Figure 1:30: Expanded view of compound **1:43B** showing the Br···Br (A, C–Br3···Br4 (3.738(5) Å, 102.2(9)°)) and H···Br (B, C–Br1···H106 (2.990(4) Å, 160.8(1)°) and C–Br2···H31A (2.979(4) Å, 129.5(9)°)) intermolecular contacts involved in the edge-on interactions. Thermal displacement is given at 50% probability. Interactions indicated by red dashed lines.

The final compound in this section is **1:43B**. The compound of **1:43B** is unique to this increasing halogen size series as it is the only solvent containing 4-halo substituted porphyrin. The halogen contact between C–Br3···Br4 (3.738(5) Å, 102.2(9)°), which is similar to the short contact seen in compound **1:45**, gives rise to edge-on interactions between the porphyrin rings and is reciprocated (Figure 1:30). On the opposite side of the macrocycle, there are two Br···H contacts, C–Br1···H106 (2.990(4) Å, 160.8(1)°) and C–Br2···H31A (2.979(4) Å, 129.5(9)°) (Figure 1:30). This binds four porphyrin macrocycles through halogen-halogen and halogen-hydrogen interactions which are repeated and expressed throughout the unit cell. This is shown quite clearly in the Hirshfeld surfaces analysis for compound **1:43B**, where all Br···H contacts can be seen to interact with the ethyl and aryl

moieties to one side of the molecule (Figure 1:31). The packing for compound **1:43B** is where the true difference lies, however. The basic structure is much the same as that of compound **1:45**, with the formation of the channel type pattern, driven by the same type of Br···H and Br···Br interactions (Figure 1:32). However, there is a clear difference when looking at the cupping motif. It has been essentially eliminated due to the presence of the CH_2Cl_2 solvent molecules throughout the structure and has created a second perpendicular channel which is occupied exclusively by solvent molecules, whereas the original channel motif is completely solvent free. This change in crystal packing is a direct result of the inclusion of the solvent.

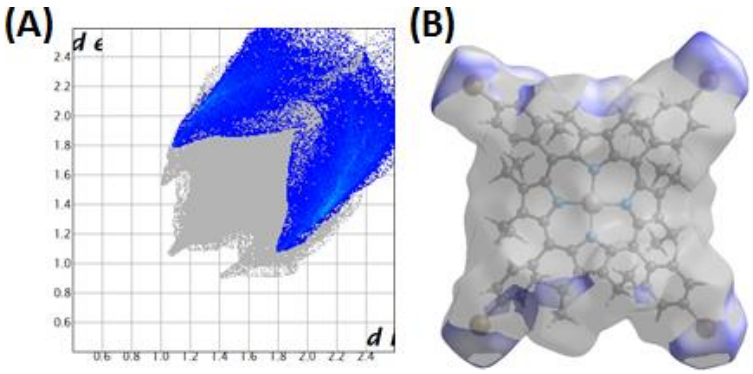

Figure 1:31: Fingerprint plots (A) and Hirshfeld surfaces (B) of compound **1:43B** showing the H···Br interactions which occupy 22.9% of total surface contacts. H···Br interactions represented in the Hirschfeld surface (B) are coloured blue. The grey areas highlight all other contacts which are not the focus of this discussion.

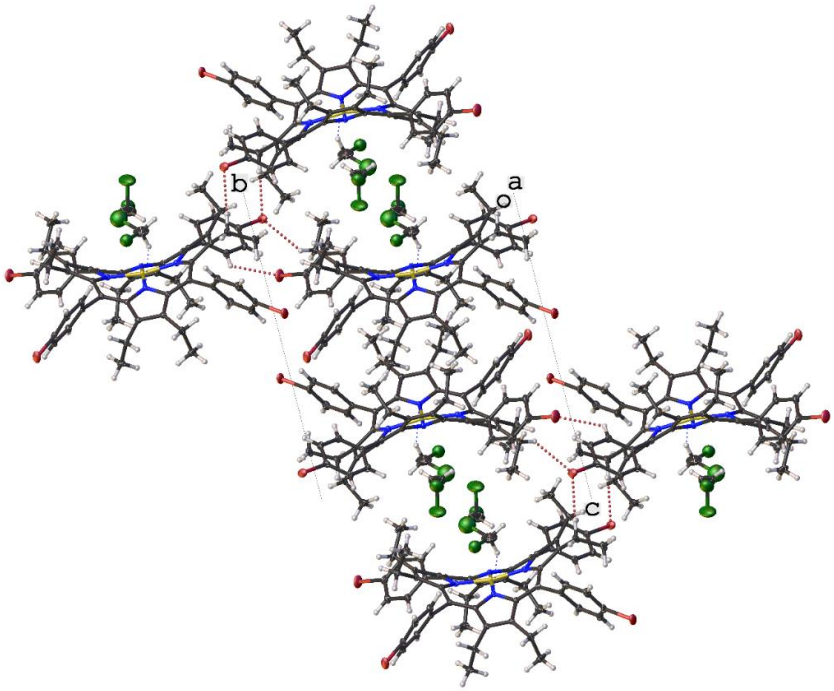

Figure 1:32: Crystal packing of compound **1:43B** looking down the *a*-axis. Thermal displacement is given at 50% probability.

From this section, it can be seen that the main difference between these compounds is due to the preferred intermolecular interactions each porphyrin demonstrates. This is indicated by the fluorine series having an equal preference for alkyl or aryl groups (*ortho*-hydrogen), the chlorine series favouring interactions between the alkyl groups, and the bromine appearing to favour the aryl (*ortho*- and *meta*-hydrogens). Although the sample size is currently limited, this halogen-hydrogen interaction preference is directed by each specific halogen. The other difference is that both fluorine and chlorine do not initiate halogen-halogen interactions, with only the bromine series showing this so far. Finally, while the effects of different metals appear to have no influence on the packing, the inclusion on the solvent has quite a stark change on the crystal packing.

Changing the Position of the Halogen.

In this section, the effects of altering the substitution pattern of a halogen from 4-position to the 2,6-position will be investigated. Six new 2,6-di-halo-substituted structures were obtained (**1:6A**, **1:49**, **1:51A**, **1:52**, **1:53**, and **1:53A**). In general terms, this has some significant effects on the type of interactions that are now available to the porphyrin macrocycle, namely the presence of intramolecular interactions. The effects will be discussed with regards to their 4-substituted derivates.

The first structure is that of compound **1:49** where the aryl ring of the porphyrin contains a di-*ortho*-fluoro substitution. In this structure, two independent molecules were present in the asymmetric unit. From Figure 1:33 the inclusion of intramolecular H···F bonds is quite evident. In fact, this is the most common type of interaction seen in this structure. In both residue one and two, the fluorine atoms show a high preference for interacting with the CH_2 hydrogen atoms of the ethyl chain. This is exemplified in the Hirshfeld surface analysis (Figure 1:34) where the density of F···H interactions surrounding the ethyl and aryl groups is higher than that in compound **1:37**. As impressive as this interaction is, this has little effect on the actual packing of the molecule. Instead, there are several other H···F short contacts present in the structure that result in three distinct intermolecular interactions, forming the overall packing arrangement (Figure 1:35). The first two are the edge-to-face interactions between the two residues aided by H···F contacts between F4_2···H13E_1, F5_2···H12D_1, and F3_1···H17E_2. The second type is

an edge-on interaction between the aryl rings aided by F5_1···H53_1 and F1_1···H53_1. The combination of these two types of interactions results in a densely packed crystal structure with individual porphyrin molecules held at right angles to each other through H···F contacts (Figure 1:36). This type of packing is quite different from that of compound **1:37** as the overlapped cupping pattern has been replaced by an edge-to-face packing arrangement.

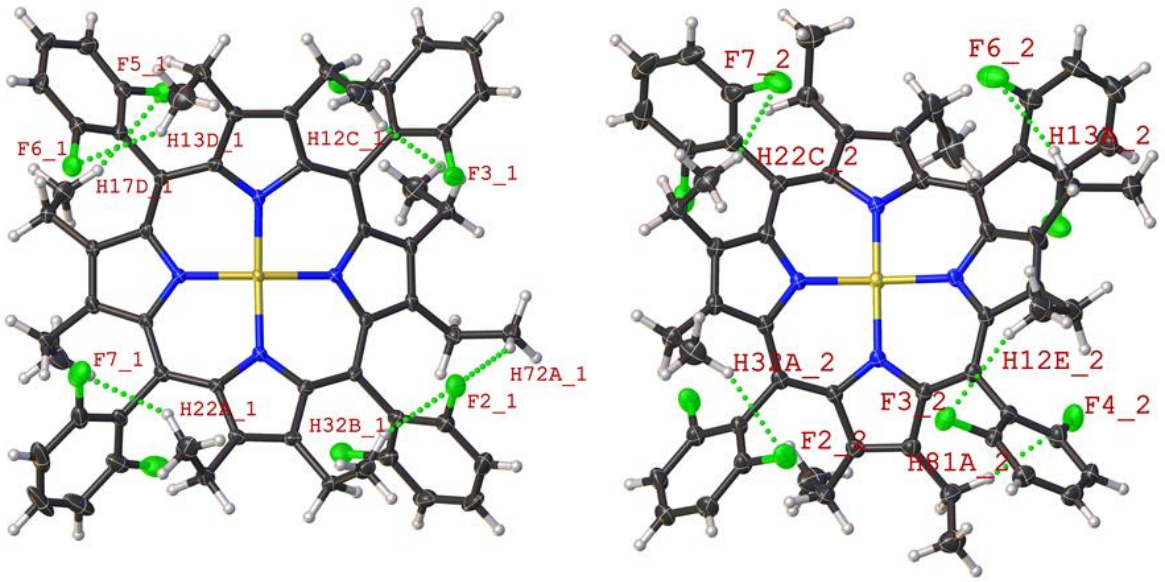

Figure 1:33: The molecular structure of the two crystallographic independent molecules in the structure of **1:49** shows the intermolecular F···H interactions. Thermal displacement is given as 50% probability.

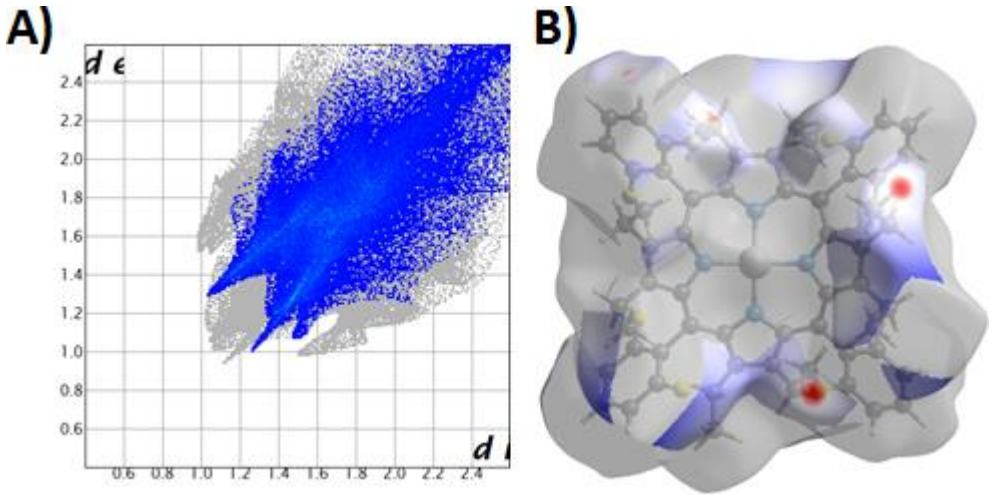

Figure 1:34: Fingerprint plots (A) and Hirshfeld surfaces (B) of compound **1:49** showing the H···F interactions which occupy 27.0% of total surface contacts. H···F interactions represented in the Hirschfeld surface (B) are coloured blue and red. The grey areas highlight all other contacts which are not the focus of this discussion.

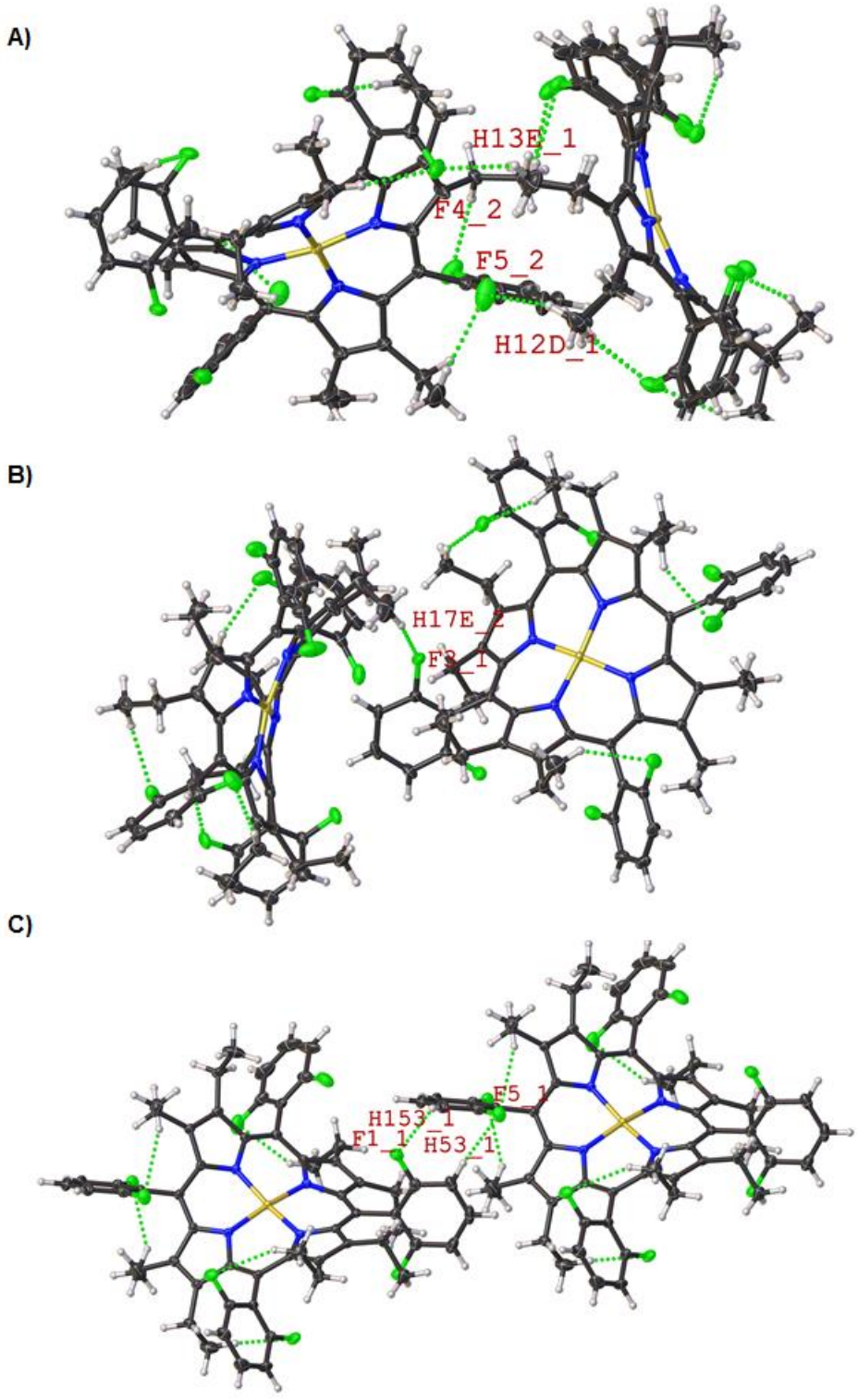

Figure 1:35: Expanded view of the three intermolecular interactions of compound **1:49** showing the H···F intermolecular (A, C–F4_2···H13E_1 (2.405(2) Å, 118.0(1)°) and C–F5_2···H12D_1 (2.645(2) Å, 117.3(1)°)) (B, C–F3_1···H17E_2 (3.377(2) Å, 137.7(1)°)) contact involved in the face-to-face or edge-on (C, C–F5_1···H53_1 (2.730(1) Å, 104.2(1)°) and C–F1_1···H53_1 (2.602(2) Å, 100.7(1)°)) interactions. Thermal displacement is given at 50% probability. Interactions indicated by green dashed lines. Each image is a separate view of the crystal structure to allow for the simple presentation of each interaction independently.

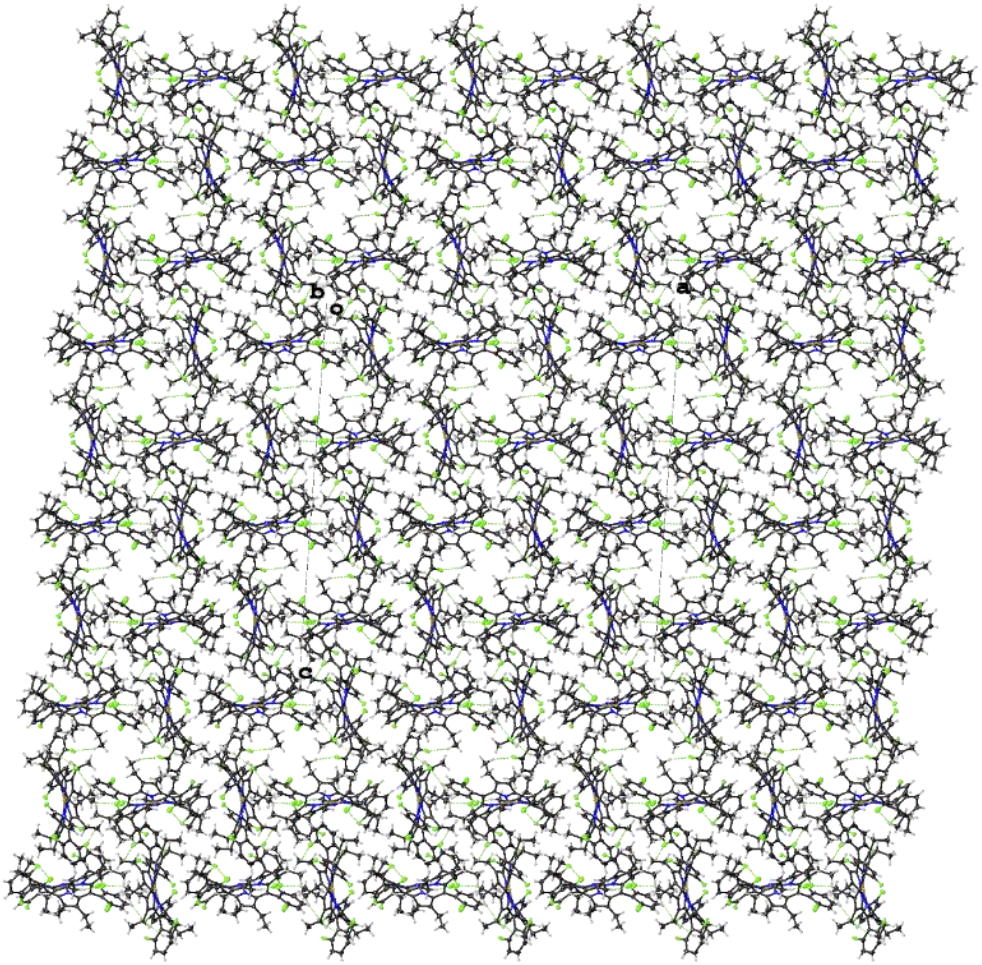

Figure 1:36: Crystal packing of compound **1:49** looking down the *b*-axis. Thermal displacement is given at 50% probability.

The next five structures (**1:6A**, **1:51A**, **1:52**, **1:53**, and **1:53A**) all belong to the series of 2,6-dichlorophenyl substituted porphyrin complexes with a variety of free base, metal(II) centres, and solvent ($CDCl_3$) included. This is the largest family of structures in this work and offers the best dataset to investigate subtle differences within the OETArXP series. There are some general features that all these structures share. This is the propensity to partake in intramolecular interactions between the chlorine atoms and the terminal hydrogen atoms of the ethyl chains. This feature is apparently typical of the 2,6-halo series, as both the chlorine and fluorine derivatives share this motif. The pattern in which these intramolecular interactions take place is not identical from structure to structure, such as, 2,6-dichlorophenyl substituted at the 15-position of **1:6A** does not partake in this intramolecular interaction. These differences can be due to several factors such as the intermolecular contacts or solvent inclusion/exclusion. However, it should be noted that these intramolecular interactions play no role in packing or any particular

binding motif, and therefore should not be considered an important structural factor. For completeness, the basic intramolecular interactions have been compiled into Figure 1:37 for each of the 2,6-dichlorophenyl substituted porphyrins in this section. Figure 1:37 also includes the Hirshfeld surface analysis and fingerprint plots of the 2,6-dichlorophenyl substituted porphyrin. Looking at these plots we can see only minor changes due to the inclusion of solvent which results in a higher density of Cl···H interactions in the core of the porphyrin. Other noticeable features are the Cl···H contacts which are mostly due to the intramolecular interactions and as such obscure any possible analysis of the intermolecular interactions using this method.

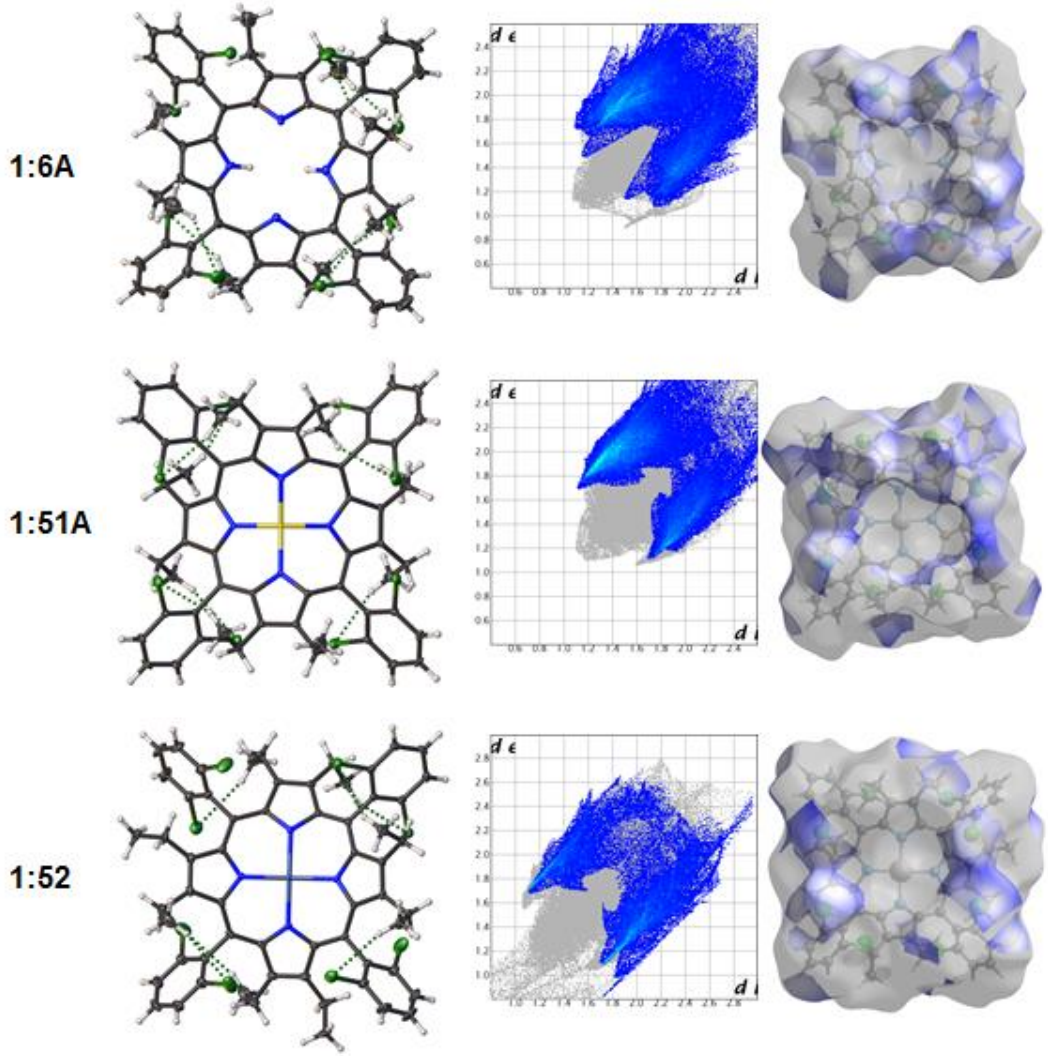

Figure 1:37: Molecular structures, fingerprint plots, and Hirshfeld surface analysis of the 2,6-dichlorophenyl substituted porphyrins. The molecular structures show the intramolecular Cl···H interactions. Thermal displacement is given as 50% probability. Fingerprint plots and Hirshfeld surfaces indicate all Cl···H interactions. H···Cl interactions represented in the Hirschfeld surface are coloured blue. The grey areas highlight all other contacts which are not the focus of this discussion. The percentage of surface contacts that are due to Cl···H interactions, **1:6A** (45.3%), **1:51A** (39.2%), **1:52** (30.0%), **1:53** (30.0%), and **1:53A** (39.4%).

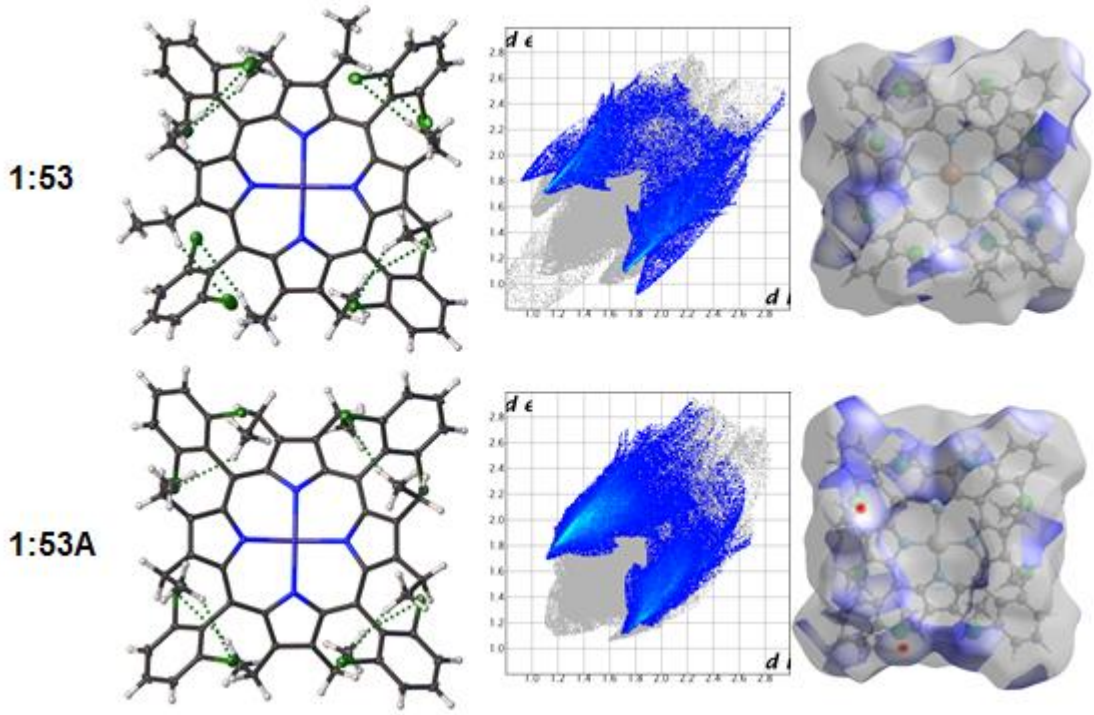

Figure 1:37 (continued): Molecular structure, fingerprint plots, and Hirshfeld surface analysis of the 2,6-dichlorophenyl substituted porphyrins. The molecular structures show the intermolecular Cl···H interactions. Thermal displacement is given as 50% probability. Fingerprint plots and Hirshfeld surfaces indicate all Cl···H interactions. H···Cl interactions represented in the Hirschfeld surface are coloured blue and red. The grey areas highlight all other contacts which are not the focus of this discussion. The percentage of surface contacts that are due to Cl···H interactions, **1:6A** (45.3%), **1:51A** (39.2%), **1:52** (30.0%), **1:53** (30.0%), and **1:53A** (39.4%).

The structure of **1:6A** contains one intermolecular interactions C–Cl7···H154 (2.935(3) Å, 78.5(4)°) which creates an edge-on contact between the porphyrin macrocycle similar to that of compound **1:40** (Figure 1:38). However, whereas the Cl of compound **1:40** interacts with the ethyl groups, in **1:6A** they interact with the aryl groups exclusively. As this structure is both free base and solvated with $CDCl_3$, the structure is separated into layers of porphyrin with a solvent channel between them. This alters the packing pattern slightly compared to the *para*-chloro-substituted **1:40** resulting in a wider packing pattern, Figure 1:39. This is due to both the solvent inclusion and the alternate intermolecular interaction as stated above.

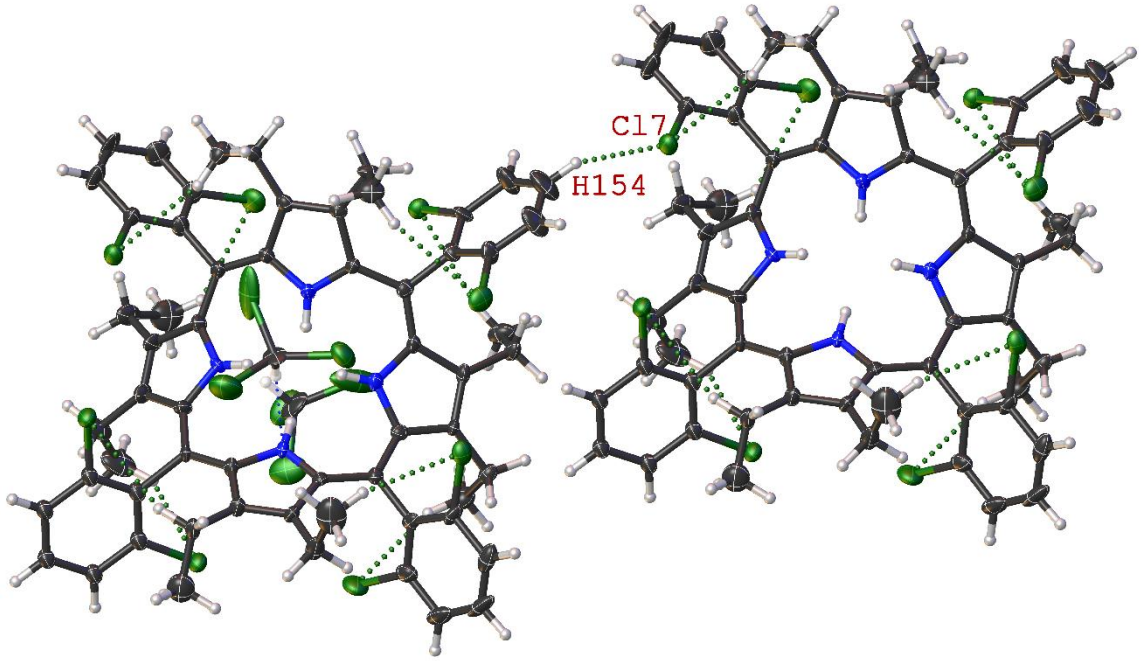

Figure 1:38: Expanded view of compound **1:6A** showing the Cl···H intermolecular contact (C–Cl7···H154 (2.935(3) Å, 78.5(4)°)). Thermal displacement is given at 50% probability. Interactions indicated by green dashed lines.

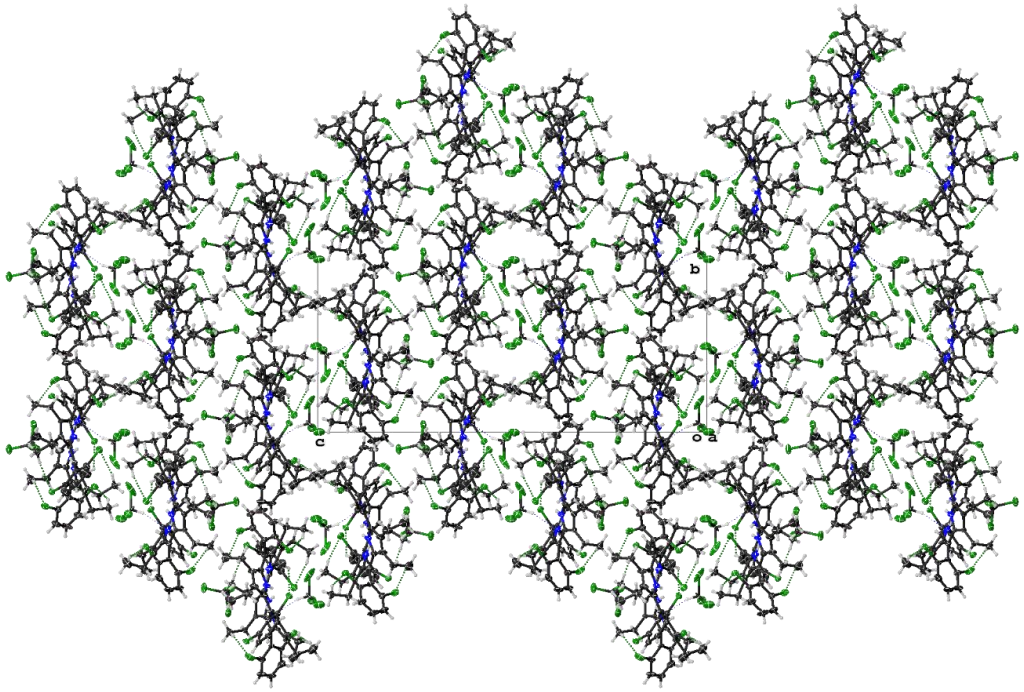

Figure 1:39: Crystal packing of compound **1:6A** looking down the *a*-axis. Thermal displacement is given at 50% probability.

The structure of **1:51A** is the Ni(II) version of **1:6A**. In Figure 1:40, it is shown that compound **1:51A** appears to favour a face-to-face interaction between the porphyrin macrocycles through Cl8···H82A, as opposed to the edge-on interaction favoured by compound **1:6A**. This is clearly seen in the packing diagram, as even though the

primary intermolecular interactions are quite different the overall crystal packing is almost identical, indicating that these differences are minimal compared to the solvent interactions (Figure 1:41). This suggests two things are occurring in the crystal packing. The first and most obvious is that the solvent has more of an impact on the packing of the structure than the inclusion of a metal to the core of the porphyrin. The second and more subtle is that the metal(II) centre has a minor effect on the changing the intermolecular interaction from an edge-on interaction towards a face-to-face interaction.

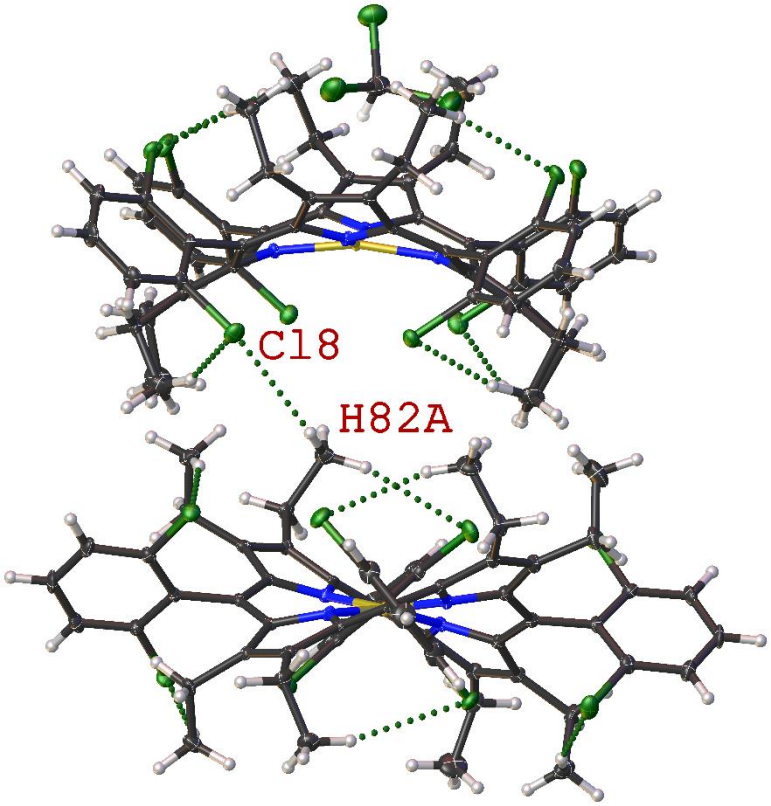

Figure 1:40: Expanded view of compound **1:51A** showing the Cl···H intermolecular contact involved in the face-to-face interactions (C–Cl8···H82A (2.876(1) Å, 169.4(1)°)). Thermal displacement is given at 50% probability. Interactions indicated by green dashed lines.

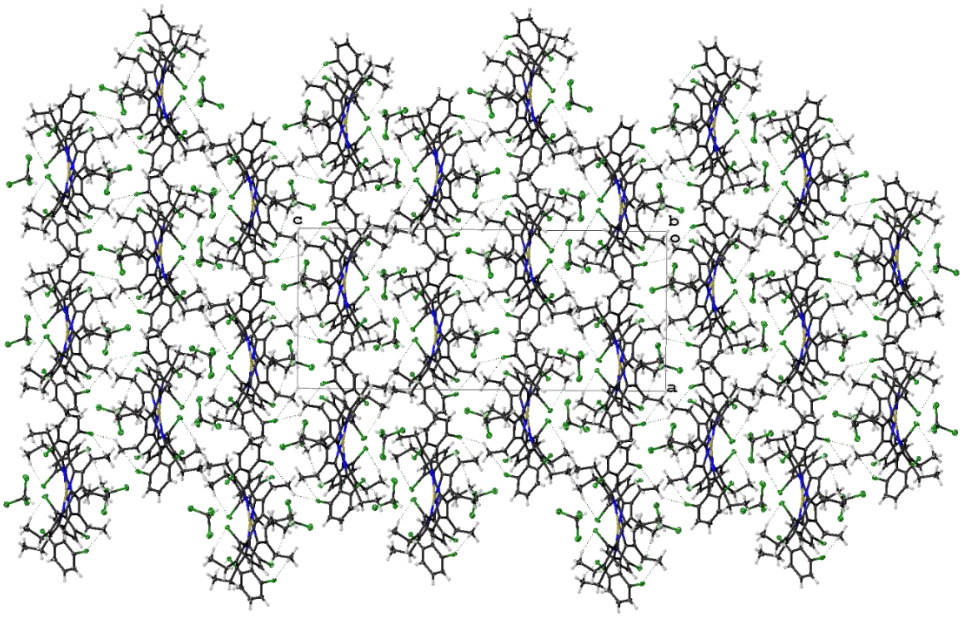

Figure 1:41: Crystal packing of compound **1:51A** looking down the *b*-axis. Thermal displacement is given at 50% probability.

The structure of **1:52** is that of the Pd(II) derivative of the 2,6-dichlorophenyl series. This is the first of two non-solvated structures in this series. Where the main difference arises is with the intermolecular interactions. In this structure, a new type of contact is observed in which the edge of one porphyrin macrocycle interacts with the face of its nearest neighbouring porphyrin macrocycle (Figure 1:42). This is aided by two Cl···H interactions (Cl2···H82A and Cl4···H32A) and is reproduced on the opposite side of the porphyrin ring, due to symmetry. This results in forming a network, where one porphyrin macrocycle is essentially sandwiched between the face of two other porphyrin rings. This is also the position which was previously occupied by $CDCl_3$ making this interaction profile unique to the non-solvated structures in this series. The effect these interactions have on the packing is quite stark. Rather than the alternating layers of porphyrins and solvent previously seen in this series, there is now a highly ordered stacked system, in which the phenyl rings are stacked on top with each other (Figure 1:43), as opposed to the solvent driven packing as seen before in compound **1:51A**.

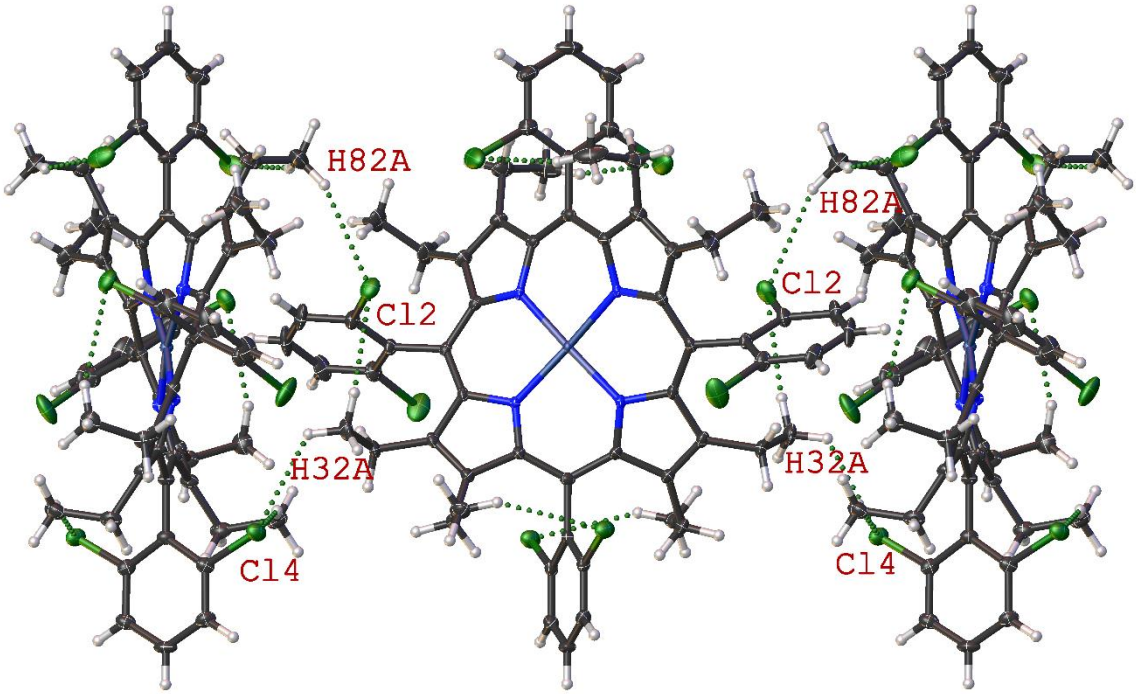

Figure 1:42: Expanded view of compound **1:52** showing the Cl···H intermolecular contacts involved in the face-to-edge interactions (C–Cl2···H82A (2.907(8) Å, 109.8(1)°) and C–Cl4···H32A (2.851(8) Å, 141.8(1)°). Thermal displacement is given at 50% probability. Interactions indicated by green dashed lines.

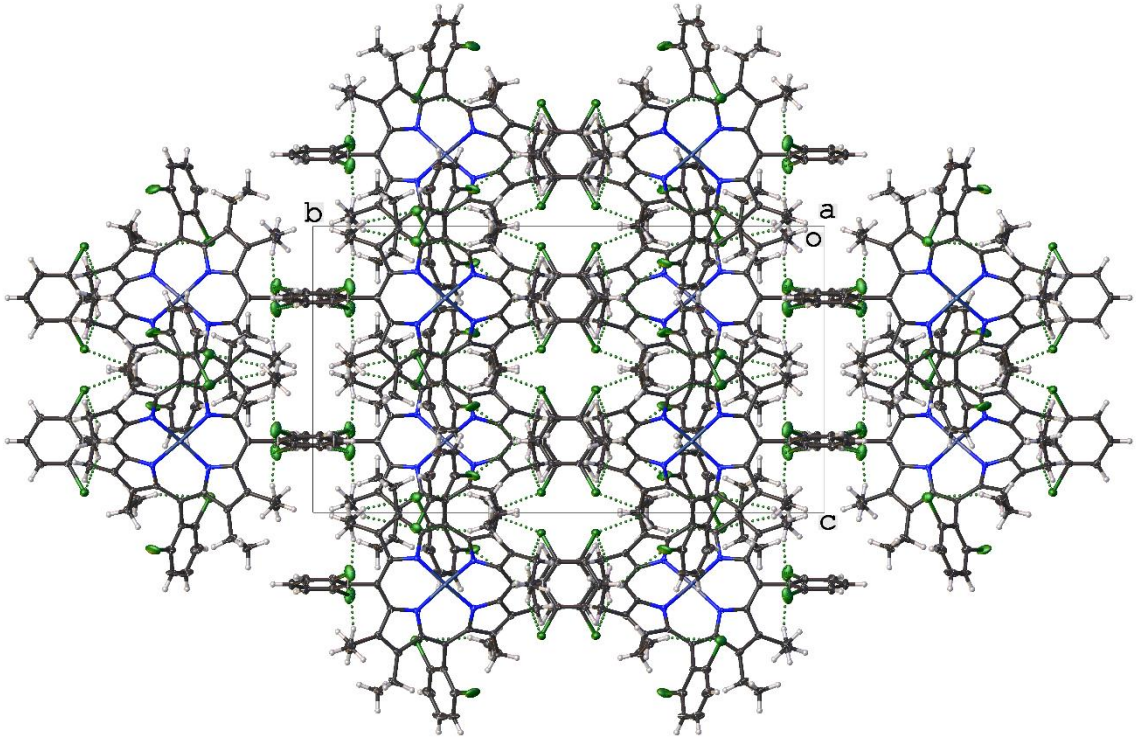

Figure 1:43: Crystal packing of compound **1:52** looking down the *a*-axis. Thermal displacement is given at 50% probability.

The structure of compound **1:53** is the Cu(II) derivative of the 2,6-dichlorophenyl series. This is the second of the two non-solvated structures in this series. This structure is almost identical to that of compound **1:52**. The intermolecular interactions are the exact same as seen in compound **1:52**, where the one porphyrin ring is held between the faces of two other porphyrin macrocycle in a face-to-edge packing pattern. The interactions involved in this motif are C–Cl1···H22A (2.900(6) Å, 103.6(8)°) and C–Cl3···H72A (2.882(6) Å, 143.9(2)°) and are reproduced on opposite side of the porphyrin ring due to symmetry, Figure 1:44. When looking at the packing of compound **1:53**, it is clear that there are little to no differences between it and that of compound **1:52**, (Figure 1:45). This is a clear indication that the metal(II) centres chosen in this project, have little to no effect on the overall structure and packing of these compounds in this 2,6-di-substituted series.

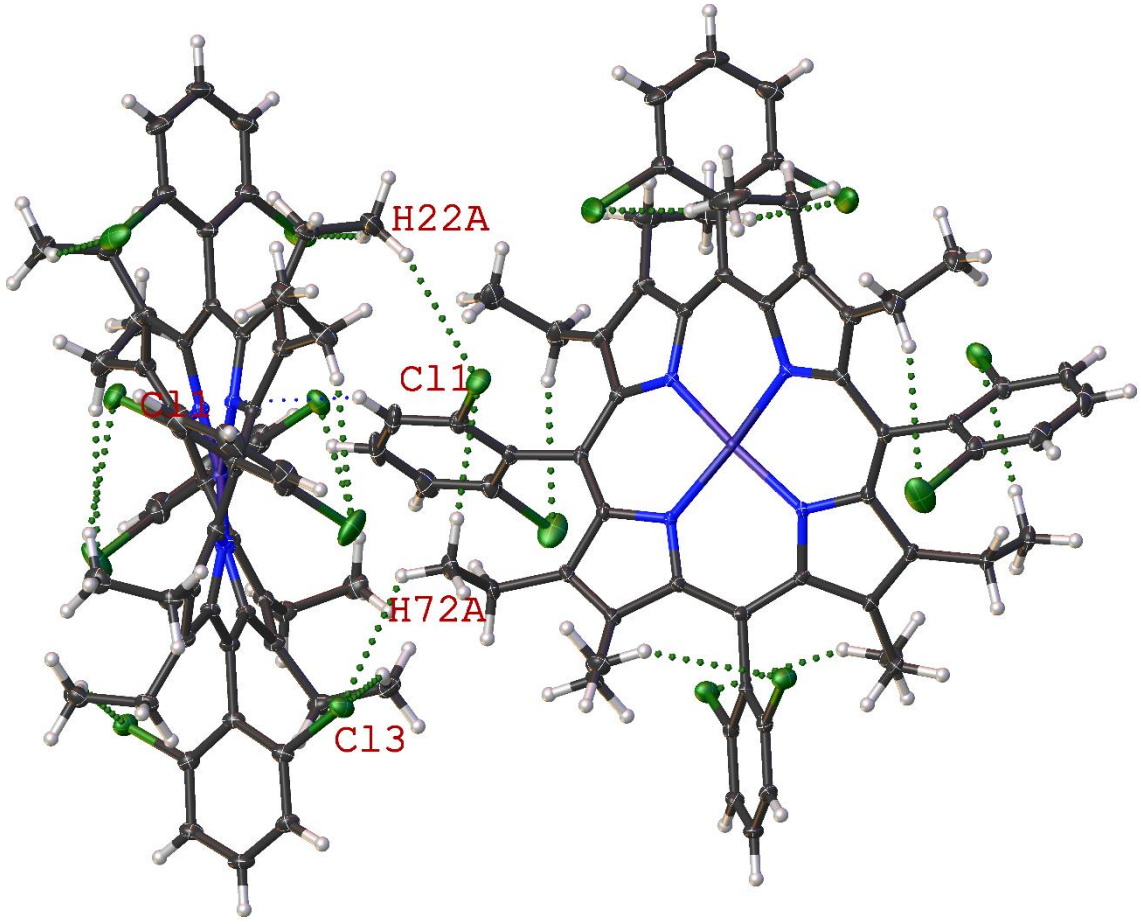

Figure 1:44: Expanded view of compound **1:53** showing the Cl···H intermolecular contacts involved in the face-to-edge interactions (C–Cl1···H22A (2.900(6) Å, 103.6(8)°) and C–Cl3···H72A (2.882(6) Å, 143.9(2)°)). Thermal displacement is given at 50% probability. Interactions indicated by green dashed lines.

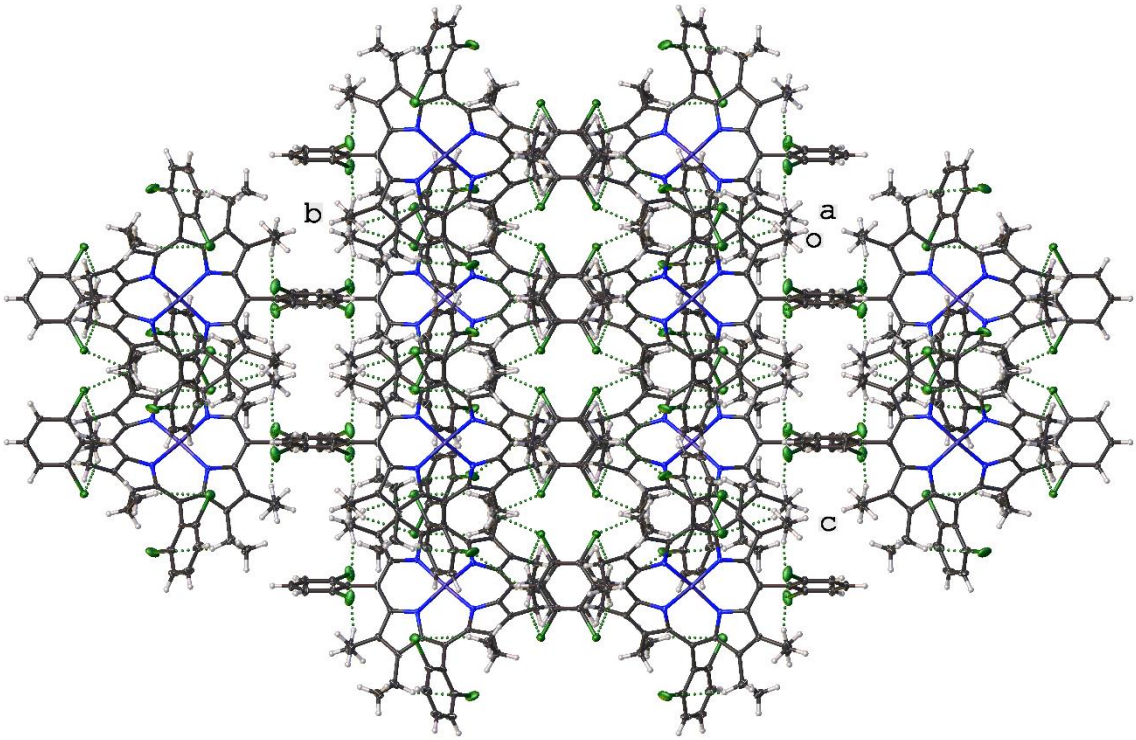

Figure 1:45: Crystal packing of compound **1:53** looking down the *a*-axis. Thermal displacement is given at 50% probability.

The structure of compound **1:53A** is the $CDCl_3$ solvated structure of porphyrin **1:53** and as such, is the first case in which only the solvent effects can be examined without any other external factors. The intermolecular interactions of compound **1:53A** in this structure are different from those of **1:53**. Rather than the face-to-edge interactions previously seen in **1:53**, compound **1:53A** shows an offset face-to-face network, which is aided by a Cl···H network (C–Cl4···H17C (2.943(1) Å, 125.9(2)°)). This is repeated throughout the structure in a wave-like pattern, tethering lines of porphyrin together, Figure 1:46. However, the crystal packing is identical to that of **1:51A** and **1:6A** which indicates the solvent inclusion is more directive in the crystal packing than the intramolecular/intermolecular interactions, Figure 1:47.

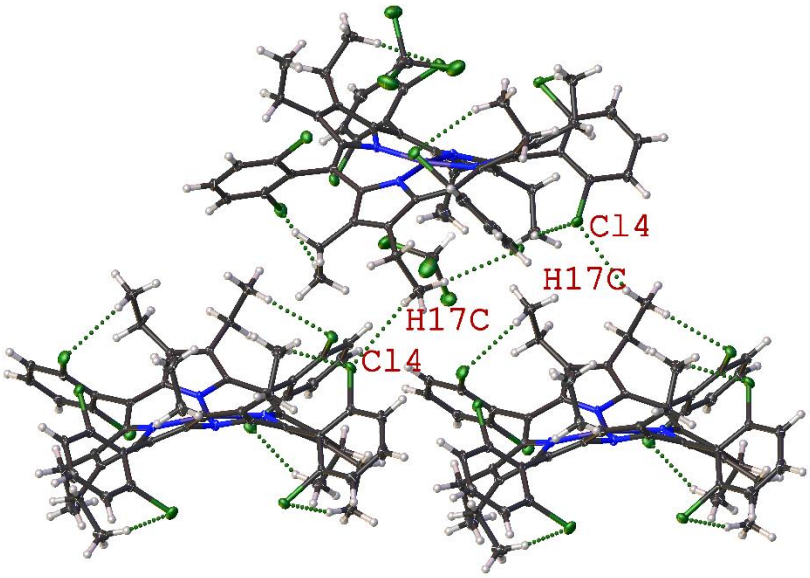

Figure 1:46: Expanded view of compound **1:53A** showing the Cl···H intermolecular contact involved in the face-to-face interactions (C–Cl4···H17C (2.943(1) Å, 125.9(2)°)). Thermal displacement is given at 50% probability. Interactions indicated by green dashed lines.

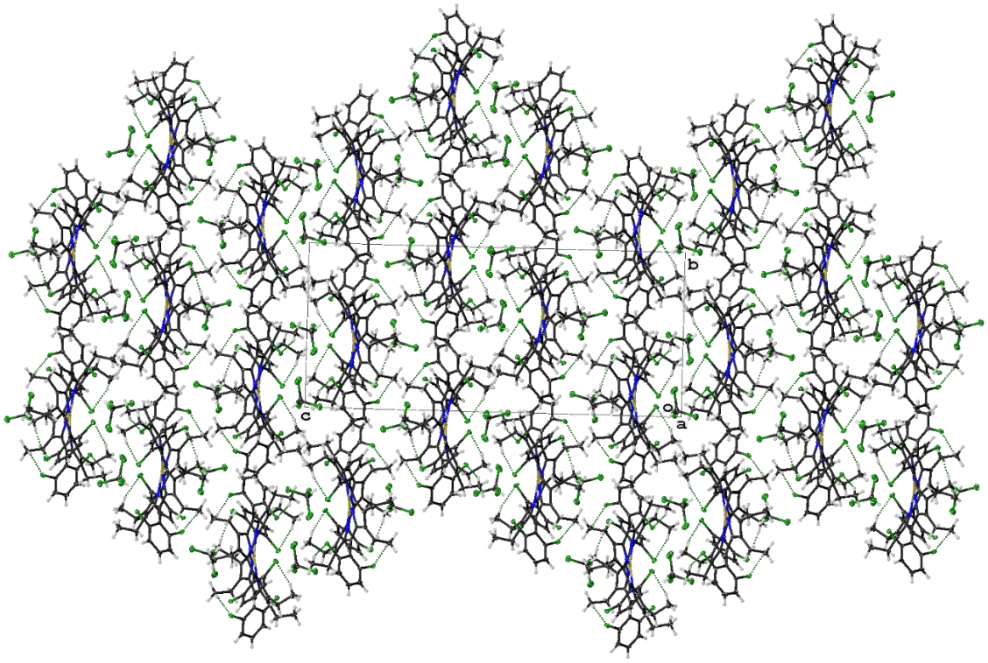

Figure 1:47: Crystal packing of compound **1:53A** looking down the *a*-axis. Thermal displacement is given at 50% probability.

Overall, this section highlights some key features. The first of these is that the metal(II) centres have very little effects on the overall crystal packing. This is indicated by the fact that, even if structures contain Pd(II), Cu(II), Ni(II) or no metal at all, the only difference observed is when the structure contains a solvent or not. This leads to the second observation. The inclusion or exclusion of solvent is the

main driving force in packing. The metal(II) centres do appear to have a minor effect, however, when it comes to intermolecular interactions as without a metal these structures seem to favour an edge-on interaction like the *para*-halo-substituted structure **1:40**. However, with a metal(II) centre the face-to-face overlap is exclusively observed in the solvated structures.

Nitrile OETArXP – a Z-Shaped Hydrogen Bonding Framework.

For the nitrile porphyrins, compound **1:54** is atypical of a rigid hydrogen-bond acceptor. This is exemplified in Figure 1:48, where the cyano group is seen to be directive towards *ortho*-aryl hydrogen atoms in a bifurcated fashion. This is directed through C–N1···H52 (2.720(1) Å, (130.5(1)°) and C–N1···H206 (2.730(1) Å, 95.8(1)°), in which the two interacting porphyrin molecules are orthogonal to each other. The second interaction profile is seen between C–N2···H53 (2.675(2) Å, 131.6(1)°) (Figure 1:49). This results in an interesting feature in which these two porphyrin macrocycles are held at an angle of 59.1(3)° as measured by their 24-atom least-squares plane. This motif is repeated throughout the structure and results in a Z-shaped pattern through the layer of porphyrin rings (Figure 1:50). These two interaction profiles combine to make the packing of this porphyrin exclusively on the periphery. Looking at the Hirshfeld surface analysis it is clear that all N···H interactions happen on the edge of the porphyrin macrocycle and strictly involve the aryl hydrogen atoms (Figure 1:51). This results in the tightly ordered packing seen in Figure 1:52.

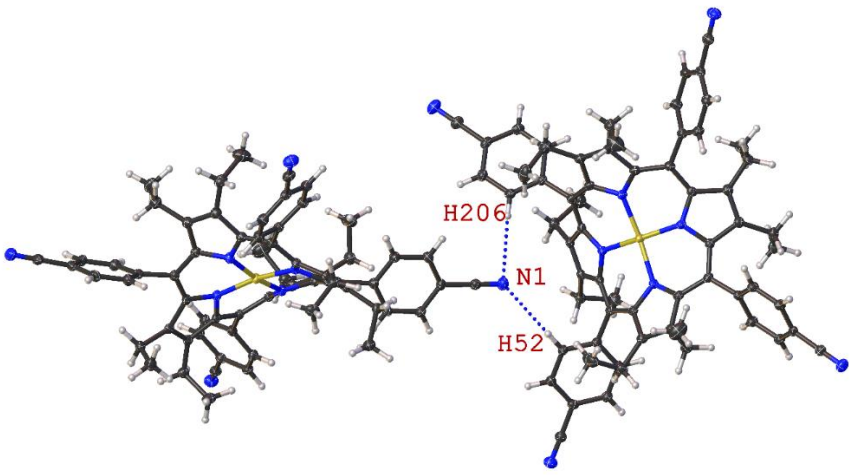

Figure 1:48: Expanded view of compound **1:54** showing the N···H intermolecular contacts involved in the bifurcated interactions (C–N1···H52 (2.720(1) Å, (130.5(1)°) and C–N1···H206 (2.730(1) Å, 95.8(1)°)). Thermal displacement is given at 50% probability. Interactions indicated by blue dashed lines.

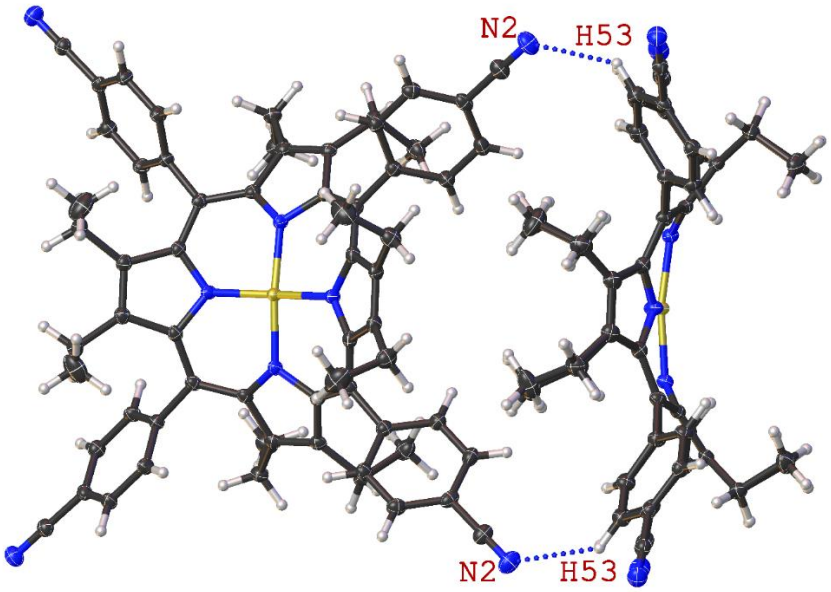

Figure 1:49: Expanded view of compound **1:54** showing the N···H intermolecular contacts involved in the edge-on interactions (C–N2···H53 (2.675(2) Å, 131.6(1)°)). Thermal displacement is given at 50% probability. Interactions indicated by blue dashed lines.

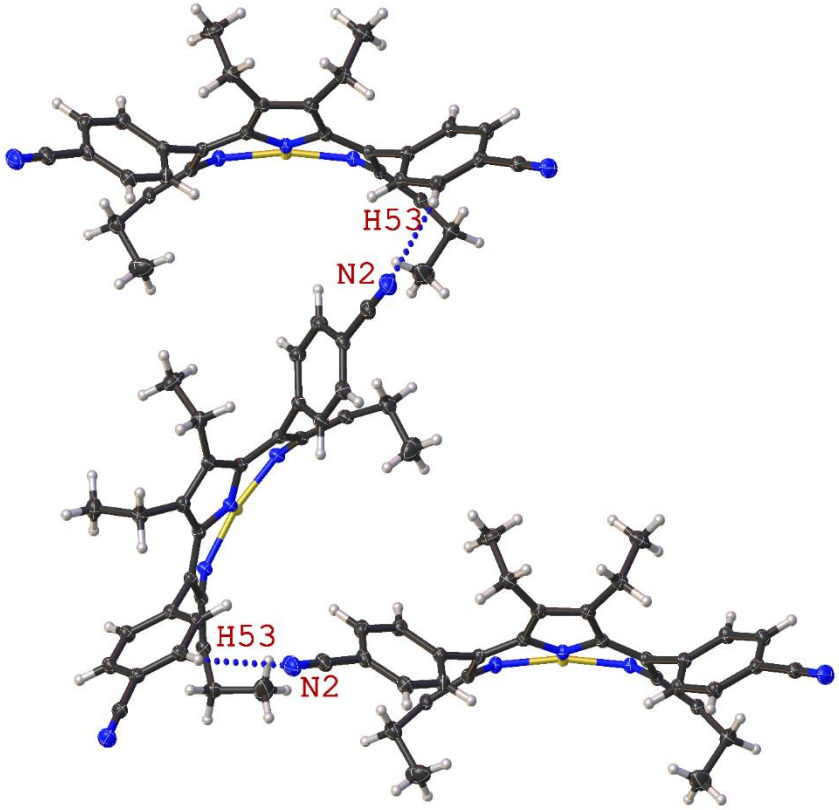

Figure 1:50: Expanded view of compound **1:54** showing the N2···H53 intermolecular contacts (C–N2···H53 (2.675(2) Å, 131.6(1)°)) involved in the Z-shaped pattern through the layer of porphyrin rings. Thermal displacement is given at 50% probability. Interactions indicated by blue dashed lines.

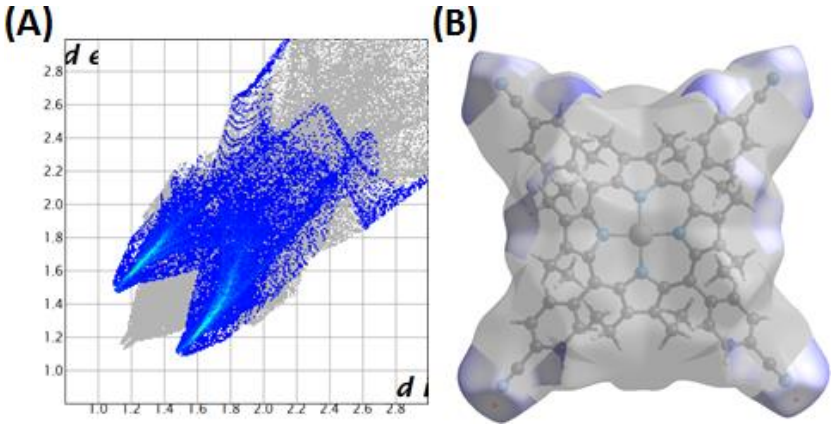

Figure 1:51: Fingerprint plots (A) and Hirshfeld surfaces (B) of compound **1:54** showing the H···N interactions which occupy 21.5% of total surface contacts. H···N interactions represented in the Hirschfeld surface (B) are coloured blue. The grey areas highlight all other contacts which are not the focus of this discussion.

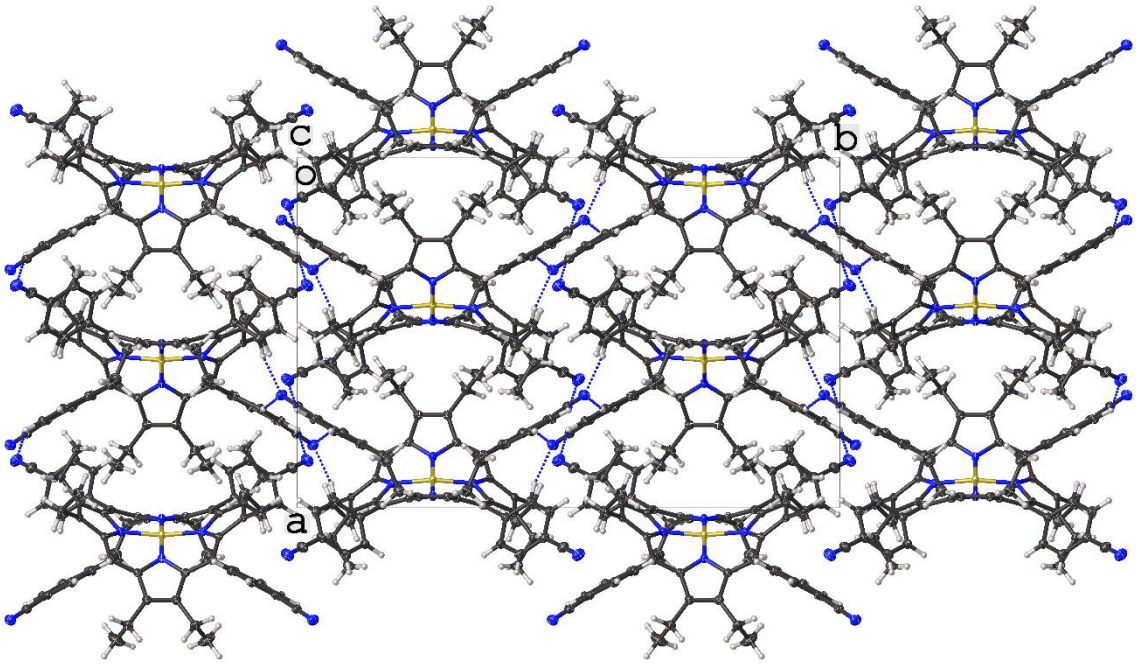

Figure 1:52: Crystal packing of compound **1:54** looking down the *c*-axis. Thermal displacement is given at 50% probability.

Shaking Hands – Aliphatic Side Chain Core Interaction.

The topic in this section is that of inner core binding motifs. While conducting this project a very unexpected result was achieved. This was the inner core interaction between the nitrogen atoms and long alkyl chains. This was accomplished through the crystallisation of compounds **1:57** and **1:59**. Initially, it was expected that the butyl chains of compound **1:57** would possibly interact with each other through some form of non-classical hydrogen-bonding or hydrophobic interaction and that the benzyloxy chain of compound **1:59** would result in a complex that would interact

with some sort of π-system. However, what actually happens is much more interesting.

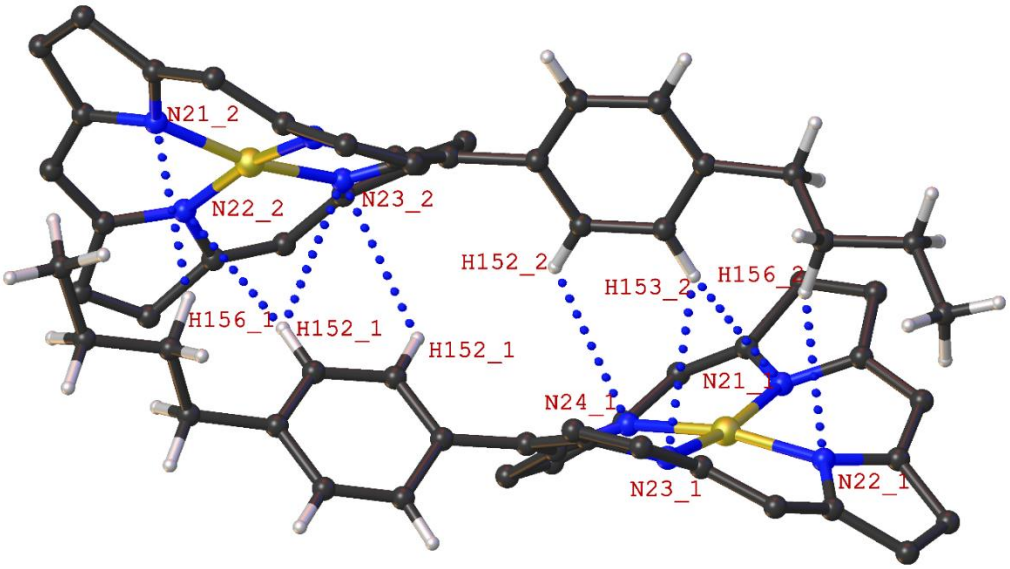

Figure 1:53: Expanded view of compound **1:57** showing the N···H core interactions (C–H152_2···N23_1 (2.968(2) Å, 123.8(5)°), C–H153_2···N23_1 (2.917(2) Å, 127.6(3)°), C–H153_2···N22_1 (2.981(2) Å, 168.6(1)°), C–H156_2···N21_1 (3.225(2) Å, 152.1(3)°), C–H152_1···N24_2 (3.159(2) Å, 129.6(4)°), C–H153_1···N21_2 (3.222(3) Å, 151.1(3)°), C–H153_1···N23_2 (3.141(2) Å, 130.1(2)°), and C–H156_1···N22_2 (3.143(2) Å, 156.3(2)°)). All peripheral substituents bar those involved in the core interactions have been omitted to make it easier to view the core overlap. The structure was drawn isotropically. Interactions indicated by blue dashed lines.

Taking compound **1:57** first, there are two sets of core interactions. As there are two independent molecules in the asymmetric unit all atoms have been assigned a residue number in the form of '_#'. The first set of core interactions are between the butylphenyl substituent of the second residue and the core of the porphyrin in the first residue. This is seen through several core interactions C–H152_2···N23_1 (2.968(2) Å, 123.8(5)°), C–H153_2···N23_1 (2.917(2) Å, 127.6(3)°) and C–H153_2···N22_1 (2.981(2) Å, 168.6(1)°), which are between the core and the phenyl ring and C–H156_2···N21_1 (3.225(2) Å, 152.1(3)°) which is between the core and the butyl chain (Figure 1:53). The second set of core interactions are between butylphenyl substituent of the first residue and the core of the porphyrin in the second residue. These are C–H152_1···N24_2 (3.159(2) Å, 129.6(4)°), C–H153_1···N21_2 (3.222(3) Å, 151.1(3)°) and C–H153_1···N23_2 (3.141(2) Å, 130.1(2)°) which are between the core and the phenyl ring and C–H156_1···N22_2 (3.143(2) Å, 156.3(2)°) which is between the core and the butyl chain (Figure 1:53).

When looking at the Hirshfeld surface analysis, it can be seen that the N···H contacts are centred on the butyl and aryl groups in the crystal structure (Figure 1:54). This results in a rather tight packing with alkyl chains overlapping with the core of the porphyrin to give a mesh-like appearance (Figure 1:55). It should be considered that these contacts are very weak and an artefact of close packing not a true directive interaction.

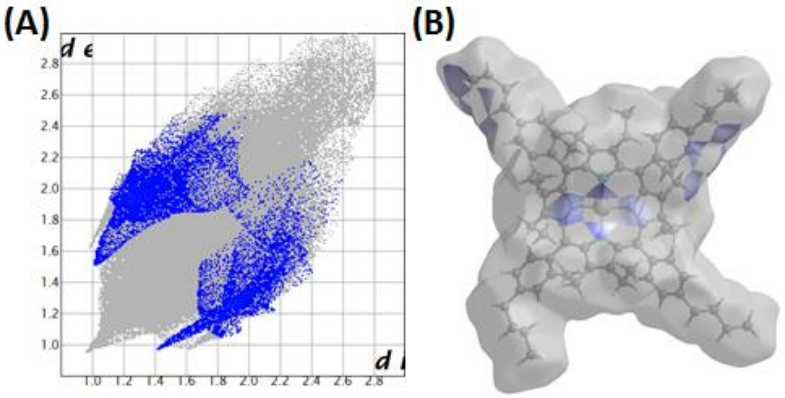

Figure 1:54: Fingerprint plots (A) and Hirshfeld surfaces (B) of compound **1:57** showing the H···N interactions which occupy 3.7% of total surface contacts. H···N interactions represented in the Hirschfeld surface (B) are coloured blue. The grey areas highlight all other contacts which are not the focus of this discussion.

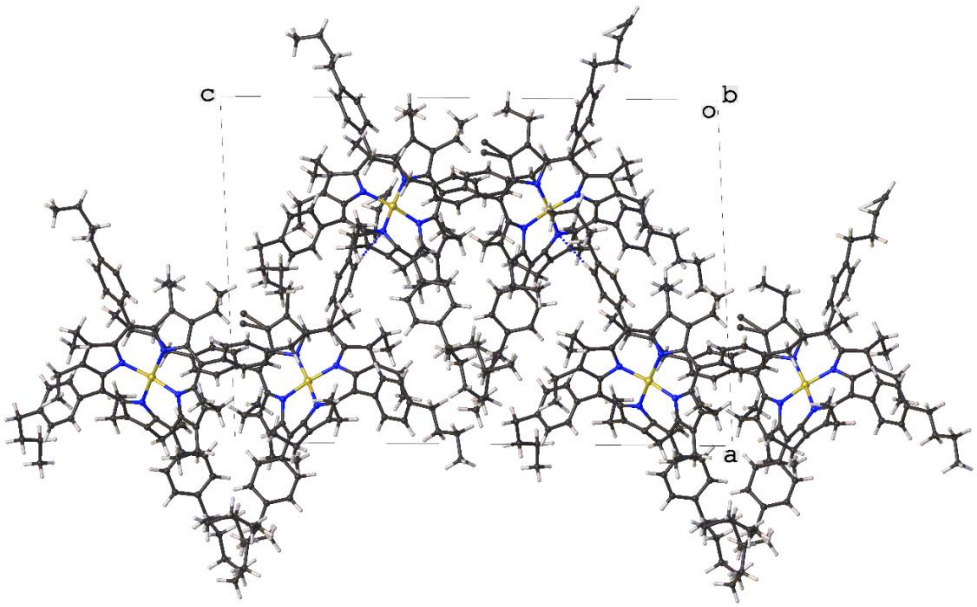

Figure 1:55: Crystal packing of compound **1:57** looking down the *a*-axis. The structure was drawn isotropically.

The structure of **1:59** shows a similar core interaction as compound **1:57**. Two independent molecules were isolated in the asymmetric unit of compound **1:59** and all atoms have been assigned a residue number in the form of '_#'. For this structure,

the core interactions have two types of motifs. The first of these is similar to that seen in compound **1:57** where the *meta*-hydrogen atom of the phenyl ring is involved in a short contact with the N21 (C103_2–H103_2···N21_1) at a distance of 2.891(4) Å (Figure 1:56). The second interaction motif is between the CH_2 hydrogen atoms of the benzyloxy chain and the nitrogen atoms N22 and N24 (C108_2–H10A_2···N22_1 (2.832(3) Å) and C108_2–H10B_2···N24_1 (3.001(4) Å)) (Figure 1:56). This interaction is interesting due to the fact that the angle caused by the inclusion of oxygen into the benzyloxy chain holds the CH_2 moiety at the same distance away from the porphyrin core as the aromatic CH which is also involved in this core interaction. When a Hirshfeld surface analysis is applied to this porphyrin structure, it can be seen that the N···H interactions are strictly centred on the aryl and benzyloxy chain, confirming that these are the only interactions involved with the core of the porphyrin (Figure 1:57). The crystal packing of this structure is also rather similar to that of compound **1:57** where the consistent overlap of the *meso*-substituent results in a tightly packed mesh-like crystal pattern (Figure 1:58).

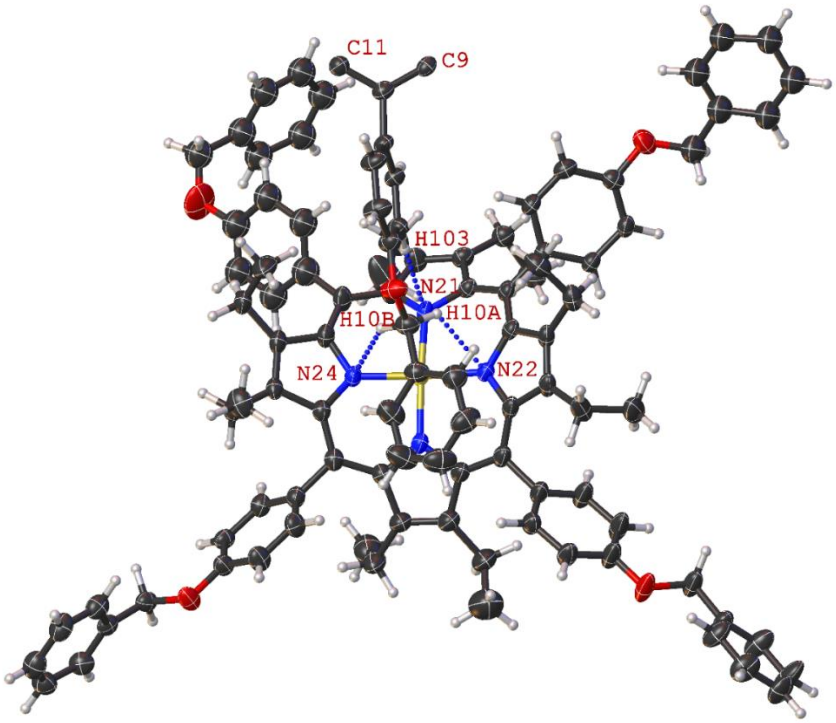

Figure 1:56: Expanded view of compound **1:59** showing the N···H core interactions. The second porphyrin has been coloured purple to allow for a clearer observation of the core interactions (C103_2–H103_2···N21_1 (2.891(4) Å, 175.6(3)°), C108_2–H10A_2···N22_1 (2.832(3) Å, 123.1(3)°) and C108_2–H10B_2···N24_1 (3.001(4) Å, 144.6(3)°)). Thermal displacement is given at 50% probability. Interactions indicated by blue dashed lines. For clarity the second porphyrin ring has been cut out of the image at C9 and C11 (these atoms are labelled) to avoid overcrowding.

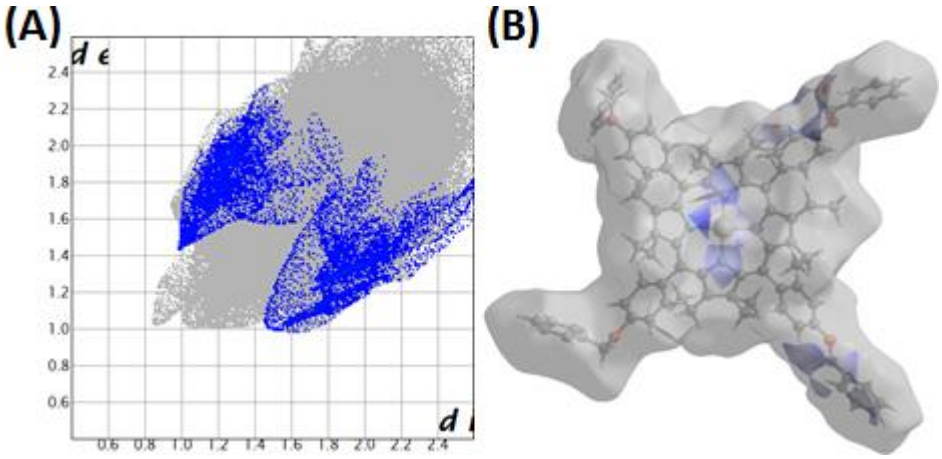

Figure 1:57: Fingerprint plots (A) and Hirshfeld surfaces (B) of compound **1:59** showing the H···N interactions which occupy 3.5% of total surface contacts. H···N interactions represented in the Hirschfeld surface (B) are coloured blue. The grey areas highlight all other contacts which are not the focus of this discussion.

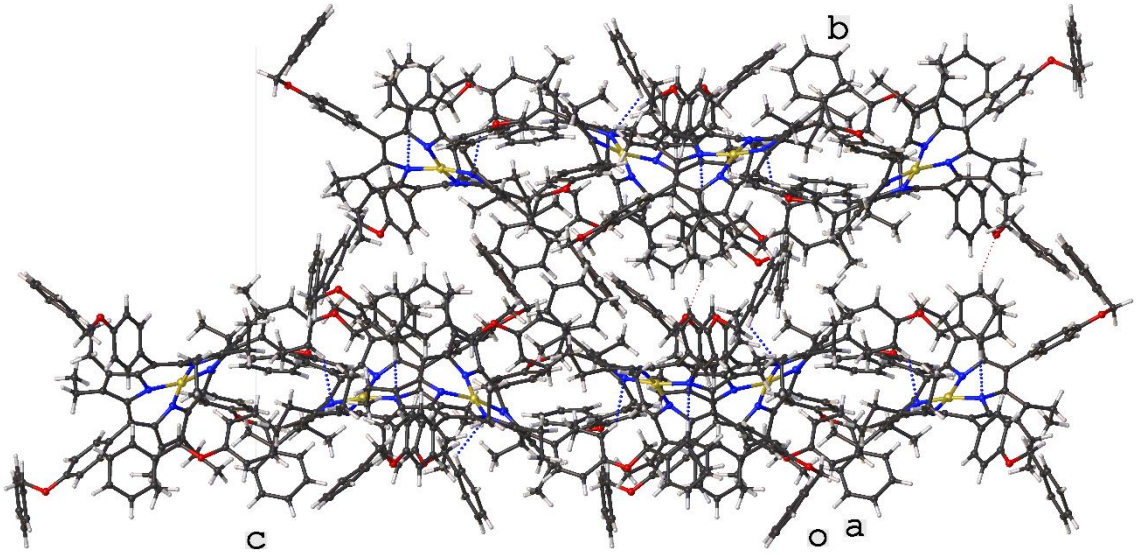

Figure 1:58: Crystal packing of compound **1:59** looking down the *a*-axis. The structure was drawn isotropically.

The Next Phase of Molecular Design of OETArXP Molecular Cages.

From the outcome of the previous OETArXP scaffold, it was decided to redesign these systems in order to circumvent the issue faced with the close-packing arrangement. With this in mind, there are two processes that may prove beneficial in the design of molecular cages. The first is to attempt to generate co-crystal with complementary functionalities (such as 4-iodophenyl and 4-cyanophenyl) to direct the intermolecular interactions between the functional group or to use more hydrogen-bonding groups as Goldberg and co-workers have previously reported.[109a] The second is to extend the arm and angle of the *meso*-substituent

so that it is in a more favourable position for direct contact.[114d] In a paper previously reported by us, one of the structures (5,10,15,20-tetrakis[(4-bromophenyl)thio]-2,3,7,8,12,13,17,18-octaethylporphyrin) showed a promising Br···H interaction in which four porphyrin molecules connected to each other in a cyclic pattern (Figure 1:59). This molecule gave an indication as to the potential of this arm-extension to facilitate the formation of molecular cages, the next layer of porphyrin in the crystal structure occupies this 'cavity' blocking any potential for a molecular cage.

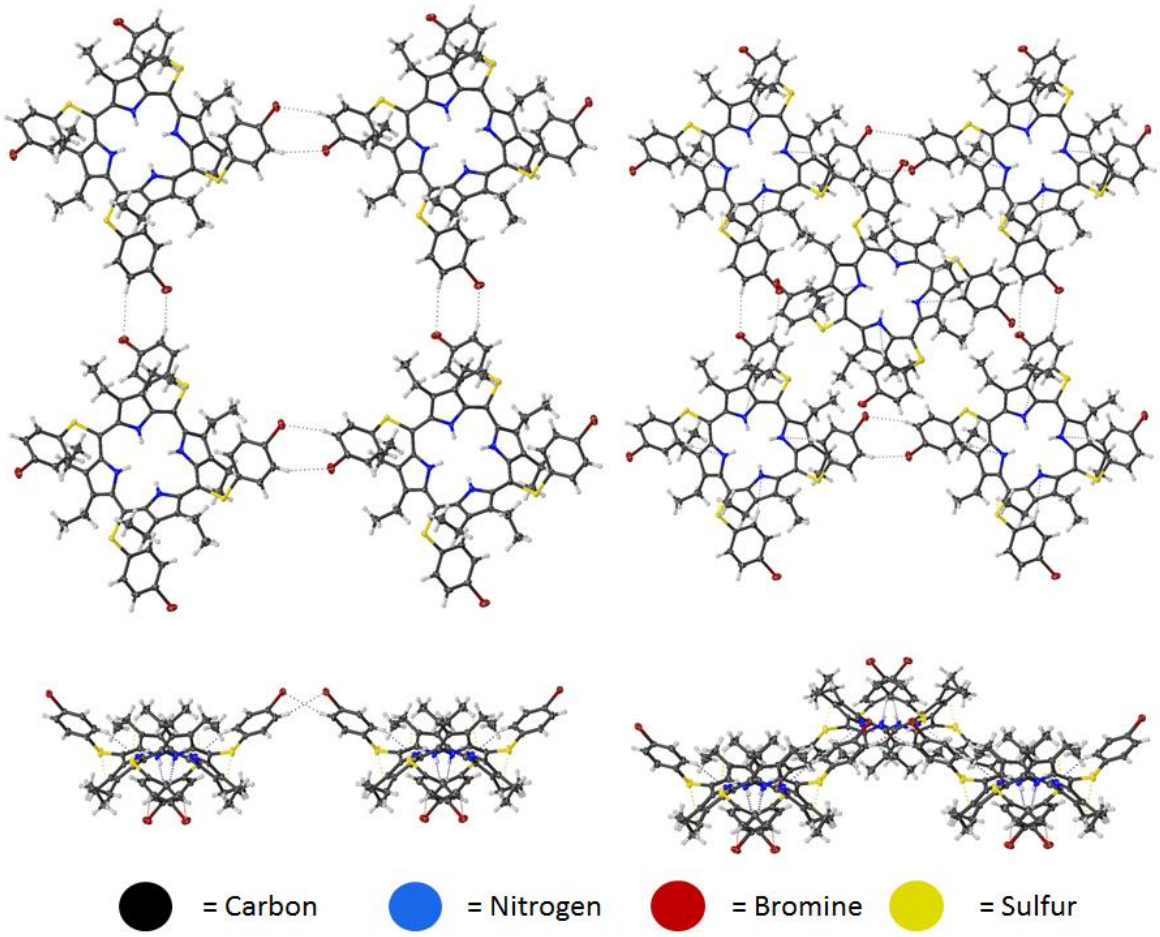

Figure 1:59: The structure (5,10,15,20-tetrakis[(4-bromophenyl)thio]-2,3,7,8,12,13,17,18-octaethylporphyrin) showing the Br···H interaction in which four porphyrin molecules connected to each other in a cyclic pattern. The left image highlights the interaction observed and the right image shows the actual packing.[114d]

To move this project forward it was decided to take an approach where the *meso*-substituted 'arms' were extended away from the porphyrin ring and a larger variety of hydrogen-bonding partners was explored. This process would have two benefits, increasing the number of functional groups at our disposal and potentially reducing the overlap of the porphyrin ring caused by the *meso*-substituents interaction with the porphyrin ring. For this, copper-catalysed azide-alkyne cycloaddition (CuAAC)

was chosen as it meets both requirements. Another benefit to this reaction was that within the series already created to this point were the compounds **1:8**, **1:58**, and **1:12** which would provide an excellent starting point for these reactions.

The first step in synthesising a library of azide partner compounds to couple with either compounds **1:8** or **1:58**. For this, a procedure outlined by Grimes *et al.*, in which the boronic acid precursor was stirred in the presence of NaN_3 for three hours in MeOH was chosen.[121] This resulted in the synthesis of **1:66**, **1:68**, **1:70**, **1:72**, and **1:74**, Scheme 1:8. The azide partner **1:76** was synthesised according to a procedure adapted from Ladmiral *et al.* where the brominated starting material was stirred in the presence of NaN_3 for 4 hours in DMF followed by precipitated from solution using toluene.[127] Following this, the arm-extended porphyrins, compounds **1:78–1:83** were synthesised by the deprotection of compound **1:58** using TBAF followed by a CuAAC using the appropriate azide in excess, Scheme 1:9.

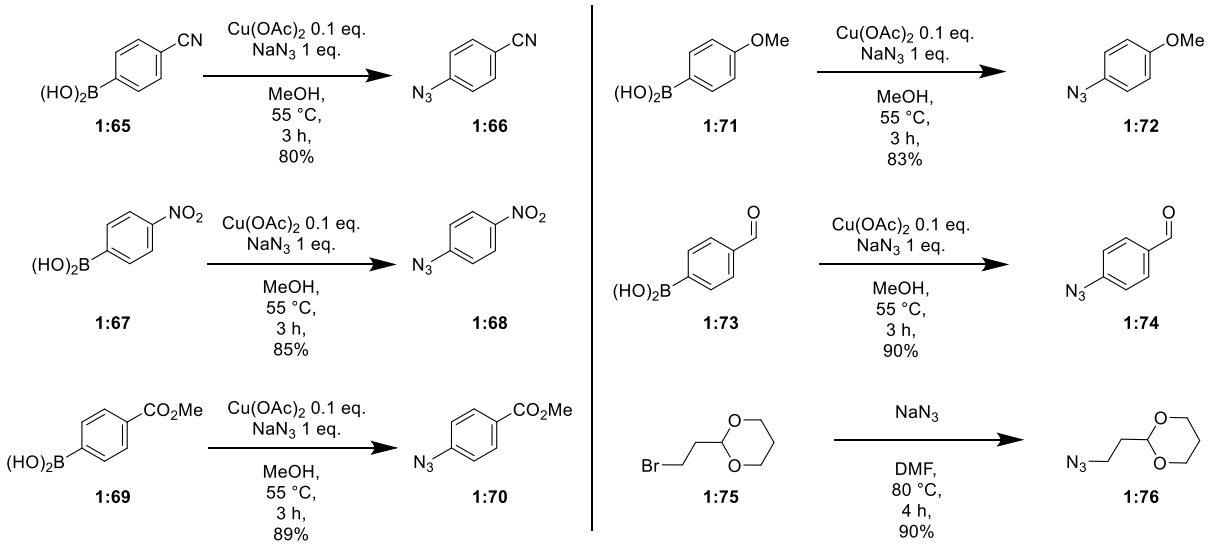

Scheme 1:8: Synthesis of azide coupling partners for arm-extended porphyrins.

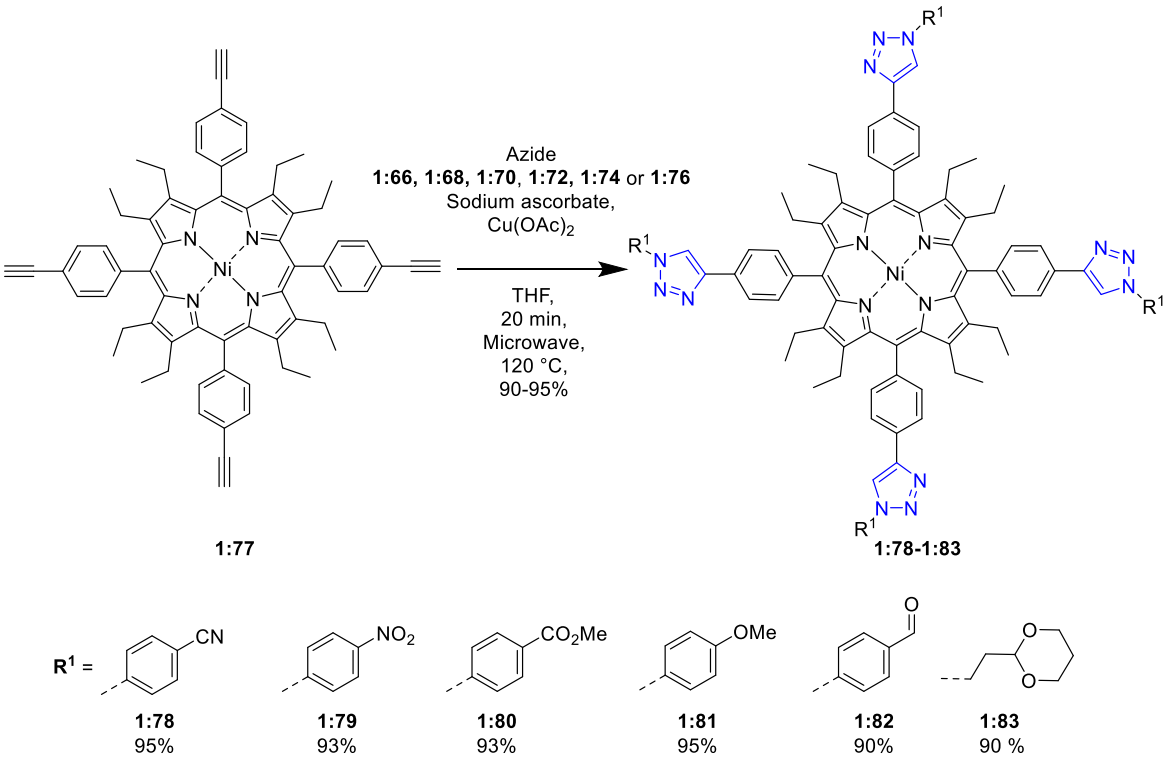

Scheme 1:9: Synthesis of arm-extended porphyrins from acetylene porphyrin.

Additionally, the synthesis of compound **1:84**, which is a regioisomer of compound **1:80** could be achieved by employing a CuAAC using porphyrin **1:12** and the reciprocal alkyne in a four-fold excess (Scheme 1:10). This reaction would demonstrate the versatility of using alternate porphyrin scaffolds to achieve compounds with almost identical functionality.

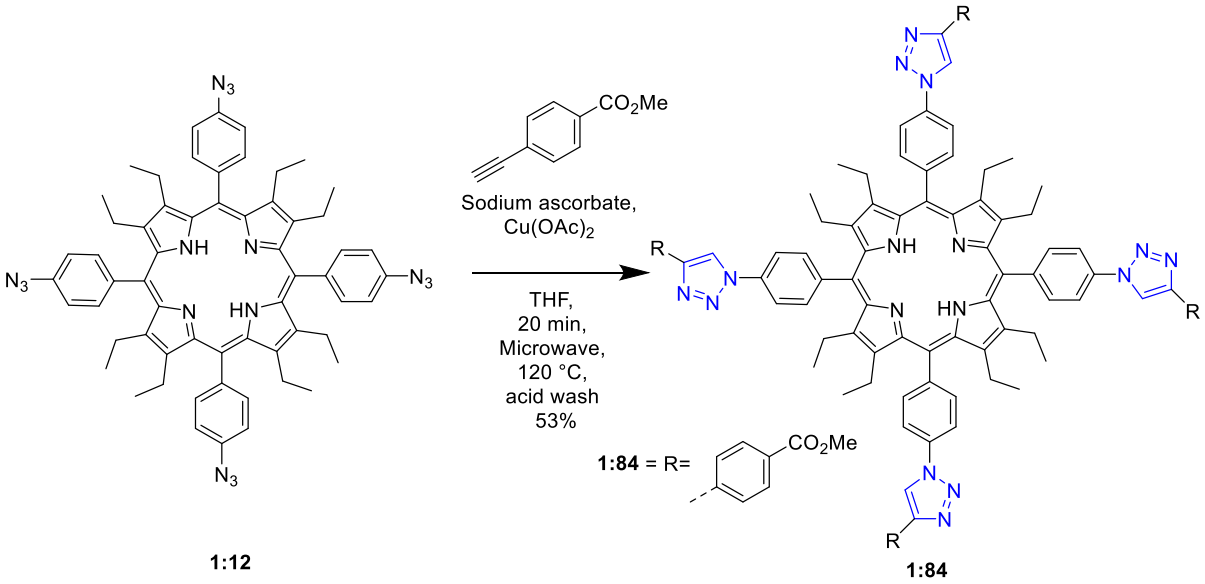

Scheme 1:10: Synthesis of arm-extended porphyrins from azide porphyrins.

The potential crystal from this project would have two desirable outcomes. First, it would extend the *meso*-substituents and help reduce the overlap of the porphyrin rings caused by the *meso*-substituents interaction with the porphyrin macrocycle. Second, it would introduce a variety of hydrogen-bonding partners to this project. As an additional benefit, this method appears to be a rapid way to synthesise a variety of new OETArXPs though a simple one-step process.

Conclusions.

In conclusion, the synthesis of several new OETArXP and their metal counterparts were undertaken. However, the main focus of this project was to establish if OETArXP could be used as a potential scaffold for the synthesis of molecular cages through non-covalent interactions. To this end, we have determined the structures of several new OETArXPs, their metal counterparts, and several solvent inclusion complexes. During this work, the aspects of substitution type and pattern, solvent inclusion, and a change of metal(II) centres was carried out in order to gauge the effect such alterations might have on the crystal packing. We have established that increasing sized halogens, effects the potential of intermolecular interactions and the resulting crystal packing in 4-halo-OETArXP complexes. Additionally, it was demonstrated that both fluorine and chlorine atoms do not partake in direct halogen-halogen interactions in OETArXP systems. For the 2,6-halo-OETArXP it was established that the change in position changes the types of the intermolecular interactions and the packing patterns observed. Additionally, it was highlighted that solvent effects play a much larger role in crystal packing than intermolecular/intramolecular interaction or metal(II) centre substitution. This indicates that the solvent effects are the major driving force behind crystal packing, while other changes such as altering the metal(II) centres have only a marginal influence on the local environment of the macrocycle, rather than in the global packing. This indicates that these structures behave like the porphyrin sponges reported by Byrn *et al*.[108] Within the chain-OETArXP series the *meso*-substituent favours interacting with the core of the porphyrin macrocycle. The cyano-OETArXP is a suitable hydrogen-bond acceptor and resulted in an interesting Z-shape network. To that end, it can be concluded that OETArXP as they currently are would not be suitable as a scaffold design of a molecular cage. The main problem with these molecules is when the solvent is excluded from the structure, they have very

tight packing patterns. This close-packing arrangement is their largest drawback for such an application.

To circumvent this issue, we synthesised a family of 'arm extended' OETArXPs where X is triazole-linked benzene group with a *para*-functionalised moiety (cyano, nitro, methyl ester, methyl ether, or aldehyde), or triazole-linked dioxane. This was done to introduce an alternate functionality to the OETArXPs by using hydrogen bonding group or functional groups that could undergo further functionalisation. This would potentially allow for a moderate reduction in the overlap of the porphyrin ring caused by the *meso*-substituents interaction. We have shown that it is possible to start from either the acetylene or azide porphyrin to achieve such compounds, however, the overall yield from the acetylene complexes are higher. Copper(II) insertion is not a problem for these complexes either as a simple acid wash is suitable to remove most metal centres. An added benefit to this family of compounds is within the chosen functional groups. By using an aldehyde, some initial studies have shown that the porphyrin can be incorporated into a chitosan hydrogel through covalent bonding to create nonplanar water-soluble porphyrin systems that can be tested for catalytic activity or inner core binding.

Outlook

While currently the compounds contained in this chapter do not from molecular cages as was initially hoped for there are areas which could still be exploited in the future. This would involve generating co-crystal with complementary functionalities (such as 4-iodophenyl and 4-cyanophenyl) to direct the intermolecular interactions between the functional group or to use more hydrogen-bonding groups as Goldberg and co-workers have previously reported.[109a] The use of such complimentary groups may prove to be sufficient in directing the *meso*-substituents towards each other, which would eliminate the overlapped structure seen. Another avenue of research one could also attempt is to study the solvent inclusion complexes in more detail. This aspect is similar to the porphyrin sponges reported by Byrn *et al*., where a variety of guests could be incorporated into the crystal structure of the OETArXPs to assess their potential to make porphyrin clathrates.[108] The use of nonplanar porphyrins as clathrates is an intriguing potential as the potential for a guest to occupy the space around the porphyrin core is a new feature compared to the previous studies done on the 5,10,15,20-tetraphenylporphyrin. Another area in

which these compounds may prove beneficial to study, is the sensing and binding of small molecules as illustrated in a review by Kielmann and Senge[115] or as an organo-catalyst as demonstrated by Roucan *et al*.[116]

The triazole-linked porphyrin provides a synthetically attractive scaffold for the continuation of this project. Not only are the yields sufficiently high, but reaction times are also quick and working with either the azide or acetylene derivatives of OETArXP can be used as a starting point for a truly large variety of compound through a one-step process. There are many applications that these compounds could be used for for example, the aldehyde derivative can be incorporated into a chitosan hydrogel to examine nonplanar porphyrin organo-catalysis described by Roucan *et al*. in an aqueous media.[116]

Chapter 1.2 Investigation into the structure of *N*-substituted porphyrins.

Introduction.

The *N*-substitution of porphyrins is an often-neglected path towards nonplanar porphyrins. *N*-Substituted porphyrins, the so-called “green pigments”, are a unique class of molecules relevant to medicine and biochemistry.[128] In nature, they are strong inhibitors of ferrochelatase.[128a, 129] However, over the past few decades this area has been neglected. A recent publication by Roucan *et al*. in which an optimised and simplified synthesis of *N*-substituted porphyrins and their conformation analysis (which is the basis of this chapter section) has spawned a renaissance in this area.[93] As stated before, the conformational distortion of porphyrins is crucially related to their biological function.[[72]] However, most previous structural studies focused on systems with peripheral steric strain (highly substituted porphyrins) while only a few crystallographic reports have addressed metal-free *N*-substituted porphyrins. During the course of this project, we were able to obtain structures for five new macrocycle structures (**1:86**, **1:87**, **1:90**, **1: [91]$^+$**, and **1: [99]$^+$**) and use these in conjunction with published structures (see Figure 1:60 and Table 1:2) for the first comprehensive analysis of the structural properties of *N*-substituted porphyrins.[88-89, 105, 114e, 130] The compounds in this chapter were provided by Marie Roucan from the Senge group and the X-ray crystal structures were collected by myself..

Results and Discussion.

Two new structures of *N*-methyl substituted porphyrins (N^{21}-mono (**1:86**) and N^{21},N^{23}-di (**1:87**)) have been determined. Several trends can be seen when comparing against the literature compounds 5,10,15,20-tetraphenylporphyrin (**1:85**) and N^{21},N^{22},N^{23}-trimethyl-5,10,15,20-tetraphenylporphyrin (**1:[88]$^+$**) (Figure 1:61).[114e, 130a] Inspection of the average deviation of the 24-atom mean plane (Δ24) reveals an interesting trend for the overall macrocycle distortion as a result of *N*-methylation. The first insertion shows a large increase in the Δ24 from **1:85** to **1:86**. When a second methyl group is inserted (**1:86** to **1:87**), a second larger increase in Δ24 is observed due to crowding in the porphyrin core. When the third methyl group is inserted into the porphyrin core (**1:[88]$^+$**), a moderate decrease in the Δ24 (**1:87** to **1:[88]$^+$**) is noted. This is due to the fact that the third methyl group insertion is now below the macrocycle plane, at the most extreme distance available from the

other two methyl groups and has a moderated effect by decreasing the overall 24-atom ring strain applied by core substitutions. These trends are followed for deviation of the *α* and *β* carbon atoms (C_a and C_b), while the *meso* carbons (C_m) appear to follow the trend of **1:85**<**1:87**<**1:86**<**1:[88]$^+$**.

This is also represented in the normal-coordinate structural decomposition (NSD) analysis[131] (Figure 1:62), where the out-of-plane distortion of **1:85** favours the $E_g(y)$ wave distortion mode with the second largest, albeit small, contribution by the $E_g(x)$ wave distortion mode. However, upon insertion of one methyl group (**1:86**), a large preference for the B_{2u} distortion mode with the second largest contribution to the $E_g(x)$ wave distortion mode is observed. For **1:87**, a much larger contribution to the B_{2u} saddled distortion mode is observed in comparison to **1:86** with the second largest contribution now present in the A_{2u} propeller distortion mode.

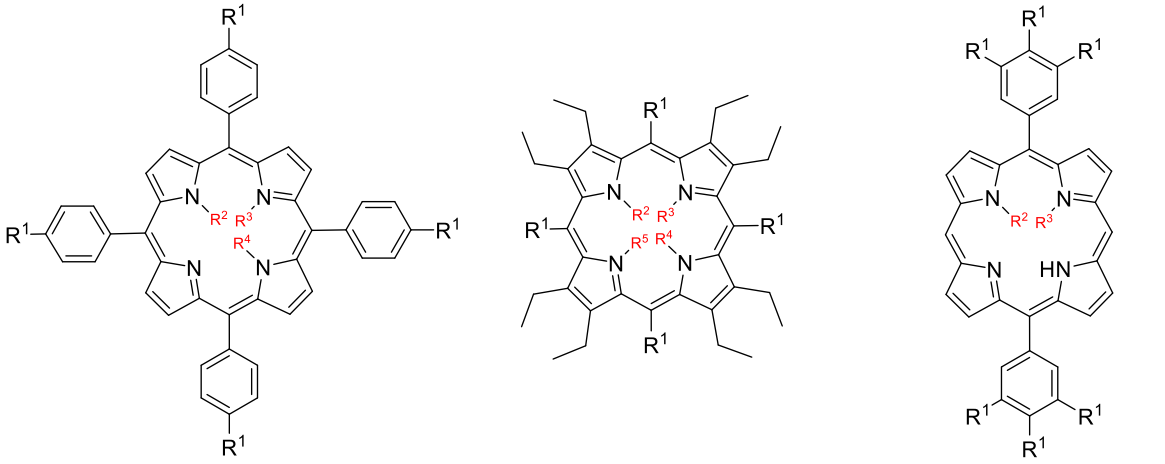

X	R^1	R^2	R^3	R^4
1:85	H	H	H	H
1:86	H	CH_3	H	H
1:87	H	CH_3	H	CH_3
1:[88]$^+$	H	CH_3	CH_3	CH_3
1:89	OMe	H	H	H
1:90	OMe	CH_3	H	H
1:[91]$^+$	OMe	CH_3	CH_3	CH_3
1:92	Br	CH_3	H	H

X	R^1	R^2	R^3	R^4	R^5
1:93	Ph	H	H	H	H
1:94	Ph	CH_3	H	CH_3	H
1:[95]$^+$	Ph	CH_3	CH_3	CH_3	H
1:[96]$^{2+}$	Ph	CH_3	CH_3	CH_3	CH_3
1:97	H	H	H	H	H
1:98	H	CH_3	H	CH_3	H

X	R^1	R^2	R^3
1:[99]$^+$	OMe	CH_3	CH_3

[X]$^+$ and [X]$^{2+}$ indicates salt species

Figure 1:60: List of compounds investigated in this section.

Structure **1: [88]$^+$** shows a similar contribution to the B_{2u} saddled distortion mode with the second largest contribution now present in the A_{2u} propeller distortion mode similar to **1:87**, with only a marginal decrease in values. This trend is extended to the D_{oop} with the contributions as follows **1:85**<**1:86**<**1:[88]$^+$**<**1:87**, which is representative of the Δ24 as seen in Table 1:2. Looking at the global distortion, it

shows that an increase in the core substitution[105, 130e] is a convenient and suitable method to achieve nonplanarity in previously planar porphyrin macrocycles. However, increasing from two to three inner core substituents only results in moderate additional distortion and can be considered to be almost equal in nonplanarity. Interestingly, localised distortion on specific pyrrole units is also observed in these systems. This can be illustrated by inspection of pyrrole tilt angles and the deviation from the 24-atom mean plane of internal nitrogen atoms (N21–N24) (see Table 1:2).

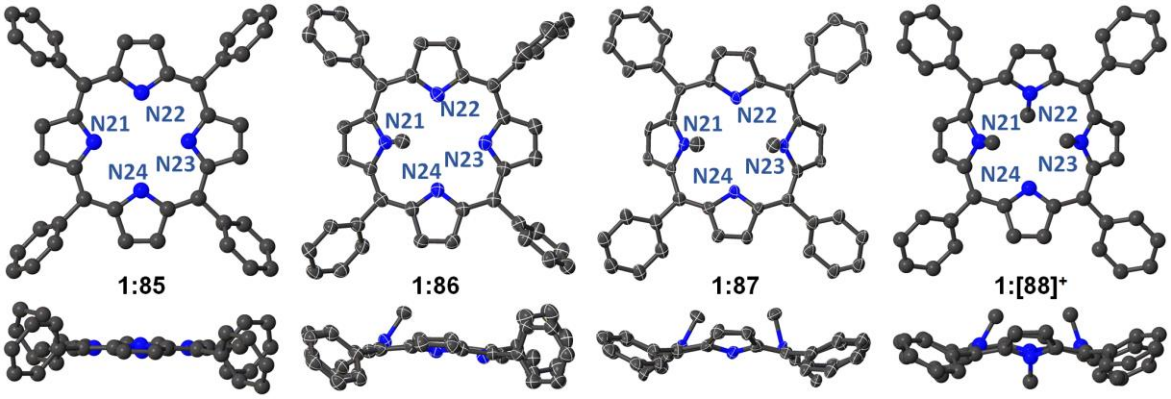

Figure 1:61: Views of molecular structures in the crystals: 5,10,15,20-tetraphenylporphyrin (**1:85**),[130a] N^{21}-monomethyl-5,10,15,20-tetraphenylporphyrin (**1:86**), N^{21},N^{23}-dimethyl-5,10,15,20-tetraphenylporphyrin (**1:87**), N^{21},N^{22},N^{23}-trimethyl-5,10,15,20-tetraphenylporphyrin **1:[88]$^+$**.[114e] X-ray structure images (top and side-on) are shown with hydrogen atoms, minor disorder, and solvent molecules are omitted for clarity. Structure of **1:86** and **1:87** have been drawn with thermal ellipsoids at 50% probability. The structures of **1:85** and **1:[88]$^+$** have been drawn isotropically.

Table 1:2: Selected structural parameters for *N*-substituted porphyrins.

	1:85[130a]	**1:86_1**	**1:86_2**	**1:87_1**	**1:87_2**	**1:[88]$^+$**[114e]
Pyrrole tilt (°)						
N21	6.545(7)	30.9(10)	28.4(10)	43.3(3)	43.1(3)	38.2(1)
N22	1.518(18)	7.5(10)	8.2(10)	28.9(3)	24.2(1)	30.4(11)
N23	6.545(7)	1.5(10)	6.1(10)	48.9(5)	38.4(3)	39.7(16)
N24	1.518(18)	11.8(9)	9.1(10)	30.6(14)	24.5(18)	18.2(12)
Structural parameters (Å)						
ΔN21[a]	-0.158	-0.427	0.422	0.247	-0.308	-0.307
ΔN22[b]	0.012	-0.083	0.020	0.035	0.002	0.183
ΔN23[c]	0.158	0.227	-0.063	0.300	-0.260	-0.328
ΔN24[d]	-0.012	0.024	-0.031	-0.013	-0.001	-0.066
ΔN[e]	0.085	0.190	0.134	0.149	0.143	0.221
Δ24[f]	0.068	0.299	0.256	0.711	0.608	0.570
ΔC_m[g]	0.023	0.062	0.075	0.037	0.048	0.076
ΔC_a[h]	0.034	0.134	0.095	0.333	0.273	0.232
ΔC_b[i]	0.063	0.431	0.368	1.171	0.999	0.933
Δ_{ip}[j]	0.199	0.161	0.232	0.588	0.315	0.152
Δ_{oop}[k]	0.261	1.388	1.161	3.372	2.857	2.644

Tables 1:2 (continued): Selected structural parameters for *N*-substituted porphyrins.

	1:89[130b]	**1:90**	**1: [91]$^+$**	**1:92**[130c]	**1:93**[89]	**1:94**[130e]
Pyrrole tilt (°)						
N21	2.7(1)	35.7(2)	42.1(15)	27.2(5)	34.3(11)	52.1(2)
N22	2.8(1)	11.9(8)	30.2(16)	10.8(18)	27.0(11)	32.7(7)
N23	2.7(1)	10.0(4)	47.9(15)	7.7(13)	29.1(11)	52.6(4)
N24	2.8(1)	7.3(5)	22.3(9)	11.3(18)	31.7(10)	36.3(4)
Structural parameters (Å)						
ΔN21[a]	-0.023	0.418	-0.308	-0.399	-0.028	0.239
ΔN22[b]	-0.030	0.070	0.109	0.073	0.111	0.164
ΔN23[c]	0.023	-0.130	-0.361	0.059	-0.107	0.254
ΔN24[d]	0.030	0.136	-0.060	0.001	0.038	0.036
ΔN[e]	0.027	0.189	0.210	0.133	0.066	0.173
Δ24[f]	0.048	0.366	0.645	0.266	0.712	0.831
ΔC_m[g]	0.069	0.127	0.050	0.182	0.036	0.038
ΔC_a[h]	0.026	0.177	0.280	0.110	0.421	0.414
ΔC_b[i]	0.031	0.540	1.057	0.361	1.156	1.367
Δ_{ip}[j]	0.200	0.283	0.407	0.246	0.515	0.856
Δ_{oop}[k]	0.220	1.705	3.041	1.209	3.460	3.973

Tables 1:2 (continued): Selected structural parameters for *N*-substituted porphyrins.

.	**1:[95_2]$^+$**[105]	**1:[95_2]$^+$**[105]	**1:[96]$^{2+}$**[130e]	**1:97**[88]	**1:[98]$^+$**[130d]	**1:[99]$^+$**
Pyrrole tilt (°)						
N21	46.7(16)	47.7(2)	46.6(12)	2.2(4)	31.2(8)	30.4(1)
N22	41.3(17)	39.3(3)	45.0(15)	1.1(3)	25.4(6)	31.0(1)
N23	52.0(17)	47.7(2)	44.3(13)	2.2(4)	7.1(19)	6.7(1)
N24	36.3(15)	35.3(3)	43.8(13)	1.1(3)	8.7(16)	0.6(1)
Structural parameters (Å)						
ΔN21[a]	-0.217	-0.235	0.200	-0.040	-0.363	-0.390
ΔN22[b]	0.102	0.099	-0.179	0.015	0.260	0.381
ΔN23[c]	-0.242	-0.235	0.177	0.040	0.111	0.212
ΔN24[d]	0.030	0.010	-0.176	-0.015	-0.133	-0.256
ΔN[e]	0.148	0.145	0.183	0.028	0.217	0.310
Δ24[f]	0.820	0.795	0.810	0.026	0.362	0.364
ΔC_m[g]	0.024	0.026	0.030	0.021	0.099	0.119
ΔC_a[h]	0.395	0.382	0.373	0.012	0.144	0.150
ΔC_b[i]	1.357	1.316	1.345	0.026	0.543	0.502
Δ_{ip}[j]	0.722	0.612	0.636	0.228	0.313	0.608
Δ_{oop}[k]	3.886	3.765	3.814	0.110	1.683	1.695

[a] Calculated deviation of N21 from the 24-atom mean plane. [b] Calculated deviation of N22 from the 24-atom mean plane. [c] Calculated deviation of N23 from the 24-atom mean plane. [d] Calculated deviation of N24 from the 24-atom mean plane. [e] Simulated displacement of the four internal nitrogen atoms from the 24-atom mean plane. [f] Average deviation from the least-squares plane of the 24-macrocycle atoms. [g] Average deviation of the *meso*-carbon atoms from the 24-atom mean plane. [h] Average deviation of the *α*-carbon atoms from the 24- atom mean plane. [i] Average deviation of the *β*-carbon atoms from the 24-atom mean plane. [j] Simulated total in-plane distortion. [k] Simulated total out-of-plane distortion.

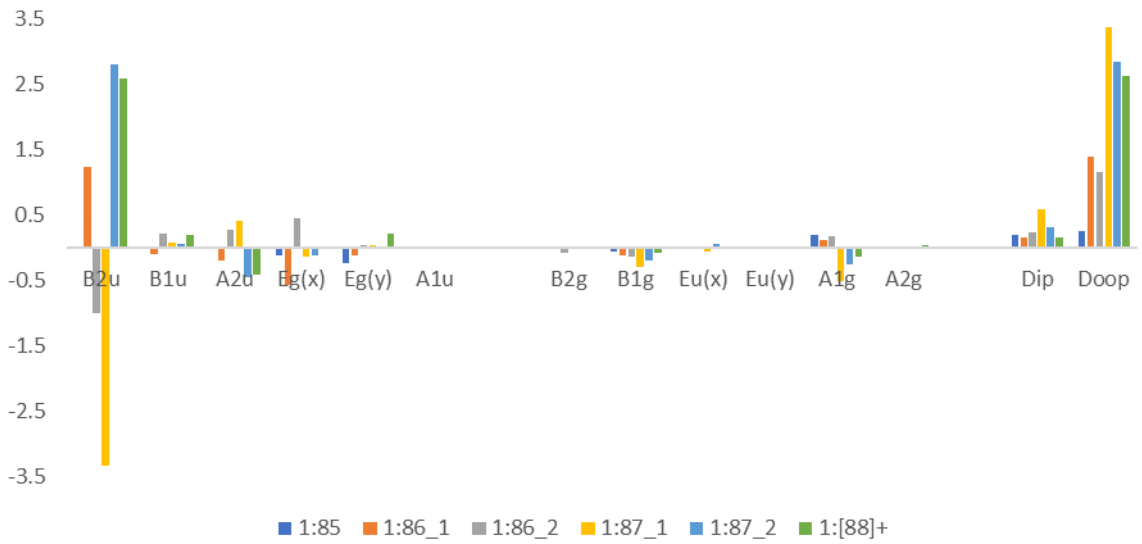

Figure 1:62. Normal-coordinate structural decomposition (NSD) analysis of the X-ray crystallographic structures of **1:85**, **1:86**, **1:87** and **1:[88]$^+$**.

Looking at the pyrrole tilt angles from the 24-atom mean plane, a similar trend is seen as above with the increase of tilt **1**:**85**<**1:86**<**1:[88]$^+$**<**1:87** for *N*-methyl substituted pyrroles. However, accessing the specific impact this has on the localised pyrroles, it is noted that the largest deviation of core nitrogen atoms from the 24-atom mean plane is located on N21 of **1:86**, being much larger than its counterparts, **1:87** and **1:[88]$^+$**. This suggests that the localised deviations (considering the deviation at one point of the 24-atom macrocycle) of N21 from the 24-atom mean plane in the *N*-monomethylated porphyrin have a larger impact than that of higher substituted porphyrins due to a lower overall distortion (the complete porphyrin macrocycle, Δ24), but higher local distortion. Conversely, the higher the overall macrocycle distortion, the lower the ΔN is observed, as is the case for **1:87**. This suggests that there is a correlation between the number of internal core substituents and nitrogen atom deviation. By taking into consideration the above situation, it appears that the inclusion of a third *N*-Me unit to the porphyrin core results in a type of 'counter-balancing' effect. With increased *N*-methyl substitution the global distortion of internal nitrogen atoms is significantly increased; however, due to their comparative planarity, lower numbers of *N*-methyl substituents result in the largest local deviation of the core nitrogen atom from the 24-atom mean plane. One of the interesting points noted from the ^{1}H NMR spectra reported by Roucan *et al.* was associated with an upfield chemical shift of core protons as a result of *N*-methylation.[93] When comparing the structures of **1:85**, **1:86**, **1:87** and **1:[88]$^+$** two factors appear to be at play. The noticeable difference in chemical shift of **1:87**

where the core methyl substitution is less than would be expected to give the increased distortion. The first case is the fact that the methyl groups point directly away from phenyl groups suggesting a decrease in the electron density of the porphyrin ring. This coupled with the alternate packing of **1:87**, where contrary to the packing diagrams of **1:86** and **1:[88]$^+$** there are fewer molecules interacting with the porphyrin ring, Figure 1:63. This creates an electron deficient environment with effects the total ring current of the porphyrin ring resulting in the unexpected shift of signals seen in the ^{1}H NMR spectra reported by Roucan *et al*.[93]

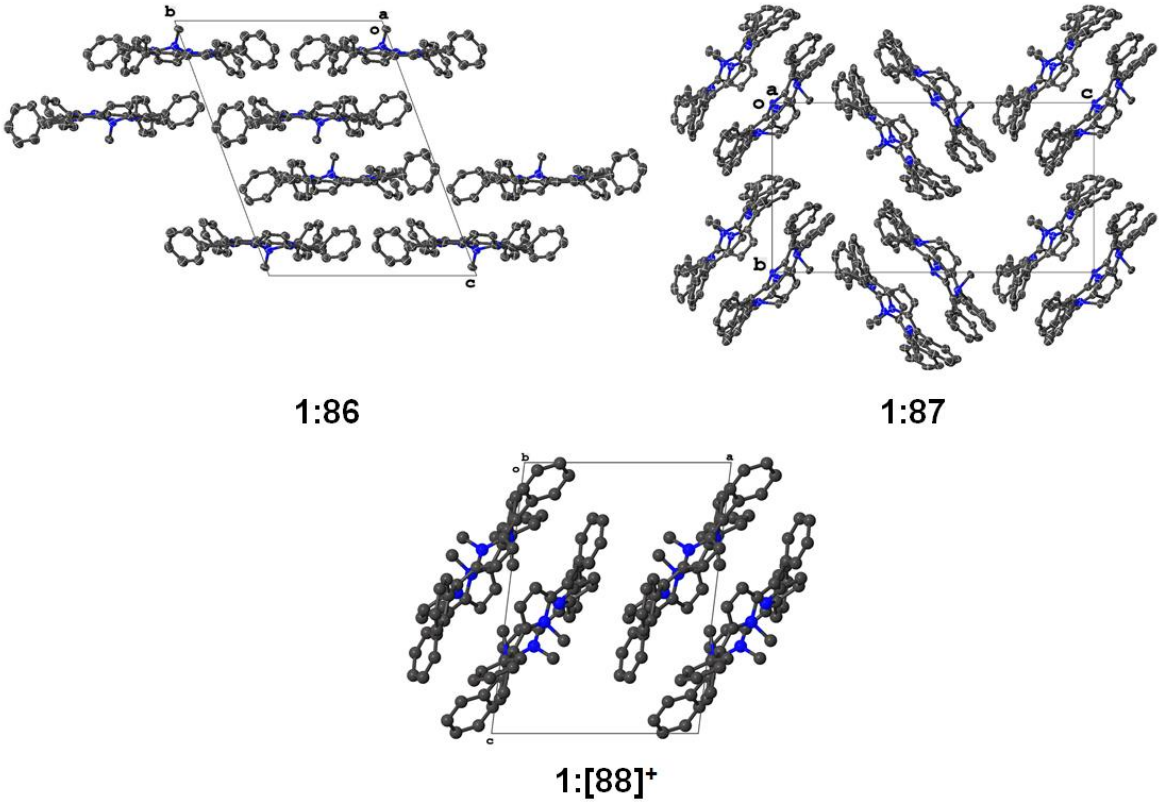

Figure 1:63: Moiety packing of compounds **1:86**, **1:87**, and **1:[88]$^+$** shown with hydrogen atoms, minor disorder, and solvent molecules omitted for clarity.

As previously indicated, nonplanar porphyrins have been implicit in small molecule binding.[92a, 115-116, 132] This is due to the tilt angle of the pyrrole rings out of the porphyrin plane, allowing for the central imine and amine motifs of the porphyrin ring to partake in hydrogen-binding with small molecules. This effect is also seen with *N*-substituted porphyrins, namely in the structure of **1:87**. The asymmetric unit of this structure contains core bound water molecules, which are interacting with the imine pyrrole units in a hydrogen-bonding fashion (Figure 1:64). The D–H···X distances and angles are listed as follows; N22_1···H2SA–O2S (2.006 (1) Å, 148.7(1)°), N24_1···H2SB–O2S (2.114 (1) Å, 144.0 (1)°), N22_2···H1SA–O1S (2.002 (1) Å,

138.5 (1)°), and N24_2···H1SA–O1S (1.831 (1) Å, 168.0 (1)°). This suggests that *N*-substituted porphyrins have a sizable capacity to bind small molecules to the porphyrin core.

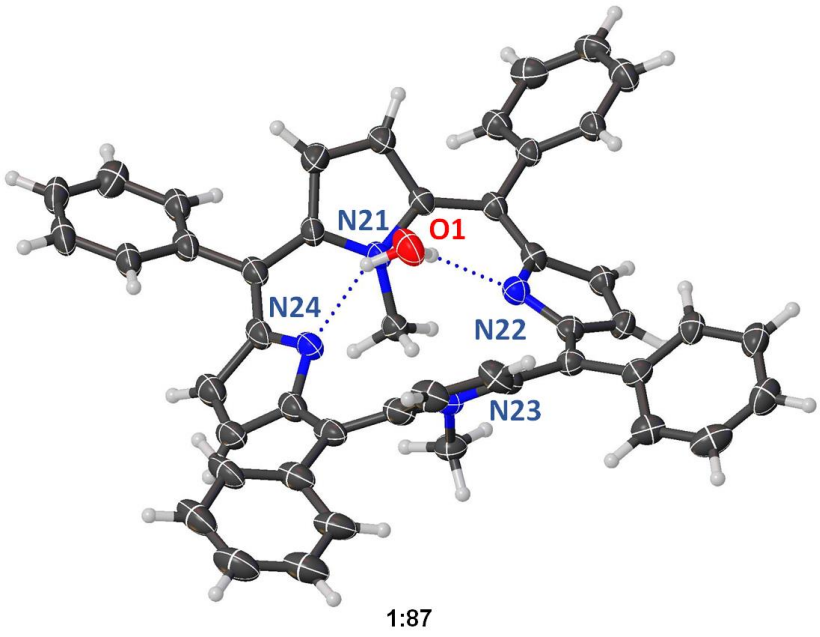

Figure 1:64: View of the molecular structure of N^{21},N^{23}-dimethyl-5,10,15,20-tetraphenylporphyrin (**1:87**) showing solvent water molecule interacting with the porphyrin core. The structure of **1:87** has been drawn with thermal ellipsoids at 50% probability.

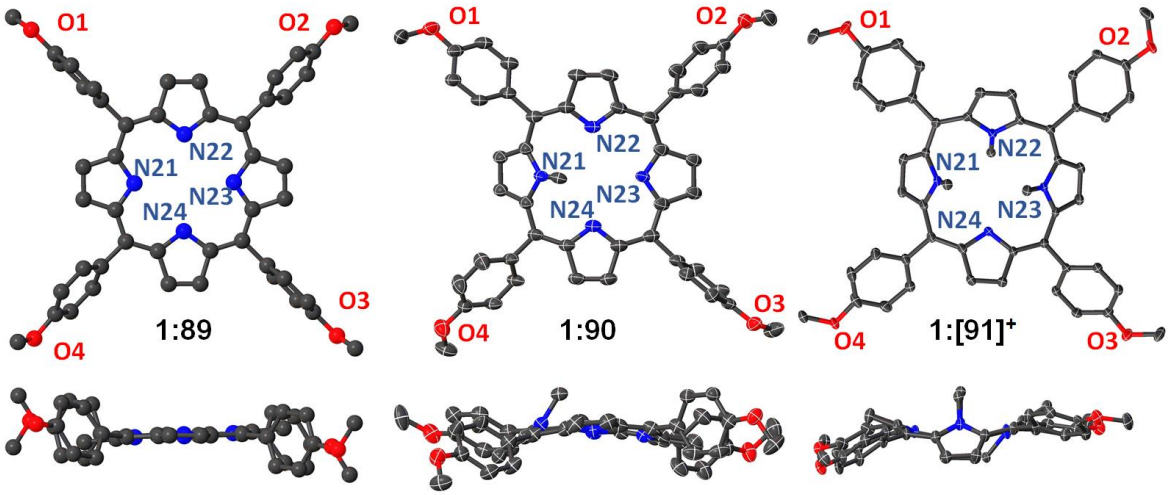

Figure 1:65: Top and side views of the molecular structure in the crystal for 5,10,15,20-tetrakis(4-methoxyphenyl)porphyrin (**1:89**),[28] N^{21}-monomethyl-5,10,15,20-tetrakis(4-methoxyphenyl)porphyrin (**1:90**) and N^{21},N^{22},N^{23}-trimethy-5,10,15,20-tetrakis(4-methoxyphenyl)porphyrin **1:[91]**$^{+}$. Hydrogen atoms, minor disorder, and solvent molecules were omitted for clarity. Structure of **1:90** and **1:[91]**$^{+}$ have been drawn with thermal ellipsoids indicate 50% probability. The structure of **1:89** has been drawn isotropically.

In the case of 5,10,15,20-tetrakis(4-methoxyphenyl)porphyrin (**1:89**), two new *N*-methyl substituted structures containing the N^{21}-mono- (**1:90**) and N^{21},$N^{22}N^{23}$-trimethylated-5,10,15,20-tetrakis(4-methoxyphenyl)porphyrin were obtained (**1:[91]$^+$**) (Figure 1:65). While looking at the global distortion as indicated by Δ24, a similar trend was observed as for the 5,10,15,20-tetraphenylporphyrin series discussed above. Compound **1:89** shows the smallest deviation in Δ24, followed by **1:90** and **1:[91]$^+$**. This **1:89**<**1:90**<**1:[91]$^+$** trend is followed for the C_a and C_b deviations from the 24-atom mean plane. However, for the C_m, **1:90** shows the largest deviation from the 24-atom mean plane with **1:[91]$^+$** showing deviations much more similar to that of porphyrin **1:89**. This is due to the larger atom deviations forcing the C_m atoms to be closer to the 24-atom mean plane. Deviations of the nitrogen atoms from the 24-atom mean plane gave similar results. Compound **1:90** shows a much larger ΔN21 then **1:[91]$^+$**. This suggests that this trend is generally applicable to *N*-substituted porphyrins.

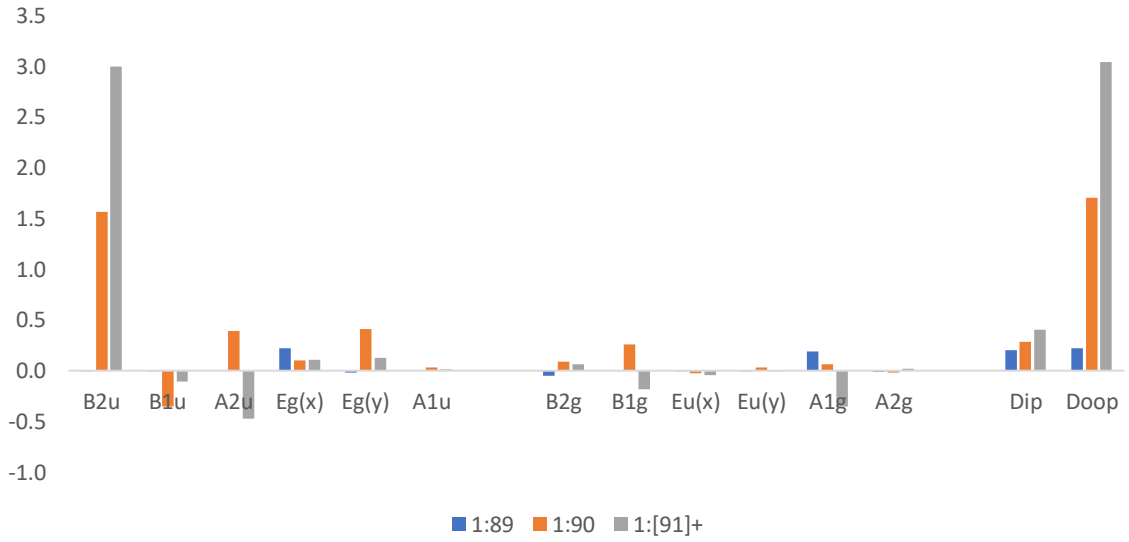

Figure 1:66: Normal-coordinate structural decomposition (NSD) analysis of the X-ray crystallographic structures of **1:89**, **1:90**, and **1:[91]$^+$**.

Using NSD analysis (Figure 1:66), the structure of **1:89** shows largest contributions from the E_g(x) wave distortion mode with a smaller contribution seen in the E_g(y) wave distortion mode. As with the TPP series, the insertion of one methyl group to the core nitrogen atom (**1:90**) results in a shift of the distortion mode to the B_{2u} saddle distortion mode with the second largest presence in the E_g(y) wave distortion mode. Similarly, a large increase is observed for the B_{2u} saddle distortion mode when three methyl groups occupy the core nitrogen atoms (**1:[91]$^+$**) with the second largest contribution to the A_{2u} domed distortion mode. There is a clear increase in

the out-of-plane distortion with **1:89**<**1:90**<**1:[91]**$^{+}$ which is similar to that seen in the TPP series.

The inclusion of electron donating and withdrawing groups (EWD and EWG) to the porphyrin macrocycle is well known to affect the electronics of the porphyrin core and thus the ability of the porphyrin core nitrogen atoms to undergo substitutions.[133] However, how the inclusion of EWG's and EDG's affect the conformation of *N*-substituted porphyrins has been less well established, due to the relative scarcity of structural examples in the literature. Here, we determined the structure of **1:90** (Figure 1:67) and the structure of **1:92** which is available in the literature.[130c]

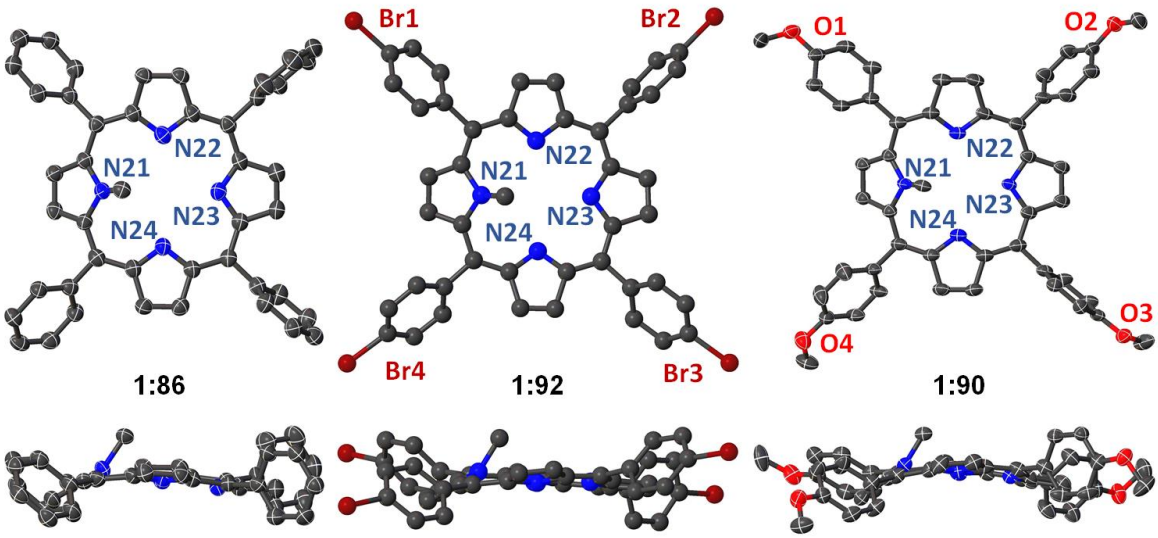

Figure 1:67: Substitution effects on distortion; N^{21}-monomethyl-5,10,15,20-tetraphenylporphyrin (**1:86**), N^{21}-monomethyl-5,10,15,20-tetrakis(4-methoxyphenyl)porphyrin (**1:90**), N^{21}-monomethyl-5,10,15,20-tetrakis(4-bromophenyl)porphyrin (**1:92**).[130c] Views of the molecular structure in the crystal: face (top) and edge-on (bottom) are shown with hydrogen atoms, minor disorder, and solvent molecules omitted for clarity. The structure of **1:86** and **1:90** have been drawn with thermal ellipsoids indicate 50% probability. The structure of **1:92** has been drawn isotropically.

As before, looking at the overall distortion of the porphyrin macrocycle, the porphyrin with strong electron-donating substituents (**1:90**) shows the largest contribution to ΔN, Δ24, ΔC_a, ΔC_b, $\Delta_{ip,}$ and Δ_{oop}. In fact, the only area in which an EWG porphyrin **1:92** shows a larger contribution is the ΔC_m. This indicates that the distortion present in *N*-substituted porphyrins, is partially dependent on the type of substitutions, with EDG's causing generally higher degrees of nonplanarity than EWG's. However, within this group of porphyrins, it should be noted that EDG porphyrins have a higher impact on the global distortion of the *N*-substituted porphyrin macrocycle. The

highest degree of distortion associated with the local pyrrole ring is located on porphyrin **1:86** with ΔN21, ΔN22, and ΔN23 being marginally larger than the more EDG of porphyrin **1:90**. The reverse of this effect is seen in the pyrrole tilt angles, in which, **1:90** shows the largest tilts for N21, N22, and N23 and the smallest tilt angle for N24. The largest N24 tilt angle is featured on porphyrin **1:86**. Compound **1:92** seems generally to lie in the middle for the pyrrole tilt angles of N22, N23, and N24, while it exhibits by far the smallest pyrrole tilt around N21.

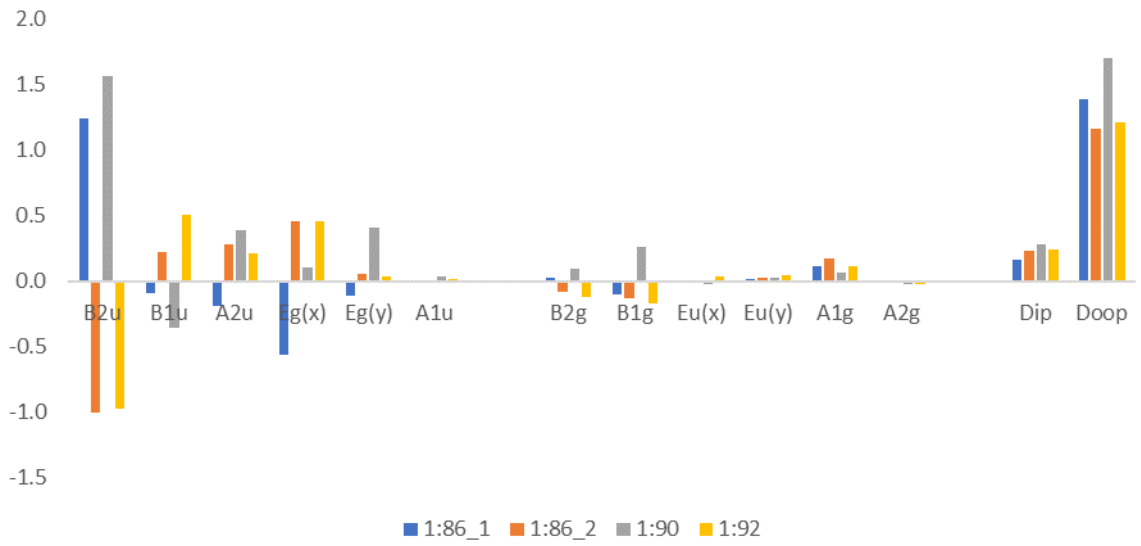

Figure 1:68: Normal-coordinate structural decomposition (NSD) analysis of the X-ray crystallographic structures of **1:86**, **1:90**, and **1:92**.

From the NSD (Figure 1:68), it can be seen that compound **1:90** shows the largest contribution to the B_{2u} distortion mode with its second largest contribution to the E_g(y) distortion mode. Compound **1:86** shows the next largest contribution to the B_{2u} distortion mode; however, it appears to favour the E_g(x) distortion mode for its second largest contribution. The structure of **1:92** shows the smallest contribution to the B_{2u} distortion mode of the three structures discussed in this section. Additionally, **1:92** appears to favour the B_{1u} distortion mode for the second largest contribution, closely followed by the E_g(x) distortion mode.

As this section deals with a discussion on the structural effect of *N*-substitutions in porphyrins, it felt prudent to include the literature examples of highly *β*-substituted *N*-substituted porphyrins. With this in mind, the previously published structures of 2,3,7,8,12,13,17,18-octaethyl-5,10,15,20-tetraphenyl *N*-substituted porphyrins were investigated (Figure 1:69).[89, 105, 130e] This series presents an interesting example of the effects of *N*-substitution on highly substituted porphyrins. It is seen

clearly from both the Δ24 (Table 1:2) and the NSD (Figure 1:70), that there is little to no difference in the degree of nonplanarity as a result of *N*-substitution. The largest atom displacement (ΔN and ΔC_b) appears to correspond to compound **1:94** baring the deviations of ΔN22 and ΔN24 of porphyrin **1:[96]$^{2+}$** due to the additional methyl units attached to these nitrogen atoms. The free base porphyrin **1:93** appears to generally have the smallest displacement of atoms from the 24-atom macrocycle except in the ΔC_m and ΔC_a. This trend is represented with the largest contribution of all compounds found in the B_{2u} distortion mode (**1:94>1:[95]$^{+}$> 1:[96]$^{2+}$>1:93**). The second largest contributions are located in the A_{2u} distortion mode for **1:94>1:[95]$^{+}$> 1:[96]$^{2+}$**. However, **1:93** appears to have a preference E_g(x) distortion mode. This indicates that when working with highly substituted porphyrins *N*-substitution only presents minimal increases to the overall distortion present.

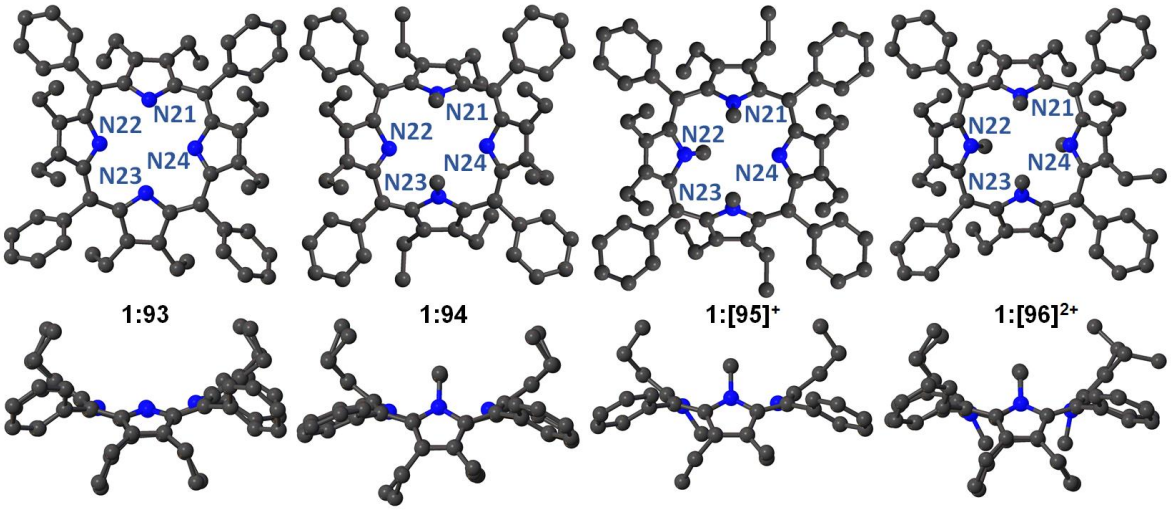

Figure 1:69: Structure of 2,3,7,8,12,13,17,18-octaethyl-5,10,15,20-tetraphenylporphyrin (**1:93**),[89] 2,3,7,8,12,13,17,18-octaethyl-N^{21},N^{23}-dimethyl-5,10,15,20-tetraphenylporphyrin (**1:94**),[130e] 2,3,7,8,12,13,17,18-octaethyl-N^{21},N^{22},N^{23}-trimethyl5,10,15,20-tetraphenylporphyrin (**1:[95]$^{+}$**),[105] 2,3,7,8,12,13,17,18-octaethyl-N^{21},N^{22},N^{23},N^{24}-tetramethyl-5,10,15,20-tetraphenylporphyrin (**1:[96]$^{2+}$**)[130e] Views of the molecular structure in the crystal: face (top) and edge-on (bottom) are shown with hydrogen atoms, minor disorder, and solvent molecules omitted for clarity. All structures are drawn isotropically.

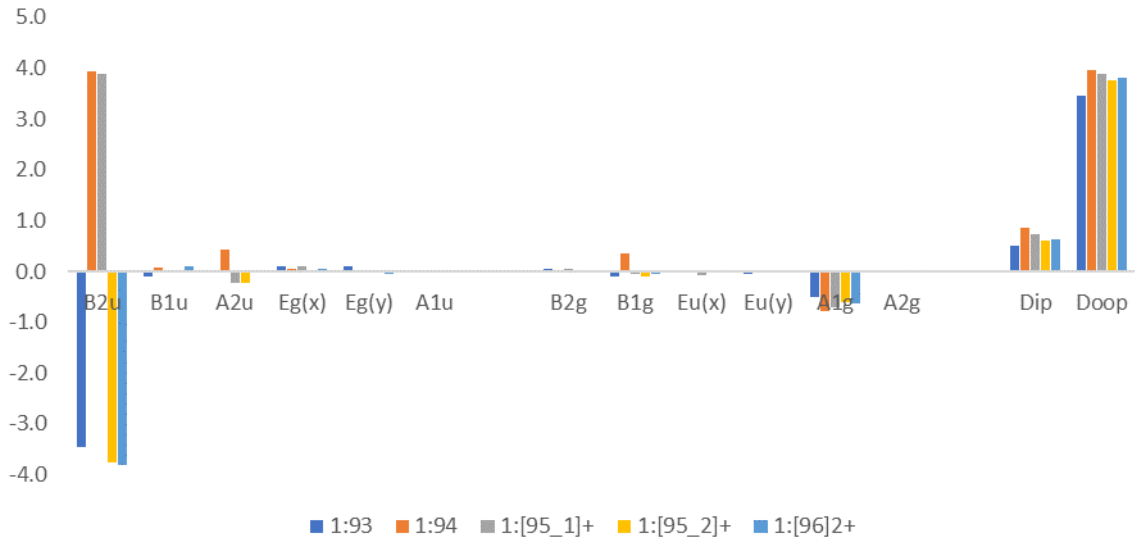

Figure 1:70: Normal-coordinate structural decomposition (NSD) analysis of the X-ray crystallographic structures of **1:93**, **1:94**, **1:[95]$^{+}$** and **1:[96]$^{2+}$**.

From the previous observations, OETPP **1:93** and the N^{21},N^{22}-dimethylated TPP **1:87** were compared (Figure 1:71) as they display similar behaviours. While considering the UV-vis results reported by Roucan *et al.*, it was noted that the bathochromic shift of the Soret band is correlated to the distortion of the macrocycle.[93] Here, compounds **1:93** (456 nm) and **1:87** (459 nm) present similar Soret bands (Table 1:3). This indicated that the distortion between these two porphyrins was comparable which is confirmed by the X-ray crystallographic studies as the overall distortion from the 24-atom mean plane are almost identical (Table 1:3).[134]

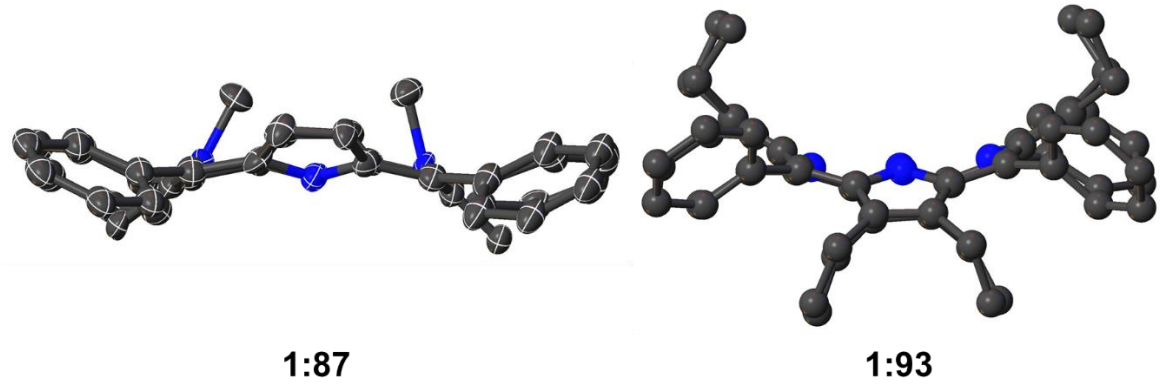

Figure 1:71: N^{21},N^{23}-Dimethyl-5,10,15,20-tetraphenylporphyrin (**1:87**) and 2,3,7,8,12,13,17,18-octaethyl-5,10,15,20-tetraphenylporphyrin (**1:93**)[89] showing the edge-on view of both compounds. Views of the molecular structure in the crystal are shown with hydrogen atoms, minor disorder, atom labels, and solvent molecules omitted for clarity. The structure of **1:87** has been drawn with thermal ellipsoids indicate 50% probability. The structure of **1:93** has been drawn isotropically.

Table 1:3: Comparison of the UV-vis data and the overall deviation of the macrocycle (Δ24) of **1:87** and **1:93**.

Entry	Porphyrin	Δ24	Δλ(nm)[a]
1	**1:87**	0.712	37(456)
2	**1:93**	0.711	40(459)

[a] Δλ represents the shift of the Soret absorption band compared to free base **1:85** (419 nm).[93]

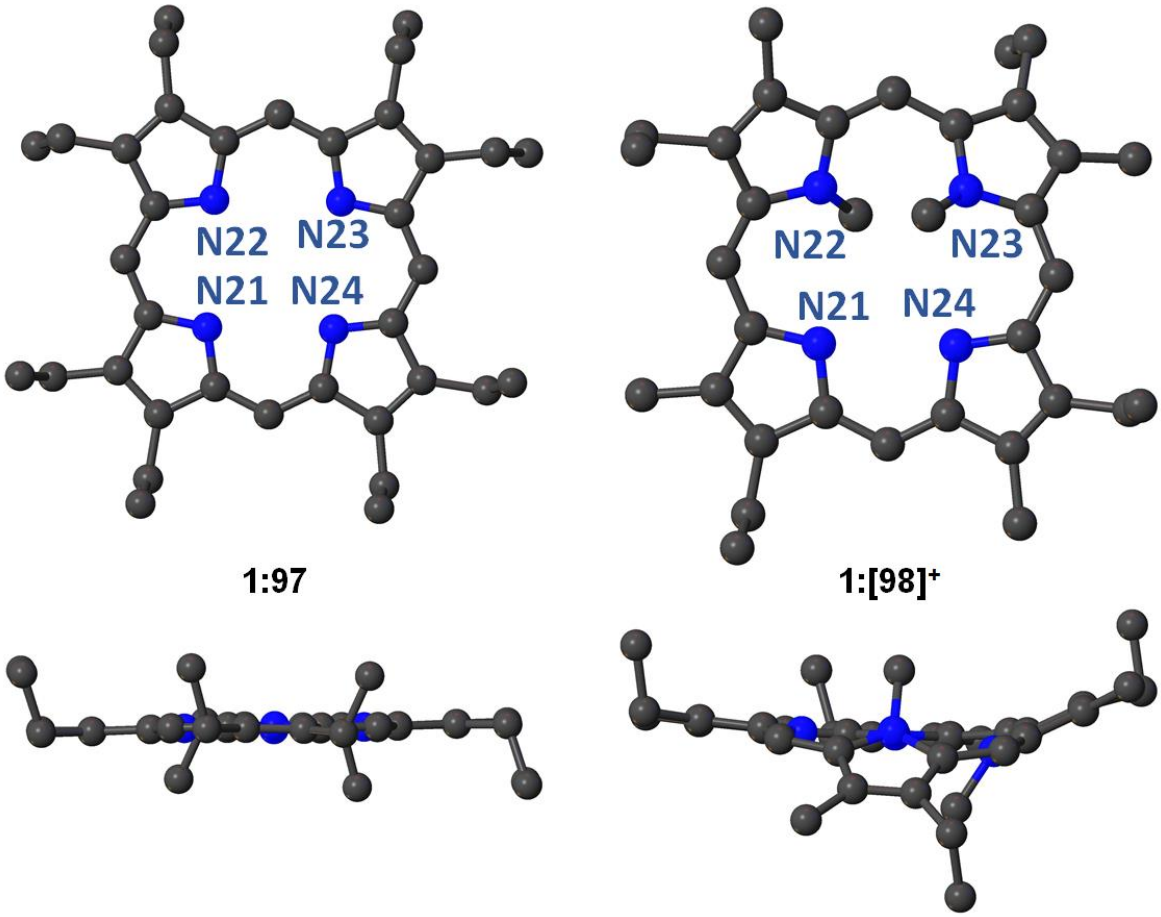

Figure 1:72: Views of the molecular structure of 2,3,7,8,12,13,17,18-octaethylporphyrin (**1:97**)[88] and 2,3,7,8,12,13,17,18-octaethyl-N^{21}-hydro-N^{22},N^{23}-dimethylporphyrin trifluoromethanesulfonate salt (**1:[98]$^+$**)[130d] Hydrogen atoms, minor disorder, and solvent molecules were omitted for clarity. Structures have been drawn isotropically.

The final case concerns the literature samples of planar 2,3,7,8,12,12,17,18-octaethylporphyrin (H_2OEP, **1:97**)[88] compared to the *N,N'*-dimethylated-OEP (**1:[98]$^+$**) (Figure 1:72).[130d] This case is notable as up to recently, compound **1:[98]$^+$** was the only confirmed structure of a N^{21},N^{22}-disubstituted crystal structure in the literature. Introduction of two methyl groups to the core nitrogen atoms of porphyrin **1:97** results in a stark change from the planar free base parent molecule to the N^{21},N^{22}-disubstituted analogue **1:[98]$^+$**. Across the board, there is a large increase

in the deviation of atoms from the 24-atom mean plane and also the pyrrole tilt angles (Table 1:2). In this case, there is a general decrease in C_m–C_m, C_a–C_b, and C_b–C_b bond lengths and increase in the N–C_a bond length (Table 1:4). This is coupled with a decrease in the C_a–N–C_a and N–C_a–C_m bond angles and an increase in the C_a–C_m–C_a and C_b–C_b–C_a bond angles. These changes in the ring structure drive the out-of-plane distortion from favouring the $E_g(x)$ distortion mode to the B_{2u} distortion mode making the whole structure become mode saddled in shape as seen in the NSD (Figure 1:73).

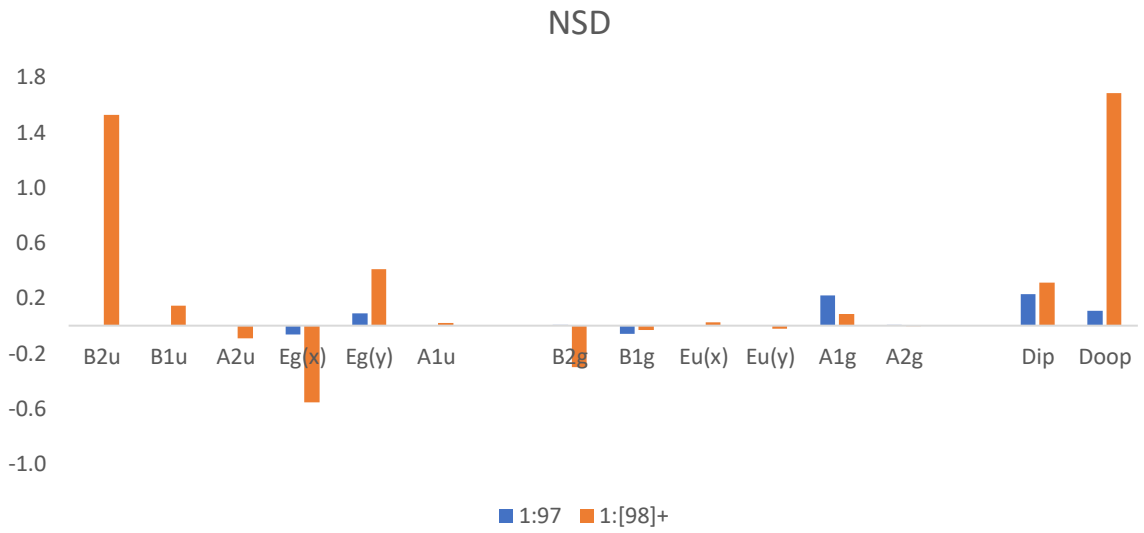

Figure 1:73: Normal-coordinate structural decomposition (NSD) analysis of the X-ray crystallographic structures of **1:97** and **1:[98]$^+$**.

The structure of **1:[99]$^+$** contains the only other example of a porphyrin crystal structure showing a N21, N22 substitution pattern, Figure 1:74. This is due to the similarities noted with example **1:97**, where the reduced substitution pattern coupled with increased electron donating capabilities of the *meso* substituents at the 5,15-positions results in an environment suitable for a N21, N22 substitution pattern. The effects of this substitution cannot be ascertained as no crystal structure is available for compound 5,15-bis(3,4,5-trimethoxyphenyl) porphyrin. However, we can see a general increase in distortion of N21, N22 side of the porphyrin macrocycle, with the N23, N24 side being relatively planar. This is also clearly represented by the fact that the *meso*-substituent is much more in plane on the N21, N22 side (5-position) of the porphyrin macrocycle than the N23, N24 side (15-position), which is logical due to the aforementioned increase in distortion.

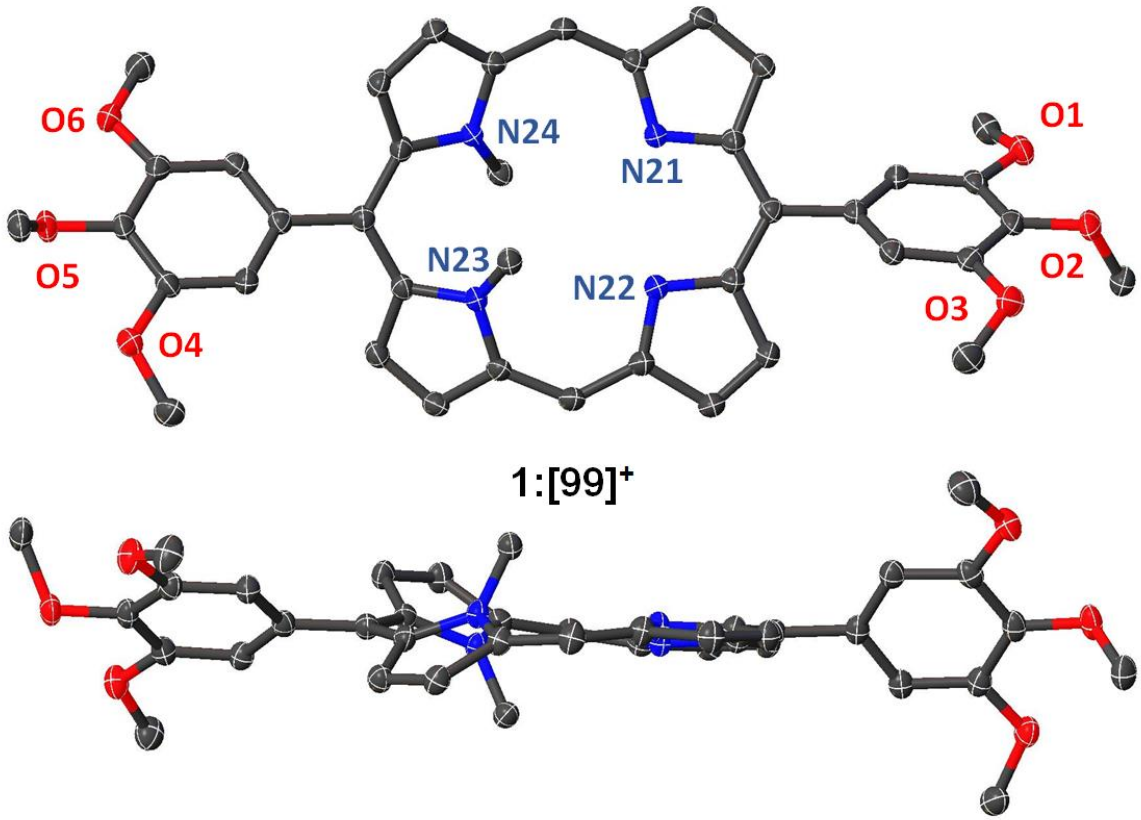

Figure 1:74: Views of the molecular structure of N^{21}-hydro-N^{23},N^{24}-dimethyl-5,15-bis(3,4,5-trimethoxyphenyl)porphyrin trifluoromethanesulfonate salt (**1:[99]$^+$**) showing top and side views. Hydrogen atoms, minor disorder, and counter-ion were omitted for clarity. The structure has been drawn with thermal ellipsoids indicate 50% probability.

Conclusions.

The intention of this section was to highlight the important structural aspects of the inclusion of core *N*-methyl groups to a porphyrin scaffold. Comparison of the new and literature crystal structures of planar free base porphyrins revealed that, from a structural point of view, *N*-methylation of planar porphyrins results in significant structural changes and macrocycle distortion. NSD was successfully applied to all the structures and used to determine the distortion modes in porphyrin structures with increasing number of *N*-substitution. In planar molecules, there is a clear increase seen in the D_{oop} distortion modes with the N^{21},$N^{22/23}$-disubstitutions showing the largest contributions. There is also the case where increasing the number of *N*-substitution, increase the global distortion of the porphyrin macrocycle. However, the local increase of distortion is more profound in lower *N*-substitutions, due to less of a 'counter-balancing' effect. This highlights the importance of global distortion *vs*. local distortion in *N*-substitution. For the electron withdrawing/donating

groups, the distortion present in *N*-substituted, is partially dependent on the type of substitutions, with EDG's causing generally higher degrees of nonplanarity than EWG's. In the nonplanar porphyrin series, the effect of *N*-substitution is less pronounced with only minor changes in the increase of nonplanarity. As seen in the D_{oop} distortion modes, only a minor increase to nonplanarity is noted. This is due to the already large degree of nonplanarity imparted onto these structures due to *β*-substitution. Finally, the case of N^{21},N^{22}-disubstitutions, these complexes show a significant increase in local distortion to the substituted side of the macrocycle with the unsubstituted side remaining relatively planar.

Outlook.

From the results herein we have shown that, by using inner core substation (*N*-substitution) we can achieve high distortion, comparable to nonplanar porphyrins such as 2,3,7,8,12,13,17,18-octaethyl-5,10,15,20-tetraphenyl porphyrin (**1:93**). This is important as outlined in the introduction chapter due to the characteristics specific to nonplanar porphyrins, such as increase basicity. By using *N*-substitution, macrocycles with the same distortion as nonplanar porphyrins can be achieved, while preserving all peripheral units surrounding the porphyrin available for further functionalisation. This is of benefit, as by increasing nonplanarity with large number of peripheral substituents would either complicate or eliminate the potential for further functionalization. Additionally, we have demonstrated that by controlling the degree of *N*-substitution we can tailor the degree of distortion to an extent, allowing for optimisation of conformation *vs*. application. With this in mind, using inner core substitution is an extremely versatile path to build non-native highly distorted porphyrin derivative which have potential in the design of porphyrin inhibitors for biological process. For example, using N^{21}-methylprotoporphyrin IX as a competitive enzyme inhibitor for ferrochelatase in the body.[135] Other potential uses are in the design of organo-catalysts using modified planar porphyrins (originally planar macrocycle that have been distorted by inner core substitution) *via* exposing the inner moieties resulting in an increase of their basicity and an improvement of their catalytic activity.[116] Additionally, these compounds can be used to study the effect of non-charged (not cationic or anionic) core binding of molecules to the macrocycle as seen in Figure 1:64.

This chapter has focused mainly on the uses of *N*-substituted porphyrins using methyl units, however, there is an increase interest in using more complex core substitution as a building block for supramolecular assembly materials. This would allow for the connection of macrocycle through inner core substitution. An example of these building blocks would be the *para*-substituted benzyl *N*-substituted porphyrins as shown by Callot *et al.*.[136]

Table 4: Bond lengths and angles for *N*-substituted porphyrins.

	1:85[130a]	**1:86_1**	**1:86_2**	**1:87_1**	**1:87_2**	**1:[88]**$^{+}$[114e]	**1:89**[130b]	**1:90**	**1:[91]**$^{+}$
Bond lengths (Å):									
N–C_a									
N21–C1	1.370(12)	1.391(5)	1.384(5)	1.350(9)	1.402(8)	1.379(6)	1.377(4)	1.398(6)	1.388(4)
N21–C4	1.377(16)	1.387(4)	1.402(4)	1.401(8)	1.380(8)	1.383(5)	1.367(3)	1.376(7)	1.375(4)
N22–C6	1.359(15)	1.364(5)	1.371(5)	1.367(7)	1.343(8)	1.388(5)	1.372(4)	1.371(6)	1.383(4)
N22–C9	1.369(11)	1.363(5)	1.347(5)	1.397(6)	1.379(7)	1.396(7)	1.378(4)	1.363(6)	1.393(4)
N23–C11	1.370(12)	1.371(5)	1.370(5)	1.368(7)	1.378(8)	1.375(5)	1.377(4)	1.376(5)	1.383(3)
N23–C14	1.377(16)	1.373(5)	1.390(5)	1.387(8)	1.386(8)	1.387(5)	1.367(3)	1.390(8)	1.385(5)
N24–C16	1.359(15)	1.366(4)	1.366(5)	1.391(7)	1.389(8)	1.362(6)	1.372(4)	1.365(7)	1.366(4)
N24–C19	1.369(11)	1.361(5)	1.363(5)	1.348(7)	1.362(7)	1.369(6)	1.378(4)	1.371(6)	1.362(4)
Average	1.369	1.372	1.374	1.376	1.377	1.380	1.374	1.376	1.379
C_a–C_b									
C1–C2	1.432(12)	1.425(5)	1.436(5)	1.390(10)	1.439(7)	1.426(7)	1.430(4)	1.431(5)	1.420(3)
C3–C4	1.424(11)	1.412(5)	1.418(5)	1.402(8)	1.411(8)	1.429(7)	1.413(4)	1.420(7)	1.414(4)
C6–C7	1.453(18)	1.454(5)	1.457(5)	1.414(10)	1.456(9)	1.435(7)	1.454(4)	1.464(6)	1.433(4)
C8–C9	1.454(18)	1.453(5)	1.461(5)	1.387(9)	1.448(8)	1.426(6)	1.456(4)	1.463(7)	1.428(5)
C11–C12	1.432(12)	1.438(5)	1.425(5)	1.436(9)	1.401(8)	1.419(5)	1.430(4)	1.426(5)	1.414(3)
C13–C14	1.424(11)	1.417(5)	1.424(6)	1.425(10)	1.419(7)	1.410(5)	1.413(4)	1.429(6)	1.410(4)
C16–C17	1.453(14)	1.463(6)	1.448(5)	1.439(7)	1.431(9)	1.460(6)	1.454(4)	1.457(5)	1.445(4)
C18–C19	1.454(18)	1.467(5)	1.465(5)	1.482(8)	1.421(8)	1.461(6)	1.456(4)	1.463(8)	1.446(5)
Average	1.441	1.441	1.442	1.422	1.428	1.433	1.438	1.444	1.426
C_b–C_b									
C2–C3	1.353(15)	1.367(5)	1.367(5)	1.390(10)	1.375(7)	1.354(7)	1.354(5)	1.380(6)	1.358(5)
C7–C8	1.347(10)	1.337(5)	1.336(5)	1.374(7)	1.378(1)	1.372(7)	1.330(5)	1.336(5)	1.351(5)
C12–C13	1.353(15)	1.362(6)	1.366(6)	1.357(10)	1.354(7)	1.372(7)	1.354(5)	1.365(6)	1.370(5)
C17–C18	1.347(10)	1.347(5)	1.348(5)	1.369(7)	1.351(10)	1.338(6)	1.330(5)	1.338(5)	1.343(5)
Average	1.350	1.353	1.354	1.373	1.365	1.359	1.342	1.355	1.356
C_a–C_m									
C4–C5	1.395(11)	1.405(5)	1.403(5)	1.394(10)	1.387(7)	1.410(6)	1.401(4)	1.402(5)	1.426(5)
C5–C6	1.399(11)	1.409(5)	1.400(5)	1.414(7)	1.408(9)	1.408(7)	1.399(4)	1.405(6)	1.401(5)
C9–C10	1.400(12)	1.410(5)	1.408(5)	1.398(8)	1.405(10)	1.395(6)	1.395(4)	1.412(5)	1.402(4)
C10–C11	1.402(18)	1.400(5)	1.400(5)	1.425(10)	1.420(7)	1.432(6)	1.389(4)	1.420(7)	1.425(6)
C14–C15	1.395(13)	1.409(6)	1.391(5)	1.433(8)	1.400(8)	1.424(6)	1.401(4)	1.424(5)	1.422(4)
C15–C16	1.399(11)	1.390(5)	1.398(5)	1.421(9)	1.436(9)	1.420(6)	1.399(4)	1.407(6)	1.416(5)
C19–C20	1.400(12)	1.410(5)	1.395(5)	1.403(8)	1.407(10)	1.421(6)	1.395(4)	1.404(5)	1.415(4)
C20–C1	1.402(18)	1.416(5)	1.416(5)	1.451(9)	1.399(8)	1.424(5)	1.389(4)	1.405(7)	1.412(5)
Average	1.399	1.406	1.401	1.417	1.408	1.417	1.396	1.410	1.415

Table 4 (continued): Bond lengths and angles for *N*-substituted porphyrins.

	1:85[130a]	**1:86_1**	**1:86_2**	**1:87_1**	**1:87_2**	**1:[88]**$^{+}$[114e]	**1:89**[130b]	**1:90**	**1:[91]**$^{+}$
Bond angles (°):									
C_a–N–C_a									
C1–N21–C4	109.2(7)	108.2(3)	109.2(3)	107.9(6)	109.7(3)	109.2(4)	110.0(2)	109.7(2)	109.5(3)
C6–N22–C9	106.2(7)	105.6(3)	106.4(3)	109.5(5)	108.0(5)	109.2(4)	106.7(2)	106.1(16)	108.4(3)
C11–N23–C14	109.2(7)	109.9(3)	110.2(3)	109.5(5)	109.7(3)	108.9(3)	110.0(2)	110.5(18)	108.4(2)
C16–N24–C19	106.2(7)	106.6(3)	107.1(3)	106.9(3)	108.0(6)	105.9(3)	106.7(2)	105.7(19)	106.7(3)
Average	107.7	107.6	108.2	108.5	108.9	108.3	108.4	108.0	108.3
N–C_a–C_a									
N21–C1–C2	107.4(8)	107.6(3)	106.8(3)	110.9(3)	106.1(4)	107.0(3)	106.3(3)	106.2(4)	106.2(2)
N21–C4–C3	107.4(6)	107.8(3)	106.9(3)	106.5(6)	107.3(3)	107.0(4)	107.0(2)	107.8(6)	107.2(2)
N22–C6–C7	110.2(8)	110.2(3)	109.8(3)	106.2(4)	109.1(4)	107.0(4)	109.1(3)	109.9(3)	107.6(3)
N22–C9–C8	110.2(6)	110.8(3)	110.4(3)	107.4(5)	106.1(5)	107.1(4)	109.1(3)	110.3(11)	107.3(2)
N23–C11–C12	107.4(8)	106.6(3)	107.1(3)	107.4(5)	106.7(3)	107.6(4)	106.3(3)	106.7(3)	108.1(3)
N23–C14–C13	107.4(6)	107.4(4)	106.0(3)	106.8(4)	105.6(4)	107.5(4)	107.0(2)	105.8(5)	107.5(11)
N24–C16–C17	110.2(8)	109.7(3)	109.8(3)	110.1(4)	108.4(4)	110.4(4)	109.1(3)	110.8(3)	109.4(3)
N24–C19–C18	110.2(6)	110.4(3)	109.3(3)	109.4(3)	107.8(5)	110.2(4)	109.1(3)	109.7(5)	109.8(15)
Average	108.8	108.8	108.3	108.1	107.1	108.0	107.9	108.4	107.9
N–C_a–C_m									
N21–C1–C20	126.2(5)	126.3(3)	127.3(3)	123.3(5)	125.9(3)	126.1(4)	126.9(3)	129.6(8)	125.9(2)
N21–C4–C5	125.6(6)	125.7(3)	126.5(3)	124.8(4)	123.8(3)	124.8(4)	126.6(3)	128.3(3)	124.5(2)
N22–C6–C5	126.9(5)	125.8(3)	125.5(4)	123.8(4)	123.6(5)	126.6(4)	126.3(2)	124.5(5)	125.6(19)
N22–C9–C10	125.8(6)	124.7(3)	125.5(4)	122.2(4)	125.4(5)	125.9(4)	126.6(2)	125.4(2)	124.2(2)
N23–C11–C10	126.2(5)	127.6(3)	127.3(3)	126.8(4)	123.8(3)	125.1(3)	126.9(3)	125.7(9)	123.9(15)
N23–C14–C15	125.6(6)	127.1(3)	126.9(3)	125.4(5)	126.0(3)	125.4(3)	126.6(3)	126.0(2)	126.0(2)
N24–C16–C15	126.9(5)	125.2(4)	125.0(4)	122.8(2)	125.0(5)	125.4(4)	126.3(2)	124.5(9)	123.7(18)
N24–C19–C20	125.8(6)	125.9(3)	126.8(3)	124.5(3)	123.3(5)	124.5(4)	126.6(2)	125.0(3)	124.1(2)
Average	126.1	126.0	126.4	124.2	124.6	125.5	126.6	126.1	124.7
C_a–C_m–C_a									
C4–C5–C6	125.6(6)	126.1(3)	125.9(3)	123.5(16)	125.2(16)	123.8(4)	124.4(2)	121.7(3)	124.5(14)
C9–C10–C11	125.6(7)	124.7(4)	125.6(4)	121.5(8)	125.0(16)	123.7(4)	125.6(3)	126.6(3)	121.9(15)
C14–C15–C16	125.6(6)	125.5(3)	125.4(3)	121.1(2)	124.7(15)	123.8(4)	124.4(2)	125.3(3)	124.0(14)
C19–C20–C1	125.6(7)	125.0(3)	125.1(4)	123.2(2)	123.2(10)	124.4(4)	125.6(3)	123.8(3)	123.8(12)
Average	125.6	125.3	125.5	122.3	124.5	123.9	125.0	124.4	123.6
C_a–C_b–C_a									
C1–C2–C3	107.9(8)	107.7(3)	108.3(3)	105.6(2)	107.8(4)	108.5(5)	108.0(3)	108.6(4)	108.7(15)
C2–C3–C4	108.2(15)	108.5(3)	108.7(3)	109.1(4)	109.1(4)	108.1(5)	108.7(3)	107.8(3)	108.2(11)
C6–C7–C8	107.0(8)	107.1(3)	106.9(3)	109.0(19)	106.5(2)	108.2(4)	107.8(3)	106.9(4)	108.2(2)
C7–C8–C9	106.3(7)	106.3(4)	106.6(4)	107.6(3)	110.2(3)	108.4(5)	107.2(3)	106.8(3)	108.5(10)
C11–C12–C13	107.9(8)	107.8(4)	107.9(4)	107.7(3)	108.9(3)	107.9(3)	108.0(3)	108.2(4)	107.4(2)
C12–C13–C14	108.2(15)	108.2(4)	108.9(3)	108.7(6)	109.1(4)	108.2(4)	108.7(3)	108.8(3)	108.7(10)
C16–C17–C18	107.0(8)	107.2(3)	107.1(3)	106.6(4)	106.3(11)	106.8(4)	107.8(3)	106.3(4)	107.3(19)
C17–C18–C19	106.3(7)	106.1(3)	106.7(3)	106.4(4)	109.4(3)	106.7(4)	107.2(3)	107.3(3)	106.8(9)
Average	107.4	107.4	107.6	107.6	108.4	107.9	107.9	107.6	108.0

Table 4 (continued): Bond lengths and angles for *N*-substituted porphyrins.

	1:92[130c]	**1:93**[89]	**1:94**[130e]	**1:[95_2]**$^{+}$[105]	**1:[95_2]**$^{+}$[105]	**1:[96]**$^{2+}$[130e]	**1:97**[88]	**1:98**[130d]	**1:[99]**$^{+}$
Bond lengths (Å):									
N–C_a									
N21–C1	1.410(17)	1.363(6)	1.369(13)	1.384(7)	1.382(10)	1.382(5)	1.379(10)	1.363(3)	1.381(4)
N21–C4	1.368(17)	1.372(5)	1.444(13)	1.394(8)	1.389(10)	1.398(7)	1.434(10)	1.364(3)	1.409(15)
N22–C6	1.339(18)	1.366(4)	1.230(3)	1.376(8)	1.403(10)	1.395(7)	1.392(11)	1.367(3)	1.379(2)
N22–C9	1.350(14)	1.369(6)	1.420(3)	1.392(7)	1.403(10)	1.401(5)	1.398(11)	1.367(2)	1.374(12)
N23–C11	1.369(17)	1.366(6)	1.430(17)	1.388(7)	1.389(10)	1.393(5)	1.373(11)	1.363(3)	1.397(11)
N23–C14	1.373(15)	1.374(4)	1.364(17)	1.392(7)	1.382(10)	1.373(7)	1.385(10)	1.364(3)	1.369(2)
N24–C16	1.361(18)	1.360(4)	1.372(19)	1.397(8)	1.366(9)	1.382(7)	1.338(10)	1.367(3)	1.388(3)
N24–C19	1.364(14)	1.379(5)	1.364(19)	1.355(7)	1.366(9)	1.383(5)	1.399(12)	1.367(2)	1.380(13)
Average	1.367	1.369	1.374	1.385	1.385	1.388	1.387	1.365	1.385
C_a–C_b									
C1–C2	1.398(2)	1.439(6)	1.424(7)	1.448(9)	1.445(10)	1.422(7)	1.425(11)	1.463(3)	1.428(13)
C3–C4	1.434(14)	1.429(7)	1.411(7)	1.448(9)	1.423(11)	1.445(5)	1.411(11)	1.461(2)	1.430(11)
C6–C7	1.460(17)	1.469(6)	1.440(2)	1.432(9)	1.420(11)	1.419(5)	1.448(10)	1.438(4)	1.435(5)
C8–C9	1.498(13)	1.481(5)	1.480(2)	1.445(8)	1.420(11)	1.421(8)	1.456(12)	1.438(2)	1.450(18)
C11–C12	1.452(19)	1.460(4)	1.400(2)	1.421(8)	1.423(11)	1.441(7)	1.438(12)	1.463(3)	1.424(3)
C13–C14	1.463(13)	1.453(6)	1.430(2)	1.406(9)	1.445(10)	1.441(5)	1.463(13)	1.461(2)	1.435(16)
C16–C17	1.444(16)	1.457(6)	1.460(2)	1.467(9)	1.388(15)	1.442(6)	1.493(12)	1.438(4)	1.474(14)
C18–C19	1.440(14)	1.468(6)	1.426(19)	1.485(9)	1.464(11)	1.431(7)	1.487(11)	1.438(2)	1.459(18)
Average	1.449	1.457	1.434	1.444	1.429	1.433	1.453	1.450	1.442
C_b–C_b									
C2–C3	1.333(13)	1.369(6)	1.385(5)	1.359(9)	1.390(10)	1.390(8)	1.394(13)	1.354(3)	1.375(14)
C7–C8	1.301(14)	1.365(6)	1.360(2)	1.383(9)	1.365(15)	1.387(7)	1.382(13)	1.373(2)	1.329(2)
C12–C13	1.347(14)	1.375(6)	1.360(2)	1.380(8)	1.390(10)	1.380(9)	1.359(10)	1.354(3)	1.364(14)
C17–C18	1.344(14)	1.360(6)	1.400(2)	1.368(9)	1.388(15)	1.375(6)	1.329(12)	1.373(2)	1.297(2)
Average	1.331	1.367	1.376	1.373	1.383	1.383	1.366	1.364	1.341
C_a–C_m									
C4–C5	1.419(17)	1.418(6)	1.363(7)	1.391(9)	1.437(11)	1.401(6)	1.406(12)	1.394(3)	1.404(9)
C5–C6	1.403(13)	1.408(6)	1.477(18)	1.423(9)	1.411(11)	1.426(6)	1.410(11)	1.389(2)	1.358(16)
C9–C10	1.377(18)	1.418(5)	1.400(2)	1.408(8)	1.411(11)	1.417(7)	1.391(12)	1.392(3)	1.339(2)
C10–C11	1.422(13)	1.404(5)	1.420(2)	1.423(8)	1.437(11)	1.414(7)	1.415(10)	1.393(3)	1.421(2)
C14–C15	1.397(17)	1.400(6)	1.440(19)	1.429(9)	1.406(10)	1.428(6)	1.386(12)	1.394(3)	1.405(12)
C15–C16	1.402(13)	1.422(6)	1.399(19)	1.404(9)	1.419(11)	1.415(5)	1.444(13)	1.389(2)	1.360(16)
C19–C20	1.416(18)	1.404(5)	1.380(2)	1.434(9)	1.419(11)	1.414(7)	1.374(12)	1.392(3)	1.379(2)
C20–C1	1.399(13)	1.414(6)	1.443(16)	1.395(9)	1.406(10)	1.432(7)	1.437(10)	1.393(3)	1.411(18)
Average	1.404	1.411	1.415	1.413	1.418	1.418	1.408	1.392	1.385

Table 4 (continued): Bond lengths and angles for *N*-substituted porphyrins.

	1:92[130c]	**1:93**[89]	**1:94**[130e]	**1:[95_2]**$^{+}$[105]	**1:[95_2]**$^{+}$[105]	**1:[96]**$^{2+}$[130e]	**1:97**[88]	**1:98**[130d]	**1:[99]**$^{+}$
Bond angles (°):									
C_a–N–C_a									
C1–N21–C4	108.1(6)	111.4(3)	107.6(7)	110.0(5)	109.6(6)	108.3(4)	109.2(6)	105.7(16)	108.8(9)
C6–N22–C9	107.5(6)	106.3(3)	112.0(2)	109.0(5)	107.0(9)	108.0(4)	109.9(7)	109.6(16)	110.2(9)
C11–N23–C14	109.8(6)	111.6(3)	107.4(10)	107.9(5)	109.6(6)	108.9(3)	110.9(7)	105.7(16)	108.3(10)
C16–N24–C19	105.4(5)	106.1(3)	111.2(11)	105.3(5)	106.2(9)	109.0(4)	105.9(7)	109.6(16)	105.2(11)
Average	107.7	108.9	109.6	108.1	108.1	108.6	109.0	107.7	108.1
N–C_a–C_a									
N21–C1–C2	106.4(16)	106.3(3)	110.0(6)	106.6(5)	107.1(6)	109.0(5)	108.3(7)	110.8(13)	107.8(10)
N21–C4–C3	107.7(10)	105.9(4)	105.7(5)	106.5(5)	107.8(6)	107.7(4)	105.4(6)	110.9(16)	106.9(7)
N22–C6–C7	109.7(16)	110.8(4)	109.5(19)	108.0(5)	108.1(7)	108.3(4)	107.2(7)	107.8(13)	107.2(10)
N22–C9–C8	108.7(9)	110.2(3)	102.0(17)	107.6(5)	108.1(7)	107.8(4)	106.4(7)	107.7(16)	105.0(10)
N23–C11–C12	107.9(5)	105.8(3)	107.4(11)	108.2(5)	107.1(6)	107.4(4)	106.8(6)	110.8(13)	107.5(10)
N23–C14–C13	106.5(9)	106.4(4)	108.4(11)	108.2(5)	107.8(6)	108.4(4)	105.6(6)	110.9(16)	108.5(12)
N24–C16–C17	110.7(2)	110.8(3)	108.2(12)	110.5(5)	110.9(7)	107.6(4)	111.7(8)	107.8(13)	109.3(10)
N24–C19–C18	110.6(9)	109.9(3)	105.4(12)	111.6(5)	110.9(7)	107.9(4)	108.8(7)	107.7(16)	109.6(13)
Average	108.5	108.3	107.1	108.4	108.5	108.0	107.5	109.3	107.7
N–C_a–C_m									
N21–C1–C20	125.9(7)	123.1(4)	121.9(9)	122.6(5)	123.2(7)	122.2(4)	123.6(6)	125.2(14)	124.6(8)
N21–C4–C5	126.6(3)	123.2(4)	124.1(7)	123.1(5)	122.4(7)	123.2(4)	122.2(6)	125.0(12)	122.4(9)
N22–C6–C5	125.6(7)	121.8(3)	122.2(18)	123.6(5)	122.6(7)	122.6(4)	124.8(7)	124.9(14)	123.5(8)
N22–C9–C10	126.9(3)	122.0(3)	128.2(18)	123.6(5)	122.6(7)	121.6(4)	123.5(8)	125.0(13)	128.2(8)
N23–C11–C10	126.0(3)	124.0(3)	119.1(12)	121.5(5)	122.4(7)	123.4(4)	122.5(8)	125.2(14)	124.8(9)
N23–C14–C15	127.9(2)	123.6(3)	124.2(13)	121.5(5)	123.2(7)	123.1(1)	124.9(8)	125.0(12)	122.6(9)
N24–C16–C15	124.5(7)	121.1(4)	122.9(12)	120.2(5)	122.1(7)	123.3(4)	122.4(7)	124.9(14)	122.8(9)
N24–C19–C20	124.3(2)	121.4(4)	122.9(12)	121.5(5)	122.1(7)	123.4(4)	119.6(7)	125.0(13)	124.9(9)
Average	126.0	122.5	123.2	122.2	122.6	122.9	122.9	125.0	124.2
C_a–C_m–C_a									
C4–C5–C6	125.8(7)	124.4(3)	121.3(8)	123.4(6)	123.3(7)	121.8(5)	121.7(7)	127.7(11)	127.1(9)
C9–C10–C11	124.0(7)	124.3(4)	123.9(14)	121.7(5)	123.3(7)	123.0(3)	124.5(8)	127.4(10)	130.1(9)
C14–C15–C16	126.4(7)	124.6(3)	121.0(12)	122.9(6)	123.2(7)	123.4(5)	123.5(8)	127.7(11)	127.2(10)
C19–C20–C1	124.6(7)	122.9(4)	122.4(13)	123.8(5)	123.2(7)	122.8(3)	123.5(7)	127.4(10)	130.0(8)
Average	125.2	124.1	122.2	123.0	123.3	122.8	123.3	127.6	128.6
C_a–C_b–C_a									
C1–C2–C3	110.4(6)	107.6(4)	105.9(4)	108.6(5)	107.6(7)	107.8(3)	106.9(8)	106.3(12)	108.3(7)
C2–C3–C4	107.3(10)	108.6(4)	110.5(4)	108.2(6)	107.9(6)	107.2(5)	110.1(7)	106.3(14)	108.2(5)
C6–C7–C8	108.1(7)	106.2(3)	106.6(16)	108.2(5)	108.3(4)	107.7(4)	108.0(7)	107.3(12)	107.4(10)
C7–C8–C9	106.0(1)	106.2(4)	107.1(14)	107.0(5)	108.3(4)	108.1(4)	108.2(7)	107.5(14)	110.2(1)
C11–C12–C13	107.3(6)	108.2(4)	109.0(13)	107.4(5)	107.9(6)	107.4(4)	108.6(8)	106.3(12)	108.3(11)
C12–C13–C14	108.6(9)	107.4(3)	107.7(13)	108.3(5)	107.6(7)	107.4(4)	108.1(7)	106.3(14)	107.4(12)
C16–C17–C18	106.4(7)	106.7(3)	103.4(12)	106.7(5)	105.8(4)	107.6(5)	105.7(7)	107.3(12)	107.3(11)
C17–C18–C19	106.8(10)	106.3(4)	111.2(12)	105.6(5)	105.8(4)	107.9(4)	107.7(8)	107.5(14)	108.5(13)
Average	107.6	107.2	107.7	107.5	107.4	107.6	107.9	106.9	108.2

Experimental

All commercial chemicals used were of analytical grade and supplied by Sigma Aldrich, Frontier Scientific, Inc., Tokyo Chemical Company and Acros chemicals and used without further purification unless otherwise stated. Anhydrous CH_2Cl_2 (for porphyrin synthesis) was obtained via distillation over phosphorus pentoxide. Flash column chromatography was carried out using Fluka Silica Gel 60 (230-400 mesh; Merck) or aluminium oxide (neutral, activated with 6% H_2O, Brockman Grade III). Mobile phases are described as (v/v) if isocratic, or% gradients. Analytical thin-layer chromatography (TLC) was performed using silica gel 60 (fluorescence indicator F254, precoated sheets, 0.2 mm thick, 20 cm × 20 cm; Merck) or aluminium oxide 60 (neutral, F254; Merck) plates and visualized by UV irradiation. Melting points are uncorrected and were measured with a Stuart SP-10 melting point apparatus. A Bruker Advance III 400 MHz, a Bruker DPX400 400 MHz and an Agilent 400 spectrometer were employed for ^{1}H (400.13 MHz), ^{19}F (376.60 MHz) and ^{13}C (100.61 MHz) NMR spectra and a Bruker Ultrashield 600 spectrometer was employed for ^{1}H (600.13 MHz), ^{13}C (150.90 MHz) NMR spectra. All NMR experiments were performed at room temperature, unless otherwise stated. Resonances δ, are given in ppm units and referenced either to the deuterium peak in the NMR solvent, $CDCl_3$ (δ_H = 7.26 ppm, δ_C = 77.0 ppm), C_5D_5N (δ_H = 7.19, 7.55, 8.71 ppm, δ_C = 123.5, 135.5, 149.5 ppm), or $(CD_3)_2SO$ (δ_H = 2.50 ppm, δ_C = 39.5), used as an internal standard. The assignment of the signals was confirmed by selective 2D spectra (COSY, TOCSY, ROESY, NOESY, HMBC, and HSQC). Mass spectrometry analysis was performed with a Q-Tof Premier Waters MALDI quadrupole time-of-flight (Q-TOF) mass spectrometer equipped with Z-spray electrospray ionization (ESI) and matrix-assisted laser desorption ionization (MALDI) sources either in a positive or negative mode with DCTB (*trans*-2-[3-(4-*tert*-butylphenyl)-2-methyl-2-propenylidene]malononitrile) as the matrix. ESI mass spectra were acquired in positive or negative modes as required, using a Micromass time of flight mass spectrometer (TOF) interfaced to a Waters 2960 HPLC, or a Bruker microTOF-Q III spectrometer interfaced to a Dionex UltiMate 3000 LC. APCI experiments were performed on a Bruker microTOF-Q III spectrometer interfaced to a Dionex UltiMate 3000 LC. Photophysical measurements were carried out in CH_2Cl_2 as solvent. UV-visible absorption measurements were performed using a Shimadzu MultiSpec-1501.

General Procedures.

General Procedure A: The Synthesis of Free Base OETArXPs.

Dry CH_2Cl_2 (1L), 3,4-diethylpyrrole (1 g, 8.12 mmol, 1 eq.) and aldehyde (8.12 mmol, 1 eq.) were placed in a 2 L round-bottom flask and stirred for 10 minutes. BF_3•Et_2O (0.10 mL, 0.81 mmol, 0.1 eq.) was added to the mixture and left to stir for 18 h at room temperature. DDQ (1.84 g, 8.12 mmol, 1 eq.) was added and the solution was stirred for 1 h. The reaction was quenched with TEA (0.11 mL, 0.81 mmol, 0.1 eq.). The solvent was evaporated to dryness and the residue taken up in CH_2Cl_2. The mixture was ultrasonicated for 2 min and then filtered through a plug of silica, washing with 1% MeOH in CH_2Cl_2. The eluted porphyrin fractions were evaporated to dryness and purified by silica gel chromatography using *n*-hexane:EtOAc (4:6) and dried *in vacuo* to yield the compound as green flakes.

General Procedure B: The Synthesis of Nickel(II) OETArXPs.

The free base porphyrin (1 eq.) was dissolved in toluene (5 mL) and heated to reflux with nickel(II) acetylacetonate (ca. 5 eq.) for 18 hours. The reaction was monitored by TLC control and the solvent removed under reduced pressure. The residue was dissolved in CH_2Cl_2 and the mixture filtered through silica gel, eluting with CH_2Cl_2. The solvent was removed under reduced pressure and the product dried under high vacuum. The resulting solid was dissolved in a minimal amount of CH_2Cl_2 and layered with MeOH for recrystallisation, resulting in purple crystals.

General Procedure C: The Synthesis of Copper(II) OETArXPs.

The free base porphyrin (1 eq.) was dissolved in toluene (5 mL) and heated to reflux with copper(II) acetate (ca. 5 eq.) for 18 hours. The reaction was monitored by TLC control and the solvent removed under reduced pressure. The residue was dissolved in CH_2Cl_2 and the mixture filtered through silica gel, eluting with CH_2Cl_2. The solvent was removed under reduced pressure and the product dried in high vacuum. The resulting solid was dissolved in a minimal amount of CH_2Cl_2 and layered with MeOH for recrystallisation, resulting in purple crystals.

General Procedure D: The Synthesis of Palladium(II) OETArXPs.

The free base porphyrin (1 eq.) was dissolved in toluene (5 mL) and heated to reflux with palladium(II) acetate (ca. 5 eq.) for 18 hours. The reaction was monitored by TLC control and the solvent removed under reduced pressure. The residue was dissolved in CH_2Cl_2 and the mixture filtered through silica gel, eluting with CH_2Cl_2. The solvent was removed under reduced pressure and the product dried under high vacuum. The resulting solid was dissolved in a minimal amount of CH_2Cl_2 and layered with MeOH for recrystallisation, resulting in purple crystals.

General Procedure E: The Synthesis of Click OETArXPs.

The porphyrin **1:77**, azide coupling partner, sodium ascorbate (0.4 eq.) and $Cu(OAc)_2$ (0.4 eq.) were dissolved in THF (5 mL) and heated in a microwave reactor for 20 minutes. The solvent removed under reduced pressure. The residue was dissolved in CH_2Cl_2 and the mixture filtered through silica gel, eluting with CH_2Cl_2:EtOAc (1:1). The solvent was removed under reduced pressure and the product dried under high vacuum. The resulting solid was dissolved in a minimal amount of CH_2Cl_2 and layered with MeOH for recrystallisation, resulting in purple crystals.

Free Base OETArXPs.

Synthesis of 2,3,7,8,12,13,17,18-octaethyl-5,10,15,20-tetrakis-(4-fluorophenyl)porphyrin (**1:1**).

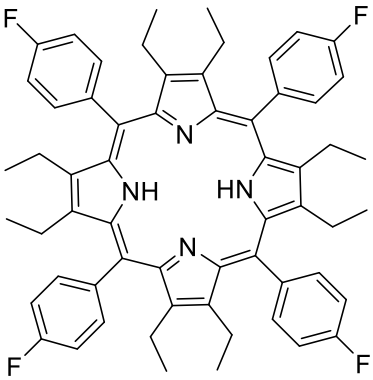

Compound **1:1** was synthesised following general procedure A outlined above using 4-fluorobenzaldehyde (1.01 g, 8.12 mmol, 1 eq.) to yield 555 mg (0.61 mmol, 30%) of green flakes. M.p. >300 °C; R_f = 0.36 (EtOAc/*n*-hexane, 1:1, v/v); ^{1}H NMR (400 MHz, $CDCl_3$): δ = 0.7 (t, 24H, J = 7.5 Hz, CH_2CH_3), 2.1 (bs, 8H, CH_2CH_3), 2. 7 (bs, 8H, CH_2CH_3), 7.6 (dd, 8H, J = 7.3 Hz, H_{meta}), 7.7 ppm (d, 8H, J = 7.3 Hz, H_{ortho}); ^{19}F NMR (377 MHz, $CDCl_3$): δ = -110.1 ppm; ^{13}C NMR (150 MHz, $CDCl_3$): δ = 1.0, 13.3, 15.9, 16.9, 18.0, 29.7, 115.8, 116.0, 128.8, 131.1, 131.2, 123.4, 134.4, 138.2, 142.8, 163.1, 172.0 ppm; UV/Vis (CH_2Cl_2): λ_{max} (log ε) = 466 (5.76), 688 nm (4.74); HRMS (MALDI) *m/z*

calcd. for [$C_{60}H_{58}F_4N_4$]: 910.4598, found 910.4553; LRMS (MALDI) *m/z*: 911.4 (100%, M^+), 883.5 (5%, M – 3F).

Synthesis of 5,10,15,20-tetrakis(4-chlorophenyl)-2,3,7,8,12,13,17,18-octaethylporphyrin (**1:2**).

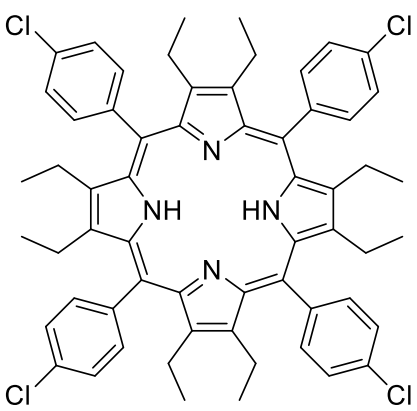

Compound **1:2** was synthesised following general procedure A outlined above using 4-chlorobenzaldehyde (1.14 g, 8.12 mmol, 1 eq.) to yield 555 mg (0.56 mmol, 28%) of green flakes. M.p. >300 °C; R_f = 0.32 (EtOAc/*n*-hexane, 1:1, v/v); ^{1}H NMR (400 MHz, $CDCl_3$): δ = 0.8 (t, 24H, J = 7.11 Hz, CH_2CH_3), 2.1 (bs, 8H, CH_2CH_3), 2.4 (bs, 8H, CH_2CH_3), 7.7 (d, 8H, J = 8.46 Hz, H_{ortho}), 7.8 ppm (d, 8H, J = 8.46 Hz, H_{meta}); UV/Vis (CH_2Cl_2): λ_{max} (log ε) = 472 (5.02), 683 nm (4.12); HRMS (MALDI) *m/z* calcd. for [$C_{60}H_{58}Cl_4N_4$]: 974.3416, found 974.3377; LRMS (MALDI) *m/z*: 977.4 (100%, M^+), 949.4 (4%, M – CH_2CH_3).

Synthesis of 5,10,15,20-tetrakis-(4-bromophenyl)-2,3,7,8,12,13,17,18-octaethylporphyrin (**1:3**).[123a]

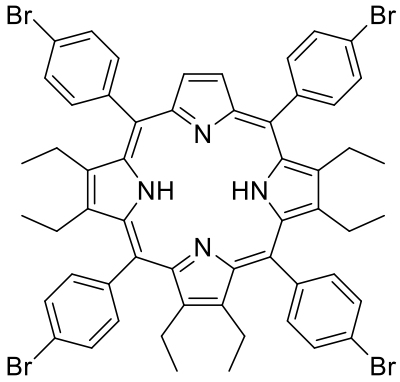

Compound **1:3** was synthesised following general procedure A outlined above using 4-bromobenzaldehyde (1.50 g, 8.12 mmol, 1 eq.) to yield 773 mg (0.67 mmol, 33%) of green flakes. M.p. >300 °C; R_f = 0.42 (EtOAc/*n*-hexane, 1:1, v/v); ^{1}H NMR (400 MHz, $CDCl_3$): δ = -2.1 (s, 2H, N*H*), 0.5 (Bs, 24H, CH_2CH_3), 1.8 (bs, 8H, CH_2CH_3), 2.6 (bs, 8H, CH_2CH_3), 7.8 (d, 8H, J = 8.4 Hz, H_{ortho}), 8.2 ppm (d, 8H, J = 8.4 Hz, H_{meta}); ^{13}C NMR (150 MHz, $CDCl_3$): δ = 16.8, 19.4, 116.8, 123.0, 130.3, 131.7, 137.1, 138.1, 139.4 ppm; UV/Vis (CH_2Cl_2): λ_{max} (log ε) = 459 (5.46), 559 nm (4.25); HRMS (MALDI) *m/z* calcd. for [$C_{60}H_{59}Br_4N_4$]: 1151.1473, found 1151.1525; LRMS (MALDI) *m/z*: 1155.1 (100%, M^+), 1097.1 (4%, M – 2 × CH_2CH_3).

Synthesis of 2,3,7,8,12,13,17,18-octaethyl-5,10,15,20-tetrakis(4-iodophenyl)porphyrin (**1:4**).

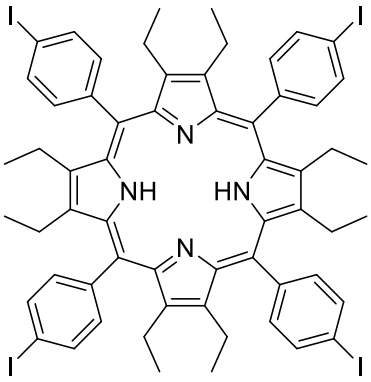

Compound **1:4** was synthesised following general procedure A outlined above using 4-iodobenzaldehyde (1.88 g, 8.12 mmol, 1 eq.) to yield 381 mg (0.28 mmol, 14%) of green flakes. M.p. >300 °C; R_f = 0.35 (EtOAc/*n*-hexane, 1:1, v/v); ^{1}H NMR (400 MHz, $CDCl_3$): δ = 1.2 (t, 24H, J = 7.1 Hz, CH_2CH_3), 1.9 (bs, 8H, CH_2CH_3), 2.3 (bs, 8H, CH_2CH_3), 7.8 (dd, 8H, J = 8.2 Hz, H_{ortho}), 7.9 ppm (dd, 8H, J = 8.2 Hz, H_{meta}); ^{13}C NMR (150 MHz, $CDCl_3$): δ = 14.2, 15.1, 15.8, 15.9, 18.3, 18.9, 21.1, 60.4, 97.5, 136.4, 136.9, 137.6, 138.1, 138.3, 142.3 ppm; UV/Vis (CH_2Cl_2): λ_{max} (log ε) = 474 (5.51), 685 nm (4.57); HRMS (MALDI) *m/z* calcd. for [$C_{60}H_{59}I_4N_4$]: 1343.0919, found 1343.0857; LRMS (MALDI) *m/z*: 1343.0 (100%, M^+).

Synthesis of 2,3,7,8,12,13,17,18-octaethyl-5,10,15,20-tetrakis(2,6-difluorophenyl)porphyrin (**1:5**).

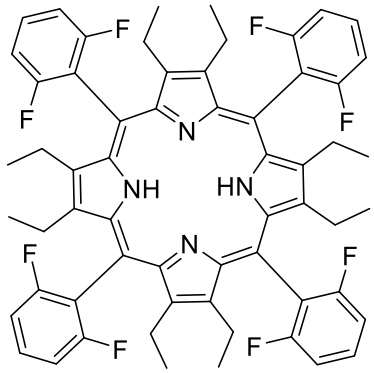

Compound **1:5** was synthesised following general procedure A outlined above using 2,6-difluorobenzaldehyde (1.15 g, 8.12 mmol, 1 eq.) to yield 399 mg (0.41 mmol, 20%) of green flakes. M.p. >300 °C; R_f = 0.35 (EtOAc/*n*-hexane, 1:1, v/v); ^{1}H NMR (400 MHz, $CDCl_3$): δ = 0.2 (bs, 24H, CH_2CH_3), 2.3 (bs, 8H, CH_2CH_3), 2.5 (bs, 8H, CH_2CH_3), 7.4 (dd, 8H, J = 8.1 Hz, H_{meta}), 7.8 ppm (t, 4H, J = 8.1 Hz, H_{para}); ^{19}F NMR (377 MHz, $CDCl_3$): δ = -115.22 ppm; UV/Vis (CH_2Cl_2): λ_{max} (log ε) = 473 (5.89), 617 (4.61), 674 nm (4.69); HRMS (MALDI) *m/z* calcd. for [$C_{60}H_{55}F_8N_4$]: 983.4299, found 983.4265; LRMS (MALDI) *m/z*: 983.40 (100%, M^+), 955.4 (17%, M –CH_2CH_3).

Synthesis of 5,10,15,20-tetrakis(2,6-dichlorophenyl)-2,3,7,8,12,13,17,18-octaethylporphyrin (**1:6**).[123b]

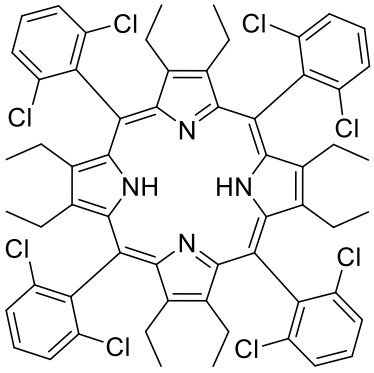

Compound **1:6** was synthesised following general procedure A outlined above using 2,6-dichlorobenzaldehyde (1.42 g, 8.12 mmol, 1 eq.) to yield 385 mg (0.34 mmol, 17%) of green flakes. M.p. >300 °C; R_f = 0.42 (EtOAc/*n*-hexane, 1:1, v/v); ^{1}H NMR (400 MHz, $CDCl_3$): δ = -1.30 (s, 2H, N*H*), 0.69 (t, 24H, J = 7.54 Hz, CH_2CH_3), 2.08 (bs, 8H, CH_2CH_3), 2.7 (bs, 8H, CH_2CH_3), 7.6 (t, 4H, J = 7.4 Hz, H_{para}), 7.7 ppm (d, 8H, J = 7.4 Hz, H_{meta}); ^{13}C NMR (150 MHz, $CDCl_3$): δ = 14.9, 18.3, 128.4, 131.3, 137.3, 140.5, 143.5 ppm; UV/Vis (CH_2Cl_2): λ_{max} (log ε) = 463 (5.07), 563 nm (4.94); HRMS (MALDI) *m/z* calcd. for [$C_{60}H_{54}Cl_8N_4$]: 1111.1935, found 1111.1885; LRMS (MALDI) *m/z*: 1115.2 (100%, M^+), 1079 (4%, M – Cl).

Synthesis of 5,10,15,20-tetrakis(4-butylphenyl)-2,3,7,8,12,13,17,18-octaethylporphyrin (**1:7**).

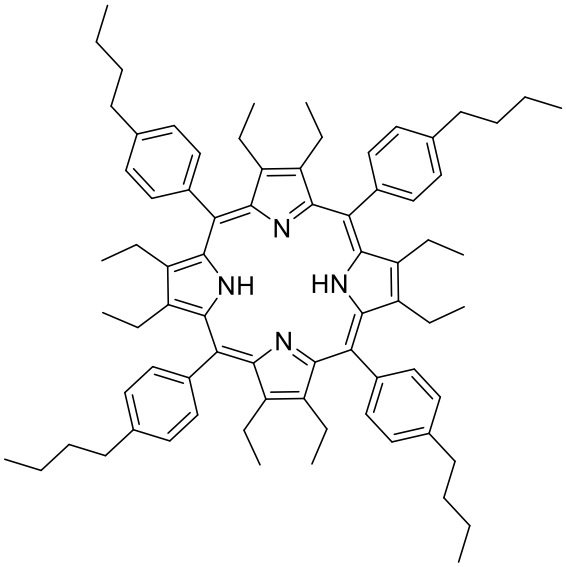

Compound **1:7** was synthesised following general procedure A outlined above using 4-butylbenzaldehyde (1.32 g, 8.12 mmol, 1 eq.) to yield 237 mg (0.22 mmol, 11%) of green flakes. M.p. >300 °C; R_f = 0.30 (EtOAc/*n*-hexane, 1:1, v/v); ^{1}H NMR (400 MHz, $CDCl_3$): δ = 0.50 (t, 24H, J = 7.40 Hz, CH_2CH_3), 1.26 (bs, 12H, butyl-CH_3), 1.80–2.14 (m, 24H, butyl-CH_2), 2.33 (bs, 8H, CH_2CH_3), 2.60 (bs, 8H, CH_2CH_3), 8.01 (t, 8H, J = 8.0 Hz, H_{ortho}), 8.38 ppm (d, 8H, J = 8.0 Hz, H_{meta}); UV/Vis (CH_2Cl_2): λ_{max} (log ε) = 486 (5.07), 697 nm (4.94); HRMS (MALDI) *m/z* calcd. for [$C_{76}H_{95}N_4$]: 1063.7557, found 1063.7585; LRMS (MALDI) *m/z*:1063.76 (100%, M^+), 1035.73 (85%, M – CH_2CH_3), 1007.70 (28%, M – $CH_2CH_2CH_2CH_3$).

Synthesis of 2,3,7,8,12,13,17,18-octaethyl-5,10,15,20-tetrakis(4-((trimethylsilyl)ethynyl)phenyl)-porphyrin (**1:8**).

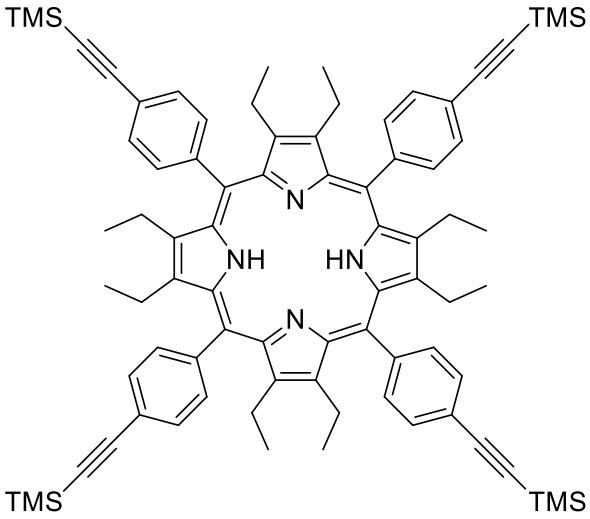

Compound **1:8** was synthesised following general procedure A outlined above using 4-((trimethylsilyl)ethynyl)benzaldehyde (1.64 g, 8.12 mmol, 1 eq.) to yield 1.29 g (1.06 mmol, 52%) of green flakes. M.p. >300 °C; R_f = 0.39 (EtOAc/*n*-hexane, 1:1, v/v); ^{1}H NMR (400 MHz, $CDCl_3$): δ = 0.50 (bs, 48H, CH_2CH_3 + TMS-CH_3), 2.10 (bs, 8H, CH_2CH_3), 2.39 (bs, 8H, CH_2CH_3), 7.96 (t, 8H, J = 6.9 Hz, H_{ortho}), 8.47 ppm (bs, 8H, J = 8.0 Hz, H_{meta}); ^{13}C NMR (150 MHz, $CDCl_3$): 0.13, 18.4, 29.8, 97.8, 104.8, 125.1, 132.0, 137.3, 142.5 ppm; UV/Vis (CH_2Cl_2): λ_{max} (log ε) = 482 (5.07), 696 nm (4.94); HRMS (MALDI) *m/z* calcd. for [$C_{80}H_{95}N_4Si_4$]: 1223.6634, found 1223.6656; LRMS (MALDI) *m/z*:1224.67 (100%, M^+), 1196.64 (50%, M – CH_2CH_3).

Synthesis of 5,10,15,20-tetrakis(4-benzyloxyphenyl)-2,3,7,8,12,13,17,18-octaethylporphyrin (**1:9**).

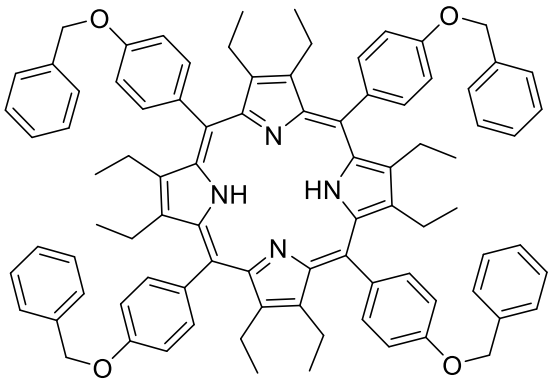

Compound **1:9** was synthesised following general procedure A outlined above using 4-benzyloxybenzaldehyde (1.72 g, 8.12 mmol, 1 eq.) to yield 949 mg (0.75 mmol, 37%) of green flakes. M.p. >300 °C; R_f = 0.42 (EtOAc/*n*-hexane, 1:1, v/v); ^{1}H NMR (400 MHz, $CDCl_3$): 0.9 (t, 24H, J = 7.2 Hz, CH_2CH_3), 2.1 (bs, 8H, CH_2CH_3), 2.3 (bs, 8H, CH_2CH_3), 5.3 (s, 8H, OCH_2), 7.6 (bs, 16H, $H_{meta/ortho}$), 7.5 (t, 8H, J = 7.3 Hz, H_{meta}), 7.6 (d, 8H, J = 7.3 Hz, H_{ortho}), 8.4 ppm (bs, 4H, H_{para}); ^{13}C NMR (150 MHz, $CDCl_3$): δ = 12.3, 12.4, 15.01, 15.3, 17.0, 18.1, 18.7, 19.0, 70.3, 70.5, 114.7, 115.2, 127.5, 127.9, 128.3, 128.4, 128.6, 128.8, 129.1, 129.8, 130.1, 131.1, 132.1, 134.6, 136.0, 136.5, 138.0, 143.2, 160.4, 163.8, 191.0, 192.6 ppm; UV/Vis (CH_2Cl_2): λ_{max} (log ε) = 473 (5.17), 694 nm (4.33); HRMS (MALDI) *m/z* calcd. for [$C_{88}H_{87}O_4N_4$]: 1263.6727, found 1263.6743; LRMS (MALDI) *m/z*: 1263.7 (100%, M^+), 1173.7

(77%, M – $CH_2C_6H_6$), 1083.6 (48%, M – 2 × $CH_2C_6H_6$), 991.5 (16%, M – 3 × $CH_2C_6H_6$), 901.5 (48%, M – 4 × $CH_2C_6H_5$)

Synthesis of 5,10,15,20-tetrakis(3,4-dibenzyloxyphenyl)-2,3,7,8,12,13,17,18-octaethylporphyrin (**1:10**).

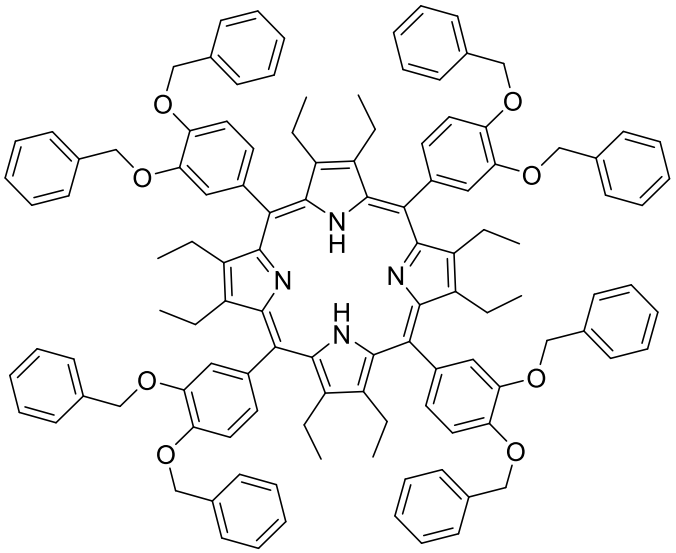

Compound **1:10** was synthesised following general procedure A outlined above using 3,4-dibenzyloxybenzaldehyde (2.58 g, 8.12 mmol, 1 eq.) to yield 959 mg (0.57 mmol, 28%) of green flakes. M.p. >300 °C; R_f = 0.42 (EtOAc/*n*-hexane, 1:1, v/v); ^{1}H NMR (400 MHz, $CDCl_3$): δ = 0.8 (bs, 24H, CH_2CH_3), 1.8 (bs, 8H, CH_2CH_3), 2.1 (bs, 8H, CH_2CH_3), 5.5 (s, 8H, OCH_2), 5.5 (s, 8H, OCH_2), 7.3 (bs, 4H, H_{meta}), 7.4 (bs, 12H, $H_{meta/ortho}$), 7.5 (bs, 12H, $H_{meta/ortho}$), 7.9 ppm (bs, 8H, H_{para}); UV/Vis (CH_2Cl_2): λ_{max} (log ε) = 480 (5.38), 696 nm (4.53); HRMS (MALDI) *m/z* calcd. for [$C_{116}H_{111}O_8N_4$]: 1687.8402, found 1687.8423; LRMS (MALDI) *m/z*: 1688.9 (100%, M^+), 1598.9 (90%, M – $CH_2C_6H_6$) 1507.8 (40%, M – 2 × $CH_2C_6H_5$), 1416.7 (24%, M – 3 x $CH_2C_6H_5$), 1325.7 (24%, M – 4 × $CH_2C_6H_5$), 1234.6 (5%, M – 5 × $CH_2C_6H_5$).

Synthesis of 5,10,15,20-tetrakis(4-cyanophenyl)-2,3,7,8,12,13,17,18-octaethylporphyrin (**1:11**).

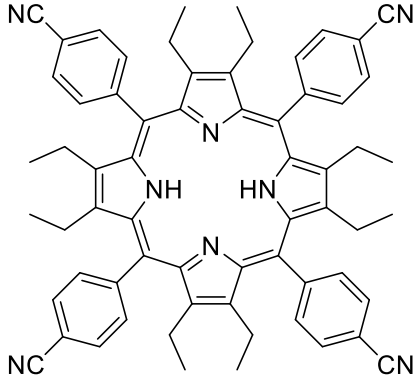

Compound **1:11** was synthesised following general procedure A outlined above using 4-cyanophenylbenzaldehyde (1.06 g, 8.12 mmol, 1 eq.) to yield 553 mg (0.55 mmol, 29%) of green flakes. M.p. >300 °C; R_f = 0.43 (EtOAc/*n*-hexane, 1:1, v/v); ^{1}H NMR (400 MHz, $CDCl_3$): δ = 0.8 (bs, 24H, CH_2CH_3), 1.9 (bs, 8H, CH_2CH_3), 2.4 (bs, 8H, CH_2CH_3), 8.2 (d, 8H, J = 8.0 Hz, H_{ortho}), 8.6 ppm (d, 8H, J = 8.0 Hz, H_{meta}); UV/Vis (CH_2Cl_2): λ_{max} (log ε) = 476 (6.07), 626 (4.95), 683 nm (4.75); HRMS (MALDI) *m/z* calcd. for [$C_{64}H_{59}N_8$]: 939.4963, found 939.4901; LRMS (MALDI) *m/z*: 939.5 (100%, M^+), 911.5 (4%, M – CH_2CH_3).

Synthesis of 5,10,15,20-tetrakis(4-azidophenyl)-2,3,7,8,12,13,17,18-octaethylporphyrin (**1:12**).

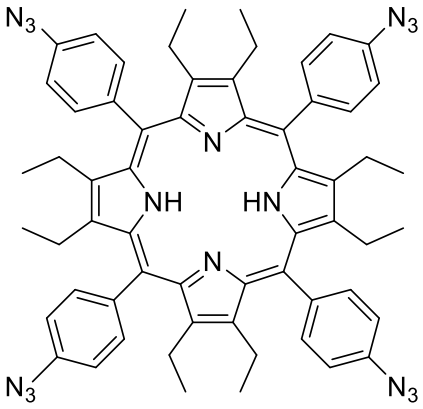

Compound **1:12** was synthesised following general procedure A outlined above using 4-cyanophenylbenzaldehyde (1.19 g, 8.12 mmol, 1 eq.) to yield 428 mg (0.43 mmol, 21%) of green flakes. M.p. >300 °C; R_f = 0.37 (EtOAc/*n*-hexane, 1:1, v/v); ^{1}H NMR (400 MHz, $CDCl_3$): δ = 0.0 (bs, 24H, CH_2CH_3), 2.1 (m, 8H, CH_2CH_3), 2.4 (m, 8H, CH_2CH_3), 7.5 (d, 8H, J = 8.3 Hz, H_{ortho}), 8.3 ppm (d, 8H, J = 8.3 Hz, H_{meta}); UV/Vis (CH_2Cl_2): λ_{max} (log ε) = 478 (5.52), 695 nm (4.64); HRMS (MALDI) *m/z* calcd. for [$C_{60}H_{59}N_{16}$]: 1003.5109, found 1003.5122; LRMS (MALDI) *m/z*: 1003.5 (100%, M^+), 977.5 (83%, M –CH_2CH_3), 962.5 (62%, M – CH_2CH_3 + CH_3), 949.5 (49%, M – 2 ×CH_2CH_3), 892.5 (32% M – 4 ×CH_2CH_3).

Nickel(II) OETArXPs.

Synthesis of [2,3,7,8,12,13,17,18-octaethyl-5,10,15,20-tetrakis(4-fluorophenyl)porphyrinato]nickel(II) (**1:37**).

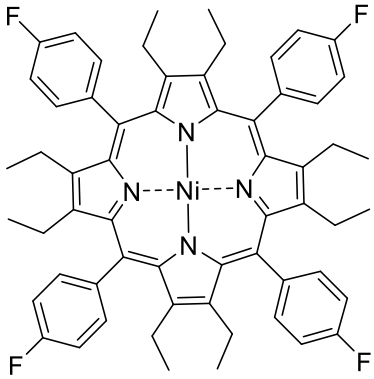

The free base porphyrin **1:1** (100 mg, 0.11 mmol) was reacted with nickel(II) acetylacetonate according to the general procedure B. Yield: 76 mg (0.08 mmol, 72%) of purple crystals. M.p. >300 °C; R_f = 0.60 (CH_2Cl_2/*n*-hexane, 1:1, v/v); ^{1}H NMR (400 MHz, $CDCl_3$): δ = 0.5 (t, 24H, J = 7.5 Hz CH_2CH_3), 2.0 (bs, 8H, CH_2CH_3), 2.5 (bs, 8H, CH_2CH_3), 7.3 (dd, 8H, J = 8.6 Hz, H_{meta}), 8.0 ppm (dd, 8H, J = 8.6 Hz, H_{ortho}); ^{19}F NMR (377 MHz, $CDCl_3$): δ = -113.6 ppm; ^{13}C NMR (150 MHz, $CDCl_3$): δ = 16.9, 19.6, 114.0, 114.2, 135.5, 144.8, 145.5 ppm; UV/Vis (CH_2Cl_2): λ_{max} (log ε) = 433 (5.24), 553 (4.04), 590 nm (4.01); HRMS (MALDI) *m/z* calcd. for [$C_{60}H_{56}F_4N_4Ni$]: 966.3795, found 966.3791; LRMS (MALDI) *m/z*: 966.4 (100%, M^+).

Synthesis of 5,10,15,20-tetrakis(4-chlorophenyl)-2,3,7,8,12,13,17,18-octaethylporphyrinato]nickel(II) (**1:40**).

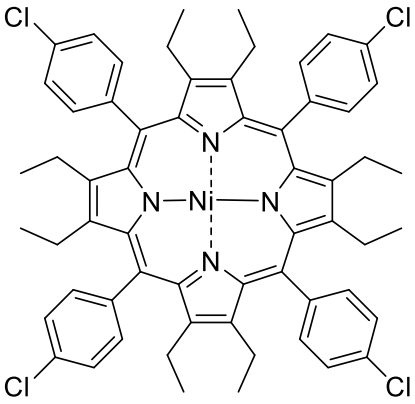

The free base porphyrin **1:2** (100 mg, 0.1 mmol) was reacted with nickel(II) acetylacetonate according to the general procedure B. Yield: 87 mg (0.84 mmol, 82%) of purple crystals. M.p. >300 °C; R_f = 0.68 (CH_2Cl_2/*n*-hexane, 1:1, v/v); ^{1}H NMR (400 MHz, $CDCl_3$): δ = 0.5 (t, 24H, J = 7.4 Hz CH_2CH_3), 2.0 (bs, 8H, CH_2CH_3), 2.5 (bs, 8H, CH_2CH_3), 7.6 (d, 8H, J = 8.4 Hz, H_{ortho}), 8.0 ppm (d, 8H, J = 8.4 Hz, H_{meta}); ^{13}C NMR (150 MHz, $CDCl_3$): δ = 17.0, 19.7, 115.9, 127.3, 134.5, 135.3, 138.4, 144.6, 145.5 ppm; UV/Vis (CH_2Cl_2): λ_{max} (log ε) = 435 (4.41), 555 (3.24), 592 nm (3.15); HRMS (MALDI) *m/z* calcd. for [$C_{60}H_{56}Cl_4N_4Ni$]: 1030.2613, found 1030.2654; LRMS (MALDI) *m/z*: 1032.3 (85%, M^+), 1001.6 (39%, M –Cl), 813.4 (100%, M – 4Cl + 3 × CH_2CH_3).

Synthesis of [5,10,15,20-tetrakis(4-bromophenyl)-2,3,7,8,12,13,17,18-octaethylporphyrinato]nickel(II) (**1:43**).[123a]

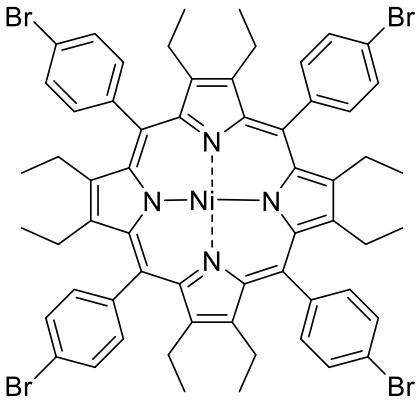

The free base porphyrin **1:3** (100 mg, 0.09 mmol) was reacted with nickel(II) acetylacetonate according to the general procedure B. Yield: 80 mg (0.07 mmol, 77%) of purple crystals. M.p. >300 °C; R_f = 0.68 (CH_2Cl_2/*n*-hexane, 1:1, v/v); ^{1}H NMR (400 MHz, $CDCl_3$): δ = 0.5 (t, 24H, J = 7.5 Hz, CH_2CH_3), 2.0 (bs, 8H, CH_2CH_3), 2.5 (bs, 8H, CH_2CH_3), 7.8 (d, 8H, J = 8.3 Hz, H_{ortho}), 7.9 ppm (d, 8H, J = 8.3 Hz, H_{meta}). ^{13}C NMR (150 MHz, $CDCl_3$): δ = 17.0, 19.7, 116.0, 122.8, 130.3, 135.7, 138.8, 144.6, 145.5 ppm; UV/Vis (CH_2Cl_2): λ_{max} (log ε) = 435 (5.18), 555 (4.01), 592 nm (3.94); HRMS (MALDI) *m/z* calcd. for [$C_{60}H_{56}Br_4N_4Ni$]: 1206.0592, found 1206.0629; LRMS (MALDI) *m/z*: 1210.1 (98%, M^+), 1055.1 (100%, M – 2Br), 898.2 (8%, M – 4Br).

Synthesis of [2,3,7,8,12,13,17,18-octaethyl-5,10,15,20-tetrakis(4-iodophenyl)porphyrinato]nickel(II) (**1:46**).

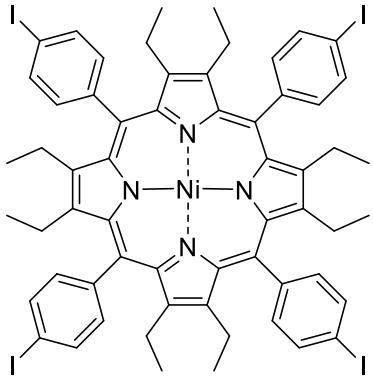

The free base porphyrin **1:4** (100 mg, 0.07 mmol) was reacted with nickel(II) acetylacetonate according to the general procedure B. Yield: 86 mg (0.06 mmol, 85%) of purple crystals. M.p. >300 °C; R_f = 0.65 (CH_2Cl_2/*n*-hexane, 1:1, v/v); ^{1}H NMR (400 MHz, $CDCl_3$): δ = 0.5 (t, 24H, J = 7.3 Hz, CH_2CH_3), 2.0 (bs, 8H, CH_2CH_3), 2.5 (bs, 8H, CH_2CH_3), 7.8 (dd, 8H, J = 8.4 Hz, H_{ortho}), 8.0 ppm (dd, 8H, J = 8.4 Hz, H_{meta}); ^{13}C NMR (150 MHz, $CDCl_3$): δ = 17.1, 19.8, 94.5, 116.2, 125.4, 128.4, 129.2, 136.1, 136.4, 139.5, 144.6, 145.6 ppm; UV/Vis (CH_2Cl_2): λ_{max} (log ε) = 436 (4.40), 554 (3.23), 589 nm (3.15); HRMS (MALDI) *m/z* calcd. for [$C_{60}H_{56}I_4N_4Ni$]: 1398.0038, found 1398.0023; LRMS (MALDI) *m/z*: 1398.0 (100%, M^+), 1227.0 (39%, M – I).

Synthesis of [2,3,7,8,12,13,17,18-octaethyl-5,10,15,20-tetrakis(2,6-difluorophenyl)porphyrinato]nickel(II) (**1:49**).

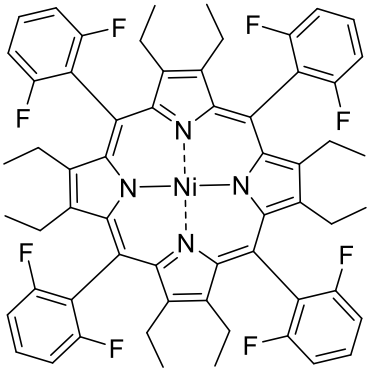

The free base porphyrin **1:5** (100 mg, 0.1 mmol) was reacted with nickel(II) acetylacetonate according to the general procedure B. Yield: 78 mg (0.08 mmol, 74%) of purple crystals. M.p. >300 °C; R_f = 0.73 (CH_2Cl_2/*n*-hexane, 1:1, v/v); ^{1}H NMR (400 MHz, $CDCl_3$): δ = 0.6 (t, 24H, J = 7.4 Hz, CH_2CH_3), 2.4 (bs, 16H, CH_2CH_3), 7.2 (m, 8H, H_{meta}), 7.6 ppm (m, 4H, H_{para}); ^{19}F NMR (377 MHz, $CDCl_3$): δ = -107.91 ppm; ^{13}C NMR (150 MHz, $CDCl_3$): δ = 16.2, 19.6, 111.2, 111.5, 131.0, 161.5, 164.2 ppm; UV/Vis (CH_2Cl_2): λ_{max} (log ε) = 429 (4.74), 556 (3.53), 595 nm (3.74); HRMS (MALDI) *m/z* calcd. for [$C_{60}H_{52}F_8N_4Ni$]: 1038.3418, found 1038.3494; LRMS (MALDI) *m/z*: 1038.4 (100%, M^+), 1010.4 (10%, M – CH_2CH_3), 954.4 (4%, M – 3 × CH_2CH_3).

Synthesis of [5,10,15,20-tetrakis(2,6-dichlorophenyl)-2,3,7,8,12,13,17,18-octaethylporphyrinato]nickel(II) (**1:51**).

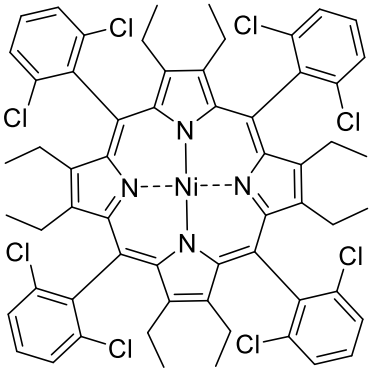

The free base porphyrin **1:6** (100 mg, 0.09 mmol) was reacted with nickel(II) acetylacetonate according to the general procedure B. Yield: 84 mg (0.07 mmol, 80%) of purple crystals. M.p. >300 °C; R_f = 0.68 (CH_2Cl_2/*n*-hexane, 1:1, v/v); ^{1}H NMR (400 MHz, $CDCl_3$): δ = 0.7 (t, 24H, J = 7.4 Hz, CH_2CH_3), 2.1 (bs, 8H, CH_2CH_3), 2.5 (bs, 8H, CH_2CH_3), 7.5 (dd, 4H, J = 8.8 Hz, H_{para}), 7.6 ppm (dd, 8H, J = 8.8 Hz, H_{meta}); ^{13}C NMR (150 MHz, $CDCl_3$): δ = 15.5, 19.1, 110.5, 127.5, 129.9, 137.1, 139.5, 143.2, 143.9 ppm; UV/Vis (CH_2Cl_2): λ_{max} (log ε) = 439 (4.98), 565 (3.83), 607 nm (3.98); HRMS (MALDI) *m/z* calcd. for [$C_{60}H_{52}Cl_8N_4Ni$]: 1166.1054, found 1166.1112; LRMS (MALDI) *m/z*: 1171.1 (100%, M^+), 1001.6 (4%, M – 2Cl).

Synthesis of [5,10,15,20-tetrakis(4-butylphenyl)-2,3,7,8,12,13,17,18-octaethylporphyrinato]nickel(II) (**1:57**).

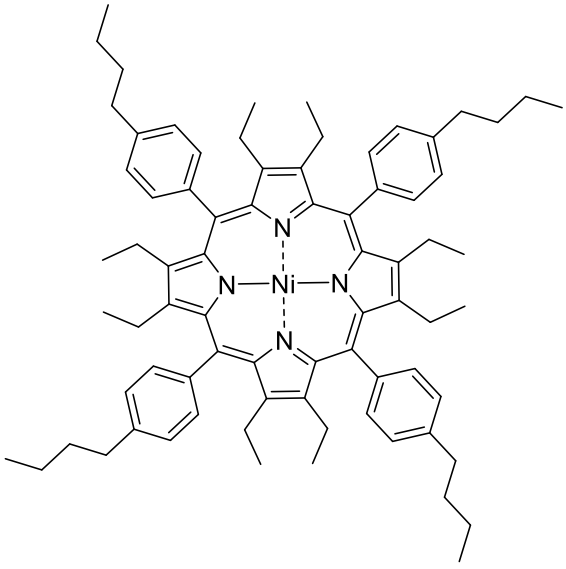

The free base porphyrin **1:7** (100 mg, 0.09 mmol) was reacted with nickel(II) acetylacetonate according to the general procedure B. Yield: 85 mg (0.08 mmol, 81%) of purple crystals. M.p. >300 °C; R_f = 0.63 (CH_2Cl_2/*n*-hexane, 1:1, v/v); ^{1}H NMR (400 MHz, $CDCl_3$): δ = 0.5 (m, 24H, CH_2CH_3), 1.0 (t, 12H, J = 7.3 Hz, butyl-CH_3), 1.5 (bs, 8H, butyl-CH_2 + CH_2CH_3), 1.8 (bs, 8H, butyl-CH_2), 2.2 (bs, 8H, CH_2CH_3), 2.8 (bs, 8H, butyl-CH_2), 7.4 (bs, 8H, H_{ortho}), 7.9 ppm (bs, 8H, H_{meta}); UV/Vis (CH_2Cl_2): λ_{max} (log ε) = 438 (4.73), 556 (3.42), 592 nm (3.66); HRMS (MALDI) *m/z* calcd. for [$C_{76}H_{92}N_4Ni$]: 1118.6675, found 1118.6685; LRMS (MALDI) *m/z*: 1118.7 (100%, M^+), 1090.6 (45%, M – CH_2CH_3), 1062.6 (15%, M – $CH_2CH_2CH_2CH_3$).

Synthesis of [2,3,7,8,12,13,17,18-octaethyl-5,10,15,20-tetrakis(4-((trimethylsilyl)ethynyl)phenyl)-porphyrin]nickel(II) (**1:58**).

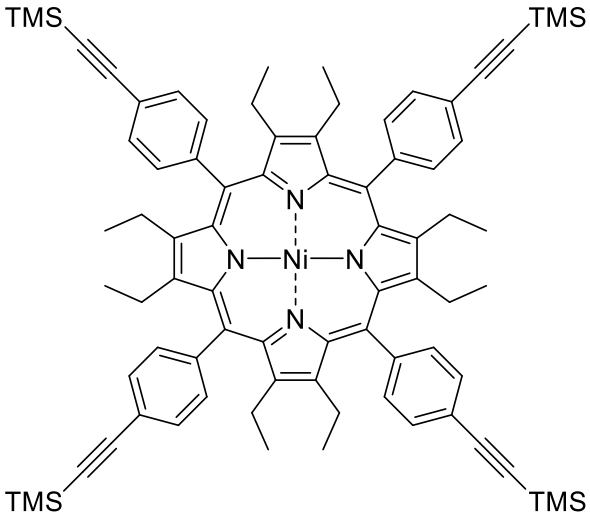

The free base porphyrin **1:8** (100 mg, 0.09 mmol) was reacted with nickel(II) acetylacetonate according to the general procedure B. Yield: 82 mg (0.06 mmol, 78%) of purple crystals. . M.p. >300 °C, R_f = 0.72 (CH_2Cl_2/ *n*-hexane, 1:1, v/v); ^{1}H NMR (600 MHz, $CDCl_3$): δ = 0.36 (bs, 36H, TMS-CH_3), 0.05 (t, 24H, J = 7.3 Hz, CH_2CH_3), 2.0 (bs, 8H, CH_2CH_3), 2.5 (bs, 8H, CH_2CH_3), 7.7 (t, 8H, J = 7.7 Hz, H_{ortho}), 8.5 ppm (bs, 8H, J = 7.7 Hz, H_{meta}); ^{13}C NMR (150 MHz, $CDCl_3$): 0.2, 17.1, 19.8, 95.3, 105.5, 116.8, 123.0, 130.8, 134.3, 140.4, 144.7, 145.6 ppm; UV/Vis (CH_2Cl_2): λ_{max} (log ε) = 441 (4.07), 558 nm (3.74); HRMS (MALDI) *m/z* calcd. for [$C_{80}H_{95}N_4Si_4Ni$]: 1278.5753, found 1278.5786; LRMS (MALDI) *m/z*:1278.60 (100%, M^+), 1235.58 (30%, M – CH_2CH_3 + CH_3).

Synthesis of [5,10,15,20-tetrakis(4-benzyloxyphenyl)-2,3,7,8,12,13,17,18-octaethylporphyrinato]nickel(II) (**1:59**).

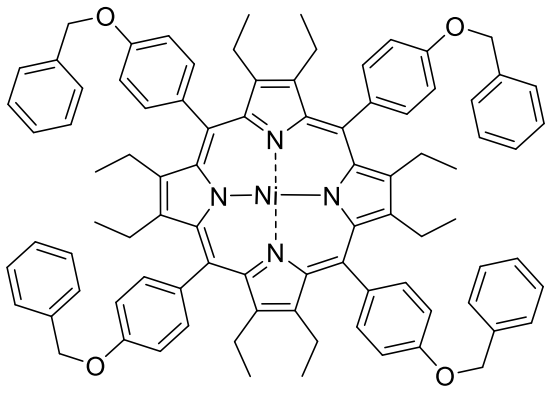

The free base porphyrin **1:9** (100 mg, 0.08 mmol) was reacted with nickel(II) acetylacetonate according to the general procedure B. Yield: 78 mg (0.06 mmol, 75%) of purple crystals. M.p. >300 °C; R_f = 0.67 (CH_2Cl_2/*n*-hexane, 1:1, v/v); ^{1}H NMR (400 MHz, $CDCl_3$): δ = 0.5 (t, 24H, J = 7.3 Hz, CH_2CH_3), 2.0 (bs, 8H, CH_2CH_3), 2.7 (bs, 8H, CH_2CH_3), 5.4 (s, 8H, OCH_2), 7.3 (d, 8H, J = 8.1 Hz, H_{meta}), 7.4 (t, 4H, J = 8.1 Hz, H_{para}), 7.5 (d, 8H, J = 8.1 Hz, H_{meta}), 7.6 (d, 8H, J = 8.1 Hz, H_{ortho}), 8.2 ppm (d, 8H, J = 8.1 Hz, H_{ortho}); ^{13}C NMR (150 MHz, $CDCl_3$): δ = 16.9, 19.3, 69.8, 113.1, 119.0, 127.2, 127.6, 128.2, 133.6, 135.3, 136.5, 143.3, 143.7, 158.5 ppm; UV/Vis (CH_2Cl_2): λ_{max} (log ε) = 437 (4.27), 553 nm (3.28); HRMS (MALDI) *m/z* calcd. for [$C_{88}H_{84}O_4N_4Ni$]: 1318.3574, found 1318.3539; LRMS (MALDI) *m/z*: 1318.6 (100%, M^+), 1228.5 (4%, M – $CH_2C_6H_5$).

Synthesis of [5,10,15,20-tetrakis(3,4-dibenzyloxyphenyl)-2,3,7,8,12,13,17,18-octaethylporphyrinato]nickel(II) (**1:62**).

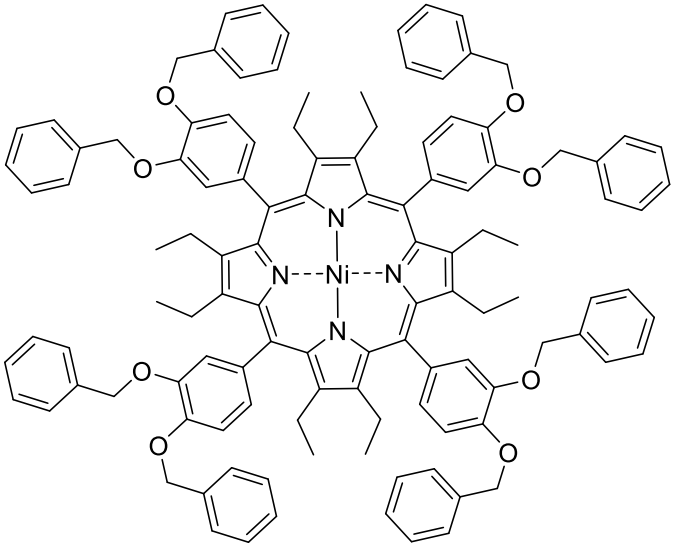

The free base porphyrin **1:10** (100 mg, 0.06 mmol) was reacted with nickel(II) acetylacetonate according to the general procedure B. Yield: 86 mg (0.05 mmol, 83%) of purple crystals. M.p. >300 °C; R_f = 0.68 (CH_2Cl_2/*n*-hexane, 1:1, v/v); ^{1}H NMR (400 MHz, $CDCl_3$): δ = 0.5 (bs, 24H, CH_2CH_3), 1.9 (bs, 8H, CH_2CH_3), 2.4 (bs, 8H, CH_2CH_3), 5.3 (s, 8H, OCH_2), 5.5 (s, 8H, OCH_2), 7.2 (bs, 4H, H_{meta}), 7.3 (bs, 8H, $H_{ortho/meta}$), 7.5 (m, 32H, $H_{ortho/meta}$), 7.6 ppm (bs, 8H, H_{para}); ^{13}C NMR (150 MHz, $CDCl_3$): δ = 17.2, 19.6, 29.8, 71.5, 114.0, 116.4, 121.2, 127.4, 127.6, 128.0, 128.6, 128.9, 133.9, 137.2, 144.6, 145.4, 147.4 ppm; UV/Vis (CH_2Cl_2): λ_{max} (log ε) = 437 (4.39), 533 nm (3.41); HRMS (MALDI) *m/z* calcd. for [$C_{116}H_{108}O_8N_4Ni$]: 1742.7521, found 1742.7593; LRMS (MALDI) *m/z*: 1743.9 (90%, M^+), 1653.8 (100%, M – $CH_2C_6H_6$), 1563.7 (35%, M – 2 × $CH_2C_6H_5$), 1473.7 (4%, M – 3 × $CH_2C_6H_5$).

Synthesis of [5,10,15,20-tetrakis(4-cyanophenyl)-2,3,7,8,12,13,17,18-octaethylporphyrinato]nickel(II) (**1:54**).

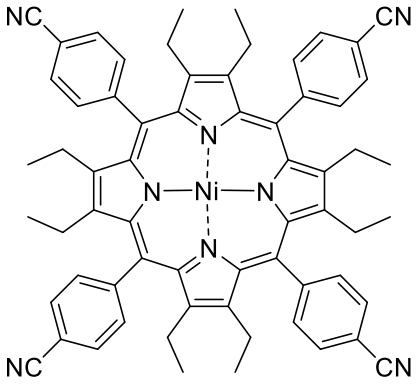

The free base porphyrin **1:11** (100 mg, 0.11 mmol) was reacted with nickel(II) acetylacetonate according to the general procedure B. Yield: 86 mg (0.09 mmol, 81%) of purple crystals. M.p. >300 °C; R_f = 0.67 (CH_2Cl_2/*n*-hexane, 1:1, v/v); ^{1}H NMR (400 MHz, $CDCl_3$): δ = 0.5 (t, 24H, J = 7.4 Hz, CH_2CH_3), 2.2 (bs, 8H, CH_2CH_3), 2.4 (bs, 8H, CH_2CH_3), 8.0 (d, 8H, J = 8.2 Hz, H_{ortho}), 8.2 ppm (d, 8H, J = 8.2 Hz, H_{meta}); ^{13}C NMR (150 MHz, $CDCl_3$): δ = 16.9, 19.7, 114.1, 116.0 135.5, 136.1, 144.8, 145.5 ppm; UV/Vis (CH_2Cl_2): λ_{max} (log ε) = 436 (4.51), 559 nm (3.36); HRMS (MALDI) *m/z* calcd. for [$C_{64}H_{56}N_4Ni$]: 994.3981, found 994.3988; LRMS (MALDI) *m/z*: 994.4 (100%, M^+), 966.3 (75%, M – CH_2CH_3).

Copper(II) OETArXPs.

Synthesis of [2,3,7,8,12,13,17,18-octaethyl-5,10,15,20-tetrakis(4-fluorophenyl)porphyrinato]copper(II) (**1:39**).

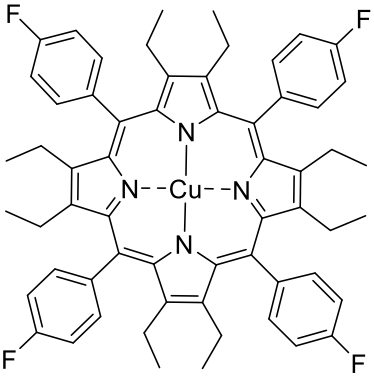

The free base porphyrin **1:1** (100 mg, 0.11 mmol) was reacted with copper(II) acetate according to the general procedure C. Yield: 95 mg (0.10 mmol, 89%) of purple crystals. M.p. >300 °C; R_f = 0.60 (CH_2Cl_2/*n*-hexane, 1:1, v/v); UV/Vis (CH_2Cl_2): λ_{max} (log ε) = 434 (4.78), 572 nm (3.68); HRMS (MALDI) *m/z* calcd. for [$C_{60}H_{56}CuF_4N_4$]: 971.3737, found 971.3699; LRMS (MALDI) *m/z*: 971.3 (48%, M^+), 927.3 (60%, M – F, CH_2CH_3)), 898.2 (100%, M – F, 2 × CH_2CH_3).

Synthesis of [5,10,15,20-tetrakis(4-chlorophenyl)-2,3,7,8,12,13,17,18-octaethylporphyrinato]copper(II) (**1:42**).

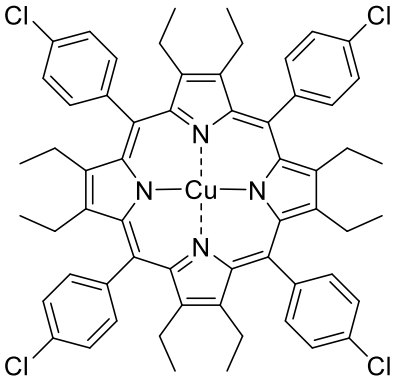

The free base porphyrin **1:2** (100 mg, 0.11 mmol) was reacted with copper(II) acetate according to the general procedure C. Yield: 83 mg (0.08 mmol, 78%) of purple crystals. M.p. >300 °C; R_f = 0.62 (CH_2Cl_2/*n*-hexane, 1:1, v/v); UV/Vis (CH_2Cl_2): λ_{max} (log ε) = 436 (5.25), 572 nm (3.35); HRMS (MALDI) *m/z* calcd. for [$C_{60}H_{56}Cl_4CuN_4$]: 1035.2555, found 1035.2518; LRMS (MALDI) *m/z*: 1037.2 (70%, M^+), 964.1 (100%, M – 2Cl), 897.2 (55%, M – 4Cl).

Synthesis of [5,10,15,20-tetrakis(4-bromophenyl)-2,3,7,8,12,13,17,18-octaethylporphyrinato]copper(II) (**1:45**).

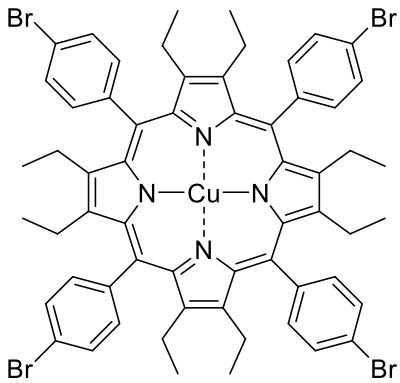

The free base porphyrin **1:3** (100 mg, 0.09 mmol) was reacted with copper(II) acetate according to the general procedure C. Yield: 99 mg (0.08 mmol, 88%) of purple crystals. M.p. >300 °C; R_f = 0.68 (CH_2Cl_2/ *n*-hexane, 1:1, v/v); UV/Vis (CH_2Cl_2): λ_{max} (log ε) = 437 (4.80), 574 nm (3.86); HRMS (MALDI) *m/z* calcd. for [$C_{60}H_{56}Br_4N_4Cu$]: 1211.0534, found

1211.0494; LRMS (MALDI) *m/z*: 1215.0 (100%, M^+). 1060 (22%, M – 2Br).

Synthesis of [2,3,7,8,12,13,17,18-octaethyl-5,10,15,20-tetrakis(4-iodophenyl)porphyrinato]copper(II) (**1:48**).

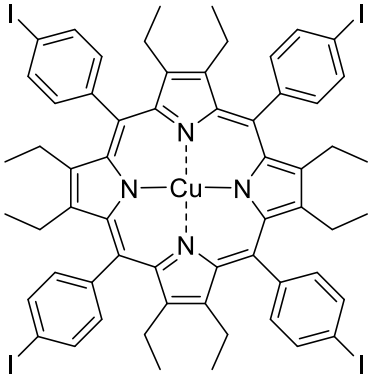

The free base porphyrin **1:4** (100 mg, 0.07 mmol) was reacted with copper(II) acetate according to the general procedure C. Yield: 89 mg (0.06 mmol, 85%) of purple crystals. M.p. >300 °C; R_f = 0.71 (CH_2Cl_2/*n*-hexane, 1:1, v/v); UV/Vis (CH_2Cl_2): λ_{max} (log ε) = 438 (4.24), 575 nm (3.31); HRMS (MALDI) *m/z* calcd. for [$C_{60}H_{52}I_8N_4Cu$]: 1402.9980, found 1402.9922; LRMS (MALDI) *m/z*: 1402.97 (100%, M^+), 1344.88 (7%, M – Cu).

Synthesis of [2,3,7,8,12,13,17,18-octaethyl-5,10,15,20-tetrakis(2,6-difluorophenyl)porphyrinato]copper(II) (**1:50**).

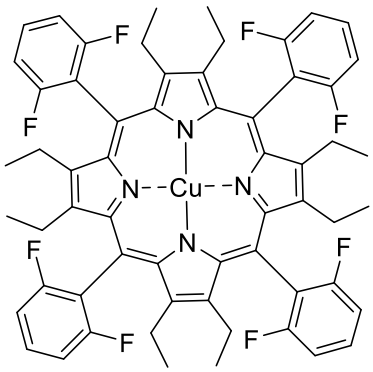

The free base porphyrin **1:5** (100 mg, 0.10 mmol) was reacted with copper(II) acetate according to the general procedure C. Yield: 85 mg (0.08 mmol, 80%) of purple crystals. M.p. >300 °C; R_f = 0.65 (CH_2Cl_2/ *n*-hexane, 1:1, v/v); UV/Vis (CH_2Cl_2): λ_{max} (log ε) = 433 (4.84), 573 (3.80), 609 nm (3.70); HRMS (MALDI) *m/z* calcd. for [$C_{60}H_{52}F_8N_4Cu$]: 1043.3360, found 1043.3344; LRMS (MALDI) *m/z*: 1043.4 (100%, M^+), 1001.6 (28%, M – 2F), 906.9 (10%, M – 7F).

Synthesis of [5,10,15,20-tetrakis(2,6-dichlorophenyl)-2,3,7,8,12,13,17,18-octaethylporphyrinato]copper(II) (**1:53**).

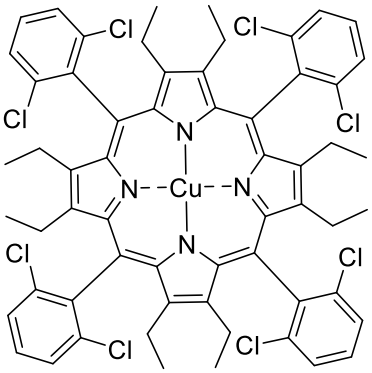

The free base porphyrin **1:6** (100 mg, 0.09 mmol) was reacted with copper(II) acetate according to the general procedure C. Yield: 91 mg (0.08 mmol, 86%) of purple crystals. M.p. >300 °C; R_f = 0.68 (CH_2Cl_2/ *n*-hexane, 1:1, v/v); UV/Vis (CH_2Cl_2): λ_{max} (log ε) = 433 (5.11), 581 (4.13), 620 nm (4.02); HRMS (MALDI) *m/z* calcd. for [$C_{60}H_{52}Cl_8N_4Cu$]: 1171.0996, found 1171.1001; LRMS (MALDI) *m/z*: 1175.1 (100%, M^+), 1101.7 (9%, M – 2Cl).

Synthesis of [5,10,15,20-tetrakis(4-cyanophenyl)-2,3,7,8,12,13,17,18-octaethylporphyrinato]copper(II) (**1:56**).

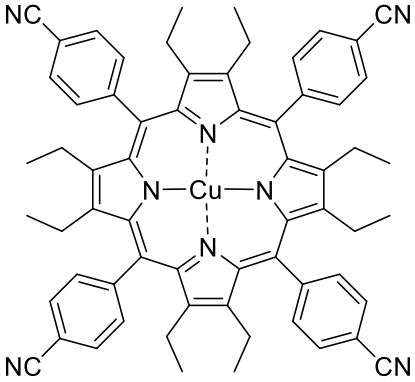

The free base porphyrin **1:11** (100 mg, 0.11 mmol) was reacted with copper(II) acetate according to the general procedure C. Yield: 91 mg (0.09 mmol, 79%) of purple crystals. M.p. >300 °C; R_f = 0.66 (CH_2Cl_2/*n*-hexane, 1:1, v/v); UV/Vis (CH_2Cl_2): λ_{max} (log ε) = 440 (4.22), 578 nm (3.28); HRMS (MALDI) *m/z* calcd. for [$C_{64}H_{56}CuN_8$]: 999.3924, found 997.3940; LRMS (MALDI) *m/z*: 999.4 (20%, M^+), 955.3 (50%, M – 3 × N), 926.3 (100%, M – 3 × CN).

Synthesis of [5,10,15,20-tetrakis(4-benzyloxyphenyl)-2,3,7,8,12,13,17,18-octaethylporphyrinato]copper(II) (**1:61**).

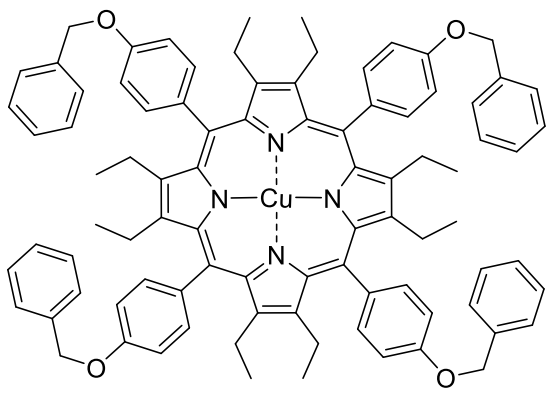

The free base porphyrin **1:9** (100 mg, 0.08 mmol) was reacted with copper(II) acetate according to the general procedure C. Yield: 89 mg (0.07 mmol, 85%) of purple crystals. M.p. >300 °C; R_f = 0.67 (CH_2Cl_2/*n*-hexane, 1:1, v/v); UV/Vis (CH_2Cl_2): λ_{max} (log ε) = 437 (4.61), 574 nm (3.68); HRMS (MALDI) *m/z* calcd. for [$C_{88}H_{84}CuN_4O_4$]: 1323.5789, found 1323.5767; LRMS (MALDI) *m/z*: 1323.5 (55%, M^+), 1232.5 (100%, M – $CH_2C_6H_5$); 1141.4 (25%, M – 2 × $CH_2C_6H_5$); 50%, M – 2 × $CH_2C_6H_5$, CH_2CH_3).

Synthesis of [5,10,15,20-tetrakis(3,4-dibenzyloxyphenyl)-2,3,7,8,12,13,17,18-octaethylporphyrinato]copper(II) (**1:64**).

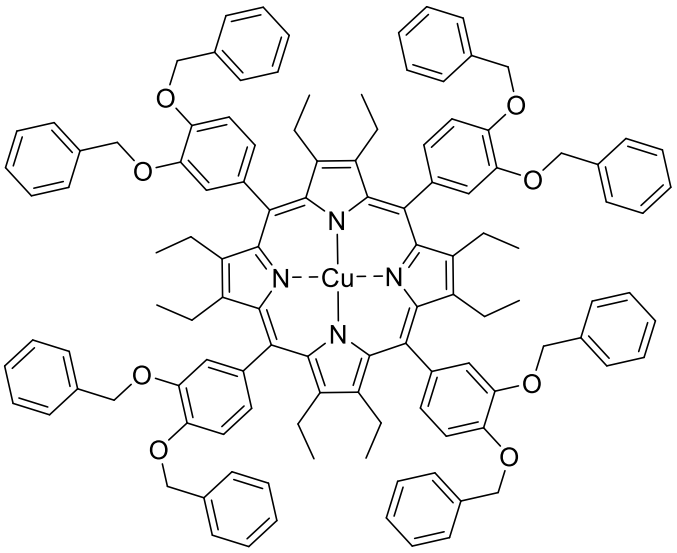

The free base porphyrin **1:10** (100 mg, 0.06 mmol) was reacted with copper(II) acetate according to the general procedure C. Yield: 84 mg (0.05 mmol, 81%) of purple crystals. M.p. >300 °C; Rf = 0.68 (CH_2Cl_2/*n*-hexane, 1:1, v/v); UV/Vis (CH_2Cl_2): λ_{max} (log ε) = 437 (5.00), 572 (4.07); HRMS (MALDI) m/z calcd. for [$C_{116}H_{108}CuN_4O_8$]: 1747.7463, found 1747.7400; LRMS (MALDI) m/z: 1748.7 (100%, M^+), 1657.7 (40%, M – $CH_2C_6H_5$), 1566.6 (45%, M – 2 × $CH_2C_6H_5$), 1474.6 (5%, M – 3 × $CH_2C_6H_5$).

Palladium(II) Porphyrins.

Synthesis of [2,3,7,8,12,13,17,18-octaethyl-5,10,15,20-tetrakis(4-fluorophenyl)porphyrinato]palladium(II) (**1:38**).

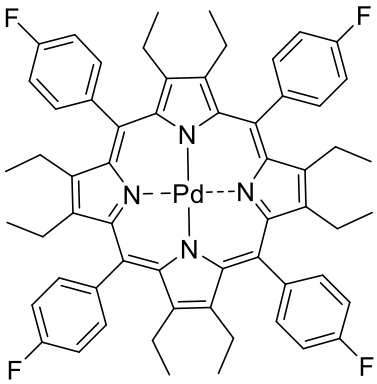

The free base porphyrin **1:1** (100 mg, 0.11 mmol) was reacted with palladium(II) acetate according to the general procedure D. Yield: 95 mg (0.10 mmol, 85%) of purple crystals. M.p. >300 °C; R_f = 0.60 (CH_2Cl_2/*n*-hexane, 1:1, v/v); ^{1}H NMR (400 MHz, $CDCl_3$): δ = 0.6 (t, 24H, J = 7.3 Hz CH_2CH_3), 2.0 (bs, 8H, CH_2CH_3), 2.6 (bs, 8H, CH_2CH_3), 7.8 (dd, 8H, J = 8.1 Hz, H_{meta}), 8.0 ppm (dd, 8H, J = 8.1 Hz, H_{ortho}); ^{19}F NMR (377 MHz, $CDCl_3$): δ = -110.9 ppm; ^{13}C NMR (150 MHz, $CDCl_3$): δ = 17.1, 19.8, 116.1, 122.9, 125.5, 128.4, 129.2, 130.4, 135.8, 139.0, 144.7, 145.6 ppm; UV/Vis (CH_2Cl_2): λ_{max} (log ε) = 434 (4.32), 546 (3.07), 582 nm (3.03); HRMS (MALDI) *m/z* calcd. for [$C_{60}H_{56}F_4N_4Pd$]: 1014.3476, found 1014.3514.

Synthesis of [5,10,15,20-tetrakis(4-chlorophenyl)-2,3,7,8,12,13,17,18-octaethylporphyrinato]palladium(II) (**1:41**).

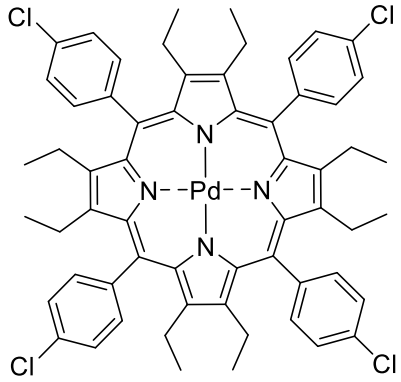

The free base porphyrin **1:2** (100 mg, 0.11 mmol) was reacted with palladium(II) acetate according to the general procedure D. Yield: 70 mg (0.06 mmol, 63%) of purple crystals. M.p. >300 °C; R_f = 0.69 (CH_2Cl_2/*n*-hexane, 1:1, v/v); ^{1}H NMR (400 MHz, $CDCl_3$): δ = 0.5 (t, 24H, J = 7.4 Hz CH_2CH_3), 2.0 (bs, 8H, CH_2CH_3), 2.7 (bs, 8H, CH_2CH_3), 7.7 (d, 8H, J = 8.4 Hz, H_{meta}), 8.2 ppm (dd, 8H, J = 8.4 Hz, H_{ortho}); ^{13}C NMR (150 MHz, $CDCl_3$): δ = 17.3, 19.8, 118.0, 127.3, 134.8, 135.9, 139.1, 143.4, 144.3 ppm; UV/Vis (CH_2Cl_2): λ_{max} (log ε) = 437 (4.26), 549 (3.27), 585 nm (3.08); HRMS (MALDI) *m/z* calcd. for [$C_{60}H_{56}Cl_4N_4Pd$]: 1078.2294, found 1078.2272.

Synthesis of [5,10,15,20-tetrakis(4-bromophenyl)-2,3,7,8,12,13,17,18-octaethylporphyrinato]palladium(II) (**1:44**).

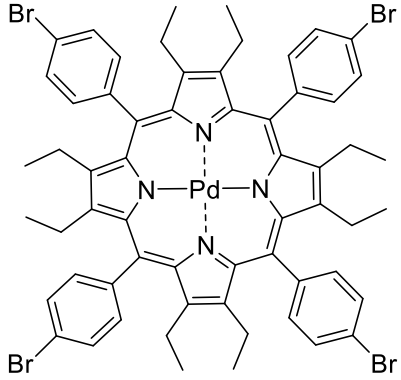

The free base porphyrin **1:3** (100 mg, 0.09 mmol) was reacted with palladium(II) acetate according to the general procedure D. Yield: 68 mg (0.05 mmol, 62%) of purple crystals. M.p >300 °C; R_f = 0.73 (CH_2Cl_2/ *n*-hexane, 1:1, v/v); ^{1}H NMR (400 MHz, $CDCl_3$): δ = 0.5 (t, 24H, J = 7.3 Hz CH_2CH_3), 2.0 (bs, 8H, CH_2CH_3), 2.6 (bs, 8H, CH_2CH_3), 7.8 (d, 8H, J = 8.3 Hz, H_{ortho}), 8.1 ppm (dd, 8H, J = 8.3 Hz, H_{meta}); ^{13}C NMR (150 MHz, $CDCl_3$): δ = 17.2, 19.9, 123.1, 127.0, 127.7, 127.8, 129.5, 130.3, 136.2, 143.3, 144.3, ppm; UV/Vis (CH_2Cl_2): λ_{max} (log ε) = 437 (4.62), 548 nm (3.62), 583 nm (3.42); HRMS (MALDI) *m/z* calcd. for [$C_{60}H_{56}Br_4N_4Pd$]: 1254.0273, found 1254.0236; LRMS (MALDI) *m/z*: 1258.1 (50%, M^+), 1180.2 (100%, M – Br), 1100.3 (79%, M – 2Br), 1022.3 (45%, M – 3Br), 942.3 (4%, M – 4Br).

Synthesis of [2,3,7,8,12,13,17,18-octaethyl-5,10,15,20-tetrakis(4-iodophenyl)porphyrinato]palladium(II) (**1:47**).

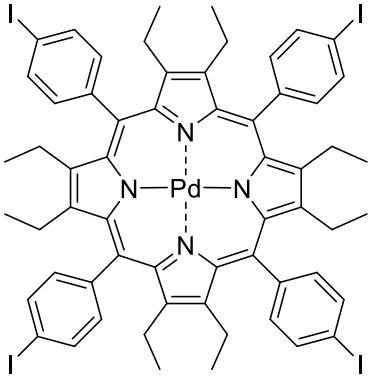

The free base porphyrin **1:4** (100 mg, 0.07 mmol) was reacted with palladium(II) acetate according to the general procedure D. Yield: 61 mg (0.04 mmol, 57%) of purple crystals. M.p. >300 °C; $R_f = 0.58$ (CH_2Cl_2/*n*-hexane, 1:1, v/v); ^{1}H NMR (400 MHz, $CDCl_3$): $\delta = 0.5$ (bs, 24H, CH_2CH_3), 2.0 (bs, 8H, CH_2CH_3), 2.6 (bs, 8H, CH_2CH_3), 7.5 (dd, 8H, $J = 8.1$ Hz, H_{meta}), 8.03 ppm (dd, 8H, $J = 8.1$ Hz, H_{ortho}); UV/Vis (CH_2Cl_2): λ_{max} (log ε) = 437 (4.39), 548 nm (3.41); HRMS (MALDI) *m/z* calcd. for [$C_{60}H_{56}I_4N_4Pd$]: 1445.9719, found 1445.9767; LRMS (MALDI) *m/z*: 1446 (15%, M^+), 1320 (40%, M – I), 942 (20%, M – 4I).

Synthesis of [5,10,15,20-tetrakis(2,6-dichlorophenyl)-2,3,7,8,12,13,17,18-octaethylporphyrinato]palladium(II) (**1:52**).

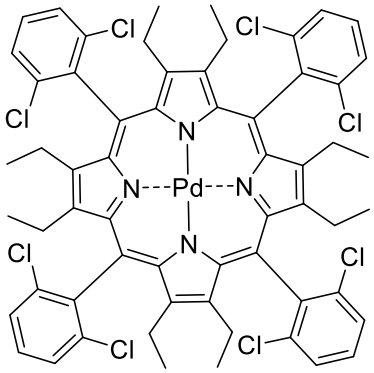

The free base porphyrin **1:6** (100 mg, 0.09 mmol) was reacted with palladium(II) acetate according to the general procedure D. Yield: 69 mg (0.05 mmol, 63%) of purple crystals. M.p. >300 °C; $R_f = 0.73$ (CH_2Cl_2/ *n*-hexane, 1:1, v/v); ^{1}H NMR (400 MHz, $CDCl_3$): $\delta = 0.7$ (t, 24H, $J = 7.5$ Hz, CH_2CH_3), 2.1 (bs, 8H, CH_2CH_3), 2.6 (bs, 8H, CH_2CH_3), 7.5–7.6 (m, 4H, H_{para}), 7.7 ppm (d, 8H, $J = 8.1$ Hz, H_{meta}); ^{13}C NMR (150 MHz, $CDCl_3$): $\delta = 16.1$, 19.9, 113.8, 128.3, 130.7, 138.3, 140.6, 142.8, 143.4 ppm; UV/Vis (CH_2Cl_2): λ_{max} (log ε) = 430 (4.98), 548 (3.73), 586 nm (3.98); HRMS (MALDI) *m/z* calcd. for [$C_{60}H_{52}Cl_8N_4Pd$]: 1214.0735, found 1214.0751.

Synthesis of [5,10,15,20-tetrakis(4-benzyloxyphenyl)-2,3,7,8,12,13,17,18-octaethylporphyrinato]palladium(II) (**1:60**).

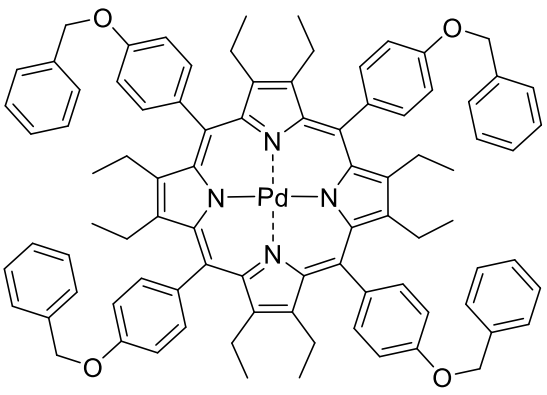

The free base porphyrin **1:9** (100 mg, 0.08 mmol) was reacted with palladium(II) acetate according to the general procedure D. Yield: 81 mg (0.06 mmol, 75%) of purple crystals. M.p. >300 °C; R_f = 0.69 (CH_2Cl_2/*n*-hexane, 1:1, v/v); ^{1}H NMR (400 MHz, $CDCl_3$): δ = 0.5 (t, 24H, J = 7.3 Hz, CH_2CH_3), 2.0 (bs, 8H, CH_2CH_3), 2.7 (bs, 8H, CH_2CH_3), 5.4 (s, 8H, OCH_2), 7.3 (d, 8H, J = 8.4 Hz, H_{meta}), 7.4 (t, 4H, J = 8.4 Hz, H_{para}), 7.5 (d, 8H, J = 8.4 Hz, H_{meta}), 7.6 (d, 8H, J = 8.4 Hz, H_{ortho}), 8.2 ppm (d, 8H, J = 8.4 Hz, H_{ortho}); ^{13}C NMR (150 MHz, $CDCl_3$): δ = 16.9, 19.3, 69.8, 113.1, 119.0, 127.2, 127.6, 128.2, 133.6, 135.3, 136.5, 143.3, 143.7, 158.5 ppm; UV/Vis (CH_2Cl_2): λ_{max} (log ε) = 439 (4.26), 548 nm (3.27); HRMS (MALDI) *m/z* calcd. for [$C_{88}H_{84}O_4N_4Pd$]: 1366.5527, found 1366.5505; LRMS (MALDI) *m/z*: 1366.5 (23%, M^+), 1275.5 (100%, M – $CH_2C_6H_5$).

Synthesis of [5,10,15,20-tetrakis(2,6-dibenzyloxyphenyl)-2,3,7,8,12,13,17,18-octaethylporphyrinato]palladium(II) (**1:63**).

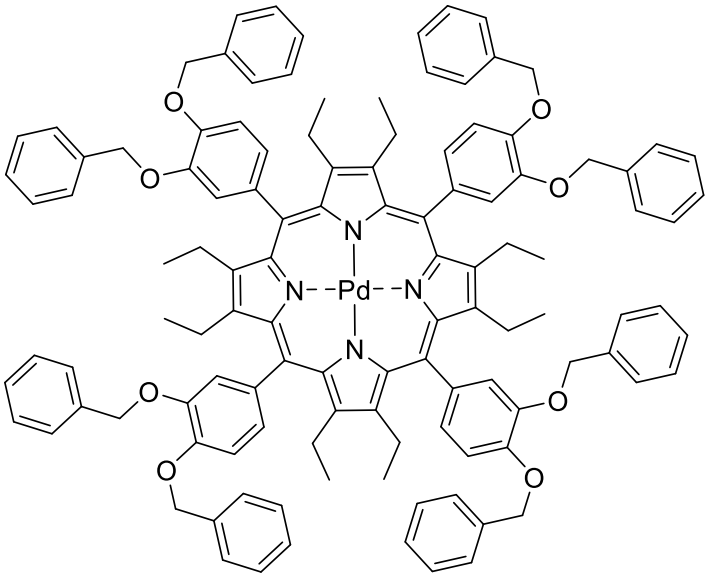

The free base porphyrin **1:10** (100 mg, 0.06 mmol) was reacted with palladium(II) acetate according to the general procedure D. Yield: 71 mg (0.04 mmol, 67%) of purple crystals. M.p. >300 °C; R_f = 0.69 (CH_2Cl_2/*n*-hexane, 1:1, v/v); ^{1}H NMR (400 MHz, $CDCl_3$): δ = 0.5 (bs, 24H, CH_2CH_3), 2.0 (bs, 8H, CH_2CH_3), 2. 6 (bs, 8H, CH_2CH_3), 5.4 (s, 8H, OCH_2), 5.5 (s, 8H, OCH_2), 7.2 (m, 4H, H_{meta}), 7.4 (bs, 8H, $H_{ortho/meta}$), 7.54 (m, 32H, $H_{ortho/meta}$), 7.66 ppm (bs, 8H, H_{para}); ^{13}C NMR (150 MHz, $CDCl_3$): δ = 17.4, 19.6, 20.6, 21.2, 21.6, 29.8, 71.6, 121.6, 124.1, 124.3, 125.8, 125.8, 126.3, 126.9, 127.1, 127.1, 127.2, 127.3, 127.4, 127.5, 127.7, 127.8, 127.8, 128.0, 128.0, 128.3,

129.6, 128.6, 128.8, 128.9, 129.1, 129.5, 129.8, 129.9, 130.00, 130.3, 130.3, 137.3, 137.7, 138.3, 138.5, 141.4, 142.0, 143.6, 144.2, 147.4 ppm; UV/Vis (CH_2Cl_2): λ_{max} (log ε) = 439 (4.26), 548 nm (3.28); HRMS (MALDI) *m/z* calcd. for [$C_{116}H_{108}O_8N_4Pd$]: 1790.7202, found 1790.7202; LRMS (MALDI) *m/z*: 1792.7 (100%, M^+), 1699.7 (96%, M – $CH_2C_6H_5$), 1608 (43%, M – 2 × $CH_2C_6H_5$).

Synthesis of [5,10,15,20-tetrakis(4-cyanophenyl)-2,3,7,8,12,13,17,18-octaethylporphyrinato]palladium(II) (**1:55**).

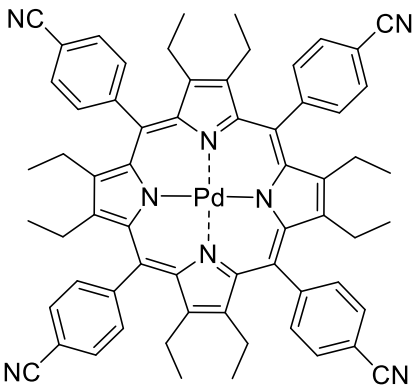

The free base porphyrin **1:11** (100 mg, 0.11 mmol) was reacted with palladium(II) acetate according to the general procedure D. Yield: 96 mg (0.09 mmol, 86%) of purple crystals. M.p. >300 °C; R_f = 0.65 (CH_2Cl_2/*n*-hexane, 1:1, v/v); ^{1}H NMR (400 MHz, $CDCl_3$): δ = 0.5 (t, 24H, J = 7.4 Hz, CH_2CH_3), 1.8 (bs, 8H, CH_2CH_3), 2.5 (bs, 8H, CH_2CH_3), 7.9 (d, 8H, J = 8.1 Hz, H_{ortho}), 8.1 ppm (d, 8H, J = 8.2 Hz, H_{meta}); ^{13}C NMR (150 MHz, $CDCl_3$): δ = 16.9, 19.7, 130.9, 134.8, 144.3, 145.7 ppm; UV/Vis (CH_2Cl_2): λ_{max} (log ε) = 439 (4.15), 577 nm (3.21); HRMS (MALDI) *m/z* calcd. for [$C_{64}H_{56}PdN_8$]: 1042.3663, found 1042.3342.

Click Reactions.

[2,3,7,8,12,13,17,18-octaethyl-5,10,15,20-tetrakis(4-ethynylphenyl)porphyrinato]nickel(II) (**1:77**)

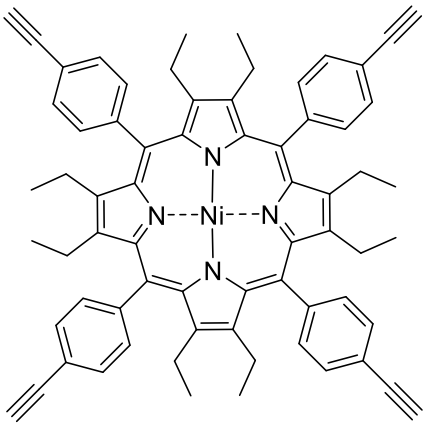

Porphyrin **1:58** (100 mg, 0.08 mmol, 1 eq.) was dissolved in 6 mL of THF in a 50 mL round-bottom flask. 2.2 mL of TBAF was added to the solution and left to stir for 1 h. The resultant mixture was evaporated to dryness and the residue taken up in CH_2Cl_2. The mixture filtered through a plug of silica, using CH_2Cl_2 as an eluent. The eluted porphyrin fraction was evaporated to dryness. Yield: 70 mg (0.07 mmol, 90%) of purple crystals. M.p. >300 °C; R_f = 0.76 (EtOAc/*n*-hexane, 1:1, v/v); ^{1}H NMR (400 MHz, $CDCl_3$): δ = 0.5 (bs, 24H, CH_2CH_3), 2.1 (bs, 8H, CH_2CH_3), 2.4 (bs, 8H, CH_2CH_3), 3.3 (s, 4H, C≡C*H*), 7.7 (d, 8H, J = 7.0 Hz, H_{ortho}), 8.1 ppm (d,

8H, *H*$_{meta}$); UV/Vis (CH_2Cl_2): λ_{max} (log ε) = 440 (5.34), 559 (4.19), 594 nm (4.07); HRMS (MALDI) *m/z* calcd. for [$C_{68}H_{60}N_8Ni$]: 990.4171, found 990.4184.

[2,3,7,8,12,13,17,18-octaethyl-5,10,15,20-tetrakis(4-(1-(4-cyanophenyl)-1H-1,2,3-triazol-4-yl)phenyl)porphyrinato] nickel(II)
(**1:78**)

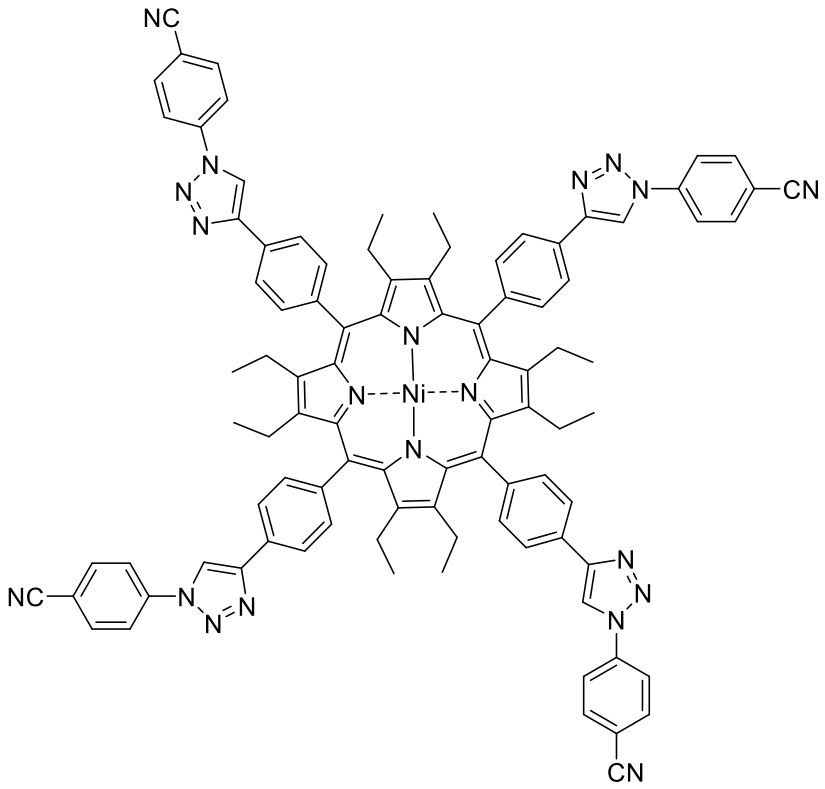

Porphyrin **1:77** (45 mg, 0.05 mmol, 1 eq.) was reacted with azide **1:66** (65 mg, 0.45 mmol, 10 eq.) following general procedure E. Yield: 67 mg (0.04 mmol, 95%) of purple crystals. M.p. >300 °C; R_f = 0.63 (*n*-hexane/EtOAc, 10:1, v/v); ^{1}H NMR (400 MHz, $CDCl_3$): δ = 0.6 (bs, 24H, CH_2CH_3), 2.4 (bs, 8H, CH_2CH_3), 2.6 (bs, 8H, CH_2CH_3), 7.9 (d, 8H, J = 8.0 Hz, Ar*H*), 8.0 (d, 8H, J = 8.0 Hz, Ar*H*), 8.2 (bs, 16H, Ar*H*), 8.5 ppm (s, 4H, triazole-C*H*); UV/Vis (CH_2Cl_2): λ_{max} (log ε) = 441 (5.37), 557 (4.22), 592 nm (4.04); HRMS (MALDI) *m/z* calcd. for [$C_{96}H_{76}N_{20}Ni$]: 1566.5915, found 1566.5830.

[2,3,7,8,12,13,17,18-octaethyl-5,10,15,20-tetrakis(4-(1-(4-nitrophenyl)-1H-1,2,3-triazol-4-yl)phenyl)porphyrinato] nickel(II)
(**1:79**)

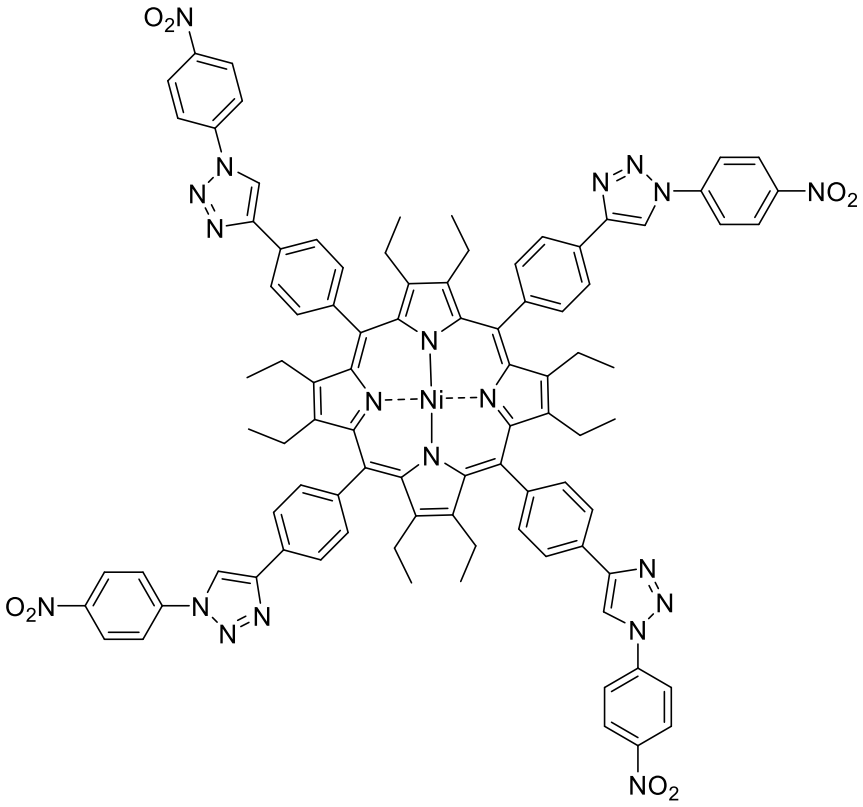

Porphyrin **1:77** (45 mg, 0.05 mmol, 1 eq.) was reacted with azide **1:68** (74 mg, 0.45 mmol, 10 eq.) following general procedure E. Yield: 70 mg (0.04 mmol, 93%) of purple crystals. M.p. >300 °C; R_f = 0.87 (*n*-hexane/EtOAc, 10:1, v/v); ^{1}H NMR (400 MHz, $CDCl_3$): δ = 0.6 (bs, 24H, CH_2CH_3), 2.7 (bs, 16H, CH_2CH_3), 8.1 (d, 8H, J = 8.3 Hz, Ar*H*), 8.2 (bs, 20H, Ar*H* + triazole-C*H*), 8.5 ppm (d, 8H, J = 9.1 Hz, Ar*H*); UV/Vis (CH_2Cl_2): λ_{max} (log ε) = 441 (5.21), 567 (4.08), 590 nm (3.89); HRMS (MALDI) *m/z* calcd. for [$C_{92}H_{76}N_{20}O_8Ni$]: 1646.5508, found 1646.5509.

[2,3,7,8,12,13,17,18-octaethyl-5,10,15,20-tetrakis(4-(1-(4-methoxy carbonylphenyl)-1H-1,2,3-triazol-4-yl)phenyl)porphyrinato] nickel(II) (**1:80**)

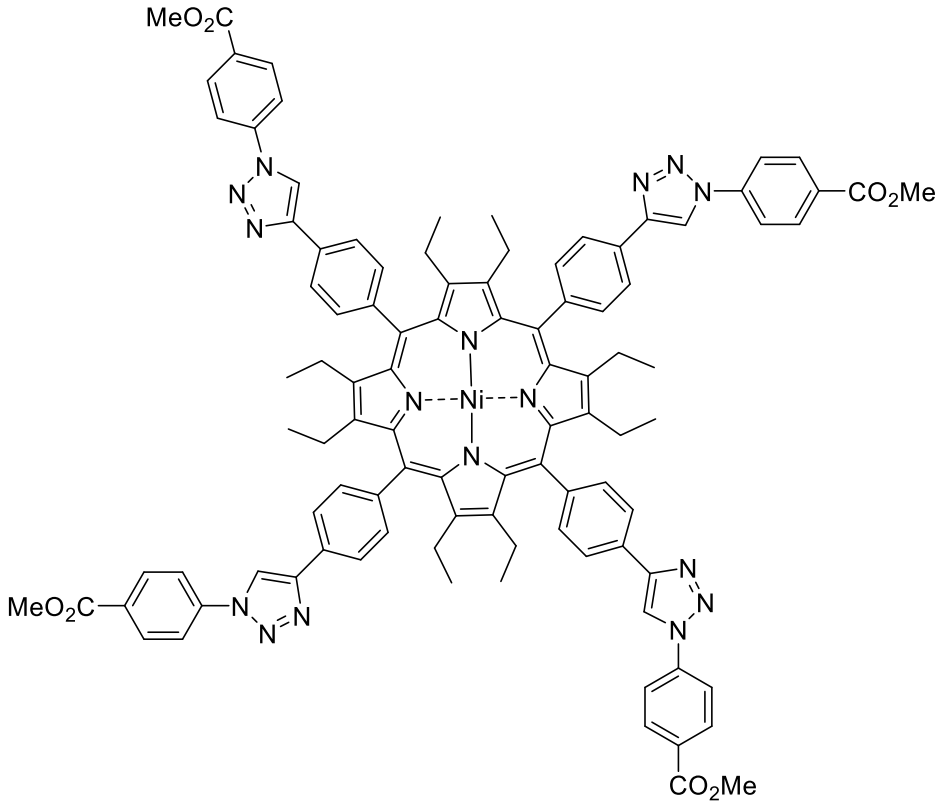

Porphyrin **1:77** (45 mg, 0.05 mmol, 1 eq.) was reacted with azide **1:70** (80 mg, 0.45 mmol, 10 eq.) following general procedure E. Yield: 71 mg (0.04 mmol, 93%) of purple crystals. M.p. >300 °C; R_f = 0.52 (*n*-hexane/EtOAc, 10:1, v/v); ^{1}H NMR (400 MHz, $CDCl_3$): δ = 0.6 (bs, 24H, CH_2CH_3), 1.8 (bs, 8H, CH_2CH_3), 2.4 (bs, 8H, CH_2CH_3), 3.9 (s, 12H, -O_2CH_3), 7.1 (d, 8H, J = 8.6 Hz, Ar*H*), 7.8 (d, 8H, J = 7.4 Hz, Ar*H*), 8.2 (bs, 16H, Ar*H*), 8.4 ppm (s, 4H, triazole-C*H*); UV/Vis (CH_2Cl_2): λ_{max} (log ε) = 442 (5.39), 556 (4.28), 591 nm (4.09); HRMS (MALDI) *m/z* calcd. for [$C_{100}H_{88}N_{16}O_8Ni$]: 1698.6325, found 1698.6387.

[2,3,7,8,12,13,17,18-octaethyl-5,10,15,20-tetrakis(4-(1-(4-methoxyphenyl)-1H-1,2,3-triazol-4-yl)phenyl)porphyrinato]nickel(II) (**1:81**)

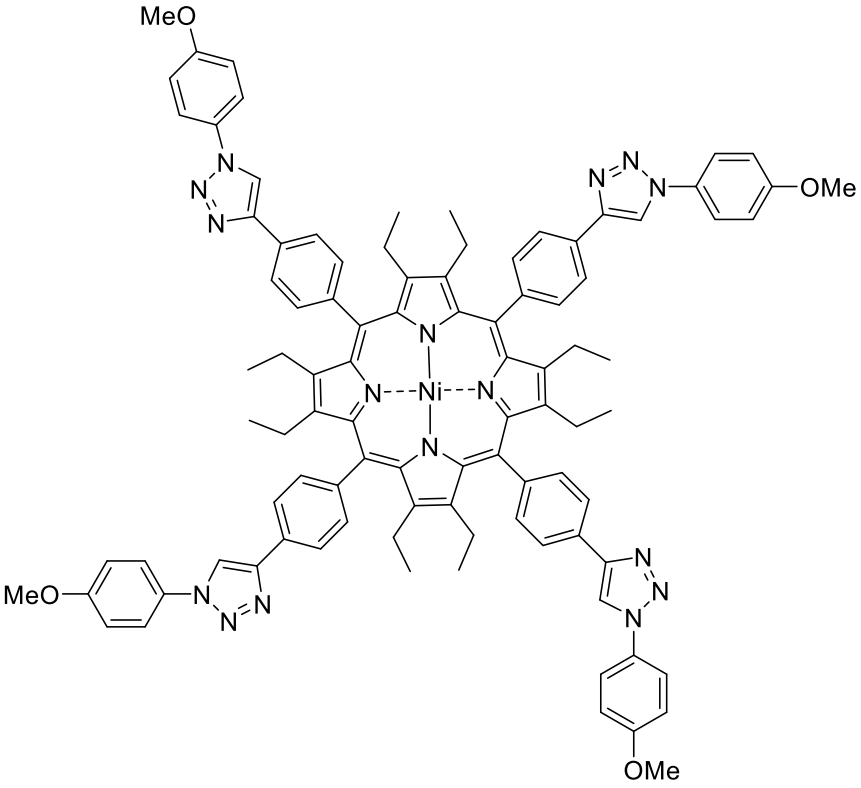

Porphyrin **1:77** (45 mg, 0.05 mmol, 1 eq.) was reacted with azide **1:72** (67 mg, 0.45 mmol, 10 eq.) following general procedure E. Yield: 68 mg (0.04 mmol, 95%) of purple crystals. M.p. >300 °C; R_f = 0.58 (*n*-hexane/EtOAc, 10:1, v/v); ^{1}H NMR (400 MHz, $CDCl_3$): δ = 0.6 (bs, 24H, CH_2CH_3), 2.1 (bs, 8H, CH_2CH_3), 2.5 (bs, 8H, CH_2CH_3), 3.9 (s, 12H, $-O_2CH_3$), 7.1 (d, 8H, J = 8.9 Hz, Ar*H*), 7.8 (d, 8H, J = 8.9 Hz, Ar*H*), 8.2 (bs, 16H, Ar*H*), 8.3 ppm (s, 4H, triazole-C*H*); UV/Vis (CH_2Cl_2): λ_{max} (log ε) = 441 (5.31), 556 (4.16), 593 nm (3.99); HRMS (MALDI) *m/z* calcd. for [$C_{96}H_{88}N_{16}O_4Ni$]: 1586.6528, found 1586.6556.

[2,3,7,8,12,13,17,18-octaethyl-5,10,15,20-tetrakis(4-(1-(4-formylphenyl)-1H-1,2,3-triazol-4-yl)phenyl)porphyrinato]nickel(II) (**1:82**)

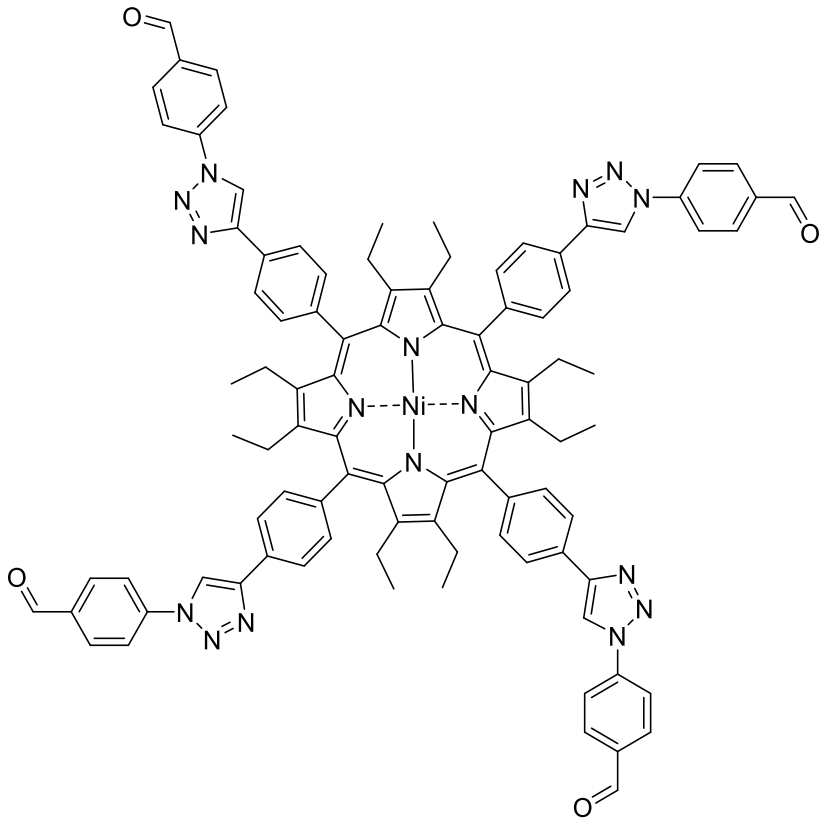

Porphyrin **1:77** (45 mg, 0.05 mmol, 1 eq.) was reacted with azide **1:74** (67 mg, 0.45 mmol, 10 eq.) following general procedure E. Yield: 66 mg (0.04 mmol, 90%) of purple crystals. M.p. >300 °C; R_f = 0.20 (*n*-hexane/EtOAc, 10:1, v/v); ^{1}H NMR (400 MHz, $CDCl_3$): δ = 0.6 (bs, 24H, CH_2CH_3), 2.4 (bs, 8H, CH_2CH_3), 2.6 (bs, 8H, CH_2CH_3), 8.1 (m, 16H, Ar*H*), 8.2 (m, 16H, Ar*H*), 8.5 (s, 4H, triazole-C*H*), 10.1 ppm (s, 4H, C*H*O); UV/Vis (CH_2Cl_2): λ_{max} (log ε) = 441 (5.24), 557 (4.09), 591 nm (3.91); HRMS (MALDI) *m/z* calcd. for [$C_{96}H_{80}N_{16}O_4Ni$]: 1578.5902, found 1578.5980.

[5,10,15,20-tetrakis(4-(4-(2-(1,3-dioxan-2-yl)ethyl)-1H-1,2,3-triazol-1-yl)phenyl)-2,3,7,8,12,13,17,18-octaethylporphyrinato]nickel(II) (**1:83**)

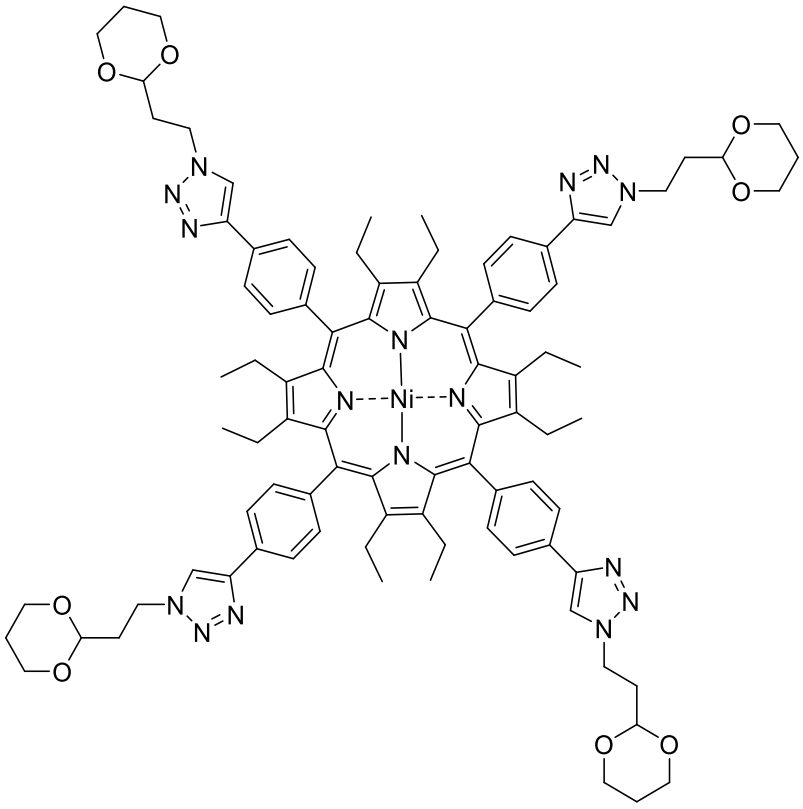

Porphyrin **1:77** (45 mg, 0.05 mmol, 1 eq.) was reacted with azide **1:76** (71 mg, 0.45 mmol, 10 eq.) following general procedure E. Yield: 66 mg (0.04 mmol, 90%) of purple crystals. M.p. >300 °C; R_f = 0.25 (CH_2Cl_2/EtOAc, 1:1, v/v); ^{1}H NMR (400 MHz, $CDCl_3$): δ = 0.5 (bs, 24H, CH_2CH_3), 1.4 (bs, 4H, $OCH_2CH_{2[Eq]}$), 2.1 (m, 8H, $OCH_2CH_{2[Ax]}$), 2.3 (dd, 8H, J = 6.7, 11.7 Hz, NCH_2CH_2), 2.1–2.4 (bs, 16H, CH_2CH_3), 3.8 (t, 8H, J = 11.2 Hz, $OCH_{2[Eq]}$), 4.2 (dd, 8H, J = 4.6, 11.3 Hz, $OCH_{2[Eq]}$), 4.6 (t, 8H, J = 7.0 Hz, NCH_2), 4.7 (t, 4H, J = 4.6 Hz, OC*H*), 8.0 (s, 4H, triazole-C*H*), 8.1 ppm (bs, 16H, Ar*H*); UV/Vis (CH_2Cl_2): λ_{max} (log ε) = 442 (5.41), 459 (4.27), 593 nm (4.10); HRMS (MALDI) *m/z* calcd. for [$C_{92}H_{104}N_{16}O_8Ni$]: 1618.7577, found 1618.7488.

2,3,7,8,12,13,17,18-octaethyl-5,10,15,20-tetrakis(4-(4-(4-methoxy carbonylphenyl)-1H-1,2,3-triazol-1-yl)phenyl)porphyrin (**1:84**)

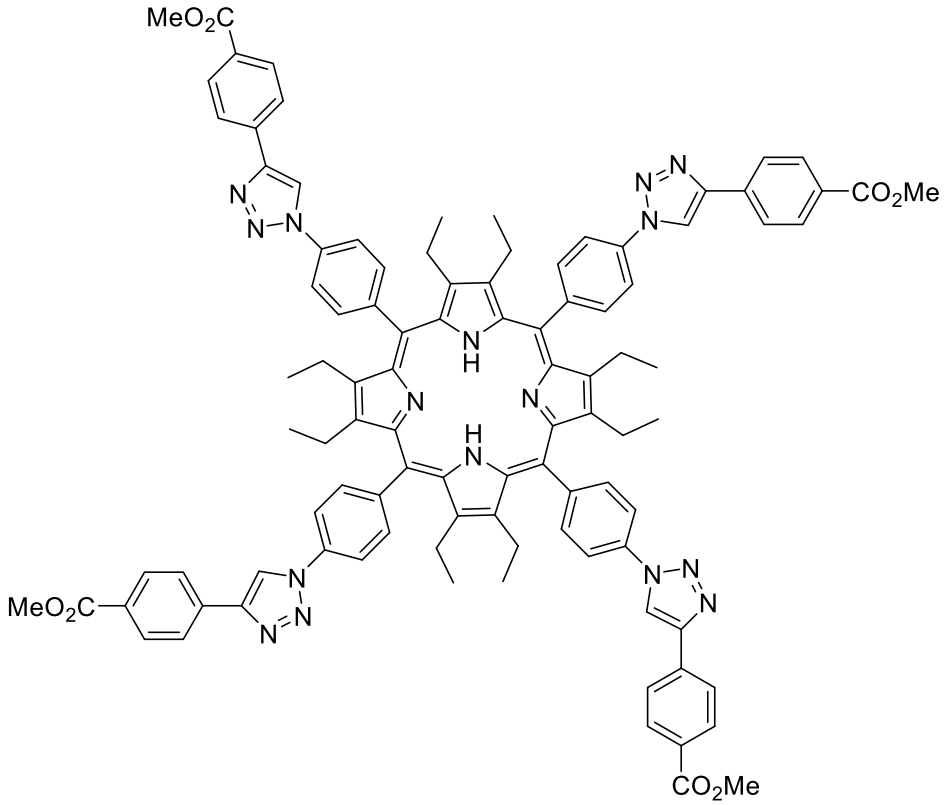

Porphyrin **1:12** (45 mg, 0.05 mmol, 1 eq.), methyl 4-ethynylbenzoate (71 mg, 0.45 mmol, 10 eq.), sodium ascorbate (0.4 eq.) and Cu(II)$(OAc)_2$ (0.4 eq.) were dissolved in 2 mL of THF in a 5 mL microwave vial. The vial was sealed and reacted for 20 minutes at 120°C in a microwave reactor. The resultant mixture was diluted with CH_2Cl_2 and 0.01 mL of H_2SO_4 was added. The solution was then washed with sodium bicarbonate solution, brine, and water, and then dried over $MgSO_4$. The solution was then evaporated to dryness, dissolved in *n*-hexane and purified by silica gel column chromatography using *n*-hexane:EtOAc (1:1) and dried *in vacuo*. Yield: 39 mg (0.02 mmol, 53%) of green flakes. M.p. >300 °C; R_f = 0.34 (CH_2Cl_2/EtOAc, 1:1, v/v); ^{1}H NMR (400 MHz, $CDCl_3$): δ = 0.4 (bs, 24H, CH_2CH_3), 2.2 (bs, 8H, CH_2CH_3), 2.4 (bs, 8H, CH_2CH_3), 4.0 (s, 12H, -O_2CH_3), 8.1 (d, 8H, J = 8.2 Hz, Ar*H*), 8.2 (d, 8H, J = 8.2 Hz, Ar*H*), 8.4 (d, 8H, J = 8.5 Hz, Ar*H*), 8.7 (s, 4H, triazole-C*H*), 8.8 ppm (d, 8H, J = 8.3 Hz, Ar*H*); UV/Vis (CH_2Cl_2): λ_{max} (log ε) = 488 (5.21), 700 nm (4.34); HRMS (MALDI) *m/z* calcd. for [$C_{100}H_{90}N_{16}O_8$]: 1643.7206, found 1643.7231.

Crystallisation Methods.

During this project there were two types of crystallisation techniques were used to obtain single crystals suitable for XRD. These were liquid diffusion and slow evaporation. For the liquid diffusion the most common vessel this was set up in are the crystallisation tubes seen in Figure 1:75A. These tubes have a bulb which is usually filled with a 5mL concentrated solution of the sample and layered with a second solvent which is over lower density, miscible with the first solvent, and the compound you are trying to crystallise is not highly soluble in. Typically, multiple attempts of the same sample – varying the solvents used – are set up simultaneously, sealed with parafilm, and left in the dark in an isolated are for several weeks. Over this time the lower solvent layer will slowly diffuse into the upper solvent layer and crystals should for where these two solvents meet. In practical terms this is more an art of trial and error with majority of samples failing. However, with time and repeated attempts the chances of getting a desired crystal go up. This is a low maintenance method of crystallising compounds. For compounds which only ever form very small crystals or crystallites, it was found that heating the solution up to just below its boiling point and then adding in an enough of the compound under investigation to get a super concentrated solution, adding this solution to the tube, allowing this to cool down and then layering with a second solvent, sometimes gave larger crystals. This is completely more art than science at this stage with greater number of attempts allowing for better results.

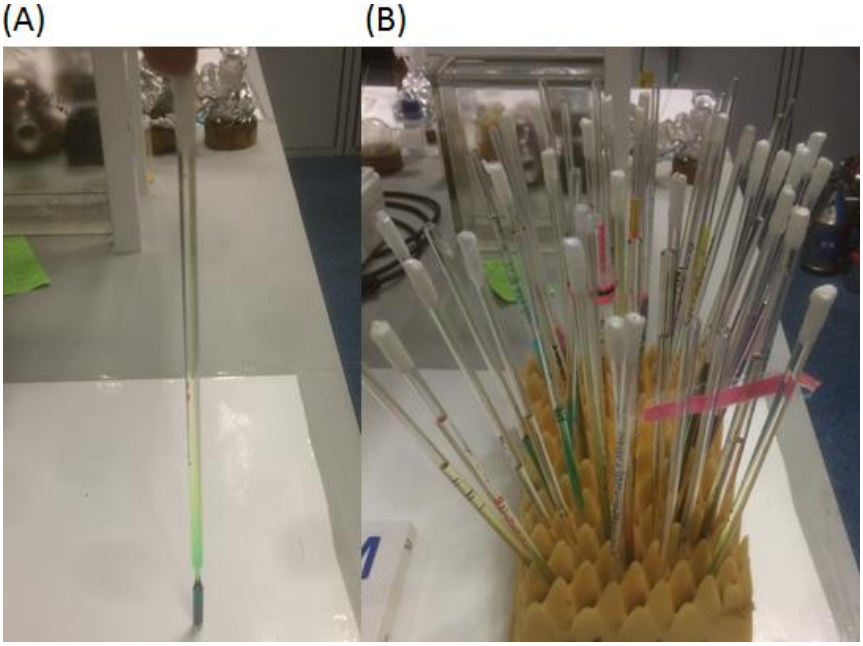

Figure 1:75: Photo of a typical solvent diffusion set up used throughout this thesis.

The second method used during this project was slow evaporation. Usually if the above method did not work (no crystals formed after several weeks) the seal was removed, and the tubes were allowed to evaporate to dryness. This sometimes can provide crystals suitable for XRD. A second less common method was finding crystals in your NMR tube after leaving them for a few days. Several of the structures (those containing $CDCl_3$ in the unit cell) were obtained this way by pure chance. These methods were used for all crystals obtained in this thesis unless otherwise stated.

Crystallographic Data.

Crystals were grown following the protocol developed by Hope by dissolving the compounds in either DCM, a DCM/MeOH mixture, or $CDCl_3$ and layering with a second solvent (MeOH or hexane) for liquid diffusion or allowing for slow evaporate over time.[137] Single crystal X-ray diffraction data for all compounds were collected on a Bruker APEX 2 DUO CCD diffractometer by using graphite-monochromated MoK_α (λ = 0.71073 Å) radiation and Incoatec IμS CuK_α (λ = 1.54178 Å) radiation. Crystals were mounted on a MiTeGen MicroMount and collected at 100(2) K by using an Oxford Cryosystems Cobra low-temperature device. Data were collected by using omega and phi scans and were corrected for Lorentz and polarization effects by using the APEX software suite.[138] Using Olex2, the structure was solved with the XT structure solution program, using the intrinsic phasing solution method and refined against $|F^2|$ with XL using least squares minimization.[139] Hydrogen atoms were generally placed in geometrically calculated positions and refined using a riding model. Details of data refinements can be found in Table E1:1–E1:5. All images were prepared by using Olex2.[139a]

Normal-coordinate Structural Decomposition (NSD) Analysis. The theoretical background and development of this method have been described by Shelnutt and co-workers.[72b, 131] NSD is a conceptually simple method that employs the decomposition of the conformation of the macrocycle by a basis set composed of its various normal modes of vibration, affording clear separation of the contributing distortions to the macrocycle conformation in a quantitative fashion. For calculations, we used the NSD engine program as provided by Shelnutt.[140]

Crystal Data for compound 1:6A: The two internal hydrogen atoms were modelled over two positions in a 50:50% occupancy. The 2,6-dichlorophenyl substitute at C5 was modelled over two positions in a 75:25% occupancy using restraints (SADI) and constraints (EADP). The structure is refined as an inversion twin. The C and N bound H atoms were placed in their expected calculated positions and refined as riding model: N–H = 0.88 Å, C–H = 0.95–0.98 Å, with U_{iso}(H) = 1.5U_{eq}(C) for methyl H atoms and 1.2U_{eq} (C, N) for all other atoms other H atoms.

Crystal Data for compound 1:37: The C and N bound H atoms were placed in their expected calculated positions and refined as riding model: N–H = 0.88 Å, C–H = 0.95–0.98 Å, with U_{iso}(H) = 1.5U_{eq}(C) for methyl H atoms and 1.2U_{eq} (C, N) for all other atoms other H atoms.

Crystal Data for compound 1:38: The C and N bound H atoms were placed in their expected calculated positions and refined as riding model: N–H = 0.88 Å, C–H = 0.95–0.98 Å, with U_{iso}(H) = 1.5U_{eq}(C) for methyl H atoms and 1.2U_{eq} (C, N) for all other atoms other H atoms.

Crystal Data for compound 1:40: The 4-chlorophenyl group at C5_1 was modelled over two positions in a 64:36% occupancy using restraints (ISOR) and constraints (EAPD). Residual density and two C-alerts in the check cif indicate that there are possibly one or more positions that could be modelled for this group. However, due to no reliable solution being found this modelling was omitted. The C and N bound H atoms were placed in their expected calculated positions and refined as riding model: N–H = 0.88 Å, C–H = 0.95–0.98 Å, with U_{iso}(H) = 1.5U_{eq}(C) for methyl H atoms and 1.2U_{eq} (C, N) for all other atoms other H atoms.

Crystal Data for compound 1:43A: The C and N bound H atoms were placed in their expected calculated positions and refined as riding model: N–H = 0.88 Å, C–H = 0.95–0.98 Å, with U_{iso}(H) = 1.5U_{eq}(C) for methyl H atoms and 1.2U_{eq} (C, N) for all other atoms other H atoms.

Crystal Data for compound 1:45: The C and N bound H atoms were placed in their expected calculated positions and refined as riding model: N–H = 0.88 Å, C–H = 0.95–0.98 Å, with U_{iso}(H) = 1.5U_{eq}(C) for methyl H atoms and 1.2U_{eq} (C, N) for all other atoms other H atoms.

Crystal Data for compound 1:49: The ethyl group at C13_2 (C131, C132, C131_2, C132_2) was modelled over two positions in a 57 and 43% occupancy. The C and N bound H atoms were placed in their expected calculated positions and refined as riding model: N–H = 0.88 Å, C–H = 0.95–0.98 Å, with U_{iso}(H) = 1.5U_{eq}(C) for methyl H atoms and 1.2U_{eq} (C, N) for all other atoms other H atoms.

Crystal Data for compound 1:51A: The structure was solved as a two-component twin. The C and N bound H atoms were placed in their expected calculated positions and refined as riding model: N–H = 0.88 Å, C–H = 0.95–0.98 Å, with U_{iso}(H) = 1.5U_{eq}(C) for methyl H atoms and 1.2U_{eq} (C, N) for all other atoms other H atoms.

Crystal Data for compound 1:52: The ethyl group at C7 (C71a, C72a, C71b, C72b) was modelled over two positions in a 67 and 33% occupancy using constraint (EADP). The C and N bound H atoms were placed in their expected calculated positions and refined as riding model: N–H = 0.88 Å, C–H = 0.95–0.98 Å, with U_{iso}(H) = 1.5U_{eq}(C) for methyl H atoms and 1.2U_{eq} (C, N) for all other atoms other H atoms.

Crystal Data for compound 1:53: The ethyl group at C3 was modelled over two positions in a 75:25% occupancy using restraints (SADI) and constraints (EADP). The C and N bound H atoms were placed in their expected calculated positions and refined as riding model: N–H = 0.88 Å, C–H = 0.95–0.98 Å, with U_{iso}(H) = 1.5U_{eq}(C) for methyl H atoms and 1.2U_{eq} (C, N) for all other atoms other H atoms.

Crystal Data for compound 1:54: The structure contains a large solvent-accessible void in which a reasonably strong residual density is located. However, no reasonable solution could be modelled for likely solvents and the structure was squeezed.[141] The C and N bound H atoms were placed in their expected calculated positions and refined as riding model: N–H = 0.88 Å, C–H = 0.95–0.98 Å, with U_{iso}(H) = 1.5U_{eq}(C) for methyl H atoms and 1.2U_{eq} (C, N) for all other atoms other H atoms.

Crystal Data for compound 1:53A: The structure was refined as a two-component twin. The C and N bound H atoms were placed in their expected calculated positions and refined as riding model: N–H = 0.88 Å, C–H = 0.95–0.98 Å, with U_{iso}(H) = 1.5U_{eq}(C) for methyl H atoms and 1.2U_{eq} (C, N) for all other atoms other H atoms.

Crystal Data for compound 1:57: The C and N bound H atoms were placed in their expected calculated positions and refined as riding model: N–H = 0.88 Å, C–H

= 0.95–0.98 Å, with U_{iso}(H) = 1.5U_{eq}(C) for methyl H atoms and 1.2U_{eq} (C, N) for all other atoms other H atoms.

Crystal Data for compound 1:59: The structure was extensively modelled with regards to the benzyloxy side chains. The benzyloxyphenyl chain at C20_1 was modelled over two positions in a 75:25% occupancy using restraints (SADI, SIMU, ISOR, DFIX). The benzyloxy chain at O57_1 was modelled over two positions in a 65:35% occupancy using restraints (SADI, SIMU, DFIX). The ethyl group at C12_1 was modelled over two positions in a 75:25% occupancy. The benzyloxyphenyl chain at C5_2 was modelled over two positions in a 63:37% occupancy using restraints (SADI, SIMU, ISOR). The benzyloxy chain at C204_2 was modelled over two positions in an 80:20% occupancy using restraints (SIMU, ISOR). The beta-carbons and ethyl chains associated with N23_2 were modelled over two positions in a 75:25% occupancy using restraints (SIMU, DFIX). The C and N bound H atoms were placed in their expected calculated positions and refined as riding model: N–H = 0.88 Å, C–H = 0.95–0.98 Å, with U_{iso}(H) = 1.5U_{eq}(C) for methyl H atoms and 1.2U_{eq} (C, N) for all other atoms other H atoms.

Crystal Data for compound 1:86: The structure was solved with two independent molecules in the asymmetric unit. However, in the sum formula, it should be noted that this formula only represents one molecule. This is due to Z' = 0.5 and a large degree of overlap between the two structures. Solvent molecules (H_2O) in the structure was squeezed using platon squeeze as no reliable solution could be modelled.[141] The C and N bound H atoms were placed in their expected calculated positions and refined as riding model: N–H = 0.88 Å, C–H = 0.95–0.98 Å, with U_{iso}(H) = 1.5U_{eq}(C) for methyl H atoms and 1.2U_{eq} (C, N) for all other atoms other H atoms. Large K value in the analysis of variance is associated with the very weak reflections in the high angle data. Low bond precision on C–C bonds are associated with the very weak reflections in the high angle data. Missing reflection is associated with only 97.3% of collected data.

Crystal Data for compound 1:87: The structure was solved with two independent porphyrin molecules and three fully occupied water molecules in the asymmetric unit. Additional water molecules (around 8.5) were squeezed from the structure as no reliable structure could be obtained.[141] This resulted in one alert due to a D–H without an acceptor. The hydrogen atoms attached to the oxygen of the water

molecules were placed in their expected calculated positions and refined as riding model: O–H = 0.98 Å, with U_{iso}(H) = 1.5U_{eq}(O) for water H atoms. The O–H distances were restrained using the DFIX restraint and the H–H distances in the water molecules were fixed using the DFIX restraint. The phenyl ring (C156_1, C155_1, C154_1, C153_1, and C152_1) were fixed using the restraint (SIMU). The C and N bound H atoms were placed in their expected calculated positions and refined as riding model: N–H = 0.88 Å, C–H = 0.95–0.98 Å, with U_{iso}(H) = 1.5U_{eq}(C) for methyl H atoms and 1.2U_{eq} (C, N) for all other atoms other H atoms. Low bond precision on C–C bonds are associated with the very weak reflections in the high angle data.

Crystal Data for compound 1:90: The pyrrole units at N21 and N23 were modelled over two positions (80:20% occupancy) using restraints (SADI, DFIX, and SIMU). The methoxy group O1–C57 was modelled over two positions (80:20% occupancy) using restraints (SADI and SIMU). Solvent molecules (H_2O, $CDCl_3$) in the structure were squeezed using platon squeeze as no reliable solution could be modelled.[141] The C and N bound H atoms were placed in their expected calculated positions and refined as riding model: N–H = 0.88 Å, C–H = 0.95–0.98 Å, with U_{iso}(H) = 1.5U_{eq}(C) for methyl H atoms and 1.2U_{eq} (C, N) for all other atoms other H atoms. Large K value in the analysis of variance is associated with the very weak reflections in the high angle data.

Crystal Data for compound 1:[91]$^+$[CF_3SO_3]$^-$: The structure was solved containing one unit in the asymmetric cell one trifluoromethanesulfonate solvate. The structure was modelled over two positions at C26 (C26A) in an 80:20% occupancy. No restraints or constraints were necessary. The trifluoromethanesulfonate solvate was modelled over two positions (80:20% occupancy) using restraints (SIMU and SADI). The C and N bound H atoms were placed in their expected calculated positions and refined as riding model: N–H = 0.88 Å, C–H = 0.95–0.98 Å, with U_{iso}(H) = 1.5U_{eq}(C) for methyl H atoms and 1.2U_{eq} (C, N) for all other atoms other H atoms. Large K value in the analysis of variance is associated with the very weak reflections in the high angle data.

Crystal Data for compound 1:[99]$^+$[CF_3SO_3]$^-$: The structure was solved containing one unit in the asymmetric cell one trifluoromethanesulfonate solvate. The trifluoromethanesulfonate solvate was modelled over two positions (75:25%

occupancy) using restraints (SIMU and ISOR). Solvent molecules (CH_2Cl_2) in the structure was squeezed using platon squeeze as no reliable solution could be modelled.[141] The C and N bound H atoms were placed in their expected calculated positions and refined as riding model: N–H = 0.88 Å, C–H = 0.95–0.98 Å, with U_{iso}(H) = 1.5U_{eq}(C) for methyl H atoms and 1.2U_{eq} (C, N) for all other atoms other H atoms. Large K value in the analysis of variance is associated with the very weak reflections in the high angle data. Missing reflection is associated with only 99.9% of the collected data.

Table E1:1: Details of XRD data refinement.

Compound	**1:6A**	**1:37**	**1:38**	**1:40**
Empirical formula	$C_{61}H_{54}Cl_{11}DN_4$	$C_{60}H_{56}F_4N_4Ni$	$C_{60}H_{56}F_4N_4Pd$	$C_{60}H_{56}Cl_4N_4Ni$
Formula weight	1235.04	967.79	1015.48	1033.59
Temperature/K	99.99	100.0	100.02	100.0
Crystal system	Orthorhombic	Triclinic	Triclinic	Monoclinic
Space group	$P2_12_12_1$	$P\bar{1}$	$P\bar{1}$	$P2_1/n$
a/Å	14.0489(4)	13.0162(9)	13.017(7)	27.5338(12)
b/Å	14.0504(4)	13.8530(9)	13.881(8)	12.7176(6)
c/Å	31.7547(9)	14.8981(10)	14.956(8)	30.0947(12)
α/°	90	64.7800(10)	64.87(2)	90
β/°	90	85.1460(10)	84.99(2)	96.2200(10)
γ/°	90	78.2160(10)	78.48(3)	90
Volume/Å^3	6268.1(3)	2379.0(3)	2397(2)	10476.0(8)
Z	4	2	2	8
D_{calc} g/cm^3	1.181	1.351	1.407	1.311
μ/mm^{-1}	3.576	0.469	0.448	0.617
F(000)	2312.0	1016.0	1052.0	4320.0
Crystal size/mm^3	0.29×0.25×0.24	0.38×0.08×0.07	0.27×0.09×0.03	0.40×0.30×0.07
Radiation	CuK_α	MoK_α	MoK_α	MoK_α
Wavelength/Å	λ = 1.54178	λ = 0.71073	λ = 0.71073	λ = 0.71073
2θ/°	5.566–135.958	3.022–53.66	5.308–56.752	3.48–50.752
Reflections collected	61675	80173	36156	232027
Independent reflections	11124	10143	11922	19221
R_{int}	0.0411	0.0341	0.0452	0.0493
R_{sigma}	0.0370	0.0213	0.0540	0.0233
Restraints	4	0	0	84
Parameters	622	622	630	1251
GooF	1.094	1.026	1.035	1.128
R_1 [I> 2σ (I)]	0.0596	0.0297	0.0359	0.0437
wR_2 [I> 2σ (I)]	0.1586	0.0688	0.0676	0.0888
R_1 [all data]	0.0599	0.0402	0.0510	0.0558
wR_2 [all data]	0.1588	0.0738	0.0726	0.0931
Largest peak/e Å^{-3}	0.92	0.34	0.56	0.74
Deepest hole/e Å^{-3}	-0.80	-0.32	-0.83	-0.54
Flack parameter	0.149(19)	--	--	--

Table E1:2: Details of XRD data refinement.

Compound	**1:43A**	**1:45**	**1:49**	**1:51A**
Empirical formula	$C_{62}H_{60}Br_4Cl_4N_4Ni$	$C_{60}H_{56}Br_4CuN_4$	$C_{120}H_{104}F_{16}N_8Ni_2$	$C_{62}H_{52}Cl_{14}D_2N_4Ni$
Formula weight	1381.29	1216.26	2079.53	1412.11
Temperature/K	100.0	100.01	99.98	100.01
Crystal system	Triclinic	Monoclinic	Monoclinic	Orthorhombic
Space group	$P\bar{1}$	$P2_1/n$	C2/c	$P2_12_12_1$
a/Å	12.4193(5)	19.8627(12)	38.624(2)	13.9245(8)
b/Å	15.2923(6)	12.6204(8)	14.0574(7)	13.924
c/Å	17.0496(7)	21.0706(13)	39.598(2)	32.0685(19)
α/°	100.525(2)	90	90	90
β/°	98.460(2)	97.508(2)	94.202(2)	90
γ/°	109.3600(10)	90	90	90
Volume/Å³	2927.3(2)	5236.6(6)	21442(2)	6217.8(5)
Z	2	4	8	4
D_{calc} *g/cm³*	1.567	1.543	1.288	1.508
μ/mm⁻¹	3.287	3.512	0.432	0.958
F(000)	1392.0	2452.0	8640.0	2880.0
Crystal size/mm³	0.20×0.20×0.05	0.21×0.18×0.05	0.80×0.30×0.13	0.60×0.40×0.20
Radiation	MoK_α	MoK_α	MoK_α	MoK_α
Wavelength/Å	λ = 0.71073	λ = 0.71073	λ = 0.71073	λ = 0.71073
2θ/°	3.332–52.748	2.65–50.852	3.06–52.212	1.27–52.998
Reflections collected	84477	50886	304281	51167
Independent reflections	11971	9645	21253	12467
R_{int}	0.0420	0.1153	0.0852	0.0259
R_{sigma}	0.0274	0.1032	0.0386	0.0471
Restraints	117	0	0	0
Parameters	783	630	1351	739
GooF	1.018	0.984	1.026	1.020
R_1 *[I> 2σ (I)]*	0.0343	0.0470	0.0438	0.240
wR_2 *[I> 2σ (I)]*	0.0745	0.0741	0.0907	0.0610
R_1 *[all data]*	0.0477	0.1202	0.0677	0.0249
wR_2 *[all data]*	0.0794	0.0861	0.0964	0.0614
Largest peak/e Å⁻³	1.38	0.47	0.55	0.36
Deepest hole/e Å⁻³	-1.11	-0.57	-0.52	-0.22
Flack parameter	--	--	--	-0.176(5)

Table E1:3: Details of XRD data refinement.

Compound	**1:52**	**1:53A**	**1:53**	**1:54**
Empirical formula	$C_{60}H_{52}Cl_8N_4Pd$	$C_{62}H_{50}Cl_{14}CuD_2N_4$	$C_{60}H_{52}Cl_8CuN_4$	$C_{64}H_{56}N_8Ni$
Formula weight	1219.05	1414.93	1176.19	995.87
Temperature/K	100.01	99.99	99.99	100.01
Crystal system	Orthorhombic	Orthorhombic	Orthorhombic	Orthorhombic
Space group	Pcca	$P2_12_12_1$	Pcca	Pnma
a/Å	14.8707(10)	13.9521(9)	14.8686(9)	16.2405(6)
b/Å	25.6212(17)	13.9842(9)	25.5584(16)	25.1800(10)
c/Å	14.3556(10)	31.929(2)	14.3378(9)	14.4853(6)
α/°	90	90	90	90
β/°	90	90	90	90
γ/°	90	90	90	90
Volume/Å^3	5469.6(6)	6229.7(7)	5448.6(6)	5923.6(4)
Z	4	4	4	4
D_{calc} g/cm^3	1.480	1.509	1.434	1.117
μ/mm^{-1}	0.774	0.995	0.837	0.371
F(000)	2488.0	2876.0	2420.0	2096.0
Crystal size/mm^3	0.50×0.38×0.07	0.37×0.15×0.12	0.22×0.17×0.05	0.40×0.15×0.12
Radiation	MoK_α	MoK_α	MoK_α	MoK_α
Wavelength/Å	λ = 0.71073	λ = 0.71073	λ = 0.71073	λ = 0.71073
2θ/°	4.252–51.998	3.18–56.996	3.186–54.21	3.234–53.838
Reflections collected	33760	15775	36482	186498
Independent reflections	5384	15775	6006	6525
R_{int}	0.0411	Merged	0.0565	0.0321
R_{sigma}	0.0265	0.0158	0.0389	0.0096
Restraints	18	0	13	0
Parameters	339	739	339	338
GooF	1.091	1.033	1.047	1.075
R_1 [I> 2σ (I)]	0.0376	0.0188	0.0365	0.0357
wR_2 [I> 2σ (I)]	0.0776	0.0451	0.0724	0.0883
R_1 [all data]	0.0474	0.0199	0.0583	0.0427
wR_2 [all data]	0.0803	0.0456	0.0800	0.0945
Largest peak/e Å^{-3}	1.22	0.36	0.56	0.34
Deepest hole/e Å^{-3}	-0.52	-0.32	-0.45	-0.29
Flack parameter	--	-0.0355(14)	--	--

Table E1:4: Details of XRD data refinement.

Compound	**1:57**	**1:59**	**1:86**	**1:87**
Empirical formula	$C_{75}N_4Ni$	$C_{176}H_{168}N_8Ni_2O_8$	$C_{45}H_{32}N_4$	$C_{92}H_{74}N_8O_3$
Formula weight	1015.50	2640.59	628.74	1339.59
Temperature/K	100.0	99.98	100(2)	100(2)
Crystal system	Monoclinic	Monoclinic	triclinic	monoclinic
Space group	$P2_1/n$	$P2_1/n$	$P\bar{1}$	Pn
a/Å	20.0407(16)	20.0808(9)	13.7893(7)	14.7319(11)
b/Å	21.6454(18)	23.3563(10)	14.9069(8)	12.3812(9)
c/Å	28.815(3)	29.9530(13)	19.3164(10)	24.5671(18)
α/°	90	90	108.234(2)	90
β/°	92.928(6)	94.604(2)	96.992(3)	107.071(2)
γ/°	90	90	101.614(3)	90
Volume/Å³	12483.4(18)	14003.0(11)	3620.5(3)	4283.6(5)
Z	8	4	4	2
D_{calc} *g/cm³*	1.187	1.253	1.154	1.039
μ/mm⁻¹	0.791	0.334	0.526	0.063
F(000)	4796.0	5600.0	1320.0	1412.0
Crystal size/mm³	0.50×0.07×0.05	0.50×0.30×0.20	0.32×0.19×0.08	0.50×0.20×0.10
Radiation	CuK_α	MoK_α	CuK_α	MoK_α
Wavelength/Å	λ = 1.54178	λ = 0.71073	λ = 1.54178	λ = 0.71073
2θ/°	5.108–109.724	2.214–52.966	7.464–136.972	3.290–50.760
Reflections collected	100657	420323	36917	87884
Independent reflections	15282	28792	12845	15659
R_{int}	0.2766	0.0557	0.0676	0.0413
R_{sigma}	0.1542	0.0282	0.0760	0.0328
Restraints	0	71	0	34
Parameters	1504	1676	886	945
GooF	1.865	1.082	1.094	1.062
R_1 *[I> 2σ (I)]*	0.2132	0.0901	0.0779	0.0632
wR_2 *[I> 2σ (I)]*	0.5196	0.2133	0.2189	0.1637
R_1 *[all data]*	0.2585	0.1290	0.1038	0.0751
wR_2 *[all data]*	0.5397	0.2487	0.2436	0.1722
Largest peak/e Å⁻³	1.13	1.29	0.48	0.55
Deepest hole/e Å⁻³	-0.79	-0.96	-0.41	-0.27
Flack parameter	--	--		

Table E1:5 (Continued): Details of XRD data refinement.

Compound	**1:90**	**1:[91]$^+$**	**1:[99]$^+$**
Empirical formula	$C_{49}H_{40}N_4O_4$	$C_{52}H_{46}F_3N_4O_7S$	$C_{41}H_{39}F_3N_4O_9S$
Formula weight	748.85	927.99	820.82
Temperature/K	100(2)	100(2)	100(2)
Crystal system	monoclinic	monoclinic	Monoclinic
Space group	$P2_1/c$	$P2_1/c$	P21/c
a/Å	13.818(7)	16.1055(6)	7.6298(3)
b/Å	15.957(9)	8.0297(3)	29.1766(9)
c/Å	20.117(11)	34.4166(14)	19.2119(6)
α/°	90	90	90
β/°	92.552(14)	102.3050(10)	95.085(2)
γ/°	90	90	90
Volume/Å^3	4431(4)	4348.6(3)	4260.0(3)
Z	4	4	4
D_{calc} g/cm^3	1.122	1.417	1.280
μ/mm^{-1}	0.072	0.149	1.277
F(000)	1576.0	1940.0	1712.0
Crystal size/mm^3	0.45×0.33×0.19	0.37×0.15×0.08	0.30×0.14×0.02
Radiation	MoK_α	MoK_α	CuK_α
Wavelength/Å	λ = 0.71073	λ = 0.71073	λ = 1.54178
2θ/°	3.902–52.906	5.216–50.996	5.522–133.482
Reflections collected	119390	66623	50790
Independent reflections	9059	8092	7526
R_{int}	0.0400	0.1140	0.0628
R_{sigma}	0.0168	0.0496	0.0357
Restraints	224	71	18
Parameters	638	712	607
GooF	1.088	1.039	1.025
R_1 [I> 2σ (I)]	0.0615	0.0521	0.0490
wR_2 [I> 2σ (I)]	0.1384	0.1289	0.1351
R_1 [all data]	0.0773	0.0726	0.0549
wR_2 [all data]	0.1485	0.1404	0.1406
Largest peak/e Å^{-3}	0.41	0.65	0.84
Deepest hole/e Å^{-3}	-0.23	-0.54	-0.39
Flack parameter			

Chapter 2:
Crystal Engineering of BODPIPY and Tris(Dipyrrinato)metal(III) Complex.

Introduction.

Dipyrromethanes (DPM) are of wide interest as building blocks in organic synthesis, namely, in the preparation of porphyrins and porphyrin analogues such as *meso*-substituted corroles, chlorins, expanded porphyrins, and calix[4]pyrroles.[142] More recently, there has been a growing interest in various other applications of dipyrromethanes, which led to an increase in the synthetic methodologies available for their preparation, including 1,9-disubstituted derivatives.[142e] Functionalised dipyrromethanes are also potentially attractive structures for the development of new optical anion sensors, for application in biological systems.[142e, 143]

Dipyrromethanes are also the precursors of BODIPY dyes[144] (4,4-difluoro-4-bora-3a,4a-diaza-s-indacenes). BODIPY dyes, tend to be strongly UV-absorbing small molecules that emit relatively sharp fluorescence bands with high quantum yields.[145] They are relatively insensitive to the polarity and pH of their environment and are reasonably stable under physiological conditions. Small modifications to their structures enable tuning of their fluorescence characteristics; consequently, these dyes are widely used to label proteins[146], DNA,[147] and more recently sensing singlet oxygen.[148]

Nomenclature of DPM and BODIPYs.

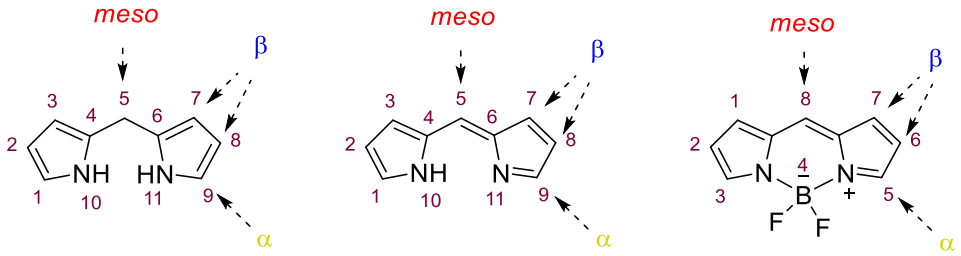

Figure 2:1: Nomenclature of DPM and BODIPYs, current IUPAC numbering scheme and traditional nomenclature.

Figure 2:1 shows the current IUPAC numbering scheme and traditional nomenclature for dipyrrole complexes.[68b] As DPM complexes are essentially half a porphyrin, the naming and numbering scheme is an extension of what is usually found in porphyrins. In BODIPY, however, since the seminal work by Treibs and Kreuzer, the numbering changes in comparison to their DPM parent molecules as seen in Figure 2:1.[144] However, for both compounds, the traditional naming scheme (*meso*, *α*, and *β*) are used interchangeably in literature frequently.

Chapter 2.1: The Structure of BODIPY Dyads.

Crystal Engineering of BODIPY.

With over a 1000 structures deposited into the CCDC as of this year, BODIPYs can be considered a treasure trove of knowledge for a crystal engineer.[149] Over the years the Senge group has made several ventures into the chemistry of BODIPYs ranging from; photo up-conversion[150] to hydrogels[151] and scaffold chemistry[152] Due to their inherent properties as mentioned above, many groups have studied these incredible dyes, including detailed X-ray studies on their structures in order to understand how they are relevant to their photophysical properties.[145, 153] There are many such studies due to the fact that the conformation of BODIPY has an effect on the photophysical properties of the molecule, especially in dyad systems where the *meso*-substituent can freely rotate in solution and adopt a planar, orthogonal, or anything in-between, conformation.[145, 153] BODIPY systems have even been designed with a fixed orthogonal geometry (usually found in di-BODIPY systems) to improve their ability to generate singlet oxygen.[154] This demonstrates a strong relationship between crystal structure and photophysical properties, however, crystal engineering has been somewhat overlooked in this discussion. As covered in the general introduction crystal engineering focuses on the identification of intermolecular and supramolecular features. How does this effect BODIPY? The basic structure of BODIPY is the core and this feature must be in every derivative of BODIPY. The core is where the BF_2 moiety lies and, as also stated in the introduction, fluorine can behave as a hydrogen-bond partner. This feature means that every BODIPY structure has an incorporated hydrogen-bond partner. So, the question is, does this BF_2 moiety have any effect on the outcome of the supramolecular structure? This is the question that will be answered in this thesis chapter for BODIPY-dyads (*meso*-substituted, anthracene, pyrene, or perylene). This chapter will focus on the investigation of fluorine···hydrogen (F···H) interactions within a family of BODIPY dyads in an attempt to answer this question.

Objectives.

This chapter (Chapter 2.1) will encompass two areas of structural studies. The first part will examine the structure of several new BODIPY compounds bearing either an anthracene, pyrene, or perylene moiety on the *meso*-position and a variety of alkyl core substituents (methyl or ethyl). The objective of this section is to establish

if there is a structural relationship between the alkyl-substitution pattern and to examine if there are any effects between the BODIPY and the *meso*-substituent within the structure. This will be combined with an investigation into how the H···F interactions behave in the crystal packing to determine their potential as directive contacts in the crystal structure.

In part two, we will discuss the formation of three new epoxide or ring expanded compounds which are formed by subjecting a BODIPY-anthracene-dyad to oxygen in the presence of light. In this section, the crystal structure of the product and parent compounds will be investigated to examine if there are any structural effects which may contribute to the formation of these compounds.

Part 1: BODIPY Dyads and Their Structural Properties.

To examine the effect of the alkyl substitution and aromatic donor units on the molecular geometry of the dyads, we obtained single crystals for BODIPYs **2:2-2:12** (Figure 2:4-2:6) suitable for X-ray crystallography by slow evaporation of CH_2Cl_2, $CDCl_3$ or toluene.[148, 155] The original compounds were provided by Dr. Mikhail Filatov during his work in the Senge group and the X-ray crystal structures were collected by myself.

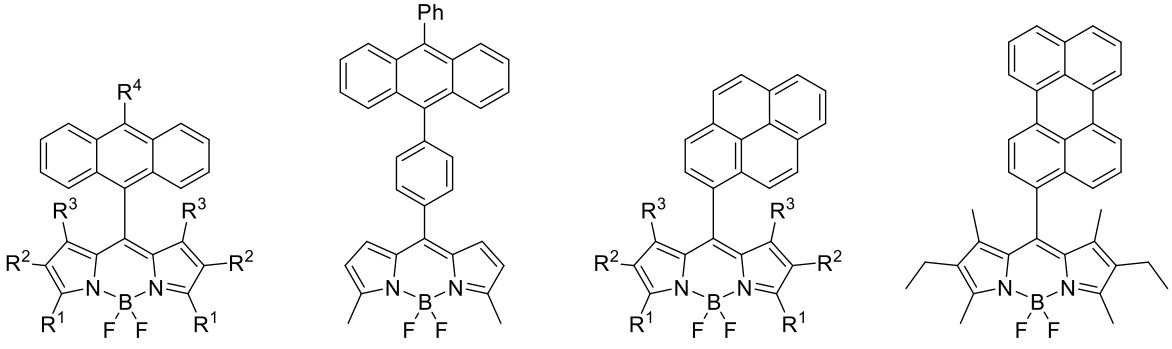

2:1 = R^1 = H, R^2 = H, R^3 = H, R^4 = H
2:2 = R^1 = H, R^2 = H, R^3 = H, R^4 = Me
2:3 = R^1 = Me, R^2 = H, R^3 = H, R^4 = Me
2:4 = R^1 = Me, R^2 = H, R^3 = Me, R^4 = Me
2:4-T = R^1 = Me, R^2 = H, R^3 = Me, R^4 = Me
2:5 = R^1 = Me, R^2 = Et, R^3 = Me, R^4 = Me
2:6 = R^1 = Me, R^2 = H, R^3 = H, R^4 = H
2:7 = R^1 = Me, R^2 = H, R^3 = H, R^4 = Ph

2:9 = R^1 = H, R^2 = H, R^3 = H
2:10 = R^1 = Me, R^2 = H, R^3 = Me
2:11 = R^1 = Me, R^2 = Et, R^3 = Me

Figure 2:2: BODIPY dyad systems that are being investigated in this section.

For analysis, we measured atom deviations from the least-squares-planes of the BODIPY core and the substitution at C8 (anthracene, pyrene, or perylene), the

carbon-carbon bond lengths of C8–C15 and the rotations around the C8–C15 bond designated ψ (Figure 2:3). Additionally, in the packing arrangement, we evaluated the model packing (head-to-head or head-to-tail), solvent effects, and the formation of any halogen short contacts between fluorine atoms and hydrogens (bond lengths given with respects to H···F distance and angles quoted for C–H···F). All structural features of interest are summarised in Table 2:1.

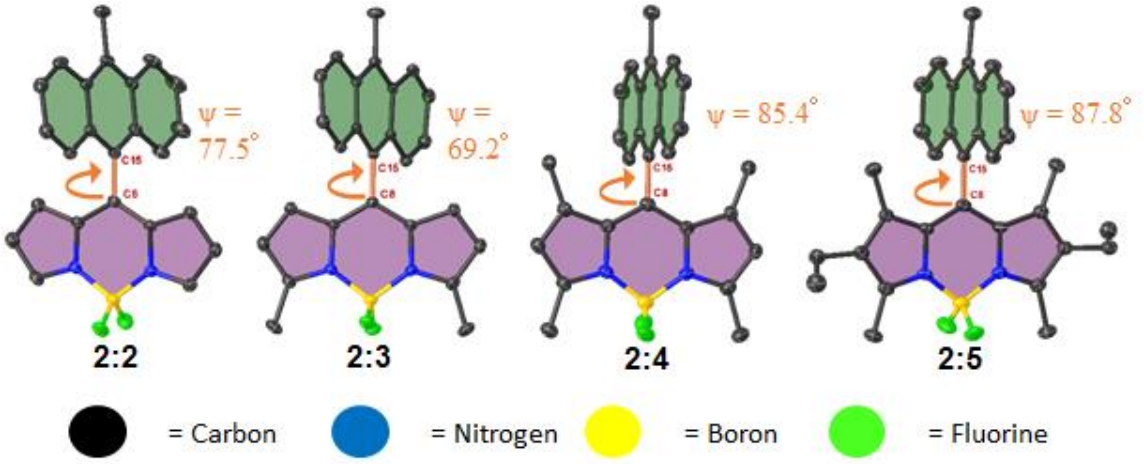

Figure 2:3: BODIPY structural features under investigation. Green denotes the anthracene plane. Purple denotes the BODIPY plane. Orange denotes the bond used to get the C8–C15 bond length. ψ-angle rotations determined by taking the dihedral angle between the green and purple planes. Thermal ellipsoids displacement shown as 50% probability, hydrogen atoms have been omitted for clarity.

Regarding the BODIPY anthracene dyad (BAD) complexes, we can see there is quite a variety in ψ rotations with no directly visible trends in substitution pattern around the BODIPY core. This suggests a large degree of freedom is available around this bond. However, for directly-linked BODIPY anthracene systems, the structures studied here prefer to be crystallised in an almost orthogonal (69-88°) orientation as seen in Table 2:1. What is interesting to note is that as the substitution pattern increases around the BODIPY core, the C8–C15 bond length displays a moderate decrease in length from 1.499 Å in the unsubstituted BODIPY, **2:2** (Figure **2:4B**), to 1.481 Å for the hexafunctionalised BODIPY, **2:5** (Figure **2:4F**). However, upon substituting the 10-position of the anthracene (C22 in the figures below), only a small variation in C8–C15 bond length observed. In comparison, the previously published structure of 8-(anthracen-9-yl)-4,4-difluoro-4-bora-3a,4a-diaza-s-indacene (**2:1**), with a completely unsubstituted BODIPY and anthracene moieties, contain the largest C8–C15 bond length (1.501 Å).[156]

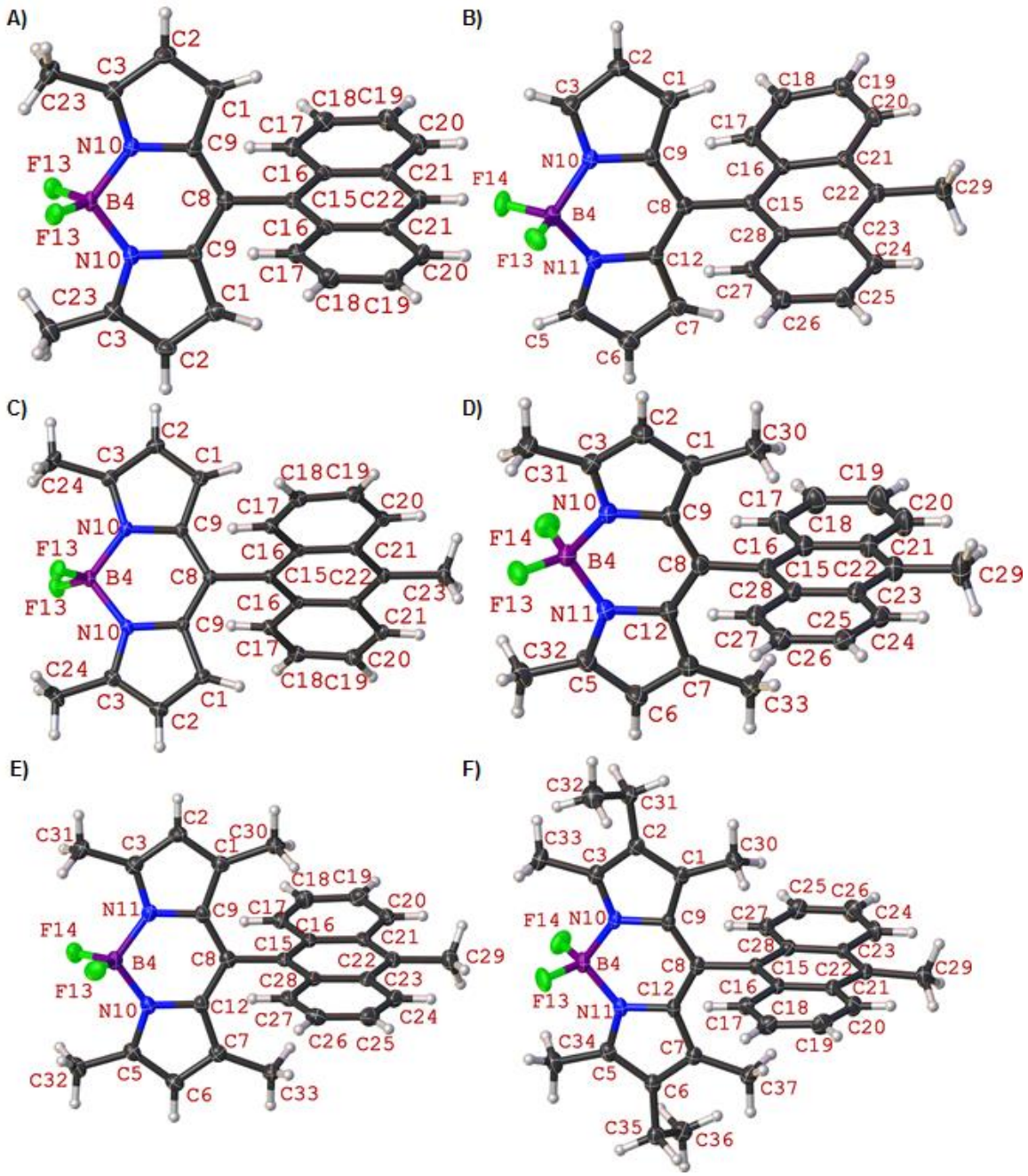

Figure 2:4: Molecular structure of **2:6** (A, (C8–C15 = 1.505(1) Å)), **2:2** (B, (C8–C15 = 1.499(1) Å)), **2:3** (C, (C8–C15 = 1.494(1) Å)), **2:4–T** (D, (C8–C15 = 1.492(1) Å)), **2:4** (E, (C8–C15 = 1.492(1) Å)), and **2:5** (F, (C8–C15 = 1.481(1) Å)) (thermal displacement 50%). Minor disorder moieties and solvent molecules have been omitted for clarity.

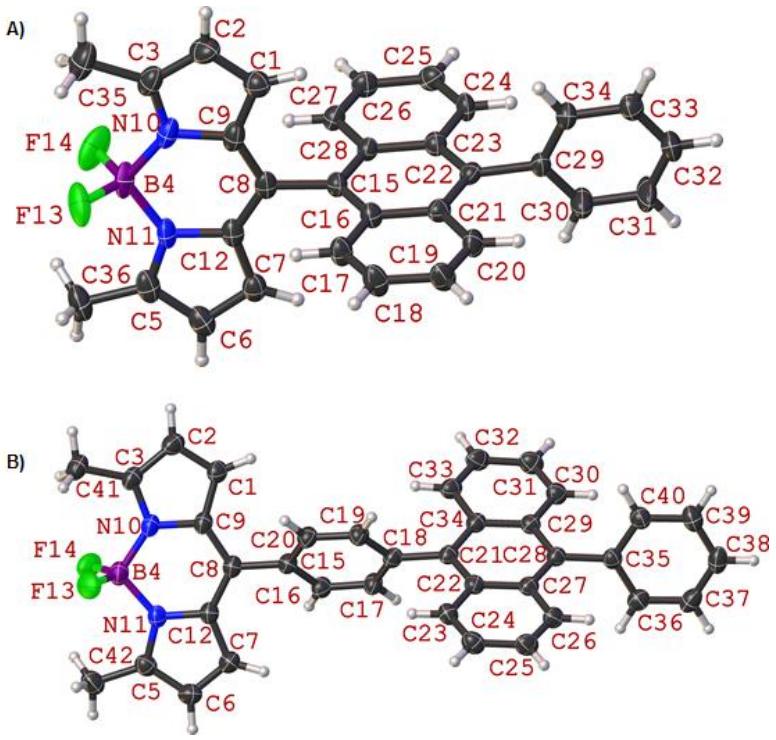

Figure 2:5: Molecular structure of **2:7** (A, (C8–C15 = 1.496(1) Å)) and **2:8** (B, (C8–C15 = 1.484(3)–1.486(3) Å)) (thermal displacement 50%).

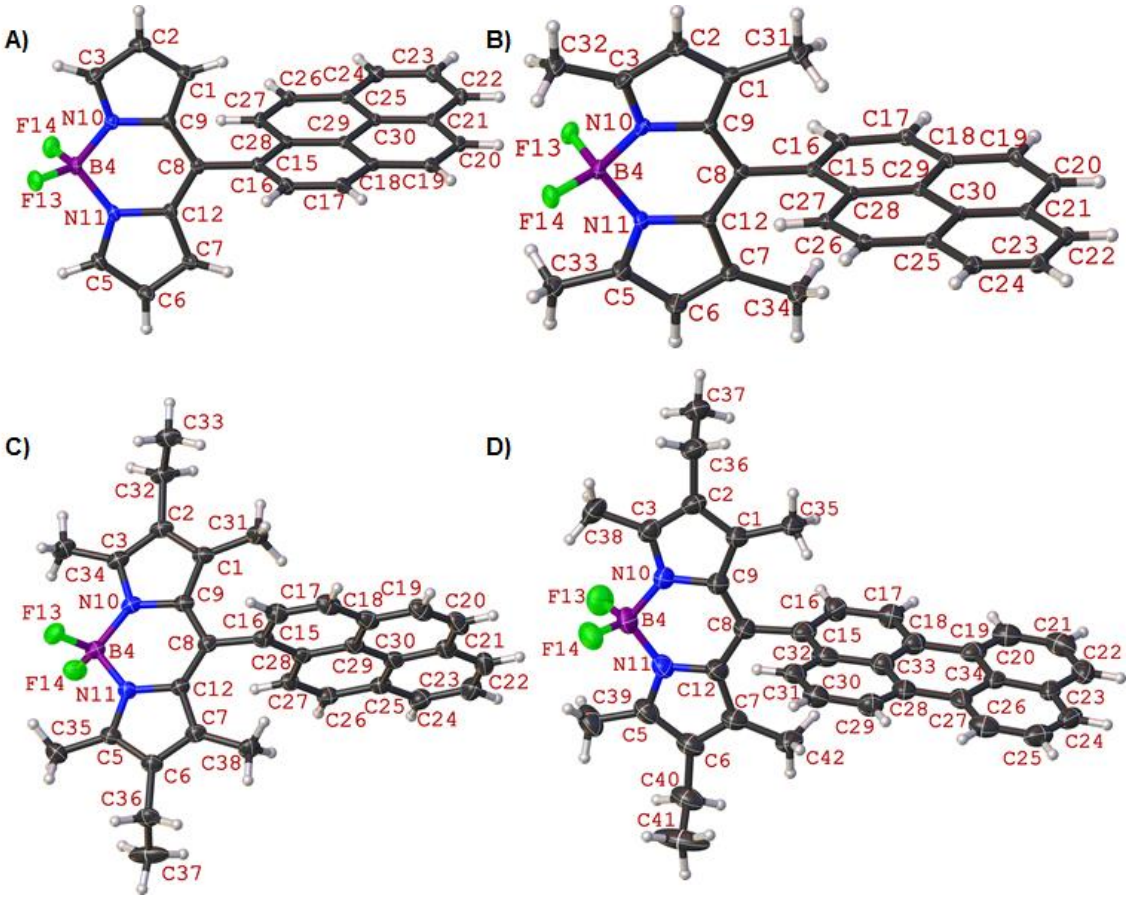

Figure 2:6: Molecular structure of **2:9** (A, (C8–C15 = 1.499(1) Å)), **2:10** (B, (C8–C15 = 1.490(1) Å)), **2:11** (C, (C8–C15 = 1.495(1)–1.498(1) Å)), and **2:12** (D, (C8–C15 = 1.493(1)–1.495(1) Å)) (thermal displacement 50%). Minor disordered moieties have been omitted for clarity.

Table 2:1: Selected structural details for rotations angles, bond length, planar distortions.

	[d]ψ (°)	C8–C15 (Å)	[e]ΔB (Å)	[f]ΔA/P (Å)	Ref
Anthracene					
2:1	98.5	1.501	0.035	0.041	[156]
2:2[a]	77.5(16)	1.499(1)	0.036	0.016	[155]
2:2[a]	73.9(16)	1.499(1)	0.126	0.074	[155]
2:3	69.2(3)	1.494(1)	0.026	0.057	[155]
2:4	78.3(5)	1.492(1)	0.066	0.028	[148b]
2:4-T*	85.4(6)	1.492(1)	0.070	0.011	[155]
2:5	87.8(3)	1.481(1)	0.015	0.030	[155]
2:6[a]	75.3(4)	1.505(1)	0.020	0.025	[155]
2:6[a]	81.2(6)	1.493(1)	0.014	0.012	[155]
2:7	86.7(2)	1.496(1)	0.041	0.015	[155]
2:8[a]	42.0(1)[b]	5.804(1)[c]	0.067	0.026	[155]
2:8[a]	53.0(1)[b]	5.798(1)[c]	0.071	0.043	[155]
Pyrene					
2:9	84.0(1)	1.499(1)	0.071	0.023	[148a]
2:10	81.1(1)	1.490(1)	0.062	0.024	[148a]
2:11[a]	87.5(2)	1.495(1)	0.018	0.020	[148a]
2:11[a]	88.7(1)	1.498(1)	0.061	0.018	[148a]
2:11-N[#](PAVRAG)	75.3	1.495	0.009	0.051	[157]
Perylene					
2:12[a]	85.7(2)	1.495(1)	0.022	0.048	[148a]
2:12[a]	84.5(2)	1.493(1)	0.016	0.095	[148a]

[*] Isostructural to **2:4**, however, includes solvent toluene. [#] Isostructural to **2:11**, however, includes solvent nitromethane [a]Two independent molecules in the asymmetric unit and both structural factors are reported. [b] rotation angle between the BODIPY plane and the anthracene plane. [c]Bond length is given for C8–C21 (9-position of the anthracene unit) due to the presence of a phenyl spacer unit. [d]Dihedral angle between the mean planes of the BODIPY and substituted plane (anthracene, pyrene, or perylene). [e]Deviation of atoms from the mean plane of the BODIPY. [f]Deviation of atoms from the mean plane of the substituted anthracene, pyrene, or perylene.

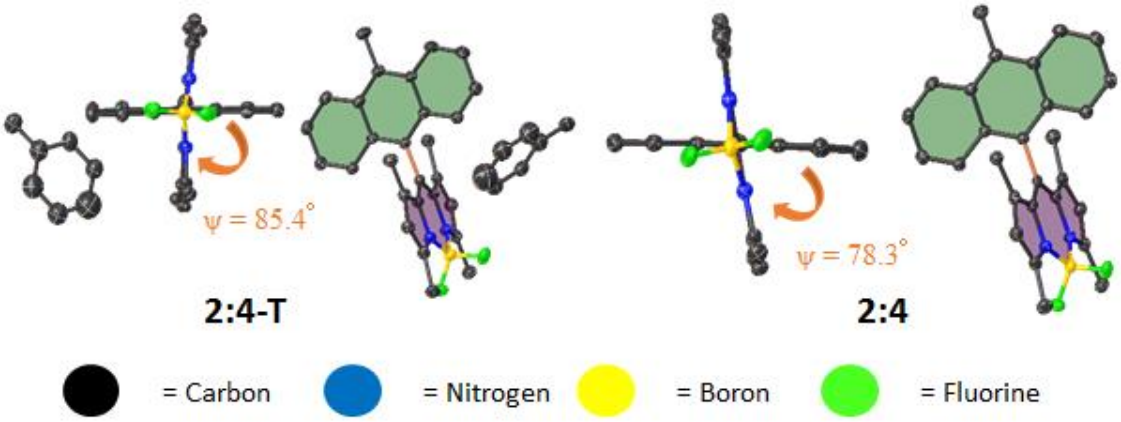

Figure 2:7: Structure of **2:4-T** (left) and **2:4** (right) showing the difference in ψ-angle due to the inclusion of a solvent toluene molecule in **2:4**. Orange arrows are an indication the rotation around the C8–C15 bond and the ψ-angle is representative of the dihedral angle between the anthracene (green) and BODIPY (purple) planes. Thermal ellipsoids displacement is shown as 50% probability. Hydrogen atoms have been omitted for clarity.

In compound **2:4**, a short contact is present between C26–H26···F14 (2.329(1) Å, 132.1(1)°), which is the 2-position on the anthracene unit (Figure 2:8A). Additionally, **2:4** shows a short contact between C31–H31C···F14 (2.517(1) Å, 121.1(1)°), which forms the head-to-head dimer. This head-to-head dimer is preserved throughout the crystal packing of the structure (Figure 2.8B). The structures of **2:4** and **2:4-T** (where T indicates toluene solvate) are isostructural, varying only by the inclusion of a toluene solvent molecule and ~1 Å increase in the *a*-axis of the unit cell for **2:4-T**. The inclusion toluene molecule displays an isolating effect, causing the previously seen head-to-head dimer in the structure **2:4** to be replaced by a head-to-tail interaction (Figure 2:9A and 2:9B). In the structure of **2:4-T** there is a bifurcated H···F contact between the C24–H24···F14 (2.579(2) Å, 125.7(1)°) and C25–H25···F14 (2.639(1) Å, 122.5(1)°) (Figure 2:9A) which is the 4-position of the anthracene unit.

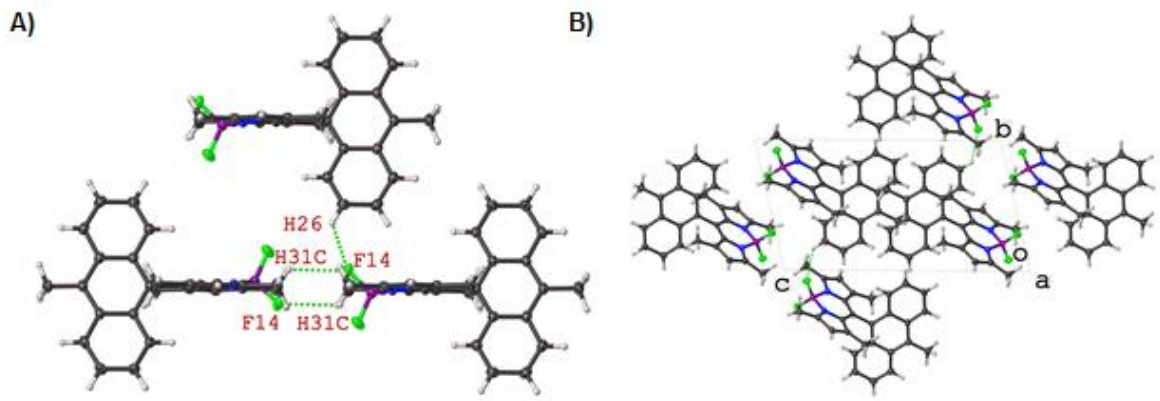

Figure 2:8: (A): Expanded structure of **2:4** displaying the H···F close contacts present in the structure (C26–H26···F14 (2.329(1) Å, 132.1(1)°) and C31–H31C···F14 (2.517(1) Å, 121.1(1)°)) (thermal displacement 50%). (B): Moiety packing of **2:4** looking down the *a*-axis showing the repeating head-to-head interactions between individual molecules within the unit cell.

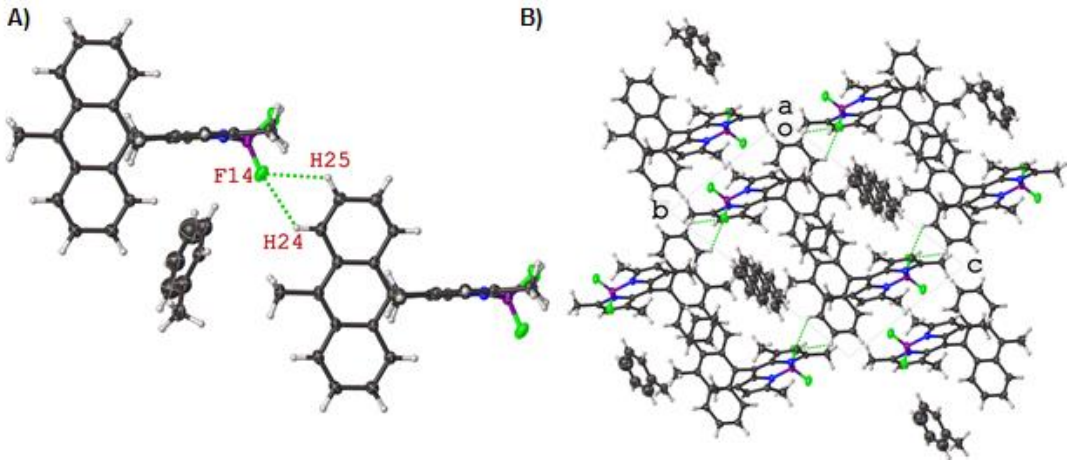

Figure 2:9: (A) Expanded structure of **2:4-T** displaying the H···F close contacts present in the structure (C24–H24···F14 (2.579(2) Å, 125.7(1)°) and C25–H25···F14 (2.639(1) Å, 122.5(1)°)) (thermal displacement 50%). (B): Moiety packing of **2:4-T** looking down the *a*-axis showing the repeating head-to-tail interactions between individual molecules within the unit cell.

In the remaining BAD systems, there are two major forms of packing seen. The first is the head-to-head arrangement of compound **2:2** (Figure 2:10). This is strongly favoured due to the formation of a dimer utilising two C–H···F halogen-bonds, C5_1–H5_1···F13 (2.181(1) Å, 145.0(1)°) and C5_2–H5_2···F14 (2.498(8) Å, 154.1(1)°). BODIPY **2:5** (Figure 2:11) and **2:7** (Figure 2:12) features a predominantly head-to-head overlapped structure, aided by short contacts between the fluorine atoms of the BODIPY and anthracene subunit. In **2:5**, a C–H···F short contact is seen between C26–H26···F14 (2.479(1) Å, 157.2(1)°). This is systematically referred to as the 2-position of the anthracene subunit and preserves the head-to-head structure in the crystal packing. **2:7** displays a similar packing to **2:5**, however, in this case, the short C–H···F contact is present between C17–H17···F13 (2.309(1) Å, 167.9(1)°), which is commonly referred to as the 1-position of the anthracene subunit.

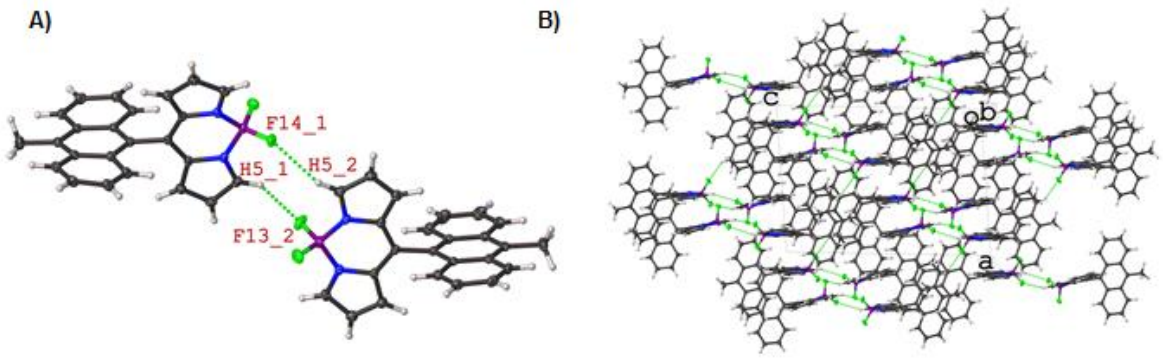

Figure 2:10: (A): Expanded structure of **2:2** displaying the H···F close contacts present in the structure (C5_1–H5_1···F13 (2.181(1) Å, 145.0(1)°) and C5_2–H5_2···F14 (2.498(8) Å, 154.1(1)°)) (thermal displacement 50%). (B): Moiety packing of **2:2** looking down the *b*-axis showing the repeating head-to-head interactions between individual molecules within the unit cell.

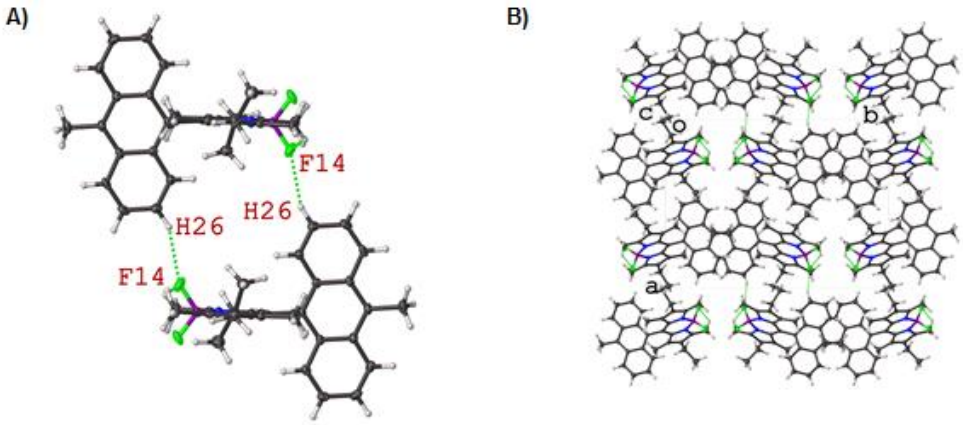

Figure 2:11: (A): Expanded structure of **2:5** displaying the H···F close contacts present in the structure (C26–H26···F14 (2.479(1) Å, 157.2(1)°)) (thermal displacement 50%). (B): Moiety packing of **2:5** looking down the *c*-axis showing the repeating head-to-head interactions between individual molecules within the unit cell.

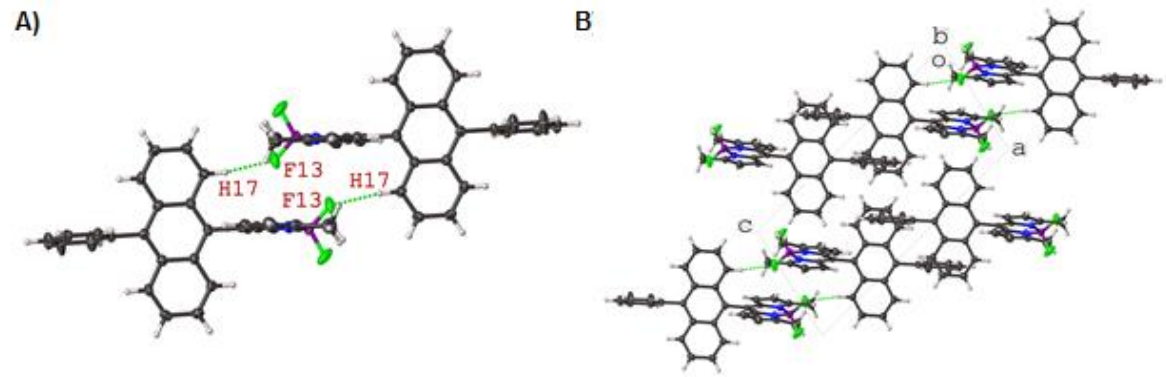

Figure 2:12: (A): Expanded structure of **2:7** displaying the H···F close contacts present in the structure (C17–H17···F13 (2.309(1) Å, 167.9(1)°)) (thermal displacement 50%). (B): Moiety packing of **2:7** looking down the *b*-axis showing the repeating head-to-head interactions between individual molecules within the unit cell.

The second type of packing is a head-to-tail overlap within the unit cell. This is the main feature observed for **2:6** (Figure 2:13), **2:3** (Figure 2:14), **2:4** (Figure 2:8), and **2:4-T** (Figure 2:9). The packing of **2:6** displays a highly ordered in-line packing of molecules in the unit cell. This results in two close contacts between C22_1–H22_1···F13_1 (2.491(2) Å, 152.8(3)°) and its symmetry equivalent C22_1–H22_1···F13_1 (2.491(2) Å, 152.8(3)°), forming a bifurcated interaction between the BODIPY and the 10-position of the anthracene unit. This feature is unique to this structure, due to the presence of methyl or phenyl moieties on the 10-position of the remaining anthracene units within this set. When compared to the literature structure of **2:1**, we can see this type of H···F interaction is favoured, provided the anthracene subunit is unhindered.[156] Additionally, in the structure of **2:6** the presence of a close contact between C23_1–H23_1···F13_2 (2.418(2) Å, 172.9(1)°) form a H···F close contact systems between neighbouring molecules related by an almost orthogonal rotation. Compound **2:3** shows a packing independent of close contacts between H···F, in which the BAD units are in a head-to-tail conformation. This is due to the presence of a methyl group which shields the fluorine atoms from forming close contacts with the methyl substituted anthracene unit. Quite interestingly the structure of **2:3** is the only structure to show any π-interactions with a π-π stacking between the anthracene rings (C16, C17, C18, C19, C20, and C21 and its symmetry equivalent) (centroid···centriod distance of 3.794(1) Å and a shift distance of 1.648(1) Å).

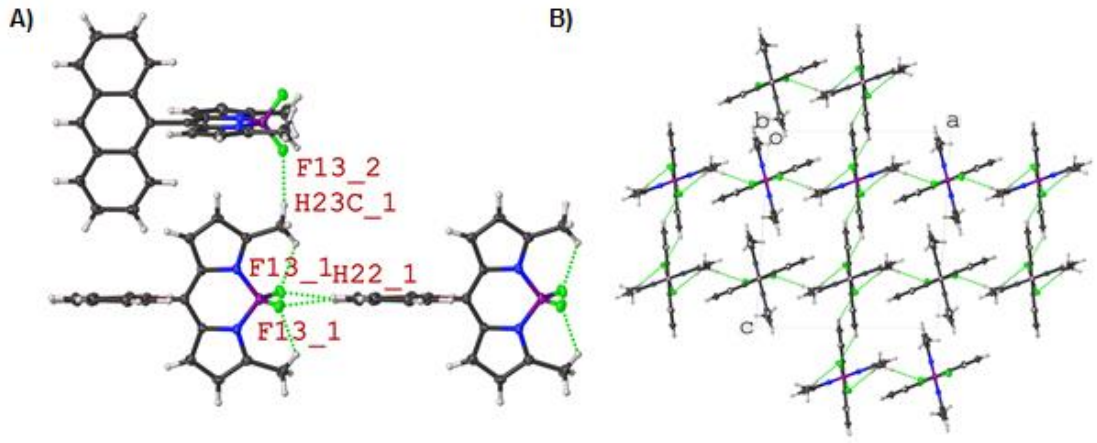

Figure 2:13: (A): Expanded structure of **2:6** displaying the H···F close contacts present in the structure (C22_1–H22_1···F13_1 (2.491(2) Å, 152.8(3)°) and C23_1–H23_1···F13_2 (2.418(2) Å, 172.9(1)°)) (thermal displacement 50%). (B): Moiety packing of **2:6** looking down the *b*-axis showing an interesting alternation intra- to intermolecular halogen-bonded network.

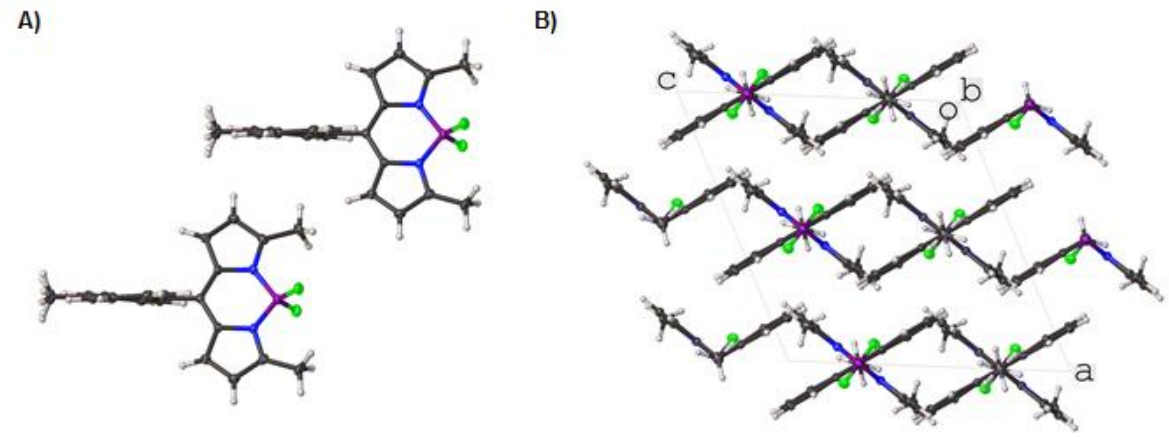

Figure 2:14: (A): Expanded structure of **2:3** displaying the absence of any H···F close contacts present in the structure (thermal displacement 50%). (B): Moiety packing of **2:3** looking down the *b*-axis showing stacking between individual BODIPY and anthracene subunits.

The structure of **2:8** (Figure **2:15**) in which a phenyl spacer is included between the BODIPY core and anthracene subunit displays a significantly decreased ψ-angle of 42.0(1)° and 53.0(1)° (structure has two molecules in asymmetric unit)

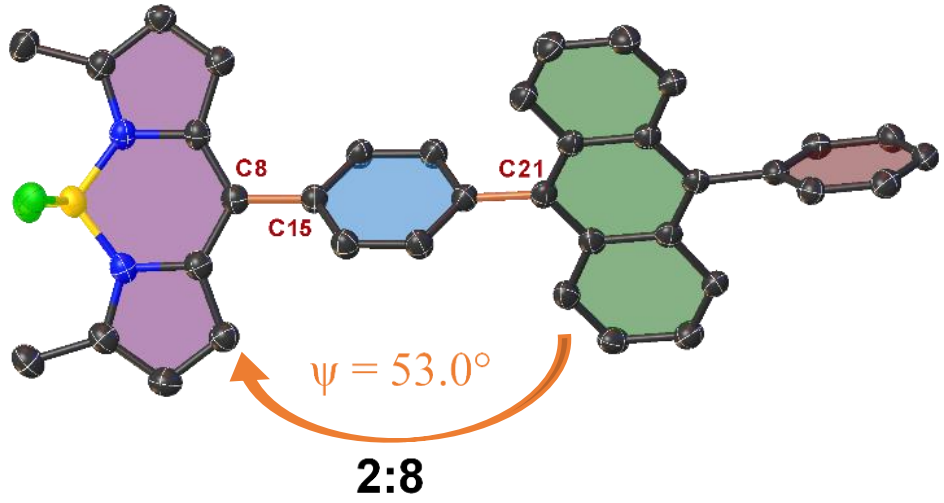

Figure 2:15: BODIPY structural features under investigation. Green denotes the anthracene plane. Purple denotes the BODIPY plane. The distance between the anthracene and BODIPY planes was measured by taking the distance between C8 and C21. ψ-angle rotations determined by taking the dihedral angle between the green and purple planes. Thermal ellipsoids displacement is shown as 50% probability. Hydrogen atoms have been omitted for clarity.

in comparison to the BAD systems outlined previously. Additionally, it features one of the smallest C8–C15 bond lengths at 1.484–1.486(2) Å. However, it should be noted that due to the phenyl spacer, **2:8** displays the largest distance between the

BODIPY core and the anthracene subunit at 5.798–5.804(1) Å. Compound **2:8** (Figure 2:15) features a predominantly head-to-head overlapped structure, aided by short contacts between the fluorine atoms of the BODIPY and anthracene or phenyl subunit. The structure of **2:8** shows a similar head-to-head overlap as seen in **2:7**, C33_1–H33_1···F14_1 (2.602(3) Å, 142.5(1)°), the 1-position of the anthracene moiety. However, as two independent molecules are present in the asymmetric unit, a second C–H···F is present between the BODIPY and the terminal phenyl, C39_2–H39_2···F14_2 (2.405(4) Å, 167.4(2)°) (Figure 2**:**16).

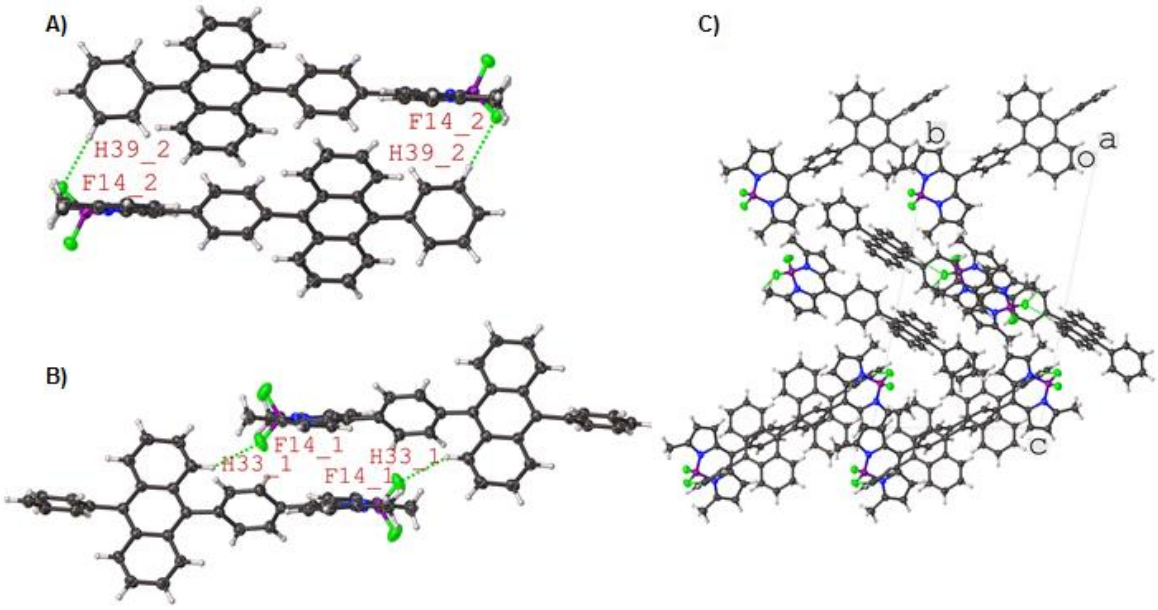

Figure 2:16: (A): Expanded structure of **2:8** displaying both independent molecules and the H···F close contacts present in each motif (C33_1–H33_1···F14_1 (2.602(3) Å, 142.5(1)° and C39_2–H39_2···F14_2 (2.405(4) Å, 167.4(2)°) (thermal displacement 50%). (B): Moiety packing of **2:8** looking down the *a*-axis showing the repeating head-to-head interactions between individual molecules within the unit cell.

In the BODIPY-pyrene-dyad (BPyrD) systems, the ψ-angles of these structures do not vary as much as seen in the BADs (Figure 2:17). The literature structure of **2:11-N** (PAVRAG), which is isostructural to **2:11** differing by the inclusion of a nitromethane molecule in the unit cell, shows the only substantial difference in the ψ-angle.[157] A similar conclusion is drawn from the C8–C15 carbon bond length. In the packing of **2:9** (Figure 2:18), a similar head-to-head dimer connected by a halogen-bond between C5–H5···F14 (2.470(2) Å, 160.0(1)°) is observed, as seen in **2:2**. The difference lies in the bulk of the pyrene moiety which inhibits the formation of the neatly stacked structure of **2:2** in favour of an X-crossed lattice to accommodate the extra ‘bulk’, resulting in an additional halogen-bond between C2–

H2···F14 (2.544(2) Å, 144.2(3)°) and C16–H16···F13 (2.589(3) Å, 145.5(1)°). The packing of **2:10** (Figure 2:19) shows that the formation of head-to-tail is evident through a short contact between C22–H22···F13 (2.544(2) Å, 144.2(3)°). This type of packing is reminiscent of that seen in the unsubstituted anthracene structures **2:1** and **2:6**. However, this seems to be a result of the now hindered fluorine atoms due to the presence of the methyl substitution on C3 and C5, making this packing arrangement more favourable than the head-to-head dimer. The packing structure of **2:11** (Figure 2:20) shows two molecules in the asymmetric unit interacting with each other through one H···F contact at C35_1–H35C_1···F14_2 (2.576 (1) Å, 136.5(1)°) in a head-to-head fashion. Each of the independent molecules also contains a head-to-head overlap which results in the formation of a H···F contact between the fluorine and the pyrene moiety (C26_1–H26_1···F13_1 (2.351(1) Å, 155.6(2)°), and C20_2–H20_2···F13_2 (2.391(2) Å, 144.1(3)°)). With the inclusion of a nitromethane molecule, as in the case of **2:11-N** (PAVRAG), the head-to-head packing pattern gets shifted to form a stepwise dimer due to the nitromethane occupying the cavity previously inhabited by the pyrene moiety.

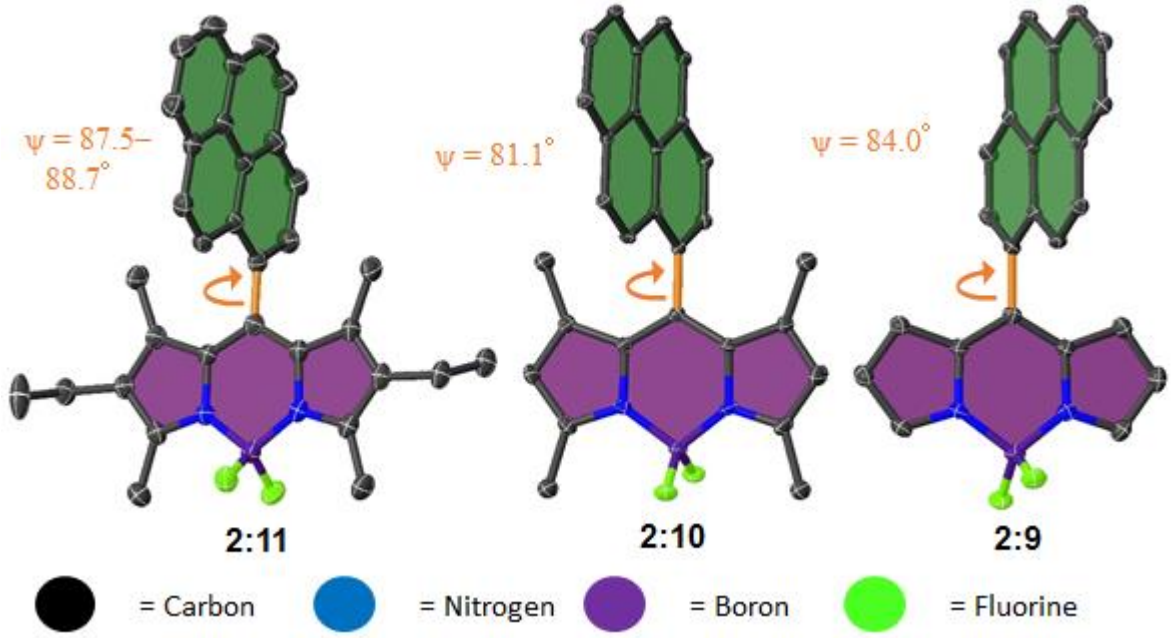

Figure 2:17: Structural features of the dyads under investigation. Orange denotes the bond used to C8–C15 bond length. ψ-angle rotations were determined by measuring the dihedral angle between the pyrene (green) and BODIPY (purple) least squares plane. Thermal ellipsoids displacement shown as 50% probability, hydrogen atoms have been omitted for clarity.

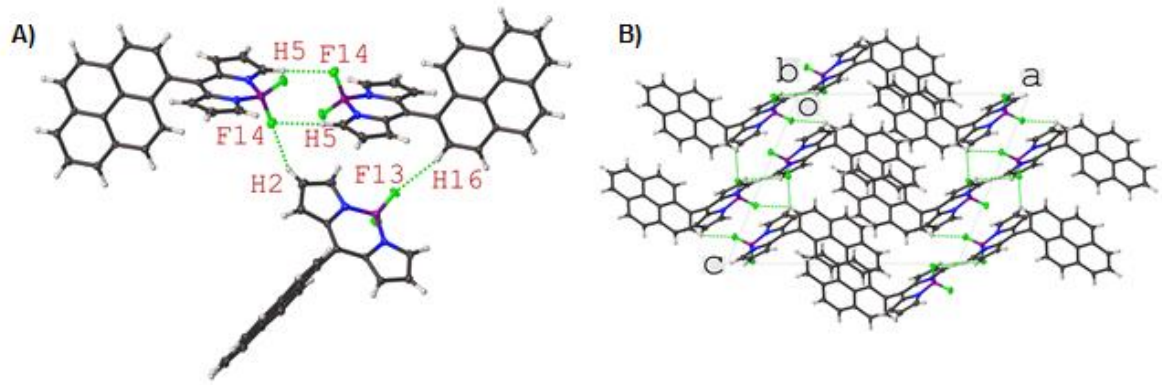

Figure 2:18: (A): Expanded structure of **2:9** displaying the H···F close contacts present in the structure (C5–H5···F14 (2.470(2) Å, 160.0(1)°), C2–H2···F14 (2.544(2) Å, 144.2(3)°)) and C16–H16···F13 (2.589(3) Å, 145.5(1)°). (thermal displacement 50%). (B): Moiety packing of **2:9** looking down the *b*-axis showing the repeating head-to-head interactions between individual molecules within the unit cell.

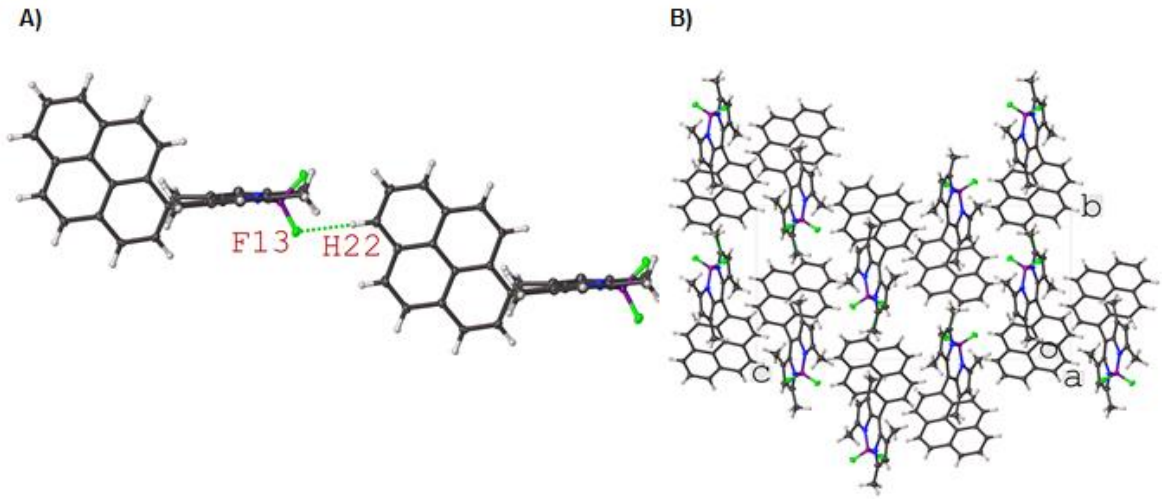

Figure 2:19: (A): Expanded structure of **2:10** displaying the H···F close contacts present in the structure (C22–H22···F13 (2.544(2) Å, 144.2(3)°)) (thermal displacement 50%). (B): Moiety packing of **2:10** looking down the *a*-axis showing the repeating head-to-tail interactions between individual molecules within the unit cell.

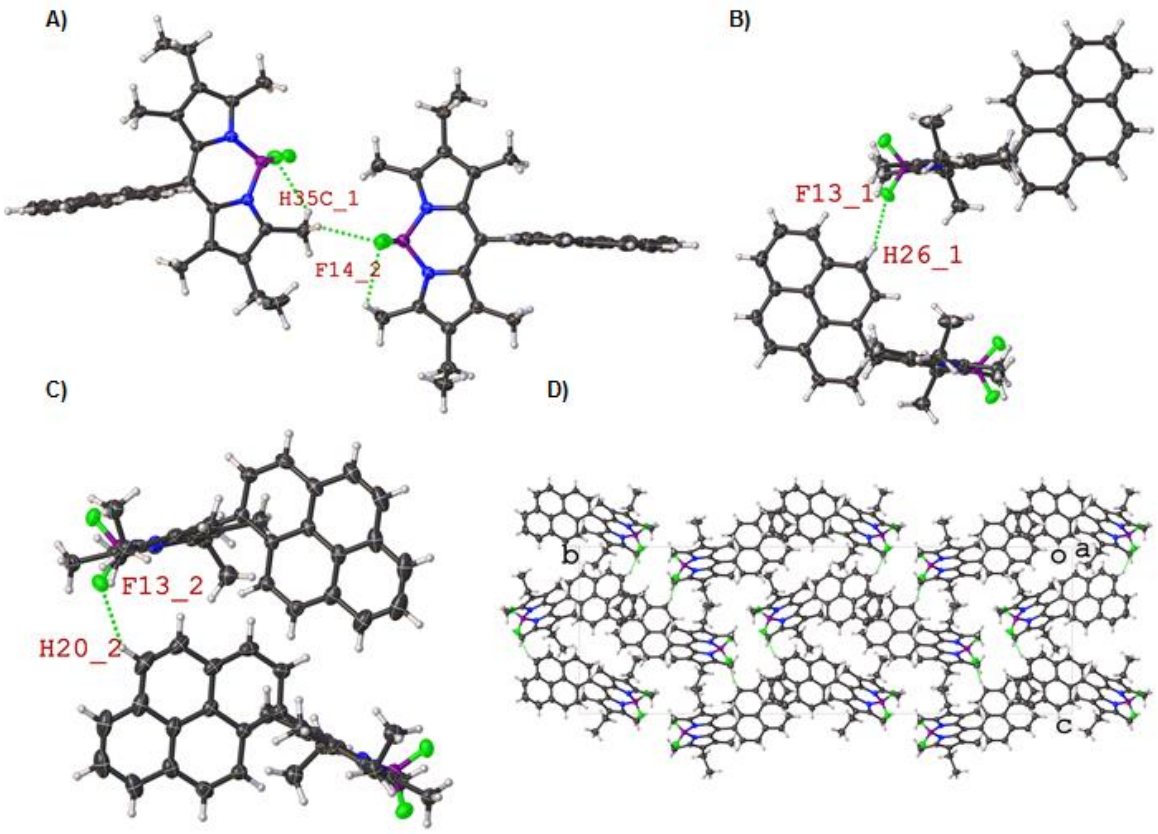

Figure 2:20: (A-C): Expanded structure of **2:11** displaying the H···F close contacts present in the structure (C35_1–H35C_1···F14_2 (2.576(1) Å, 136.5(1)°), C26_1–H26_1···F13_1 (2.351(1) Å, 155.6(2)°), and C20_2–H20_2···F13_2 (2.391(2) Å, 144.1(3)°)) (thermal displacement 50%). (D): Moiety packing of **2:11** looking down the *a*-axis showing the repeating head-to-head interactions between individual molecules within the unit cell.

The final class is the BODPIY-perylene-dyad (BPerD) system, of which only one example of a crystal structure was obtained. **2:12** (Figure **2:21** and **2:22**) is an interesting example as two individual molecules are presents in the unit cell. The hydrogen atoms associated with the 6- and 7-positions of the perylene moiety form a bifurcated close contact to the fluorine of the BODIPY at 2.369(1) Å (173.2(1)°) for C20_2–H20_2···F13_1 and 2.449(1) Å (148.1(1)°) for C17_2–H17_2···F13_1. Additionally, the presence of the two independent molecules results in a mixture of head-to-head interactions coupled with a head-to-tail overlap in the unit cell.

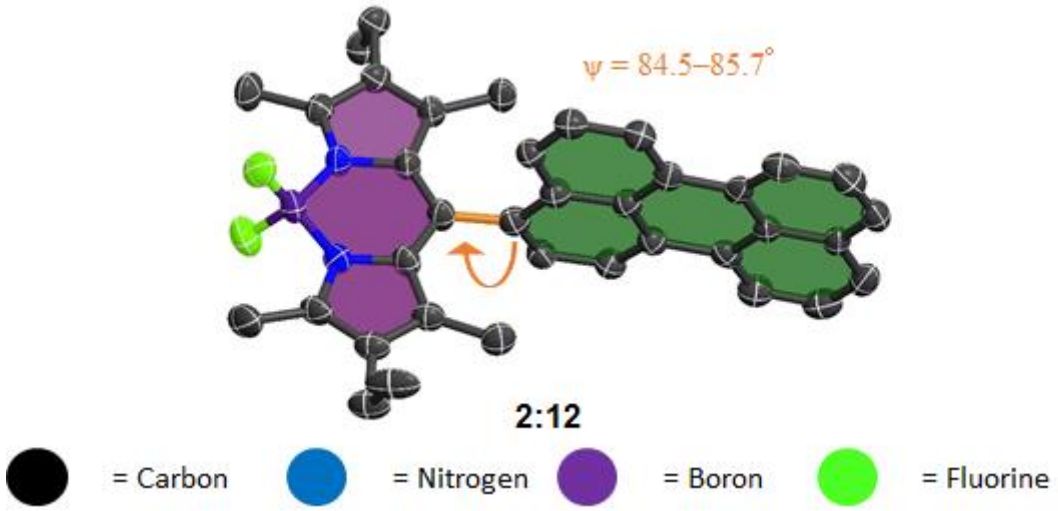

Figure 2:21: Structural features of the dyads (**2:12**) under investigation. Orange denotes the bond used to C8–C15 bond length. ψ-angle rotations were determined by measuring the dihedral angle between the perylene (green) and BODIPY (purple) least squares plane. Thermal ellipsoids displacement shown as 50% probability, hydrogen atoms have been omitted for clarity.

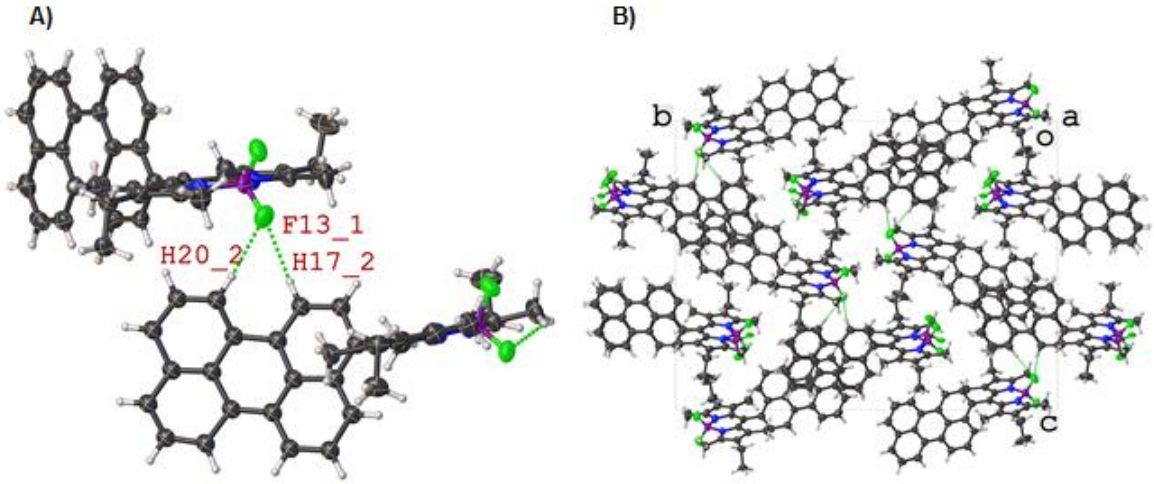

Figure 2:22: (A): Expanded structure of **2:12** displaying the H···F close contacts present in the structure (C20_2–H20_2···F13_1 (2.369(1) Å, 173.2(1)°) and C17_2–H17_2···F13_1 (2.449(1) Å, (9148.1(1)°)) (thermal displacement 50%). (B): Moiety packing of **2:12** looking down the *a*-axis showing to exhibiting a mix of both head-to-head and head-to-tail interactions within the unit cell.

Conclusion.

In conclusion, the rotation of the dyad group (anthracene, pyrene, or perylene), as designated by the ψ-angle is dependant, in the solid state, on the environment of the substitution pattern around both the BODIPY and the *meso*-substituent (anthracene, pyrene, or perylene). This is most evident while observing the BAD systems. Additionally, it was noted that while most of the H···F interactions are within sufficient distance and angle to be considered hydrogen bonds, they are comparably

weak interactions. This is evident by the fact that simple modifications to the BODIPY core or C8 substituent (anthracene, pyrene, or perylene) result in radical changes to the H···F interactions observed. Rather than being directional globally throughout each structure, the H···F interactions appear to be subject to structural changes. However, there is sufficient evidence in the crystal packing that indicates that in the individual structures these H···F interactions are one of the driving forces in crystal packing. There are too many possible interactions that could occur, so only the least hindered conformation occurs due to structural changes in this family of compounds.

Aside from this, there are some key structural features we can use to predict the type of packing which will occur with these structures. The first of these is with a completely unsubstituted anthracene unit, the H···F contacts are directed towards the hydrogen atom at the 10-position of the anthracene moiety in a head-to-tail linear network. When this position contains a substituent such as the introduction of methyl groups at the anthracene 10-position, this greatly favours head-to-head dimer formation, while the introduction of methyl groups to the C3 and C5 positions make this interaction less favourable. The *meso*-substitution type tends to only affect the efficiency in stacking in the unit cell as bulkier subunits such as the pyrene tend to eliminate the neat row stacking seen in the majority of the BAD systems. Finally, the inclusion of solvents, while not always having the largest effect on the overall packing (changing head-to-head to head-to-tail, or *vice-versa*), leads to aggregation in pockets that would have been previously occupied by the *meso*-substituent, such as in the case of **2:4** and **2:4-T**.

Outlook.

While the results presented herein provide a detailed account of conformational and structural changes present in BODIPY-X-Dyad systems (BXD, where X is anthracene, pyrene, or perylene) they have great potential for future work. One of these areas is the comparison between conformation and photophysical properties such as singlet oxygen yields or fluorescence quantum yields. The recent publications by Filatov *et al*. tabulate the fluorescence quantum yields for all of the BXD systems included in this chapter.[148a, 155] By comparing these photophysical measurements with the structural information obtained herein, it is possible to start generating hypotheses on the relationship of conformation *vs.* activity. The only

drawback to committing to such a study at this moment in time is that most of the structure's in the series reported by Filatov *et al*. are currently not determined by XRD.[148a, 155] Therefore, the first step in such an investigation would be to gather the crystal structure data for all compounds and include their solvent counterpart (in the publications by Filatov *et al*. the measurement we conducted in several solvents [DMF, DCM, CH_3CN, EtOH, toluene, and hexane]).[148a, 155] These structures would then be categorised with regards to the value of the ψ-angle, bond distance between the donor and acceptor of the dyads, and distortion of both the donor core and the acceptor core to gauge how the photophysical properties are affected in the solid state structure. Research like this could be beneficial in designing specific motifs in BXD systems to target desirable photophysical properties.

One final area which could be investigated would be to use these BXD systems as clathrates like that showed in porphyrins by Byrn *et al*.[108] We have seen that the structure of **2:4** and **2:11** have been shown to incorporate solvent molecules within the crystal lattice (**2:4-T** and **2:11-N**), which indicates a potential to form host-guest inclusion compounds that would be held together with van der Waals forces, such as H···F interactions.

Part 2: Cycloaddition and Subsequent Rearrangement Reaction in BADs.

During photochemical experiments, carried out by Dr. Mikhail Filatov, on the compounds **2:3** and **2:4** in the previous section, an interesting reaction was observed. It was found that upon broad-band visible light irradiation of air-saturated solutions of **2:4** in a range of polar solvents, the formation of compound **2:13** was observed.[148b] This compound was isolated in 5% yield, along with recovered unreacted starting material (Scheme 2:1).

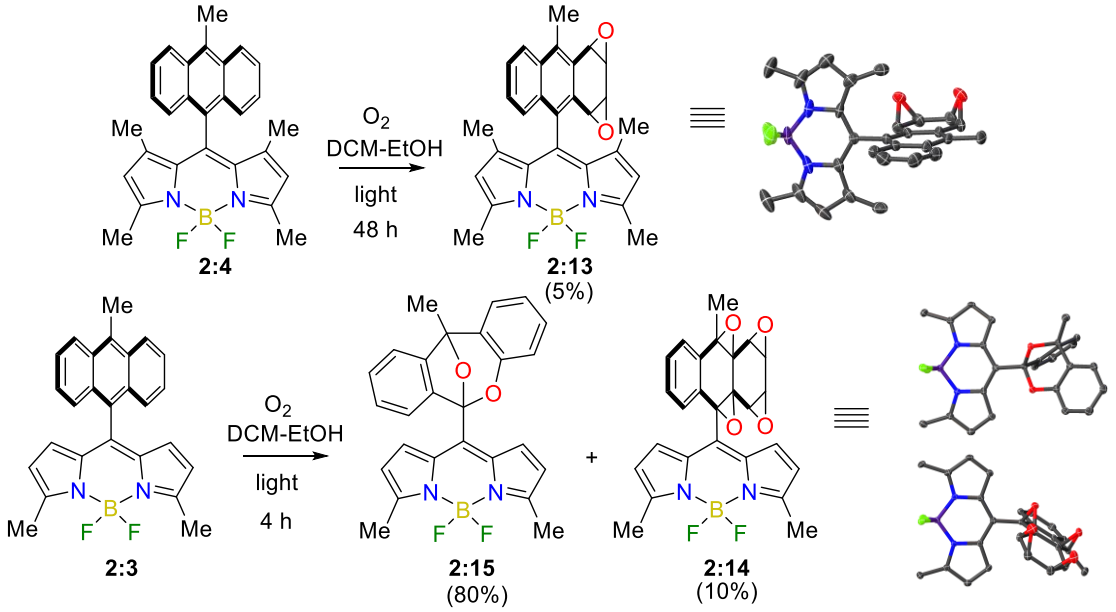

Scheme 2:1: Photo-induced transformations of **BADs** in the presence of oxygen.

In contrast, irradiation of **2:3** under the same conditions resulted in complete conversion of the substrate and formation of two products, bicyclic acetal derivative (**2:15**) and the tetraepoxide (**2:14**), which were isolated in 80% and 10% yields, respectively (Scheme 2:1).[148b] From these results the mechanism in Scheme 2:2 was suggested. The formation of these products appears to be due to the sensitisation of oxygen and subsequent [4+2] cycloaddition of the resulting $^1O_2$, which is typical for anthracene derivatives.[158] The X-ray structures of all products were determined. This led to the question; why did both compounds result in two different substitution patterns and the formation of three distinct products? Using the X-ray structures (Figure 2:23-2:25) this question could be addressed by looking at the structure of the parent compounds. In the XRD data, the *β*-methyl substituents in **2:4** are forming a steric-like shield of the C-9 position of the anthracene unit. Introduction of methyl groups into the BODIPY pyrrole rings shields the inner ring of the orthogonal anthracene residue, making the approach of $^1O_2$ molecule difficult. As for the structure of compound **2:3**, this is not an issue, as the orthogonal

anthracene residue is not encumbered by the methyl units, allowing for rearrangement product seen in compound **2:15** and the tetraepoxide formation of compound **2:14**.

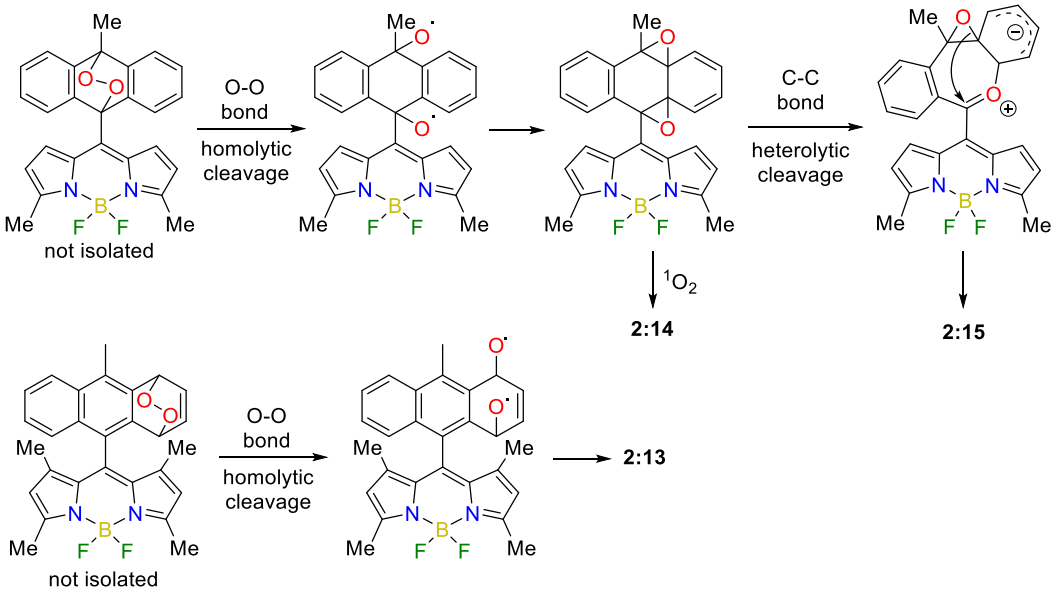

Scheme 2:2: Suggested mechanism of the fluorescent products formation.

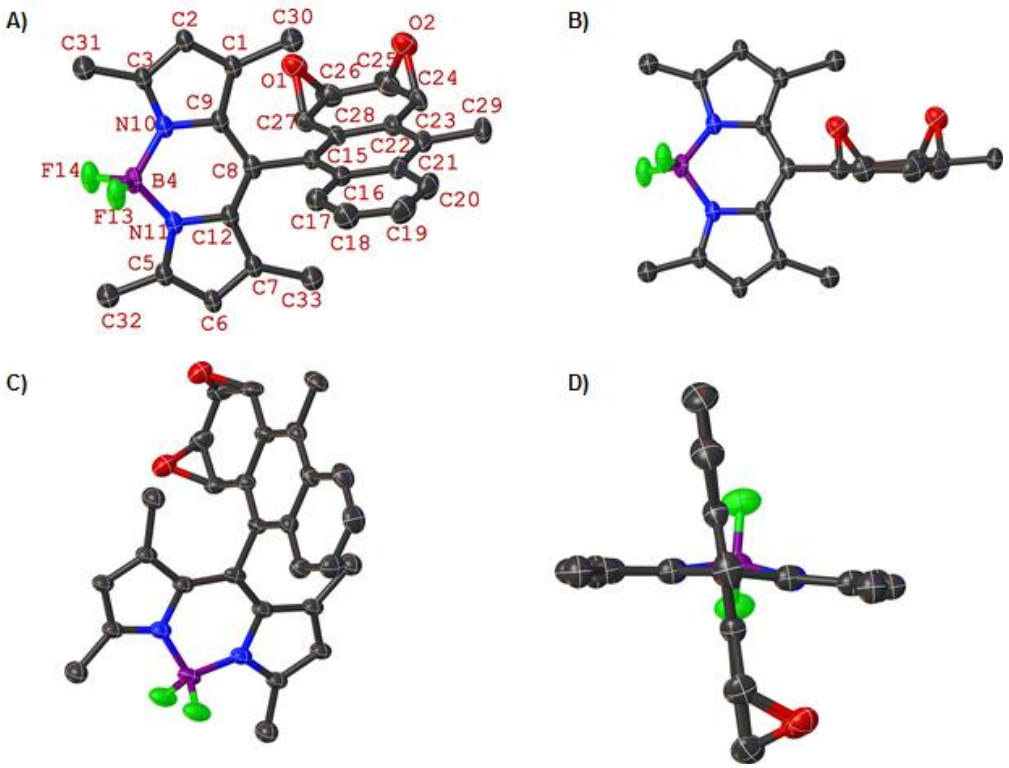

Figure 2:23: Molecular structure of **2:13** (thermal displacement 50%) showing the major disordered moiety (occupancy 74%). Images are taken at different views, ((A) offset to the *c*-axis; (B) offset to the *a*-axis; (C) offset to the *c*-axis; (D) offset to the *b*-axis), to illustrate the angles between the BODIPY plane and the substituent at C8 position, demonstrating the effect of the epoxides on the anthracene ring. The hydrogen atoms have been omitted for clarity.

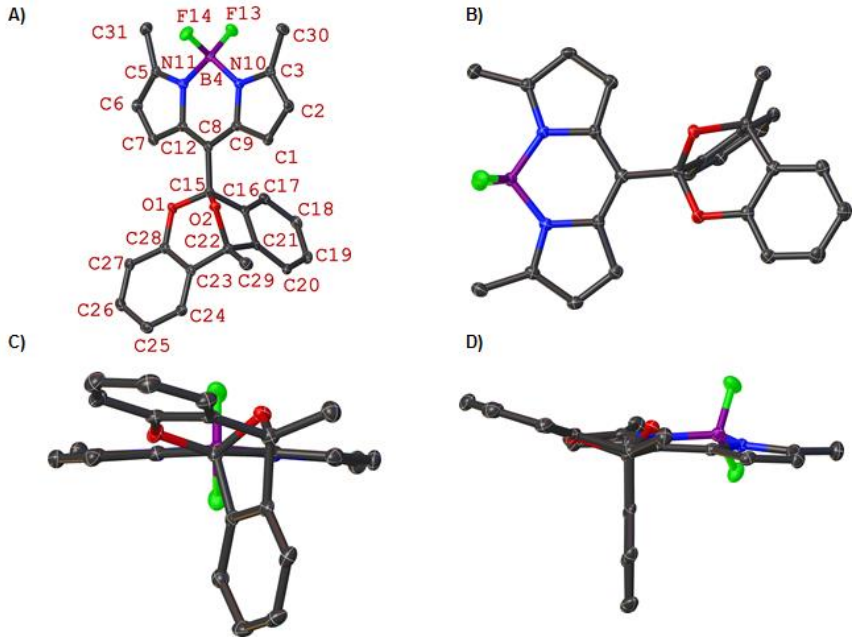

Figure 2:24: Molecular structure of **2:15** (thermal displacement 50%). Images are taken at different views, ((A) offset to the *b*-axis; (B) offset to the *a*-axis; (C) offset to the *c*-axis; (D) offset to the *c*-axis), to illustrate the angles between the BODIPY plane and the substituent at C8 position, demonstrating the effect of the insertion of the epoxide into the anthracene ring. The hydrogen atoms and solvent CH_2Cl_2 molecule have been omitted for clarity.

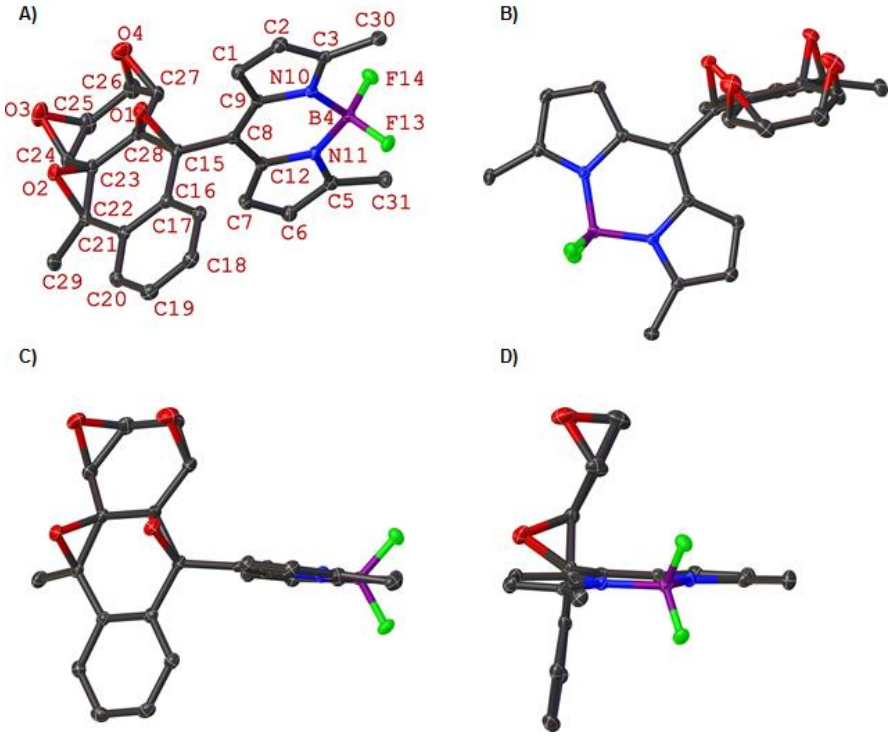

Figure 2:25: Molecular structure of **2:14** (thermal displacement 50%) showing the major disordered moiety. Images are taken at different views, ((A) offset to the *b*-axis; (B) offset to the *b*-axis; (C) offset to the *a*-axis; (D) offset to the *c*-axis), to illustrate the angles between the BODIPY plan and the substituent at C8 position, demonstrating the effect of the epoxides on the anthracene ring. The hydrogen atoms have been omitted for clarity.

Conclusion.

From this brief section, we have shown that the BIDIPY-anthracene dyad systems will undergo a photoinduced ring arrangement from the endoperoxide to form the bis-/tetraepoxides and the bicyclic acetal. Additionally, we have outlined how the substitution pattern on the BODIPY (substituted or unsubstituted C1 and C7 position) determines the degree of epoxide to the anthracene ring. This is also a structural confirmation of the rearrangement products determined by Aubry *et al.*.[158]

Outlook

Moving forward from this, one area which the focus of future research could entail is to expand the current structural data to encompass all of the molecules shown in part 1 with regards to the rearrangement/epoxide formation. This would give us a much larger library to establish the determinants (substitution type and pattern) which drive the formation of the various rearrangement or ring expansion products in the BAD, BPerD, and BPyrD systems. This would allow for a direct comparison with the observations of Aurbry *et al*. to validate how the structure and conformation of these dyads effects the substitution of polycyclic aromatic hydrocarbons.[158]

Chapter 2.2: Tris(dipyrrinato)metal(III) Complex – a Kaleidoscope of Crystals.

Introduction.

This chapter will discuss a new type of tris(dipyrrinato)metal(III) complex interaction which was published recently with their synthesis and activity against tumors and bacteria.[159] The structural elucidation of tris(dipyrrinato)metal(III) complexes was first reported in 1997 by Brückner *et al.* and over the following decades, several such structures have been deposited to the Cambridge Crystallographic Data Centre (CCDC) database.[149, 160] These compounds have found a variety of uses with one of the main features being their incorporation into metal-organic frameworks and non-covalent networks.[161] This is due to their characteristic octahedral shape that the tris(dipyrrinato) motifs form around their metal(III) centres, the planar conformation of the dipyrrin ligand, and a variety of short contacts that can be achieved due to various substitutes on the dipyrrin ligand. These features typically generate an artistic packing pattern for metal-organic frameworks or host-guest complexes. For the compounds studied herein, these characteristics will be the focus of the discussion, as well as how the presentation of fluorine atoms on the aromatic rings adds a unique element to the packing pattern of tris(dipyrrinato) metal complexes, which to date, has not been studied. In this section, five new tris(dipyrrinato)metal(III) complexes, with either indium(III), gallium(III), or iron(III) centres, are described.

Objective.

This chapter will discuss the structure of five new structures of tris(dipyrrinato)metal(III) complexes containing either an iron(III), gallium(III), or indium(III) centre. The structural difference between the metal(III) complexes of the *meso*-pentafluorophenyl structures and their *para*-substituted derivatives will be investigated. Additionally, this section will examine if the presentation of fluorine atoms on the aromatic rings adds a unique element to the packing pattern of tris(dipyrrinato)metal(III) complexes, which for this family of compounds is a new area of study.

Results and Discussion.

For this section five new tris(dipyrrinato)metal(III) complexes were obtained from the lab of Dr. Arno Wiehe and the X-ray crystal structure were collected by myself

(Figure 2.26). The obtained compounds were dissolved in CH_2Cl_2 and left to slowly evaporate over time. This resulted in single crystal suitable for X-ray diffraction studies.

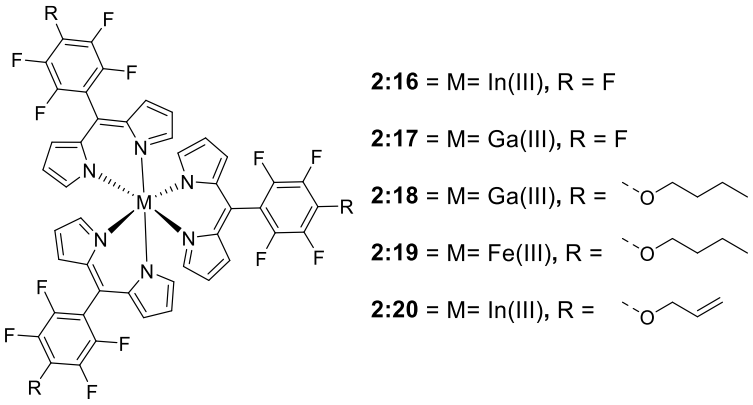

Figure 2:26: Tris(dipyrrinato)metal(III) complexes under investigation in this section.

The structure of compounds **2:16** and **2:17** (Figures 2:27 and 2:30) shows the first examples of tris(dipyrrinato)metal(III) complexes bearing a pentafluorophenyl (PFP) unit on the *meso*-position. These two structures have two separate packing patterns. However, both structures feature several F···H contacts, which appear to be directional within each respective structure. The packing of compound **2:16** and **2:17** seem to be influenced by the metal(III) centre due to N–M bond lengths, which adds to the distinction of their packing patterns. Both compounds **2:16** and **2:17** were solved with one complete molecule in the asymmetric unit. For simplicity, the dipyrrin units surrounding the metal(III) centres in structures have been labelled A, B, and C following the atom label, as seen in Figures 2:27and 2**:**30.

In structure of compound **2:16** There are two major interactions of note C3A–H3A···F3B (2.519(1) Å, 162.9(1)°) and are C2A–H2A···F3A (2.525(1) Å, 147.3(1)°). The combination of these interactions is repeated throughout the unit cell to form a H···F network holding the individual molecules together (Figure 2:28). This forms the rather complex packing pattern seen in Figure 2**:**29. There is an almost octahedral orientation of ligands around the metal(III) centre with an N–In–N angle range of 84.6(5)–95.2(5)° and an N–In bond length range of 2.188(1)–2.243(1) Å. Additionally, there is an In···In the separation of 8.402(1)–9.347(1) Å to the nearest neighbouring molecule. Interestingly, the C-subunit in this structure forms no interactions or short contacts.

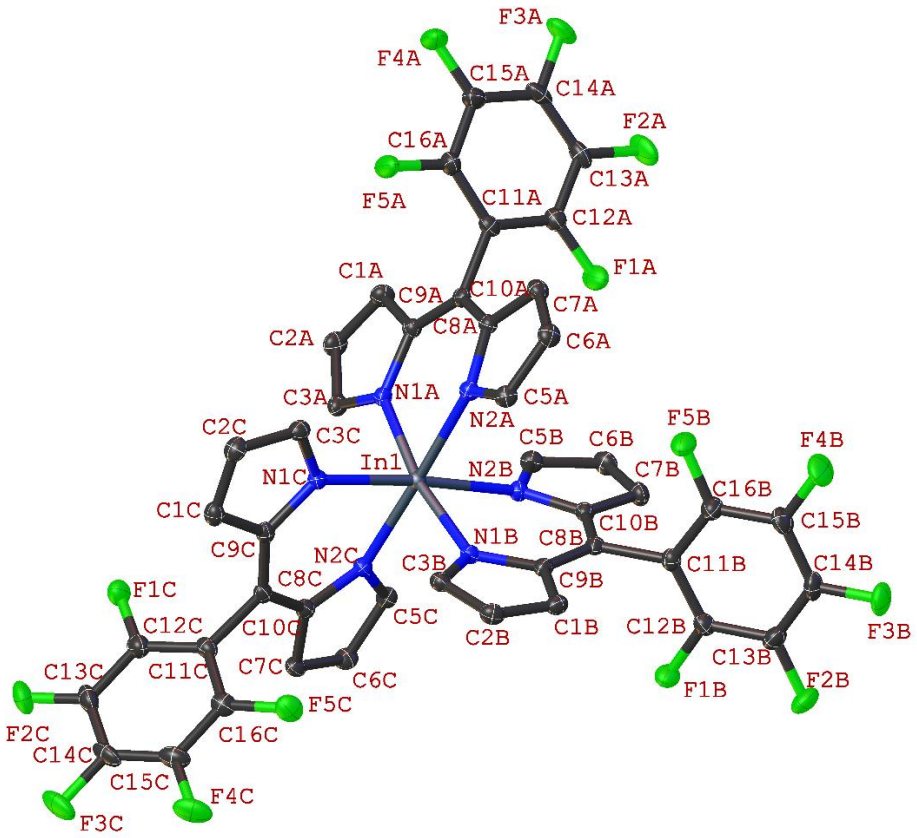

Figure 2:27: View of the molecular structure of complex **2:16** in the crystal. Hydrogen atoms have been omitted for clarity. Thermal ellipsoids give 50% probability.

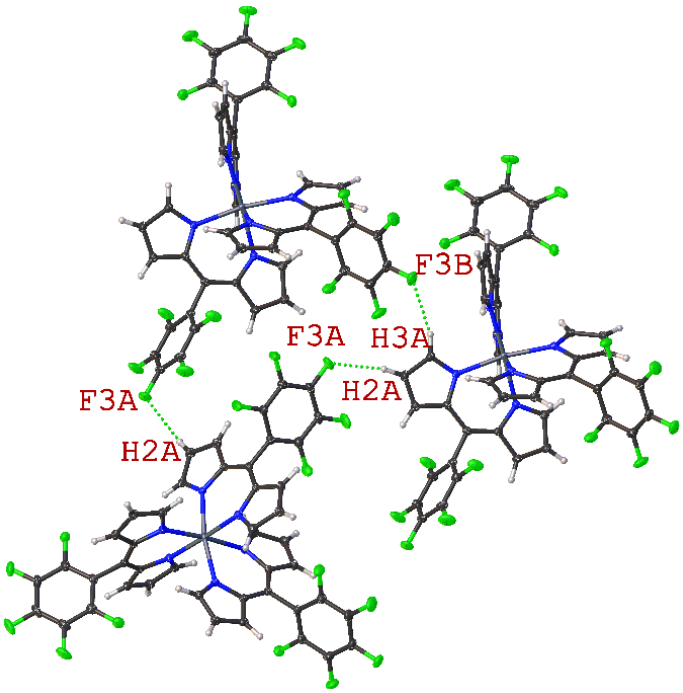

Figure 2.28: Expanded structure of **2:16** showing the most notable intermolecular H···F interactions (C3A–H3A···F3B (2.519(1) Å, 162.9(1)°) and C2A–H2A···F3A (2.525(1) Å, 147.3(1)°)).

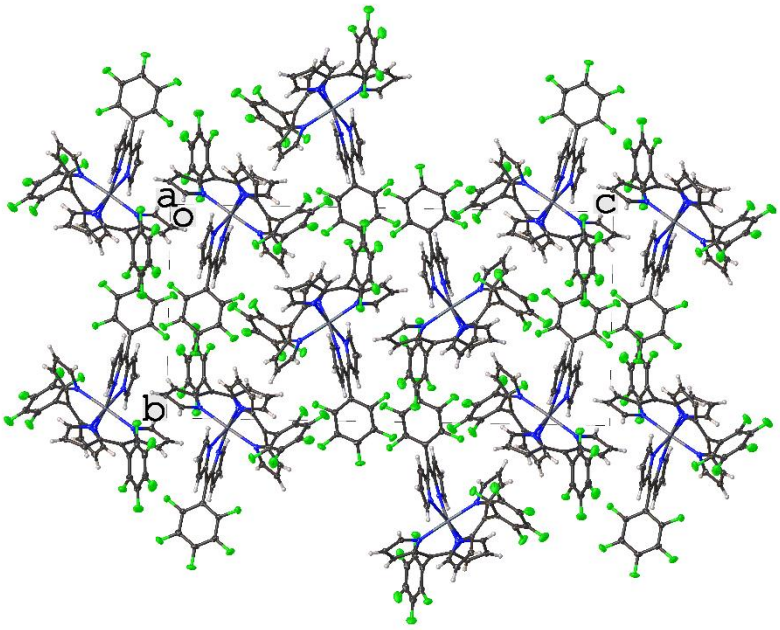

Figure 2:29: View of the crystal packing of complex **2:16** along the *a*-axis. Thermal ellipsoids give 50% probability.

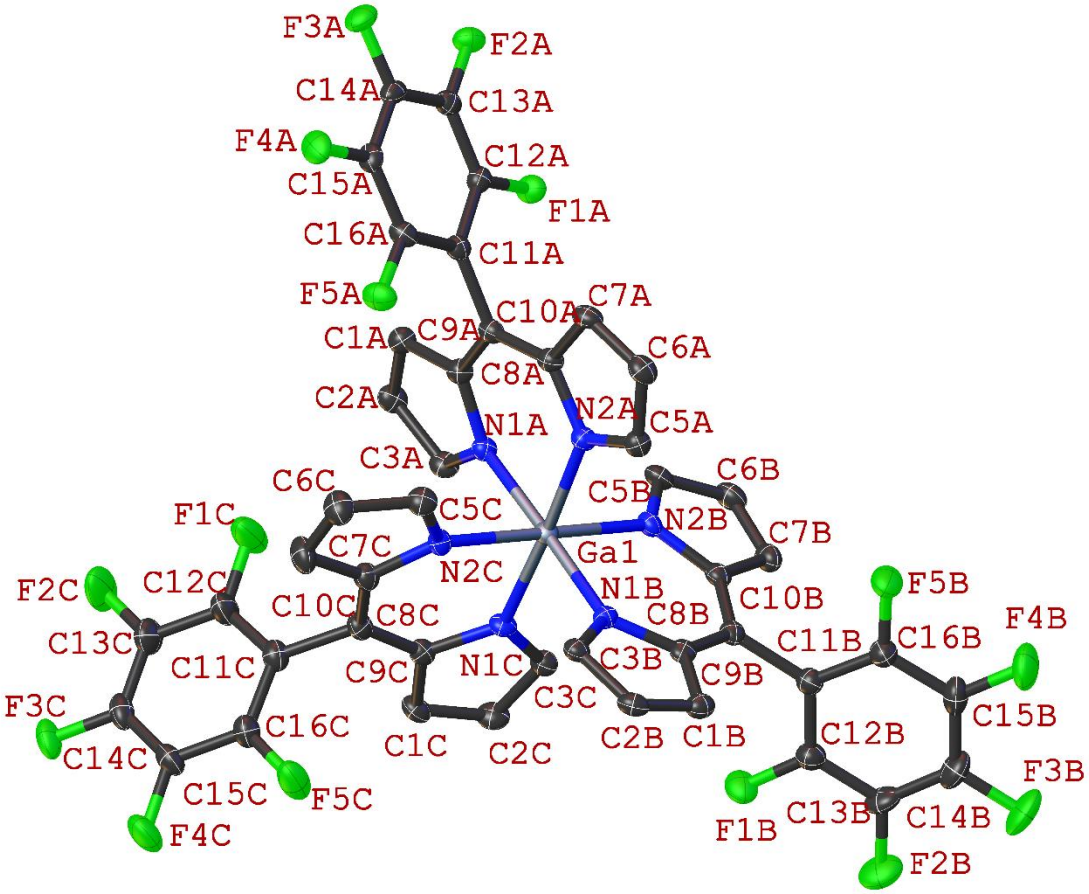

Figure 2:30: View of the molecular structure of complex **2:17** in the crystal. Hydrogen atoms have been omitted for clarity. Thermal ellipsoids give 50% probability.

In compound **2:17**, the F···H interactions observed are much simpler than those of **2:16**. The F···H contacts of C7A–H7A···F1A (2.458(2) Å, 173.0(2)°) and C7B–H7B···F5B (2.435(2) Å, 141.9(2)°) are repeated between all units (Figure 2.31), holding the structure at a Ga···Ga distance of 8.837(1)–8.904(1) Å to the nearest neighbouring molecule. This is clearly represented in the moiety packing of compound **2:17**, Figure 2:32. Additionally, the N–Ga–N angle range of 88.3(1)–92.6(1)° and an N–Ga bond length range of 2.046(3)–2.084(3) Å forms an octahedral complex around the Ga(III) metal centre.

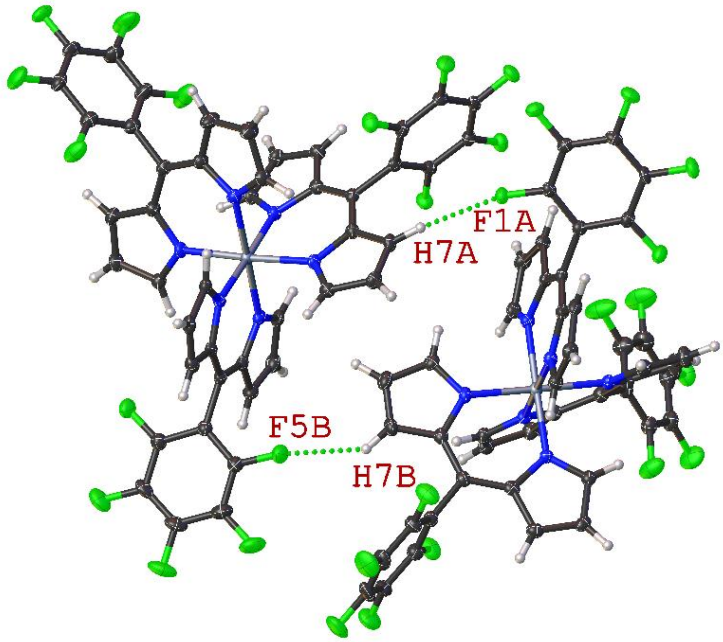

Figure 2.31: Expanded structure of **2:17** showing the most notable intermolecular H···F interactions (C7A–H7A···F1A (2.458(2) Å, 173.0(2)°) and C7B–H7B···F5B (2.435(2) Å, 141.9(2)°)).

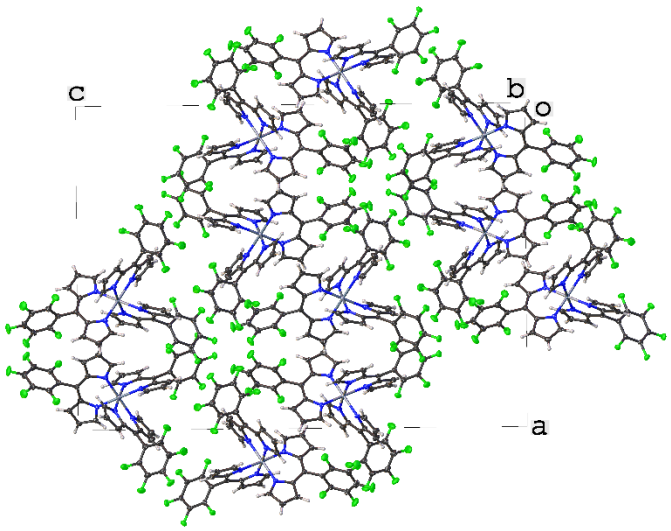

Figure 2.32: View of the crystal packing of complex **2:17** along the *b*-axis.

There are only minor differences between compounds **2:16** and **2:17** due to the metal(III) centres, which results in compound **2:16** having a longer N–M bond length between the ligand and metal(III) centre and a larger N–M–N angle. Aside from this, both structures result in an octahedral complex. This difference appears to impact the potential F···H networks formed in both samples, with compound **2:16** containing many more short contacts compared to compound **2:17**.

The structure of **2:18** (Figure 2:33) was solved with only 1/3 of the molecule present in the asymmetric unit. This structure differs from compound **2:17** due to the now substituted 4-position, which contains a butoxy group. This alternate substitution has quite an impact on the F···H networks formed and results in an artistic kaleidoscope–type pattern of packing in the unit cell, (Figure 2:34). The structure of **2:18** shows two major F···H contacts, C17–H17A···F3 (2.405(1) Å, 158.2(1)°) and C6–H6···F1 (2.406(1) Å, 157.8(1)°) (Figure 2:35). However, due to the high symmetry within this structure, these interactions are repeated three times in one unit creating an elaborate F···H network within the structure. This results in a shorter Ga···Ga distance of 7.595(1) Å to the nearest neighbouring molecule, as compared to compound **2:17**. The N–Ga–N angle range of 88.3(1)–90.6(1)° and an N–Ga bond length range of 2.052(1)–2.055(1) Å is similar to compound **2:17**. While viewed along the *c*-axis, the structure of compound **2:18** appears to be rotated by ~90° to the next layer, resulting in the aforementioned kaleidoscope–type pattern.

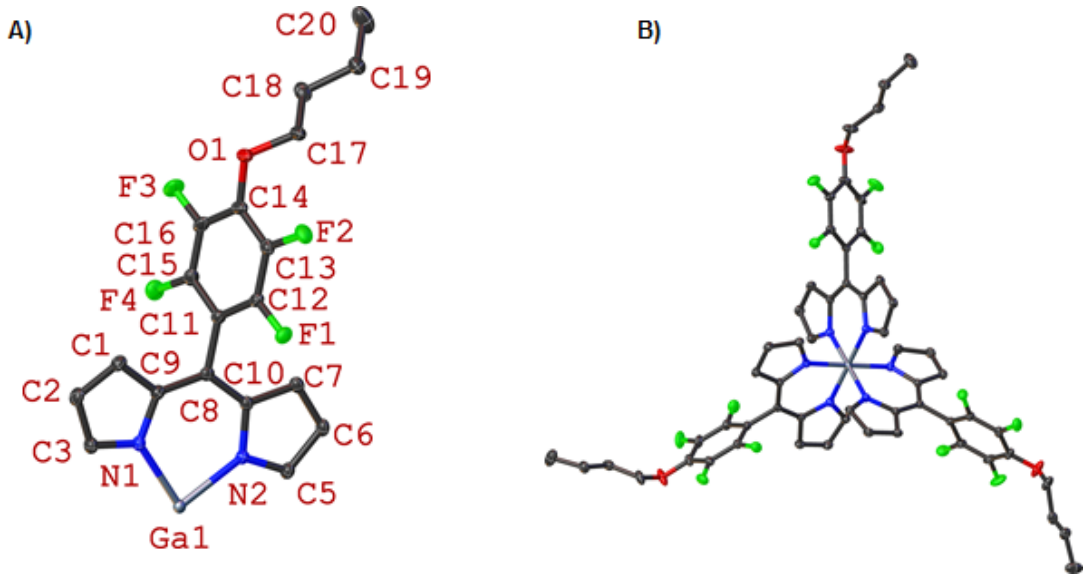

Figure 2:33: View of the asymmetric unit of with all non-hydrogen atoms labelled (A) and the complete molecular structure without labels (B) of complex **2:18** in the crystal. Hydrogen atoms have been omitted for clarity. Thermal ellipsoids give 50% probability.

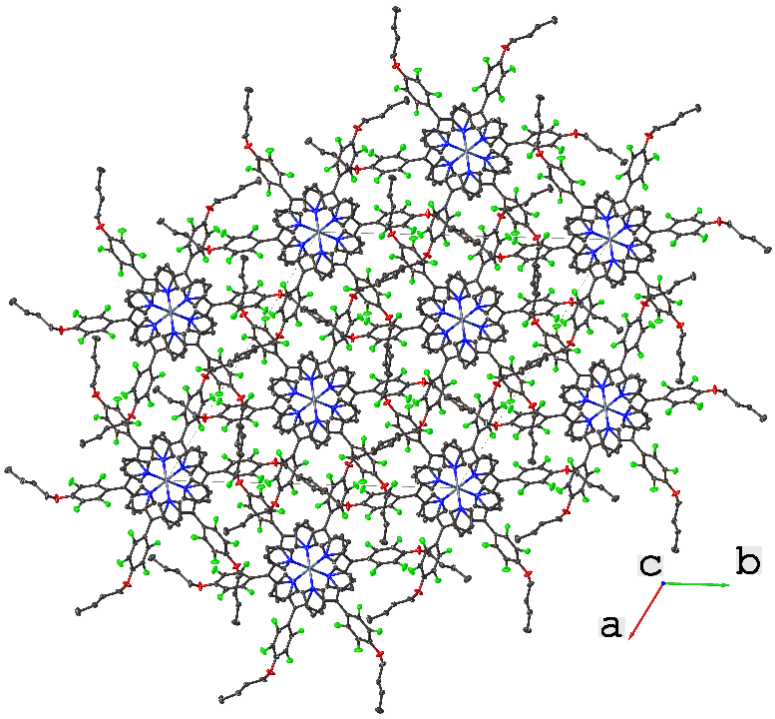

Figure 2:34: View of the crystal packing of complex **2:18** along the *c*-axis. Hydrogen atoms have been omitted for clarity.

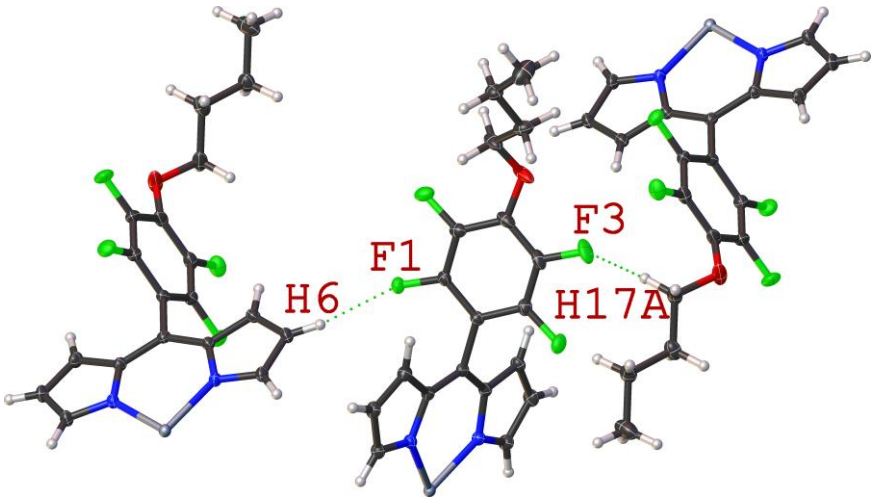

Figure 2:35: Expanded structure of complex **2:18** (only the asymmetric unit is shown to give a clearer image of the interactions) showing the most notable intermolecular H···F interactions, (C17–H17A···F3 (2.405(1) Å, 158.2(1)°) and C6–H6···F1 (2.406(1) Å, 157.8(1)°)). Thermal ellipsoids give 50% probability.

The complex **2:19** (Figures 2:36) was solved with 1/3 of the molecule present in the asymmetric unit similar to that of **2:18**. The structure of **2:19** contains two major F···H contacts, C17–H17A···F2 (2.380(2) Å, 157.2(3)°), C2–H2···F4 (2.410(2) Å, 154.3(2)°) (Figure 2:37). Just as in compound **2:18** above, the interactions are reciprocated and repeated three times over the symmetry resulting in an extensive F···H network. The overall geometry of compound **2:19** is an octahedral orientation of the ligands around the metal(III) centre. There is a N–Fe–N angle range of 86.2(1)–91.8(1)° and a N–Fe bond length range of 1.964(3)–1.970(3) Å.

Additionally, there is a Fe···Fe distance of 7.522(2) Å to the nearest neighbouring molecule. The structures of **2:19** shows a similar F···H network as seen in compound **2:18**, resulting in a similar artistic packing pattern. While viewed along the *c*-axis with layers rotated by ~90° to each other, resulting in a kaleidoscope–type pattern (Figure 2:38).

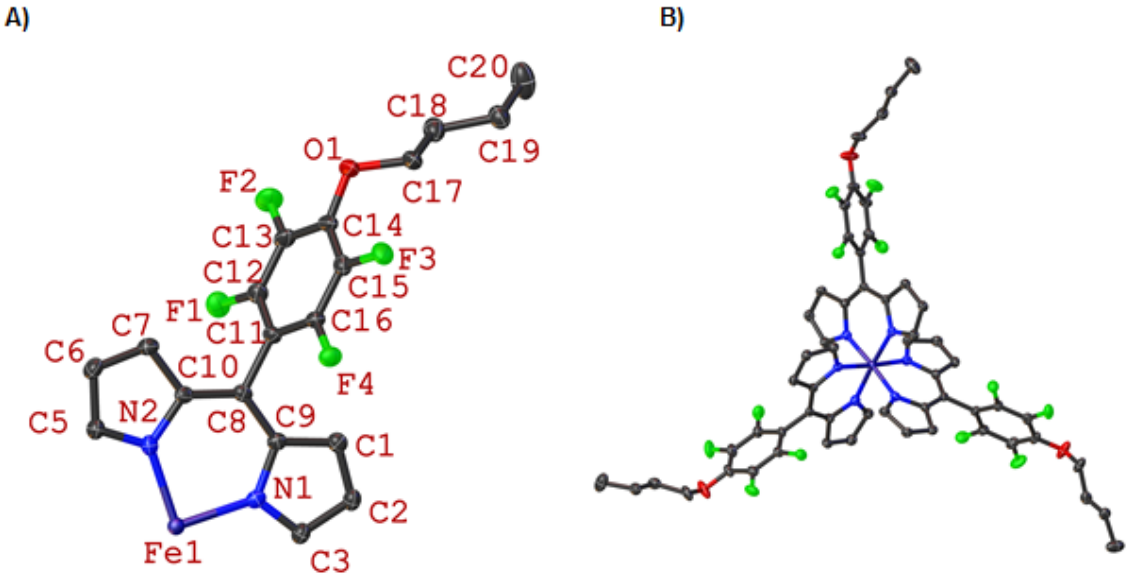

Figure 2:36: View of the asymmetric unit of with all non-hydrogen atoms labelled (A) and the complete molecular structure without labels (B) of complex **2:19**. Hydrogen atoms have been omitted for clarity. Thermal ellipsoids give 50% probability.

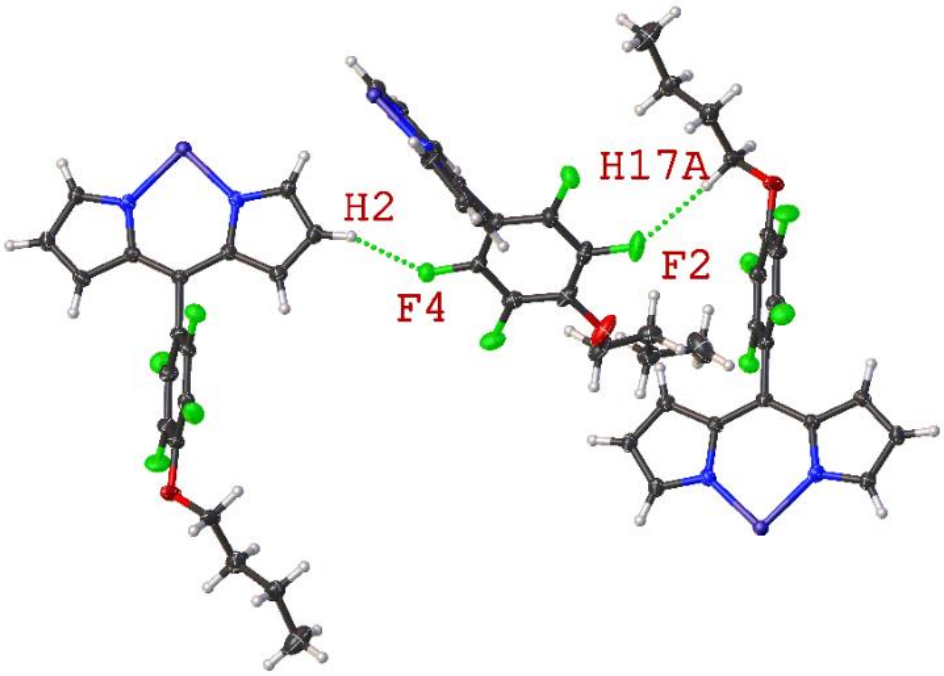

Figure 2:37: Expanded structure of complex **2:19** (only the asymmetric unit is shown to give a clearer image of the interactions) showing the most notable intermolecular H···F interactions, (C17–H17A···F2 (2.380(2) Å, 157.2(3)°), C2–H2···F4 (2.410(2) Å, 154.3(2)°)). Thermal ellipsoids give 50% probability.

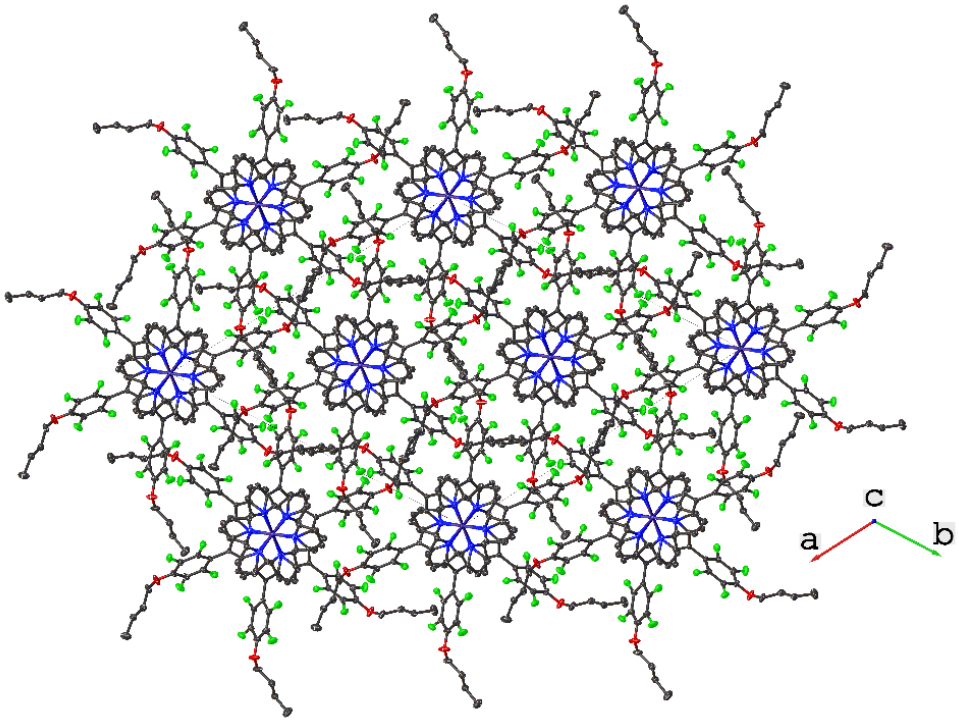

Figure 2:38: View of the crystal packing of complex **2:19** along the *c*-axis. Hydrogen atoms have been omitted for clarity. Thermal ellipsoids give 50% probability.

The structure of **2:20** (Figure 2:39) contains one major F···H contact, C17–H17B···F4 (2.319(1) Å, 134.1(1)°) (Figure 2:40), which, just like in **2:18** and **2:19** above, is reciprocated and repeated three times due to symmetry. This results in the allyloxy chains being tethered to the fluorine groups of the phenyl ring through a F···H network. Additionally, the presence of a F···F short contact, F2···F4 (2.765(2) Å, 129.6(2)°) (Figure 2:40) results in an aggregation of phenyl rings within the unit cell (Figure 2:39). The overall geometry of compound **2:20** is an octahedral orientation of the ligands around the metal(III) centre. There is an N–In–N angle range of 83.6(1)–95.2(1)° and an N–In bond length range of 2.218(2)–2.221(2) Å. Additionally, there is an In···In separation of 7.564(2) Å to the nearest neighbouring molecule. Similar to the structure of **2:18** and **2:19** above, looking down the *c*-axis the reveals the layers rotated by ~90° to each other, resulting in a kaleidoscope–type pattern (Figure 2:41).

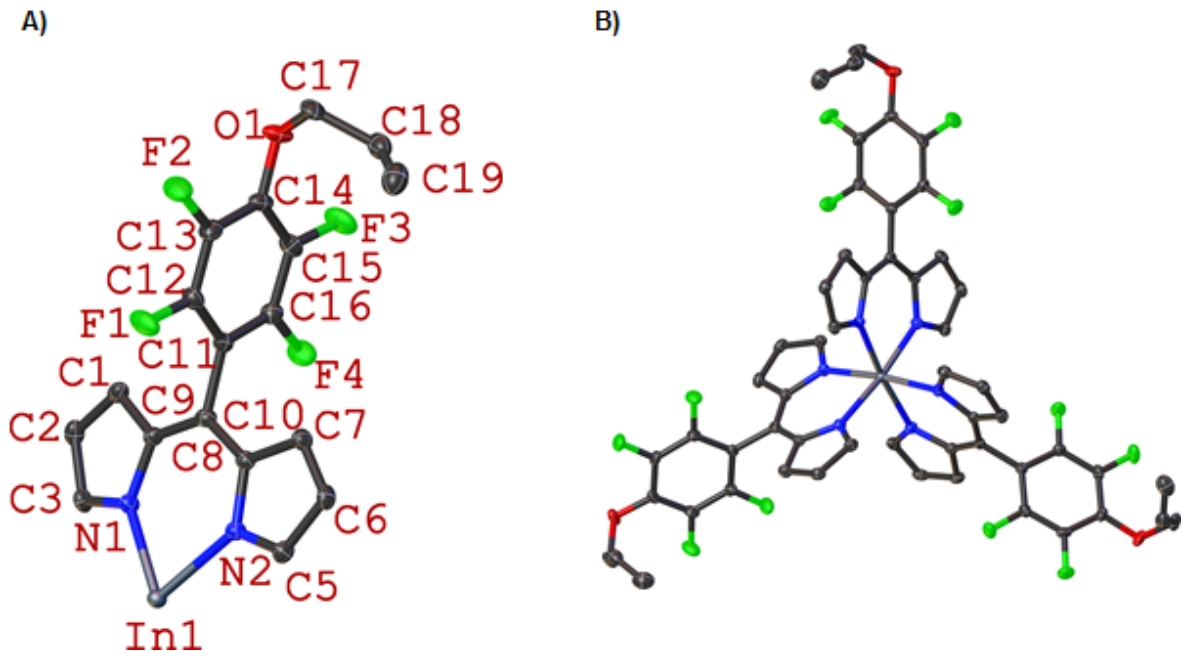

Figure 2:39: View of the asymmetric unit of with all non-hydrogen atoms labelled (A) and the complete molecular structure without labels (B) of complex **2:20**. Hydrogen atoms have been omitted for clarity. Thermal ellipsoids give 50% probability.

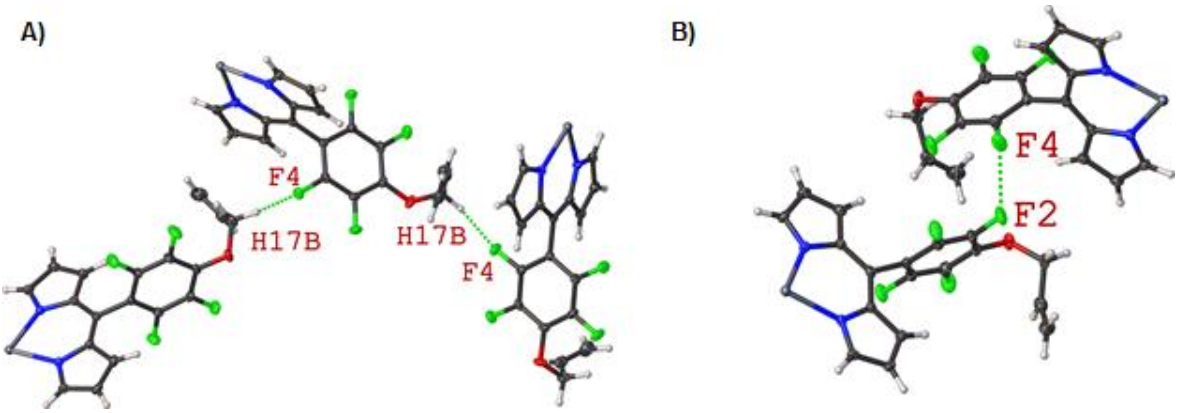

Figure 3:40: Expanded structure of complex **2:20** (only the asymmetric unit is shown to give a clearer image of the interactions) showing the intermolecular H···F interactions (A) C17–H17B···F4 (2.319(1) Å, 134.1(1)°) and the F···F contact (B) (F2···F4 (2.765(2) Å, 129.6(2)°). Thermal ellipsoids give 50% probability.

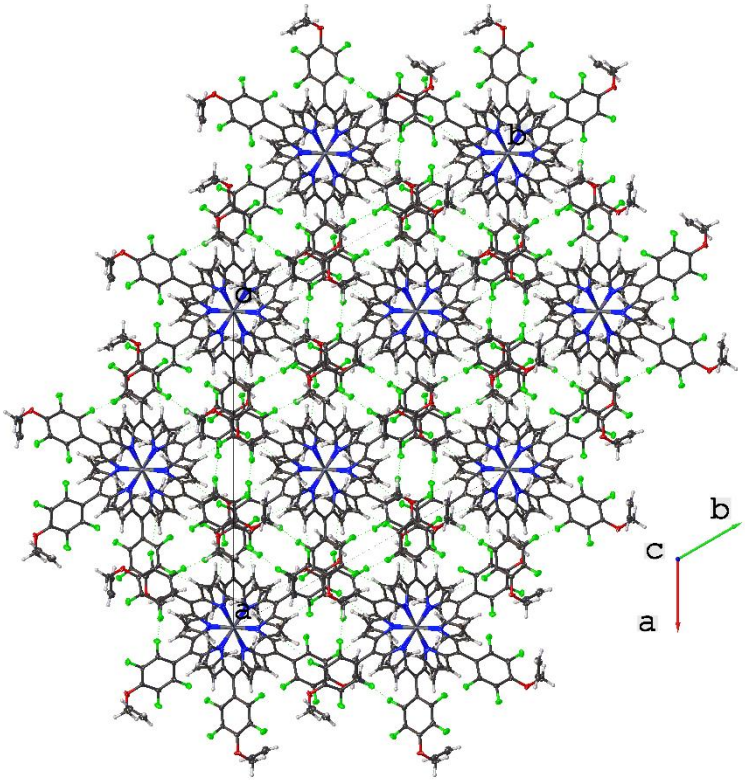

Figure 2:41: View of the crystal packing of complex **2:20** along the *c*-axis. Thermal ellipsoids give 50% probability.

Overall, the structures of **2:18**, **2:19**, and **2:20** form a tight packing pattern. Both the structure of **2:18** and **2:20** displays a shorter distance between the metal(III) centres of neighbouring molecules (compound **2:17** and **2:16**, respectfully). In comparison to PFP counterpart (**2:16**), compound **2:20**. The main difference between packing of compound **2:18**–**2:20** and with the PFP complexes **2:16** and **2:17**, is the participation of the substituted 4-position (**2:20:** allyloxy, **2:18** and **2:19:** butoxy) with interactions to fluorine groups rather than the pyrrole rings exclusively. This results in more space around the fluorinated phenyl rings, causing the metal(III) centres to be closer together, forming an attractive highly symmetric packing pattern. Comparing the space groups of compounds (**2:17** with **2:18** and **2:20** with **2:16**) shows a marked increase in the symmetry, going from orthorhombic (Pbca) to triagonal ($R\bar{3}$) for **2:17** and monoclinic ($P2_1/n$) to trigonal ($R\bar{3}$) for compound **2:20**. With the Fe(III) complex also favouring the trigonal ($R\bar{3}$) and containing similar short contacts suggests that while the H···F contacts may be weak interactions, they are highly favoured in these *para*-substituted analogues.

Conclusion.

To conclude, in this section, there are two effects. The first is caused by the metal(III) centres. This is clearly seen by the difference in the packing of compound **2:16** and **2:17**, where two compounds with the same DPM ligand, resulting in two distinct sets of F···H interactions, which affect the packing of both structures. The differences in N–M bond length between the ligand and metal(III) centre and a larger N–M–N angle impact the potential F···H interaction and cause the formation of two distinct packing types. The second effect is caused by the substitution of the *para*-fluorine of the PFP moiety where the introduction of the alkyl chains introduces a hydrogen-rich moiety, increasing the potential for F···H interactions to occur. Rather than complicating the packing pattern further, the opposite effect is seen when the symmetry of the structure is increased and the resulting packing pattern is less determined by the metal(III) centre. This also forms a highly artistic packing pattern resulting in the kaleidoscope of crystals.

Outlook.

For the future work of this project, it would be necessary to examine how alternate functional groups substituted to the *para*-position of the phenyl ring can affect the crystal packing of such structures. As we have shown, the H···F interactions will interact in the most favourable conformation, moving from pyrrole hydrogen contacts to that of the ether chain. This has the effect of moving from low symmetry space groups to high symmetry space groups. By doing this one can also investigate how different functional group will interact with fluorine atoms (either promoting interactions or isolating them) and how this will affect the packing of these structures. As shown by Gutsche *et al*. the para-fluorine atom is highly susceptible nucleophilic substitution which offers great potential in modifying the molecules shown herein. The final path one could take is to examine how the use of alternate metal centres, such as molybdenum, iridium, aluminium, etc. and how they would affect the packing.

Experimental.

Crystals were grown following the protocol developed by Hope by dissolving the compounds in either DCM or a DCM/MeOH mixture and allowing for slow evaporate over time.[137] Single crystal X-ray diffraction data for all compounds were collected on a Bruker APEX 2 DUO CCD diffractometer by using graphite-monochromated MoK_α (λ = 0.71073 Å) radiation and Incoatec IμS CuK_α (λ = 1.54178 Å) radiation. Crystals were mounted on a MiTeGen MicroMount and collected at 100(2) K by using an Oxford Cryosystems Cobra low-temperature device. Data were collected by using omega and phi scans and were corrected for Lorentz and polarization effects by using the APEX software suite.[138] Using Olex2, the structure was solved with the XT structure solution program, using the intrinsic phasing solution method and refined against $|F^2|$ with XL using least squares minimization.[139] Hydrogen atoms were generally placed in geometrically calculated positions and refined using a riding model. Details of data refinements can be found in Table E2:1–E2:5. All images were prepared by using Olex2.[139a]

Crystal Data for compound 2:2: The C-bound H atoms were placed in their expected calculated positions and refined as riding model: C–H = 0.95–0.98 Å, with U_{iso}(H) = 1.5 U_{eq}(C) for methyl H atoms and 1.2 U_{eq} (C) for all other atoms other H atoms. Due to a large solvent-accessible void but no significant density to model, the structure was squeezed using platon squeeze.[141]

Crystal Data for compound 2:3: The C-bound H atoms were placed in their expected calculated positions and refined as riding model: C–H = 0.95–0.98 Å, with U_{iso}(H) = 1.5 U_{eq}(C) for methyl H atoms and 1.2 U_{eq} (C) for all other atoms other H atoms. No constraints or restraints were applied.

Crystal Data for compound 2:4: The C-bound H atoms were placed in their expected calculated positions and refined as riding model: C–H = 0.95–0.98 Å, with U_{iso}(H) = 1.5 U_{eq}(C) for methyl H atoms and 1.2 U_{eq} (C) for all other atoms other H atoms. No constraints or restraints were applied.

Crystal Data for compound 2:4-T: The C-bound H atoms were placed in their expected calculated positions and refined as riding model: C–H = 0.95–0.98 Å, with U_{iso}(H) = 1.5 U_{eq}(C) for methyl H atoms and 1.2 U_{eq} (C) for all other atoms other H atoms. The structure was modelled containing one toluene molecule that was

projected over symmetry in a 50:50% occupancy. This toluene molecule was fixed using restraints (ISOR, DFIX, SADI, FLAT, RIGU, and SIMU). The methyl group at C29 was modelled over two positions in a 36:64% occupancy using a constraint (EADP). Missing reflections are a result of only 99.4% completion of the collection.

Crystal Data for compound 2:5: The C-bound H atoms were placed in their expected calculated positions and refined as riding model: C–H = 0.95–0.98 Å, with U_{iso}(H) = 1.5 U_{eq}(C) for methyl H atoms and 1.2 U_{eq} (C) for all other atoms other H atoms. Two C-alerts present in the cifcheck relating to the high value of R_{int} and large K value are associated with the very weak reflections in the high angle data.

Crystal Data for compound 2:6: The C-bound H atoms were placed in their expected calculated positions and refined as riding model: C–H = 0.95–0.98 Å, with U_{iso}(H) = 1.5 U_{eq}(C) for methyl H atoms and 1.2 U_{eq} (C) for all other atoms other H atoms. Solvent chloroform molecules were modelled over four positions and fixed using restraints (SADI, DFIX, and ISOR) in a 50:27:13:10% occupancy.

Crystal Data for compound 2:7: The C-bound H atoms were placed in their expected calculated positions and refined as riding model: C–H = 0.95–0.98 Å, with U_{iso}(H) = 1.5 U_{eq}(C) for methyl H atoms and 1.2 U_{eq} (C) for all other atoms other H atoms. Solvent molecules (CH_2Cl_2 and MeOH) the structure was squeezed using platon squeeze as no reliable solution could be modelled.[141] Large K value in the Analysis of Variance is associated with the very weak reflections in the high angle data. No C-C Bonds with Positive Residual Density is associated with the very weak reflections in the high angle data.

Crystal Data for compound 2:8: The C-bound H atoms were placed in their expected calculated positions and refined as riding model: C–H = 0.95–0.98 Å, with U_{iso}(H) = 1.5 U_{eq}(C) for methyl H atoms and 1.2 U_{eq} (C) for all other atoms other H atoms. Missing reflections are a result of only 99% completion of the collection.

Crystal Data for compound 2:9: The C-bound H atoms were placed in their expected calculated positions and refined as riding model: C–H = 0.95–0.98 Å, with U_{iso}(H) = 1.5 U_{eq}(C) for methyl H atoms and 1.2 U_{eq} (C) for all other atoms other H atoms. No restraint or constraints were applied.

Crystal Data for compound 2:10: The C-bound H atoms were placed in their expected calculated positions and refined as riding model: C–H = 0.95–0.98 Å, with U_{iso}(H) = 1.5 U_{eq}(C) for methyl H atoms and 1.2 U_{eq} (C) for all other atoms other H atoms. The methyl groups at the α-positions (C3 and C5) and the β-positions (C1 and C7) were modelled in two positions using restraints (ISOR, SADI, and DFIX) and constraint (EDAP) in a 90:10% occupancy.

Crystal Data for compound 2:11: The C-bound H atoms were placed in their expected calculated positions and refined as riding model: C–H = 0.95–0.98 Å, with U_{iso}(H) = 1.5 U_{eq}(C) for methyl H atoms and 1.2 U_{eq} (C) for all other atoms other H atoms. Two individual data collections on one crystal were merged together to get complete data for this structure. The overall structure was refined as a two-component inversion twin.

Crystal Data for compound 2:12: The C-bound H atoms were placed in their expected calculated positions and refined as riding model: C–H = 0.95–0.98 Å, with U_{iso}(H) = 1.5 U_{eq}(C) for methyl H atoms and 1.2 U_{eq} (C) for all other atoms other H atoms. The perylene unit to the second residue was modelled over two positions to using restraints (ISOR and SADI) and constraints (EADP) in a 50:50% occupancy. The boron difluoride moiety of residue two was modelled over two positions in an 87:13% occupancy. Theta full value too low is associated with the very weak reflections in the high angle data. Residual electron density larger than normal close to C17_1 is due to the large disorder around the perylene moiety. Due to the high disorder and weak high angle data, a high wR2 value is noted with the structure. Residual electron density larger than normal close to C17_1 is due to the large disorder around the perylene moiety. Due to the large disorder associated with perylene moiety a large residual density is noted within the structure. Low bond precision on C-C bonds is associated with the very weak reflections in the high angle data. Large K value in the analysis of variance is associated with the very weak reflections in the high angle data. Missing reflection is associated with the very weak reflections in the high angle data.

Crystal Data for compound 2:13: The C-bound H atoms were placed in their expected calculated positions and refined as riding model: C–H = 0.95–0.98 Å, with U_{iso}(H) = 1.5 U_{eq}(C) for methyl H atoms and 1.2 U_{eq} (C) for all other atoms other H atoms. The BODIPY moiety was modelled over two positions and the constraint

(EAPD) was applied in a 75:25% occupancy. The epoxide units have been modelled over two positions mirroring each other either the side of the anthracene molecule. The constraint (EAPD) was applied in a 75:25% occupancy.

Crystal Data for compound 2:14: The C-bound H atoms were placed in their expected calculated positions and refined as riding model: C–H = 0.95–0.98 Å, with U_{iso}(H) = 1.5 U_{eq}(C) for methyl H atoms and 1.2 U_{eq} (C) for all other atoms other H atoms. The alert B referring to a small average Tau for a cyclohexane C23 -C28 has been reviewed and has no implications to this structure. Crystal structures with an almost completely planar ring have been reported20 indicating that this is not an independent or unique feature to this structure. The hydrogen atoms of the methyl group C16 have been modelled over two positions in a 51 and 49% occupancy ratio. The length of the hydrogen-oxygen distance of the methanol group (O36-H36) was restrained using the DFIX command. The molecule contains several chiral centres at C17 (R), C24 (R), C26 (S), and C29 (R).

Crystal Data for compound 2:15: The C-bound H atoms were placed in their expected calculated positions and refined as riding model: C–H = 0.95–0.98 Å, with U_{iso}(H) = 1.5 U_{eq}(C) for methyl H atoms and 1.2 U_{eq} (C) for all other atoms other H atoms. The CH_2Cl_2 group was modelled at half occupancy and for the attached hydrogen atoms their distance was fixed using restraints (DFIX).

Crystal Data for compound 2:16: The C-bound H atoms were placed in their expected calculated positions and refined as riding model: C–H = 0.95–0.99 Å, with U_{iso}(H) = 1.2 U_{eq} (C) for H atoms. No constraints or restraints were applied.

Crystal Data for compound 2:17: The C-bound H atoms were placed in their expected calculated positions and refined as riding model: C–H = 0.95–0.99 Å, with U_{iso}(H) = 1.2 U_{eq} (C) for H atoms. No constraints or restraints were applied.

Crystal Data for compound 2:18: The C-bound H atoms were placed in their expected calculated positions and refined as riding model: C–H = 0.95–0.98 Å, with U_{iso}(H) = 1.5 U_{eq}(C) for methyl H atoms and 1.2 U_{eq} (C) for all other atoms other H atoms. No constraints or restraints were applied.

Crystal Data for compound 2:19: The C-bound H atoms were placed in their expected calculated positions and refined as riding model: C–H = 0.95–0.98 Å, with

U_{iso}(H) = 1.5 U_{eq}(C) for methyl H atoms and 1.2 U_{eq} (C) for all other atoms other H atoms. No constraints or restraints were applied.

Crystal Data for compound 2:20: The C-bound H atoms were placed in their expected calculated positions and refined as riding model: C–H = 0.95–0.99 Å, with U_{iso}(H) = 1.2 U_{eq} (C) for H atoms. No constraints or restraints were applied.

Table E2:1: Details of XRD data refinement

Compound	**2:2**	**2:3**	**2:4**	**2:4-T**
Empirical formula	$C_{24}H_{17}BF_2N_2$	$C_{26}H_{21}BF_2N_2$	$C_{28}H_{25}BF_2N_2$	$C_{63}H_{58}B_2F_4N_4$
Formula weight	382.20	410.26	438.31	968.75
Temperature/K	99.99	100.0	100.0	100.0
Crystal system	Monoclinic	Monoclinic	Triclinic	Triclinic
Space group	$P2_1/n$	C2/c	$P\bar{1}$	$P\bar{1}$
a/Å	14.2177(13)	13.2460(6)	7.2381(6)	8.5680(10)
b/Å	13.2738(11)	12.7829(6)	9.7454(9)	9.7581(11)
c/Å	19.7784(17)	12.8418(6)	16.9374(15)	15.2034(18)
α/°	90	90	75.307(3)	101.961(2)
β/°	95.067(2)	114.6700(10)	83.691(2)	91.811(2)
γ/°	90	90	70.111(4)	99.856(2)
Volume/Å^3	3718.1(6)	1975.94(16)	1086.37(17)	1222.2(2)
Z	8	4	2	1
D_{calc} g/cm^3	1.366	1.379	1.340	1.316
μ/mm^{-1}	0.094	0.093	0.09	0.087
F(000)	1584.0	856.0	460.0	510.0
Crystal size/mm^3	0.30×0.12×0.12	0.29×0.15×0.14	0.30×0.10×0.10	0.53×0.43×0.24
Radiation	MoKα	MoKα	MoKα	MoKα
Wavelength/Å	λ = 0.71073	λ = 0.71073	λ = 0.71073	λ = 0.71073
2θ/°	3.39–55.04	4.648–55.032	4.568–50.998	4.34–51.052
Reflections collected	61492	31215	14965	25783
Independent reflections	8548	2391	4042	4651
R_{int}	0.0521	0.0312	0.0509	0.0417
R_{sigma}	0.0349	0.0125	0.0562	0.0296
Restraints	0	0	0	166
Parameters	525	153	303	360
GooF	1.012	1.053	1.016	1.055
R_1 [I> 2σ (I)]	0.0416	0.0395	0.0440	0.0570
wR_2 [I> 2σ (I)]	0.0914	0.1016	0.1015	0.1524
R_1 [all data]	0.0672	0.0474	0.0831	0.0781
wR_2 [all data]	0.1032	0.1066	0.1129	0.1717
Largest peak/e Å^{-3}	0.30	0.38	0.28	0.66
Deepest hole/e Å^{-3}	-0.24	-0.22	-0.25	-0.51
Flack parameter	--	--		--

Table E2:2: Details of XRD data refinement

Compound	**2:5**	**2:6**	**2:7**	**2:8**
Empirical formula	$C_{32}H_{33}BF_2N_2$	$C_{26}H_{20}BCl_3F_2N_2$	$C_{31}H_{23}BF_2N_2$	$C_{37}H_{27}BF_2N_2$
Formula weight	494.41	515.60	472.32	548.41
Temperature/K	100.0	100.0	100.01	100.0
Crystal system	Monoclinic	Monoclinic	Triclinic	Triclinic
Space group	$P2_1/c$	P2/c	$P\bar{1}$	$P\bar{1}$
a/Å	15.836(6)	14.2315(15)	8.9484(18)	10.3605(16)
b/Å	20.573(7)	11.3053(12)	9.6443(19)	13.301(2)
c/Å	7.781(3)	15.4276(16)	17.849(4)	21.611(4)
α/°	90	90	87.62(3)	76.897(3)
β/°	101.878(8)	93.737(2)	77.07(3)	82.836(6)
γ/°	90	90	68.24(3)	73.801(5)
Volume/Å^3	2480.7(15)	2476.9(5)	1392.9(6)	2779.5(8)
Z	4	4	2	4
D_{calc} g/cm^3	1.324	1.383	1.126	1.311
μ/mm^{-1}	0.087	0.403	0.075	0.680
F(000)	1048.0	1056.0	492.0	1144.0
Crystal size/mm^3	0.6×0.05×0.05	0.28×0.2×0.06	0.18×0.09×0.02	0.26×0.1×0.03
Radiation	MoKα	MoKα	MoKα	CuKα
Wavelength/Å	λ = 0.71073	λ = 0.71073	λ = 0.71073	λ = 1.54178
2θ/°	3.29–51	3.602–50.98	2.344–52.336	4.206–136.41
Reflections collected	58475	30226	37805	54487
Independent reflections	4627	4620	5542	10075
R_{int}	0.1328	0.0633	0.0934	0.0617
R_{sigma}	0.0715	0.0395	0.0758	0.0420
Restraints	0	307	0	0
Parameters	341	421	327	761
GooF	1.013	1.013	1.021	1.054
R_1 [I>=2σ (I)]	0.0483	0.0480	0.0563	0.0473
wR_2 [I>=2σ (I)]	0.0937	0.1102	0.1156	0.1227
R_1 [all data]	0.1076	0.0849	0.1163	0.0645
wR_2 [all data]	0.1125	0.01289	0.1348	0.1347
Largest peak/e Å^{-3}	0.19	0.37	0.22	0.17
Deepest hole/e Å^{-3}	-0.23	-0.45	-0.24	-0.29
Flack parameter	--	--	--	--

Table E2:3: Details of XRD data refinement

Compound	**2:9**	**2:10**	**2:11**	**2:12**
Empirical formula	$C_{25}H_{15}BF_2N_2$	$C_{29}H_{23}BF_2N_2$	$C_{33}H_{31}BF_2N_2$	$C_{37}H_{33}BF_2N_2$
Formula weight	392.20	448.30	504.41	554.46
Temperature/K	100.01	99.99	99.99	100.01
Crystal system	Monoclinic	Orthorhombic	Monoclinic	Monoclinic
Space group	$P2_1/c$	$P2_12_12_1$	Cc	$P2_1/n$
a/Å	17.082(17)	8.5915(4)	7.8654(2)	7.8092(3)
b/Å	8.600(12)	11.3514(6)	44.0642(11)	30.8205(11)
c/Å	13.632(14)	23.2887(11)	14.9251(4)	23.4106(9)
α/°	90	90	90	90
β/°	112.854(15)	90	91.213(2)	95.314(2)
γ/°	90	90	90	90
Volume/Å³	1845(4)	2271.24(19)	5171.6(2)	5610.3(4)
Z	4	4	8	8
D_{calc} *g/cm³*	1.412	1.311	1.296	1.313
μ/mm⁻¹	0.097	0.087	0.676	0.675
F(000)	808.0	936.0	2128.0	2336.0
Crystal size/mm³	0.37×0.27×0.03	0.60×0.10×0.07	0.50×0.20×0.06	0.26×0.09×0.03
Radiation	MoKα	MoKα	CuKα	CuKα
Wavelength/Å	λ = 0.71073	λ = 0.71073	λ = 1.54178	λ = 1.54178
2θ/°	5.176–54.268	3.498–62.28	4.01–135.99	4.752–136.504
Reflections collected	43889	92743	60945	48293
Independent reflections	4028	7314	9342	10233
R_{int}	0.0304	0.0651	0.0505	0.0685
R_{sigma}	0.0104	0.0303	0.0311	0.0576
Restraints	0	78	2	896
Parameters	271	309	698	934
GooF	1.034	1.022	1.043	1.039
R_1 *[I>=2σ (I)]*	0.0354	0.0408	0.0392	0.0873
wR_2 *[I>=2σ (I)]*	0.0875	0.0916	0.1050	0.2367
R_1 *[all data]*	0.0464	0.0536	0.0407	0.1094
wR_2 *[all data]*	0.0952	0.0981	0.1063	0.2561
Largest peak/e Å⁻³	0.29	0.33	0.22	0.86
Deepest hole/e Å⁻³	-0.22	-0.65	-0.21	-0.36
Flack parameter	--	-0.06(18)	0.23(13)	--

Table E2:4: Details of XRD data refinement

Compound	**2:13**	**2:14**	**2:15**	**2:16**
Empirical formula	$C_{28}H_{21}BF_2N_2O_2$	$C_{27}H_{25}BF_2N_2O_5$	$(C_{26}H_{21}BF_2N_2O_2)$ $0.5(CH_2Cl_2)$	$C_{45}H_{18}F_{15}InN_6$
Formula weight	466.28	506.30	484.72	1042.47
Temperature/K	100.0	99.99	100.0	100.04
Crystal system	Monoclinic	Triclinic	Monoclinic	Monoclinic
Space group	Cc	$P\bar{1}$	$P2_1/n$	$P2_1/n$
a/Å	14.9120(5)	6.3949(3)	17.3115(10)	10.5034(8)
b/Å	21.0584(7)	9.4233(5)	6.4766(4)	13.5594(11)
c/Å	7.2943(3)	20.1050(10)	20.9257(12)	28.179(2)
α/°	90	80.269(2)	90	90
β/°	101.100(2)	83.793(2)	107.061(2)	93.7280(10)
γ/°	90	70.715(2)	90	90
Volume/Å^3	2247.73(14)	1125.33(10)	2242.9(2)	4004.7(5)
Z	4	2	4	4
D_{calc} g/cm^3	1.378	1.494	1.435	1.729
μ/mm^{-1}	0.805	0.113	0.216	0.704
F(000)	968.0	528.0	1004.0	2056.0
Crystal size/mm^3	0.20×0.10×0.05	0.50×0.20×0.09	0.20×0.20×0.08	0.34×0.11×0.10
Radiation	CuKα	MoKα	MoKα	MoK_α
Wavelength/Å	λ = 1.54178	λ = 0.71073	λ = 0.71073	0.71073
2θ/°	7.356–136.53	5.324–55.39	5.39–50.78	2.90-50.75
Reflections collected	16154	24467	33492	49555
Independent reflections	4076	5164	4113	7365
R_{int}	0.0386	0.0494	0.0916	0.0162
R_{sigma}	0.0355	0.0421	0.0476	0.0096
Restraints	10	1	1	0
Parameters	356	425	336	604
GooF	1.044	1.036	1.036	1.092
R_1 [I>=2σ (I)]	0.0751	0.0481	0.0426	0.0204
wR_2 [I>=2σ (I)]	0.2031	0.1051	0.0856	0.0460
R_1 [all data]	0.0780	0.0762	0.0773	0.0220
wR_2 [all data]	0.2081	0.1164	0.0977	0.0469
Largest peak/e Å^{-3}	0.91	0.35	0.23	0.31
Deepest hole/e Å^{-3}	-0.28	-0.48	-0.31	-0.34
Flack parameter	0.3(4)	--	--	--

Table E2:5: Details of XRD data refinement

Compound	**2:17**	**2:18**	**2:19**	**2:20**
Empirical formula	$C_{45}H_{18}F_{15}GaN_6$	$C_{57}H_{45}F_{12}GaN_6O_3$	$C_{57}H_{45}F_{12}FeN_6O_3$	$C_{54}H_{33}F_{12}InN_6O_3$
Formula weight	997.37	1159.71	1145.84	1156.68
Temperature/K	100(2)	100(2)	100.01	100(2)
Crystal system	Orthorhombic	Trigonal	Trigonal	Trigonal
Space group	Pbca	$R\bar{3}$	$R\bar{3}$	$R\bar{3}$
a/Å	25.7650(8)	24.0883(10)	24.0020(11)	23.433(3)
b/Å	8.8371(3)	24.0883(10)	24.0020(11)	23.433(3)
c/Å	35.7783(11)	15.2527(7)	15.1852(9)	15.332(5)
α/°	90	90	90	90
β/°	90	90	90	90
γ/°	90	120	120	120
Volume/Å^3	8146.3(5)	7664.6(7)	7576.1(8)	7291(3)
Z	8	6	6	6
D_{calc} g/cm^3	1.626	1.508	1.507	1.581
μ/mm^{-1}	1.940	0.635	3.253	0.585
F(000)	3968.0	3552.0	3522.0	3480.0
Crystal size/mm^3	0.37×0.16×0.09	0.5×0.08×0.08	0.6×0.06×0.02	0.5×0.03×0.03
Radiation	CuK_α	MoK_α	CuK_α	MoK_α
Wavelength/Å	1.54178	0.71073	1.54178	0.71073
2θ/°	4.94-136.59	3.31-63.02	7.21-138.40	4.81-52.58
Reflections collected	52826	93276	31292	48936
Independent reflections	7436	5684	3129	3274
R_{int}	0.0834	0.0443	0.1428	0.0954
R_{sigma}	0.0519	0.0247	0.0980	0.0385
Restraints	0	0	0	0
Parameters	604	239	239	229
GooF	1.044	1.046	1.056	1.027
R_1 [I>=2σ (I)]	0.477	0.341	0.0605	0.0308
wR_2 [I>=2σ (I)]	0.1127	0.0710	0.1562	0.0591
R_1 [all data]	0.0679	0.0528	0.0739	0.0533
wR_2 [all data]	0.1234	0.0778	0.1686	0.0656
Largest peak/e Å^{-3}	0.59	0.45	0.47	0.33
Deepest hole/e Å^{-3}	-0.44	-0.40	-0.51	-0.42
Flack parameter	--	--	--	--

Chapter 3:
Cubane Crystal Engineering.

Introduction.

Cubanes.

Cubane, since its discovery has been a hallmark molecule in organic chemistry due to its exceptional structure, symmetry, and pronounced strain.[162] It holds the top position for highest density hydrocarbon known and as a results has an incredibly high strain energy which leads cubane to be used in fields such as high energy fuels and explosives.[163]

Due to its geometry, the cubane system departures from classical sp^3 hybridisation. To alleviate ring strain, the C–C bonds adopt more p-character while the exocyclic carbon orbital used for the C–H bond compensates by becoming more s-electron rich. By calculating the ^{13}C-^{1}H coupling constant of 150.5 Hz, Della *et al.* have estimated the s-character of the C–H bonds in cubane as 30.1%.[164] This compares with a value of around 26% in adamantane and more closely approximates as an sp^2 hybridised system (33% s) than an sp^3 (25% s). This has the knock-on effect of causing the hydrogen atoms of cubane to be more acidic in character compared to conventional saturated hydrocarbons. For example the kinetic acidity of cubane is approximately 63,000 times greater than that of cyclohexane.[165] While this is still too low to be of direct synthetic use, this nature of the acidic hydrogens has strong potential as a non-classical hydrogen-bonding system in terms of crystal engineering.

Considering the geometry of cubane, it is noteworthy that the distance across the cube (the body diagonal) is 2.72 Å, which is almost equivalent to the distance across a benzene ring, (2.79 Å).[166] This implies that, given robust substitution procedures, cubane could conceivably be used as a (nontoxic) isostere of benzene.[167] With this in mind there is a need to determine how cubane and its derivatives interact with their environment to determine if there is more potential for this simple scaffold in the realm of crystal engineering.

Crystal Engineering of Cubane Complexes.

While cubanes offer diverse and intriguing possibilities due to their inherent 3D geometry for interaction studies, this field has been limited due to their complex synthesis and lack of derivatives. Recently, we published an improved methodology for aryl-cubane cross-coupling through the use of redox-active esters as developed

by the Baran group, to improve the scope of potential cubane compounds.[168] This now allows for the investigation of previously unobtainable cubane complexes with regard to unseen interaction patterns in the solid state using single crystal X-ray diffraction.

Why cubane interactions? While this question has many answers, ranging from their aesthetic beauty to fundamental relevance, one reason is the subject of bioisosteres. In 1992, Eaton postulated that cubane, due to its size and shape, would make an ideal bioisostere for a phenyl ring.[162a] In this regards, there has been plenty of research into the use of cubane-containing molecules as pharmaceutical and agrochemical compounds.[169] This was further verified by Chalmers *et al*.. Another application for cubane is as a rigid linker in materials chemistry as recently highlighted by us.[168a, 170]

Knowing how a drug which has been modified interacts with its environment is one of the keys to drug design and as such an important path to crystal engineering. Therefore, an interactive study into the structure of cubane and its functionalized derivatives is warranted and with over 100 structures data sets of 1,4-disubstituted cubane structures available in the CCDC database the time for such a study is ideal.

Previous studies by Desiraju and co-workers on the crystal engineering of cubane scaffolds focused on the series of 4-R-substituted-1-cubanecarboxylic acids.[171] Within this series, they demonstrated the presence of rare *syn-anti* catemers in the formation of the hydrogen-bonds (Figure 3:1). This was theorized to be a direct result of a secondary binding motif between the cubane hydrogen and carbonyl groups leading to a more favoured *syn-anti* catemer formation. Additionally, when halogens were incorporated into the 4-position of the cubane scaffold they were seen to occupy a centrosymmetric void present in these structures further stabilizing the network. When an ester (CO_2Me) is placed in the 4-position of the cubane scaffold a noticeable shift is observed towards the formation of cyclic patterns with the ester partaking in hydrogen-bonding with the hydrogen of the cubane scaffold. Moreover, in cases where the substituent at the 4-position is small (H) or large (Ph) or when an equally competitive hydrogen-bonding partner is included ($CONH_2$), the catemer is no longer formed and a more classical dimer is observed.

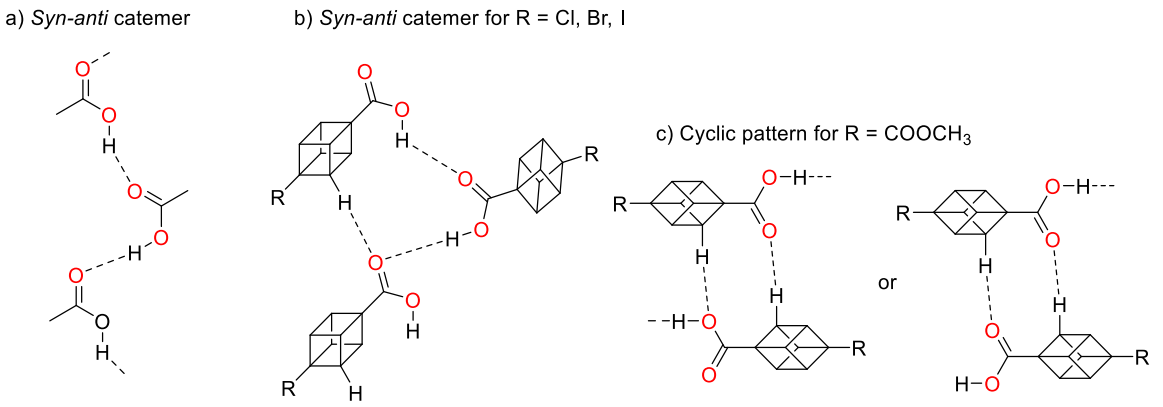

Figure 3:1: Different hydrogen-bonding interactions for 1,4-substituted cubane carboxylic acids.[172]

A further study investigated how the C–H bond of cubane is activated toward hydrogen-bond formation and its ability to support a framework with stabilizing C–H···O bonds.[173] Initially, the authors chose to work with primary cubane carboxamides to observe the formation of N–H···O hydrogen-bonds.[172b] Similar to what is observed in carboxylic acid dimers, the common motif observed for primary carboxamides is the centrosymmetric dimer with *syn*-oriented N–H groups. Additionally, *anti*-oriented N–H groups can be seen to form either a linear pattern with or without a glide plane (shallow-glide motif). Characteristically, the motif without the glide plane is related by a 5.1 Å translation to the next succeeding molecule. When a linear pattern without a glide plan occurs, the dimer motif of the commonly occurring translational ribbon synthon is formed. Notably, the primary cubane carboxamides have been shown not to utilize the ribbon motif, because the cubane skeleton is considered too bulky for the 5.1 Å translation and this results in the formation of the less sterically demanding shallow glide conformation. As before, it appears that this conformation is further reinforced by the formation of a hydrogen-bond between oxygen atoms and the cubane hydrogen (Figure 3:2). This ability is attributed to the large C-C-H pyramidality angle of the interacting hydrogen atoms present due to the tertiary and rigidity of the carbon atoms.[174] Other structural reports on cubane scaffolds exist in the literature, however, none go into quite as much detail on potential interactions. With this in mind, we performed broad scale crystallographic studies, reporting 12 new cubane structures and, together with data from the CCDC investigated the range of interactions available to cubane scaffolds and their potential implications in the field of crystal engineering. The original compound for the crystal structures was provided by Dr. Stefan Bernhard during his work in the Senge group and the X-ray crystal structure were collected by myself.

Furthermore, this work allows us to consider the possibility of structure isomers between cubane and its phenyl derivatives and how this concept may be beneficial for the prediction of a packing system in cubane analogues for crystal engineering purposes.

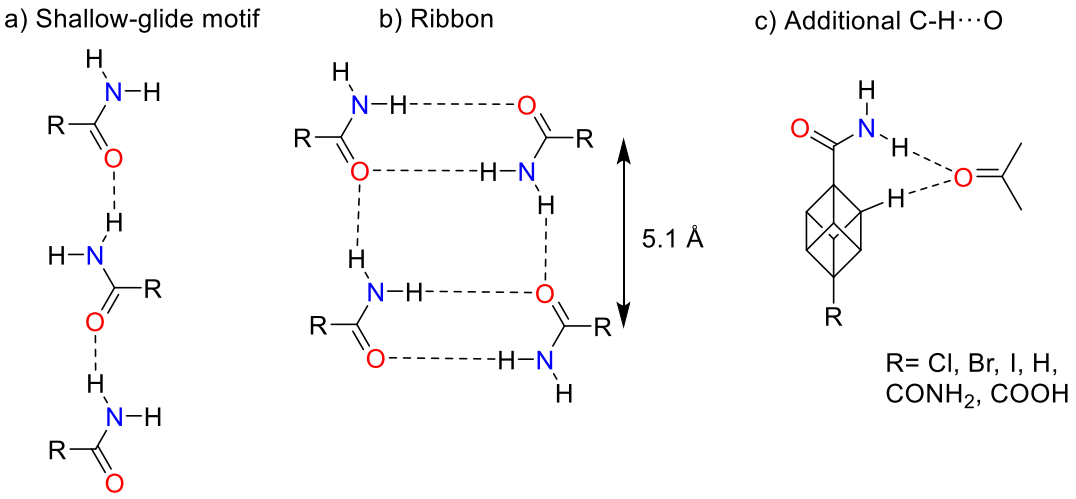

Figure 3:2: Different hydrogen-bonding motifs for 1,4-substituted cubane carboxamide compounds.[172b]

Objectives.

The objective of this chapter is to assess the environment of cubane in terms of its interaction potential. As highlighted in the general introduction, the crystal engineering expands by identifying potential synthons and applying the data to novel systems. With this in mind, this chapter will have a two-fold process. The first will be the compilation of all 1,4-disubstituted cubane structures that have been submitted to the CCDC. This will be combined in addition with recent cubane structures. The second step will be to sort all this data out into families of ,4-disubstituted cubane structures and conduct an investigation into all their intermolecular and close-packing interactions in order to discover the secrets this exotic hydrocarbon scaffold has to offer in terms of crystal engineering.

Results and Discussion.

Benzene *vs*. Cubane.

As mentioned previously, cubane has been used to an extent as a bioisostere. This topic was covered by Chalmers *et al.* among others where cubane containing drugs showed equal or increased bioactivity for *in vivo* or *in vitro* tests.[167, 169, 175] In these studies, the authors have focused on solubility, stability, tractability and the

availability of suitable precursors as the main concerns for using cubane as a bioisostere for a benzene ring.[167] However, when considering the shape of cubane and benzene, there is a world of differences between a flat molecule, i.e. benzene and the 3D architecture of cubane. As discussed by Luh *et al*. the kinetic acidity of cubane is similar to that of benzene.[165] Therefore, both compounds have an equal potential to form C–H···A contacts (where A is any hydrogen acceptor). However, cubane has two more hydrogen atoms that can participate in C–H···A contacts and the orientation of the hydrogen atoms are very different to that of benzene.

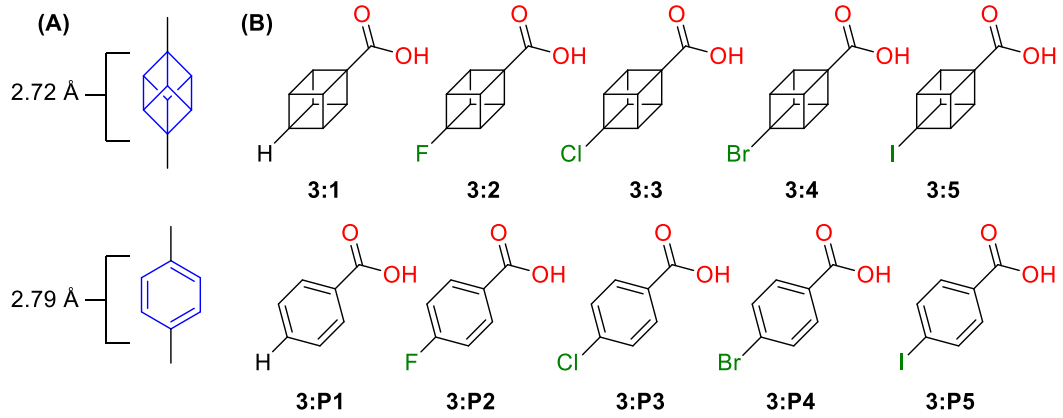

Figure 3:3: (A) Schematic representation of the distance between the 1,4-positions in cubane and benzene. (B) Literature structures of 1-carboxylic acid-4-(R)-cubane and 4-(R)-benzoic acid (where R is H, F, Cl, Br, or I).[171, 173, 176]

As a small case study, we examined the interaction profiles of 1-carboxylic acid-4-(R)-cubane and 4-(R)-benzoic acid (where R is H, F, Cl, Br, or I) to assess their differences (Figure 3:3 and 3:4). In Figure 3:4 (B, D, F, H, and J) there is a clear trend in the 4-(R)-benzoic acid compounds where the carboxylic acid moieties all form head-to-head dimers. The benzene hydrogen atoms are also seen to have favourable interactions with the carboxylic acid moiety forming a linear C–H···O network. This motif is preserved in all examples and only varies by the interactions of the substituent at the *para*-position of the benzene moiety with either halogen···halogen or halogen···hydrogen interactions observed. This is not the case for the cubane derivatives. In Figure 3:4 (A, C, E, G, and I), there is no standard pattern observed and each C–H···O network in compounds **3:1**–**3:6** is unique in the crystal packing. This shows that as the cubane scaffold has both more hydrogen atoms and 3D orientation incorporated the potential for unique packing patterns is increased dramatically. In the case of the 4-(R)-benzoic acid there is a clear case of predictability in the interaction profile. Whereas, cubane, due to its inherent

properties, makes predicting the interactions profile much harder. This leads to the current problem of using cubane as a bioisostere for a benzene or a phenyl ring. While both molecules may be of similar size, they are not of similar interaction profiles. Basing such studies on this concept relies more on trial and error than it does on design, which highlights the importance of understanding the potential interactions between the cubane hydrogen atoms and appropriate acceptor groups.

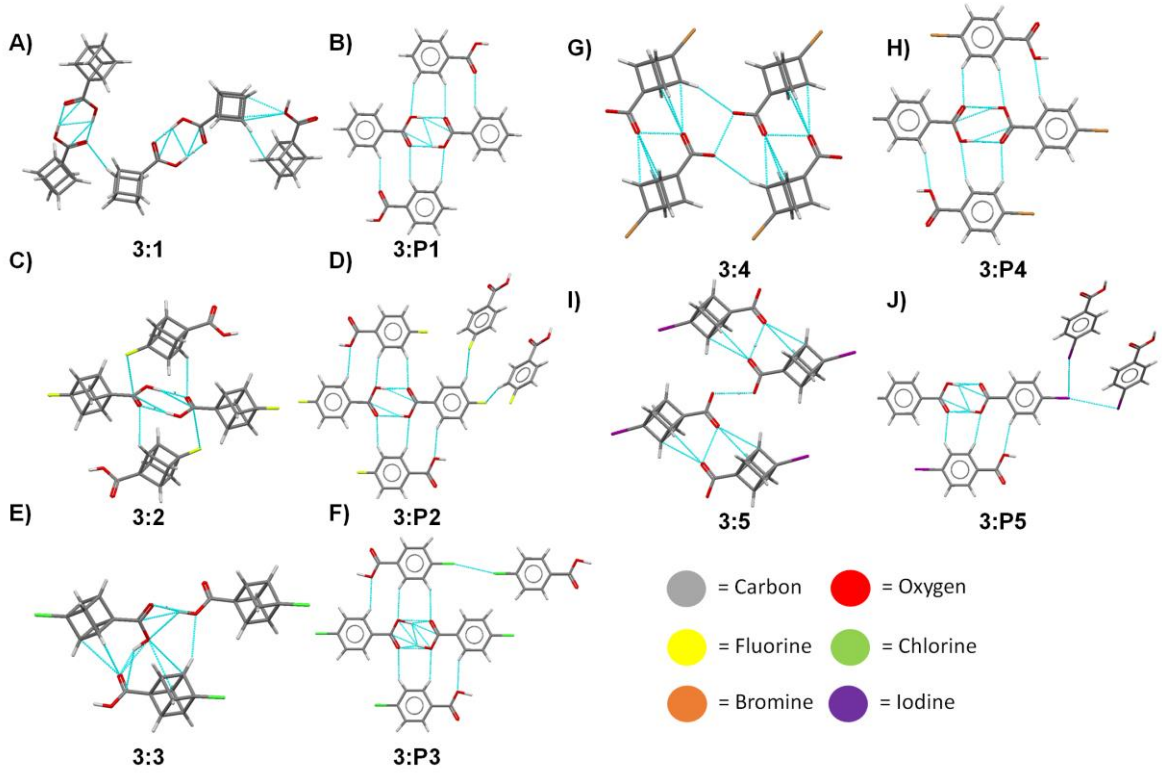

Figure 3:4: View of the molecular arrangement in the crystal of compounds **3:1** (A), **3:P1** (B), **3:2** (C), **3:P2** (D), **3:3** (E), **3:P3** (F), **3:4** (G), **3:P4** (H), **3:5** (I), and **3:P5** (J) showing the hydrogen-bonding between the carboxylic acid and the cubane/benzene hydrogen atoms. Interactions are indicated by dashed blue lines.

Carboxylic acids.

When considering acid substitution and its effects on the crystal packing of cubane structure it is necessary to look at the previous work done by Desiraju and co-workers.[171] As outlined in the introduction carboxylic acid derivatives of cubane tend to favour the formation of *syn-anti* catemers or at least this motif is more prevalent in cubane crystal structures than their phenyl counterparts. (Figure 3:5, bond lengths and angles are given in Table SI3:1).[171, 173, 177] From this relatively small sample size, it is rather interesting to note that six out of eleven of the published structures favour this *syn-anti* catemers formation. Given that the average

occurrence for this motif in the literature is quite low, this high average, within a specific family, is quite unique. Das and Desiraju have previously stated that the propensity for this motif is that it is stabilized by a supportive C–H···O interaction.[172a] It appears that the natural 3D conformation of cubane containing six available C–H interactive groups in a spatially defined pattern increases the potential of these interactions. This feature has been highlighted by Fleischer *et al*. in which the bent bonds of cubane allow for acid hydrogen atoms to be presented in several directions which are unavailable to its benzene counter-part.[178] However, this effect is only seen in certain cubane carboxylic acids (**3:3**–**3:6**, **3:9** and **3:10**). It can be seen that the 4-substituted position with the cubane scaffold plays an important role in catemer formation. In cases where the 4-position is small (**3:1** and **3:2**) or large (**3:7**), or when an equally competitive hydrogen-bonding partner is included (**3:8**), the catemer is no longer formed and a more classical dimer is observed. Additionally, when looking at the structure of compound **3:11** there is an interesting development as the NO_2 group has now taken over the interacting possible interactions with the cubane scaffold resulting in the formation of the common dimer form being observed. Further inspection of the crystal structure of **3:1**–**3:11** shows that when the *syn-anti* catemer is formed the 4-substituted position interacts less with the acidic hydrogens of the cubane scaffold than when the *syn-anti* catemer is not formed. This suggests that there is a possible competition between these interactions.

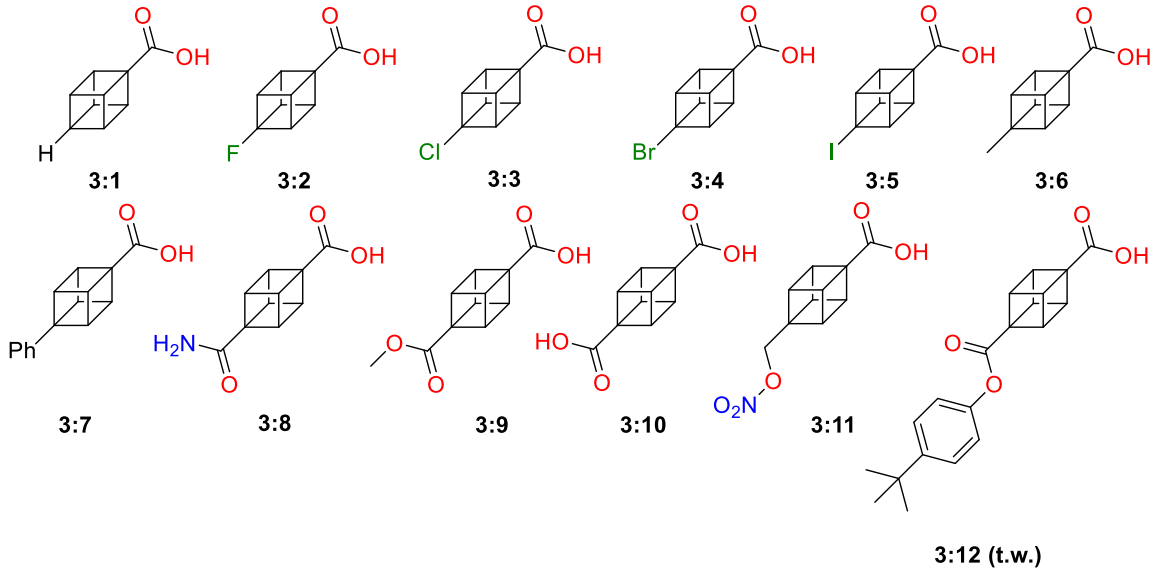

Figure 3:5: Available structures of 1,4-substituted cubane carboxylic acid derivatives. 't.w.' indicates structures obtained as part of this work. [171, 173, 177]

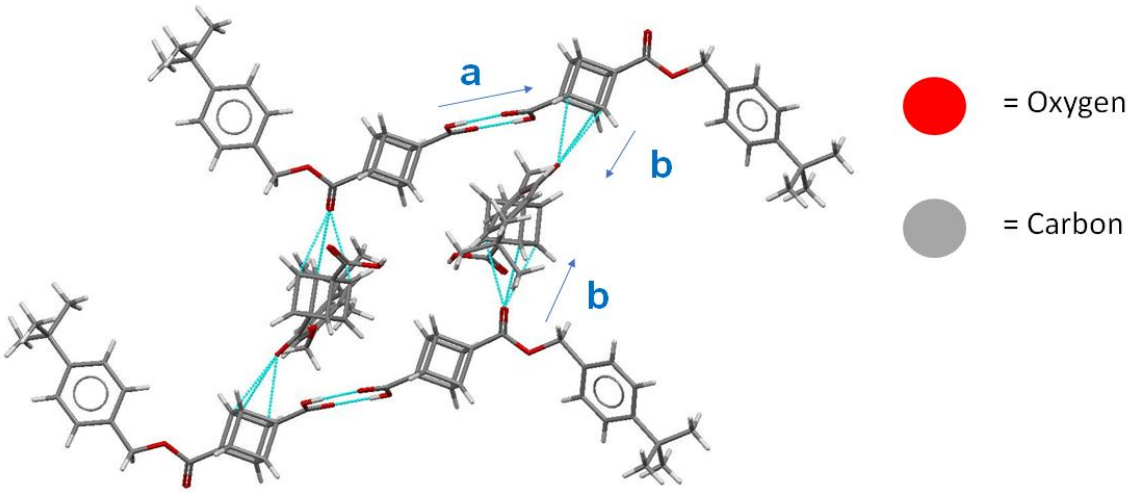

Figure 3:6: View of the molecular arrangement in the crystal of compound **3:12** showing the hydrogen-bonding between the carboxylic acid and the cubane ester interactions resulting in rotated layers. Interactions are indicated by blue dashed lines. 'a' indicated the head-to-head interactions between the carboxylic acid moiety and 'b' the interactions between the cubane and the ester group. Bond lengths and angles are given in Table 3:1 below.

Table 3:1: List of bond lengths and angles shown in Figure 3:6.

#	Interaction	H···A (Å)	D–H···A (°)
3:12	$C–H_{cubane}\cdots O$	2.713	145.0
	$C–H_{cubane}\cdots O$	2.641	131.7
	$C–H_{cubane}\cdots O$	2.682	139.7
	$C–H_{cubane}\cdots O$	2.567	134.4
	$C–H_{cubane}\cdots O$	2.705	117.1
	$C–H_{cubane}\cdots O$	2.816	87.3
	$C–H_{cubane}\cdots O$	2.945	84.2
	$C–H_{cubane}\cdots O$	3.084	81.3
	$C–H_{cubane}\cdots O$	2.568	143.6
	$C–H_{cubane}\cdots O$	2.671	131.7
	$C–H_{cubane}\cdots O$	2.710	142.6
	$C–H_{cubane}\cdots O$	2.859	84.2
	$C–H_{cubane}\cdots O$	2.938	82.5
	$C–H_{cubane}\cdots O$	2.951	81.9
	O–H···O	1.796	176.5
	O–H···O	1.806	176.9
	O–H···O	1.801	175.0
	O–H···O	1.801	175.0

One new structure has been added to this group of 1-carboxylic acid-4(R)-cubane structures. When looking at the structure of **3:12** we can see head-to-head dimer formation as expected due to the relatively large size of the 4-position substitution, Figure 3:6. There is no evidence of catemer formation within the structure and the presence of a C–H···O interaction between the ester and the cubane scaffold results in an almost orthogonal rotation between the crystal layers in the unit cell. The result is a mesh-like a hydrogen-bonded network in two directions.

Carboxamides.

In the 1-carboxamides 4-(R)-cubane structures shown in Figure 3:7 (for bond lengths and angles see Table SI3:2) an alternative hydrogen-bonding network is observed.[171, 172b] Due to the nature of these groups (**3:8**, **3:13–3:15**) and the strong hydrogen-bonding properties of carboxamides, the dimer formation is much more prevalent and thus, there is no formation of the *syn/anti* catemers which results in a greater number of interactions between the 4-position and the cubane scaffold. As shown by Kuduva *et al*. this series of structures adopt a dimer formation combined with a shallow glide motif which is unusual for carboxamides.[172b] However, it was highlighted that due to the steric bulk of cubane, the average sectional distance of 5.4 Å is too large to fit into a 5.1 Å translational motif. What is equally interesting as a counterpoint to 1-carboxylic acid-4-(R)-cubane, the 4-substituted position always aids in the formation of this shallow glide motif through halo-cubane/hydrogen-cubane interactions. Interestingly, the structure of **3:8** forms the only head-to-tail dimer present in this set which results in an *a*-glide motif.

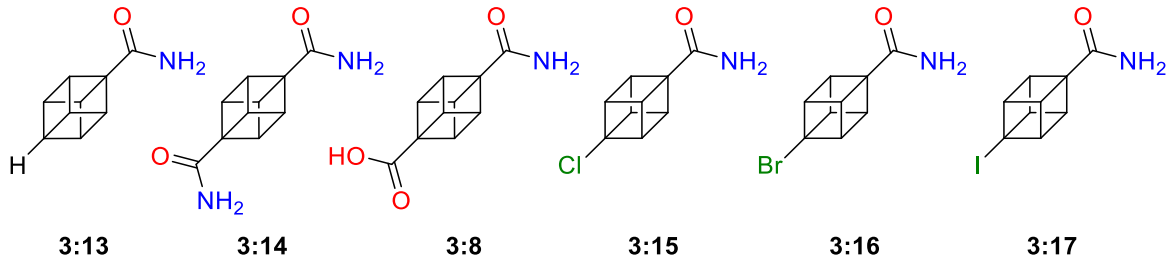

Figure 3:7: Available structures of 1,4-substituted cubane carboxamide derivatives.[171, 172b]

Esters.

To this point, we have discussed interactions that have been previously described by Desiraju and co-workers, however, a section that has not been covered until now is the connections between cubane and esters. To date, there have been 27

published structures of cubanes bearing esters in the 1-position submitted to the CCDC database (Figures 3:8, 3:21 and 3:27 and data in Table SI3:3).[168a, 171, 179] For simplicity, in each structure the oxygen atoms that are involved in each contact are numbered in Figures 3:8, 3:21 and 3:27 to allow clear indication of the atoms being discussed.

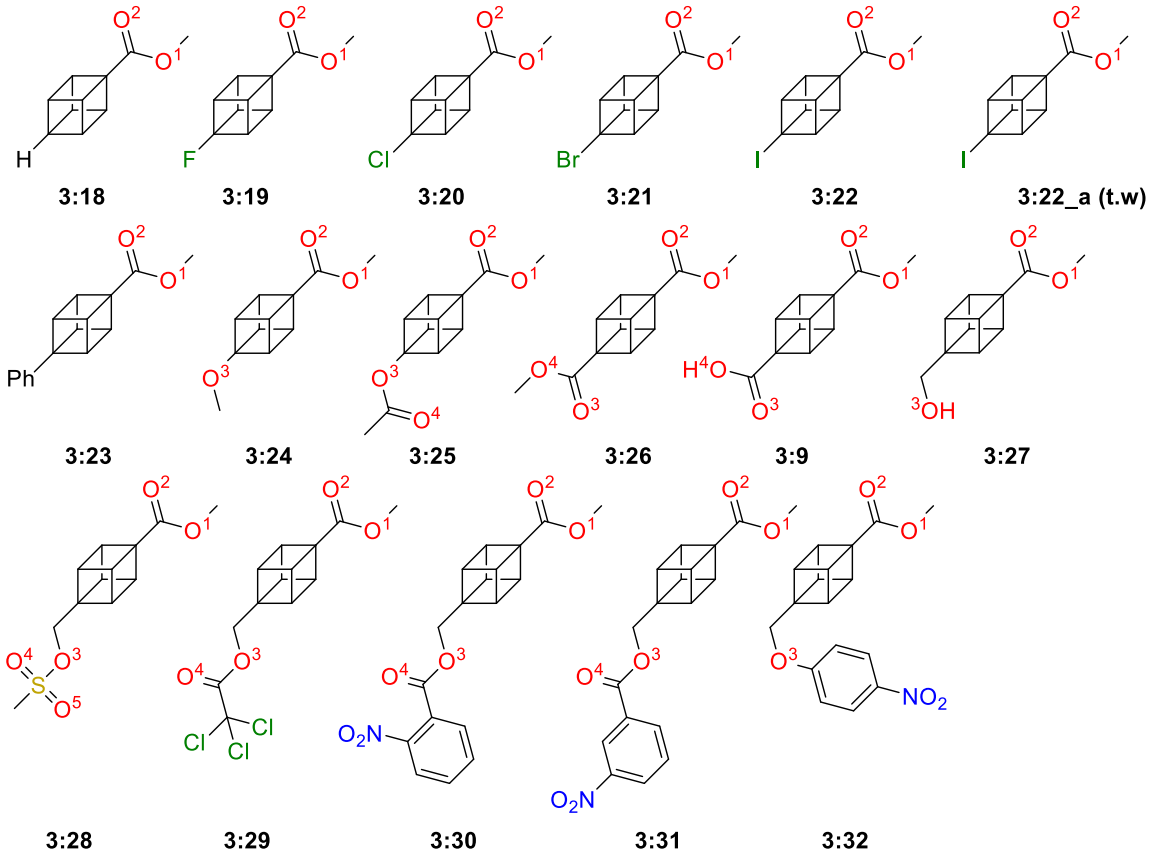

Figure 3:8: List of methoxy ester containing 1,4-disubstituted cubane structures. 't.w.' indicates structures obtained as part of this work.[171, 173, 179a, 179c, 179f, 179h, 179l]

While other functionalities are present in these structures, their interactions and effects shall be discussed briefly here, but in more detail in their relevant sections. Esters themselves provide a very interesting case. Generally, they cannot perform as a hydrogen-bond donor due to a lack of suitable hydrogen to donate, however, they can and do participate frequently as hydrogen-bond acceptors. Previously we have published on this with very simple molecules, such as 4-(methoxycarbonyl)phenylboronic acid, in which the methoxy ester is clearly seen to participate as a hydrogen-bond acceptor to create an alternate zig-zag stacking pattern compared to its carboxylic acid derivative.[180] For cubane, this aspect offers much more potential due to the previously mentioned propensity of the acidic hydrogens of the cubane scaffold to act as hydrogen-bond donors in a non-classical

fashion. This results in a large number of interactions between cubane hydrogen atoms and ester groups in a hydrogen-bonding fashion that can be identified (Table SI3:3). The first section is the methyl esters as outlined in Figure 3:8, all of which feature a methyl ester in the 1-position of the cubane scaffold.

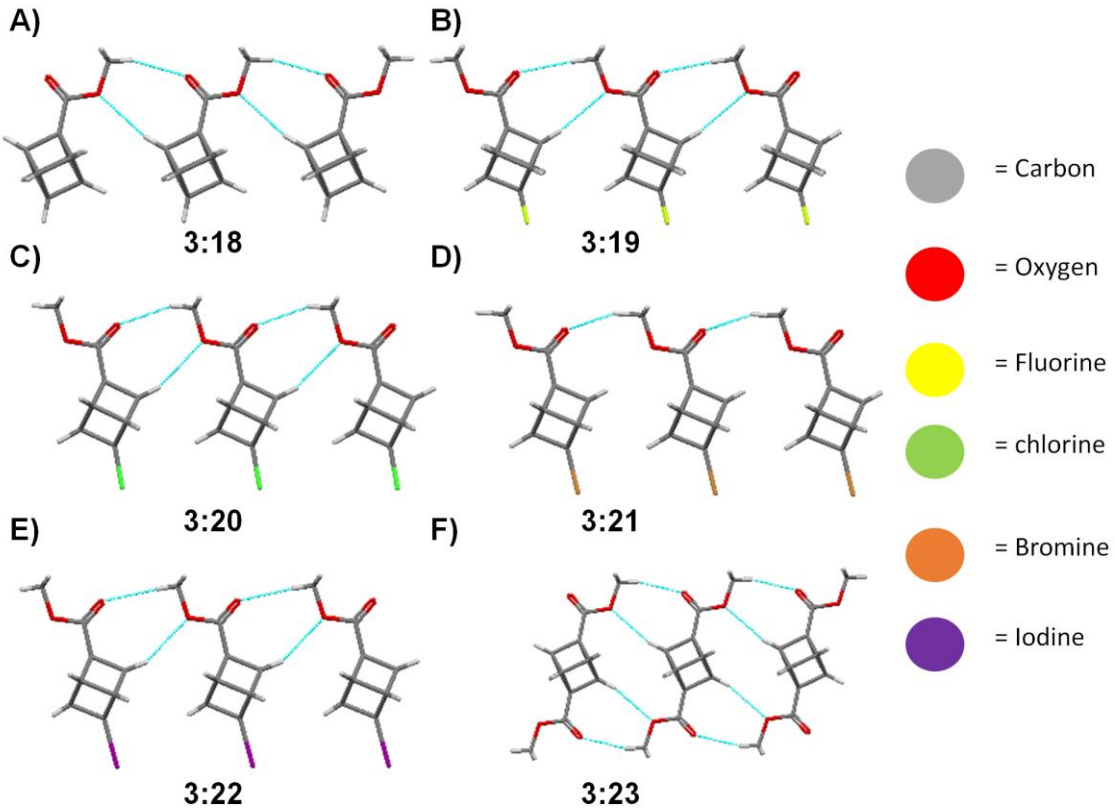

Figure 3:9: View of the molecular arrangement in the crystal of compound **3:18** (A), **3:19** (B), **3:20** (C), **3:21** (D), **3:22** (E), and **3:26** (F) represented as a stick model. Each model shows the preference for ester interactions within the given structure. Interactions are indicated by blue dashed lines. Bond lengths and angles are given in Table 3:2 below.

Table 3:2: List of bond lengths and angles shown in Figure 3:9.

#	Interaction	H···A (Å)	D–H···A (°)
3:18	$C–H_{cubane}\cdots O^1$	2.652	167.3
	$C–H_{OMe}\cdots O^2$	2.413	162.4
3:19	$C–H_{cubane}\cdots O^1$	2.645	175.0
	$C–H_{OMe}\cdots O^2$	2.390	171.0
3:20	$C–H_{cubane}\cdots O^1$	2.692	156.1
	$C–H_{OMe}\cdots O^2$	2.353	161.1
3:21	$C–H_{OMe}\cdots O^2$	2.184	158.4
	$C–H_{OMe}\cdots C_{cubane}$	2.895	167.8
3:22	$C–H_{OMe}\cdots O^2$	2.428	176.2
	$C–H_{OMe}\cdots C_{cubane}$	2.762	174.2
3:26	$C–H_{cubane}\cdots O^1$	2.684	165.8
	$C–H_{OMe}\cdots O^2$	2.437	165.3

When looking at 1-(methoxycarbonyl) cubane (**3:18**) there is an interaction between O^1 and the cubane hydrogen atoms which is combined with a short contact between O^2 and the methyl hydrogen atoms (Figure 3:9A).[173] These interactions result in a linear network between the cubane molecules directed by the ester group. When moving to more functionalized cubane scaffolds such as the halogen series **3:19**–**3:22** we see that this trend is preserved (Figure 3:9A–E).[179h] The halogens themselves partake in certain directive interactions (see halogen section below) but the main linear network of cubane ester interactions is preserved. However, **3:21** appears to deviate from this trend slightly favouring a more head-to-tail overlap between cubane and the methyl ester.[179h] The structure of **3:22_a** (which is the same as **3:22**) shows a slight difference to its previously determined counterpart. The literature structure **3:22** was determined at 218 K whereas the structure of **3:22_a** was determined at 100 K. This results in a shift in cell axis (*a* = 24.986, *b* = 6.551, *c* = 5.777 for **3:22** and *a* = 15.493, *b* = 7.129, *c* = 8.394 for **3:22_a**) due to a change in space group from Pnma (**3:22**) to $P2_1/c$ (**3:22_a**). This translates to a shift in short contacts with **3:22_a** now showing much more overlap between the ester units with $C–H_{cubane}\cdots C$ interactions between the methyl moiety and the cubane scaffold (Figure 3:10). In the structure of **3:23**, the ester O^2 now interacts with the methyl hydrogen atoms rather than the cubane scaffold, suggesting that competition for hydrogen contacts is possible with alternate groups (Figure 3:11).[179f]

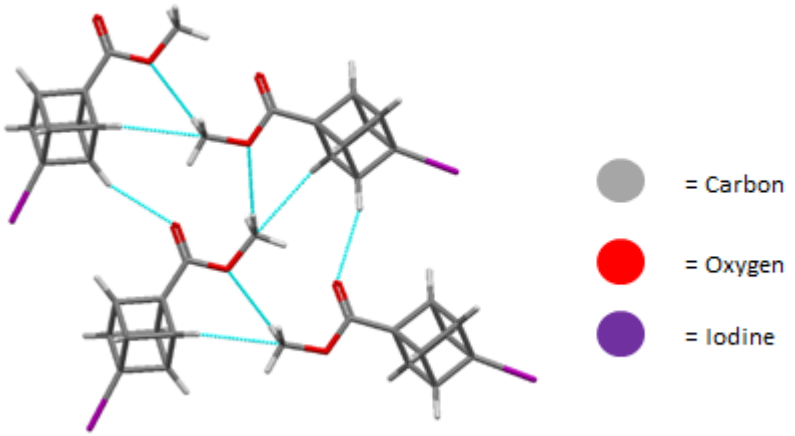

Figure 3:10: View of the molecular arrangement in the crystal of 4-iodo-1-methoxycarbonyl cubane (**3:22_a**) represented as a stick model showing the alternate carbonyl interactions due to a change in space group, as a result of the lower collection temperature. Interactions are indicated by blue dashed lines. Bond lengths and angles are given in Table 3:3 below.

Table 3:3: List of bond lengths and angles shown in Figure 3:10.

#	Interaction	H···A (Å)	D–H···A (°)
3:22_a	$C–H_{cubane}\cdots C$	2.769	140.1
	$C–H_{OMe}\cdots O^1$	2.719	161.0
	$C–H_{cubane}\cdots O^2$	2.509	156.0
	$C–H_{cubane}\cdots O^2$	2.705	130.0

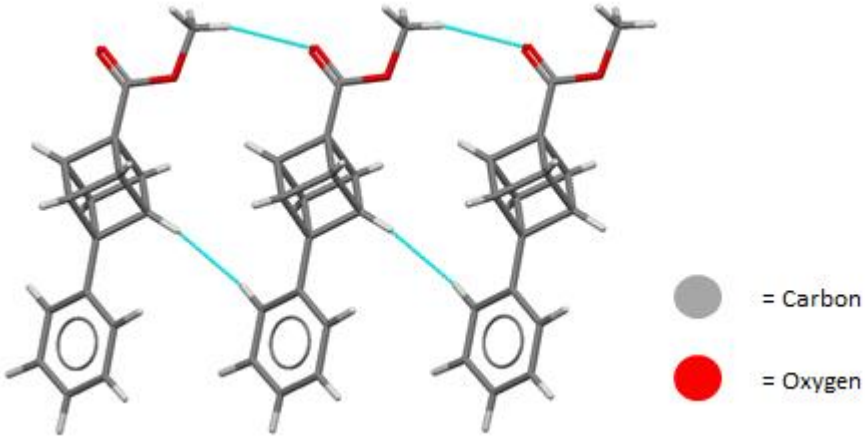

Figure 3:11: View of the molecular arrangement in the crystal of 4-phenyl-1-methoxycarbonyl cubane (**3:23**) represented as a stick model showing the ester oxygen interacting with the methyl hydrogen atoms rather than the cubane scaffold and the cubane hydrogens interaction with the phenyl hydrogens. Interactions are indicated by blue dashed lines. Bond lengths and angles are given in Table 3:4 below.

Table 3:4: List of bond lengths and angles shown in Figure 3:11.

#	Interaction	H···A (Å)	D–H···A (°)
3:23	$C–H_{OMe}\cdots O^2$	2.486	163.9
	$C–H_{cubane}\cdots H_{Ph}$	2.358	149.98

The structure of **3:26** (1,4-dimethoxycarbonyl-cubane) preserves the motif seen in **3:18** but this time it is twofold on both sides of the cubane scaffold (Figure 3:9F).[179c] However, by simply substituting one side of the cubane scaffold for a methyl ether (**3:24**) O^2 becomes the dominant side at which the cubane hydrogen atoms interact with the ester moiety.[179a] Additionally, the methyl ester is involved in a reciprocal dimer formation with its nearest neighbour, changing the packing from a linear network to a twofold network of head-to-head dimers (Figure 3:12). When substituted with a carboxylic acid (**3:9**) on one side of the cubane scaffold we not only see the cubane partaking in catemer formation as mention above, we see a bifurcated interaction between O^2 and the cubane hydrogen (Figure 3:13).[171] Substitution for an acetoxy group (**3:25**) shows a similar network to **3:26**; however, instead of the ester group partaking in interaction with the cubane hydrogens, the acetoxy appears to be more dominant with O^3 and O^4 involved in the formation of a linear network (Figure 3:14).[179a] The ester side shows more preference in forming dimers like **3:24** and an additional reciprocated bifurcated interaction between the hydrogens of the terminal carbonyl group is observed.

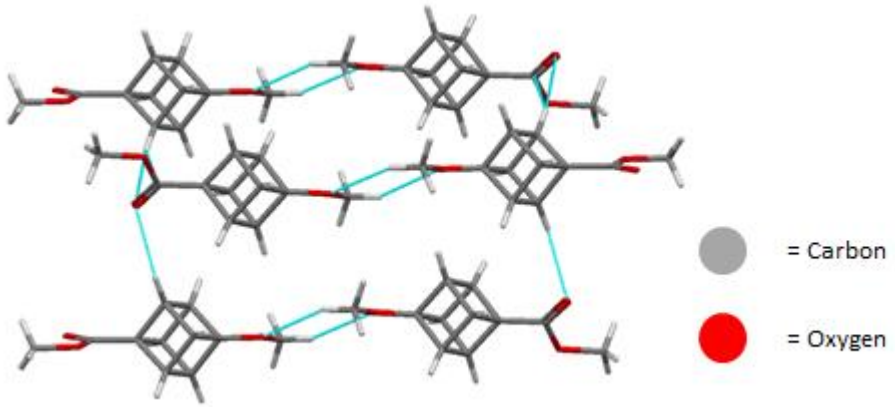

Figure 3:12: View of the molecular arrangement in the crystal of 4-methoxy-1-methoxycarbonyl cubane (**3:24**) represented as a stick model showing the methyl ester partakes in a reciprocal dimer formation with the methyl ester of its nearest neighbour and the cubane hydrogen interacting with the carbonyl oxygen resulting in a two-fold network of head-to-head dimers. Interactions are indicated by blue dashed lines. Bond lengths and angles are given in Table 3:5 below.

Table 3:5: List of bond lengths and angles shown in Figure 3:12.

#	Interaction	H···A (Å)	D–H···A (°)
3:24	$C–H_{cubane}\cdots O^2$	2.525	166.9
	$C–H_{cubane}\cdots O^2$	2.445	160.5
	$C–H_{OMe}\cdots O^3$	2.491	147.1
	$C–H_{OMe}\cdots O^3$	2.497	147.1

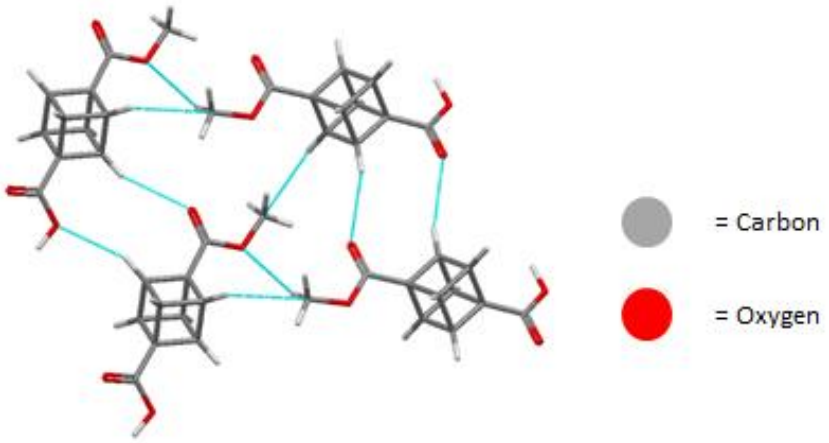

Figure 3:13: View of the molecular arrangement in the crystal of 4- methoxycarbonyl-1-cubane carboxylic acid (**3:9**) represented as a stick model showing the catemer formation between the acid and ester moieties with the cubane hydrogens. Interactions are indicated by blue dashed lines. Bond lengths and angles are given in Table 3:6 below.

Table 3:6: List of bond lengths and angles shown in Figure 3:13.

#	Interaction	H···A (Å)	D–H···A (°)
3:9	$C–H_{OMe}\cdots O^1$	2.716	148.2
	$C–H_{cubane}\cdots O^2$	2.700	124.4
	$C–H_{cubane}\cdots O^2$	2.689	156.3
	$C–H_{cubane}\cdots O^3$	2.651	150.5
	$C–H_{cubane}\cdots O^3$	2.523	159.4
	$C–H_{cubane}\cdots O^4$	2.670	153.3
	$C–H_{cubane}\cdots O^4$	2.660	144.7
	$C–H_{cubane}\cdots O^4$	2.936	90.4
	$C–H_{cubane}\cdots O^4$	3.090	86.6
	$C–H_{cubane}\cdots O^4$	3.095	86.6
	$O^4–H\cdots O^3$	1.650	170.4
	$O^4–H\cdots O^3$	1.665	159.9

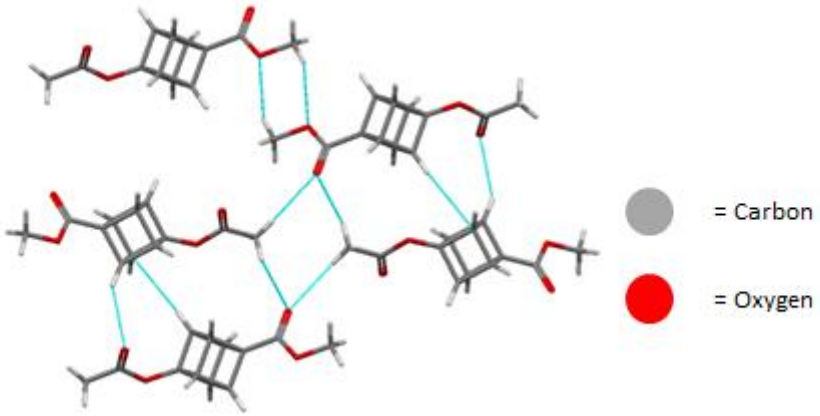

Figure 3:14: View of the molecular arrangement in the crystal of 4-acetoxy-1-methoxycarbonyl cubane (**3:25**) represented as a stick model showing the preference for acetoxy oxygen atoms for interaction with cubane hydrogens and the ester oxygens to form dimers between the esters. Interactions are indicated by blue dashed lines. Bond lengths and angles are given in Table 3:7 below.

Table 3:7: List of bond lengths and angles shown in Figure 3:14.

#	Interaction	H···A (Å)	D–H···A (°)
3:25	$C–H_{OMe}\cdots O^1$	2.647	152.1
	$C–H_{cubane}\cdots O^1$	2.588	161
	$C–H_{OMe}\cdots O^2$	2.570	160.9
	$C–H_{cubane}\cdots O^3$	2.487	175.5
	$C–H_{cubane}\cdots O^4$	2.680	165.3
	$C–H_{cubane}\cdots O^4$	2.563	145.2

In the structure of compound **3:27** the hydroxymethyl groups from a type of catemer partially stabilised by cubane hydrogen atoms interacting with O^3.[179l] There is also the appearance of a short hydrogen contact between O^2 and cubane hydrogen to form a simple linear network. Both of these interaction motifs together form a rather complex looking packing system (Figure 3:15). When a methyl methanesulfonate is inserted to the 4-position (**3:28**) of the cubane scaffold there is a preference for forming a head-to-tail overlapped network of cubane hydrogens interacting with the O^2 on one side and O^1 on the other which is repeated to form this network.[179l] The 4-((methylsulfonyl)oxy)methyl moiety has several interactions, one of these being an interaction between O^4 and the cubane hydrogen (Figure 3:16). However, it is more common to see the methyl ester interacting with the cubane than the 4-((methylsulfonyl)oxy)methyl. The substitution of a 4-((2,2,2-trichloroacetoxy)methyl) group to the cubane scaffold (**3:29**) results in cubane hydrogen interacting with O^1

forming a linear network in a head-to-head fashion and with O^2 in a head-to-tail overlapped dimers (Figure 3:17).[179l] Additionally, the chlorine atoms can interact with the cubane scaffold and other chlorine atoms in a halogen-bonding fashion to form head-to-head dimers. The structure of **3:30** features an *ortho*-nitrobenzoyloxy at the 4-position of the cubane scaffold.[179l] There are two interactive group types here, namely the ester type (Figure 3:18A) and the nitro type (Figure 3:18B). When looking at the ester type this is featured around O^4 to the cubane hydrogen and augmented by an O^2 interacting with a phenyl hydrogen to form an alternating pattern of head-to-head dimers. The nitro group works in a similar fashion to form a stacked hydrogen-bonded network with the cubane scaffold. When this nitro group is moved to the *meta*-position, as is the case in compound **3:31**, the packing pattern is shifted significantly.[179l] The O^1 is now forming head-to-tail dimers with the cubane hydrogen atoms and this is augmented by O^4 interacting with the cubane hydrogens from the opposite side of the cubane. The nitro groups can be seen to interact with both the cubane hydrogen on one oxygen. and the phenyl hydrogens on the other oxygen atom. This forms a relatively stacked head-to-head network facilitated by the nitro group (Figure 3:19). The final compound in this section is one with the *para*-nitrobenzloxy on the 4-position of the cubane scaffold (**3:32**).[179l] The cubane hydrogen atoms are interacting with O^1 in a head-to-head overlapped fashion with a secondary interaction seen between O^2 and the phenyl hydrogens, Figure 3:20. The nitro group in this structure appears to be less directive as seen with the similar structures of **3:30** and **3:31**, as short contacts to this group can be seen forming towards to the methyl hydrogens of the methyl ester.

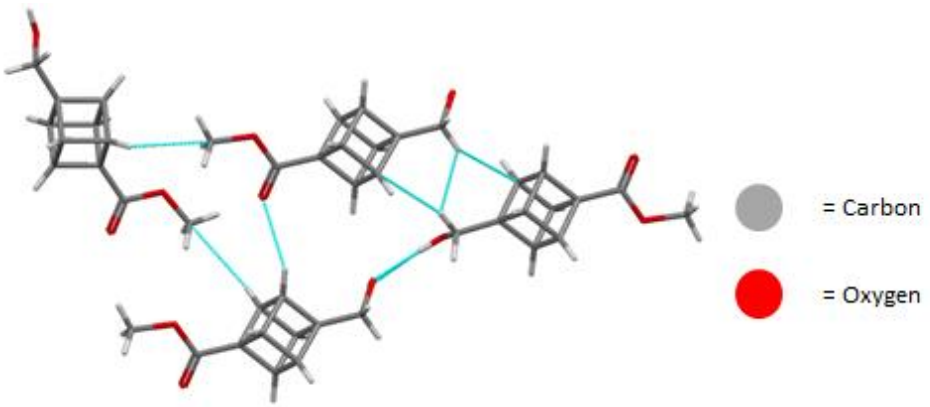

Figure 3:15: View of the molecular arrangement in the crystal of 4-acetoxy-1-methoxycarbonyl cubane (**3:27**) represented as a stick model showing the hydroxymethyl groups from a type of catemer partially stabilized by cubane hydrogen atoms interacting with an oxygen atom. Interactions are indicated by blue dashed lines. Bond lengths and angles are given in Table 3:8 below.

Table 3:8: List of bond lengths and angles shown in Figure 3:15.

#	Interaction	H···A (Å)	D–H···A (°)
3:27	$C–H_{cubane}\cdots O^{2}$	2.565	153.4
	$O–H\cdots O^{3}$	1.887	177.4
	$C–H_{cubane}\cdots O^{3}$	2.786	166.14
	$O–H\cdots O^{3}$	1.912	177.00

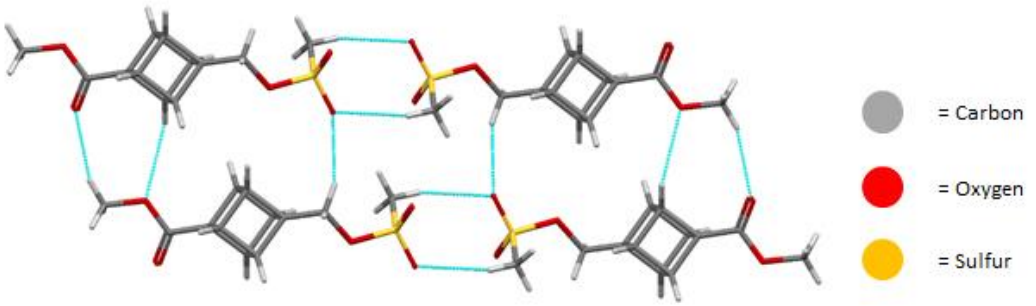

Figure 3:16: View of the molecular arrangement in the crystal of 4-((methylsulfonyl)oxy)methyl-1-methoxycarbonyl cubane (**3:28**) represented as a stick model showing the head-to-head interactions between the (methylsulfonyl)oxy)methyl moiety and the head-to-head overlap between the ester moieties through C–H···O interactions. Interactions are indicated by blue dashed lines. Bond lengths and angles are given in Table 3:9 below.

Table 3:9: List of bond lengths and angles shown in Figure 3:16.

#	Interaction	H···A (Å)	D–H···A (°)
3:28	$C–H_{cubane}\cdots O^{1}$	2.682	143.3
	$C–H_{cubane}\cdots O^{2}$	2.647	156.4
	$C–H_{OMe}\cdots O^{2}$	2.453	160.9
	$C–H_{SMe}\cdots O^{2}$	2.377	168.8
	$C–H_{cubane}\cdots O^{4}$	2.562	148.3
	$C–H_{SMe}\cdots O^{5}$	2.566	143.5
	$C–H_{S}\cdots O^{5}$	2.461	159.2

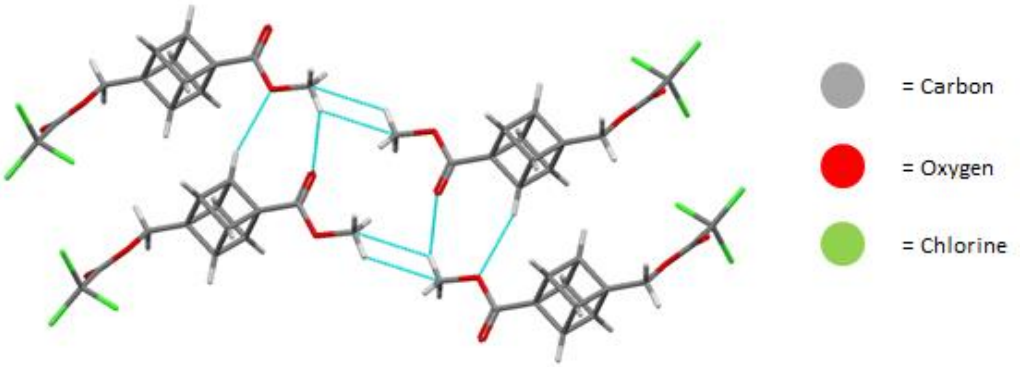

Figure 3:17: View of the molecular arrangement in the crystal of 4-((2,2,2-trichloroacetoxy)methyl)-1-methoxycarbonyl cubane (**3:29**) represented as a stick model showing the head-to-head overlap between the ester moieties through C–H···O interactions. Interactions are indicated by blue dashed lines. Bond lengths and angles are given in Table 3:10 below.

Table 3:10: List of bond lengths and angles shown in Figure 3:17.

#	Interaction	H···A (Å)	D–H···A (°)
3:29	C–H···O^{4}	2.572	124.3
	C–H$_{cubane}$···Cl	3.085	101.6
	C–Cl···Cl	3.410	148.1

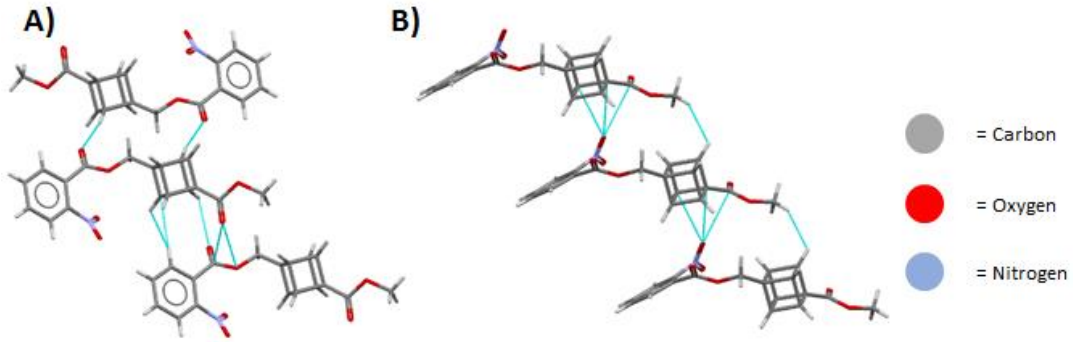

Figure 3:18: View of the molecular arrangement in the crystal of 4-(((2-nitrobenzoyl)oxy)methyl)-1-methoxycarbonyl cubane (**3:30**) represented as a stick model showing the ester C–H···O interactions (A) and interactions between the nitro groups and the cubane scaffold (B). Interactions are indicated by blue dashed lines. Bond lengths and angles are given in Table 3:11 below.

Table 3:11: List of bond lengths and angles shown in Figure 3:18.

#	Interaction	H···A (Å)	D–H···A (°)
3:30	C–H$_{Ph}$···O^{2}	2.525	125.1
	C–H$_{cubane}$···O(NO$_2$)	2.753	102.5

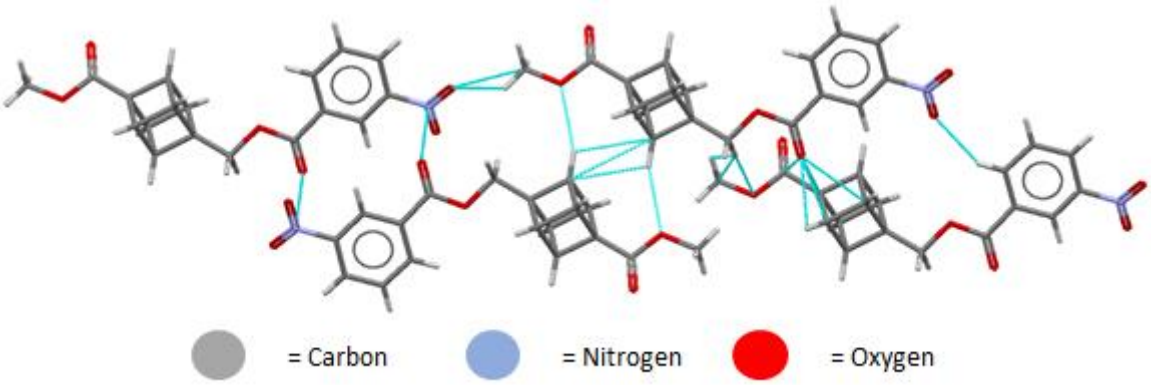

Figure 3:19: View of the molecular arrangement in the crystal of 4-(((3-nitrobenzoyl)oxy)methyl)-1-methoxycarbonyl cubane (**3:31**) represented as a stick model showing the head-to-tail overlapped structure aided by the C–H···O ester interactions, N···O interactions, and the C–H···C interactions between cubane moieties. Interactions are indicated by blue dashed lines. Bond lengths and angles are given in Table 3:12 below.

Table 3:12: List of bond lengths and angles shown in Figure 3:19.

#	Interaction	H···A (Å)	D–H···A (°)
3:31	$C–H_{cubane}\cdots O^4$	2.695	92.6
	$C–H_{cubane}\cdots O^4$	2.696	85.9
	$C–H_{cubane}\cdots O(NO_2)$	2.547	120.4
	$C–H_{OMe}\cdots O(NO_2)$	2.574	115.9
	$C–H_{Ph}\cdots O(NO_2)$	2.447	144.8
	$C–H_{cubane}\cdots \pi$	2.721	129.4

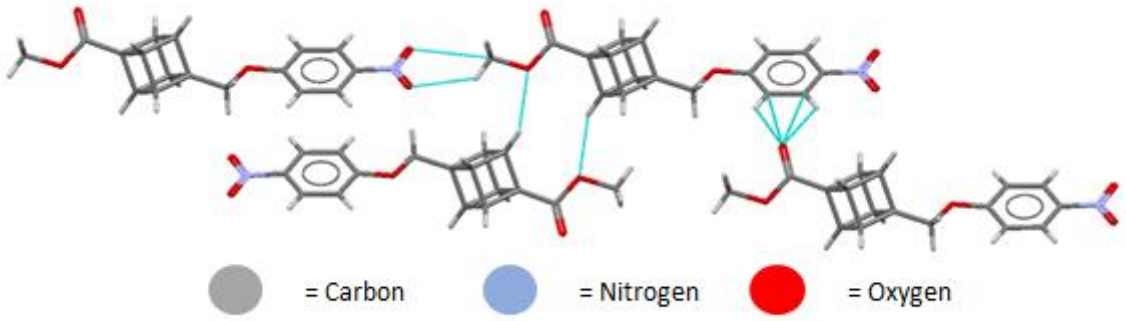

Figure 3:20: View of the molecular arrangement in the crystal of 4-((4-nitrophenoxy)methyl)-1-methoxycarbonyl cubane (**3:32**) represented as a stick model showing the head-to-head overlap aided by C–H···O ester interactions, N···O interactions. Interactions are indicated by blue dashed lines. Bond lengths and angles are given in Table 3:13 below.

Table 3:13: List of bond lengths and angles shown in Figure 3:20.

#	Interaction	H···A (Å)	D–H···A (°)
3:32	C–H···O^1	2.498	153.1
	$C–H_{Ph}···O^2$	2.480	124.9
	$C–H_{Ph}···O^2$	2.597	119.8
	$C–H_{OMe}···O(NO_2)$	2.652	133.3

When including larger ester groups (Figure 3:21, bond lengths and angles are shown in Table SI3:4) it is noted that the cubane hydrogens are less likely to interact with the ester groups due to the increased competition of functionalized moieties within the cubane framework. Looking at the structure of **3:33** we can see that the cubane has now ceased forming hydrogen-bonded pairs with the ester.[179i] In fact, there appears to be a preference for C–H···C_{cubane} short contacts present rather than any typical hydrogen-bond (Figure 3:22). Moving to the propyl ester (**3:34**), we see a return to the cubane interacting with O^1 accepting a hydrogen from the cubane scaffold and O^2 interacting with a CH_2 of the propyl chain to form a timer type complex (Figure 3:23A).[179i] In this structure, the presence of C–H···C short contacts is also noted between the cubane scaffolds. For **3:35** there are no hydrogen atoms included the structure, so no interactions can be deduced.[179b]

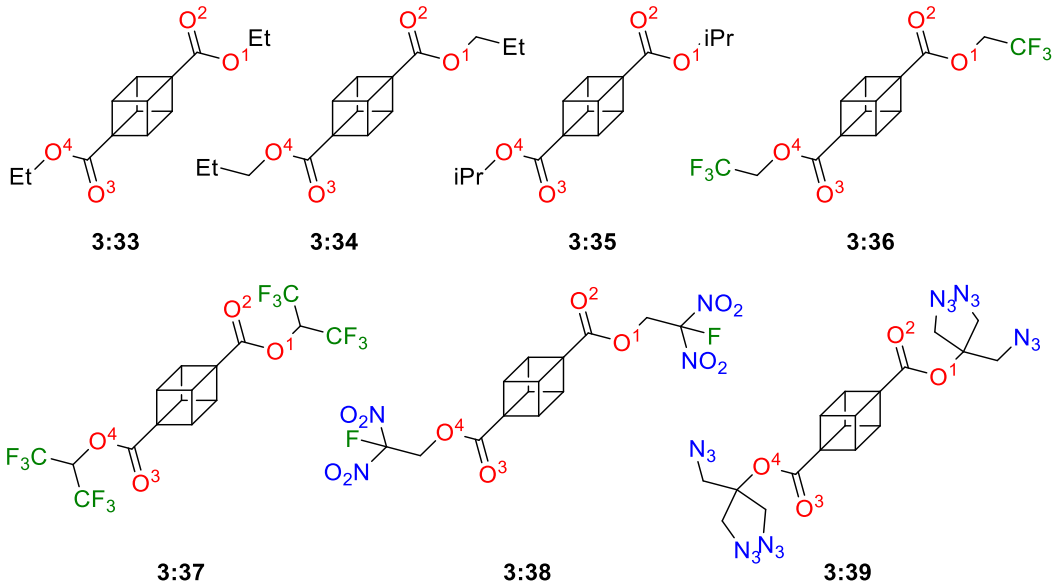

Figure 3:21: List of previously published extended ester 1,4-disubstituted cubane structures.[179e, 179i]

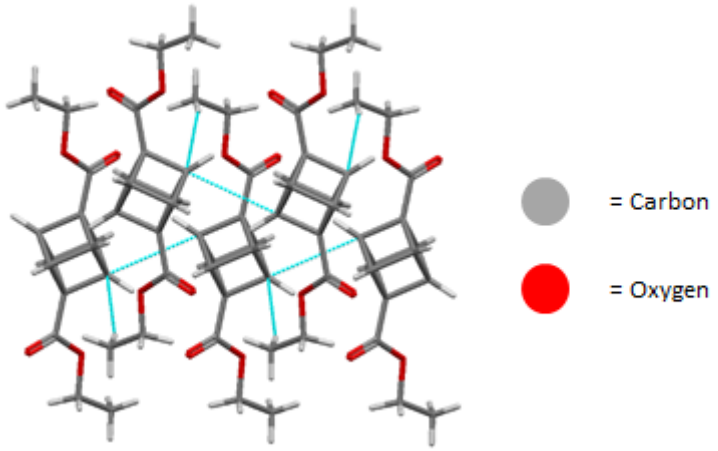

Figure 3:22: View of the molecular arrangement in the crystal of 1,4-di-ethoxycarbonly cubane (**3:33**) represented as a stick model showing its preference for C–H···C short contacts. Interactions are indicated by blue dashed lines. Bond lengths and angles are given in Table 3:14 below.

Table 3:14: List of bond lengths and angles shown in Figure 3:22.

#	Interaction	H···A (Å)	D–H···A (°)
3:33	$C–H_{OMe}\cdots C_{cubane}$	2.900	153.9
	$C_{cubane}\cdots C_{cubane}$	3.362	91.3

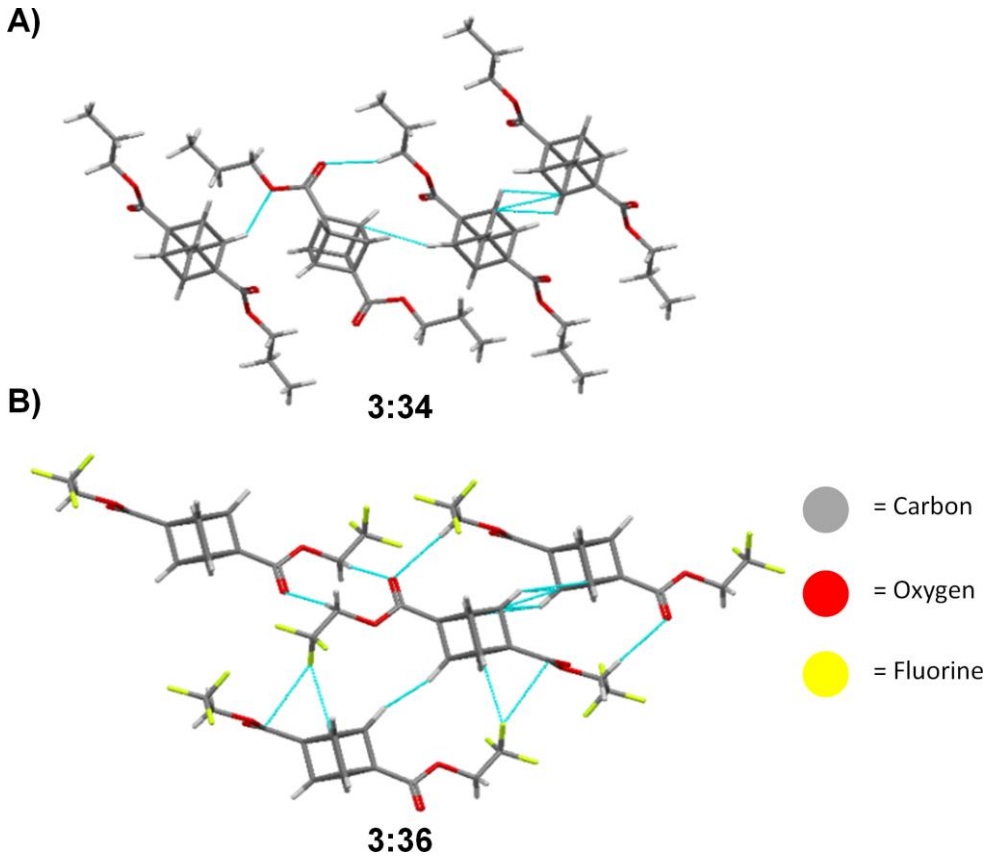

Figure 3:23: View of the molecular arrangement in the crystal of compound **3:34** (A) and **3:36** (B) represented as a stick model. Each model shows the preference for ester interactions within the given structure. Interactions are indicated by blue dashed lines. Bond lengths and angles are given in Table 3:15 below.

Table 3:15: List of bond lengths and angles shown in Figure 3:23.

#	Interaction	H···A (Å)	D–H···A (°)
3:34	$C–H_{cubane}\cdots O^{1}$	2.693	142.2
	$C–H_{OPr}\cdots O^{2}$	2.653	150.3
	$C–H_{cubane}\cdots C_{cubane}$	2.835	158.6
	$C–H_{cubane}\cdots C_{cubane}$	2.891	110.87
3:36	$C–F\cdots C_{cubane}$	3.068	144.6
	$C–F\cdots C_{cubane}$	3.068	144.6
	$C–H\cdots O^{2}$	2.430	163.4
	$C–H\cdots O^{2}$	2.646	145.5
	$C–H\cdots O^{3}$	2.430	163.4
	$C–H\cdots O^{3}$	2.646	145.5
	$C–H_{cubane}\cdots C_{cubane}$	2.772	113.6

Compound **3:36** shows an interesting case, the CF_3 groups show some partial preference for halogen-bonding with the cubane scaffold, but the ester functionality is seen to form a dimer through $O^{2/3}$ and the CH_2 hydrogens (Figure 3:23B).[179i] The cubane scaffold appears to be held in a position where C–H···C short contacts are present. In structure of **3:37** this is changed due to the large bulk contributed by two CF_3 moieties. In this case, there is a clear linear network created through the $O^{2/3}$ interacting with the CH hydrogen (Figure 3:24). No close contacts appear around the cubane scaffold. The structure **3:38** shows a staggered linear network formed between the cubane scaffold and the terminal nitro groups in a reciprocated fashion (Figure 3:25).[179i] However, as no hydrogens were provided in this structure no distances can be measured. The structure of **3:39** shows a linear network formed by the azide moiety yielding two close contacts. The first is the dimer formed between the CH_2 hydrogens with the terminal nitrogen of the azide group. The second is the linear network formed between cubane hydrogen and the nitrogen atom connected to the carbon skeleton (Figure 3:26).[179e]

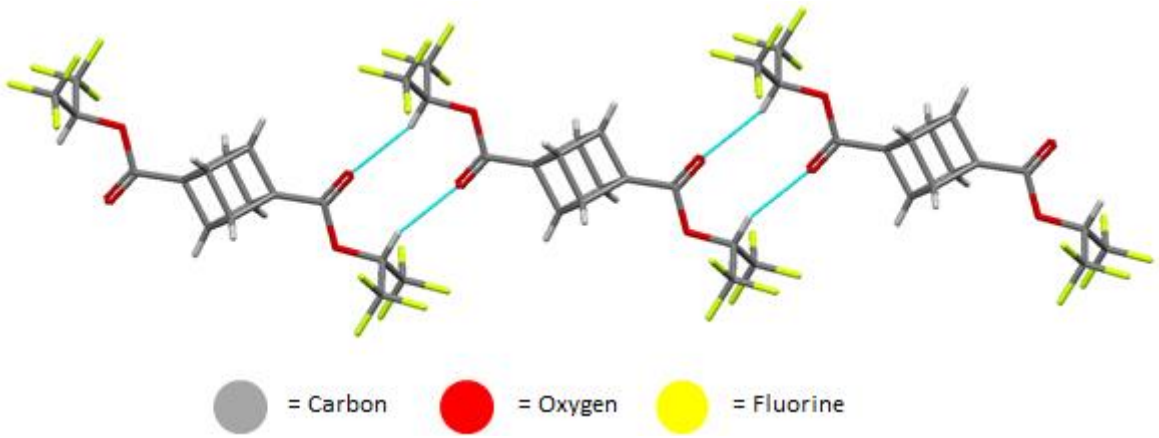

Figure 3:24: View of the molecular arrangement in the crystal of 1,4-di-((1',1',1',3',3',3'-hexafluoropropan-2-yl)oxycarbonyl cubane (**3:37**) represented as a stick model showing the linear network formed through the C–H···O interactions ester interactions. Interactions are indicated by blue dashed lines. Bond lengths and angles are given in Table 3:16 below.

Table 3:16: List of bond lengths and angles shown in Figure 3:24.

#	Interaction	H···A (Å)	D–H···A (°)
3:37	C–H···O^{2}	2.347	159.8
	C–H···O^{3}	2.347	159.8

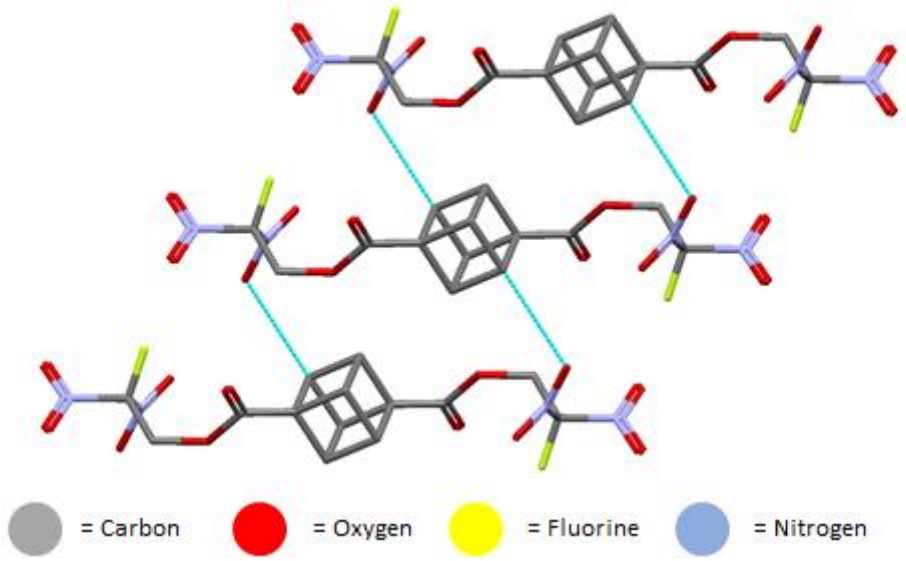

Figure SI3:25: View of the molecular arrangement in the crystal of 1,4-(2-fluoro-2',2''-dinitroethoxy)carbonyl cubane (**3:38**) represented as a stick model showing the interactions between the cubane scaffold and the nitro groups. Interactions are indicated by blue dashed lines.

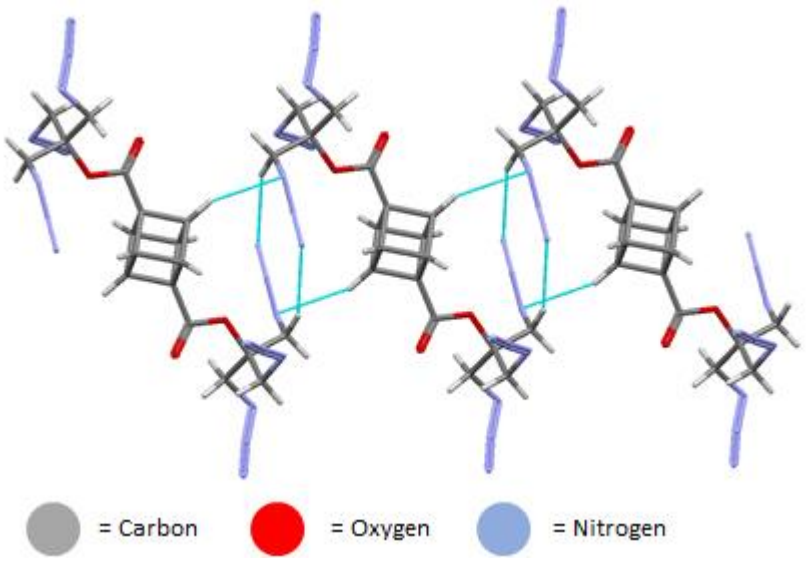

Figure 3:26: View of the molecular arrangement in the crystal of 1,4-((1',3'-diazido-2''-(azidomethyl)propan-2'''-yl)oxycarbonyl cubane (**3:39**) represented as a stick model showing the interactions between the cubane hydrogens and the azide moiety. Interactions are indicated by blue dashed lines. Bond lengths and angles are given in Table 3:18 below.

Table 3:18: List of bond lengths and angles shown in Figure 3:26.

#	Interaction	H···A (Å)	D–H···A (°)
3:39	C–H···N	2.740	155.2
	$C–H_{cubane}···N$	2.710	145.3

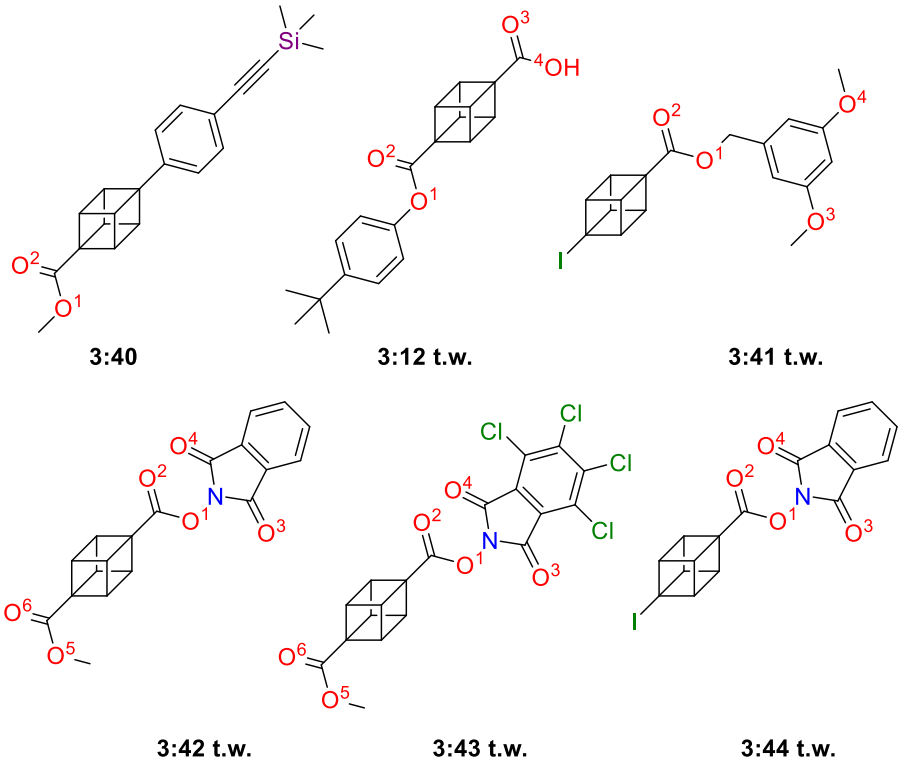

Figure 3:27: 1,4-Disubstituted cubane ester structures that are submitted as part of this work. 't.w.' indicates structures obtained as part of this work.[168a]

The final group of the esters features new compounds recently published by our group (**3:40**) and several determined as part of this work (**3:12**, **3:41**–**3:44**) (Figure 3:27, Table SI5).[168a] The structure of **3:40** is an interesting example of what occurs when an extended rigid arm is present in the 4-position of a methyl ester cubane. The O···H interactions observed for compound **40** are similar to that of compound **24**. The cubane hydrogen atoms interacts with O^1 in a dimer formation and O^2 in a head-to-head overlapped fashion (Figure 3:28A). Additionally, we see the first aspects where the cubane hydrogen atoms are interacting with the ethynyl group in a C–H···π fashion. However, as there are more compounds like this, this will be discussed in more detail in the ethynyl section below. As discussed previously in the acid section above, compound **3:12** results in the ester-forming a rotated linear network between the O^2 and the cubane hydrogen atoms (Figure 3:13). The structure of **3:41** shows more prevalent contacts between the methyl ether of the phenyl ring and the cubane hydrogens. This type of interaction is aided by a halogen-bond between the methyl ether and the iodine of the cubane scaffold which facilitates overlapped dimers (Figure 3:28B and 3:28C). The structure of **3:41** shows that when sufficient competing groups are introduced to the cubane scaffold, the ester is less likely to form hydrogen-bonds with the cubane scaffold.

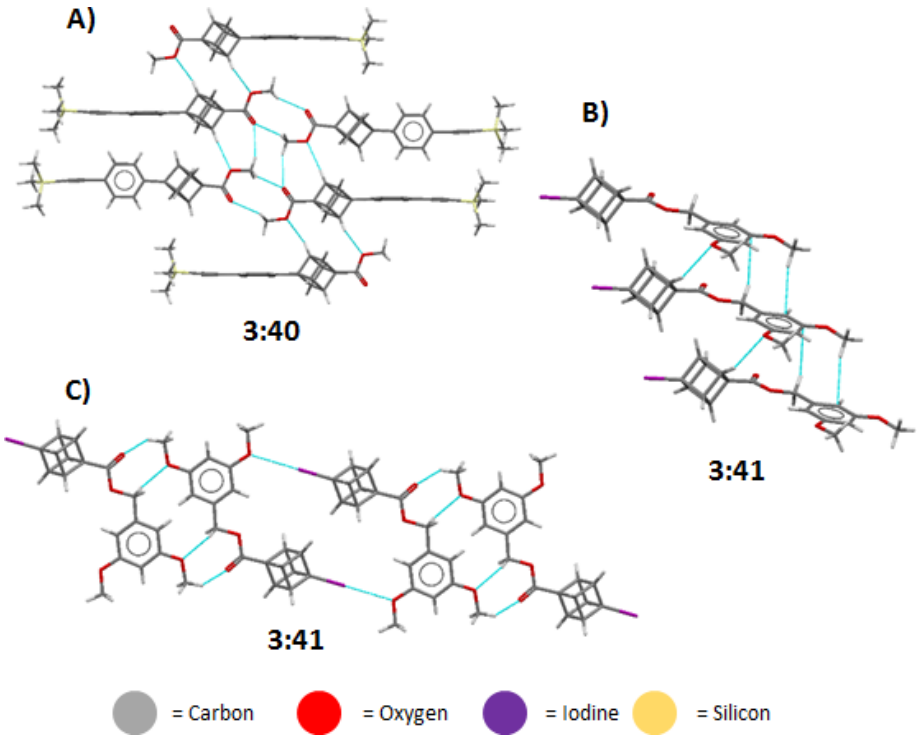

Figure 3:28: View of the molecular arrangement in the crystal of compound **3:40** (A) and **3:41** (B and C), represented as a stick model. Each view shows the preference for ester interactions within the given structure. Interactions are indicated by blue dashed lines. Bond lengths and angles are given in Table 3:19 below.

Table 3:19: List of bond lengths and angles shown in Figure 3:28.

#	Interaction	H···A (Å)	D–H···A (°)
3:40	$C–H_{cubane}\cdots O^1$	2.394	155.3
	$C–H_{cubane}\cdots O^1$	2.416	162.1
	$C–H\cdots O^1$	2.615	157.9
	$C–H\cdots O^2$	2.512	157.5
	$C–H\cdots O^2$	2.476	157.8
	$C–H\cdots O^2$	2.392	147.4
	$C–H_{cubane}\cdots O^2$	2.608	120.2
3:41	$C–H_{Ph}\cdots O^2$	2.643	146.8
	$C–H\cdots O^2$	2.695	124.3
	$C–H_{cubane}\cdots O^3$	2.554	148.6
	$C–I\cdots O^3$	3.201	169.7
	$C–H\cdots O^4$	2.713	151.
	$C–H\cdots O^4$	2.497	157.1

This leaves the final section of the esters section which concerns redox-active ester. These compounds had previously been synthesized by our group as a method to functionalize the 4-position of a cubane scaffold through a radical-mediated mechanism.[168a] Through this project, three such redox active esters were crystallized to a quality sufficient for X-ray diffraction analysis (**3:42**–**3:44**). The structure of **3:42** shows an interesting head-to-tail overlapped network through the cubane hydrogen atoms interacting with O^1 and O^5.[168a] This is stabilized though $O^2\cdots\pi$ and $O^6\cdots H–C_{(Me)}$ interactions (Figure 3:29A and 3:29B). The cubane scaffold is also held at an ideal distance to partake in $C–H_{cubane}\cdots C_{cubane}$ short contacts with the nearest cubane unit. Furthermore, in Figure 3:29A and 3:29B, we can see that the additional oxygen atoms included in the redox active ester can be seen to interact with the cubane hydrogen atoms on one side ($C–H_{(cubane)}\cdots O^4$) and the indoline hydrogens on the other side $C–H_{(In)}\cdots O^3$) which results in an offset pattern of parallel sheets. When the redox active ester is substituted with chlorine atoms (**3:43**) we see a similar pattern emerge with cubane hydrogen atoms interacting with O^1 and O^5 to form the same head-to-tail overlap. The same $O^2\cdots\pi$ and $O^6\cdots H–C_{(Me)}$ interactions are observed in this structure to form the stacked network. The main differences occur due to the chlorine atoms occupying the indoline moiety removing any hydrogen-bonding aspects. This results in a head-to-tail overlapped structure

due to hydrogen-bonding interactions between C–$H_{(cubane)}$···O^3, C–$H_{(Me)}$···O^4, and C–$H_{(cubane)}$···O^5 (Figure 3:29C and 3:29D). Also evident in this structure are several halogen-bonds between C–Cl···O^2, C–Cl···O^4, C–Cl···O^6, C–Cl···H, C–Cl···H, and C–Cl···Cl which increase the space surrounding the phenyl moiety resulting in an increase in the *b*- and *c*-axis lengths by 0.5–1 Å, compared to compound **3:42**. When the methyl ester is replaced by an iodine atom (**3:44**) some unique changes occur. Specifically, in the stacking (Figure 3:29E and 3:29F), there is no head-to-tail overlap as seen in **3:42** or **3:43**, due to the absence of the ester. Rather, there is quite a beautiful threefold interaction sequence of hydrogen-bonding (C–$H_{(cubane)}$···O^1), halogen (C–I···$H_{(cubane)}$), and a close contact (C–O^2···O^3) which is repeated to form a neat stacking pattern. The secondary interactions of note are C–$H_{(cubane)}$···O^4, C–$H_{(In)}$···O^4, C–$H_{(cubane)}$···O^3, C–I···$H_{(In)}$, C–I···$H_{(In)}$, and C–$H_{(In)}$···$C_{(cubane)}$ which results in a wedge shape packing pattern.

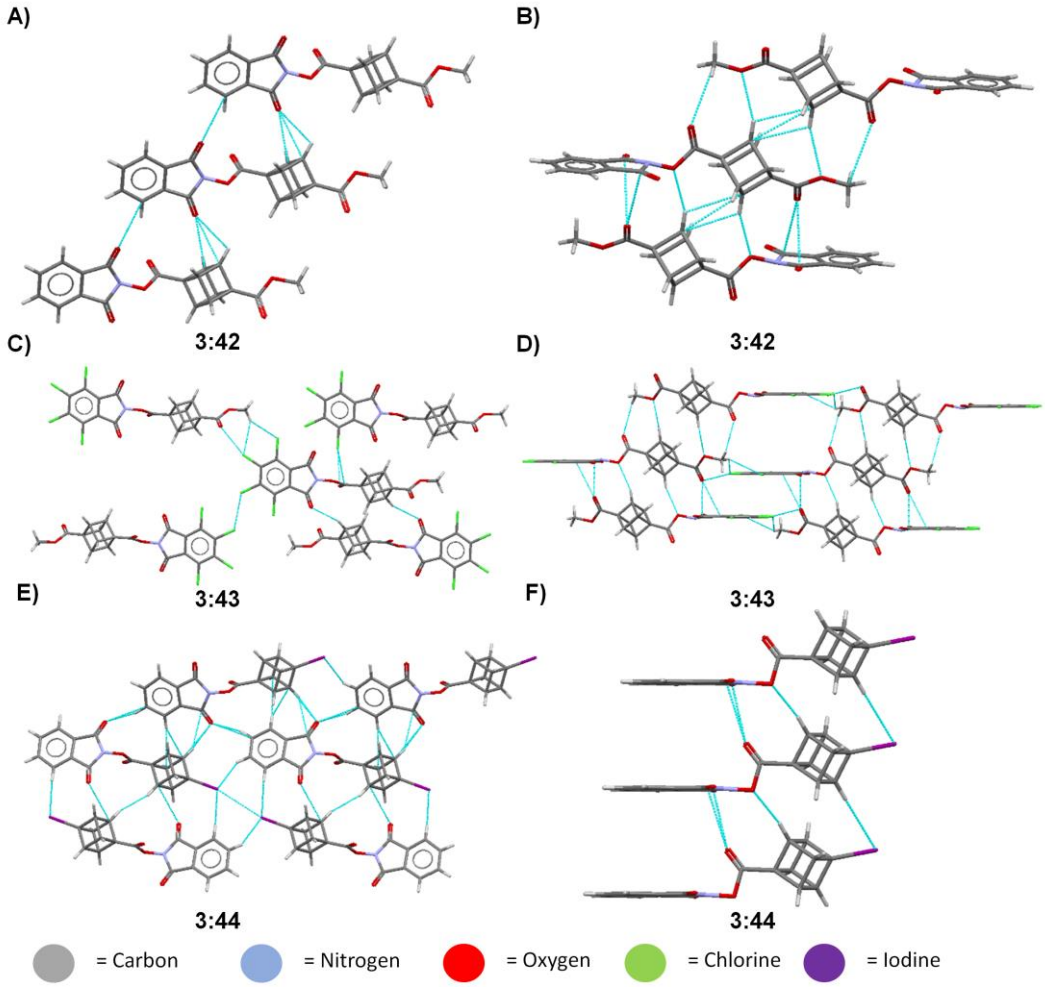

Figure 3:29: View of the molecular arrangement in the crystal of compound **3:42** (A and B), **3:43** (C and D), and **3:44** (E and F) represented as a stick model. Each model shows the preference for ester interactions within the given structure. Interactions are indicated by blue dashed lines. Bond lengths and angles are given in Table 3:20 below.

Table 3:20: List of bond lengths and angles shown in Figure 3:29.

#	Interaction	H···A (Å)	D–H···A (°)
3:42	$C–H_{cubane}\cdots O^{1}$	2.368	158.8
	$C–H\cdots O^{2}$	2.858	102.2
	$C–H_{In}\cdots O^{3}$	2.785	107.4
	$C–H_{cubane}\cdots O^{4}$	2.686	102.2
	$C–H_{cubane}\cdots O^{4}$	2.848	97.5
	$C–H_{cubane}\cdots O^{5}$	2.559	158.6
	$C–H_{cubane}\cdots O^{5}$	2.435	158.9
	$C–O^{6}\cdots \pi$	2.964	136.1
	$C–H_{Ph}\cdots O^{6}$	2.708	123.6
3:43	$C–H_{cubane}\cdots O^{1}$	2.455	163.1
	$C–H\cdots O^{2}$	2.694	126.2
	$C–H_{cubane}\cdots O^{3}$	2.625	157.2
	$C–H\cdots O^{4}$	2.560	116.1
	$C–H_{cubane}\cdots O^{5}$	2.505	154.6
	$C–H_{cubane}\cdots O^{5}$	2.517	149.5
	$C–O^{6}\cdots \pi$	2.953	163.1
	$C–Cl\cdots O^{2}$	3.103	159.6
	$C–Cl\cdots O^{4}$	3.227	170.4
	$C–Cl\cdots O^{6}$	3.011	157.5
	$C–Cl\cdots H$	2.930	109.6
	$C–Cl\cdots H$	2.871	111.9
	$C–Cl\cdots Cl$	3.277	127.3
3:44	$C–H_{cubane}\cdots O^{1}$	2.377	167.1
	$C–O^{2}\cdots O^{3}$	2.851	152.7
	$C–I\cdots H_{cubane}$	3.178	69.2
	$C–H_{cubane}\cdots O^{4}$	2.222	169.3
	$C–H_{In}\cdots O^{4}$	2.484	125.1
	$C–H_{cubane}\cdots O^{3}$	2.963	94.0
	$C–I\cdots H_{In}$	3.064	107.8
	$C–I\cdots H_{In}$	3.173	97.4
	$C–H_{In}\cdots C_{cubane}$	2.865	118.1
	$C–I\cdots \pi$	4.041	97.2

Halogens.

As of yet, there have been no studies into the effects that halogen-bonding has on the cubane hydrogen interactions. Halogen contacts, as outlined in the general introduction, are one of the most common ways next to hydrogen-bonds, to achieve chemical directionality in a crystal structure. Some of these compounds have been covered in previous sections with regards to their second functionality (either methyl ester or carboxylic acid). This section shall focus mainly on the how the cubane scaffold directly interacts with halogens atoms.

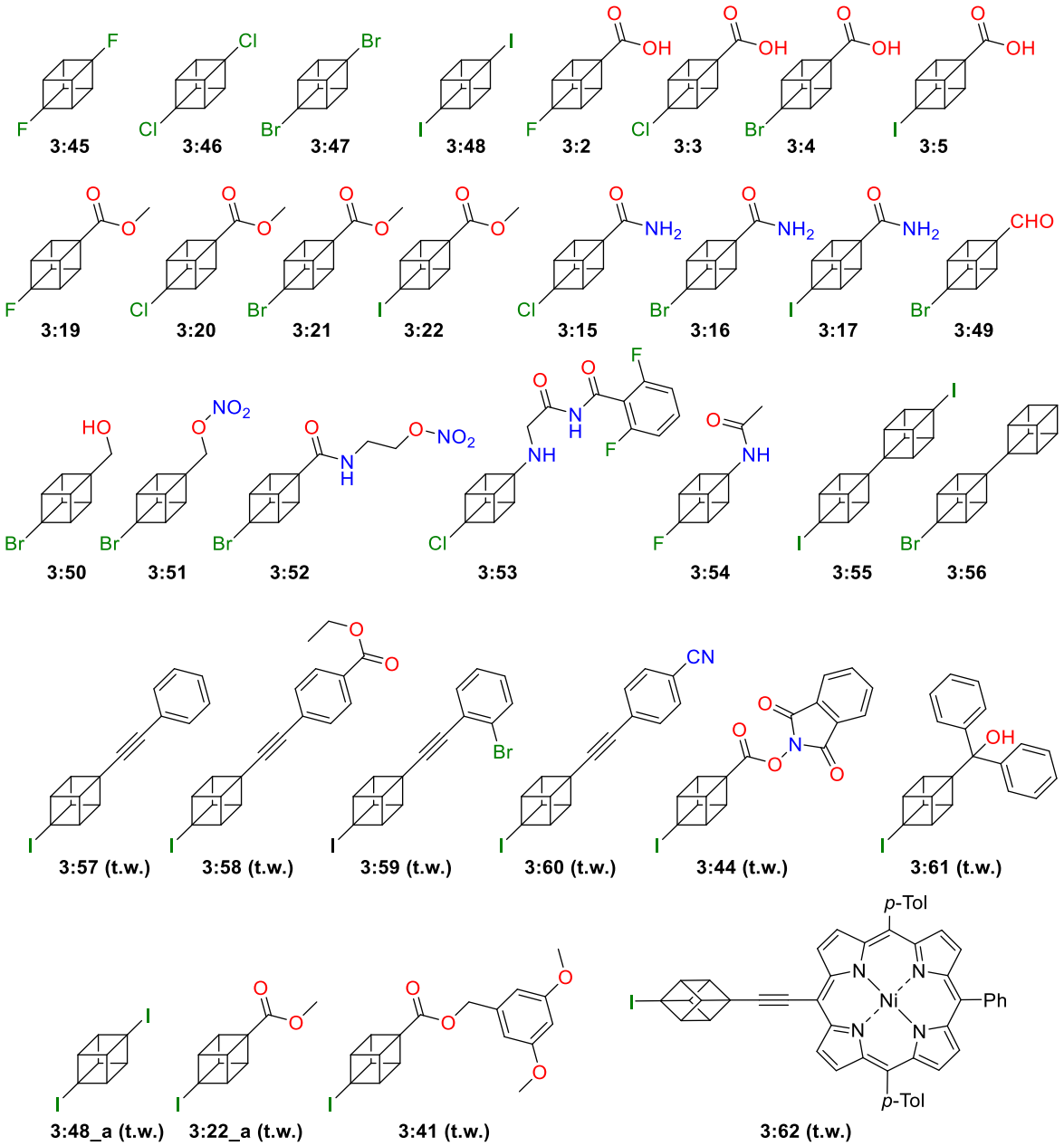

Figure 3:30: List of all 1,4-disubstituted cubane structures with a halogen attached to the 4-position. 't.w.' indicates structures obtained as part of this work.[167-168, 171, 172b, 173, 177a, 179a, 179h, 181]

Figure 3:30 shows all the published 4-halogeno-1-(R)-substituted cubane structures and structures determined as part of this work (bond lengths and angles are given in Table SI3:6). The 1,4-dihalocubanes (**3:45**–**3:48**) show typical hydrogen-halogen interactions (Figure 3:31).[179a, 181a, 181b]

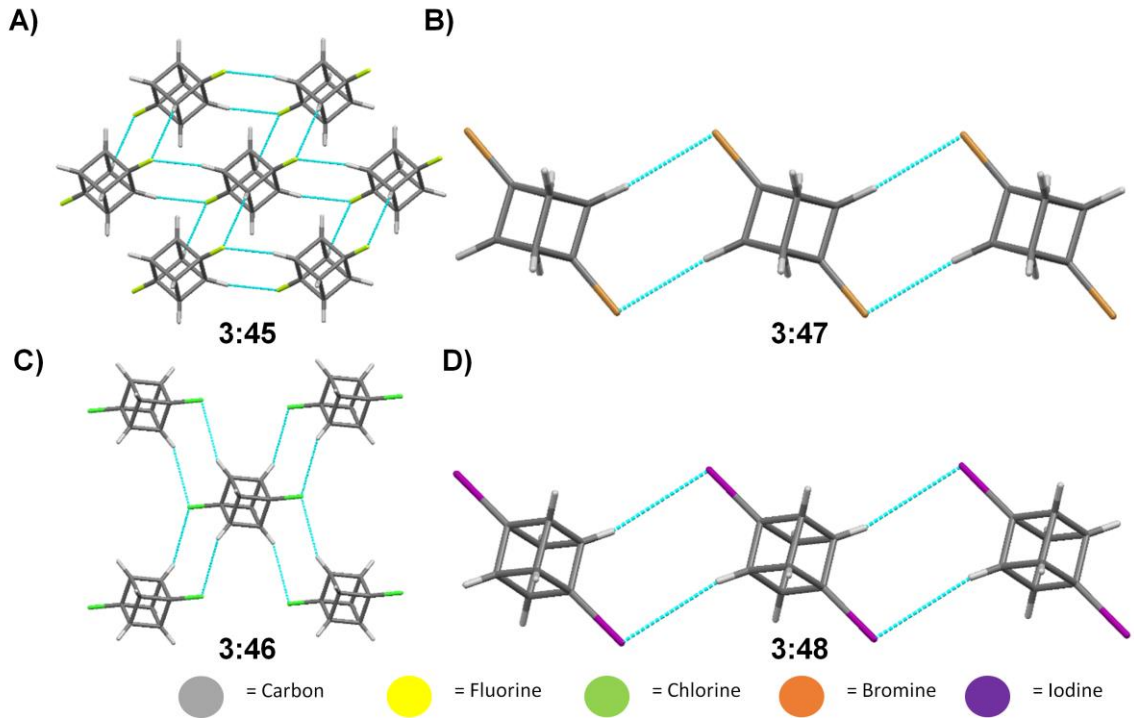

Figure 3:31: View of the molecular arrangement in the crystal of compound **3:45** (A), **3:47** (B), **3:46** (C), and **3:48** (D) represented as a stick model. Each model shows the preference for halogen interactions within the given structure. Interactions are indicated by blue dashed lines. Bond lengths and angles are given in Table 3:21 below.

Table 3:21: List of bond lengths and angles shown in Figure 3:31.

#	Interaction	H···A (Å)	D–H···A (°)
3:45	C–H_{cubane}···F	2.639	131.8
	C–H_{cubane}···F	2.499	170.5
3:46	C–H_{cubane}···Cl	3.001	154.8
	C–H_{cubane}···Cl	3.067	158.9
3:47	C–H_{cubane}···Br	2.893	157.4
3:48	C–H_{cubane}···I	3.330	156.2

This is due to the fact that these are the only functional groups present in these structures. This is curious as no direct halogen-halogen interactions are observed, which would be expected in such cases, for unhindered halogens. This suggests the effect that the acidic hydrogens of the cubane scaffold are much more directive

and favourable in these molecules than the expected halogen-halogen interactions. The only exception to this is the short contacts seen in **3:46**, which are larger than one would expect for a halogen-hydrogen interaction. There is also some correlation between atom size and the packing pattern observed. The difluoro cubane **3:45** shows a tighter packing, but also that the interactions are consistently bifurcated centring on the fluorine atom. The dichloro cubane **3:46** shows only short contacts and as a result, a much looser packing pattern is observed. The dibromo cubane **3:47** and the diiodo (**3:48**) show much looser packing patterns and appear to form linear networks rather than cage like networks seen in **3:45** and **3:46**. The structure of **3:48_a**, which is the updated structure of **3:48** (**3:48** originally determined at room temperature, **3:48_a** determined at 100 K). Both structures have the same unit cell and as a result have the same short contacts present for compound **3:48_a** as **3:48** with only a minor decrease in bond length (Figure 3:32).

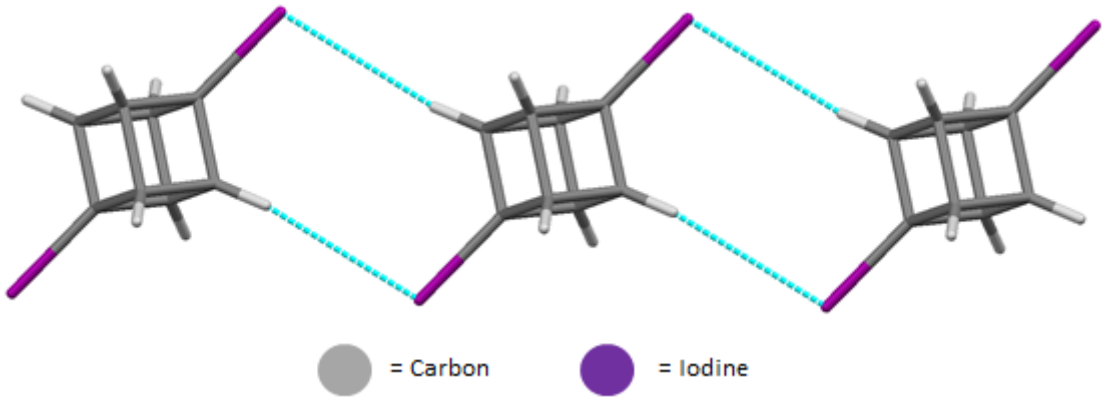

Figure 3:32: View of the molecular arrangement in the crystal of 1,4-diiodocubane (**3:48_a**) represented as a stick model showing the H···I interactions. Interactions are indicated by blue dashed lines. Interactions are indicated by blue dashed lines. Bond lengths and angles are given in Table 3:22 below.

Table 3:22: List of bond lengths and angles shown in Figure 3:31.

#	Interaction	H···A (Å)	D–H···A (°)
3:48_a	C–H_{cubane}···I	3.227	156.4

When alternate functionalities are incorporated onto the 1-position of the cubane scaffold as seen with carboxylic acids (**3:2**–**3:5**), methyl esters (**3:19**–**3:22**), or primary carboxamides (**3:15**–**3:17**), the hydrogen-bond donor/acceptor groups appear to form the primary interactions in these complexes with the halogen functionality appearing to be secondary in terms of directing packing.[171, 172b, 173, 179h] In the carboxylic acid group, the 4-fluoro cubane (**3:2**) forms dimers, complementary

to the head-to-head dimer of the acid, through an overlap of H···F contacts resulting in a staggered hydrogen-bonding halogen-bonding system (Figure 3:33). The use of a larger halogen atom, such as chlorine, for compound **3:3** results in linking two catemer hydrogen-bonded networks with H···Cl interaction channels to form an alternate network of hydrogen-bonding and halogen-bonding interactions (Figure 3:34A). Moving to bromine, the structure of **3:4** shows predominantly hydrogen-bonded networks in which the bromine atoms interact with the hydrogen on the cubane in the next layer rather than the cubane which is in the same layer as seen with **3:2** and **3:3** (Figure 3:34D). The structure of compound **3:5** is the first example where a direct halogen-halogen-bond is observed. The iodine atoms are interacting directly, allowing for an alternating linear network of halogen and hydrogen interactions, which are periodically tethered together in layers by cubane hydrogen interacting with the carboxylic acid (Figure 3:35). For the esters, the story is a little different. Unlike the carboxylic acids the esters do not have a hydrogen-bond donating ability and as a result, the ester moiety tends to stack with the cubane moiety in a dimer fashion. This forms two types of packing based on halogen size. Both the 4-fluoro (**3:19**) and 4-chloro derivatives (**3:20**) from tight networks where the esters can interact face-to-face. However, due to the size difference, fluorine interacts in a bifurcated fashion with the nearest hydrogen to the halogen substitute (Figure 3:36), whereas chlorine interacts with the hydrogens diagonal closest to the ester function group (Figure 3:34B).[173]

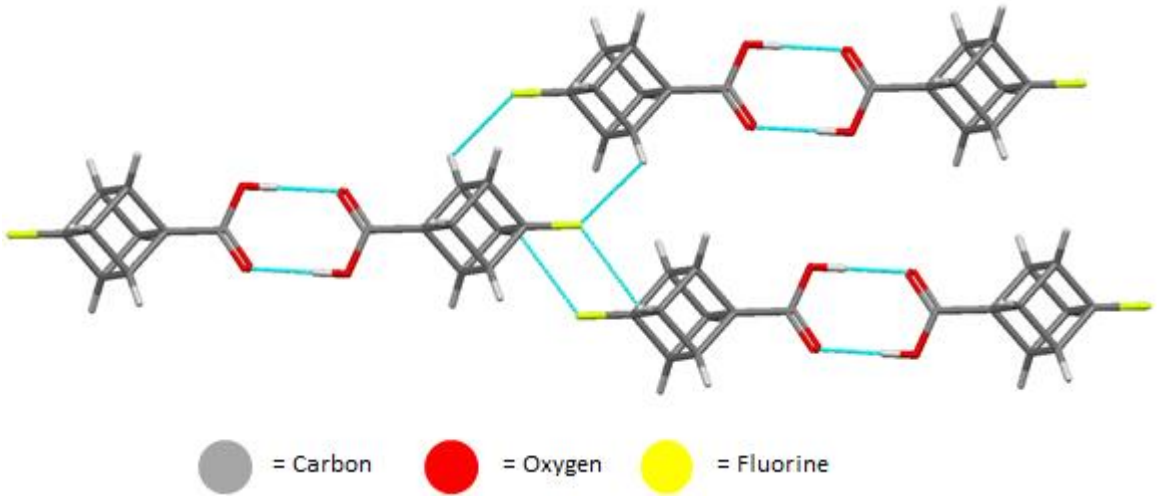

Figure 3:33: View of the molecular arrangement in the crystal of 4-fluorocubane-1-carboxylic acid (**3:2**) represented as a stick model showing the head-to-head dimers between the acid moieties and the F···H interactions. Interactions are indicated by blue dashed lines. Bond lengths and angles are given in Table 3:23 below.

Table 3:23: List of bond lengths and angles shown in Figure 3:33.

#	Interaction	H···A (Å)	D–H···A (°)
3:2	C–H_{cubane}···F	2.481	120.9
	C–H_{cubane}···F	2.730	101.3

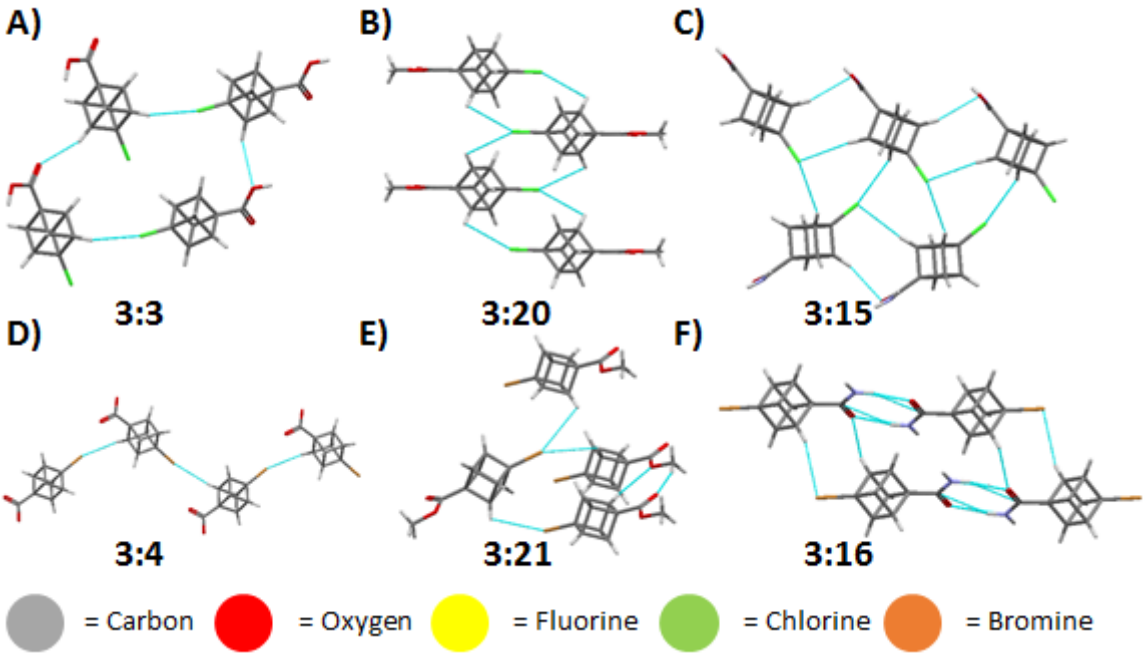

Figure 3:34: View of the molecular arrangement in the crystal of compound **3:3** (A), **3:20** (B), **3:15** (C), **3:4** (D), **3:21** (E), and **3:16** (F) represented as a stick model. Each model shows the preference for halogen interactions within the given structure. Interactions are indicated by blue dashed lines. Bond lengths and angles are given in Table 3:24 below.

Table 3:24: List of bond lengths and angles shown in Figure 3:34.

#	Interaction	H···A (Å)	D–H···A (°)
3:3	C–H_{cubane}···Cl	2.945	165.3
3:15	C–H_{cubane}···Cl	2.932	154.35
	C–H_{cubane}···Cl	3.152	99.9
3:20	C–H_{cubane}···Cl	3.106	103.0
3:4	C–H_{cubane}···Br	3.189	168.8
3:21	C–H_{cubane}···Br	3.234	105.4
3:16	C–H_{cubane}···Br	3.008	153.7

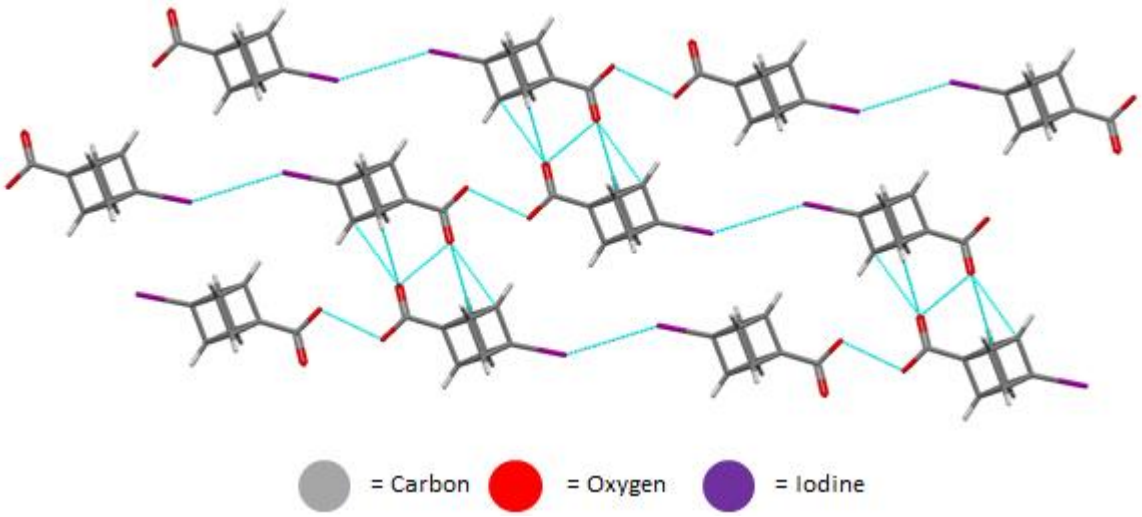

Figure 3:35: View of the molecular arrangement in the crystal of 4-iodocubane-1-carboxylic acid (**3:5**) represented as a stick model showing the head-to-head overlap between the ester moieties with the cubane scaffold and the I···I interactions. Interactions are indicated by blue dashed lines. Bond lengths and angles are given in Table 3:25 below.

Table 3:25: List of bond lengths and angles shown in Figure 3:35.

#	Interaction	H···A (Å)	D–H···A (°)
3:5	C–I···I	3.835	150.5

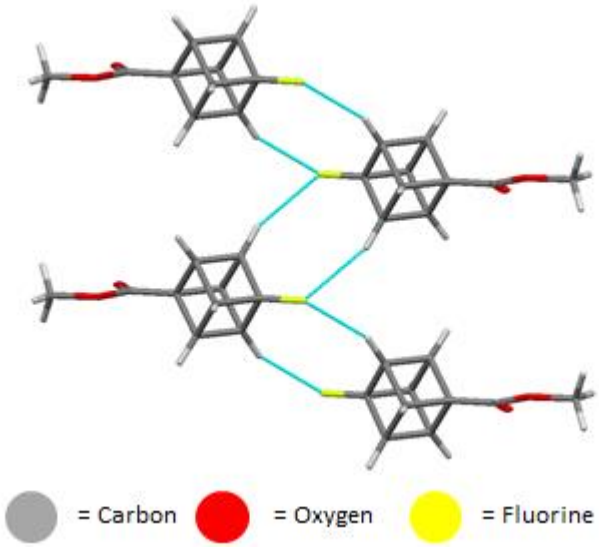

Figure 3:36: View of the molecular arrangement in the crystal of 4-fluoro-1-methoxycarbonyl cubane (**3:19**) represented as a stick a model showing the H···F interactions. Interactions are indicated by blue dashed lines. Bond lengths and angles are given in Table 3:26 below.

Table 3:26: List of bond lengths and angles shown in Figure 3:36.

#	Interaction	H···A (Å)	D–H···A (°)
3:19	C–H_{cubane}···F	2.618	156.3

Both the 4-bromo (**3:21**) and the 4-iodo (**3:22**) compound show a more staggered and wider packing pattern. Due to the larger size of a halogen atom, the halogen interacts with the cubane in the above and below layers, as opposed to the inline contacts observed for compounds **3:19** and **3:20**. Interestingly, the converse is observed with the bromine interacting with the hydrogens closest to the ester function group (Figure 3:34E) and the iodine interacts with the nearest hydrogen to the halogen substitute (Figure 3:37A), both in a bifurcated fashion. Additionally, when looking at the low-temperature structure **3:22_a** there is a shift to more distance between the halogen side of the cubane scaffold with a direct I···I interaction now visible (Figure 3:37B).

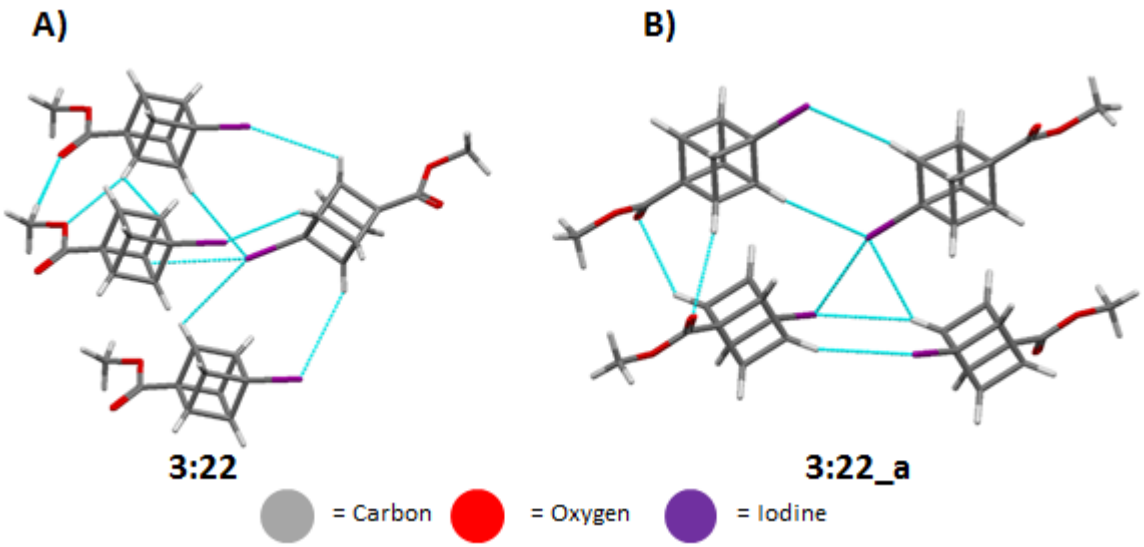

Figure 3:37: View of the molecular arrangement in the crystal of 4-iodo-1-methoxycarbonyl cubane (**3:22** (A) and **3:22_a** (B)) represented as a stick model showing the H···I and I···I interactions. Interactions are indicated by blue dashed lines. Bond lengths and angles are given in Table 3:27 below.

Table 3:27: List of bond lengths and angles shown in Figure 3:37.

#	Interaction	H···A (Å)	D–H···A (°)
3:22	C–H_{cubane}···I	3.364	148.6
3:22_a	C–H_{cubane}···I	3.278	160.9
	C–I···I	3.984	153.5

The carboxamides cubanes show mainly dimer formation between the carboxamides moieties as mentioned above. This results in a head-to-head interaction between carboxamides leaving the halogen atoms to point towards each other. The 4-chloro derivative **3:15** shows two short Cl···H interactions which form an alternating network with layers of halogen-bonding and hydrogen-bonding

interactions orthogonal to each other in a zig-zag pattern (Figure 3:34C). Moving to the 4-bromo cubane structure **3:16** a change to a stacked Br···H network occurs (Figure 3:34F). This is compounded by the face-to-face of the carboxamides to create overset lines of overlapping dimers. The 4-iodo cubane structure **3:17** shows two short contacts with an I···H network similar to compound **3:15** and an I···I network. Together these form an alternating network with layers of halogen-bonding interactions and hydrogen-bonding interactions (Figure 3:38). As seen in Figure 3:34, moving from carboxylic acid to methoxy ester to carboxamide, there is a clear shift in preference to packing patterns which are not directed by the halogen, indicating that any interactions seen are secondary to the hydrogen-bonding motif.

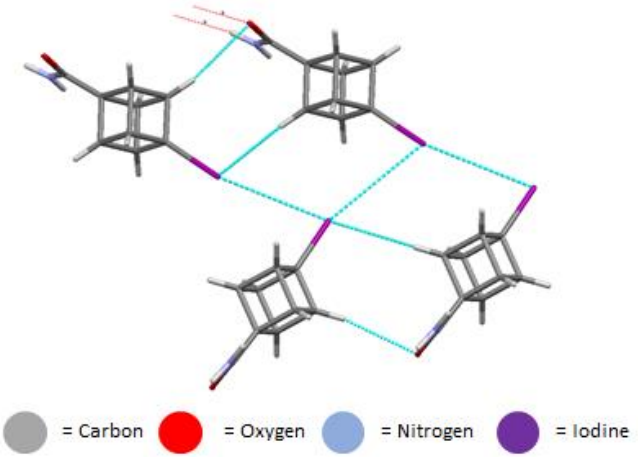

Figure 3:38: View of the molecular arrangement in the crystal of 4-iodo-1-carboxamide cubane (**3:17**) represented as a stick model showing the H···I and I···I interactions. Interactions are indicated by blue dashed lines.

Table 3:28: List of bond lengths and angles shown in Figure 3:38.

#	Interaction	H···A (Å)	D–H···A (°)
3:17	C–H_{cubane}···I	3.215	152.4
	C–I···I	4.131	74.0

Several 4-bromocubane samples with alternate substitution patterns and size have been deposited to the CCDC over the past few years. The 4-bromocubane-1-carbaldehyde **3:49** is a structure that is highly disordered, with the bromine and aldehyde being modelled over each other, and hydrogens atoms have not been assigned in the deposited structure.[181c] Therefore, not much detail can be gleaned, however, the stacking appears linear with cubane scaffolds stacked in lines (Figure 3:39). The structure of 4-bromo-1-(hydroxymethyl)cubane **3:50** shows the alcohol moiety in a linear hydrogen-bonding fashion, Figure 3:40.[181d] This allows the

bromine atoms to interact with the hydrogen of the cubane in the next layer to create a 3D lattice. When substituting hydroxymethyl for a nitrox methyl (**3:51**) the NO_2 group interacts with the cubane and the CH_2 hydrogens.[177a] This leaves bromine atoms close to each other to form a direct halogen-bonded network (Figure 3:41). The structure of **3:52**, 2-(4-bromocubane-1-carboxamido)ethyl nitrate, shows a similar linear hydrogen-bond network to that of the carboxamide **3:16**, and a Br···H network that interacts with the cubanes hydrogens in the next layer (Figure 3:42).[181e]

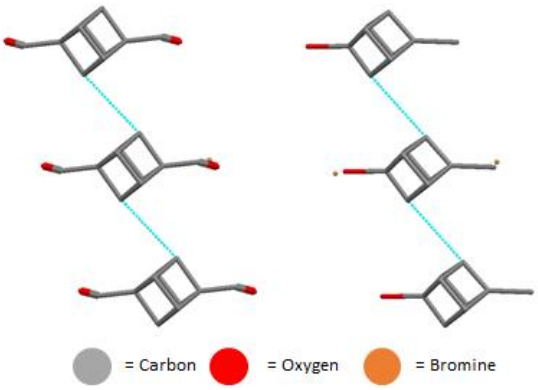

Figure 3:39: View of the molecular arrangement in the crystal of 4-bromocubane-1-carbaldehyde (**3:49**) represented as a stick model showing the potential interactions between the cubane scaffolds. Interactions are indicated by blue dashed lines. As no hydrogens were provided in the submitted data they could not be drawn in this figure.

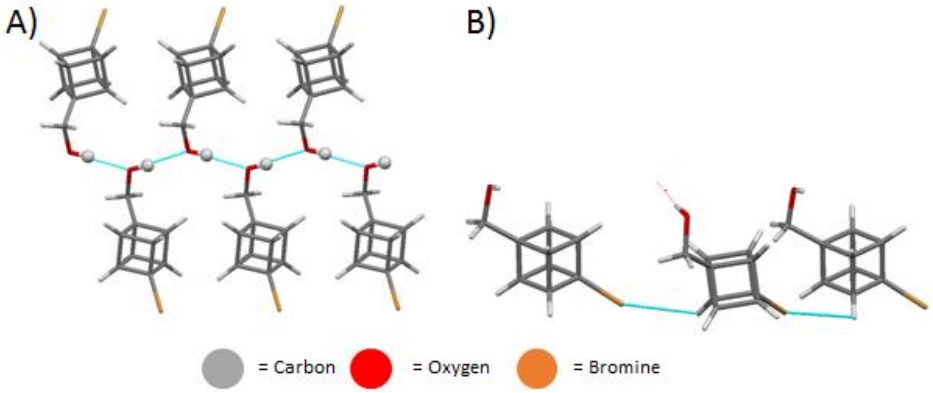

Figure 3:40: View of the molecular arrangement in the crystal of 4-bromo(cuban-1-yl)methanol (**3:50**) represented as a stick model showing the O···H interactions (A) and Br···H interactions (B). Interactions are indicated by blue dashed lines. Bond lengths and angles are given in Table 3:29 below.

Table 3:29: List of bond lengths and angles shown in Figure 3:40.

#	Interaction	H···A (Å)	D–H···A (°)
3:50	C–H_{cubane}···Br	3.120	100.9
	O–H···O	1.973	173.6

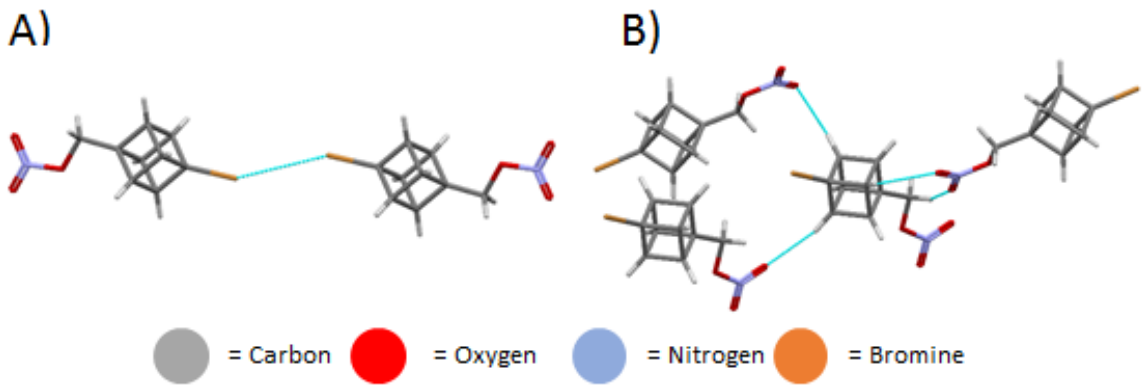

Figure 3:41: View of the molecular arrangement in the crystal of 4-bromo(cuban-1-yl)methyl nitrate (**3:51**) represented as a stick model showing the Br···Br interactions (A) and N–O···H with the cubane scaffold (B). Interactions are indicated by blue dashed lines. Bond lengths and angles are given in Table 3:30 below.

Table 3:30: List of bond lengths and angles shown in Figure 3:41.

#	Interaction	H···A (Å)	D–H···A (°)
3:51	C–Br···Br	3.685	152.8
	$C–H_{cubane}···O$	2.665	125.7
	$C–H_{cubane}···O$	2.465	149.1
	$C–H_{cubane}···O$	2.514	157.5
	$C–H_{CH2}···O$	2.405	140.1

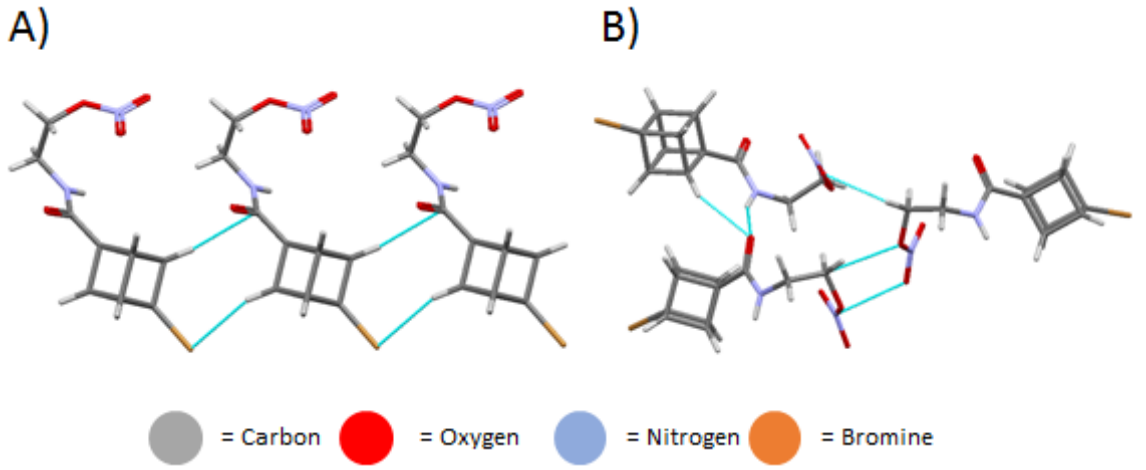

Figure 3:42: View of the molecular arrangement in the crystal of 2-(4-bromocuban-1-carboxamide)ethyl nitrate (**3:52**) represented as a stick model showing the Br···H interactions (A) and O···H interactions (B). Interactions are indicated by blue dashed lines. Bond lengths and angles are given in Table 3:31 below.

Table 3:31: List of bond lengths and angles shown in Figure 3:42.

#	Interaction	H···A (Å)	D–H···A (°)
3:52	$C–H_{cubane}\cdots Br$	2.824	148.0
	$C–H_{cubane}\cdots Br$	2.869	146.7
	$C–H_{CH2}\cdots O$	2.526	141.7
	N–O···N	3.050	110.8
	$C–H_{CH2}\cdots O$	2.891	98.5
	N–H···O	1.930	155.6

The *N*-(4-chlorocuban-1-yl)glycyl)-2,6-difluorobenzamide) (**3:53**) is probably the most functionalized 4-halocubane structure currently published (Figure 3:43).[167] With an amine, carbonyl, and halogen functional groups available for potential interactions, competition for the cubane hydrogens is rather high. A bifurcated interaction is noted centring on the chlorine atom with a cubane hydrogen and a benzene hydrogen atom. Other noticeable cubane contacts are between the fluorine atoms of the benzene ring and the oxygen of the carbonyl furthest from the cubane, both of which interact with the cubane in a bifurcated fashion. Additionally, the second fluorine atoms interact with a cubane hydrogen atom on the opposite side. The remaining interactions are a plethora of dimers formed between the amide type linkers through classical hydrogen-bonding.

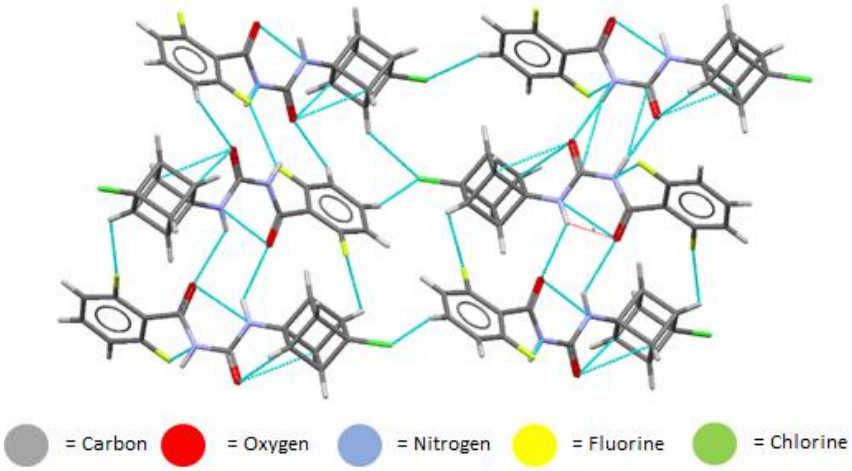

Figure 3:43: View of the molecular arrangement in the crystal of *N*-((4-chlorocuban-1-yl)glycyl)-2,6-difluorobenzamide (**3:53**) represented as a stick model showing the plethora of interactions between the O···H, H···F, and H···Cl interactions. Interactions are indicated by blue dashed lines. Bond lengths and angles are given in Table 3:32 below.

Table 3:32: List of bond lengths and angles shown in Figure 3:43.

#	Interaction	H···A (Å)	D–H···A (°)
3:53	$C–H_{cubane}\cdots Cl$	2.922	122.0
	$C–H_{cubane}\cdots F$	2.585	128.2
	$C–H_{cubane}\cdots F$	2.609	115.8
	$C–H_{cubane}\cdots O$	2.581	137.1
	$C–H_{Ph}\cdots Cl$	2.947	159.8
	C–F···F	2.777	140.8
	C–F···O	2.957	145.6
	N–H···O	1.947	159.1
	N–H···O	2.549	138.0

Compound **3:54** contains an acetamide on one side and a fluorine on the other.[179a] This structure shows the similar bifurcated interaction between fluorine and hydrogen atoms as seen in compound **3:19** and **3:2**. This is in addition to the N–H···O interactions, which are rotated at 90° to each other, resulting in an alternating packing of hydrogen-bonding and halogen-bonding partners (Figure 3:44).

The next two cubanes are directly linked cubane scaffolds with a halogen substitute (**3:55** and **3:56**).[181f, 181g] In these structures, rather than the halogen-hydrogen contacts, the non-classical hydrogen-bond between cubane scaffolds is much more common. This is due to the second cubane scaffold include in these structures which allows for the free cubane sides to interact more with each other. Compound **3:55** is a prime example of this, as even though two halogens are present, there are no interactions between them or any cubane hydrogen atoms. This results in a highly ordered system where the halogens are held between layers of cubanes but do not interact with the cubane scaffold directly (Figure 3:45). On the other hand, the mono-halogenated compound **3:56**, shows that the bromine atoms will interact with hydrogen atoms due to a tighter packing as a result of the less symmetric molecule (Figure 3:46).

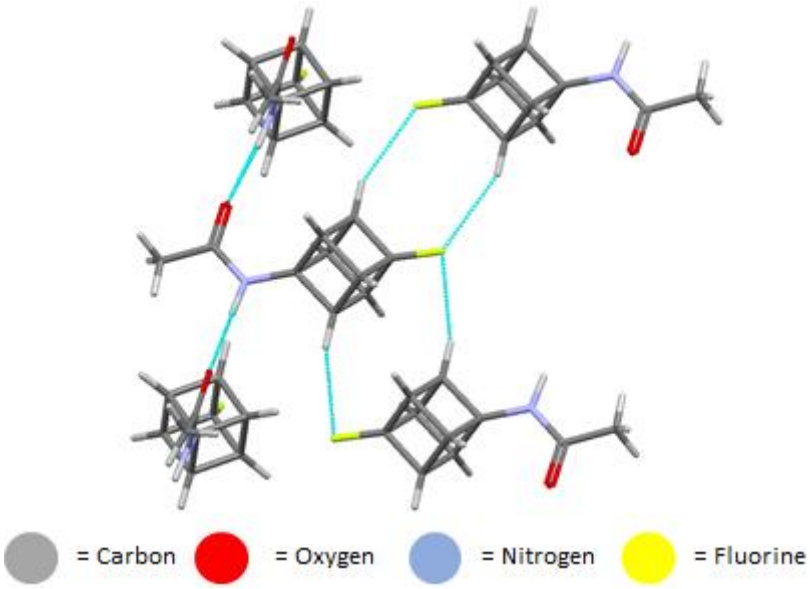

Figure 3:44: View of the molecular arrangement in the crystal of *N*-(4-fluorocuban-1-yl)acetamide (**3:54**) represented as a stick model showing the O···H and H···F interactions. Interactions are indicated by blue dashed lines. Bond lengths and angles are given in Table 3:33 below.

Table 3:33: List of bond lengths and angles shown in Figure 3:44.

#	Interaction	H···A (Å)	D–H···A (°)
3:54	C–H_{cubane}···F	2.612	155.8
	C–H_{cubane}···F	2.592	161.5
	C–H···F	2.654	152.0
	N–H···O	1.882	174.1

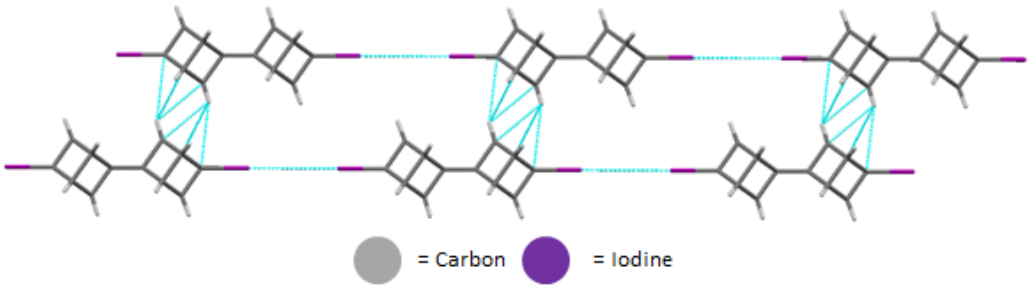

Figure 3:45: View of the molecular arrangement in the crystal of 4,4'-diiodo-1,1'-bi(cubane) (**3:55**) represented as a stick model showing the cubane···cubane and I···I interactions. Interactions are indicated by blue dashed lines. Bond lengths and angles are given in Table 3:34 below.

Table 3:34: List of bond lengths and angles shown in Figure 3:45.

#	Interaction	H···A (Å)	D–H···A (°)
3:55	C–I···I	4.258	180.0
	C–H_{cubane}···C	2.770	112.7

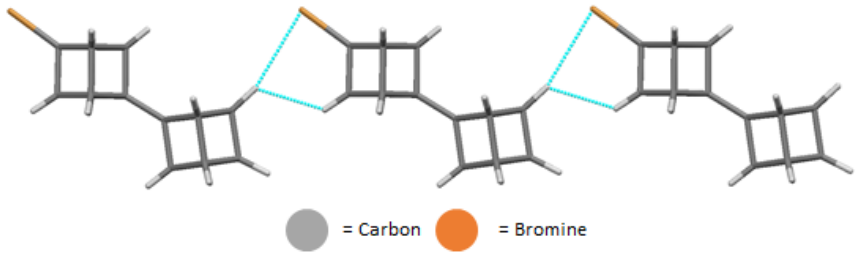

Figure 3:46: View of the molecular arrangement in the crystal of 4-bromo-1,1'-bi(cubane) (**3:56**) represented as a stick model showing the Br···H interactions. Interactions are indicated by blue dashed lines. Bond lengths and angles are given in Table 3:35 below.

Table 3:35: List of bond lengths and angles shown in Figure 3:46.

#	Interaction	H···A (Å)	D–H···A (°)
3:56	C–H_{cubane}···Br	2.955	163.6

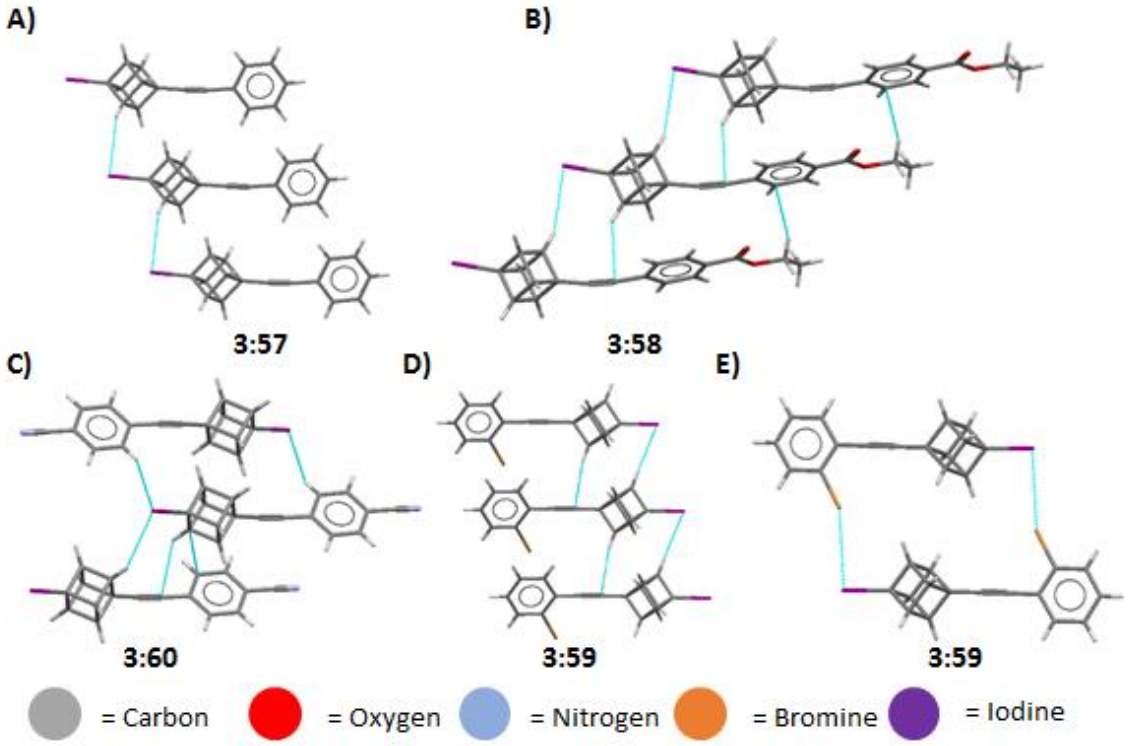

Figure 3:47: View of the molecular arrangement in the crystal of compound **3:57** (A), **3:58** (B), **3:60** (C), and **3:59** (D and E) represented as a stick model. Each view shows the preference for halogen interactions within the given structure. Interactions are indicated by blue dashed lines. Bond lengths and angles are given in Table 3:36 below.

Table 3:36: List of bond lengths and angles shown in Figure 3:47.

#	Interaction	H···A (Å)	D–H···A (°)
3:57	C–H_{cubane}···I	3.201	128.7
	C–H_{cubane}···I	3.263	129.0
	C–H_{cubane}···π	2.948	140.5
3:58	C–H_{cubane}···I	3.113	151.34
	C–H_{cubane}···π	2.843	150.9
3:59	C–H_{cubane}···I	3.028	169.9
	C–Br···I	3.756	155.8
	C–H_{cubane}···π	2.684	155.9
	C–H_{cubane}···π	3.052	167.4
3:60	C–H_{cubane}···I	3.079	150.0
	C–H_{Ph}···I	3.061	151.2
	C–H_{cubane}···π	2.692	158.4
	C–H_{cubane}···π	2.984	145.6
	C–H_{Ph}···N	2.701	144.4
	C–H_{Ph}···N	2.721	176.4

The next set of the structure have been previously published by our group (**62**) or will be as part of this section (**3:44**, **3:41**, and **3:57**–**3:61**).[168a] The first four structures (**3:57**–**3:60**) vary only by the substitution of the benzene ring. Using compound **3:57** as a base model for this set, the first contacts of note is two C–H_{cubane}···I interactions that aid in lateral stacking and one C–H_{cubane}···π interaction that allows for vertical stacking (Figure 3:47A). The inclusion of the ethyl ester, **3:58** shows the addition of a C–H_{cubane}···π of the ethynyl moiety to stabilize a C–H_{cubane}···I lateral network (Figure 3:47B). This is in addition to the ester cubane interactions which are mainly involved in a head-to-tail overlapped stacked structure (Figure 3:48). Upon the inclusion of a cyano group to the para-position of the benzene ring (**3:60**), two I···H networks are seen between the halogen and cubane hydrogens in a stacking type pattern and the halogen and aromatic hydrogens in a head-to-tail dimer fashion (Figure 3:47C). This is aided by two cubane hydrogens interacting with the ethynyl–π system, which seems typical for these types of compounds. Additionally, there is a hydrogen-bonding interaction between cyano groups and the benzene rings in a bifurcated fashion due to the space taken up by the iodine atoms. This results in a head-to-head dimer and an orthogonal interaction between another pair of molecules to form a 2×2 layering crossover pattern (Figure 3:49). The 2-bromophenyl derivative **3:59** shows a similar I···H and C–H_{cubane}···π network common for this series. However, the main feature is the direct I···Br halogen-bond to create a head-to-tail dimer between the molecules (Figure 3:47D and 3:47E).

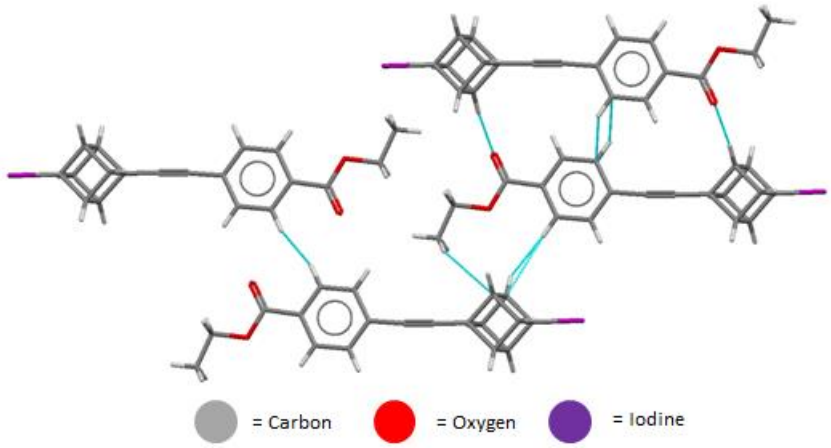

Figure 3:48: View of the molecular arrangement in the crystal of ethyl 4'-((4-iodocuban-1-yl)ethynyl)benzoate (**3:58**) represented as a stick model showing the ester cubane interactions which are involved in a head-to-tail overlapped vertical stack. Interactions are indicated by blue dashed lines. Bond lengths and angles are given in Table 3:37 below.

Table 3:37: List of bond lengths and angles shown in Figure 3:48.

#	Interaction	H···A (Å)	D–H···A (°)
3:58	$C–H_{cubane}\cdots I$	3.113	151.34
	$C–H_{cubane}\cdots \pi$	2.843	150.9

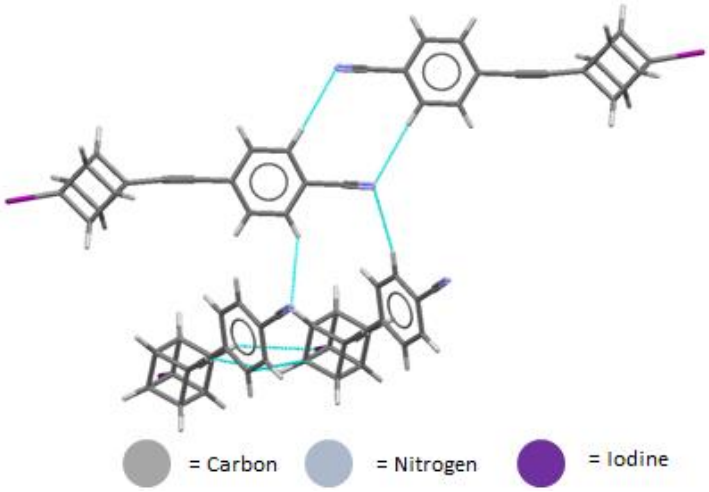

Figure 3:49: View of the molecular arrangement in the crystal of 4-(4-iodocuban-1-yl)ethynyl)benzonitrile (**3:60**) represented as a stick model showing the hydrogen-bonding interaction between cyano groups and the phenyl rings which results in a head-to-head dimer and an orthogonal interaction between another pair of molecules to form a 2×2 layering crossover pattern. Interactions are indicated by blue dashed lines.

The two halo-ester cubane structures **3:44** and **3:41**, previously covered in the ester section, show the effect of including a halogen atom. The structure of **3:44** shows one interaction between the cubane hydrogens and the iodine atoms in a similar

fashion seen in the structures of **3:57**–**3:60**. Coupled with the ester interaction there are several I···H short contacts between the indoline hydrogen atoms. Of most interest is the direct I···I halogen-bond in a type I manner forming a head-to-head contact (Figure 3:29E and 3:29F). The structure of **3:41** is much simpler with the only cubane interaction involved with the methyl ester of the benzene ring. The only noticeable halogen interaction is between the iodine and the oxygen of the methyl ester (Figure 3:28C).

The final two 4-halogeno-cubane structures are possibly the most unique structures available. The first, **3:61**, shows the inclusion of a highly bulky substitute around the cubane scaffold. There are clear short contacts between the cubane hydrogens and the phenyl π-ring in a dimer fashion as seen in Figure 3:50A. The O–H shows short contacts towards the phenyl π-ring. The only halogen interaction is seen between the phenyl hydrogens creating a linear network. This shows the noticeable effects a large group can cause in shielding the cubane scaffold. The final structure, **3:62**, has the largest substituent attached to a cubane scaffold. The addition of a porphyrin molecule has an interesting effect on the cubane structure. The tolyl substituents of the porphyrins 'sandwich' the cubane scaffold and it is tethered with a C–I···π to form a tightly packed structure (Figure 3:50B).

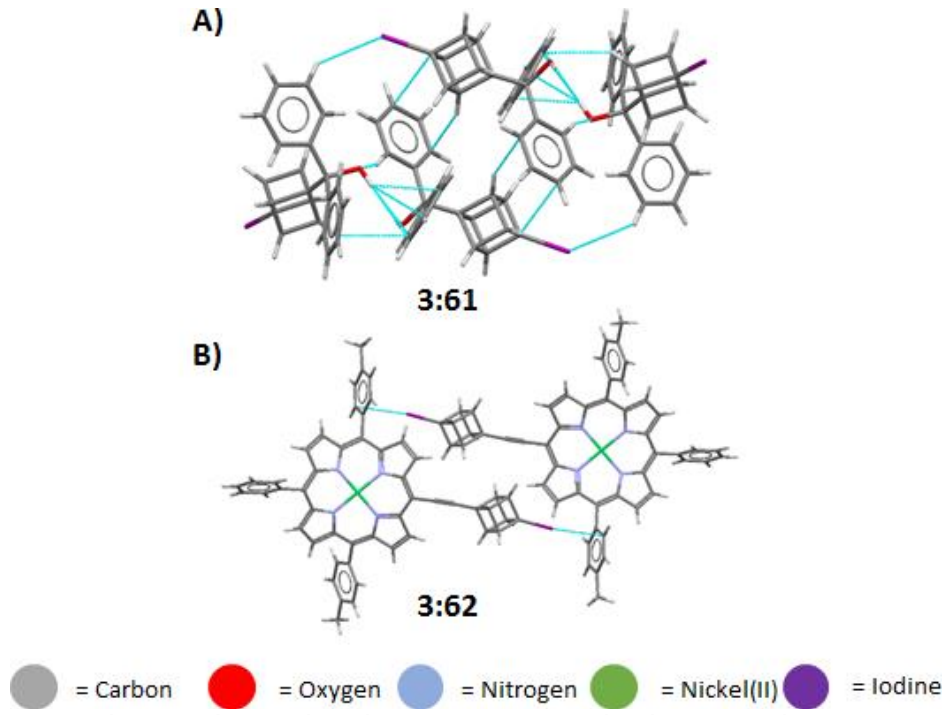

Figure 3:50: View of the molecular arrangement in the crystal of compound **3:61** (A) and **3:62** (B) represented as a stick model. Each model shows the preference for halogen interactions within the given structure. Interactions are indicated by blue dashed lines. Bond lengths and angles are given in Table 3:38 below.

Table 3:38: List of bond lengths and angles shown in Figure 3:50.

#	Interaction	H···A (Å)	D–H···A (°)
3:61	$C–H_{Ph}\cdots I$	3.151	139.7
3:62	C–I···π	3.688	80.7
	$C–H_{Ph}\cdots C_{cubane}$	2.895	149.4

By looking at the interactions and packing of the 4-halo-1-(R)-cubane structures, it is clear, as is the case from acid, ester, or carboxamide cubane derivatives, that there are a substantial number of halogen···hydrogen interactions with few halogen···halogen interactions present in most structures. However, in these structures, the halogen interactions are less directive than the acid, ester, or carboxamide interactions. This is clearly seen in Figure 3:34, with the three alternate functionalities causing three different packing patterns. When moving to the rod-like structures (Figure 3:47), the most common motif is the C–I···H interaction between the cubane scaffolds. This is typically stabilized with a $C–H\cdots C_{ethynyl}$ interaction. The only structure which differs from this packing order is compound **3:60** where the -CN group results in a detailed $C\equiv N\cdots H_{Bz}$ network which results in a rotated system leaving more space in the crystal for interactions between C–I···H of the iodine group and phenyl hydrogens. These results indicate the importance of the cubane hydrogen and halogen atoms.

Acetylene.

When looking at compounds **3:40**, **3:57–3:60**, **3:62** it was noted that there is a surprisingly high frequency of ethylene moieties interacting with the cubane scaffold in a type of non-classical hydrogen-bond (C–H···π). This prompted a further investigation to see if this feature was shared by other cubane structures with a similar moiety. In the literature, there are only five examples, so this is the smallest of these sections, but one that warrants consideration. This section will focus mainly on the interactions between the ethylene moiety and the cubane hydrogens, with alternate functionalities and the resultant interactions already covered in the previous section, unless the structure only appears in this section. Figure 3:51 shows the ethynyl bearing cubane scaffolds from the literature and six structures determined by us as part of this work. Bond lengths and angles are shown in Table SI3:7.

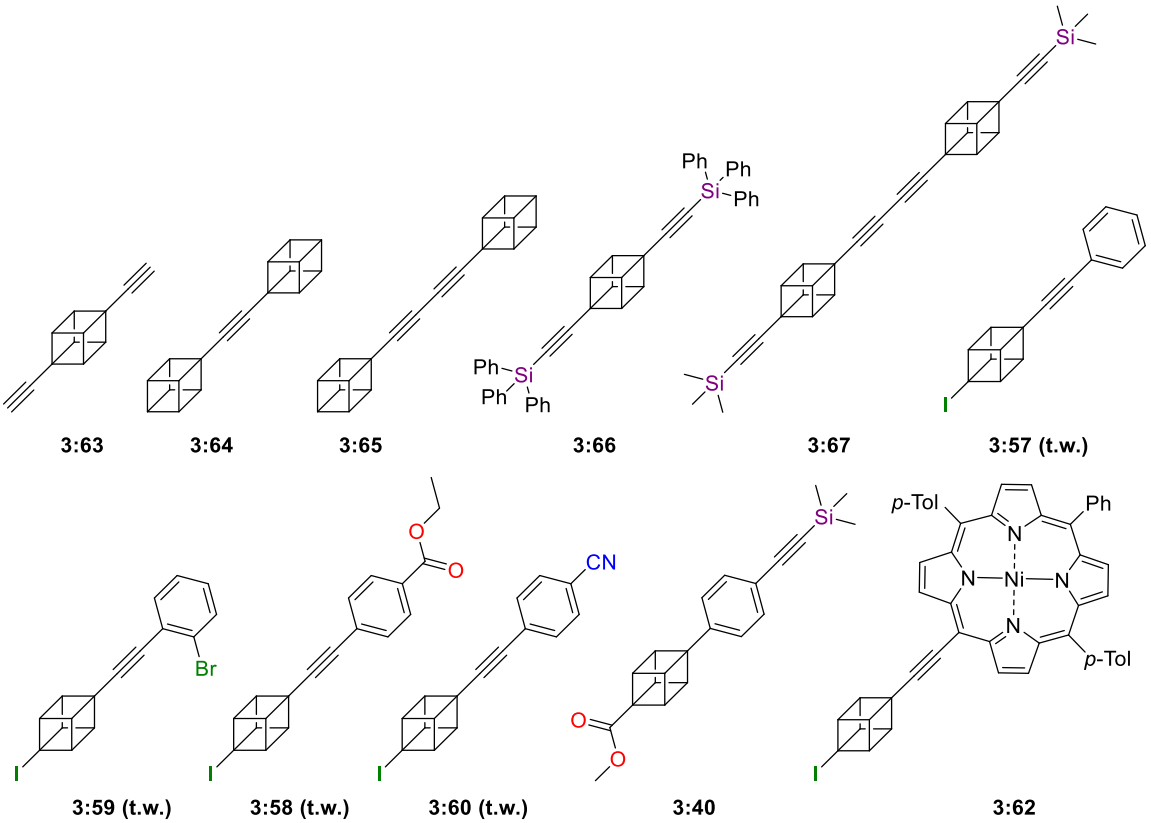

Figure 3:51: Ethynyl bearing 1,4-disubstituted cubane structures. 't.w.' indicates structures obtained as part of this work. [168a, 182]

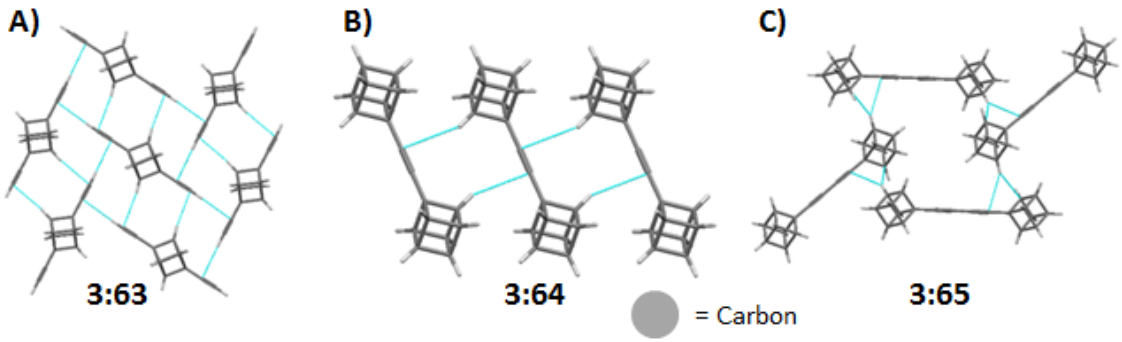

Figure 3:52: View of the molecular arrangement in the crystal of compound **3:63** (A), **3:64** (B), and **3:65** (C) represented as a stick model. Each model shows the preference for C–H_{cubane}···$C_{ethynyl}$ interactions within the given structure. Interactions are indicated by blue dashed lines. Bond lengths and angles are given in Table 3:39 below.

Table 3:39: List of bond lengths and angles shown in Figure 3:52.

#	Interaction	H···A (Å)	D–H···A (°)
3:63	C–H_{cubane}···C_{cubane}	2.838	152.6
	C–H_{cubane}···$C_{ethynyl}$	2.804	169.6
	C–$H_{ethynyl}$···$C_{ethynyl}$	2.707	167.1
3:64	C–H_{cubane}···$C_{ethynyl}$	2.879	143.6
	C–H_{cubane}···$C_{ethynyl}$	2.874	142.1
	C–H_{cubane}···$C_{ethynyl}$	2.879	144.2
3:65	C–H_{cubane}···$C_{ethynyl}$	2.879	150.0
	C–H_{cubane}···$C_{ethynyl}$	2.875	142.0
	C–H_{cubane}···C_{cubane}	2.853	145.7

The structure of **3:63** is the simplest and the most characteristic of the structures provided for the C–H_{cubane}···$C_{ethynyl}$ interactions under consideration.[182a] Due to its small size and simple structure, it is, quite literally, surrounded by the non-classical hydrogen-bonds that make up the subject of this section. This is mainly seen in the form of C–$H_{ethynyl}$···$C_{ethynyl}$ on one side of the triple bond with a complimentary C–H_{cubane}···$C_{ethynyl}$ on the other to form a herringbone network (Figure 3:52A). This holds each individual molecule in perfect alignment in a highly ordered system. When this structure is inverted, as is the case for **3:64**, no C–$H_{ethynyl}$···$C_{ethynyl}$ can possibly form. The structure is then compiled of multiple C–H_{cubane}···$C_{ethynyl}$ interactions in a similar fashion to **3:63**; however, in a much more staggered linear network, both vertically and laterally (Figure 3:52B).[182a] When this linker is extended between two cubane scaffolds (**3:65**), the extra spacer between the two cubane scaffolds allows the cubane itself to occupy a space that is otherwise too small.[182a] This results in, not only the C–H_{cubane}···$C_{ethynyl}$ interactions associated with this family of compounds, but now C–H_{cubane}···C_{cubane} interactions, which previously were disfavoured due to space constraints. This structure forms an interesting pattern of layers of molecules staggered at roughly 45° to each other as shown in Figure 3:52C. Compound **3:66** shows what happens by increasing the size of the substituent around the cubane scaffold.[182a] In direct contrast to **3:63**, there are no C–H_{cubane}···$C_{ethynyl}$ interactions. Rather, every interaction is taken up by the phenyl groups in a C–H_{phenyl}···$C_{ethynyl}$ or C–H_{phenyl}···C_{cubane} fashion (Figure 3:53). This indicates that low steric hindrances favour C–H_{cubane}···$C_{ethynyl}$, while large bulk inhibits such interactions. This is exemplified in the structure of **3:67** which is a

combination of **3:66** and **3:65**.[182b] In this structure C–H_{cubane}···$C_{ethynyl}$ interactions return as the main linkage between molecules; however, due to the comparatively smaller but still significantly bulky trimethylsilyl group, no C–H_{cubane}···C_{cubane} interactions are observed, forming a relatively ordered staggered packing (Figure 3:54).

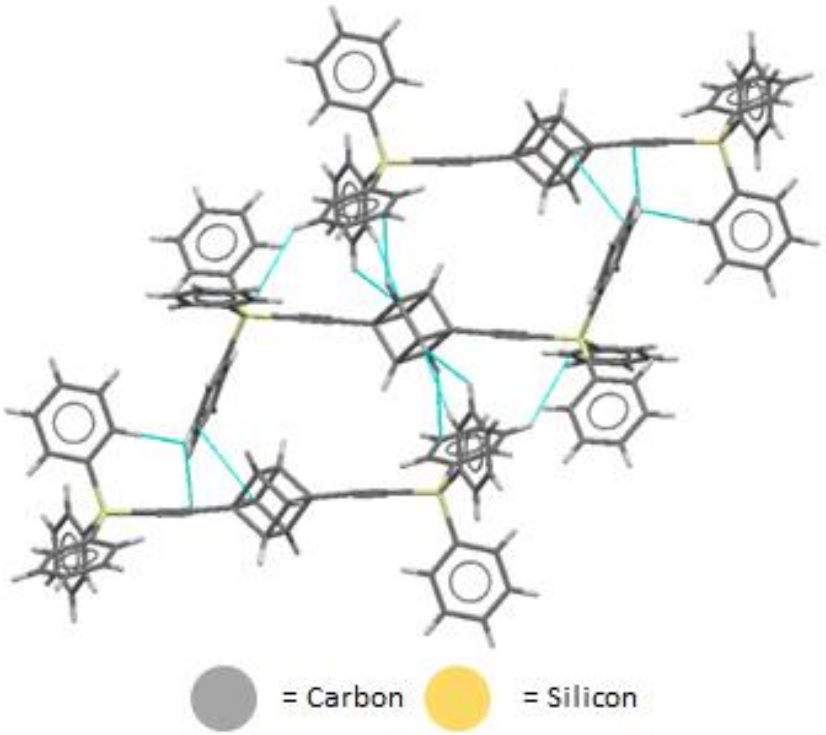

Figure 3:53: View of the molecular arrangement in the crystal of 1,4-bis((triphenylsilyl)ethynyl)cubane (**3:66**) represented as a stick model showing the C···H interactions and ethynyl C···H interactions. Interactions are indicated by blue dashed lines. Bond lengths and angles are given in Table 3:40 below.

Table 3:40: List of bond lengths and angles shown in Figure 3:53.

#	Interaction	H···A (Å)	D–H···A (°)
3:66	C–H_{Ph}···C_{cubane}	2.846	153.7
	C–H_{Ph}···C_{cubane}	2.771	137.3
	C–H_{cubane}···C_{Ph}	2.883	156.7
	C–H_{Ph}···$C_{ethynyl}$	2.716	150.0
	C–H_{Ph}···C_{Ph}	2.388	129.1
	C–H_{Ph}···C_{Ph}	2.858	137.4

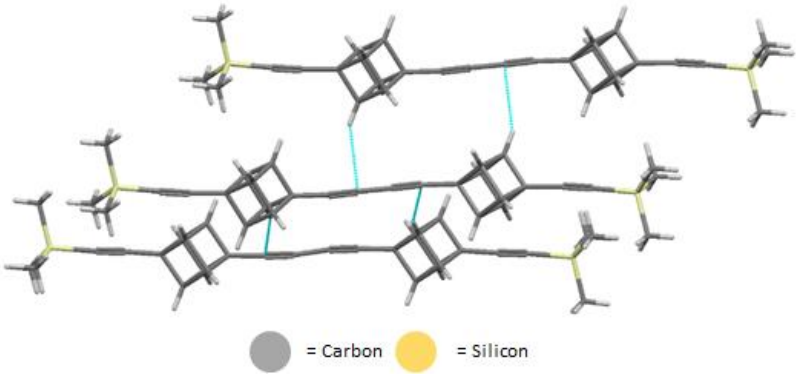

Figure 3:54: View of the molecular arrangement in the crystal of 1,4-bis(4-((trimethylsilyl)ethynyl)cuban-1-yl)buta-1,3-diyne (**3:67**) represented as a stick model showing the ethynyl C···H interactions with cubane. Interactions are indicated by blue dashed lines. Bond lengths and angles are given in Table 3:41 below.

Table 3:41: List of bond lengths and angles shown in Figure 3:54.

#	Interaction	H···A (Å)	D–H···A (°)
3:67	$C–H_{cubane}\cdots C_{ethynyl}$	2.871	159.9
	$C–H_{cubane}\cdots C_{ethynyl}$	2.871	159.9
	$C–H_{cubane}\cdots C_{ethynyl}$	2.822	152.0
	$C–H_{cubane}\cdots C_{ethynyl}$	2.822	152.0
	$C–H_{cubane}\cdots C_{ethynyl}$	2.871	159.9
	$C–H_{cubane}\cdots C_{ethynyl}$	2.871	159.9

Of the structures to be included in this section (**3:40 and 3:62** previously published by us), this $C–H_{cubane}\cdots C_{ethynyl}$ interaction is rather quite common, except strangely enough in **3:57**.[168a] In fact, **3:57** has no noticeable interactions at all, which is rather rare as shown here. The structure of **3:59** has an interesting network of $C–H_{cubane}\cdots C_{ethynyl}$ interactions that accommodate a head-to-head overlap in one direction and a head-to-tail interaction in the other to form a repeating quartet throughout the crystal. This is aided by the I···H and I···Br interactions previously mentioned in the halogen section above (Figure 3:55A). The structure of **3:58** has an overlapped network of $C–H_{cubane}\cdots C_{ethynyl}$ interactions which from the head-to-head structure, aided by I···H. The ester in this structure plays a nominal role in forming head-to-tail dimers but has no interaction visible with the ethynyl group, baring occupying cubane hydrogens that may otherwise be involved with the ethynyl group as seen in **3:59** (Figure 3:55B). The structure of **3:60** shows $C–H_{cubane}\cdots C_{ethynyl}$ interactions in a trimer formation. This is aided by the I···H interactions, as seen in both **3:59** and **3:58**, and the roughly 70° rotation of one of the contributing molecules (Figure 3:55C). The structure of **3:40**, even though does not have the same base motif, shows favourable $C–H_{cubane}\cdots C_{ethynyl}$ contacts as a result of head-to-tail stacked network (Figure 3:55D). The final structure, **3:62**, shows no $C–H_{cubane}\cdots C_{ethynyl}$ interactions, rather, it is similar to the bulky triphenyl silyl of **3:66**, preferring to form $C–H_{Ph}\cdots C_{ethynyl}$ interactions (Figure 3:55E).

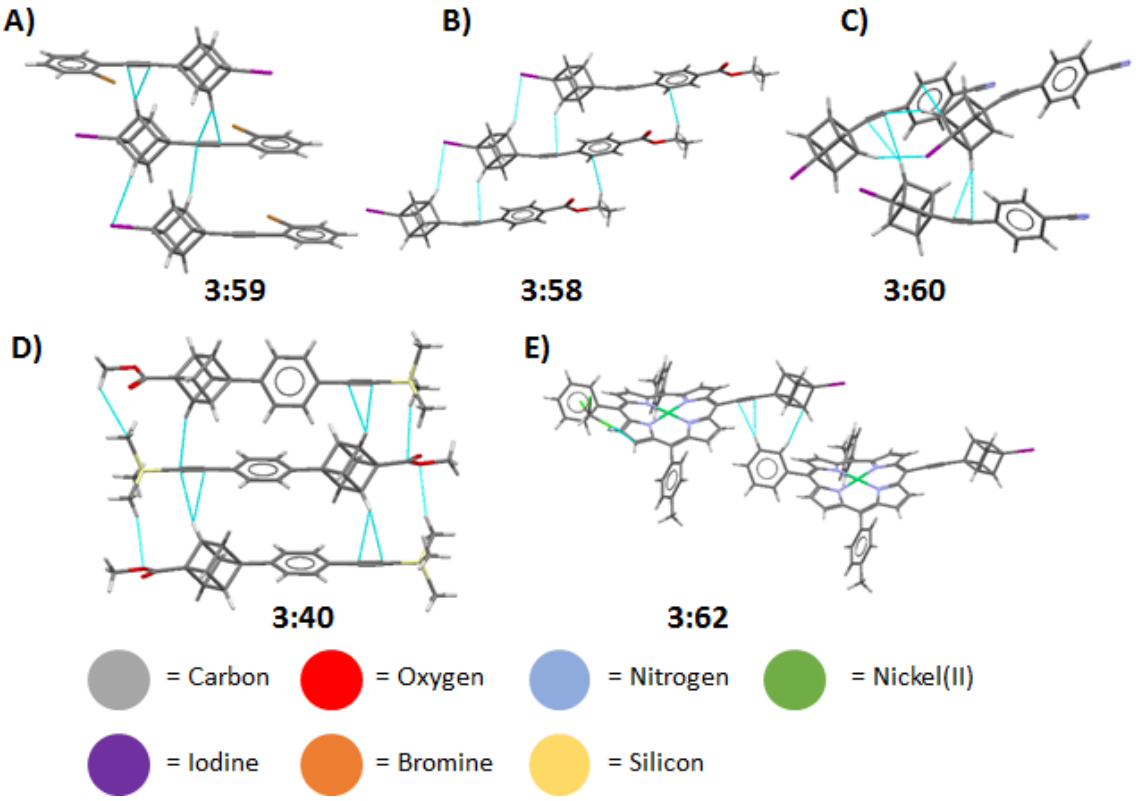

Figure 3:55: View of the molecular arrangement in the crystal of a compound of **3:59** (A), **3:58** (B), **3:60** (C), **3:40** (D), and **3:62** (E) represented as a stick model. Each model shows the preference for C–H_{cubane}···$C_{ethynyl}$ interactions within the given structure. Interactions are indicated by blue dashed lines. Bond lengths and angles are given in Table 3:42 below.

Table 3:42: List of bond lengths and angles shown in Figure 3:54.

#	Interaction	H···A (Å)	D–H···A (°)
3:59	C–H_{cubane}···$C_{ethynyl}$	2.695	147.8
	C–H_{cubane}···$C_{ethynyl}$	2.804	159.1
	C–H_{cubane}···$C_{ethynyl}$	2.881	163.4
3:58	C–H_{cubane}···$C_{ethynyl}$	2.760	141.1
3:60	C–H_{cubane}···$C_{ethynyl}$	2.756	156.8
	C–H_{cubane}···$C_{ethynyl}$	2.761	153.5
	C–H_{cubane}···$C_{ethynyl}$	2.890	138.0
3:40	C–H_{cubane}···$C_{ethynyl}$	2.869	163.4
	C–H_{cubane}···$C_{ethynyl}$	2.881	167.8
	C–H_{cubane}···$C_{ethynyl}$	2.863	143.9

By looking at these structures (**3:40**, **3:57–3:60**, **3:62–3:67**) there is a clear preference for the formation of C–H_{cubane}···$C_{ethynyl}$ regardless of the alternate functionality. This makes the C–H_{cubane}···$C_{ethynyl}$ partially directive, but the alternate

functional group or bulk of the alternate group has a more significant effect on the packing pattern.

Other Cubanes.

The final section will cover the remaining 1,4-substituted cubane structures published in the literature that either did not fit into the above categories or are too limited in number (Figures 3:56; for bond lengths and angles see Tables SI3:8 and SI3:9). This section will focus mainly on aspects that revolve around the cubane hydrogen atoms with a brief discussion on other notable interaction within this group. The first examples bear a nitro or amine functionality as a common aspect of their architecture. Compounds **3:68** and **3:69** display the effects of a nitro group directly attached to a cubane scaffold (Figure 3:57 and 3:58).[183] Compound **3:68** shows three C–H_{cubane}···O interactions with a complicated packing pattern, whereas **3:69** shows a more direct interaction with cubane face to form a neater layered structure and, as expected, twice the amount of interactions (Figure 3:58). The structure of **3:70** shows the similar preference for C–H_{cubane}···O interactions as seen in **3:68** and **3:69**, but also the presence of the CH allows for additional non-classical hydrogen-bonding aspects to occur (Figure 3:59).[184] The structures of **3:71** and **3:72** have no hydrogen atoms provided within the submitted data. **3:71** indicate the possibility though directed short contacts similar to **3:68**, where the nitro group interacts with the cubane molecule.[185] There is also some indication of the amine group interacting with the nitro group. Due to the amine group, the nitro group is now held at an angle that appears to favour potential intramolecular interactions between the cubane and the nitro groups. However, as no hydrogen atoms are provided with this is only hypothetical (Figure 3:60). For compound **3:72** we see this same potential for intramolecular interactions with the nitro group and both the cubane and phenyl moieties. This is due again to the specific angle at which the nitro group is placed in the structure and similar to compound **3:71**; however, again this is only hypothetical (Figure 3:61). For compound **3:73** a clear preference for cubane hydrogen interactions is seen between the nitro groups and the cubane scaffold with the two nitro groups forming a hydrogen-bonded network with the cubane hydrogens of its nearest neighbours which is reciprocated to its cubane hydrogens to form a square plane.[177a]

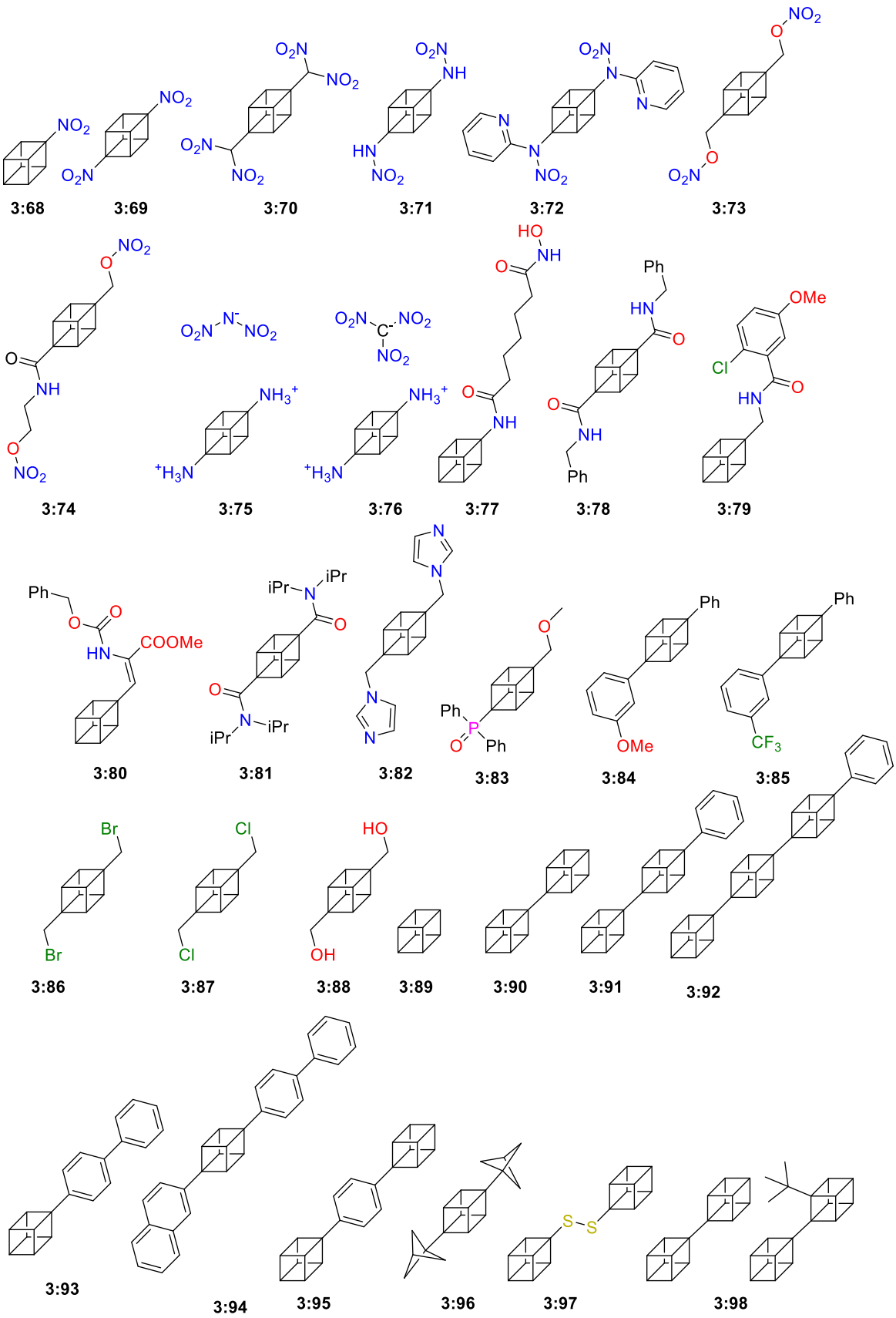

Figure 3:56: Remaining 1,4-disubstituted cubane structures.[3a, 167, 168b, 169e, 177a, 179a, 181f, 183-184, 186]

This is complemented by a cubane stacking above and below the 'plane' to form an almost octahedral geometry with one cubane at its centre (Figure 3:62). In compound **3:74** when one of the arms is extended, breaking the symmetry, the packing as expected is altered significantly.[177a] Now, two features seen are the head-to-head overlap which is tethered together through cubane hydrogens and the nitro group, and the hydrogen-bond between the amine and the carbonyl resulting in a head-to-tail hydrogen-bond network (Figure 3:63).

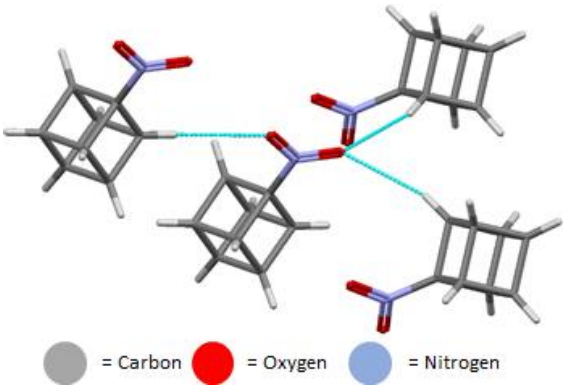

Figure 3:57: View of the molecular arrangement in the crystal of 1-nitrocubane (**3:68**) represented as a stick model showing the N···H interactions. Interactions are indicated by blue dashed lines. Bond lengths and angles are given in Table 3:43 below.

Table 3:43: List of bond lengths and angles shown in Figure 3:57.

#	Interaction	H···A (Å)	D–H···A (°)
3:68	C–H_{cubane}···O	2.515	161.3
	C–H_{cubane}···O	2.515	161.3
	C–H_{cubane}···O	2.580	177.3

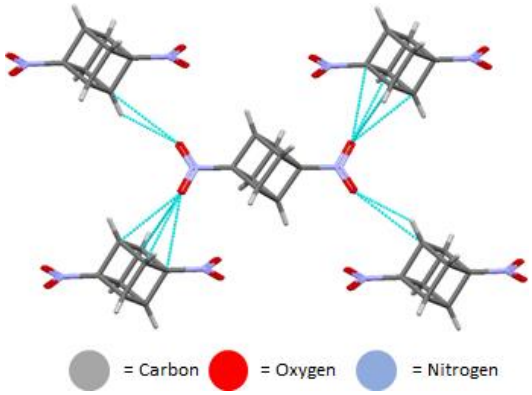

Figure 3:58: View of the molecular arrangement in the crystal of 1,4-dinitrocubane (**3:69**) represented as a stick model showing the interactions between the cubane and the nitro groups. Interactions are indicated by blue dashed lines. Bond lengths and angles are given in Table 3:44 below.

Table 3:44: List of bond lengths and angles shown in Figure 3:58.

#	Interaction	H···A (Å)	D–H···A (°)
3:69	C–H_{cubane}···O	2.528	139.6
	C–H_{cubane}···O	2.662	166.9
	C–H_{cubane}···O	2.930	89.3
	C–H_{cubane}···O	2.957	86.3
	C–H_{cubane}···O	3.070	85.8

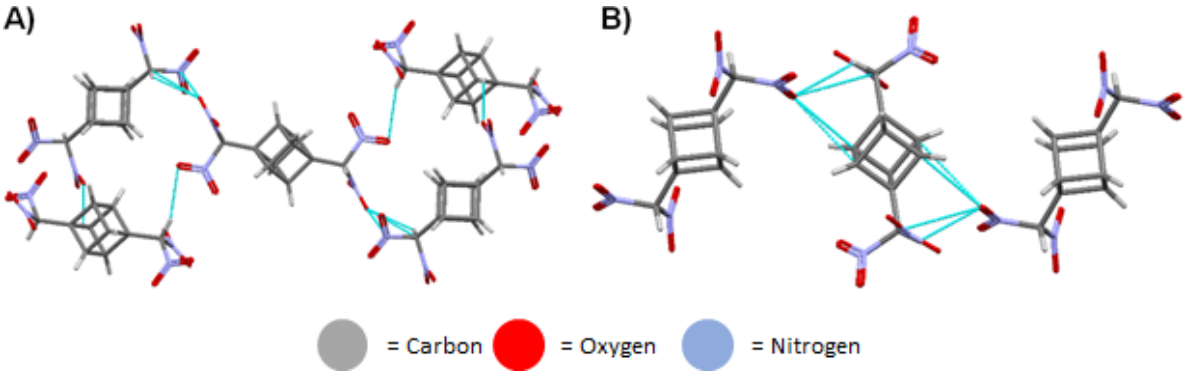

Figure 3:59: View of the molecular arrangement in the crystal of 1,4-bis(dinitromethyl)cubane (**3:70**) represented as a stick model showing the interactions between the nitro groups. Interactions are indicated by blue dashed lines. Bond lengths and angles are given in Table 3:45 below.

Table 3:45: List of bond lengths and angles shown in Figure 3:59.

#	Interaction	H···A (Å)	D–H···A (°)
3:70	C–H_{cubane}···O	2.502	131.0
	C–H_{cubane}···O	2.765	96.5
	C–H_{cubane}···O	3.084	89.1
	C–H···O	2.530	129.1
	C–H···O	2.671	137.2

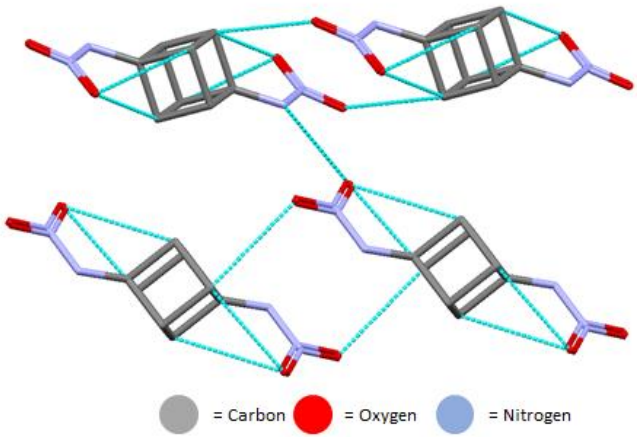

Figure 3:60: View of the molecular arrangement in the crystal of *N*,*N*'-(cubane-1,4-diyl)dinitramide (**3:71**) represented as a stick model showing the showing potential the intra- and intermolecular interactions between the cubane and the nitro groups. Interactions are indicated by blue dashed lines. The submitted data did not have hydrogen atoms included and therefore could not be drawn in the above figure.

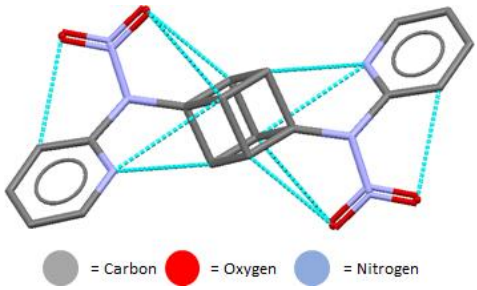

Figure 3:61: View of the molecular structure in the crystal of *N*,*N*'-(cubane-1,4-diyl)bis(*N*-(pyridin-2-yl)nitramide) (**3:72**) represented as a stick model showing potential the intramolecular interactions between the nitro or pyridyl interactions and the cubane scaffold. Interactions are indicated by blue dashed lines. The submitted data did not have hydrogen atoms included and therefore could not be drawn in the above figure.

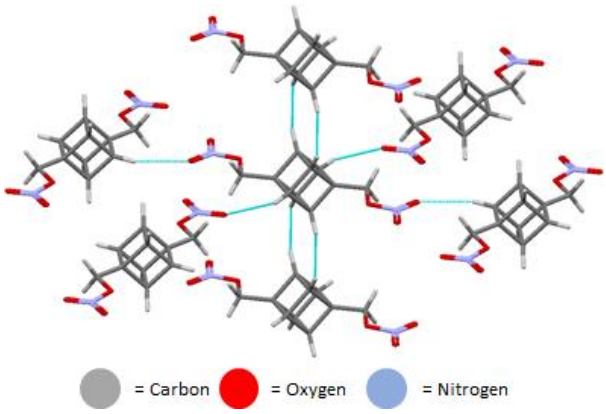

Figure 3:62: View of the molecular arrangement in the crystal of (cubane-1,4-diyl)bis(methylene) dinitrate (**3:73**) represented as a stick model showing the interactions between the cubane scaffolds or the nitro groups and cubane hydrogens. Interactions are indicated by blue dashed lines. Bond lengths and angles are given in Table 3:46 below.

Table 3:46: List of bond lengths and angles shown in Figure 3:62.

#	Interaction	H···A (Å)	D–H···A (°)
3:73	C–H_{cubane}···O	2.530	151.3
	C–H_{cubane}···H	2.335	144.4

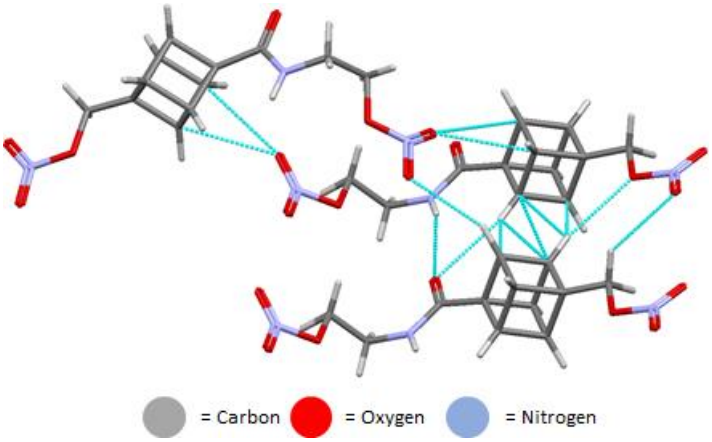

Figure 3:63: View of the molecular arrangement in the crystal of 4-((2-(nitrooxy)ethyl)carbamoyl)cuban-1-yl)methyl nitrate (**3:74**) represented as a stick model showing the interactions between the cubane scaffolds or the nitro groups and cubane hydrogens. Interactions are indicated by blue dashed lines. Bond lengths and angles are given in Table 3:47 below.

Table 3:47: List of bond lengths and angles shown in Figure 3:63.

#	Interaction	H···A (Å)	D–H···A (°)
3:74	C–H_{cubane}···O	2.477	153.1
	C–H_{cubane}···O	2.625	155.0
	C–H_{cubane}···O	2.679	151.2
	C–H_{cubane}···O	2.621	154.9
	C–H_{cubane}···C	2.814	130.8
	C–H_{cubane}···C	2.743	110.4
	C–H_{cubane}···C	2.743	110.3
	C–H_{cubane}···C	2.820	130.8
	C–H···O	2.696	126.0
	N–H···O	2.330	152.5

Two cubane cation crystal structures are reported in the literature and provide a good example of how such charged species direct cubane interactions. Compound **3:75**, which is charge balanced with a di-nitroamide, shows the amine anion to have a preference for cubane hydrogens to form a hydrogen-bonds, whereas the nitro

groups interact exclusively with the cubanes amine cation (Figure 3:64).[186a] This is exemplified in **3:76** where the nitro groups interact with the cubane amine cation and no interactions are observable for the cubane hydrogens (Figure 3:65).[186b]

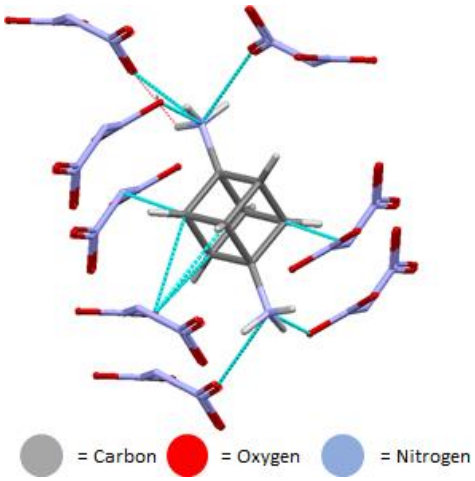

Figure 3:64: View of the molecular arrangement in the crystal of 1,4-diaminium-cubane dinitroamide solvate (**3:75**) represented as a stick model showing the nitro interactions between the cubane and the aminium counterion. Interactions are indicated by blue dashed lines. Bond lengths and angles are given in Table 3:48 below.

Table 3:48: List of bond lengths and angles shown in Figure 3:64.

#	Interaction	H···A (Å)	D–H···A (°)
3:75	C–H_{cubane}···O	2.526	134.8
	C–H_{cubane}···O	2.540	132.5
	C–H_{cubane}···O	2.744	89.3
	C–H_{cubane}···O	2.835	87.2
	C–H_{cubane}···O	3.051	82.5
	N–H···O	2.286	148.2
	N–H···O	2.459	129.2
	N–H···O	2.627	103.3
	N–H···O	2.550	108.2
	N–H···O	2.198	152.8
	N–H···O	2.690	112.1
	N–H···O	2.560	134.3
	N–H···O	2.329	134.7
	N–H···N	2.447	138.1

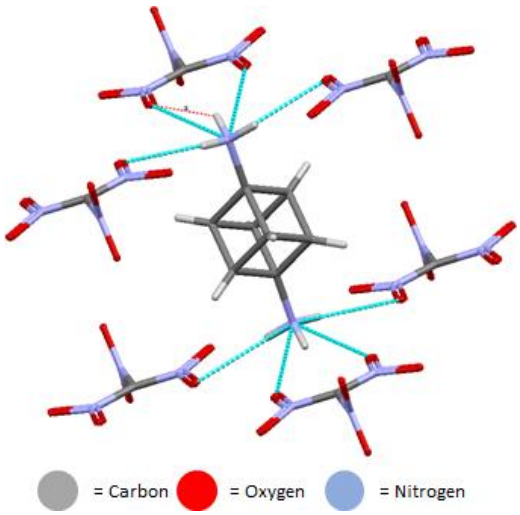

Figure 3:65: View of the molecular arrangement in the crystal of 1,4-diaminium-cubane trinitromethanide solvate (**3:76**) represented as a stick model showing the nitro interactions between the cubane and the aminium counterion. Interactions are indicated by blue dashed lines. Bond lengths and angles are given in Table 3:49 below.

Table 3:49: List of bond lengths and angles shown in Figure 3:65.

#	Interaction	H···A (Å)	D–H···A (°)
3:76	N–H···O	2.196	139.4
	N–H···O	2.365	153.9
	N–H···O	2.215	148.8

The final nitrogen bearing compounds (**3:77**–**3:82**) are only loosely related, but show examples such as amide functionality, functional group competition, and long chain *vs*. aryl substitutions.[3a, 167, 169e, 177a, 179a, 182b, 183-184, 186a-d] Compound **3:77** is an example of a long chain amide cubane structure.[167] Here, the main features are how the long chains line together in a head-to-tail fashion though N–H···O and O–H···O interactions coupled with the cubane C–H_{cubane}···C_{cubane} interactions forming a network. There is a clear preference for the long chain to aggregate leaving the cubane to interact with itself, similar to what would nominal be considered a bi-layer (Figure 3:66). The structure of **3:78**, N^1,N^4-dibenzylcubane-1,4-dicarboxamide, shows a hydrogen-bonded network through the carboxamides which result in an intricate cross-over pattern (Figure 3:67).[3a] The cubane hydrogens do not interact with the arm, but instead, are occupied by acetic acid contained within the voids of the structure. The structure of **79** with a mono-2-chloro-5-methoxy-benzamide substituent shows the same cross-over pattern seen between the amides of the structure.[169e] However, as there is only one substituent this time the cubane

scaffold appears to be able to interact with each other in a C–H_{cubane}···C_{cubane} non-classical hydrogen-bonding fashion (Figure 3:68). Additionally, the methoxy group is seen to from head-to-head dimers and the chlorine atom participates in some short contacts with the cubane scaffold and the nitrogen atom due to its pointing directly towards the cubane. The structure of **3:80** is an interesting example of a hydrogen-bond donor to one side and an exclusive hydrogen-bond acceptor to the other of the cubane scaffold.[186c] This results in a staggered hydrogen-bonding network through the N–H and the ester oxygen of the CO_2Me.

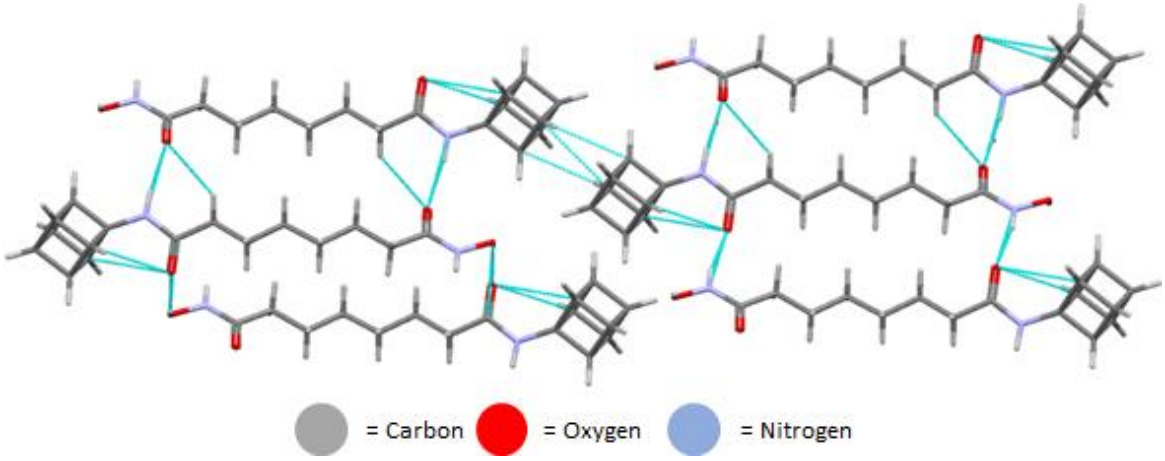

Figure 3:66: View of the molecular arrangement in the crystal of N^1-(cuban-1-yl)-N^7-hydroxyheptanediamide (**3:77**) represented as a stick model showing the showing how the long chain line together to in a head-to-tail fashion though N–H···O and O–H···O interactions coupled with the cubane C–H_{cubane}···C_{cubane} interactions to form a network. Interactions are indicated by blue dashed lines. Bond lengths and angles are given in Table 3:50 below.

Table 3:50: List of bond lengths and angles shown in Figure 3:66.

#	Interaction	H···A (Å)	D–H···A (°)
3:77	C–H_{cubane}···H	2.851	121.5
	C–H_{cubane}···N	2.728	137.3
	N–H···O	2.073	167.7
	N–H···O	1.998	160.8
	O–H···O	2.057	146.9

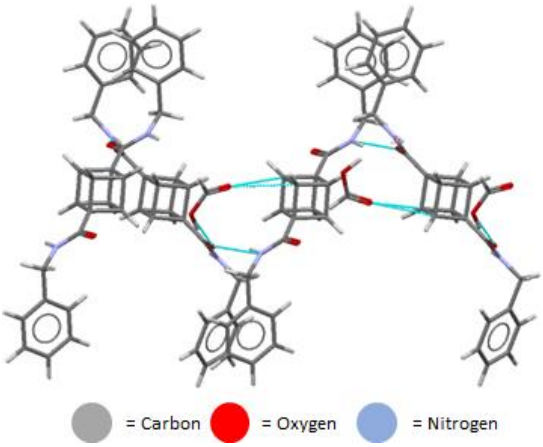

Figure 3:67: View of the molecular arrangement in the crystal of N^1,N^4-dibenzylcubane-1,4-dicarboxamide (**3:78**) represented as a stick model showing the hydrogen-bonded network through the carboxamides which results in an intricate cross-over pattern. Interactions are indicated by blue dashed lines. Bond lengths and angles are given in Table 3:51 below.

Table 3:51: List of bond lengths and angles shown in Figure 3:67.

#	Interaction	H···A (Å)	D–H···A (°)
3:78	O–H···C_{cubane}	2.869	124.3
	C–H_{Ph}···C_{cubane}	2.888	130.1
	N–H···O	1.981	149.2
	C–H_{Ph}···C	2.653	160.5
	C–H_{Ph}···O	2.665	154.5
	C–H_{Ph}···C	2.891	122.9

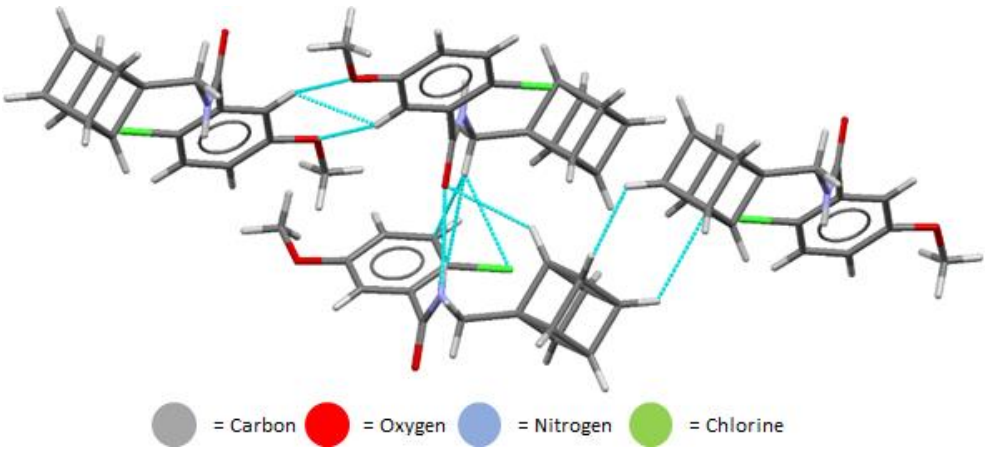

Figure 3:68: View of the molecular arrangement in the crystal of 2-chloro-*N*-cuban-1-yl)methyl)-5-methoxybenzamide (**3:79**) represented as a stick model showing the cross-over pattern seen between the amides of the structure, the cubane scaffold interacting with each other in a C–H_{cubane}···C_{cubane} non-classical hydrogen-bonding fashion and a head-to-head dimer formation between the methoxy groups and the phenyl hydrogens. Interactions are indicated by blue dashed lines. Bond lengths and angles are given in Table 3:52 below.

Table 3:52: List of bond lengths and angles shown in Figure 3:68.

#	Interaction	H···A (Å)	D–H···A (°)
3:79	$C–H_{cubane}\cdots H$	2.115	169.6
	$C–H_{cubane}\cdots H$	2.885	123.8
	$C–H_{cubane}\cdots O$	2.664	141.3
	C–H···Cl	2.893	139.0
	N–H···O	2.193	161.0
	$C–H_{Ph}\cdots O$	2.614	145.2
	$C–H\cdots C_{Ph}$	2.727	154.8
	$C–H\cdots C_{Ph}$	2.894	128.0
	$C–H\cdots C_{Ph}$	2.681	161.9
	$C–H\cdots C_{Ph}$	2.838	144.0

This is also accompanied by two O···H interactions of the carbonyls with the methyl of the ester and the CH_2 of the structure. This leaves the opposite side of the cubane complete free of interactions with the nearest cubane in a $C–H_{cubane}\cdots C_{cubane}$ interaction (Figure 3:69). The structure of **3:81** is an example of when the steric bulk of substitutes is increased and hydrogen-bond donors are removed from the structure.[186d] Here, the oxygen atoms partake in a bifurcated hydrogen short contact linear network. The cubane hydrogens appear to be partaking in a C–H···C non-classical hydrogen-bonding network with the isopropyl groups (Figure 3:70). The structure of **3:82** is seen to have a few short contacts related to the cubane scaffold in the form of non-classical hydrogen short contacts between $C–H_{cubane}\cdots H$ and interactions between the imidazole ring and the water molecules (Figure 3:71).[179a] Other contacts that make up the structure are between the nitrogen of the imidazole ring and the solvent water molecules. From this section, it is clear that nitro groups show a significant preference for the cubane hydrogens. Additionally, the amide functionalities show a preference for forming dimers and allow the $C–H_{cubane}\cdots C_{cubane}$ non-classical hydrogen-bonding to engage between the cubane scaffolds.

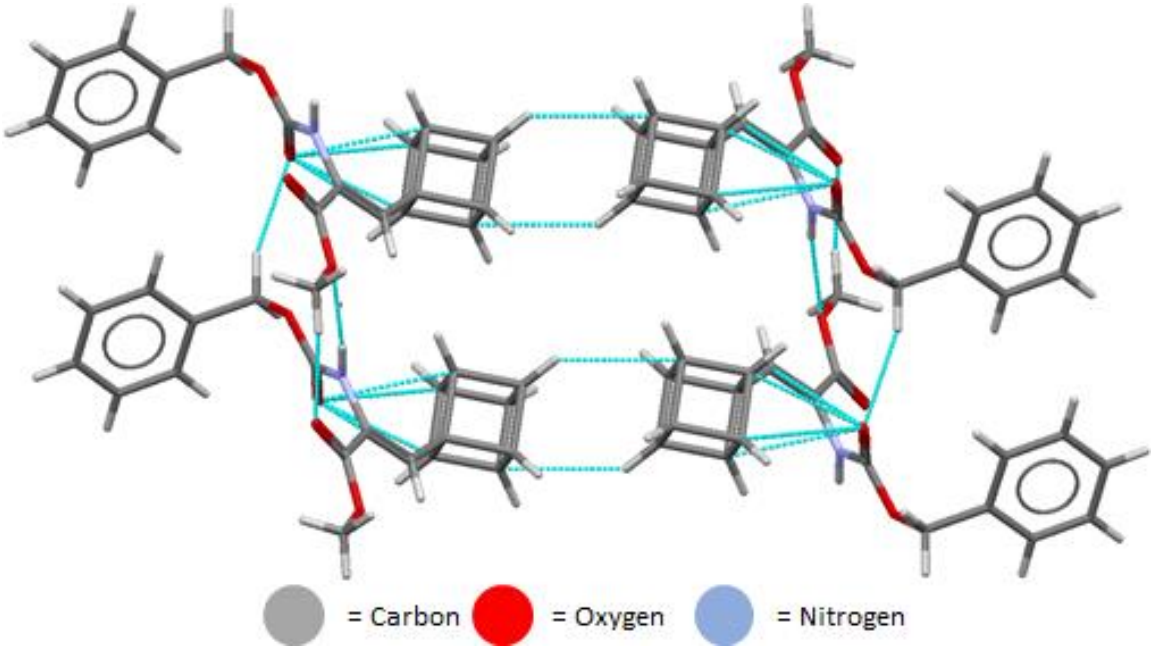

Figure 3:69: View of the molecular arrangement in the crystal of methyl 2-(((benzyloxy)carbonyl)amino)-3-(cuban-1-yl)acrylate (**3:80**) represented as a stick model showing the staggered hydrogen-bonding network through the N–H and the ester oxygen of the CO_2Me. This is also accompanied by two O···H interactions of the carbonyls with the methyl of the ester and the CH_2 of the structure coupled with cubane interactions with the nearest cubane in a $C–H_{cubane}\cdots C_{cubane}$ interaction. Interactions are indicated by blue dashed lines. Bond lengths and angles are given in Table 3:53 below.

Table 3:53: List of bond lengths and angles shown in Figure 3:69.

#	Interaction	H···A (Å)	D–H···A (°)
3:80	$C–H_{cubane}\cdots H$	2.347	129.3
	$C–H_{cubane}\cdots C$	2.838	137.3
	C–H···C	2.888	124.4
	C–H···C	2.894	134.8
	C–O···H	2.433	140.4
	N–H···O	2.455	174.0
	C–O···H	2.372	141.4

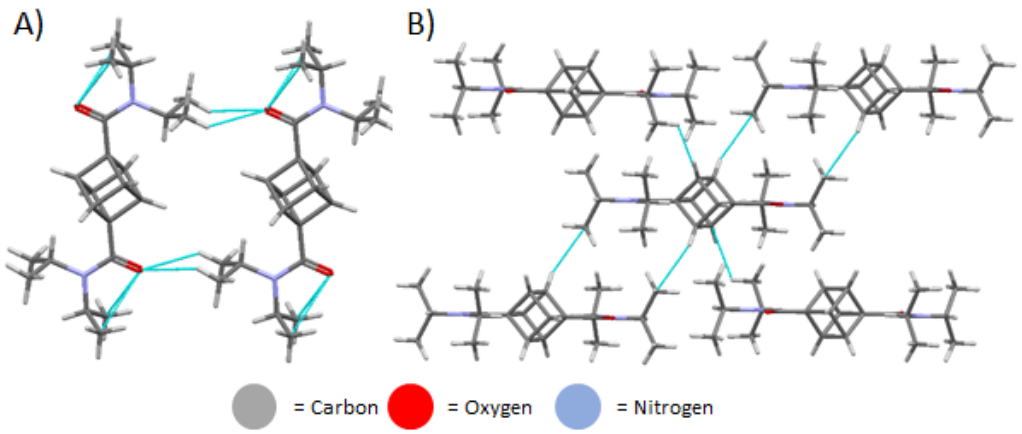

Figure 3:70: View of the molecular arrangement in the crystal of N^1,N^1,N^4,N^4-tetraisopropylcubane-1,4-dicarboxamide (**3:81**) represented as a stick model showing the bifurcated hydrogen short contact linear network between the isopropyl and the carboxamide oxygen atoms (A) and the cubane hydrogens partaking in a C–H···C non-classical hydrogen-bonding network with the isopropyl groups (B). Interactions are indicated by blue dashed lines. Bond lengths and angles are given in Table 3:54 below.

Table 3:54: List of bond lengths and angles shown in Figure 3:70.

#	Interaction	H···A (Å)	D–H···A (°)
3:81	C–H_{cubane}···C	2.874	128.9
	C–H···C_{cubane}	2.891	113.9
	C–H···O	2.664	133.8
	C–H···O	2.673	136.4

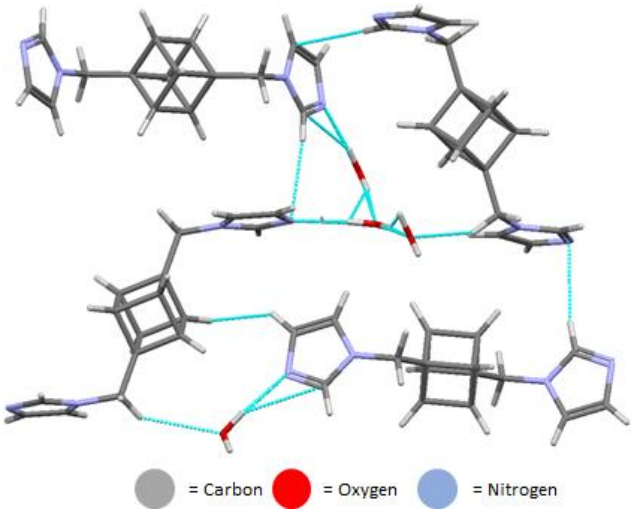

Figure 3:71: View of the molecular arrangement in the crystal of 1,4-di((1*H*-imidazol-1-yl)methyl)cubane water solvate (**3:82**) represented as a stick model showing the non-classical hydrogen short contacts between C–H_{cubane}···H and interactions between the imidazole ring and the water molecules. Interactions are indicated by blue dashed lines. Bond lengths and angles are given in Table 3:55 below.

Table 3:55: List of bond lengths and angles shown in Figure 3:71.

#	Interaction	H···A (Å)	D–H···A (°)
3:82	$C–H_{cubane}\cdots C$	2.894	134.4
	$C–H_{cubane}\cdots H$	2.365	113.2
	$C–H_{cubane}\cdots H$	2.373	118.1
	C–H···O	2.421	159.6
	O–H···N	1.933	175.8
	C–H···N	2.633	158.3
	C–H···C	2.672	164.2

The structure of **3:83** is an interesting example of a cubane structure bearing a diphenylphosphine oxide.[186e] This structure resembles compound **3:61** with a diphenylmethanol substituent; however, the packing could never be more different. The oxygen atoms are actively engaging in two hydrogen-bonding contacts with the phenyl rings and one of the cubane hydrogens to form a head-to-tail dimer (Figure 3:72). The methyl ether is also seen to form a head-to-head dimer between each other on the opposite end of the molecule. This results in an intriguing hydrogen-bonded network.

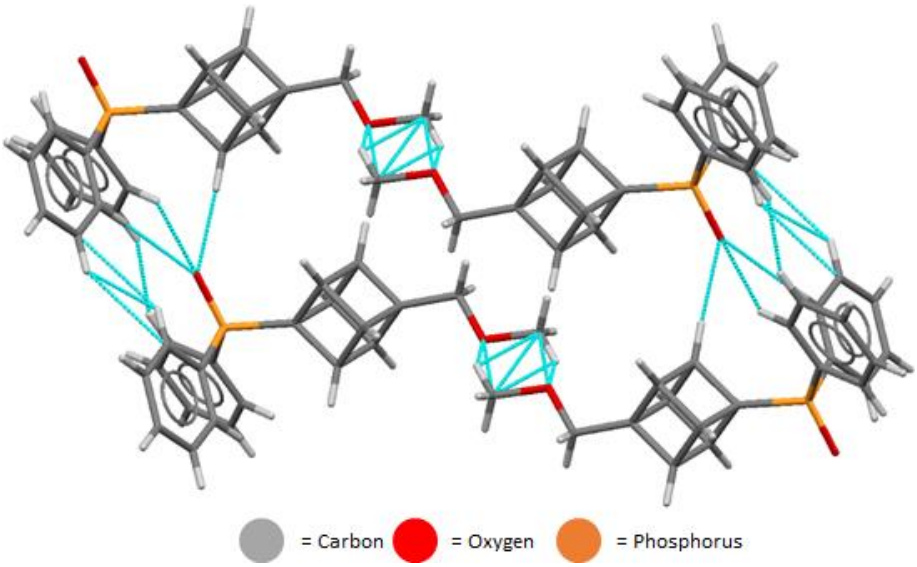

Figure 3:72: View of the molecular arrangement in the crystal of 4-(methoxymethyl)cuban-1-yl)diphenylphosphine oxide (**3:83**) represented as a stick model showing the oxygen atoms parking in hydrogen bonding with the phenyl rings and one of the cubane hydrogens to form a head-to-tail dimer, also showing the methyl ether is also seen to form a head-to-head dimer between each other on the opposite end of the molecule. Interactions are indicated by blue dashed lines. Bond lengths and angles are given in Table 3:56 below.

Table 3:56: List of bond lengths and angles shown in Figure 3:72.

#	Interaction	H···A (Å)	D–H···A (°)
3:83	$C–H_{cubane}\cdots C$	2.839	165.9
	$C–H_{cubane}\cdots H$	2.392	121.4
	$C–H_{cubane}\cdots O$	2.428	149.0
	$C–H_{Ph}\cdots O$	2.531	148.7
	$C–H_{Ph}\cdots O$	2.567	166.7
	$C–H_{Me}\cdots O$	2.334	132.3

The next two structures **3:84** and **3:85** are similar to each other, except with regards to their *meta*-substituent.[168b] Compound **3:84** shows a variety of $C–H_{cubane}\cdots C_{cubane}$ interactions resulting in a staggered head-to-tail overlap network which is aided by phenyl hydrogens interacting with the oxygen in the methyl ether (Figure 3:73).

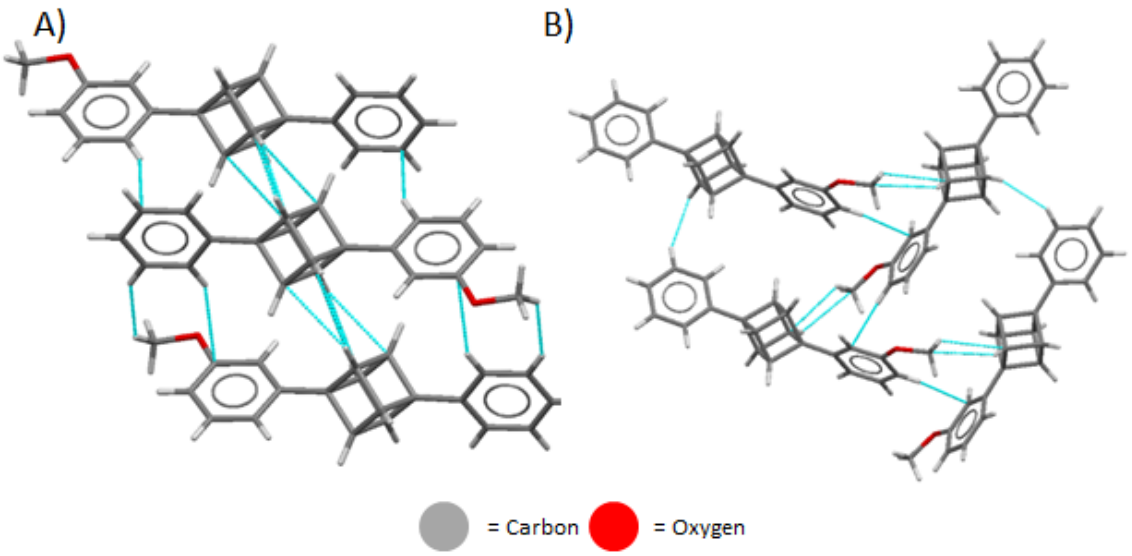

Figure 3:73: View of the molecular arrangement in the crystal of 1-(3-methoxyphenyl)-4-phenylcubane (**3:84**) represented as a stick model showing a variety of $C–H_{cubane}\cdots C_{cubane}$ resulting in a staggered head-to-tail overlap network which is aided by phenyl hydrogens interacting with the oxygen in the methyl ether (A) and several interactions can be seen between the cubane scaffold and the phenyl hydrogens. The final interaction is between the cubane scaffold and methoxy ether which results in an edge-on interaction (B). Interactions are indicated by blue dashed lines. Bond lengths and angles are given in Table 3:57 below.

Table 3:57: List of bond lengths and angles shown in Figure 3:73.

#	Interaction	H···A (Å)	D–H···A (°)
3:84	$C–H_{cubane}\cdots C$	2.766	112.7
	$C–H_{cubane}\cdots C$	2.785	135.1
	$C–H_{cubane}\cdots C$	2.745	131.9
	$C–H_{cubane}\cdots C$	2.843	109.3
	$C–H_{cubane}\cdots C$	2.876	139.0
	$C–H_{Ph}\cdots C$	2.868	147.9
	$C–H_{Ph}\cdots C$	2.872	136.8
	$C–H_{cubane}\cdots C$	2.811	120.9
	$C–H_{Me}\cdots C$	2.859	118.3
	$C–H_{Ph}\cdots C$	2.806	150.7
	$C–H_{Ph}\cdots C$	2.845	153.6

Several interactions can be seen between the cubane scaffold and the phenyl hydrogens. The final contact is between the cubane scaffold and methoxy ether which results in edge-on interaction. Replacing the methoxy with CF_3 group results in some minor changes. The structure of **3:85** shows a variety of $C–H_{cubane}\cdots C_{cubane}$ networks similar to **3:84** but with linear head-to-head structure (Figure 3:74). This is augmented through a H···F interaction between the cubane and the CF_3 group in an alternating cross-over pattern as a result of the angle of the *meta*-substituent. The final interaction results in $C–H_{cubane}\cdots C_{Ph}$ contacts which result in an edge-on interaction as seen in **3:84**.

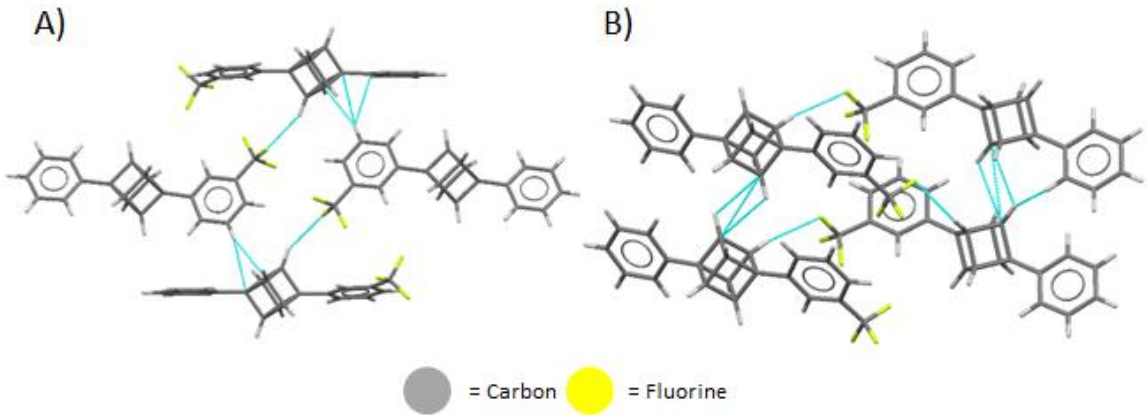

Figure 3:74: View of the molecular arrangement in the crystal of 1-phenyl-4-(3-(trifluoromethyl)phenyl)cubane (**3:85**) represented as a stick a model showing the H···F interaction between the cubane and the CF_3 group and the $C–H_{cubane}\cdots C_{cubane}$ networks (B). Interactions are indicated by blue dashed lines. Bond lengths and angles are given in Table 3:58 below.

Table 3:58: List of bond lengths and angles shown in Figure 3:74.

#	Interaction	H···A (Å)	D–H···A (°)
3:85	$C–H_{cubane}\cdots C$	2.809	114.4
	$C–H_{cubane}\cdots C$	2.812	114.1
	$C–H_{cubane}\cdots C$	2.853	113.0
	$C–H_{cubane}\cdots C$	2.848	113.2
	$C–H_{Ph}\cdots C$	2.885	140.7
	$C–H_{Ph}\cdots C$	2.702	155.3
	$C–H_{cubane}\cdots C$	2.887	136.8
	$C–H_{Ph}\cdots C$	2.873	131.6
	$C–H_{Ph}\cdots C_{cubane}$	2.773	150.4
	$C–H_{Ph}\cdots C_{cubane}$	2.741	154.4
	$C–H_{Ph}\cdots C_{cubane}$	2.858	126.6
	$C–H_{Ph}\cdots C_{cubane}$	2.882	139.2
	$C–H_{cubane}\cdots F$	2.544	153.9

The next three structures are a small collective of methyl-X-disubstituted derivatives (X = bromo (**3:86**), chloro (**3:87**), and methanol (**3:88**)).[186f, 186g] The structure of **3:86** shows quite a typical halogen-bonded network between the bromine atoms and the cubane scaffold to form a flat layer of cubane molecules (Figure 3:75). The structure of **3:87** shows a slightly altered pattern with the halogen preferring to interact with the CH_2 moiety. This allows for space around the cubane scaffold for a direct $C–H_{cubane}\cdots C$ interactions in a non-classical hydrogen-bonding pattern (Figure 3:76). Compound **3:88** exhibits an alternate interaction pattern due to hydrogen-bonding network that results in a beautiful hexamer of molecules that is a hydrogen-bond of the alcohol groups that is reminiscent of a six-membered ring. This is repeated on both sides of the molecules to create a large repeating network. This is coupled with $C–H\cdots C_{cubane}$ form as a result of the layer of cubanes (Figure 3:77).

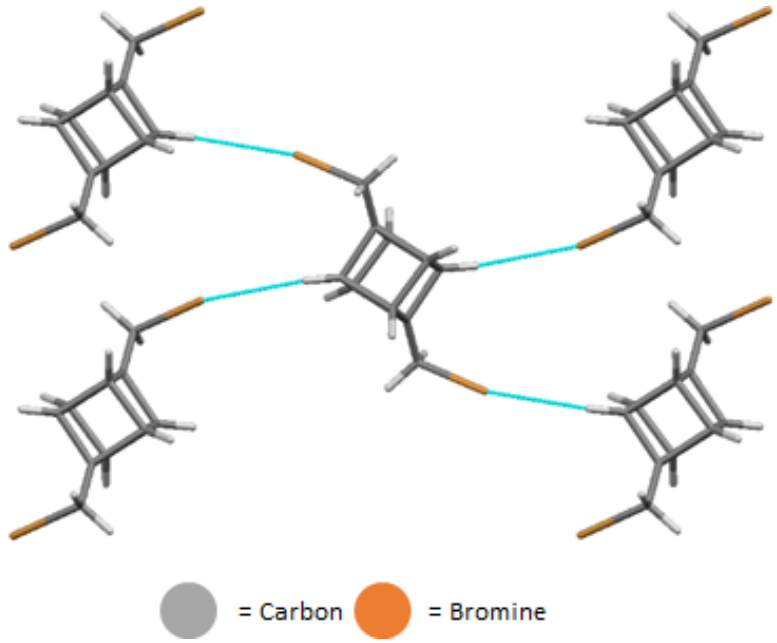

Figure 3:75: View of the molecular arrangement in the crystal of 1,4-bis(bromomethyl)cubane (**3:86**) represented as a stick model showing the Br···H interactions. Interactions are indicated by blue dashed lines. Bond lengths and angles are given in Table 3:59 below.

Table 3:59: List of bond lengths and angles shown in Figure 3:75.

#	Interaction	H···A (Å)	D–H···A (°)
3:86	C–H_{cubane}···Br	3.037	128.4

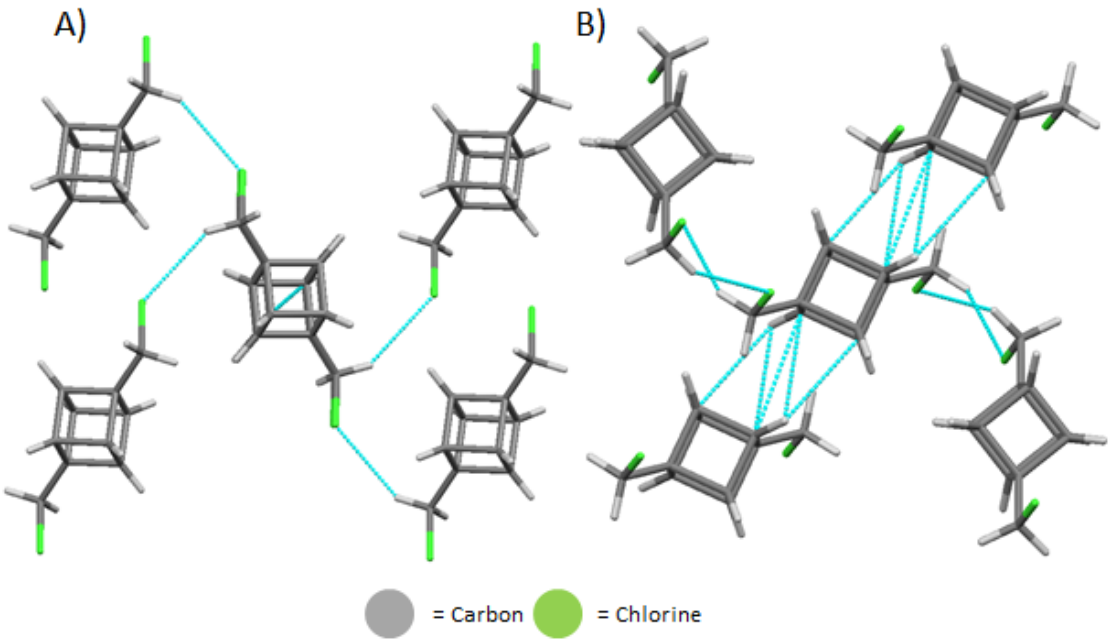

Figure 3:76: View of the molecular arrangement in the crystal of 1,4-bis(chloromethyl)cubane (**3:87**) represented as a stick model showing the Cl···H interactions (A) and the C–H_{cubane}···C_{cubane} interactions (B). Interactions are indicated by blue dashed lines. Bond lengths and angles are given in Table 3:60 below.

Table 3:60: List of bond lengths and angles shown in Figure 3:74.

#	Interaction	H···A (Å)	D–H···A (°)
3:87	C–H_{cubane}···C	2.792	132.2
	C–H_{cubane}···C	2.807	110.0
	C–Cl···H	2.755	122.2

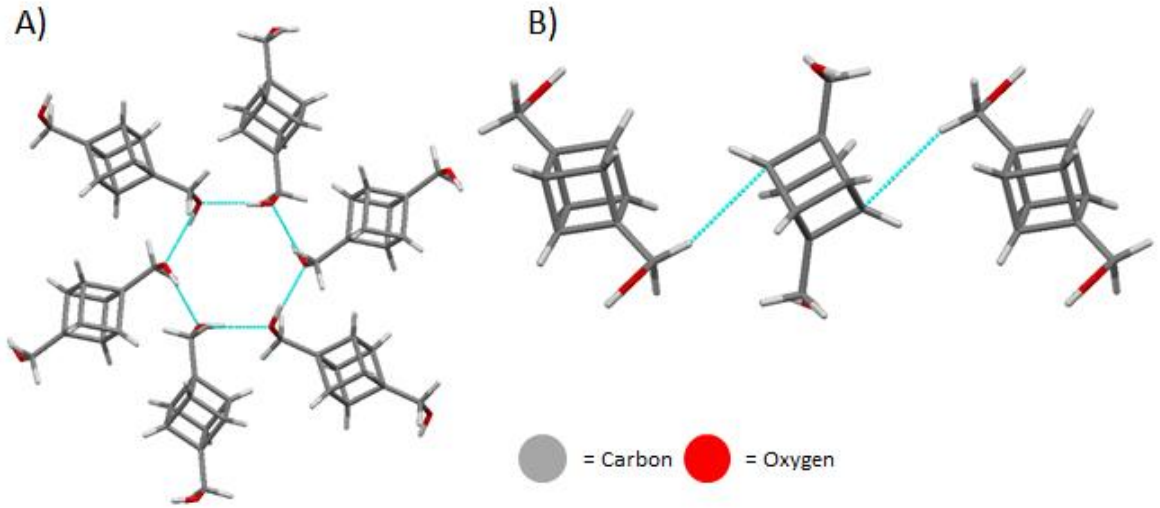

Figure 3:77: View of the molecular arrangement in the crystal of (cubane-1,4-diyl)dimethanol (**3:88**) represented as a stick model showing the O···H between the methanol units (A) and the C–H···C_{cubane} interactions (B). Interactions are indicated by blue dashed lines. Bond lengths and angles are given in Table 3:61 below.

Table 3:61: List of bond lengths and angles shown in Figure 3:77.

#	Interaction	H···A (Å)	D–H···A (°)
3:88	C–H···C_{cubane}	2.858	160.9
	O–H···O	1.828	168.4

The next section of cubanes features a variety of cubane scaffolds that all bear either aromatic rings or cubane substitutes. This allows C–H_{cubane}···C interactions to be much more prevalent and to avoid being dominated by other moieties. Cubane **3:89** shows none of these interactions in either the seminal structure or the more improved structure determined by Fleischer and co-workers.[166a, 178] However, the di-cubane structure **3:90** shows four C–H_{cubane}···C interactions with one molecule interacting with four of its nearest neighbours, (Figure 3:78).[181f] In comparison to the iodo- (**3:55**) and the bromo- (**3:56**) derivatives there are less C–H_{cubane}···C interactions; however, these contacts are more linear in compounds **55**–**56**, compared to **3:90**. Adding a phenyl group to the structure of **3:90** results in

compound **3:91**.[181f] This forms a short contact between the cubane hydrogens and the phenyl ring (Figure 3:79). With three cubane scaffolds as seen as in **3:92**, the cubane hydrogens show a large increase in the number of $C–H_{cubane}\cdots C$ interactions in a non-classical hydrogen-bonding pattern which surrounds each molecule with four others (Figure 3:80).[181f] Going the opposite direction with increase the phenyl groups around the cubane scaffold as with **3:93** and **3:94**.[181f, 186h] The structure of **3:93** results in a delightful head-to-head network of $C–H_{cubane}\cdots C$ interactions between the cubane heads of the molecule to form a linear network. this is complemented by a $C–H_{Ph}\cdots\pi$ interactions of the phenyl rings that form a head-to-tail overlap that is seen throughout the structure allowing for the tightest stacking possible (Figure 3:81). The structure of **3:94**, although more complex than **3:93**, results in a simpler interaction network. This is seen through a short $C–H_{cubane}\cdots H$ interaction between the cubane and the biphenyl that results offset stacking of the planes shifted plane against each other (Figure 3:82). Additionally, there is a C–H···C interaction between the biphenyl which results in a tilt angle between them. The structure of **3:95**, where two cubanes are tethered by a phenyl ring, surprisingly appears to have no C–H···H interaction similar to the structure of **3:89**.[181f] With two bicyclo[1.1.1]pentan-1-yl (BCP) substituents in compound **96** results in quite an interesting interaction pattern (Figure 3:83).[186i] The first is the $C–H_{cubane}\cdots C$ interactions that are the common motif of cubanes which results in the linear network. The second is a $C–H\cdots C_{cubane}$ interacting between the BCP hydrogens and the cubane scaffold. The structure of **3:97** is a nice example of a di-cubane tethered by a disulfide.[186j] This structure has a wave-like linear chain pattern which is facilitated by two $C–H_{cubane}\cdots C$ interactions (Figure 3:84). The final structure of this story is compound **3:98**.[186k] It features a co-crystallization of compound **90** and its *iso*-butyl derivative. Several $C–H_{cubane}\cdots C$ are seen holding the two compounds together with the *iso*-butyl derivative surrounding the di-cubane structure. Additionally, there are multiple cubane–cubane dimers between the *iso*-butyl derivatives which are facilitated by $C–H_{cubane}\cdots C$ interactions (Figure 3:85).

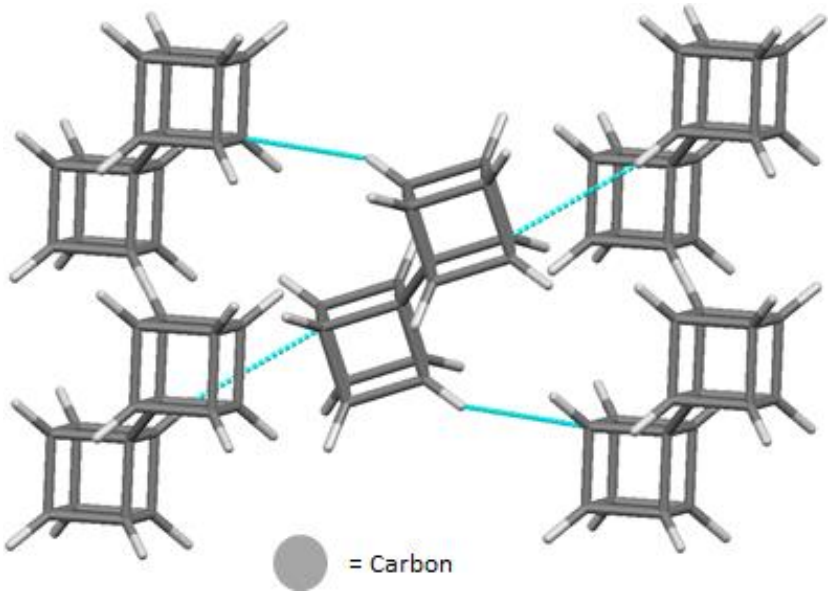

Figure 3:78: View of the molecular arrangement in the crystal of 1,1'-di(cubane) (**3:90**) represented as a stick model showing the C–H_{cubane}···C_{cubane} interactions. Interactions are indicated by blue dashed lines. Bond lengths and angles are given in Table 3:62 below.

Table 3:62: List of bond lengths and angles shown in Figure 3:78.

#	Interaction	H···A (Å)	D–H···A (°)
3:90	C–H_{cubane}···C	2.857	156.4

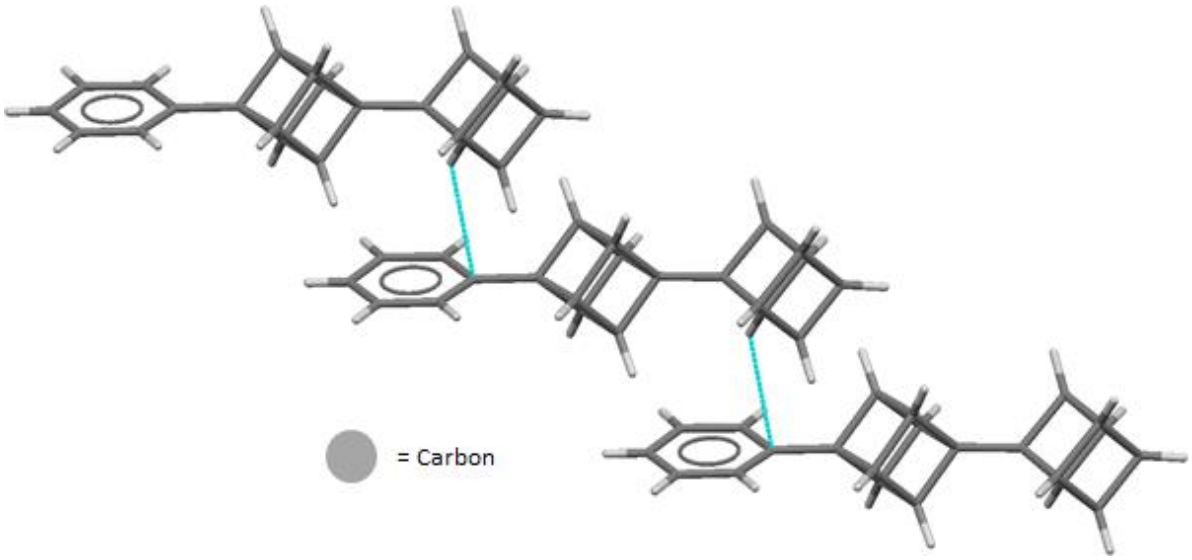

Figure 3:79: View of the molecular arrangement in the crystal of 4-phenyl-1,1'-bi(cubane) (**3:91**) represented as a stick model showing the C–H_{cubane}···C_{phenyl} interactions. Interactions are indicated by blue dashed lines. Bond lengths and angles are given in Table 3:63 below.

Table 3:63: List of bond lengths and angles shown in Figure 3:79.

#	Interaction	H···A (Å)	D–H···A (°)
3:91	C–H_{cubane}···C	2.889	134.4

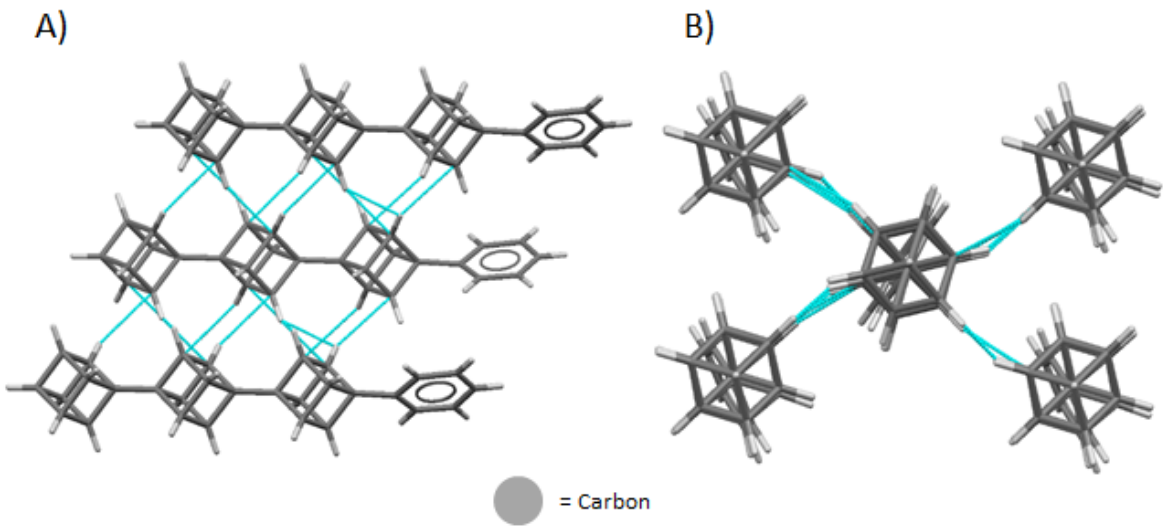

Figure 3:80: View of the molecular arrangement in the crystal of 4-phenyl-1,1',4'-tri(cubane) (**3:92**) represented as a stick model showing the C–H_{cubane}···C_{cubane} interactions. Interactions are indicated by blue dashed lines. Bond lengths and angles are given in Table 3:64 below.

Table 3:64: List of bond lengths and angles shown in Figure 3:80.

#	Interaction	H···A (Å)	D–H···A (°)
3:92	C–H_{cubane}···C	2.858	152.1
	C–H_{cubane}···C	2.881	157.6
	C–H_{cubane}···C	2.840	154.8
	C–H_{cubane}···C	2.798	152.2
	C–H_{cubane}···C	2.848	148.9
	C–H_{cubane}···C	2.879	154.0
	C–H_{cubane}···C	2.834	156.3
	C–H_{cubane}···C	2.801	148.4
	C–H_{cubane}···C	2.819	148.6
	C–H_{cubane}···C	2.802	149.3
	C–H_{cubane}···C	2.808	152.8
	C–H_{cubane}···C	2.764	147.7
	C–H_{cubane}···C	2.867	149.1
	C–H_{cubane}···C	2.850	159.0
	C–H_{cubane}···C	2.897	147.0
	C–H_{cubane}···C	2.873	159.7

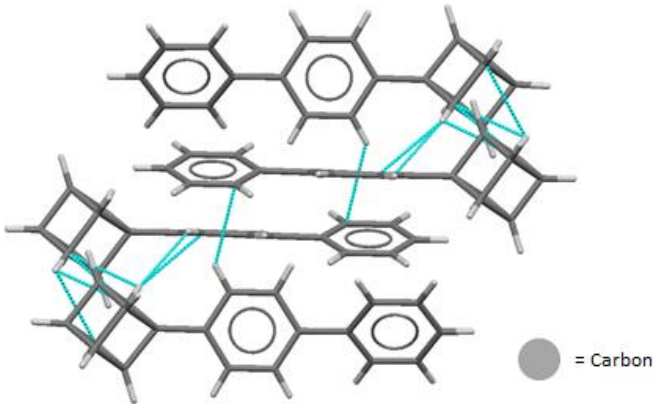

Figure 3:81: View of the molecular arrangement in the crystal of 1-([1,1'-biphenyl]-4-yl)cubane (**3:93**) represented as a stick model showing the C–H_{cubane}···C_{cubane} interactions and the C–H_{phenyl}···C_{phenyl} interactions. Interactions are indicated by blue dashed lines. Bond lengths and angles are given in Table 3:65 below.

Table 3:65: List of bond lengths and angles shown in Figure 3:81.

#	Interaction	H···A (Å)	D–H···A (°)
3:93	C–H_{cubane}···C	2.825	107.8
	C–H_{cubane}···C	2.816	109.7
	C–H_{cubane}···C	2.869	158.6
	C–H_{cubane}···C	2.881	148.6
	C–H_{cubane}···C	2.891	123.8
	C–H_{cubane}···C	2.894	120.1
	C–H_{cubane}···C	2.899	120.4
	C–H_{cubane}···C	2.851	145.5
	C–H_{cubane}···π	2.910	152.4

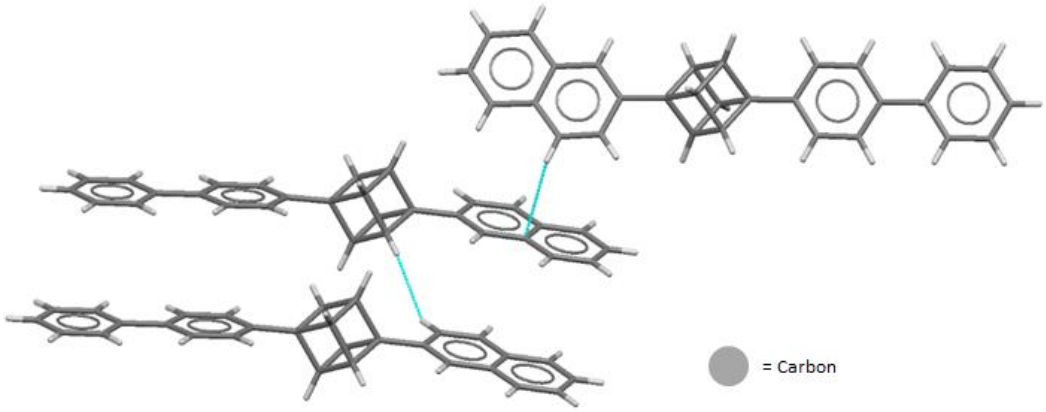

Figure 3:82: View of the molecular arrangement in the crystal of 1-([1,1'-biphenyl]-4-yl)-4-(naphthalen-2-yl)cubane (**3:94**) represented as a stick model showing the short C–H_{cubane}···H contacts and the naphthalene interactions. Interactions are indicated by blue dashed lines. Bond lengths and angles are given in Table 3:66 below.

Table 3:66: List of bond lengths and angles shown in Figure 3:82.

#	Interaction	H···A (Å)	D–H···A (°)
3:94	C–H_{cubane}···H	2.380	146.1
	C–H···C	2.795	141.6

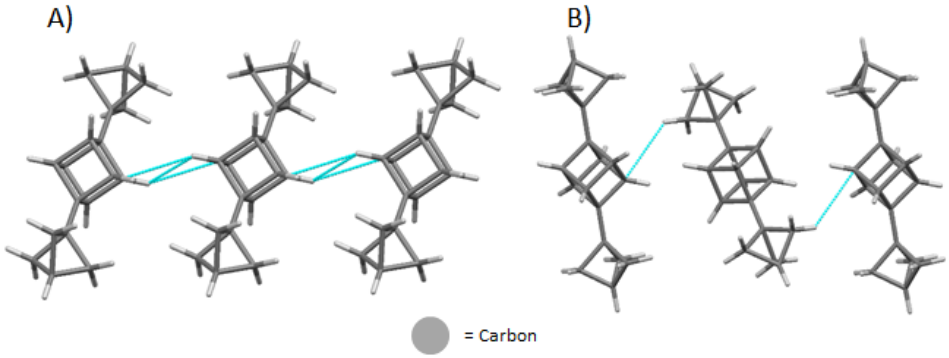

Figure 3:83: View of the molecular arrangement in the crystal of 1,4-di(bicyclo[1.1.1]pentan-1-yl)cubane (**3:96**) represented as a stick model showing the C–H_{cubane}···C_{cubane} interactions (A) and the C–H_{BCP}···C_{cubane} interactions (B). Interactions are indicated by blue dashed lines. Bond lengths and angles are given in Table 3:67 below.

Table 3:67: List of bond lengths and angles shown in Figure 3:83.

#	Interaction	H···A (Å)	D–H···A (°)
3:96	C–H_{cubane}···C	2.854	128.3
	C–H_{BCP}···C	2.898	128.4

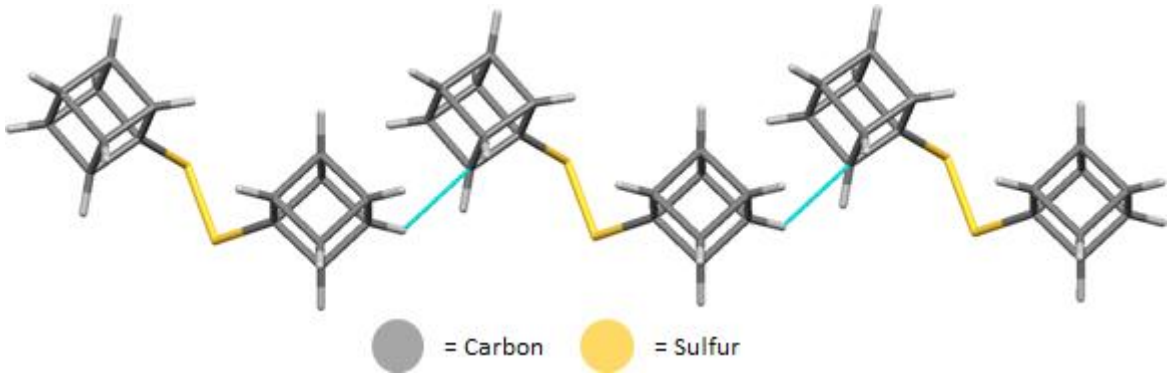

Figure 3:84: View of the molecular arrangement in the crystal of 1,2-di(cuban-1-yl)disulfane (**3:97**) represented as a stick model showing the C–H_{cubane}···C_{cubane} interactions. Interactions are indicated by blue dashed lines. Bond lengths and angles are given in Table 3:68 below.

Table 3:68: List of bond lengths and angles shown in Figure 3:84.

#	Interaction	H···A (Å)	D–H···A (°)
3:97	C–H_{cubane}···C	2.879	134.4

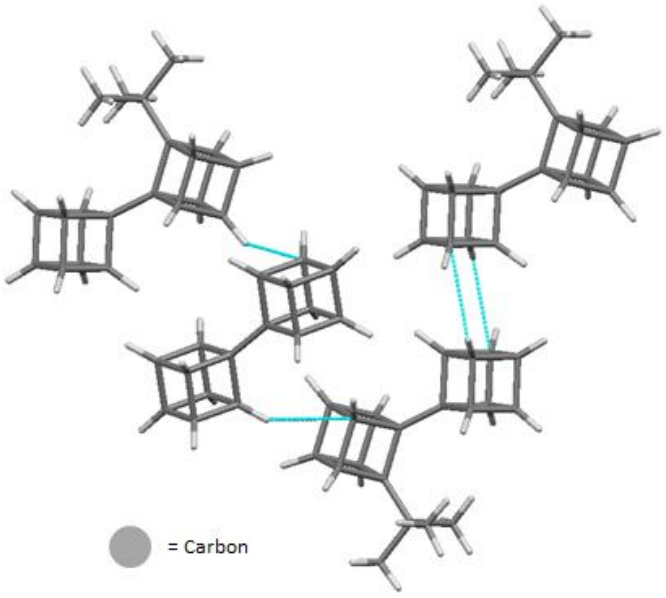

Figure 3:85: View of the molecular arrangement in the crystal of the co-crystal structure of 2-(tert-butyl)-1,1'-bi(cubane) and 1,1'-bi(cubane) (**3:98**) represented as a stick model showing the C–H_{cubane}···C_{cubane} interactions. Interactions are indicated by blue dashed lines. Bond lengths and angles are given in Table 3:69 below.

Table 3:69: List of bond lengths and angles shown in Figure 3:85.

#	Interaction	H···A (Å)	D–H···A (°)
3:98	C–H_{cubane}···C	2.880	142.0
	C–H_{cubane}···C	2.894	131.0
	C–H_{cubane}···C	2.868	130.6

This final section shows the importance of C–H_{cubane}···C non-classical hydrogen-bonding. The structure of compounds **3:86**–**3:88** show typical halogen or hydrogen interactions. however, in compounds **3:89**–**3:98**, there is a significant C–H_{cubane}···C interaction with the increasing number of cubane scaffolds and a decrease of alternate functionalities. This suggests, as seen in previous sections, that C–H_{cubane}···C interactions are competitive with other functional groups.

Conclusion.

In conclusion, we have investigated the structure of 1,4-substituted cubane scaffolds with regards to all potential interactions (Figure 3:86). With this, we have highlighted the contacts between esters, halogens, ethynyl, nitrogen bearing groups and all remaining 1,4-substituted cubane structures existing in the literature, which has built

on the previous work by Desiraju and co-workers on the interactions between cubane hydrogen atoms and acid or carboxamide moieties. This has revealed many interesting points, not only the contacts of the previously reported carboxylic acids and carboxamides, but also a plethora of connections are seen between the cubane scaffold and other heteroatoms groups. Interestingly the non-classical hydrogen-bonding between the cubane H-atoms and other moieties such as another cubane scaffold or ethynyl groups appears to be just as directive as compared to the more classical hydrogen-bonding systems seen in the works of Desiraju.

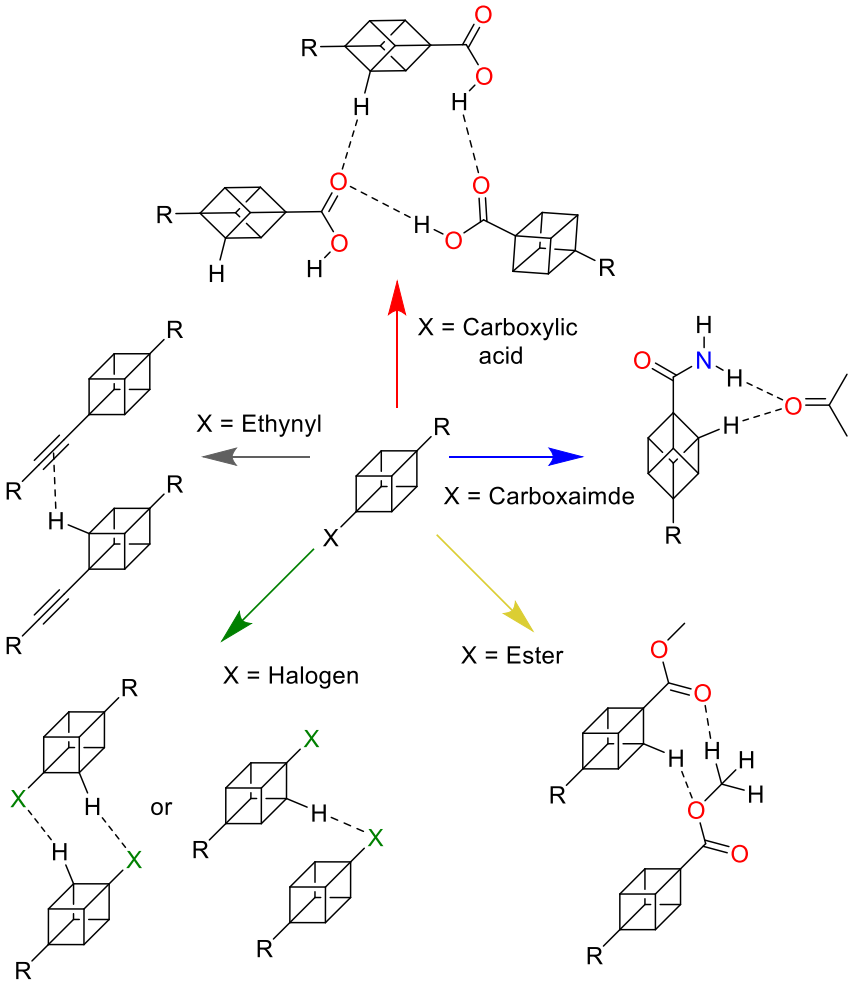

Figure 3:86: Summary image of the 1,4-disubstituted cubane structure interactions.

We have also highlighted the fact that halogen atoms, while they do change the packing motif, appear to be secondary in directing the packing regarding other hydrogen-bonding groups such as carboxylic acids, esters, or carboxamides. Additionally, the halogen functionalized cubane structures appear to favour halogen-hydrogen contacts above that of halogen-halogen interactions with only a handful of structures appearing to have any contribution to the latter. Ester functionalized cubane structures appear to form similar types of catemer formation

as seen with the carboxylic acids previously studied. As esters are exclusively hydrogen-bond acceptors, this is complementary to the hydrogen-bond donating ability of the cubane hydrogen atoms. In short, cubane is structurally close in size to a benzene ring along the 1,4-axis. However, the higher number of hydrogen atoms and the directions in which they are aligned is quite different to a benzene or a phenyl ring. This results in a multidirectional hydrogen-bond donor system which shows a larger potential of interactions possible and alternate packing systems. These packing systems are altered by the direction in which the hydrogens point as shown in the case study with the carboxylic acids. This demonstrates that the hydrogen atoms of the cubane may play much more of a role than previously discussed, a facet which should be also considered when substituting cubane as an isostere for benzene or phenyl rings.

Outlook.

This work was aimed at an initial investigation into the interaction profile of cubane to better understand which moieties and substituent pattern will give rise to specific patterns. The next steps to this investigation are to combine the knowledge gained here and compare the cubane structures directly with all their benzene counter-parts. This would allow for a direct comparison to the differences and similarities seen in both cubanes and benzene interaction profiles. Following this, there are additional small molecule scaffold systems such as bicyclo[1.1.1]pentane, which can be added as components in further structural studies in the future.[170] There are many potential avenues to expand this study in the future. The first of these is to cross reference the structures herein with that of neutron diffraction studies to obtain super fine structural details of the position of the cubane hydrogen atoms and their interactions. Additional studies comparing the bond strength to a bond distance of the interactions outlined here would provide more understanding of the nature of cubane hydrogen interactions included in this current study.

Supplementary Tables.

Table SI3:1: Bond lengths and angles of interactions between 1,4-substituted cubane carboxylic acid derivatives.

#	Interaction	H···A(Å)	D–H···A (°)	Ref
3:1	C–H_{cubane}···O	2.956	94.9	[171]
	C–H_{cubane}···O	2.936	90.5	
	C–H_{cubane}···O	3.059	87.6	
	C–H_{cubane}···O	3.122	86.1	
	O–H···O[a]	1.613	179.9	
	O–H···O[a]	1.645	179.7	
3:2	C–H_{cubane}···O	2.574	128.8	[173]
	O–H···O	1.783	178.4	
3:3	C–H_{cubane}···O	2.979	89.7	[171]
	C–H_{cubane}···O	3.109	87.0	
	C–H_{cubane}···O	2.934	90.0	
	C–H_{cubane}···O	3.060	87.5	
	C–H_{cubane}···O	3.122	86.1	
	O–H···O	1.648	164.2	
	O–H···O	1.699	153.9	
3:4	C–H_{cubane}···O	2.623	157.1	[171]
	C–H_{cubane}···O	2.703	121.0	
	C–H_{cubane}···O	2.835	90.7	
	C–H_{cubane}···O	2.980	84.5	
	C–H_{cubane}···O	3.125	87.7	
	O–H···O[a]	1.697	180.0	
	O–H···O[a]	1.573	179.9	
3:5	C–H_{cubane}···O	2.853	91.3	[171]
	C–H_{cubane}···O	2.974	88.6	
	O–H···O[a,b]	1.592	179.7	
	O–H···O[a,b]	1.697	179.5	
3:6	C–H_{cubane}···O	2.687	156.1	[173]
	O–H···O[a]	1.753	150.3	
	O–H···O[a]	1.774	163.7	
3:8	C–H_{cubane}···O	2.557	154.2	[171]
	C–H_{cubane}···O	2.678	122.9	
	O–H···O	1.610	171.8	
	N–H···O	1.874	166.0	
	N–H···O	2.003	151.9	
3:9	C–H_{OMe}···O	2.716	148.2	[171]
	C–H_{cubane}···O	2.700	124.4	
	C–H_{cubane}···O	2.689	156.3	
	C–H_{cubane}···O	2.651	150.5	
	C–H_{cubane}···O	2.670	153.3	
	C–H_{cubane}···O	2.660	144.7	
	C–H_{cubane}···O	2.936	90.4	
	C–H_{cubane}···O	3.090	86.6	
	C–H_{cubane}···O	3.095	86.6	
	O–H···O	1.650	170.4	
	O–H···O	1.665	159.9	
3:10	C–H_{cubane}···O	2.997	89.5	[177b]
	C–H_{cubane}···O	2.916	90.7	
	C–H_{cubane}···O	3.083	88.0	
	C–H_{cubane}···O	2.511	160.6	
	O–H···O	1.726	165.6	
	O–H···O	1.774	165.7	
3:11	C–H_{cubane}···O	2.716	149.0	[177a]
	C–H_{cubane}···O	2.614	107.5	
	C–H_{cubane}···H	2.338	121.2	
	C–H···O	2.557	143.3	
	O–H···O	1.756	166.9	

Table SI3:1 (continued): Bond lengths and angles of interactions between 1,4-substituted cubane carboxylic acid derivatives.

#	Interaction	H···A(Å)	D–H···A(°)	Ref	#	Interaction	H···A (Å)	D–H···A (°)	Ref
3:12	C–H_{cubane}···O	2.713	145.0			C–H_{cubane}···O	2.671	131.7	
	C–H_{cubane}···O	2.641	131.7			C–H_{cubane}···O	2.710	142.6	
	C–H_{cubane}···O	2.682	139.7			C–H_{cubane}···O	2.859	84.2	
	C–H_{cubane}···O	2.567	134.4			C–H_{cubane}···O	2.938	82.5	
	C–H_{cubane}···O	2.705	117.1			C–H_{cubane}···O	2.951	81.9	
	C–H_{cubane}···O	2.816	87.3			O–H···O	1.796	176.5	
	C–H_{cubane}···O	2.945	84.2			O–H···O	1.806	176.9	
	C–H_{cubane}···O	3.084	81.3			O–H···O	1.801	175.0	
	C–H_{cubane}···O	2.568	143.6			O–H···O	1.801	175.0	

Table SI3:2: Bond lengths and angles of interactions between 1,4-substituted cubane carboxamide derivatives.

#	Interaction	H···A (Å)	D–H···A (°)	Ref	#	Interaction	H···A (Å)	D–H···A (°)	Ref
3:13	C–H_{cubane}···O	2.616	163.3	[172b]	**3:8**	O–H···O	1.610	171.8	[171]
	N–H···O	2.044	171.6		**3:15**	C–H_{cubane}···O	2.540	164.5	[172b]
	N–H···O	2.011	165.2			N–H···O	2.016	175.3	
3:14	C–H_{cubane}···O	2.708	155.5	[172b]		N–H···O	1.971	178.1	
	N–H···O	2.103	157.0		**3:16**	C–H_{cubane}···O	2.602	164.2	[172b]
	N–H···O	2.071	165.3			N–H···O	1.977	163.9	
3:8	C–H_{cubane}···O	2.557	154.2	[171]		N–H···O	2.037	169.2	
	C–H_{cubane}···O	2.678	122.9		**3:17**	N–H···O	2.035	164.8	[172b]
	N–H···O	2.003	151.9			N–H···O	2.093	171.1	
	N–H···O	1.874	166.0						

Table SI3:3: Bond lengths and angles of interactions between 1-methoxycarbonyl-4-(R)-cubane complexes (where R is a second functional group).

#	Interaction	H···A (Å)	D–H···A (°)	Ref
3:18	C–H_{cubane}···O^1	2.652	167.3	[179h]
	C–H_{OMe}···O^2	2.413	162.4	
3:19	C–H_{cubane}···O^1	2.645	175.0	[179h]
	C–H_{OMe}···O^2	2.390	171.0	
	C–H_{cubane}···F	2.618	156.3	
	C–H_{cubane}···F	2.618	156.3	
3:20	C–H_{cubane}···O^1	2.692	156.1	[179h]
	C–H_{OMe}···O^2	2.353	161.1	
	C–H_{cubane}···Cl	3.106	103.0	
	C–H_{cubane}···Cl	3.106	103.0	
	C···O^2	3.218	95.0	
3:21	C–H_{OMe}···O^2	2.184	158.4	[179h]
	C–H_{OMe}···C_{cubane}	2.895	167.8	
3:22	C–H_{OMe}···O^2	2.428	176.2	[179h]
	C–H_{OMe}···C_{cubane}	2.762	174.2	
3:22_a	C–H_{cubane}···C	2.769	140.1	
	C–H_{OMe}···O^1	2.719	161.0	
	C–H_{cubane}···O^2	2.509	156.0	
	C–H_{cubane}···O^2	2.705	130.0	
3:23	C–H_{OMe}···O^2	2.486	163.9	[179f]
	C–H_{cubane}···H_{Ph}	2.358	149.98	
3:24	C–H_{cubane}···O^2	2.525	166.9	[179a]
	C–H_{cubane}···O^2	2.445	160.5	
	C–H_{OMe}···O^3	2.491	147.1	
	C–H_{OMe}···O^3	2.497	147.1	
3:25	C–H_{OMe}···O^1	2.647	152.1	[179a]
	C–H_{cubane}···O^1	2.588	161	
	C–H_{OMe}···O^2	2.570	160.9	
	C–H_{cubane}···O^3	2.487	175.5	
	C–H_{cubane}···O^4	2.680	165.3	
	C–H_{cubane}···O^4	2.563	145.2	
3:26	C–H_{cubane}···O^1	2.684	165.8	[179c]
	C–H_{OMe}···O^2	2.437	165.3	
	C–H_{OMe}···O^3	2.437	165.3	
	C–H_{cubane}···O^4	2.684	165.8	
3:9	C–H_{OMe}···O^1	2.716	148.2	[171]
	C–H_{cubane}···O^2	2.700	124.4	
	C–H_{cubane}···O^2	2.689	156.3	
	C–H_{cubane}···O^3	2.651	150.5	
	C–H_{cubane}···O^3	2.523	159.4	
	C–H_{cubane}···O^4	2.670	153.3	
	C–H_{cubane}···O^4	2.660	144.7	
	C–H_{cubane}···O^4	2.936	90.4	
	C–H_{cubane}···O^4	3.090	86.6	
	C–H_{cubane}···O^4	3.095	86.6	
	O^4–H···O^3	1.650	170.4	
	O^4–H···O^3	1.665	159.9	

Table SI3:3 (continued): Bond lengths and angles of interactions between 1-methoxycarbonyl-4-(R)-cubane complexes (where R is a second functional group).

#	Interaction	H···A (Å)	D–H···A (°)	Ref
3:27	$C–H_{cubane}\cdots O^2$	2.565	153.4	[179l]
	$O–H\cdots O^3$	1.887	177.4	
	$C–H_{cubane}\cdots O^3$	2.786	166.14	
	$O–H\cdots O^3$	1.912	177.00	
3:28	$C–H_{cubane}\cdots O^1$	2.682	143.3	[179l]
	$C–H_{cubane}\cdots O^2$	2.647	156.4	
	$C–H_{OMe}\cdots O^2$	2.453	160.9	
	$C–H_{SMe}\cdots O^2$	2.377	168.8	
	$C–H_{cubane}\cdots O^4$	2.562	148.3	
	$C–H_{SMe}\cdots O^5$	2.566	143.5	
	$C–H_{S}\cdots O^5$	2.461	159.2	
3:29	$C–H\cdots O^4$	2.572	124.3	[179l]
	$C–H_{cubane}\cdots Cl$	3.085	101.6	
	$C–Cl\cdots Cl$	3.410	148.1	
3:30	$C–H_{Ph}\cdots O^2$	2.525	125.1	[179l]
	$C–H_{cubane}\cdots O(NO_2)$	2.753	102.5	
3:31	$C–H_{cubane}\cdots O^4$	2.695	92.6	[179l]
	$C–H_{cubane}\cdots O^4$	2.696	85.9	
	$C–H_{cubane}\cdots O(NO_2)$	2.547	120.4	
	$C–H_{OMe}\cdots O(NO_2)$	2.574	115.9	
	$C–H_{Ph}\cdots O(NO_2)$	2.447	144.8	
	$C–H_{cubane}\cdots\pi$	2.721	129.4	
3:32	$C–H\cdots O^1$	2.498	153.1	[179l]
	$C–H_{Ph}\cdots O^2$	2.480	124.9	
	$C–H_{Ph}\cdots O^2$	2.597	119.8	
	$C–H_{OMe}\cdots O(NO_2)$	2.652	133.3	

Table SI3:4: Bond lengths and angles of interactions between 1,4-di-ester-cubane complexes.

#	Interaction	H···A (Å)	D–H···A (°)	Ref
3:33	$C–H_{OMe}\cdots C_{cubane}$	2.900	153.9	[179i]
	$C_{cubane}\cdots C_{cubane}$	3.362	91.3	
3:34	$C–H_{cubane}\cdots O^1$	2.693	142.2	[179i]
	$C–H_{OPr}\cdots O^2$	2.653	150.3	
	$C–H_{cubane}\cdots C_{cubane}$	2.835	158.6	
	$C–H_{cubane}\cdots C_{cubane}$	2.891	110.87	
3:36	$C–F\cdots C_{cubane}$	3.068	144.6	[179i]
	$C–F\cdots C_{cubane}$	3.068	144.6	
	$C–H\cdots O^2$	2.430	163.4	
3:36	$C–H\cdots O^2$	2.646	145.5	[179i]
	$C–H\cdots O^3$	2.430	163.4	
	$C–H\cdots O^3$	2.646	145.5	
	$C–H_{cubane}\cdots C_{cubane}$	2.772	113.6	
3:37	$C–H\cdots O^2$	2.347	159.8	[179i]
	$C–H\cdots O^3$	2.347	159.8	
3:39	$C–H\cdots N$	2.740	155.2	[179e]
	$C–H_{cubane}\cdots N$	2.710	145.3	

Table SI3:5: Bond lengths and angles of interactions between 1-ester-4-(R)-cubane complexes (where R is a second functional group).

#	Interaction	H···A (Å)	D–H···A (°)	Ref
3:40	$C–H_{cubane}···O^1$	2.394	155.3	[168a]
	$C–H_{cubane}···O^1$	2.416	162.1	
	$C–H···O^1$	2.615	157.9	
	$C–H···O^2$	2.512	157.5	
	$C–H···O^2$	2.476	157.8	
	$C–H···O^2$	2.392	147.4	
	$C–H_{cubane}···O^2$	2.608	120.2	
3:12	$C–H_{cubane}···O^4$	2.713	145.0	
	$C–H_{cubane}···O^3$	2.641	131.7	
	$C–H_{cubane}···O^4$	2.682	139.7	
	$C–H_{cubane}···O^3$	2.567	134.4	
	$C–H_{cubane}···O^1$	2.705	117.1	
	$C–H_{cubane}···O^2$	2.816	87.3	
	$C–H_{cubane}···O^2$	2.945	84.2	
	$C–H_{cubane}···O^2$	3.084	81.3	
	$C–H_{cubane}···O^3$	2.568	143.6	
	$C–H_{cubane}···O^3$	2.671	131.7	
	$C–H_{cubane}···O^4$	2.710	142.6	
	$C–H_{cubane}···O^3$	2.859	84.2	
	$C–H_{cubane}···O^3$	2.938	82.5	
	$C–H_{cubane}···O^3$	2.951	81.9	
	$O^4–H···O^3$	1.796	176.5	
	$O^3–H···O^4$	1.806	176.9	
	$O^3–H···O^4$	1.801	175.0	
	$O^3–H···O^4$	1.801	175.0	
3:41	$C–H_{Ph}···O^2$	2.643	146.8	
	$C–H···O^2$	2.695	124.3	
	$C–H_{cubane}···O^3$	2.554	148.6	
	$C–I···O^3$	3.201	169.7	
	$C–H···O^4$	2.713	151.	
	$C–H···O^4$	2.497	157.1	

#	Interaction	H···A (Å)	D–H···A (°)	Ref
3:42	$C–H_{cubane}···O^1$	2.368	158.8	
	$C–H···O^2$	2.858	102.2	
	$C–H_{Ph}···O^3$	2.785	107.4	
	$C–H_{cubane}···O^4$	2.686	102.2	
	$C–H_{cubane}···O^4$	2.848	97.5	
	$C–H_{cubane}···O^5$	2.559	158.6	
	$C–H_{cubane}···O^5$	2.435	158.9	
	$C–O^6···\pi$	2.964	136.1	
	$C–H_{Ph}···O^6$	2.708	123.6	
3:43	$C–H_{cubane}···O^1$	2.455	163.1	
	$C–H···O^2$	2.694	126.2	
	$C–H_{cubane}···O^3$	2.625	157.2	
	$C–H···O^4$	2.560	116.1	
	$C–H_{cubane}···O^5$	2.505	154.6	
	$C–H_{cubane}···O^5$	2.517	149.5	
	$C–O^6···\pi$	2.953	163.1	
	$C–Cl···O^2$	3.103	159.6	
	$C–Cl···O^4$	3.227	170.4	
	$C–Cl···O^6$	3.011	157.5	
	C–Cl···H	2.930	109.6	
	C–Cl···H	2.871	111.9	
	C–Cl···Cl	3.277	127.3	
3:44	$C–H_{cubane}···O^1$	2.377	167.1	
	$C–O^2···O^3$	2.851	152.7	
	$C–I···H_{cubane}$	3.178	69.2	
	$C–H_{cubane}···O^4$	2.222	169.3	
	$C–H_{Ph}···O^4$	2.484	125.1	
	$C–H_{cubane}···O^3$	2.963	94.0	
	$C–I···H_{Ph}$	3.064	107.8	
	$C–I···H_{Ph}$	3.173	97.4	
	$C–H_{Ph}···C_{cubane}$	2.865	118.1	
	$C–I···\pi$	4.041	97.2	

Table SI3:6: Bond lengths and angles of interactions between 4-halo-1-(R)-cubane complexes (where R is a second functional group).

#	Interaction	H···A (Å)	D–H···A (°)	Ref
3:45	C–H_{cubane}···F	2.639	131.8	[179a]
	C–H_{cubane}···F	2.499	170.5	
3:46	C–H_{cubane}···Cl	3.001	154.8	[179a]
	C–H_{cubane}···Cl	3.067	158.9	
3:47	C–H_{cubane}···Br	2.893	157.4	[181b]
3:48	C–H_{cubane}···I	3.330	156.2	[181a]
3:48_a	C–H_{cubane}···I	3.227	156.4	
3:2	C–H_{cubane}···F	2.481	120.9	[173]
	C–H_{cubane}···F	2.730	101.3	
3:3	C–H_{cubane}···Cl	2.945	165.3	[173]
3:4	C–H_{cubane}···Br	3.189	168.8	[173]
3:5	C–I···I	3.835	150.5	[173]
	C–H_{cubane}···I	3.238	169.8	
3:19	C–H_{cubane}···F	2.618	156.3	[179h]
3:20	C–H_{cubane}···Cl	3.106	103.0	[179h]
3:21	C–H_{cubane}···Br	3.234	105.4	[179h]
3:22	C–H_{cubane}···I	3.364	148.6	[179h]
3:22_a	C–H_{cubane}···I	3.278	160.9	
	C–I···I	3.984	153.5	
3:15	C–H_{cubane}···Cl	2.932	154.35	[172b]
	C–H_{cubane}···Cl	3.152	99.9	
3:16	C–H_{cubane}···Br	3.008	153.7	[172b]
3:17	C–H_{cubane}···I	3.215	152.4	[172b]
	C–I···I	4.131	74.0	
3:50	C–H_{cubane}···Br	3.120	100.9	[181d]
	O–H···O	1.973	173.6	
3:51	C–Br···Br	3.685	152.8	[177a]
	C–H_{cubane}···O	2.665	125.7	
	C–H_{cubane}···O	2.465	149.1	
	C–H_{cubane}···O	2.514	157.5	
	C–H_{CH2}···O	2.405	140.1	
3:53	C–H_{cubane}···Cl	2.922	122.0	[167]
	C–H_{cubane}···F	2.585	128.2	
	C–H_{cubane}···F	2.609	115.8	
	C–H_{cubane}···O	2.581	137.1	
	C–H_{Ph}···Cl	2.947	159.8	
	C–F···F	2.777	140.8	
	C–F···O	2.957	145.6	
	N–H···O	1.947	159.1	
	N–H···O	2.549	138.0	
3:54	C–H_{cubane}···F	2.612	155.8	[179a]
	C–H_{cubane}···F	2.592	161.5	
	C–H···F	2.654	152.0	
	N–H···O	1.882	174.1	
3:56	C–H_{cubane}···Br	2.955	163.6	[181g]
3:57	C–H_{cubane}···I	3.201	128.7	
	C–H_{cubane}···I	3.263	129.0	
	C–H_{cubane}···π	2.948	140.5	
3:58	C–H_{cubane}···I	3.113	151.34	
	C–H_{cubane}···π	2.843	150.9	
3:52	C–H_{cubane}···Br	2.824	148.0	[181e]
	C–H_{cubane}···Br	2.869	146.7	
	C–H_{CH2}···O	2.526	141.7	
	N–O···N	3.050	110.8	
	C–H_{CH2}···O	2.891	98.5	
	N–H···O	1.930	155.6	
3:59	C–H_{cubane}···I	3.028	169.9	
	C–Br···I	3.756	155.8	
	C–H_{cubane}···π	2.684	155.9	
	C–H_{cubane}···π	3.052	167.4	

Table SI3:6(continued): Bond lengths and angles of interactions between 4-halo-1-(R)-cubane complexes (where R is a second functional group).

#	Interaction	H···A (Å)	D–H···A (°)	Ref
3:60	C–H_{cubane}···I	3.079	150.0	
	C–H_{Ph}···I	3.061	151.2	
	C–H_{cubane}···π	2.692	158.4	
	C–H_{cubane}···π	2.984	145.6	
	C–H_{Ph}···N	2.701	144.4	
	C–H_{Ph}···N	2.721	176.4	
3:44	C–H_{cubane}···I	3.178	173.6	
	C–H_{Ph}···I	3.064	166.4	
3:44	C–H_{Ph}···I	3.173	128.9	
	C–I···I	3.640	167.8	
	C–I···π	4.041	97.2	
3:61	C–H_{Ph}···I	3.151	139.7	
3:41	C–I···O	3.201	169.7	
3:62	C–H_{Ph}···I	3.688	80.7	[168a]
	C–H_{Ph}···C_{cubane}	2.895	149.4	

Table SI3:7: Bond lengths and angles of interactions between ethynyl bearing 1,4-substituted cubane structures.

#	Interaction	H···A (Å)	D–H···A (°)	Ref
3:63	C–H_{cubane}···C_{cubane}	2.838	152.6	[182a]
	C–H_{cubane}···$C_{ethynyl}$	2.804	169.6	
	C–$H_{ethynyl}$···$C_{ethynyl}$	2.707	167.1	
3:64	C–H_{cubane}···$C_{ethynyl}$	2.879	143.6	[182a]
	C–H_{cubane}···$C_{ethynyl}$	2.874	142.1	
	C–H_{cubane}···$C_{ethynyl}$	2.879	144.2	
3:65	C–H_{cubane}···$C_{ethynyl}$	2.879	150.0	[182a]
	C–H_{cubane}···$C_{ethynyl}$	2.875	142.0	
	C–H_{cubane}···C_{cubane}	2.853	145.7	
3:66	C–H_{Ph}···C_{cubane}	2.846	153.7	[182a]
	C–H_{Ph}···C_{cubane}	2.771	137.3	
	C–H_{cubane}···C_{Ph}	2.883	156.7	
	C–H_{Ph}···$C_{ethynyl}$	2.716	150.0	
	C–H_{Ph}···C_{Ph}	2.388	129.1	
	C–H_{Ph}···C_{Ph}	2.858	137.4	
3:67	C–H_{cubane}···$C_{ethynyl}$	2.871	159.9	[182b]
	C–H_{cubane}···$C_{ethynyl}$	2.871	159.9	
	C–H_{cubane}···$C_{ethynyl}$	2.822	152.0	
	C–H_{cubane}···$C_{ethynyl}$	2.822	152.0	
	C–H_{cubane}···$C_{ethynyl}$	2.871	159.9	
	C–H_{cubane}···$C_{ethynyl}$	2.871	159.9	
3:59	C–H_{cubane}···$C_{ethynyl}$	2.695	147.8	
	C–H_{cubane}···$C_{ethynyl}$	2.804	159.1	
	C–H_{cubane}···$C_{ethynyl}$	2.881	163.4	
3:58	C–H_{cubane}···$C_{ethynyl}$	2.760	141.1	
3:60	C–H_{cubane}···$C_{ethynyl}$	2.756	156.8	
	C–H_{cubane}···$C_{ethynyl}$	2.761	153.5	
	C–H_{cubane}···$C_{ethynyl}$	2.890	138.0	
3:40	C–H_{cubane}···$C_{ethynyl}$	2.869	163.4	[168a]
	C–H_{cubane}···$C_{ethynyl}$	2.881	167.8	
	C–H_{cubane}···$C_{ethynyl}$	2.863	143.9	

Table SI3:8: Bond lengths and angles of interactions between 1,4-substituted nitrogen bearing cubane.

#	Interaction	H···A (Å)	D–H···A (°)	Ref
3:68	C–H_{cubane}···O	2.515	161.3	[183a]
	C–H_{cubane}···O	2.515	161.3	
	C–H_{cubane}···O	2.580	177.3	
3:69	C–H_{cubane}···O	2.528	139.6	[183b]
	C–H_{cubane}···O	2.662	166.9	
	C–H_{cubane}···O	2.930	89.3	
	C–H_{cubane}···O	2.957	86.3	
	C–H_{cubane}···O	3.070	85.8	
3:70	C–H_{cubane}···O	2.502	131.0	[184]
	C–H_{cubane}···O	2.765	96.5	
	C–H_{cubane}···O	3.084	89.1	
	C–H···O	2.530	129.1	
	C–H···O	2.671	137.2	
3:73	C–H_{cubane}···O	2.530	151.3	[177a]
	C–H_{cubane}···H	2.335	144.4	
3:74	C–H_{cubane}···O	2.477	153.1	[177a]
	C–H_{cubane}···O	2.625	155.0	
	C–H_{cubane}···O	2.679	151.2	
	C–H_{cubane}···O	2.621	154.9	
	C–H_{cubane}···C	2.814	130.8	
	C–H_{cubane}···C	2.743	110.4	
	C–H_{cubane}···C	2.743	110.3	
	C–H_{cubane}···C	2.820	130.8	
	C–H···O	2.696	126.0	
	N–H···O	2.330	152.5	
3:75	C–H_{cubane}···O	2.526	134.8	[186a]
	C–H_{cubane}···O	2.540	132.5	

#	Interaction	H···A (Å)	D–H···A (°)	Ref
3:75	C–H_{cubane}···O	2.744	89.3	[186a]
	C–H_{cubane}···O	2.835	87.2	
	C–H_{cubane}···O	3.051	82.5	
	N–H···O	2.286	148.2	
	N–H···O	2.459	129.2	
	N–H···O	2.627	103.3	
	N–H···O	2.550	108.2	
	N–H···O	2.198	152.8	
	N–H···O	2.690	112.1	
	N–H···O	2.560	134.3	
	N–H···O	2.329	134.7	
	N–H···N	2.447	138.1	
3:76	N–H···O	2.196	139.4	[186b]
	N–H···O	2.365	153.9	
	N–H···O	2.215	148.8	
3:77	C–H_{cubane}···H	2.851	121.5	[167]
	C–H_{cubane}···N	2.728	137.3	
	N–H···O	2.073	167.7	
	N–H···O	1.998	160.8	
	O–H···O	2.057	146.9	
3:78	O–H···C_{cubane}	2.869	124.3	[3a]
	C–H_{Ph}···C_{cubane}	2.888	130.1	
	N–H···O	1.981	149.2	
	C–H_{Ph}···C	2.653	160.5	
	C–H_{Ph}···O	2.665	154.5	
	C–H_{Ph}···C	2.891	122.9	

Table SI3:8 (continued): Bond lengths and angles of interactions between 1,4-substituted nitrogen bearing cubane.

#	Interaction	H···A (Å)	D–H···A (°)	Ref
3:79	$C–H_{cubane}···H$	2.115	169.6	[169e]
	$C–H_{cubane}···H$	2.885	123.8	
	$C–H_{cubane}···O$	2.664	141.3	
	C–H···Cl	2.893	139.0	
	N–H···O	2.193	161.0	
	$C–H_{Ph}···O$	2.614	145.2	
	$C–H···C_{Ph}$	2.727	154.8	
	$C–H···C_{Ph}$	2.894	128.0	
	$C–H···C_{Ph}$	2.681	161.9	
	$C–H···C_{Ph}$	2.838	144.0	
3:80	$C–H_{cubane}···H$	2.347	129.3	[186c]
3:80	$C–H_{cubane}···C$	2.838	137.3	[186c]
	C–H···C	2.888	124.4	
	C–H···C	2.894	134.8	
	C–O···H	2.433	140.4	
	N–H···O	2.455	174.0	
	C–O···H	2.372	141.4	
3:81	$C–H_{cubane}···C$	2.874	128.9	[186d]
	$C–H···C_{cubane}$	2.891	113.9	
	C–H···O	2.664	133.8	
	C–H···O	2.673	136.4	
3:82	$C–H_{cubane}···C$	2.894	134.4	[179a]
	$C–H_{cubane}···H$	2.365	113.2	
	$C–H_{cubane}···H$	2.373	118.1	
	C–H···O	2.421	159.6	
	O–H···N	1.933	175.8	
	C–H···N	2.633	158.3	
	C–H···C	2.672	164.2	

Table SI3:9: Bond lengths and angles of interactions between the remaining 1,4-substituted cubane complexes.

#	Interaction	H···A (Å)	D–H···A (°)	Ref
3:83	$C–H_{cubane}\cdots C$	2.839	165.9	[186e]
	$C–H_{cubane}\cdots H$	2.392	121.4	
	$C–H_{cubane}\cdots O$	2.428	149.0	
	$C–H_{Ph}\cdots O$	2.531	148.7	
	$C–H_{Ph}\cdots O$	2.567	166.7	
	$C–H_{Me}\cdots O$	2.334	132.3	
3:84	$C–H_{cubane}\cdots C$	2.766	112.7	[168b]
	$C–H_{cubane}\cdots C$	2.785	135.1	
	$C–H_{cubane}\cdots C$	2.745	131.9	
	$C–H_{cubane}\cdots C$	2.843	109.3	
	$C–H_{cubane}\cdots C$	2.876	139.0	
	$C–H_{Ph}\cdots C$	2.868	147.9	
	$C–H_{Ph}\cdots C$	2.872	136.8	
	$C–H_{cubane}\cdots C$	2.811	120.9	
	$C–H_{Me}\cdots C$	2.859	118.3	

#	Interaction	H···A (Å)	D–H···A (°)	Ref
3:84	$C–H_{Ph}\cdots C$	2.806	150.7	[168b]
	$C–H_{Ph}\cdots C$	2.845	153.6	
3:85	$C–H_{cubane}\cdots C$	2.809	114.4	[168b]
	$C–H_{cubane}\cdots C$	2.812	114.1	
	$C–H_{cubane}\cdots C$	2.853	113.0	
	$C–H_{cubane}\cdots C$	2.848	113.2	
	$C–H_{Ph}\cdots C$	2.885	140.7	
	$C–H_{Ph}\cdots C$	2.702	155.3	
	$C–H_{cubane}\cdots C$	2.887	136.8	
	$C–H_{Ph}\cdots C$	2.873	131.6	
	$C–H_{Ph}\cdots C_{cubane}$	2.773	150.4	
	$C–H_{Ph}\cdots C_{cubane}$	2.741	154.4	
	$C–H_{Ph}\cdots C_{cubane}$	2.858	126.6	
	$C–H_{Ph}\cdots C_{cubane}$	2.882	139.2	
	$C–H_{cubane}\cdots F$	2.544	153.9	

Table SI3:9 (continued): Bond lengths and angles of interactions between the remaining 1,4-substituted cubane complexes.

#	Interaction	H···A (Å)	D–H···A (°)	Ref
3:86	C–H_{cubane}···Br	3.037	128.4	[186f]
3:87	C–H_{cubane}···C	2.792	132.2	[186f]
	C–H_{cubane}···C	2.807	110.0	
	C–Cl···H	2.755	122.2	
3:88	C–H···C_{cubane}	2.858	160.9	[186g]
	O–H···O	1.828	168.4	
3:90	C–H_{cubane}···C	2.857	156.4	[181f]
3:91	C–H_{cubane}···C	2.889	134.4	[181f]
3:92	C–H_{cubane}···C	2.858	152.1	[181f]
	C–H_{cubane}···C	2.881	157.6	
	C–H_{cubane}···C	2.840	154.8	
	C–H_{cubane}···C	2.798	152.2	
	C–H_{cubane}···C	2.848	148.9	
	C–H_{cubane}···C	2.879	154.0	
	C–H_{cubane}···C	2.834	156.3	
	C–H_{cubane}···C	2.801	148.4	
	C–H_{cubane}···C	2.819	148.6	
	C–H_{cubane}···C	2.802	149.3	
	C–H_{cubane}···C	2.808	152.8	
	C–H_{cubane}···C	2.764	147.7	
	C–H_{cubane}···C	2.867	149.1	
3:92	C–H_{cubane}···C	2.850	159.0	[181f]
	C–H_{cubane}···C	2.897	147.0	
	C–H_{cubane}···C	2.873	159.7	
3:93	C–H_{cubane}···C	2.825	107.8	[181f]
	C–H_{cubane}···C	2.816	109.7	
	C–H_{cubane}···C	2.869	158.6	
	C–H_{cubane}···C	2.881	148.6	
	C–H_{cubane}···C	2.891	123.8	
	C–H_{cubane}···C	2.894	120.1	
	C–H_{cubane}···C	2.899	120.4	
	C–H_{cubane}···C	2.851	145.5	
	C–H_{cubane}···π	2.910	152.4	
3:94	C–H_{cubane}···H	2.380	146.1	[186h]
	C–H···C	2.795	141.6	
3:96	C–H_{cubane}···C	2.854	128.3	[186i]
	C–H_{BCP}···C	2.898	128.4	
3:97	C–H_{cubane}···C	2.879	134.4	[186j]
3:98	C–H_{cubane}···C	2.880	142.0	[186k]
	C–H_{cubane}···C	2.894	131.0	
	C–H_{cubane}···C	2.868	130.6	

Experimental.

All published data was obtained from the CCDC using the program ConQuest version 1.22.[149] All bond angles and bond lengths were measured using the program Mercury CSD version 3.10.2.[187] All images in this chapter were prepared by using Mercury CSD version 3.10.2. Thermal ellipsoid plots are included for all structures determined as part of this chapter in the SI and were prepared using Olex2.[139a]

Crystals were grown following the protocol developed by Hope by dissolving the compounds in either DCM or a DCM/MeOH mixture and allowing for slow evaporation over time.[137] Single crystal X-ray diffraction data for all compounds were collected on a Bruker APEX 2 DUO CCD diffractometer by using graphite-monochromated MoK_α (λ = 0.71073 Å) radiation and Incoatec IμS CuK_α (λ = 1.54178 Å) radiation. Crystals were mounted on a MiTeGen MicroMount and collected at 100(2) K by using an Oxford Cryosystems Cobra low-temperature device. Data were collected by using omega and phi scans and were corrected for Lorentz and polarization effects by using the APEX software suite.[138] Using Olex2, the structure was solved with the XT structure solution program, using the intrinsic phasing solution method and refined against $|F^2|$ with XL using least squares minimization.[139] Hydrogen atoms were generally placed in geometrically calculated positions and refined using a riding model. Details of data refinements can be found in Table E3:1–E3:4.

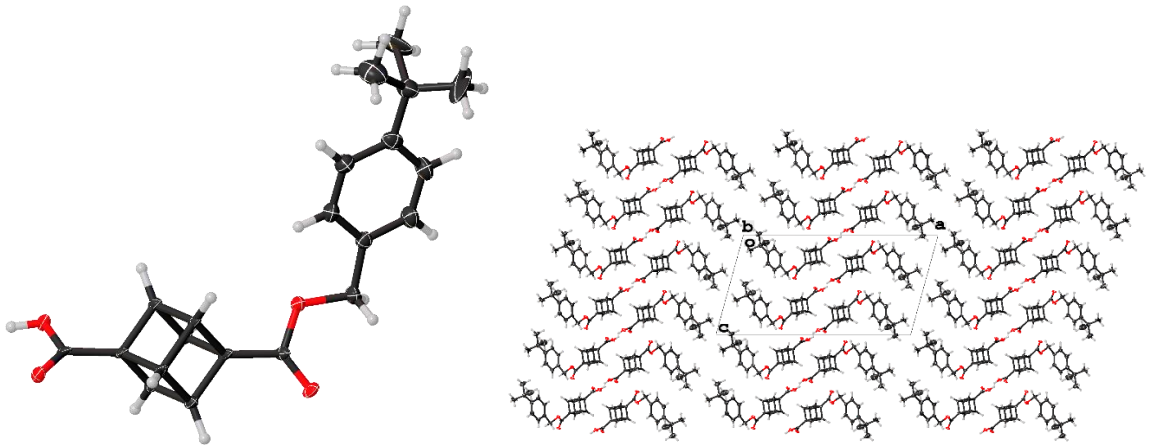

Figure E3:1: The molecular structure of compound **3:12** (left) and moiety packing looking down the *b*-axis (right). Thermal displacement gives 50% probability.

Crystal Data for compound 3:12: The C-bound and O-bound H atoms were placed in their expected calculated positions and refined as riding model: C–H = 0.95–0.98 Å, with U_{iso}(H) = 1.5 U_{eq}(C) for methyl and oxygen H atoms and 1.2 U_{eq} (C) for all other atoms other H atoms. The *tert*-butyl group at C18B was modelled over three positions in a 40:30:30% occupancy using restraints (SADI) and the constraint (EADP).

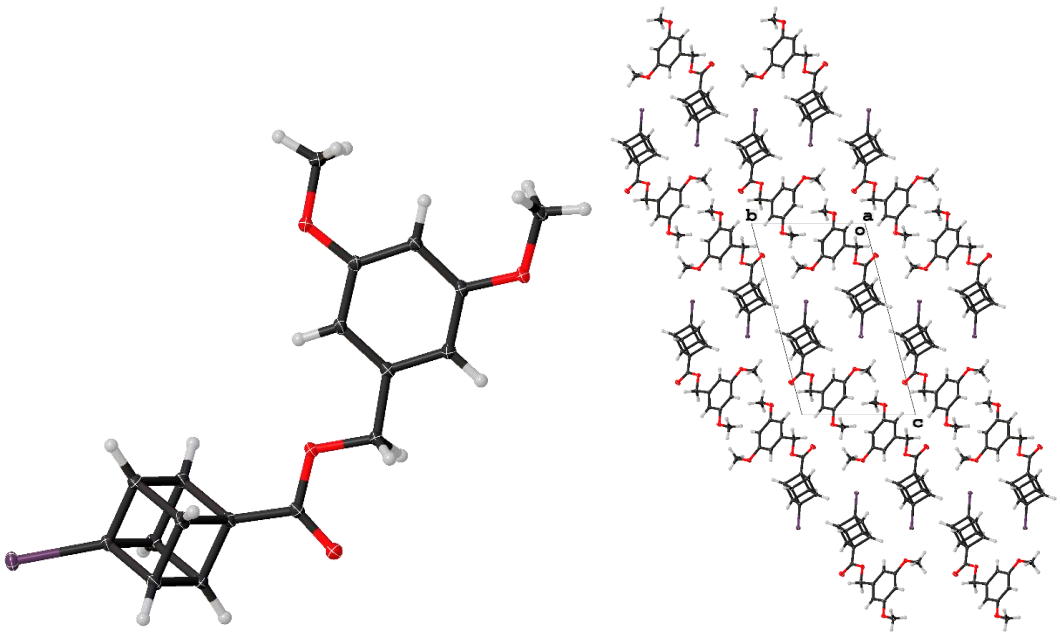

Figure E3:2: The molecular structure of compound **3:41** (left) and moiety packing looking down the *a*-axis (right). Thermal displacement gives 50% probability.

Crystal Data for compound 3:41: The C-bound H atoms were placed in their expected calculated positions and refined as riding model: C–H = 0.95–0.98 Å, with U_{iso}(H) = 1.5 U_{eq}(C) for methyl H atoms and 1.2 U_{eq} (C) for all other atoms other H atoms. No constraints or restraints were applied.

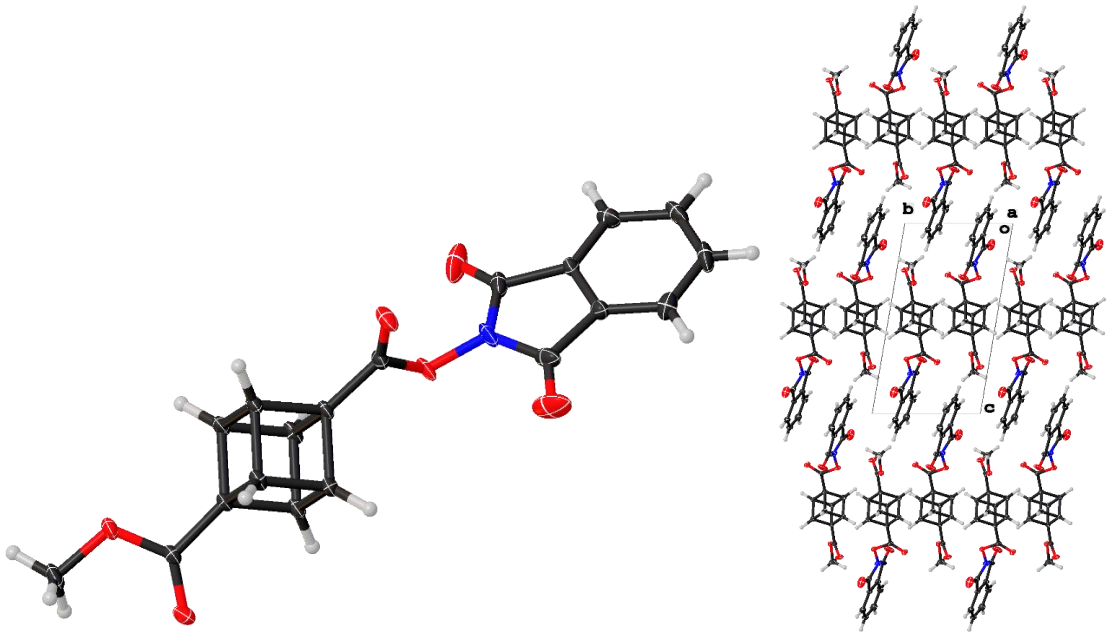

Figure E3:3: The molecular structure of compound **3:42** (left) and moiety packing looking down the *a*-axis (right). Thermal displacement gives 50% probability.

Crystal Data for compound 3:42: The C-bound H atoms were placed in their expected calculated positions and refined as riding model: C–H = 0.95–0.98 Å, with U_{iso}(H) = 1.5 U_{eq}(C) for methyl H atoms and 1.2 U_{eq} (C) for all other atoms other H atoms. The ester group oxygen atoms (O3 and O4) were modelled over two positions in a 56:44% occupancy using the restraint (ISOR).

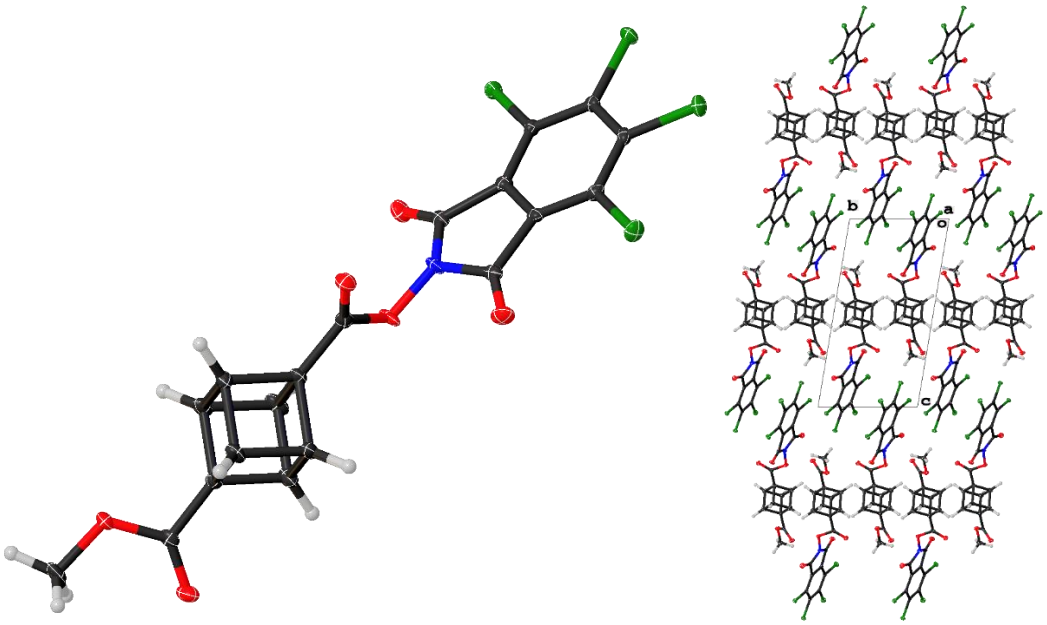

Figure E3:4: The molecular structure of compound **3:43** (left) and moiety packing looking down the *a*-axis (right). Thermal displacement gives 50% probability.

Crystal Data for compound 3:43: The C-bound H atoms were placed in their expected calculated positions and refined as riding model: C–H = 0.95–0.98 Å, with

U_{iso}(H) = 1.5 U_{eq}(C) for methyl H atoms and 1.2 U_{eq} (C) for all other atoms other H atoms. No constraints or restraints were applied.

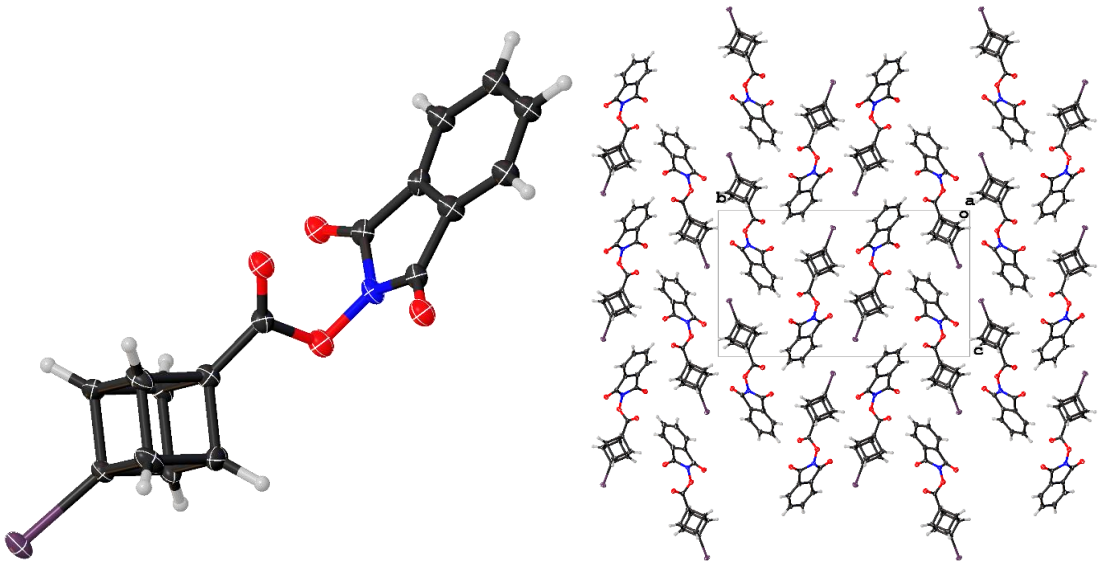

Figure E3:5: The molecular structure of compound **3:44** (left) and moiety packing looking down the *a*-axis (right). Thermal displacement gives 50% probability.

Crystal Data for compound 3:44: The C-bound H atoms were placed in their expected calculated positions and refined as riding model: C–H = 0.95–0.98 Å, with U_{iso}(H) = 1.2 U_{eq}(C) for all CH groups. The redox active ester was modelled over two positions in a 93:7% occupancy using the restraints (DFIX, SADI, and FLAT) and the constraint (EADP).

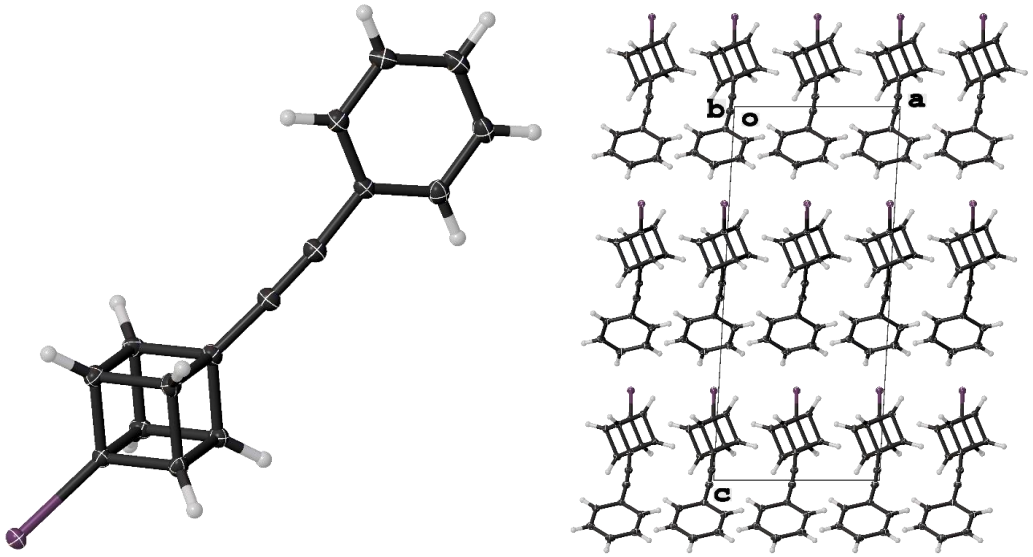

Figure E3:6: The molecular structure of compound **3:57** (left) and moiety packing looking down the *b*-axis (right). Thermal displacement gives 50% probability.

Crystal Data for compound 3:57: The C-bound H atoms were placed in their expected calculated positions and refined as riding model: C–H = 0.95–0.98 Å, with U_{iso}(H) = 1.2 U_{eq}(C) for all CH groups. No constraints or restraints were applied.

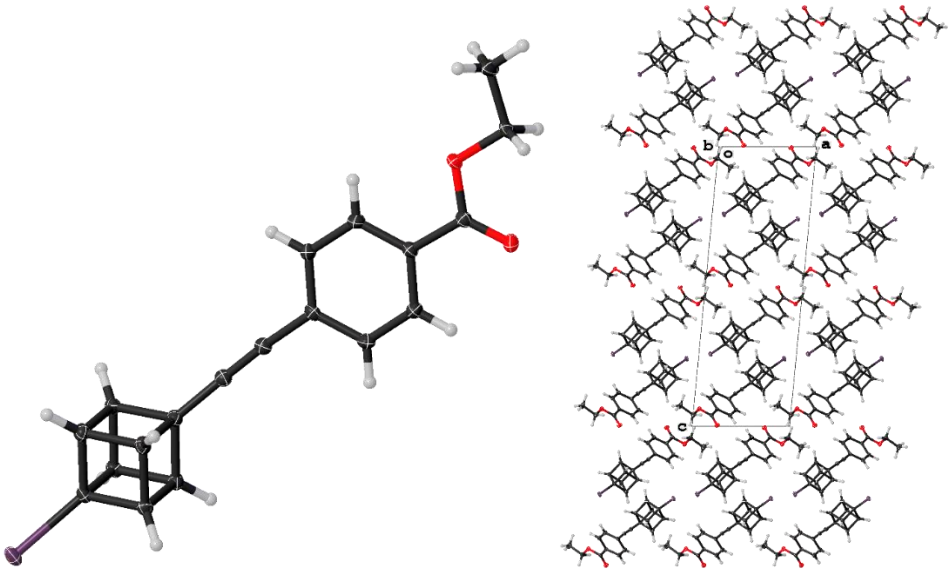

Figure E3:7: The molecular structure of compound **3:58** (left) and moiety packing looking down the *b*-axis (right). Thermal displacement gives 50% probability.

Crystal Data for compound 3:58: The C-bound H atoms were placed in their expected calculated positions and refined as riding model: C–H = 0.95–0.98 Å, with U_{iso}(H) = 1.5 U_{eq}(C) for methyl H atoms and 1.2 U_{eq} (C) for all other atoms other H atoms. No constraints or restraints were applied.

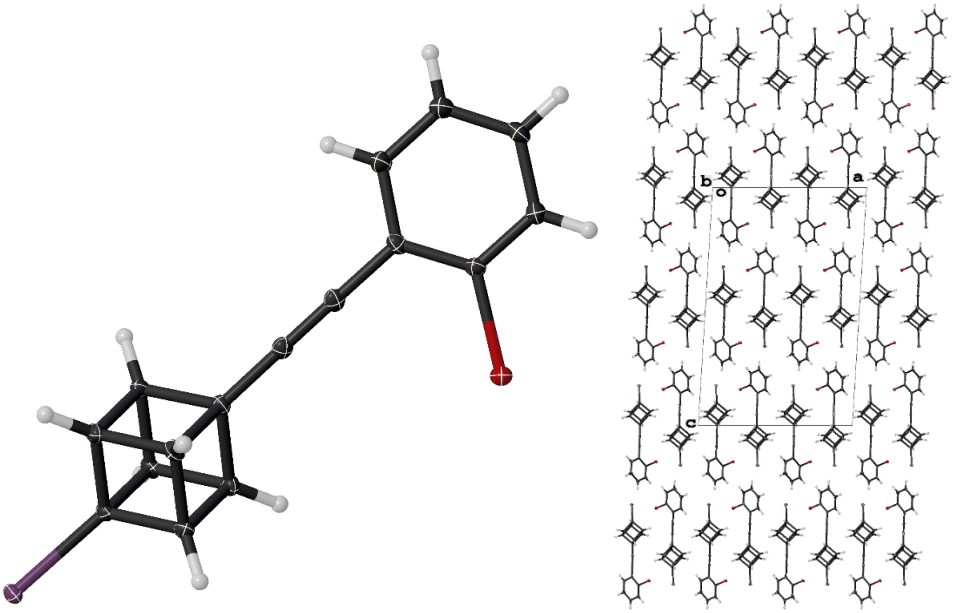

Figure E3:8: The molecular structure of compound **3:59** (left) and moiety packing looking down the *b*-axis (right). Thermal displacement gives 50% probability.

Crystal Data for compound 3:59: The C-bound H atoms were placed in their expected calculated positions and refined as riding model: C–H = 0.95–0.98 Å, with U_{iso}(H) = 1.2 U_{eq}(C) for all CH groups. No constraints or restraints were applied.

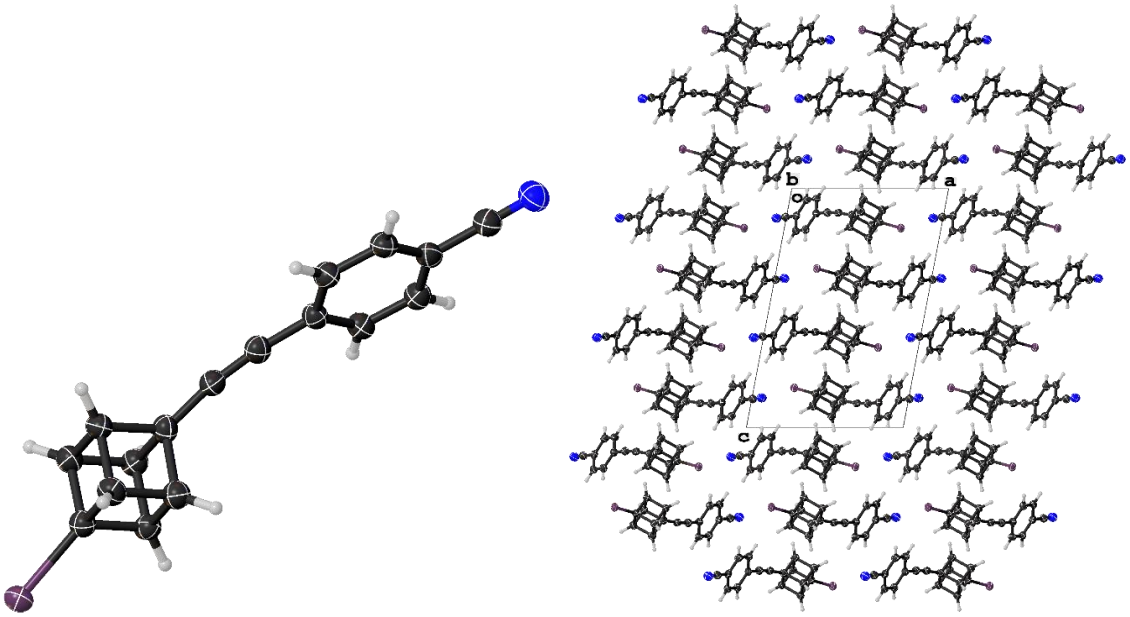

Figure E3:9: The molecular structure of compound **3:60** (left) and moiety packing looking down the *b*-axis (right). Thermal displacement gives 50% probability.

Crystal Data for compound 3:60: The C-bound H atoms were placed in their expected calculated positions and refined as riding model: C–H = 0.95–0.98 Å, with U_{iso}(H) = 1.2 U_{eq}(C) for all CH groups. No constraints or restraints were applied.

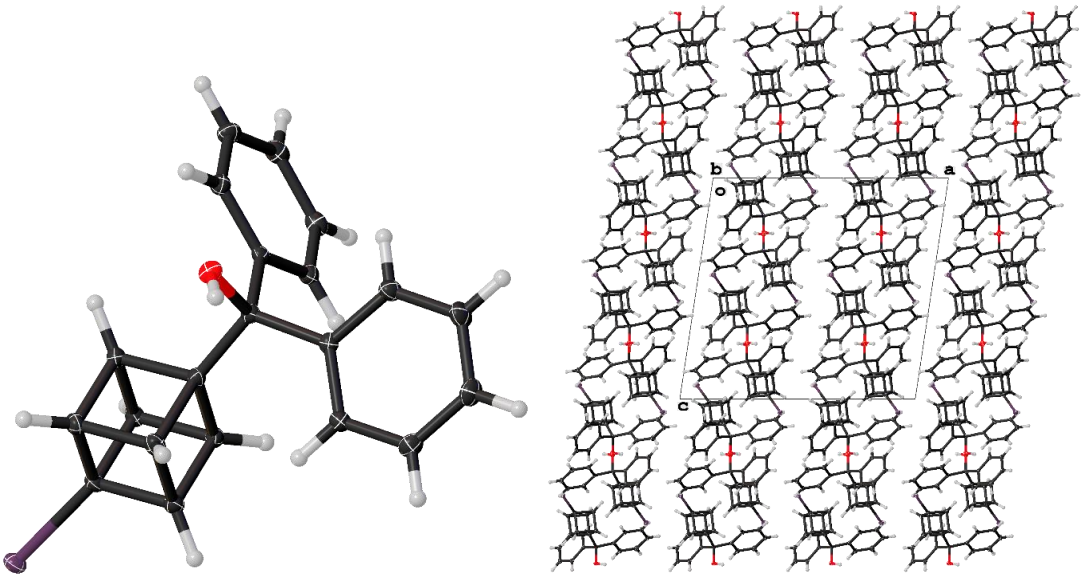

Figure E3:10: The molecular structure of compound **3:61** (left) and moiety packing looking down the *b*-axis (right). Thermal displacement gives 50% probability.

Crystal Data for compound 3:61: The C-bound H atoms were placed in their expected calculated positions and refined as riding model: C–H = 0.95–0.98 Å, with U_{iso}(H) = 1.2 U_{eq}(C) for all CH groups. The O-bound hydrogen atom was allowed to freely refine with a riding model: O–H = 0.84 Å, with U_{iso}(H) = 1.5 U_{eq}(C). No constraints or restraints were applied.

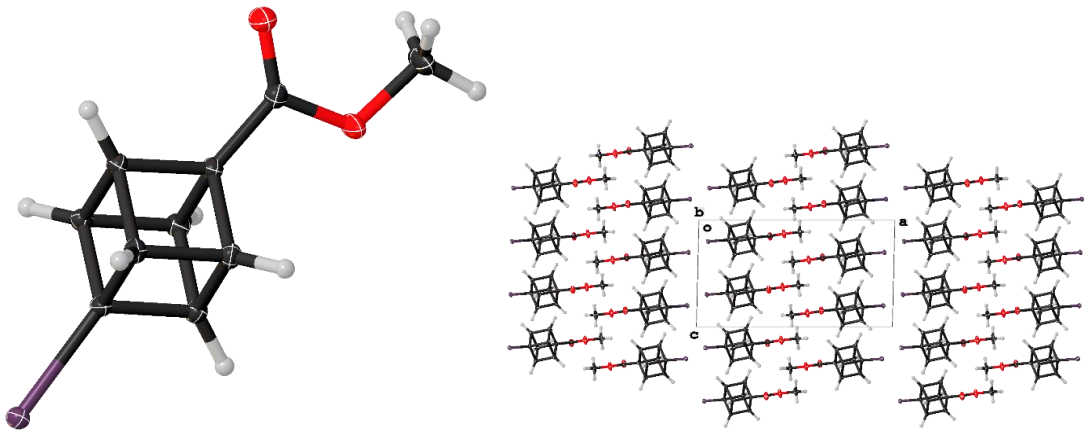

Figure E3:11: The molecular structure of compound 3:22_a (left) and moiety packing looking down the b-axis (right). Thermal displacement gives 50% probability.

Crystal Data for compound 3:22_a: The C-bound H atoms were placed in their expected calculated positions and refined as riding model: C–H = 0.95–0.98 Å, with U_{iso}(H) = 1.5 U_{eq}(C) for methyl H atoms and 1.2 U_{eq} (C) for all other atoms other H atoms. No constraints or restraints were applied.

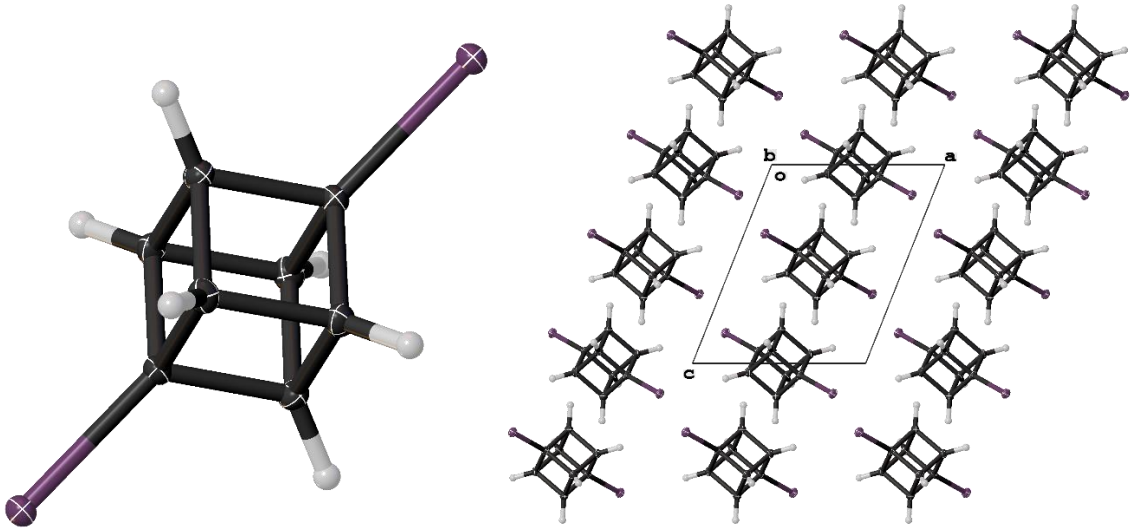

Figure E3:12: The molecular structure of compound **3:48_a** (left) and moiety packing looking down the *b*-axis (right). Thermal displacement gives 50% probability.

Crystal Data for compound 3:48_a: The C-bound H atoms were placed in their expected calculated positions and refined as riding model: C–H = 0.95–0.98 Å, with U_{iso}(H) = 1.2 U_{eq}(C) for all CH groups. No constraints or restraints were applied.

Table E3:1: Details of XRD data refinement

Compound	**3:12**	**3:41**	**3:42**
Empirical formula	$C_{21}H_{22}O_4$	$C_{18}H_{17}IO_4$	$C_{19}H_{13}NO_6$
Formula weight	338.38	424.21	351.30
Temperature/K	100.01	100(2)	100.18
Crystal system	monoclinic	triclinic	Triclinic
Space group	$P2_1/c$	$P\bar{1}$	$P\bar{1}$
a/Å	24.7224(16)	5.6752(3)	7.4355(3)
b/Å	16.7554(9)	9.2156(5)	7.7279(3)
c/Å	13.1561(8)	16.1963(9)	14.1773(5)
α/°	90	103.3140(10)	80.4500(10)
β/°	105.427(2)	99.4640(10)	76.6340(10)
γ/°	90	96.8950(10)	89.593(2)
Volume/Å^3	5253.3(5)	802.01(8)	781.17(5)
Z	12	2	2
D_{calc} g/cm^3	1.284	1.757	1.494
μ/mm^{-1}	0.088	2.014	0.113
F(000)	2160.0	420.0	364.0
Crystal size/mm^3	0.20×0.20×0.10	0.42×0.20×0.13	0.30× 0.20×0.15
Radiation	MoKα	MoKα	MoKα
Wavelength/Å	λ = 0.71073	λ = 0.71073	λ = 0.71073
2θ/°	2.972–50.806	4.604–59.426	2.996–66.404
Reflections collected	145064	30595	47837
Independent reflections	9612	4515	5965
R_{int}	0.0810	0.0216	0.0258
R_{sigma}	0.0297	0.0126	0.0152
Restraints	90	0	42
Parameters	748	210	256
GooF	1.109	1.073	1.039
R_1 [I> 2σ (I)]	0.0825	0.0132	0.0389
wR_2 [I> 2σ (I)]	0.2250	0.0328	0.1025
R_1 [all data]	0.110	0.0144	0.0485
wR_2 [all data]	0.2463	0.0332	0.1097
Largest peak/e Å^{-3}	0.48	0.43	0.48
Deepest hole/e Å^{-3}	-0.38	-0.38	-0.33
Flack parameter	--	--	--

Table E3:2: Details of XRD data refinement

Compound	**3:43**	**3:44**	**3:57**
Empirical formula	$C_{19}H_9Cl_4NO_6$	$C_{17}H_{10}INO_4$	$C_{16}H_{11}I$
Formula weight	489.07	419.16	330.15
Temperature/K	100.01	100.0	100.0
Crystal system	Triclinic	monoclinic	Monoclinic
Space group	$P\bar{1}$	$P2_1/n$	Cc
a/Å	7.5439(5)	5.4000(2)	8.7045(9)
b/Å	8.0568(5)	21.9713(7)	7.2485(8)
c/Å	15.4703(8)	12.8131(4)	19.649(2)
α/°	80.486(2)	90	90
β/°	84.620(2)	97.5180(10)	93.209(3)
γ/°	89.840(2)	90	90
Volume/Å^3	923.18(10)	1507.14(9)	1237.8(2)
Z	2	4	4
D_{calc} g/cm^3	1.759	1.847	1.772
μ/mm^{-1}	0.683	2.145	2.560
F(000)	492.0	816.0	640.0
Crystal size/mm^3	0.23×0.11×0.08	0.35×0.27×0.25	0.42×0.19×0.08
Radiation	MoK_α	MoK_α	MoK_α
Wavelength/Å	λ = 0.71073	λ = 0.71073	λ = 0.71073
2θ/°	5.126–55.366	3.704–50.818	4.152–65.606
Reflections collected	13353	25290	90886
Independent reflections	4309	2787	4560
R_{int}	0.0460	0.0203	0.0280
R_{sigma}	0.0543	0.0098	0.0099
Restraints	0	18	2
Parameters	272	204	154
GooF	1.011	1.152	1.142
R_1 [I> 2σ (I)]	0.0377	0.0258	0.0099
wR_2 [I> 2σ (I)]	0.0717	0.0552	0.0240
R_1 [all data]	0.0632	0.0269	0.0100
wR_2 [all data]	0.0802	0.0558	0.0240
Largest peak/e Å^{-3}	0.40	0.71	0.380
Deepest hole/e Å^{-3}	-0.38	-0.47	-0.43
Flack parameter	--	--	-0.007(3)

Table E3:3: Details of XRD data refinement

Compound	**3:58**	**3:59**	**3:60**
Empirical formula	$C_{19}H_{15}IO_2$	$C_{16}H_{10}BrI$	$C_{17}H_{10}IN$
Formula weight	402.21	409.05	355.16
Temperature/K	100.0	100.0	100.0
Crystal system	monoclinic	monoclinic	Monoclinic
Space group	$P2_1/c$	C2/c	$P2_1/c$
a/Å	8.9935(2)	18.0814(4)	11.1835(5)
b/Å	6.7146(2)	5.28060(10)	6.8868(3)
c/Å	25.9161(7)	28.0303(6)	17.3236(8)
α/°	90	90	90
β/°	95.4450(10)	93.4590(10)	100.776(2)
γ/°	90	90	90
Volume/Å^3	1557.95(7)	2671.48(10)	1310.71(10)
Z	4	8	4
D_{calc} g/cm^3	1.715	2.034	1.800
μ/mm^{-1}	2.060	5.366	19.046
F(000)	792.0	1552.0	688.0
Crystal size/mm^3	0.26×0.22×0.21	0.30×0.18×0.15	0.22×0.15×0.09
Radiation	MoK_α	MoK_α	CuK_α
Wavelength/Å	λ = 0.71073	λ = 0.71073	λ = 1.54178
2θ/°	2.972–50.806	2.912–59.996	8.048–136.668
Reflections collected	79327	28745	14335
Independent reflections	3584	3909	2408
R_{int}	0.0810	0.0250	0.0647
R_{sigma}	0.0297	0.0149	0.0478
Restraints	90	0	0
Parameters	748	163	172
GooF	1.109	1.182	1.071
R_1 [I> 2σ (I)]	0.082500180	0.0198	0.0576
wR_2 [I> 2σ (I)]	0.2250	0.0379	0.1567
R_1 [all data]	0.1110	0.0223	0.0582
wR_2 [all data]	0.245800434	0.0384	0.1580
Largest peak/e Å^{-3}	0.48	0.60	0.87
Deepest hole/e Å^{-3}	-0.38	-0.80	-1.45
Flack parameter	--	--	--

Table E3:4: Details of XRD data refinement

Compound	**3:61**	**3:22_a**	**3:48_a**
Empirical formula	$C_{21}H_{17}IO$	$C_{10}H_9IO_2$	$C_8H_6I_2$
Formula weight	412.24	288.07	355.93
Temperature/K	100.01	100.01	100.01
Crystal system	monoclinic	monoclinic	Monoclinic
Space group	C2/c	$P2_1/c$	$P2_1/c$
a/Å	18.6490(15)	15.4934(8)	7.1269(4)
b/Å	9.9115(8)	7.1287(4)	7.1939(4)
c/Å	17.7047(14)	8.3942(4)	8.7838(5)
α/°	90	90	90
β/°	98.5580(10)	91.4160(10)	111.7750(10)
γ/°	90	90	90
Volume/Å^3	3236.1(4)	926.84(8)	418.21(4)
Z	8	4	2
D_{calc} g/cm^3	1.692	2.064	2.826
μ/mm^{-1}	1.981	3.416	7.439
F(000)	1632.0	552.0	320.0
Crystal size/mm^3	0.60× 0.30× 0.20	0.24×0.16×0.10	0.19×0.1× 0.10
Radiation	MoK_α	MoK_α	MoK_α
Wavelength/Å	λ = 0.71073	λ = 0.71073	λ = 0.71073
2θ/°	4.418–56.69	5.260–65.348	6.156–65.318
Reflections collected	35083	27776	9964
Independent reflections	4035	3399	1535
R_{int}	0.0212	0.0283	0.0211
R_{sigma}	0.0112	0.0168	0.0133
Restraints	1	0	0
Parameters	211	119	46
GooF	1.067	1.144	1.177
R_1 [I> 2σ (I)]	0.0155	0.0194	0.0137
wR_2 [I> 2σ (I)]	0.0372	0.0393	0.0278
R_1 [all data]	0.0180	0.0242	0.0168
wR_2 [all data]	0.0383	0.0404	0.0286
Largest peak/e Å^{-3}	0.46	1.07	0.47
Deepest hole/e Å^{-3}	-0.33	-0.68	-0.51
Flack parameter	--	--	--

References.

[1] a) R. Pepinsky, *Phys. Rev.* **1955**, *100*, 971; b) M. D. Cohen, G. M. J. Schmidt, *J. Chem. Soc.* **1964**, 1996−2000; c) G. M. J. Schmidt, *Pure Appl. Chem.* **1971**, *27*, 647−678.

[2] G. R. Desiraju, *IUCrJ* **2017**, *4*, 710–711.

[3] a) A. Anthony, G. R. Desiraju, R. K. R. Jetti, S. S. Kuduva, N. N. L. Madhavi, A. Nangia, R. Thaimattam, V. R. Thalladi, *Cryst. Eng.* **1998**, *1*, 1–18; b) R. Bishop, *Chem. Soc. Rev.* **1996**, *25*, 311–319; c) A. D. Bond, *CrystEngComm* **2012**, *14*, 2363–2366; d) A. I. Cooper, *Angew. Chem. Int. Ed.* **2012**, *51*, 7892–7894; e) S. B. Copp, S. Subramanian, M. J. Zaworotko, *J. Am. Chem. Soc.* **1992**, *114*, 8719–8720; f) M. W. Hosseini, *Acc. Chem. Res.* **2005**, *38*, 313–323; g) M. Lahav, L. Leiserowitz, R. Popovitz-Biro, C.-P. Tang, *J. Am. Chem. Soc.* **1978**, *100*, 2542–2544; h) J. M. Thomas, *Nature* **1981**, *289*, 633–634.

[4] C. Aakeroy, *Acta Cryst. Sect. B* **1997**, *53*, 569–586.

[5] a) G. R. Desiraju, *Crystal engineering : the design of organic solids*, Elsevier, Amsterdam; New York, **1989**; b) J. D. Dunitz, *X-ray Analysis and the Structure of Organic Molecules*, Cornell University Press, Ithaca, New York, **1979**.

[6] G. R. Desiraju, *J. Am. Chem. Soc.* **2013**, *135*, 9952–9967.

[7] G. Resnati, E. Boldyreva, P. Bombicz, M. Kawano, *IUCrJ* **2015**, *2*, 675–690.

[8] a) J.-M. Dumas, M. Gomel, M. Guerin, in *Halides, Pseudo-Halides and Azides (1983)*, John Wiley & Sons, Ltd., **2010**, pp. 985–1020; b) P. Metrangolo, H. Neukirch, T. Pilati, G. Resnati, *Acc. Chem. Res.* **2005**, *38*, 386–395; c) P. Metrangolo, G. Resnati, *Cryst. Growth Des.* **2012**, *12*, 5835–5838.

[9] W. H. Bragg, *Proc. Phys. Soc.* **1921**, *34*, 33–50.

[10] J. D. Bernal, D. Crowfoot, *J. Chem. Soc.* **1935**, 93–100.

[11] a) J. M. Robertson, J. G. White, *J. Chem. Soc.* **1945**, 607–617; b) J. M. Robertson, J. G. White, *J. Chem. Soc.* **1947**, 358–368.

[12] a) M. D. Cohen, Z. Ludmer, J. M. Thomas, J. O. Williams, *Proc. Royal Soc. Lond.* **1971**, *324*, 459−468; b) J. M. Thomas, *Philos. Trans. R. Soc. London, Ser. A* **1974**, *277*, 251−286.

[13] A. Kitaigorodsky, *Molecular Crystals and Molecules*, Elsevier Science, **2012**.

[14] J. A. R. P. Sarma, G. R. Desiraju, *Acc. Chem. Res.* **1986**, *19*, 222−228.

[15] a) M. C. Etter, *Acc. Chem. Res.* **1990**, *23*, 120−126; b) M. Ward, M. Hollingsworth, *Chem. Mater.* **1994**, *6*, 1093−1093; c) T. Steiner, *Crystallogr. Rev.* **2003**, *9*, 177–228.

[16] H. M. Powell, *J. Chem. Soc.* **1948**, 61−73.

[17] O. Ermer, *J. Am. Chem. Soc.* **1988**, *110*, 3747−3754.

[18] a) M. Eddaoudi, D. B. Moler, H. Li, B. Chen, T. M. Reineke, M. O'Keeffe, O. M. Yaghi, *Acc. Chem. Res.* **2001**, *34*, 319−330; b) K. Biradha, M. Fujita, *Angew. Chem. Int. Ed.* **2002**, *41*, 3392−3395; c) J. J. Vittal, *Coord. Chem. Rev.* **2007**, *251*, 1781−1795; d) B. Moulton, M. J. Zaworotko, *Chem. Rev.* **2001**, *101*, 1629−1658; e) S. Kitagawa, R. Kitaura, S.-i. Noro, *Angew. Chem. Int. Ed.* **2004**, *43*, 2334−2375.

[19] a) B. F. Hoskins, R. Robson, *J. Am. Chem. Soc.* **1989**, *111*, 5962−5964; b) B. F. Hoskins, R. Robson, *J. Am. Chem. Soc.* **1990**, *112*, 1546−1554; c) R. Robson, *Dalton Trans.* **2008**, 5113−5131.

[20] a) J. Haleblian, W. McCrone, *J. Pharm. Sci.* **1969**, *58*, 911−929; b) C. Bilton, J. A. K. Howard, N. N. Laxmi Madhavi, A. Nangia, G. R. Desiraju, F. H. Allen, C. C. Wilson, *Chem. Commun.* **1999**, 1675−1676; c) J. Bernstein, R. J. Davey, J.-O. Henck, *Angew. Chem. Int. Ed.* **1999**, *38*, 3440−3461.

[21] A. Nangia, *Cryst. Growth Des.* **2006**, *6*, 2−4.

[22] a) G. R. Desiraju, *CrystEngComm* **2003**, *5*, 466−467; b) J. D. Dunitz, *CrystEngComm* **2003**, *5*, 506−506; c) S. Aitipamula, R. Banerjee, A. K. Bansal, K. Biradha, M. L. Cheney, A. R. Choudhury, G. R. Desiraju, A. G. Dikundwar, R. Dubey, N. Duggirala, P. P. Ghogale, S. Ghosh, P. K. Goswami, N. R. Goud, R. R. K. R. Jetti, P. Karpinski, P. Kaushik, D. Kumar, V. Kumar, B. Moulton, A. Mukherjee, G. Mukherjee, A. S. Myerson, V. Puri, A. Ramanan, T. Rajamannar, C. M. Reddy, N. Rodriguez-Hornedo, R. D. Rogers, T. N. G. Row, P. Sanphui, N. Shan, G. Shete, A. Singh, C. C. Sun, J. A. Swift, R. Thaimattam, T. S. Thakur, R. Kumar Thaper, S. P. Thomas, S. Tothadi, V. R. Vangala, N. Variankaval, P. Vishweshwar, D. R. Weyna, M. J. Zaworotko, *Cryst. Growth Des.* **2012**, *12*, 2147−2152.

[23] a) K. Biradha, A. Ramanan, J. J. Vittal, *Cryst. Growth Des.* **2009**, *9*, 2969−2970; b) S. R. Batten, N. R. Champness, X.-M. Chen, J. Garcia-Martinez, S. Kitagawa, L. Öhrström, M. O'Keeffe, M. P. Suh, J. Reedijk, *CrystEngComm* **2012**, *14*, 3001−3004.

[24] G. R. Desiraju, *Angew. Chem. Int. Ed.* **2011**, *50*, 52−59.

[25] K. Merz, *Acta Cryst. Sect. C* **2003**, *59*, o65−o67.

[26] V. R. Thalladi, B. S. Goud, V. J. Hoy, F. H. Allen, J. A. K. Howard, G. R. Desiraju, *Chem. Commun.* **1996**, 401−402.

[27] a) O. Ermer, A. Eling, *J. Chem. Soc. Perkin Trans. 2* **1994**, 925−944; b) F. H. Allen, V. J. Hoy, J. A. K. Howard, V. R. Thalladi, G. R. Desiraju, C. C. Wilson, G. J. McIntyre, *J. Am. Chem. Soc.* **1997**, *119*, 3477−3480.

[28] P. Ganguly, G. R. Desiraju, *CrystEngComm* **2010**, *12*, 817–833.

[29] a) P. Waldstein, L. A. Blatz, *J. Phys. Chem.* **1967**, *71*, 2271−2276; b) W. T. M. Mooij, B. P. van Eijck, S. L. Price, P. Verwer, J. Kroon, *J. Comput. Chem.* **1998**, *19*, 459−474.

[30] a) R. J. Davey, G. Dent, R. K. Mughal, S. Parveen, *Cryst. Growth Des.* **2006**, *6*, 1788−1796; b) S. A. Kulkarni, E. S. McGarrity, H. Meekes, J. H. ter Horst, *Chem. Commun.* **2012**, *48*, 4983−4985; c) C. A. Hunter, J. F. McCabe, A. Spitaleri, *CrystEngComm* **2012**, *14*, 7115−7117; d) R. J. Davey, S. L. M. Schroeder, J. H. ter Horst, *Angew. Chem. Int. Ed.* **2013**, *52*, 2166−2179; e) C. S. Towler, R. J. Davey, R. W. Lancaster, C. J. Price, *J. Am. Chem. Soc.* **2004**, *126*, 13347−13353; f) W. Sander, S. Roy, I. Polyak, J. M. Ramirez-Anguita, E. Sanchez-Garcia, *J. Am. Chem. Soc.* **2012**, *134*, 8222–8230; g) R. Crespo-Otero, E. Sánchez-García, R. Suardíaz, L. A. Montero, W. Sander, *Chem. Phys.* **2008**, *353*, 193–201.

[31] G. R. Desiraju, *Angew. Chem. Int. Ed.* **1995**, *34*, 2311−2327.

[32] D. Chakraborty, G. N. Patey, *J. Phys. Chem. Lett.* **2013**, *4*, 573−578.

[33] F. H. Allen, W. D. Samuel Motherwell, P. R. Raithby, G. P. Shields, R. Taylor, *New J. Chem.* **1999**, *23*, 25−34.

[34] M. Du, Z.-H. Zhang, X.-J. Zhao, H. Cai, *Cryst. Growth Des.* **2006**, *6*, 114–121.

[35] a) J. D. Dunitz, A. Gavezzotti, *Cryst. Growth Des.* **2005**, *5*, 2180−2189; b) J. D. Dunitz, A. Gavezzotti, *Angew. Chem. Int. Ed.* **2005**, *44*, 1766−1787; c) J. D. Dunitz, A. Gavezzotti, *Cryst. Growth Des.* **2012**, *12*, 5873−5877; d) O. V. Shishkin, V. V. Medvediev, R. I. Zubatyuk, *CrystEngComm* **2013**, *15*, 160−167.

[36] a) S. Roy, R. Banerjee, A. Nangia, G. J. Kruger, *Chem. Eur. J.* **2006**, *12*, 3777−3788; b) G. R. Desiraju, *Angew. Chem. Int. Ed.* **2007**, *46*, 8342−8356.

[37] V. R. Thalladi, H.-C. Weiss, D. Bläser, R. Boese, A. Nangia, G. R. Desiraju, *J. Am. Chem. Soc.* **1998**, *120*, 8702−8710.

[38] G. R. Desiraju, P. S. Ho, L. Kloo, A. C. Legon, R. Marquardt, P. Metrangolo, P. Politzer, G. Resnati, K. Rissanen, *Pure Appl. Chem.* **2013**, *85*, 1711–1713.
[39] a) E. Estop, A. Alvarez-Larena, A. Belaaraj, X. Solans, M. Labrador, *Acta Cryst. Sect. C* **1997**, *53*, 1932–1935; b) K. Maartmann-Moe, *Acta Cryst.* **1966**, *21*, 979–982; c) N. A. Ahmed, A. I. Kitaigorodsky, M. I. Sirota, *Acta Cryst. Sect. B* **1972**, *28*, 2875–2877.
[40] a) C. E. Marjo, M. L. Scudder, D. C. Craig, R. Bishop, *J. Chem. Soc. Perkin Trans. 2* **1997**, 2099−2104; b) G. R. Desiraju, in *Stimulating Concepts in Chemistry* (Eds.: F. Vögtle, J. F. Stoddart, S. Shibasaki), Wiley-VCH Weinheim, **2000**, p. 293−306; c) A. Angeloni, A. G. Orpen, *Chem. Commun.* **2001**, 343−344; d) B. Dolling, A. L. Gillon, A. G. Orpen, J. Starbuck, X.-M. Wang, *Chem. Commun.* **2001**, 567−568; e) J. C. Collings, K. P. Roscoe, R. L. Thomas, A. S. Batsanov, L. M. Stimson, J. A. K. Howard, T. B. Marder, *New J. Chem.* **2001**, *25*, 1410−1417; f) K. M. Anderson, A. E. Goeta, J. W. Steed, *Cryst. Growth Des.* **2008**, *8*, 2517−2524; g) A. Mukherjee, S. Tothadi, S. Chakraborty, S. Ganguly, G. R. Desiraju, *CrystEngComm* **2013**, *15*, 4640−4654.
[41] a) M. Scudder, I. Dance, *CrystEngComm* **2001**, *12*, 1−4; b) I. Dance, M. Scudder, *CrystEngComm* **2009**, *11*, 2233−2247.
[42] a) O. Delgado-Friedrichs, M. O'Keeffe, *Acta Cryst. Sect. A* **2009**, *65*, 360–363; b) M. O'Keeffe, *Chem. Soc. Rev.* **2009**, *38*, 1215–1217; c) M. O'Keeffe, O. M. Yaghi, *Chem. Rev.* **2012**, *112*, 675–702.
[43] C. V. K. Sharma, K. Panneerselvam, T. Pilati, G. R. Desiraju, *J. Chem. Soc. Chem. Commun.* **1992**, 832–833.
[44] a) S. L. Childs, L. J. Chyall, J. T. Dunlap, V. N. Smolenskaya, B. C. Stahly, G. P. Stahly, *J. Am. Chem. Soc.* **2004**, *126*, 13335–13342; b) D.-K. Bučar, R. F. Henry, X. Lou, R. W. Duerst, T. B. Borchardt, L. R. MacGillivray, G. G. Z. Zhang, *Mol. Pharm.* **2007**, *4*, 339−346; c) B. R. Sreekanth, P. Vishweshwar, K. Vyas, *Chem. Commun.* **2007**, 2375−2377; d) L. S. Reddy, P. M. Bhatt, R. Banerjee, A. Nangia, G. J. Kruger, *Chem. Asian J.* **2007**, *2*, 505−513; e) R. Santra, N. Ghosh, K. Biradha, *New J. Chem.* **2008**, *32*, 1673−1676; f) G. P. Stahly, *Cryst. Growth Des.* **2009**, *9*, 4212−4229; g) J. Bernstein, J. J. Novoa, R. Boese, S. A. Cirkel, *Chem. Eur. J.* **2010**, *16*, 9047−9055; h) M. T. Kirchner, D. Bläser, R. Boese, *Chem. Eur. J.* **2010**, *16*, 2131−2146; i) J. N. Moorthy, P. Natarajan, P. Venugopalan, *Chem. Commun.* **2010**, *46*, 3574−3576; j) C. C. Seaton, *CrystEngComm* **2011**, *13*, 6583−6592.
[45] F. Wöhler, *Ann. Chem. Pharm.* **1844**, *51*, 145−163.
[46] Ö. Almarsson, M. J. Zaworotko, *Chem. Commun.* **2004**, 1889−1896.
[47] S. G. Fleischman, S. S. Kuduva, J. A. McMahon, B. Moulton, R. D. Bailey Walsh, N. Rodríguez-Hornedo, M. J. Zaworotko, *Cryst. Growth Des.* **2003**, *3*, 909−919.
[48] N. J. Babu, P. Sanphui, A. Nangia, *Chem. Asian J.* **2012**, *7*, 2274−2285.
[49] a) A. V. Trask, W. D. S. Motherwell, W. Jones, *Cryst. Growth Des.* **2005**, *5*, 1013–1021; b) S. Cherukuvada, N. J. Babu, A. Nangia, *J. Pharm. Sci.* **2011**, *100*, 3233–3244.
[50] S. Karki, T. Friščić, L. Fábián, P. R. Laity, G. M. Day, W. Jones, *Adv. Mater.* **2009**, *21*, 3905-3909.
[51] A. J. Smith, P. Kavuru, L. Wojtas, M. J. Zaworotko, R. D. Shytle, *Mol. Pharm.* **2011**, *8*, 1867–1876.
[52] a) C. P. Price, A. L. Grzesiak, A. J. Matzger, *J. Am. Chem. Soc.* **2005**, *127*, 5512−5517; b) M. R. Caira, *Mol. Pharm.* **2007**, *4*, 310−316; c) N. J. Babu, A. Nangia, *Cryst. Growth Des.* **2011**, *11*, 2662−2679.
[53] J. Emsley, *Chem. Soc. Rev.* **1980**, *9*, 91–124.
[54] a) A. Shokri, J. Schmidt, X.-B. Wang, S. R. Kass, *J. Am. Chem. Soc.* **2012**, *134*, 2094–2099; b) H. Dong, W. Hua, S. Li, *J. Phys. Chem. A* **2007**, *111*, 2941–2945.
[55] R. C. Johnston, P. H.-Y. Cheong, *Org. Biomol. Chem.* **2013**, *11*, 5057–5064.
[56] G. Cavallo, P. Metrangolo, R. Milani, T. Pilati, A. Priimagi, G. Resnati, G. Terraneo, *Chem. Rev.* **2016**, *116*, 2478–2601.
[57] T. Clark, M. Hennemann, J. S. Murray, P. Politzer, *J. Mol. Model.* **2007**, *13*, 291–296.
[58] C. A. Hunter, J. K. M. Sanders, *J. Am. Chem. Soc.* **1990**, *112*, 5525–5534.
[59] A. S. Mahadevi, G. N. Sastry, *Chem. Rev.* **2013**, *113*, 2100–2138.
[60] D. A. Dougherty, *Acc. Chem. Res.* **2013**, *46*, 885–893.
[61] B. L. Schottel, H. T. Chifotides, K. R. Dunbar, *Chem. Soc. Rev.* **2008**, *37*, 68–83.
[62] A. D. Bond, *Chem. Commun.* **2002**, 1664–1665.
[63] B. K. Mishra, S. Karthikeyan, V. Ramanathan, *J. Chem. Theory Comput.* **2012**, *8*, 1935–1942.
[64] a) A. K. Singh, F. S. T. Khan, S. P. Rath, *Angew. Chem. Int. Ed.* **2017**, *56*, 8849–8854; b) H. Schmidbaur, A. Schier, *Angew. Chem. Int. Ed.* **2015**, *54*, 746–784.
[65] B. Assadollahzadeh, P. Schwerdtfeger, *Chem. Phys. Lett.* **2008**, *462*, 222–228.
[66] a) W. J. Hunks, M. C. Jennings, R. J. Puddephatt, *Inorg. Chem.* **2002**, *41*, 4590–4598; b) S. S. Pathaneni, G. R. Desiraju, *J. Chem. Soc. Dalton Trans.* **1993**, 319–322.
[67] H. Schmidbaur, *Gold Bulletin* **2000**, *33*, 3–10.
[68] a) P. Karlson, *J. Clin. Chem. Clin. Biochem.* **1981**, *19*, 43–47; b) G. P. Moss, *Pure Appl. Chem.* **1987**, *59*, 779–832.
[69] W. R. Scheidt, *J. Porphyrins Phthalocyanines* **2008**, *12*, 979–992.
[70] P. J. Chmielewski, L. Latos-Grazynski, *Coord. Chem. Rev.* **2005**, *249*, 2510–2533.
[71] I. Beletskaya, V. S. Tyurin, A. Y. Tsivadze, R. Guilard, C. Stern, *Chem. Rev.* **2009**, *109*, 1659–1713.
[72] a) M. O. Senge, *Chem. Commun.* **2006**, 243–256; b) M. O. Senge, S. A. MacGowan, J. M. O'Brien, *Chem. Commun.* **2015**, *51*, 17031–17063.
[73] a) M. O. Senge, M. Fazekas, E. G. A. Notaras, W. J. Blau, M. Zawadzka, O. B. Locos, E. M. N. Mhuircheartaigh, *Adv. Mater.* **2007**, *19*, 2737–2774; b) H. S. Cho, D. H. Jeong, S. Cho, D. Kim, Y. Matsuzaki, K. Tanaka, A. Tsuda, A. Osuka, *J. Am. Chem. Soc.* **2002**, *124*, 14642–14654; c) R. Shediac, M. H. B. Gray, H. T. Uyeda, R. C. Johnson, J. T. Hupp, P. J. Angiolillo, M. J. Therien, *J. Am. Chem. Soc.* **2000**, *122*, 7017–7033.
[74] a) M. O. Senge, J. Richter, *Acta Cryst. Sect. E* **2011**, *67*, m1077; b) S. Plunkett, M. O. Senge, *ECS Trans.* **2011**, *35*, 147–157.
[75] a) S. A. MacGowan, M. O. Senge, *Inorg. Chem.* **2013**, *52*, 1228–1237; b) S. A. MacGowan, M. O. Senge, *Chem. Commun.* **2011**, *47*, 11621–11623.
[76] a) L. R. Milgrom, *The Colours of Life*, Oxford University Press, New York, **1997**; b) J. A. Shelnutt, X. Z. Song, J. G. Ma, S. L. Jia, W. Jentzen, C. J. Medforth, *Chem. Soc. Rev.* **1998**, *27*, 31–41; c) M. Ravikanth, T. K. Chandrashekar, in *Structure and Bonding, Vol. 82*, Springer, Berlin, Heidelberg, **1995**, pp. 105–188.
[77] a) M. O. Senge, M. Fazekas, M. Pintea, M. Zawadzka, W. J. Blau, *Eur. J. Org. Chem.* **2011**, 5797–5816; b) E. G. Notaras, M. Fazekas, J. J. Doyle, W. J. Blau, M. O. Senge, *Chem. Commun.* **2007**, 2166–2168; c) T. E. O. Screen, K. B. Lawton, G. S. Wilson, N. Dolney, R. Ispasoiu, T. Goodson III, S. J. Martin, D. D. C. Bradley, H. L. Anderson, *J. Mater. Chem.* **2001**, *11*, 312–320.

[78] a) S. Mathew, A. Yella, P. Gao, R. Humphry-Baker, B. F. E. Curchod, N. Ashari-Astani, I. Tavernelli, U. Rothlisberger, M. K. Nazeeruddin, M. Grätzel, *Nat. Chem.* **2014**, *6*, 242–247; b) L.-L. Li, E. W.-G. Diau, *Chem. Soc. Rev.* **2013**, *42*, 291–304; c) B. E. Hardin, H. J. Snaith, M. D. McGehee, *Nat. Photonics* **2012**, *6*, 162–169; d) A. Yella, H.-W. Lee, H. N. Tsao, C. Yi, A. K. Chandiran, M. K. Nazeeruddin, E. W.-G. Diau, C.-Y. Yeh, S. M. Zakeeruddin, M. Grätzel, *Science* **2011**, *334*, 629–634; e) D. Gust, T. A. Moore, A. L. Moore, *Acc. Chem. Res.* **2009**, *42*, 1890–1898.
[79] a) J. P. Beggan, S. A. Krasnikov, N. N. Sergeeva, M. O. Senge, A. A. Cafolla, *Nanotechnology* **2012**, *23*, 235606–235606; b) S. A. Krasnikov, C. M. Doyle, N. N. Sergeeva, A. B. Preobrajenski, N. A. Vinogradov, Y. N. Sergeeva, A. A. Zakharov, M. O. Senge, A. A. Cafolla, *Nano Res.* **2011**, *4*, 376–384; c) S. A. Krasnikov, N. N. Sergeeva, Y. N. Sergeeva, M. O. Senge, A. A. Cafolla, *Phys. Chem. Chem. Phys.* **2010**, *12*, 6666–6671.
[80] a) M. O. Senge, M. W. Radomski, *Photodiagno. Photodyn. Ther.* **2013**, *10*, 1–16; b) M. O. Senge, *Photodiagno. Photodyn. Ther.* **2012**, *9*, 170–179; c) S. Yano, S. Hirohara, M. Obata, Y. Hagiya, S.-i. Ogura, A. Ikeda, H. Kataoka, M. Tanaka, T. Joh, *J. Photochem. Photobiol. C* **2011**, *12*, 46–67; d) M. Ethirajan, Y. Chen, P. Joshi, R. K. Pandey, *Chem. Soc. Rev.* **2011**, *40*, 340–362; e) K. Ogawa, Y. Kobuke, *Anti-Cancer Agents Med. Chem.* **2008**, *8*, 269–279.
[81] K. M. Kadish, K. M. Smith, R. Guilard*, Vol. 20*, Academic Press, San Diego, **2000**.
[82] a) A. Satake, Y. Kobuke, *Org. Biomol. Chem.* **2007**, *5*, 1679–1691; b) J. Kralova, J. Koivukorpi, Z. Kejik, P. Pouckova, E. Sievanen, E. Kolehmainen, V. Kral, *Org. Biomol. Chem.* **2008**, *6*, 1548–1552; c) S. Paul, F. Amalraj, S. Radhakrishnan, *Synth. Met.* **2009**, *159*, 1019–1023; d) C. Zhang, K. S. Suslick, *J. Porphyrins Phthalocyanines* **2005**, *9*, 659–666; e) W. M. Campbell, A. K. Burrell, D. L. Officer, K. W. Jolley, *Coord. Chem. Rev.* **2004**, *248*, 1363–1379; f) C. M. Drain, G. Smeureanu, S. Patel, X. C. Gong, J. Garno, J. Arijeloye, *New J. Chem.* **2006**, *30*, 1834–1843.
[83] E. D. Sternberg, D. Dolphin, C. Bruckner, *Tetrahedron* **1998**, *54*, 4151–4202.
[84] A. M. Joussen, F. E. Kruse, M. Kaus, H. E. Völcker, *Ophthalmologe* **1997**, *94*, 428–435.
[85] J. P. Kushner, A. J. Barbuto, G. R. Lee, *J. Clin. Investig.* **1976**, *58*, 1089–1097.
[86] a) M. O. Senge, V. Gerstung, K. Ruhlandt-Senge, S. Runge, I. Lehmann, *J. Chem. Soc. Dalton Trans.* **1998**, 4187–4200; b) M. O. Senge, W. W. Kalisch, *Inorg. Chem.* **1997**, *36*, 6103–6116; c) M. O. Senge, J. Richter, I. Bischoff, A. Ryan, *Tetrahedron* **2010**, *66*, 3508–3524.
[87] M. O. Senge, in *The Porphyrin Handbook, Vol. 1*, Academic Press, **2000**, pp. 239–347.
[88] J. W. Lauher, J. A. Ibers, *J. Am. Chem. Soc.* **1973**, *95*, 5148–5152.
[89] Y. Yamamoto, A. Yamamoto, S.-y. Furuta, M. Horie, M. Kodama, W. Sato, K.-y. Akiba, S. Tsuzuki, T. Uchimaru, D. Hashizume, F. Iwasaki, *J. Am. Chem. Soc.* **2005**, *127*, 14540–14541.
[90] B. Röder, M. Büchner, I. Rückmann, M. O. Senge, *Photochem. Photobiol. Sci.* **2010**, *9*, 1152–1158.
[91] T. Ishizuka, M. Sankar, Y. Yamada, S. Fukuzumi, T. Kojima, *Chem. Commun.* **2012**, *48*, 6481–6483.
[92] a) M. O. Senge, *ECS Trans.* **2015**, *66*, 1–10; b) T. P. G. Sutter, R. Rahimi, P. Hambright, J. C. Bommer, M. Kumar, P. Neta, *J. Chem. Soc. Faraday Trans.* **1993**, *89*, 495–502.
[93] M. Roucan, K. J. Flanagan, J. O'Brien, M. O. Senge, *Eur. J. Org. Chem.* **2018**, *2018*, 6432-6446.
[94] a) M. O. Senge, T. P. Forsyth, L. T. Nguyen, K. M. Smith, *Angew. Chem. Int. Ed.* **1995**, *33*, 2485–2487; b) M. O. Senge, T. P. Forsyth, L. T. Nguyen, K. M. Smith, *Angewandte Chemie International Edition in English* **1995**, *33*, 2485–2487.
[95] W. R. Scheidt, Y. J. Lee, in *Structure and Bonding Metal Complexes with Tetrapyrrole Ligands I* (Ed.: J. W. Buchler), Springer Berlin Heidelberg, Berlin, Heidelberg, **1987**, pp. 1–70.
[96] a) M. O. Senge, K. Dahms, *Acta Cryst. Sect. E* **2014**, *70*, m251; b) M. O. Senge, K. J. Flanagan, A. A. Ryan, C. Ryppa, M. Donath, B. Twamley, *Tetrahedron* **2016**, *72*, 105–115; c) K. J. Flanagan, E. M. Mothi, L. Kötzner, M. O. Senge, *Acta Cryst. Sect. E* **2015**, *71*, 1397–1400; d) M. O. Senge, C. J. Medforth, T. P. Forsyth, D. A. Lee, M. M. Olmstead, W. Jentzen, R. K. Pandey, J. A. Shelnutt, K. M. Smith, *Inorg. Chem.* **1997**, *36*, 1149–1163.
[97] D. L. Cullen, E. F. Meyer, Jr., K. M. Smith, *Inorg. Chem.* **1977**, *16*, 1179–1186.
[98] G. De Luca, A. Romeo, L. M. Scolaro, G. Ricciardi, A. Rosa, *Inorg. Chem.* **2009**, *48*, 8493–8507.
[99] a) R. Patra, A. Chaudhary, S. K. Ghosh, S. P. Rath, *Inorg. Chem.* **2010**, *49*, 2057–2067; b) M. O. Senge, *J. Porphyrins Phthalocyanines* **1998**, *2*, 107–121.
[100] M. O. Senge, K. Ruhlandt-Senge, K. J. Regli, K. M. Smith, *J. Chem. Soc. Dalton Trans.* **1993**, 3519–3538.
[101] N. Chaudhri, N. Grover, M. Sankar, *Inorg. Chem.* **2018**, *57*, 6658–6668.
[102] a) M. Sharma, S. Banerjee, M. Zeller, C. Brückner, *J. Org. Chem.* **2016**, *81*, 12350–12356; b) Y. Saegusa, T. Ishizuka, K. Komamura, S. Shimizu, H. Kotani, N. Kobayashi, T. Kojima, *Phys. Chem. Chem. Phys.* **2015**, *17*, 15001–15011.
[103] M. O. Senge, in *Z. Naturforsch., Vol. 55B*, **2000**, p. 336.
[104] a) H. M. G. Al-Hazimi, A. H. Jackson, A. W. Johnson, M. Winter, *J. Chem. Soc. Perkin Trans. 1* **1977**, 98–103; b) A. Neuberger, J. J. Scott, *Proceedings of the Royal Society of London. Series A. Mathematical and Physical Sciences* **1952**, *213*, 307–326.
[105] M. O. Senge, W. W. Kalisch, S. Runge, *Liebigs Ann. Recl.* **1997**, 1345–1352.
[106] a) T. P. Wijesekera, J. B. Paine, III, D. Dolphin, F. W. B. Einstein, T. Jones, *J. Am. Chem. Soc.* **1983**, *105*, 6747–6749; b) L. Latos-Grażyński, E. Pacholska, P. J. Chmielewski, M. M. Olmstead, A. L. Balch, *Angew. Chem. Int. Ed.* **1995**, *34*, 2252–2254; c) L. Latos-Grazynski, J. Lisowski, M. M. Olmstead, A. L. Balch, *Inorg. Chem.* **1989**, *28*, 1183–1188.
[107] T. Chatterjee, V. S. Shetti, R. Sharma, M. Ravikanth, *Chem. Rev.* **2017**, *117*, 3254–3328.
[108] M. P. Byrn, C. J. Curtis, I. Goldberg, Y. Hsiou, S. I. Khan, P. A. Sawin, S. K. Tendick, C. E. Strouse, *J. Am. Chem. Soc.* **1991**, *113*, 6549–6557.
[109] a) Y. Diskin-Posner, G. K. Patra, I. Goldberg, *Eur. J. Org. Chem.* **2001**, 2515–2523; b) M. Shmilovits, Y. Diskin-Posner, M. Vinodu, I. Goldberg, *Cryst. Growth Des.* **2003**, *3*, 855–863; c) Y. Diskin-Posner, S. Dahal, I. Goldberg, *Angew. Chem. Int. Ed.* **2000**, *39*, 1288–1292; d) I. Goldberg, *CrystEngComm* **2008**, *10*, 637–645; e) R. D. Rogers, C. V. K. Sharma, G. A. Broker, American Chemical Society, **1999**, pp. INOR-046; f) I. Goldberg, *Chem. Commun.* **2005**, 1243–1254; g) H. M. Titi, R. Patra, I. Goldberg, *Chem. Eur. J.* **2013**, *19*, 14941–14949; h) A. Karmakar, I. Goldberg, *CrystEngComm* **2010**, *12*, 4095–4100; i) Y. Diskin-Posner, R. Krishna Kumar, I. Goldberg, *New J. Chem.* **1999**, *23*, 885–890; j) S. Lipstman, I. Goldberg, *Cryst. Growth Des.* **2013**, *13*, 942–952; k) S. Lipstman, I. Goldberg, *Cryst. Growth Des.* **2010**, *10*, 4596–4606; l) S. Lipstman, I. Goldberg, *Beilstein J. Org. Chem.* **2009**, *5*, No. 77; m) I. Goldberg, *Chem. Eur. J.* **2000**, *6*, 3863–3870.
[110] R. Patra, H. M. Titi, I. Goldberg, *Cryst. Growth Des.* **2013**, *13*, 1342–1349.
[111] K. B. Ghiassi, X. B. Powers, J. Wescott, A. L. Balch, M. M. Olmstead, *Cryst. Growth Des.* **2016**, *16*, 447–455.

[112] a) M. M. Olmstead, D. A. Costa, K. Maitra, B. C. Noll, S. L. Phillips, P. M. Van Calcar, A. L. Balch, *J. Am. Chem. Soc.* **1999**, *121*, 7090–7097; b) S. Stevenson, C. J. Chancellor, H. M. Lee, M. M. Olmstead, A. L. Balch, *Inorg. Chem.* **2008**, *47*, 1420–1427; c) T. Ishii, N. Aizawa, R. Kanehama, M. Yamashita, H. Matsuzaka, T. Kodama, K. Kikuchi, I. Ikemoto, *Inorg. Chim. Acta* **2001**, *317*, 81–90; d) N. Aizawa, H. Hara, T. Ishii, M. Yamashita, H. Miyasaka, H. Matsuzaka, T. Kodama, K. Kikuchi, I. Ikemoto, *Mol. Cryst. Liq. Cryst.* **2002**, *376*, 13–18.
[113] L. C. Gilday, N. G. White, P. D. Beer, *Dalton Trans.* **2012**, *41*, 7092–7097.
[114] a) M. O. Senge, T. Ema, K. M. Smith, *J. Chem. Soc. Chem. Comm.* **1995**, 733–734; b) M. O. Senge, W. W. Kalisch, I. Bischoff, *Chem. Eur. J.* **2000**, *6*, 2721–2738; c) W. W. Kalisch, M. O. Senge, *Angew. Chem. Int. Ed.* **1998**, *37*, 1107–1109; d) M. Kielmann, K. J. Flanagan, K. Norvaiša, D. Intrieri, M. O. Senge, *J. Org. Chem.* **2017**, *82*, 5122-5134; e) M. O. Senge, *J. Porphyrins Phthalocyanines* **1999**, *3*, 216–223.
[115] M. Kielmann, M. O. Senge, *Angew. Chem. Int. Ed.* **2018**, Accepted, DOI:10.1002/anie.201806281.
[116] M. Roucan, M. Kielmann, S. J. Connon, S. S. R. Bernhard, M. O. Senge, *Chem. Commun.* **2018**, *54*, 26–29.
[117] a) S. Kambe, H. Yasuda, *Bull. Chem. Soc. Jpn.* **1968**, *41*, 1444–1446; b) J. B. Tindall, *Ind. Eng. Chem.* **1941**, *33*, 65–66; c) I. Ugi, U. Fetzer, U. Eholzer, H. Knupfer, Offerman.K, *Angew. Chem. Int. Ed.* **1965**, *4*, 472–484.
[118] D. H. R. Barton, S. Z. Zard, *J. Chem. Soc. Chem. Commun.* **1985**, 1098–1100.
[119] S. D. Roth, T. Shkindel, D. A. Lightner, *Tetrahedron* **2007**, *63*, 11030–11039.
[120] T. Sasaki, J.-F. Morin, M. Lu, J. M. Tour, *Tetrahedron Lett.* **2007**, *48*, 5817–5820.
[121] K. D. Grimes, A. Gupte, C. C. Aldrich, *Synthesis* **2010**, *2010*, 1441–1448.
[122] J. S. Lindsey, H. C. Hsu, I. C. Schreiman, *Tetrahedron Lett.* **1986**, *27*, 4969–4970.
[123] a) J. Schindler, S. Kupfer, A. A. Ryan, K. J. Flanagan, M. O. Senge, B. Dietzek, *Coord. Chem. Rev.* **2018**, *360*, 1–16; b) A. Hoshino, Y. Ohgo, M. Nakamura, *Tetrahedron Lett.* **2005**, *46*, 4961–4964.
[124] C. J. Medforth, M. O. Senge, T. P. Forsyth, J. D. Hobbs, J. A. Shelnutt, K. M. Smith, *Inorg. Chem.* **1994**, *33*, 3865–3872.
[125] C. J. Medforth, M. O. Senge, K. M. Smith, L. D. Sparks, J. A. Shelnutt, *J. Am. Chem. Soc.* **1992**, *114*, 9859–9869.
[126] S. Gentemann, C. J. Medforth, T. P. Forsyth, D. J. Nurco, K. M. Smith, J. Fajer, D. Holten, *J. Am. Chem. Soc.* **1994**, *116*, 7363-7368.
[127] V. Ladmiral, G. Mantovani, G. J. Clarkson, S. Cauet, J. L. Irwin, D. M. Haddleton, *J. Am. Chem. Soc.* **2006**, *128*, 4823–4830.
[128] a) K. L. Kunze, P. R. Ortiz de Montellano, *J. Am. Chem. Soc.* **1981**, *103*, 4225–4230; b) P. R. Ortiz de Montellano, *Annu. Rep. Med. Chem.* **1984**, *19*, 201–211.
[129] a) P. R. Ortiz de Montellano, K. L. Kunze, B. A. Mico, *Mol. Pharmacol.* **1980**, *18*, 602–605; b) G. S. Marks, D. T. Allen, C. T. Johnston, E. P. Sutherland, K. Nakatsu, R. A. Whitney, *Mol. Pharmacol.* **1985**, *27*, 459–465.
[130] a) S. J. Silvers, A. Tulinsky, *J. Am. Chem. Soc.* **1967**, *89*, 3331–3337; b) W. Chen, M. E. El-Khouly, S. Fukuzumi, *Inorg. Chem.* **2011**, *50*, 671-678; c) D. K. Lavallee, O. P. Anderson, *J. Am. Chem. Soc.* **1982**, *104*, 4707–4708; d) A. M. Abeysekera, R. Grigg, J. Trocha-Grimshaw, K. Henrick, *Tetrahedron* **1980**, *36*, 1857–1868; e) T. E. Clement, L. T. Nguyen, R. G. Khoury, D. J. Nurco, K. M. Smith, *Heterocycles* **1970**, *45*, 651–658.
[131] a) W. Jentzen, M. C. Simpson, J. D. Hobbs, X. Song, T. Ema, N. Y. Nelson, C. J. Medforth, K. M. Smith, M. Veyrat, M. Mazzanti, R. Ramasseul, J. C. Marchon, T. Takeuchi, W. A. Goddard, J. A. Shelnutt, *J. Am. Chem. Soc.* **1995**, *117*, 11085–11097; b) W. Jentzen, X.-Z. Song, J. A. Shelnutt, *J. Phys. Chem. B* **1997**, *101*, 1684-1699; c) W. Jentzen, J.-G. Ma, J. A. Shelnutt, *Biophys. J.* **1998**, *74*, 753–763.
[132] M. O. Senge, *Z. Naturforsch.* **1999**, *54B*, 821–824.
[133] J. Barbee, A. E. Kuznetsov, *Comput. Theor. Chem.* **2012**, *981*, 73–85.
[134] K. M. Barkigia, L. Chantranupong, K. M. Smith, J. Fajer, *J. Am. Chem. Soc.* **1988**, *110*, 7566–7567.
[135] Z. Shi, G. C. Ferreira, *The Biochemical journal* **2006**, *399*, 21–28.
[136] H. J. Callot, J. Fischer, R. Weiss, *J. Am. Chem. Soc.* **1982**, *104*, 1272–1276.
[137] H. Hope, *Prog. Inorg. Chem.* **2007**, 1–19.
[138] a) in *Saint*, Version 8.37a ed., Bruker AXS, Inc., Madison, WI, **2013**; b) in *SADABS*, version 2016/2 ed., Bruker AXS, Inc, Madison, WI,, **2014**; c) in *APEX3*, Version 2016.9-0 ed., Bruker AXS, Inc., Madison, WI,, **2016**.
[139] a) O. V. Dolomanov, L. J. Bourhis, R. J. Gildea, J. A. K. Howard, H. Puschmann, *J. Appl. Crystallogr.* **2009**, *42*, 339–341; b) G. Sheldrick, *Acta Cryst. Sect. A* **2015**, *71*, 3–8.
[140] in *NSDGUI*, Version 1.3 alpha ed., Sandia National Laboratory: New Mexico, **2001**.
[141] A. L. Spek, *Acta Cryst. Sect. C* **2015**, *71*, 9–18.
[142] a) D. T. Gryko, D. Gryko, C.-H. Lee, *Chem. Soc. Rev.* **2012**, *41*, 3780–3789; b) J. S. Lindsey, *Acc. Chem. Res.* **2010**, *43*, 300–311; c) T. E. Wood, A. Thompson, *Chem. Rev.* **2007**, *107*, 1831–1861; d) P. A. Gale, P. Anzenbacher Jr, J. L. Sessler, *Coord. Chem. Rev.* **2001**, *222*, 57–102; e) N. A. M. Pereira, T. M. V. D. Pinho e Melo, *Org. Prep. Proced. Int.* **2014**, *46*, 183–213.
[143] M. Wenzel, P. A. Hiscock Jr Fau - Gale, P. A. Gale, *Chem. Soc. Rev.*, *41*, 480–520.
[144] A. Treibs, F.-H. Kreuzer, *Liebigs Ann. Chem.* **1968**, *718*, 208–223.
[145] A. Loudet, K. Burgess, *Chem. Rev.* **2007**, *107*, 4891–4932.
[146] a) J. Karolin, L. B. A. Johansson, L. Strandberg, T. Ny, *J. Am. Chem. Soc.* **1994**, *116*, 7801–7806; b) R. P. Haugland, *Handbook of fluorescent probes and research chemicals*, Molecular Probes, Eugene, OR., **1996**; c) K. Tan, L. Jaquinod, R. Paolesse, S. Nardis, C. Di Natale, A. Di Carlo, L. Prodi, M. Montalti, N. Zaccheroni, K. M. Smith, *Tetrahedron* **2004**, *60*, 1099–1106; d) M. C. Yee, S. C. Fas, M. M. Stohlmeyer, T. J. Wandless, K. A. Cimprich, *J. Biol. Chem.* **2005**, *280*, 29053–29059; e) R. W. Wagner, J. S. Lindsey, *Pure Appl. Chem.* **1996**, *68*, 1373–1380.
[147] M. L. Metzker, in *WO Patent, Vol. WO/2003/066812*, **2003**.
[148] a) M. A. Filatov, S. Karuthedath, P. M. Polestshuk, S. Callaghan, K. J. Flanagan, T. Wiesner, F. Laquai, M. O. Senge, *ChemPhotoChem* **2018**, *2*, 606–615; b) M. A. Filatov, S. Karuthedath, P. M. Polestshuk, H. Savoie, K. J. Flanagan, C. Sy, E. Sitte, M. Telitchko, F. Laquai, R. W. Boyle, M. O. Senge, *J. Am. Chem. Soc.* **2017**, *139*, 6282–6285.
[149] I. J. Bruno, J. C. Cole, P. R. Edgington, M. Kessler, C. F. Macrae, P. McCabe, J. Pearson, R. Taylor, *Acta Cryst. Sect. B* **2002**, *58*, 389–397.
[150] N. Kiseleva, M. A. Filatov, M. Oldenburg, D. Busko, M. Jakoby, I. A. Howard, B. S. Richards, M. O. Senge, S. M. Borisov, A. Turshatov, *Chem. Commun.* **2018**, *54*, 1607–1610.
[151] S. Belali, G. Emandi, A. A. Cafolla, B. O'Connell, B. Haffner, M. E. Möbius, A. Karimi, M. O. Senge, *Photochemical & Photobiological Sciences* **2017**, *16*, 1700–1708.
[152] G. Emandi, Y. M. Shaker, K. J. Flanagan, J. M. O'Brien, M. O. Senge, *Eur. J. Org. Chem.* **2017**, *2017*, 6680–6692.

[153] a) M. Laine, N. A. Barbosa, A. Kochel, B. Osiecka, G. Szewczyk, T. Sarna, P. Ziółkowski, R. Wieczorek, A. Filarowski, *Sens. Actuators B Chem.* **2017**, *238*, 548–555; b) A. A. Pakhomov, Y. N. Kononevich, A. A. Korlyukov, V. I. Martynov, A. M. Muzafarov, *Mendeleev Commun.* **2016**, *26*, 196-198; c) H. Xi, C.-X. Yuan, Y.-X. Li, Y. Liu, X.-T. Tao, *CrystEngComm* **2012**, *14*, 2087-2093; d) P. Sen, G. Y. Atmaca, A. Erdoğmuş, N. Dege, H. Genç, Y. Atalay, S. Z. Yildiz, *J. Fluoresc.* **2015**, *25*, 1225-1234.
[154] N. Epelde-Elezcano, E. Palao, H. Manzano, A. Prieto-Castañeda, A. R. Agarrabeitia, A. Tabero, A. Villanueva, S. de la Moya, Í. López-Arbeloa, V. Martínez-Martínez, M. J. Ortiz, *Chem. Eur. J.* **2017**, *23*, 4837–4848.
[155] M. A. Filatov, S. Karuthedath, P. M. Polestshuk, S. Callaghan, K. J. Flanagan, M. Telitchko, T. Wiesner, F. Laquai, M. O. Senge, *Phys. Chem. Chem. Phys.* **2018**, *20*, 8016–8031.
[156] A. C. Benniston, A. Harriman, V. L. Whittle, M. Zelzer, R. W. Harrington, W. Clegg, *Photochem. Photobiol. Sci.* **2010**, *9*, 1009–1017.
[157] J. P. Rostron, G. Ulrich, P. Retailleau, A. Harriman, R. Ziessel, *New J. Chem.* **2005**, *29*, 1241–1244.
[158] J.-M. Aubry, C. Pierlot, J. Rigaudy, R. Schmidt, *Acc. Chem. Res.* **2003**, *36*, 668–675.
[159] C. S. Gutsche, S. Gräfe, B. Gitter, K. J. Flanagan, M. O. Senge, N. Kulak, A. Wiehe, *Dalton Trans.* **2018**, *47*, 12373–12384.
[160] C. Brückner, Y. Zhang, S. J. Rettig, D. Dolphin, *Inorg. Chim. Acta* **1997**, *263*, 279–286.
[161] a) S. R. Halper, L. Do, J. R. Stork, S. M. Cohen, *J. Am. Chem. Soc.* **2006**, *128*, 15255–15268; b) S. G. Telfer, J. D. Wuest, *Cryst. Growth Des.* **2009**, *9*, 1923–1931.
[162] a) P. E. Eaton, *Angew. Chem. Int. Ed.* **1992**, *31*, 1421–1436; b) G. W. Griffin, A. P. Marchand, *Chem. Rev.* **1989**, *89*, 997–1010.
[163] a) P. E. Eaton, M. X. Zhang, R. Gilardi, N. Gelber, S. Iyer, R. Surapaneni, *Propellants Explos. Pyrotech.* **2002**, *27*, 1–6; b) P. E. Eaton, R. L. Gilardi, M. X. Zhang, *Adv. Mater.* **2000**, *12*, 1143–1148.
[164] E. W. Della, P. T. Hine, H. K. Patney, *J. Org. Chem.* **1977**, *42*, 2940–2941.
[165] T. Y. Luh, L. M. Stock, *J. Am. Chem. Soc.* **1974**, *96*, 3712–3713.
[166] a) E. B. Fleischer, *J. Am. Chem. Soc.* **1964**, *86*, 3889–3890; b) L. Hedberg, K. Hedberg, P. E. Eaton, N. Nodari, A. G. Robiette, *J. Am. Chem. Soc.* **1991**, *113*, 1514–1517.
[167] a) B. A. Chalmers, H. Xing, S. Houston, C. Clark, S. Ghassabian, A. Kuo, B. Cao, A. Reitsma, C.-E. P. Murray, J. E. Stok, G. M. Boyle, C. J. Pierce, S. W. Littler, D. A. Winkler, P. V. Bernhardt, C. Pasay, J. J. De Voss, J. McCarthy, P. G. Parsons, G. H. Walter, M. T. Smith, H. M. Cooper, S. K. Nilsson, J. Tsanaktsidis, G. P. Savage, C. M. Williams, *Angew. Chem. Int. Ed.* **2016**, *55*, 3580–3585; b) B. A. Chalmers, H. Xing, S. Houston, C. Clark, S. Ghassabian, A. Kuo, B. Cao, A. Reitsma, C.-E. P. Murray, J. E. Stok, G. M. Boyle, C. J. Pierce, S. W. Littler, D. A. Winkler, P. V. Bernhardt, C. Pasay, J. J. De Voss, J. McCarthy, P. G. Parsons, G. H. Walter, M. T. Smith, H. M. Cooper, S. K. Nilsson, J. Tsanaktsidis, G. P. Savage, C. M. Williams, *Angew. Chem. Int. Ed.* **2018**, *57*, 8359–8359.
[168] a) S. S. R. Bernhard, G. M. Locke, S. Plunkett, A. Meindl, K. J. Flanagan, M. O. Senge, *Chem. Eur. J.* **2018**, *24*, 1026–1030; b) F. Toriyama, J. Cornella, L. Wimmer, T.-G. Chen, D. D. Dixon, G. Creech, P. S. Baran, *J. Am. Chem. Soc.* **2016**, *138*, 11132–11135.
[169] a) L. T. Eremenko, L. B. Romanova, M. E. Ivanova, D. A. Nesterenko, V. S. Malygina, A. B. Ermeev, G. V. Lagodzinskaya, V. P. Lodygina, *Russ. Chem. Bull.* **1998**, *47*, 1137–1140; b) H. Gunosewoyo, J. L. Guo, M. R. Bennett, M. J. Coster, M. Kassiou, *Bioorg. Med. Chem. Lett.* **2008**, *18*, 3720–3723; c) R. Pellicciari, G. Costantino, E. Giovagnoni, L. Mattoli, I. Brabet, J.-P. Pin, *Bioorg. Med. Chem. Lett.* **1998**, *8*, 1569–1574; d) A. S. Sklyarova, V. N. Rodionov, C. G. Parsons, G. Quack, P. R. Schreiner, A. A. Fokin, *Med. Chem. Res.* **2013**, *22*, 360–366; e) S. M. Wilkinson, H. Gunosewoyo, M. L. Barron, A. Boucher, M. McDonnell, P. Turner, D. E. Morrison, M. R. Bennett, I. S. McGregor, L. M. Rendina, M. Kassiou, *ACS Chem. Neurosci.* **2014**, *5*, 335–339.
[170] G. M. Locke, S. S. R. Bernhard, M. O. Senge, *Chem. Eur. J.* **2018**, *Accepted Manuscript*, DOI: 10.1002/chem.201804225.
[171] S. S. Kuduva, D. C. Craig, A. Nangia, G. R. Desiraju, *J. Am. Chem. Soc.* **1999**, *121*, 1936–1944.
[172] a) D. Das, G. R. Desiraju, *Chem. Asian J.* **2006**, *1*, 231–244; b) S. S. Kuduva, D. Bläser, R. Boese, G. R. Desiraju, *J. Org. Chem.* **2001**, *66*, 1621–1626.
[173] D. Das, R. K. R. Jetti, R. Boese, G. R. Desiraju, *Cryst. Growth Des.* **2003**, *3*, 675–681.
[174] J. Echeverría, G. Aullón, D. Danovich, S. Shaik, S. Alvarez, *Nat. Chem.* **2011**, *3*, 323–330.
[175] a) P. K. Mykhailiuk, *Org. Biomol. Chem.* **2019**, *Accepted Manuscript*, DOI: 10.1039/C1038OB02812E; b) Y. P. Auberson, C. Brocklehurst, M. Furegati, T. C. Fessard, G. Koch, A. Decker, L. La Vecchia, E. Briard, *ChemMedChem* **2017**, *12*, 590–598; c) T. A. Reekie, C. M. Williams, L. M. Rendina, M. Kassiou, *J. Med. Chem.* **2018**, *Accepted Manuscript*, DOI: 10.1021/acs.jmedchem.1028b00888; d) T. P. Stockdale, C. M. Williams, *Chem. Soc. Rev.* **2015**, *44*, 7737–7763.
[176] a) C. L. Nygren, C. C. Wilson, J. F. C. Turner, *J. Phys. Chem. A* **2005**, *109*, 2586–2593; b) M. Kubota, S. Ohba, *Acta Cryst. Sect. B* **1992**, *48*, 849–854; c) G. Bruno, L. Randaccio, *Acta Cryst. Sect. B* **1980**, *36*, 1711–1712; d) R. S. Miller, I. C. Paul, D. Y. Curtin, *J. Am. Chem. Soc.* **1974**, *96*, 6334–6339; e) O. Kenji, K. Setsuo, H. Masao, *Bull. Chem. Soc. Jpn.* **1972**, *45*, 2651–2652.
[177] a) L. B. Romanova, L. S. Barinova, V. V. Zakharov, L. T. Eremenko, G. G. Aleksandrov, I. L. Eremenko, *Russ. Chem. Bull.* **2010**, *59*, 1051–1055; b) O. Ermer, J. Lex, *Angew. Chem. Int. Ed.* **1987**, *26*, 447–449.
[178] R. J. Doedens, P. E. Eaton, E. B. Fleischer, *Eur. J. Org. Chem.* **2017**, *2017*, 2627–2630.
[179] a) H. Irngartinger, S. Strack, F. Gredel, A. Dreuw, W. Della Ernest, *Eur. J. Org. Chem.* **1999**, *1999*, 1253–1257; b) L. T. Eremenko, L. B. Romanova, M. E. Ivanova, I. L. Eremenko, S. E. Nefedov, Y. T. Struchkov, *Russ. Chem. Bull.* **1994**, *43*, 619–623; c) H. Irngartinger, S. Strack, *Acta Cryst. Sect. C* **1994**, *50*, 2017–2019; d) D. S. Yufit, Y. T. Struchkov, L. T. Eremenko, *Russ. Chem. Bull.* **1993**, *42*, 1152–1155; e) P. R. Dave, R. Duddu, K. Yang, R. Damavarapu, N. Gelber, R. Surapaneni, R. Gilardi, *Tetrahedron Lett.* **2004**, *45*, 2159–2162; f) R. M. Moriarty, J. S. Khosrowshahi, R. S. Miller, J. Flippen-Andersen, R. Gilardi, *J. Am. Chem. Soc.* **1989**, *111*, 8943–8944; g) M. Hoshino, A. Khutia, H. Xing, Y. Inokuma, M. Fujita, *IUCrJ* **2016**, *3*, 139–151; h) H. Irngartinger, S. Strack, F. Gredel, *Liebigs Ann.* **1996**, *1996*, 311–315; i) L. T. Eremenko, L. B. Romanova, M. E. Ivanova, A. V. Shastin, I. L. Eremenko, S. E. Nefedov, *Russ. Chem. Bull.* **1998**, *47*, 441–446; j) R. M. Moriarty, M. S. C. Rao, S. M. Tuladhar, C. D'Silva, G. Williams, R. Gilardi, *J. Am. Chem. Soc.* **1993**, *115*, 1194–1196; k) Y. Inokuma, S. Yoshioka, J. Ariyoshi, T. Arai, Y. Hitora, K. Takada, S. Matsunaga, K. Rissanen, M. Fujita, *Nature* **2013**, *495*, 461–466; l) B. Harris, G. P. Savage, J. M. White, *Org. Biomol. Chem.* **2013**, *11*, 3151–3158.
[180] K. J. Flanagan, M. O. Senge, *Acta Cryst. Sect. E* **2015**, *71*, 1151–1154.
[181] a) H. L. Ammon, C. S. Choi, S. Reddy, *Acta Cryst. Sect. C* **1988**, *44*, 1671–1672; b) N. T. Kawai, D. F. R. Gilson, J. F. Britten, I. S. Butler, P. G. Farrell, *Can. J. Chem.* **1992**, *70*, 910–914; c) A. V. Shastin, V. V. Zakharov, G. P.

Bugaeva, L. T. Eremenko, L. B. Romanova, G. V. Lagodzinskaya, G. G. Aleksandrov, I. L. Eremenko, *Russ. Chem. Bull.* **2006**, *55*, 1304–1306; d) V. V. Zakharov, G. P. Bugaeva, L. S. Barinova, G. V. Lagodzinskaya, L. B. Romanova, G. G. Aleksandrov, L. T. Eremenko, I. L. Eremenko, *Russ. Chem. Bull.* **2005**, *54*, 1505–1508; e) L. T. Eremenko, L. B. Romanova, M. E. Ivanova, V. S. Malygina, L. S. Barinova, G. V. Lagodzinskaya, V. P. Lodygina, I. L. Eremenko, G. G. Aleksandrov, *Russ. Chem. Bull.* **2007**, *56*, 1408–1422; f) P. E. Eaton, K. Pramod, T. Emrick, R. Gilardi, *J. Am. Chem. Soc.* **1999**, *121*, 4111–4123; g) K. Hassenruck, J. G. Radziszewski, V. Balaji, G. S. Murthy, A. J. McKinley, D. E. David, V. M. Lynch, H. D. Martin, J. Michl, *J. Am. Chem. Soc.* **1990**, *112*, 873–874.

[182] a) P. E. Eaton, E. Galoppini, R. Gilardi, *J. Am. Chem. Soc.* **1994**, *116*, 7588–7596; b) S. D. Karlen, H. Reyes, R. E. Taylor, S. I. Khan, M. F. Hawthorne, M. A. Garcia-Garibay, *Proc. Natl. Acad. Sci. U.S.A.* **2010**, *107*, 14973–14977.

[183] a) R. Gilardi, R. J. Butcher, *J. Chem. Crystallogr.* **2003**, *33*, 281–285; b) P. E. Eaton, B. K. R. Shankar, G. D. Price, J. J. Pluth, E. E. Gilbert, J. Alster, O. Sandus, *J. Org. Chem.* **1984**, *49*, 185–186.

[184] J. R. Deschamps, R. M. Moriarty, R. D. Gilardi, *Acta Cryst. Sect. E* **2001**, *57*, o149–o150.

[185] R. J. Butcher, R. D. Gilardi, C. George, J. Flippen-Anderson, *J. Chem. Crystallogr.* **1996**, *26*, 381–388.

[186] a) R. J. Butcher, R. D. Gilardi, *J. Chem. Crystallogr.* **1998**, *28*, 95–104; b) H. L. Ammon, C. S. Choi, R. S. Damvarapu, S. Iyer, J. Alster, *Acta Cryst. Sect. C* **1990**, *46*, 295–298; c) Q. I. Churches, R. J. Mulder, J. M. White, J. Tsanaktsidis, P. J. Duggan, *Aust. J. Chem.* **2012**, *65*, 690–693; d) K. Jelínková, H. Surmová, A. Matelová, M. Rouchal, Z. Prucková, L. Dastychová, M. Nečas, R. Vícha, *Org. Lett.* **2017**, *19*, 2698–2701; e) S. Plunkett, K. J. Flanagan, B. Twamley, M. O. Senge, *Organometallics* **2015**, *34*, 1408–1414; f) A. V. Shastin, L. B. Romanova, L. T. Eremenko, V. V. Zakharov, G. V. Lagodzinskaya, G. G. Aleksandrov, I. L. Eremenko, *Russ. Chem. Bull.* **2006**, *55*, 1452–1454; g) V. V. Zakharov, G. P. Bugaeva, M. E. Ivanova, L. B. Romanova, L. T. Eremenko, S. E. Nefedov, I. L. Eremenko, *Russ. Chem. Bull.* **1998**, *47*, 1349–1352; h) R. N. Evans, R. Gilardi, T. Emrick, *Acta Cryst. Sect. E* **2003**, *59*, o1283–o1285; i) K. Hassenrueck, G. S. Murthy, V. M. Lynch, J. Michl, *J. Org. Chem.* **1990**, *55*, 1013–1016; j) R. Priefer, Y. J. Lee, F. Barrios, J. H. Wosnick, A.-M. Lebuis, P. G. Farrell, D. N. Harpp, A. Sun, S. Wu, J. P. Snyder, *J. Am. Chem. Soc.* **2002**, *124*, 5626–5627; k) R. Gilardi, M. Maggini, P. E. Eaton, *J. Am. Chem. Soc.* **1988**, *110*, 7232–7234.

[187] C. F. Macrae, I. J. Bruno, J. A. Chisholm, P. R. Edgington, P. McCabe, E. Pidcock, L. Rodriguez-Monge, R. Taylor, J. van de Streek, P. A. Wood, *J. Appl. Crystallogr.* **2008**, *41*, 466–470.